Shock and Vibration

International Conference on Structural Engineering Dynamics 2013

Guest Editors: Nuno Maia and Miguel M. Neves

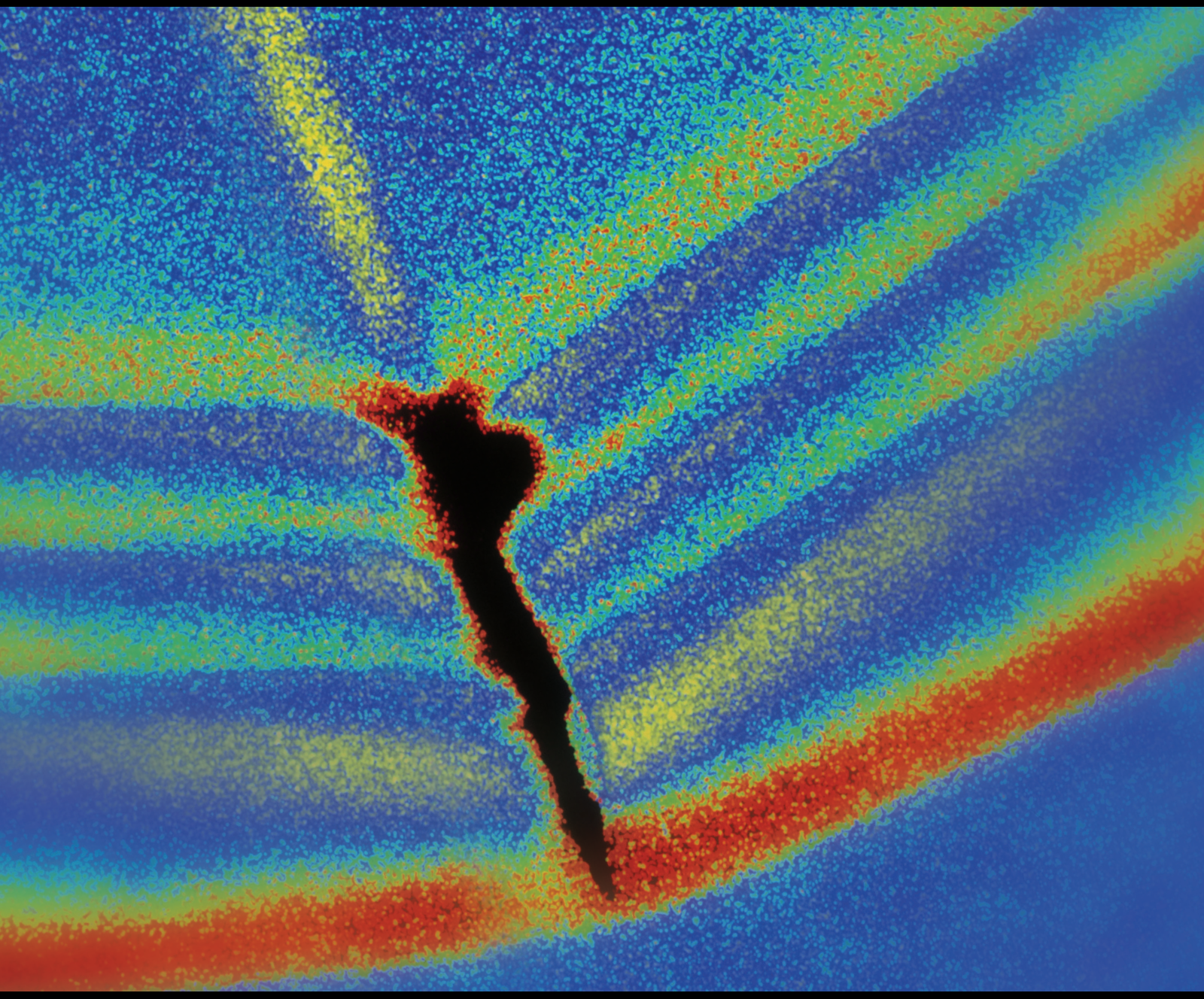

International Conference on Structural Engineering Dynamics 2013

Shock and Vibration

International Conference on Structural Engineering Dynamics 2013

Guest Editors: Nuno M. M. Maia and Miguel M. Neves

Copyright © 2014 Hindawi Publishing Corporation. All rights reserved.

This is a special issue published in "Shock and Vibration." All articles are open access articles distributed under the Creative Commons Attribution License, which permits unrestricted use, distribution, and reproduction in any medium, provided the original work is properly cited.

Editor-in-Chief

Mehdi Ahmadian, Virginia Polytechnic Institute and State University, USA

Associate Editors

Brij N. Agrawal, USA
Subhamoy Bhattacharya, UK
Dumitru I. Caruntu, USA
Peng Chen, Japan
Longjun Dong, China
Mohammad Elahinia, USA
Anindya Ghoshal, USA
Alicia Gonzalez-Buelga, UK
Hassan Haddadpour, Iran
Hamid Hosseini, Japan
Reza Jazar, Australia
Jeong-Hoi Koo, USA
Mickaël Lallart, France
Kenneth J. Loh, USA
Nuno Maia, Portugal
Tony Murmu, UK
Toshiaki Natsuki, Japan
Miguel M. Neves, Portugal
Gyuhae Park, Republic of Korea
Didier Rémond, France
Rüdiger Schmidt, Germany
Vadim V. Silberschmidt, UK
Kumar V. Singh, USA
Valder Steffen Jr, Brazil
Chao Tao, China
Senthil S. Vel, USA
Gongnan Xie, China
Peijun Xu, USA
Zaili L. Yang, UK
Ahmet S. Yigit, Kuwait
Xinjie Zhang, China
Lei Zuo, USA

Contents

Hindawi Publishing Corporation
Shock and Vibration
Volume 2014, Article ID 645026, 1 page
http://dx.doi.org/10.1155/2014/645026

Editorial

International Conference on Structural Engineering Dynamics 2013

Nuno M. M. Maia and Miguel M. Neves

LAETA, IDMEC, Instituto Superior Técnico, Universidade de Lisboa, Lisboa, Portugal

Correspondence should be addressed to Nuno M. M. Maia; nmaia@dem.ist.utl.pt

Received 12 May 2014; Accepted 12 May 2014; Published 10 September 2014

Copyright © 2014 N. M. M. Maia and M. M. Neves. This is an open access article distributed under the Creative Commons Attribution License, which permits unrestricted use, distribution, and reproduction in any medium, provided the original work is properly cited.

The last edition of the International Conference on Structural Engineering Dynamics (ICEDyn) 2013 took place in Sesimbra, a tiny fishing village in the Blue Coast Portugal, on the 17th–19th of June 2013, and was organized by the Instituto Superior Técnico (IST), from the University of Lisbon, and the Instituto de Engenharia Mecânica (IDMEC).

As it happened in previous editions of this biennial scientific event, the conference embraces a large spectrum of subjects that attract the interest of a wide community devoted to engineering dynamics, where theory and experiment mix very well. Common to all ICEDyn conferences is the high scientific standard of the submitted articles. Senior scientists, representatives of the industrial community, and young students doing their Master or Ph.D. studies were encouraged to meet and develop a healthy and stimulating interaction around the same kind of interests and objectives.

Four international renowned scientists addressed keynote lectures that preceded and framed the parallel sessions that followed them: "Operational modal analysis" (R. Brincker, Aarhus University, Denmark); "On the renewed interest for the wave propagation approach to structural dynamics" (J. R. F. Arruda, Universidade Estadual de Campinas, Brazil); "Spatial information in autonomous modal parameter estimation" (R. J. Allemang, University of Cincinnati, USA); and "Regular and chaotic dynamics of flexible plates" (J. Awrejcewicz, Łódź University of Technology, Poland). The parallel sessions covered damage/SHM (3 sessions), active control (2 sessions), experimental/operational modal analysis (2 sessions), sound and vibration generated by moving loads (2 sessions), aeronautics and aerospace (2 sessions), smart materials in structural dynamics (2 sessions), modelling, civil structures, nonlinear dynamics, analytical methods, connecting analysis and tests, and damping and updating (2 sessions).

This special issue has been carefully prepared, in order to meet the high standards of this publication and to reflect the excellent outcome of ICEDyn 2013. Those authors who had manifested an interest in publishing in SAV submitted improved versions of their articles, which have passed through a rigorous process of peer-reviewing (with at least two reviewers and most of them with three reviewers); this has contributed to the enrichment of the scientific quality of those articles. From the initial 43 papers, a total of 29 papers have been finally selected to integrate the present issue, covering various areas. It was a pleasure and an honor for us to serve as Guest Editors for this special Issue. We hope that readers will find the special issue exciting as well as useful for stimulating further research activities and conjecturing future trends in this area of structural dynamics.

Acknowledgments

Acknowledgments are due to all contributing authors and coauthors, to the reviewers for all their effort, time, and collaboration, and to our colleague of the Organizing Committee Professor Chedas Sampaio, for their support of this 2013 special issue.

Nuno M. M. Maia
Miguel M. Neves

Hindawi Publishing Corporation
Shock and Vibration
Volume 2014, Article ID 930503, 9 pages
http://dx.doi.org/10.1155/2014/930503

Research Article

Modeling and Analysis of a Piezoelectric Energy Harvester with Varying Cross-Sectional Area

Maiara Rosa and Carlos De Marqui Junior

Department of Aeronautical Engineering, Engineering School of São Carlos, University of São Paulo, Avenida Trabalhador São-Carlense, 400 Pq Arnold Schimidt, 13566-590 São Carlos, SP, Brazil

Correspondence should be addressed to Carlos De Marqui Junior; demarqui@sc.usp.br

Received 12 July 2013; Accepted 3 March 2014; Published 9 September 2014

Academic Editor: Miguel M. Neves

Copyright © 2014 M. Rosa and C. De Marqui Junior. This is an open access article distributed under the Creative Commons Attribution License, which permits unrestricted use, distribution, and reproduction in any medium, provided the original work is properly cited.

This paper reports on the modeling and on the experimental verification of electromechanically coupled beams with varying cross-sectional area for piezoelectric energy harvesting. The governing equations are formulated using the Rayleigh-Ritz method and Euler-Bernoulli assumptions. A load resistance is considered in the electrical domain for the estimate of the electric power output of each geometric configuration. The model is first verified against the analytical results for a rectangular bimorph with tip mass reported in the literature. The experimental verification of the model is also reported for a tapered bimorph cantilever with tip mass. The effects of varying cross-sectional area and tip mass on the electromechanical behavior of piezoelectric energy harvesters are also discussed. An issue related to the estimation of the optimal load resistance (that gives the maximum power output) on beam shape optimization problems is also discussed.

1. Introduction

The interest in converting vibrations into usable electrical energy has increased over the past years [1–5]. Vibration based energy harvesting is particularly useful for wireless sensor nodes and remotely operated systems with limited energy source. The aim is to provide electrical energy for such systems by using the vibrations available in their environment. Although different transduction mechanisms can be used to convert vibrations into electricity, the recent literature shows that piezoelectric transduction has drawn the most attention [1, 3, 5].

The literature on piezoelectric energy harvesting includes different models to represent the behavior of electromechanically coupled harvesters. Such models range from lumped parameter models [6, 7] to Rayleigh-Ritz type approximate distributed parameter models [7–9] as well as analytical distributed parameter solution attempts [10, 11]. The analytical distributed parameter solutions for unimorph [12] and bimorph [13] piezoelectric energy harvester configurations with closed-form expressions have been presented. The convergence of the Rayleigh-Ritz type electromechanical solution [7, 9] to the analytical solution given by Erturk and Inman [12] was reported by Elvin and Elvin [14] when a sufficient number of admissible functions were used.

The investigation into alternative configurations of electromechanical beams has also been reported in the literature. Erturk et al. [15] presented a linear distributed parameter model for predicting the electromechanical behavior of an L-shaped piezoelectric energy harvester configuration. A broadband harvester can be obtained when the first two natural frequencies of the L-shaped beam are properly tuned. The use of tapered cantilevers in order to improve the electromechanical behavior of piezoelectric energy harvesters has also been investigated [16–22]. The shape is changed from the basic rectangular configuration towards a tapered or reversed tapered geometry and the main motivation is to increase the electrical power output. The modeling of electromechanically coupled beams with nonuniform width is presented in Dietl and Garcia [21]. An optimal beam shape is determined by

an optimization code. In the cited paper [21], as well as in [2, 16, 22], the expression $1/\omega C_p$(where ω is the excitation frequency and C_p is the equivalent capacitance of piezoceramic layers) is employed for the optimum load resistance (which gives maximum power output) of a piezoelectric energy harvester. In general, the authors approximate the eigenvalues and eigenvector of electromechanically coupled beams with nonuniform width to the ones corresponding to rectangular shape beams [18–20]. Recently, the solution of eigenvalue problem of nonuniform width beams by using the differential quadrature method has been presented and the effects of beam shape on the structural natural frequencies and mode shapes are discussed [23]. An important aspect, the effect of load resistance on the electroelastic behavior of variable-shaped harvesters, is only considered in Ayed et al. [23].

An issue related to the estimate of the optimum load from the equation $1/\omega C_p$ was previously discussed [24] for a rectangular (or squared) energy harvester configuration. The piezoceramic layer of a piezoelectric energy harvester can be represented as a current source in parallel with its internal capacitance (Norton representation) or as a voltage source in series with its internal capacitance (Thévenin representation). For instance, in Norton representation, $R_{\text{opt}} = 1/\omega C_p$ is obtained only if a constant current amplitude oscillating at a frequency ω is assumed. However, regarding the electromechanical behavior of a piezoelectric energy harvesting previously discussed in the literature [13, 24, 25], the current source in Norton representation is not constant, but it depends on the load resistance, since the vibration response also depends on the load resistance. The expression $R_{\text{opt}} = 1/\omega C_p$ could be obtained from the coupled equations that govern a piezoelectric energy harvester [24] only if the electromechanical coupling term was artificially removed from the mechanical equation.

This paper reports on the modeling and experimental verification of electromechanically coupled beams with varying cross-sectional area (tapered or reversed tapered) for energy harvesting. The governing equations are formulated by the Rayleigh-Ritz method and Euler-Bernoulli assumptions. A load resistance is considered in the electrical domain of the problem for the estimate of the electric power output. The model is first verified against analytical electromechanically-coupled results of a rectangular bimorph cantilever with tip mass under base excitation reported in the literature [13]. The frequency response functions (FRFs) obtained using the model presented in this work are compared with the FRFs obtained analytically in [13]. The model is also experimentally verified for a tapered bimorph cantilever with tip mass. Finally, the effects of a varying cross-sectional area (changing from a rectangular beam to a tapered or reversed tapered configuration) and tip mass on the electrical power output of piezoelectric energy harvesters are discussed. The effects of the incorrect estimate of the optimal load resistance (which provides the maximum power output) from the expression $R_{\text{opt}} = 1/\omega C_p$ on both the electromechanical behavior of each geometric configuration and the beam shape optimization problem are discussed.

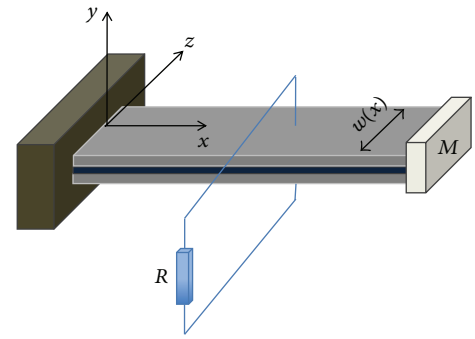

Figure 1: A bimorph piezoelectric energy harvester under clamped-free boundary conditions.

2. Mathematical Model of a Piezoelectric Energy Harvester with Varying Cross-Sectional Area

The derivation provided in this section is for a bimorph piezoelectric beam of uniform width along its length (rectangular) or nonuniform width along its length (tapered or reversed tapered). The bimorph harvester has a brass substructure bracketed by two piezoceramic layers as shown in Figure 1 (for the rectangular beam). Each piezoelectric layer is covered by continuous conductive electrodes that can be connected either in series (when piezoceramic layers are poled in the opposite direction) or in parallel (when piezoceramic layers are poled in the same direction). In this work, the pairs of electrodes covering each piezoceramic layer are connected in series. In Figure 1, R is the resistive load, $w(x)$ is the width of the beam along the length (x), and M is the tip mass attached to the free end of the harvester.

The combination of Hamilton's principle [26] and the Rayleigh-Ritz method based on the Euler-Bernoulli beam assumptions is used in the modeling approach of this paper. The generalized Hamilton's principle was applied by Hagood et al. [27], who combined the Rayleigh-Ritz method with the Euler-Bernoulli beam theory for active structural control. The Rayleigh-Ritz formulation used by Hagood et al. [27] was also implemented by duToit et al. [7] and Sodano et al. [8] for predicting the electric power output of electromechanically coupled Euler-Bernoulli beams in energy harvesting problems. Dietl and Garcia [21] combined the Rayleigh-Ritz method with the Euler-Bernoulli beam theory to model electromechanically coupled beams with a varying cross-sectional area in energy harvesting problems.

In the Euler-Bernoulli beam theory, the motion is restricted to the transverse direction and the only nonzero component of the displacement field $\mathbf{u}$ is $y(x,t)$. Furthermore, the beam strain is given by $y(x,t)$ and its partial derivatives. In the Rayleigh-Ritz procedure, the displacement $y(x,t)$ of the beam can be written as the summation of the modes and the temporal coordinate of the displacement as

$$y(x,t) = \boldsymbol{\varphi}(x)^T \mathbf{q}(t), \tag{1}$$

where $\boldsymbol{\varphi}(x)$ is a matrix of assumed mode shapes and $\mathbf{q}(t)$ is the temporal coordinate of displacement. Here, the mode

shapes are assumed to be an acceptable solution to an Euler-Bernoulli beam under a clamped-free condition,

$$\widetilde{\boldsymbol{\varphi}}_k(x) = \cos\beta_k\frac{x}{L} - \cosh\beta_k\frac{x}{L} - \sigma_k\left(\sin\beta_k\frac{x}{L} - \sinh\beta_k\frac{x}{L}\right), \tag{2}$$

where L is the length of the beam and σ_k is expressed as

$$\sigma_k = \frac{\sin\beta_k - \sinh\beta_k + \beta_k r\left(\cos\beta_k - \cosh\beta_k\right)}{\cos\beta_k + \cosh\beta_k - \beta_k r\left(\sin\beta_k - \sinh\beta_k\right)}, \tag{3}$$

where β_k is the natural frequency of the kth mode obtained from the equation given by

$$\frac{1}{r}\left(\cos\beta\cosh\beta + 1\right) + \beta\left(\cos\beta\sinh\beta - \sin\beta\cosh\beta\right) = 0, \tag{4}$$

where r is the ratio of the tip mass to the mass of the beam (substructure and piezoceramic layers).

The general form for the kth mode shape must satisfy the following equation

$$\int_0^L \varphi_k^2(x)\,\rho_l w(x)\,dx + M\varphi_k^2(L) = 1, \tag{5}$$

where the mode shape is obtained as

$$\varphi_k(x) = \frac{\widetilde{\varphi}_k(x)}{\sqrt{\int_0^L \widetilde{\varphi}_k^2(x)\,dx + r\widetilde{\varphi}_k^2(L)}}, \tag{6}$$

and ρ_l is the equivalent mass density given by

$$\rho_l = \rho_s h_s + 2\rho_p h_p, \tag{7}$$

where ρ is the mass density, h is the thickness of the layer and the subscripts s and p represent, respectively, the substructure and the piezoceramic layers.

Since piezoceramic layers are poled in the thickness direction, the nonzero electric field component (E), which is assumed to be uniform along the thickness direction, is expressed as

$$E = -\frac{\partial\psi}{\partial z} = -\frac{V}{2h_p}, \tag{8}$$

where the electric potential (ψ) is assumed to vary linearly across the electrodes and V is the voltage across the electrodes.

The previous definitions for mechanical and electrical variables should be used to define the terms in Hamilton's principle (please check Dietl and Garcia [21] or De Marqui Jr. et al. [25] for details) to provide the electromechanically coupled equations governing the beam:

$$\mathbf{M}\ddot{\mathbf{q}}(t) + \mathbf{C}\dot{\mathbf{q}}(t) + \mathbf{K}\mathbf{q}(t) - \boldsymbol{\Theta}V(t) = \mathbf{F} \tag{9}$$

$$C_p\dot{V}(t) + \frac{V(t)}{R} + \boldsymbol{\Theta}^T\dot{\mathbf{q}}(t) = 0, \tag{10}$$

where $\mathbf{M}$ is the mass matrix, $\mathbf{C}$ is the damping matrix, $\mathbf{K}$ is the stiffness matrix, $\boldsymbol{\Theta}$ is the electromechanical coupling matrix, $\mathbf{F}$ is the vector of mechanical forces (where $\mathbf{F} = \mathbf{p}^* a(t)$, where $a(t)$ is the base acceleration in function of time and $\mathbf{p}^*$ is the input matrix to be defined later), T represents the matrix transpose when superscripted, an overdot represents the time derivative, R is the load resistance, $\mathbf{q}$ is the vector of modal mechanical displacements, $V(t)$ is the voltage in function of the time, and C_p is the effective capacitance.

The mass matrix is defined as

$$\mathbf{M} = \int_0^L \rho_l w(x)\,\boldsymbol{\varphi}(x)\,\boldsymbol{\varphi}^T(x)\,dx + M\boldsymbol{\varphi}(L)\,\boldsymbol{\varphi}^T(L) \tag{11}$$

and the stiffness matrix is defined as

$$\mathbf{K} = \frac{I_{0w}}{s_p^E}\left[\int_0^L w(x)\,\boldsymbol{\varphi}''(x)\,\boldsymbol{\varphi}''^T(x)\,dx\right], \tag{12}$$

where s_p^E is the compliance measured in a constant electric field, ($''$) represents the space derivative, and I_{0w} is given by

$$I_{0w} = \frac{I_{zz}(x)}{w(x)}, \tag{13}$$

where $I_{zz}(x)$ is the moment of inertia.

The damping matrix is assumed to be proportional to the mass and stiffness matrices:

$$\mathbf{C} = \alpha\mathbf{M} + \beta\mathbf{K}, \tag{14}$$

where α and β are the constants of proportionality.

The capacitance for a bimorph harvester in series connection case is given by

$$C_p = \frac{\varepsilon_{33}^S}{2h_p}\int_0^L w(x)\,dx, \tag{15}$$

where ε_{33}^S is the dielectric constant evaluated at constant strain for an Euler-Bernoulli beam as

$$\varepsilon_{33}^S = 1730\varepsilon_0 - \frac{d_{31}}{E_p} \tag{16}$$

and ε_0 is the permittivity in free space and d_{31} is the piezoelectric coupling coefficient and E_p is Young's modulus of the piezoceramic.

The electromechanical coupling matrix is given as

$$\Theta = -\left(h_s h_p + h_p^2\right)\frac{d_{31}}{2s_p^E h_p}\left[\int_0^L w(x)\,\varphi''(x)\,dx\right] \tag{17}$$

and the input matrix is

$$\mathbf{p}^* = \int_0^L \rho_l w(x)\,\boldsymbol{\varphi}(x)\,dx + M\boldsymbol{\varphi}(L), \tag{18}$$

with all variables previously defined.

Expressions for the electromechanical FRFs (voltage across the resistive load, current passing through the resistive

Table 1: Geometric and material properties of the bimorph harvester.

Length of the beam [mm]	50.8	Mass density of the substructure [kg/m^3]	9000
Width of the beam on the clamped end [mm]	31.8	Mass density of the PZT [kg/m^3]	7800
Width of the beam on the free end [mm]	31.8	Tip mass [kg]	0.012
Thickness of the substructure [mm]	0.14 (each)	Proportional constant α (rad/s)	14.65
Thickness of the PZT [mm]	0.26 (each)	Proportional constant β (s/rad)	10^{-5}
Young's modulus of the substructure [GPa]	105	Piezoelectric coupling coefficient d_{31} [pm/V]	−190
Young's modulus of the PZT-5A [GPa]	66	Permittivity of free space [pF/m]	8.854

load, electrical power output, and relative tip motion) can be obtained from the equations of motion ((9) and (10)). The excitation is due to the harmonic motion of the base in the transverse direction, $w_B = Y_0 e^{j\omega t}$ (where $w_B(t)$ is the base displacement, Y_0 is its amplitude, ω is the excitation frequency, and j is the unit imaginary number), and the voltage output-to-base acceleration FRF can be obtained as

$$\frac{V(t)}{a(t)} = \frac{V(t)}{-\omega^2 Y_0 e^{j\omega t}} = j\omega\left(\frac{1}{R} + j\omega C_p\right)^{-1} \boldsymbol{\Theta}^T \times \left[-\omega^2 \mathbf{M} + j\omega \mathbf{C} + \mathbf{K} + j\omega\left(\frac{1}{R} + j\omega C_p\right)^{-1} \boldsymbol{\Theta}\boldsymbol{\Theta}^T\right]^{-1} \mathbf{p}^* \quad (19)$$

and the electric current FRF is obtained by dividing the voltage FRF by the load resistance of the electrical circuit and the electrical peak power FRF (since the voltage FRF is the peak voltage FRF) is the product of the voltage and current FRFs.

The relative tip motion FRF is defined as the ratio of the amplitude of the displacement at the tip of the beam (relative to the base) to the amplitude of the base displacement input and it is obtained from (9) and (10) as

$$\frac{w_{\text{rel}}}{Y_0 e^{j\omega t}} = \omega^2\left[-\omega^2 \mathbf{M} + j\omega \mathbf{C} + \mathbf{K} + j\omega\left(\frac{1}{R} + j\omega C_p\right)^{-1} \boldsymbol{\Theta}\boldsymbol{\Theta}^T\right]^{-1} \mathbf{p}^* \quad (20)$$

and the tip velocity FRF is defined as the ratio of the amplitude of velocity at the tip of the beam (relative to the fixed frame) to the gravitational acceleration. This FRF is easily obtained from the expression of the relative tip motion FRF by using

$$v_{\text{rel}} = -\frac{jg}{\omega}\left(1 + \frac{w_{\text{rel}}(L,t)}{Y_0}\right), \quad (21)$$

where g is the gravitational acceleration.

3. Case Studies

This section presents three case studies and the electromechanically coupled model described in Section 2 is employed. In the first case, the model is verified against the analytical results of a bimorph cantilever with tip mass reported in the literature [13]. The experimental verification of the model is then reported for a tapered bimorph cantilever with tip mass. Finally, a discussion regarding the calculation of the optimal load resistance (for maximum power output) is presented. The effects of varying cross-sectional area, tip mass, and estimate of optimal load resistance on the electromechanical behavior and shape optimization problems of piezoelectric energy harvesters are also discussed. It is important to mention that, in the following discussions, the power output is normalized per base acceleration (in terms of gravitational acceleration), which is assumed to be smaller than that which would cause failure in the different piezoelectric energy harvesters considered in this work.

3.1. Verification against the Analytical and Experimental Results for a Rectangular Bimorph Configuration. In the first case study, the results obtained from our electromechanical model presented for a rectangular cantilevered bimorph with a tip mass under base excitation are compared with the single mode analytical predictions of the closed-form solution presented by Erturk and Inman [13]. The bimorph harvester configuration has a brass substructure bracketed by two PZT-5A layers. The piezoceramic layers are poled in the opposite directions and therefore the combination of the layers to the electrical load results in the series connection case. The numerical input data of the bimorph is shown in Table 1.

The voltage FRF is defined here as the voltage output per gravitational acceleration ($g = 9.81$ m/s^2) to be in agreement with the analytical voltage FRFs given by Erturk and Inman [13]. Equation (19) is easily modified to provide voltage output per g. The voltage FRFs for the first mode of the harvester obtained from our model are plotted in Figure 2(a) along with the analytical solution and experimental results for eight different values of load resistance (1, 6.7, 11.8, 22, 33, 47, 100, and 470 kΩ). The voltage output increases with increasing load resistance for all excitation frequencies according to the present model and the analytical predictions. The analytical model as well as our model has predicted such frequencies as 45.7 Hz and 48.2 Hz, respectively.

The mechanical vibration FRFs of the bimorph piezoelectric harvester obtained by the present model and the analytical model are shown in Figure 2(b). The tip velocity FRF ((20) and (21)) is defined as the ratio of the amplitude of velocity at the tip of the beam (relative to the fixed

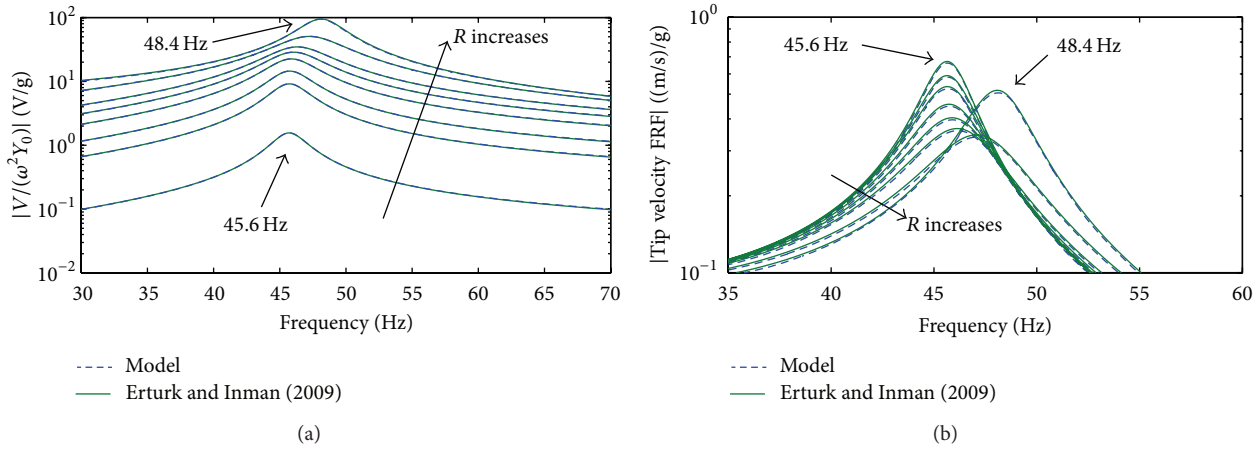

Figure 2: Voltage FRF (a) and tip velocity (FRF) (b) for eight values of load resistance.

Table 2: Geometric and material properties of the tapered bimorph harvester.

Length of the beam [mm]	50.8	Mass density of the substructure [kg/m^3]	9000
Width of the beam at the clamped end [mm]	31.5	Mass density of the PZT [kg/m^3]	7800
Width of the beam at the free end [mm]	7.25	Tip mass [kg]	0.00164
Thickness of the substructure [mm]	0.14 (each)	Proportional constant α (rad/s)	8.79
Thickness of the PZT [mm]	0.26 (each)	Proportional constant β (s/rad)	6.10^{-6}
Young's modulus of the substructure [GPa]	105	Piezoelectric coupling coefficient d_{31} [pm/V]	–190
Young's modulus of the PZT-5A [GPa]	66	Permittivity of free space [pF/m]	8.854

frame) to the gravitational acceleration. The mechanical FRFs obtained by the present model are in agreement with the analytical results. The vibration amplitude at the short circuit resonance frequency is attenuated as the load resistance is increased up to 100 kΩ due to the resistive shunt damping effect associated with power generation. Approximately after the value of 100 kΩ, increasing load resistance amplifies the vibration amplitude at the open circuit resonance frequency.

3.2. Verification against the Experimental Results for a Tapered Bimorph with Tip Mass. In this second case study, the results from our approximate model for a tapered piezoelectric energy harvester are verified against experimental results. The bimorph harvester configuration has a brass substructure bracketed by two PZT-5A layers. The piezoceramic layers are poled in the opposite directions and therefore the series connection case is studied. The geometric and material properties for the tapered beam are given in Table 2. The width of the beam at the clamped end is larger than the width at the free end and it is assumed to vary linearly along the length of the harvester.

Small magnets were attached at the free end of the tapered harvester as a tip mass in the experiments. The base acceleration was measured at the clamped end (Accelerometer Model 352C22, PCB Piezotronics), which is connected to a shaker (Model 4810, Brüel & Kjær). A digital laser vibrometer (Model PDV-100, Polytec) measures the tip velocity at the free end. The electromechanical behavior is investigated by using three different resistive loads (1 kΩ, 50 kΩ, and 1 MΩ) and the electromechanical FRFs were acquired through a Data Acquisition System (Photon II All in One System, LDS Dactron). Figure 3 shows the experimental setup.

The voltage FRFs for the first mode of the tapered harvester obtained from our model and the experimental results are plotted in Figure 4(a). The experimental short circuit and open circuit resonance frequencies for the tapered harvester are 179.1 Hz and 189.1 Hz, respectively. The present model has predicted such frequencies as 178.8 Hz and 188.9 Hz, respectively. The tip velocity FRFs obtained by the present model are in agreement with those of the experimental results, as shown in Figure 4(b).

3.3. Effects of Tip Mass, Beam Shape, and Load Resistance on the Electromechanical Behavior of a Piezoelectric Energy Harvester. In the third case study, the effects of a varying cross-sectional area (changing from a rectangular beam to a tapered or reversed tapered configuration) and tip mass on the electrical power output of piezoelectric energy harvesters are discussed. Issues related to the estimate of the optimal load resistance by using the expression $R_{\text{opt}} = 1/\omega C_p$ on the power output of each geometric configuration and on beam shape optimization problems are also discussed. The piezoceramic layers of the bimorph are poled in opposite directions and therefore the series connection case is investigated. The numerical input data of the base case studied in this section (rectangular beam) are given in Table 1.

Two different conditions are investigated in this case. In the first, the width of the clamped end ($x = 0$) is constant

FIGURE 3: Experimental setup used for the verification of relations for a tapered beam.

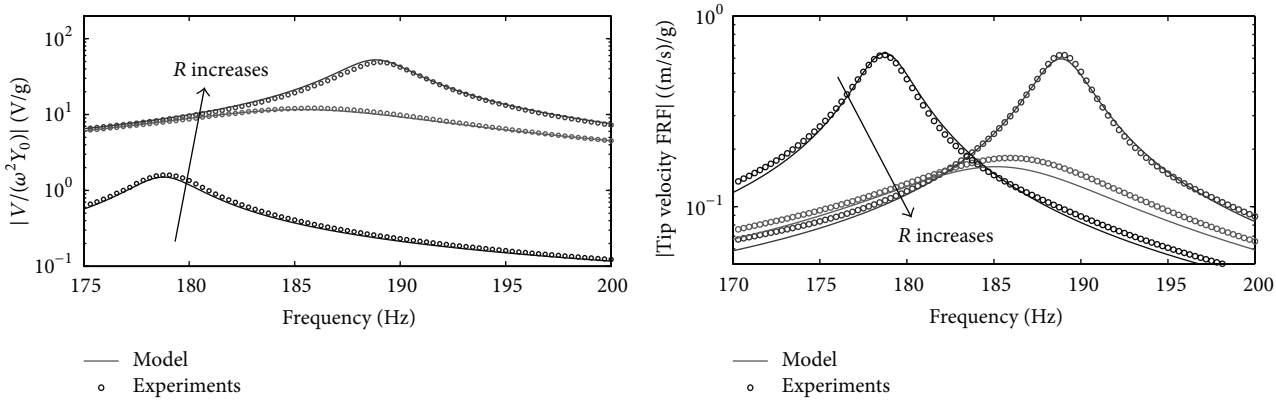

FIGURE 4: Model and experimental voltage FRFs (a) and tip velocity FRFs (b) for three values of load resistance.

($w_0 = w(0) = 31.8$ mm) and the width at the tip can be modified (tapered beam). The width (or cross-section) is linearly modified along the span, from w_0 at the clamped end to $w(L) = Pw_0$ at the free end. P may assume values from 0 (triangular beam) to 1 (rectangular shape), as shown in Figure 5(a). In the second case, the width of the free end ($x = L$) is constant ($w(L) = w_0 = 31.8$ mm) and the width of the clamped end can be modified (reversed tapered beam). The width (or cross-section) is linearly modified along the span from $w(L) = w_0$ at the clamped end to $w(0) = Qw_0$ at the free end, where Q may assume values from 0 (reversed tapered beam) to 1 (rectangular shape), as shown in Figure 5(b). The thickness and length of the composite section (substructure and piezoceramic layers) are constant in both cases and a tip mass is assumed in the free end.

The power output in each case (tapered or reversed tapered) is obtained for a range of values of tip mass and P or Q (for each case), as well as for the optimum load resistance of the short circuit resonance frequency of each configuration. Although small values of parameters P and Q are assumed in the analyses, note that $P \to 0$ and $Q \to 0$ can lead to practical issues related to fabrication and testing (tip mass position or clampling). The optimum load resistances are estimated considering (1) the Norton or Thévenin representation of the piezoelectric layers and (2) an expression for the optimum load obtained from (9) and (10) [23]. As previously discussed, when the Norton or Thévenin representations of the piezoelectric layers are assumed, the optimum load resistance is

$$R_{\text{opt}} = \frac{1}{\omega_k C_p}, \tag{22}$$

where ω_k is the short circuit resonance frequency of the desired mode. Such an expression is obtained when the backward coupling is neglected in the equations that govern the piezoelectric energy harvester. Therefore, the shift from short to open circuit resonance frequency as well as the shunt damping effect (trends reported in the previous case studies) are not observed when the load resistance is changed from short to open circuit conditions [23].

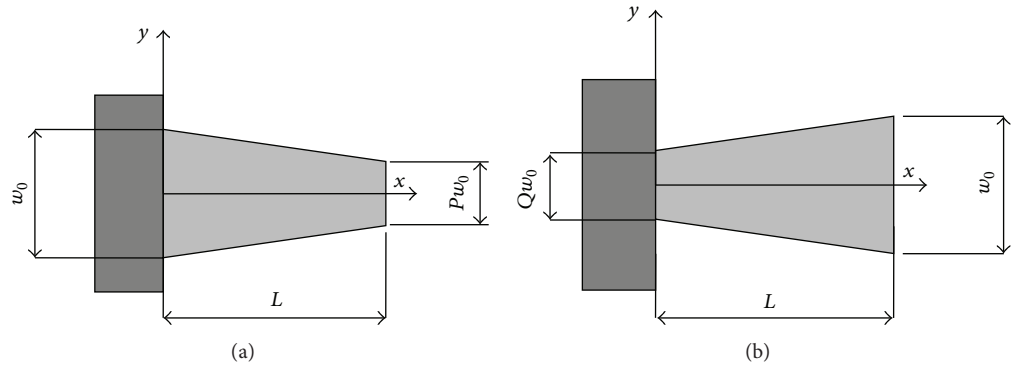

FIGURE 5: Standard shape modification of a bimorph piezoelectric harvester by parameters P and Q.

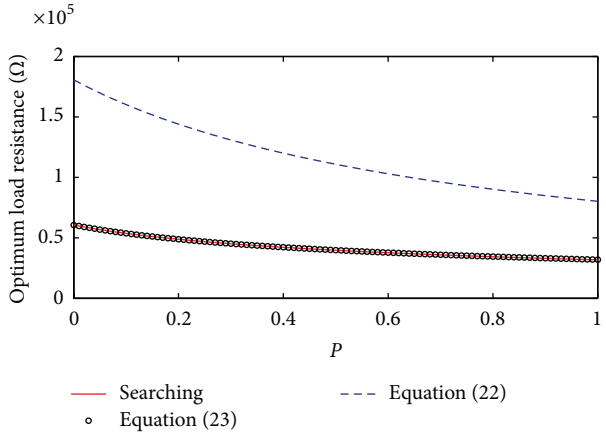

FIGURE 6: Variation of optimum load resistance with parameter P.

By considering the electromechanically coupled equations ((9) and (10)) one should obtain the expression for the optimum load as [23]

$$R_{\text{opt}} = \frac{1}{\omega_k C_p \left[1 + \left(\gamma_k / 2\zeta_k\right)^2\right]} \quad \text{where } \gamma_k = \frac{\Theta_k}{C_p \omega_k} \tag{23}$$

and ω_k is the short circuit resonance frequency of the desired mode and ζ_k is the damping ratio of the same mode and Θ_k is the modal electromechanical coupling of the mode. The optimum load resistance can also be searched by the calculation of the power output for a wide range of load resistance until the optimal one is reached [15, 24] when the system is excited at a target frequency. For instance, Figure 6 shows the variation of the optimum load resistance with parameter P for a piezoelectric energy harvester with tip mass (basic data given in Table 1) excited at the short circuit resonance frequency. The same load resistance is obtained by searching for the optimum one and by using (23). However, inaccurate predictions are obtained from (22).

The variation of power output (per squared based acceleration) with parameter P and tip mass is shown in Figure 7. The excitation is due to the harmonic motion of the clamped end in the transverse direction at the short circuit resonant frequency of the first vibration mode of each configuration. The maximum power output displayed in Figure 7(a) is obtained from the power FRF defined in Section 2 (obtained from the harmonic assumption in (9) and (10)) and the optimum load resistance (for each configuration) is calculated by using (23). Power increases with increasing tip mass for any geometric configuration (from rectangular to triangular harvester or $1 \leq P \leq 0$). This is the expected behavior, since the fundamental vibration mode of the harvester is considered in this base excitation problem. It is important to note that the forcing term in the base excitation is related to the inertia of the body itself; therefore, larger mass values result in larger strains and power output. Figure 7(a) shows that power output increases with increasing P for any tip mass. Therefore, the maximum power output is obtained from the rectangular piezoelectric energy harvester. This result contradicts the conclusions of other papers [16–22]; however, the effect of load resistance on the electromechanical behavior of a piezoelectric energy harvester is an important aspect that has not been considered previously. Ayed et al. [23] report the tapered beam as the optimum one. However, no experimental verification is provided and the open circuit condition ($R = 10^6\ \Omega$) is reported as the optimum load resistance.

The maximum power output displayed in Figure 7(b) is obtained from the power FRF defined from (9) and (10) with the electrical term in the mechanical domain (9) artificially set to zero. Therefore, the optimum load resistance (of each configuration) is calculated by (22). It is noteworthy that the power output in Figure 7(b) is larger than that in Figure 7(a). It is important to remember that the shunt damping effect was neglected in the simulations of Figure 7(b) (since electric feedback was neglected in (9)). The maximum power output in Figure 7(b) is obtained for the largest tip mass and for $P = 0.23$. The simple representation of the piezoelectric layers as constant electrical sources (Norton or Thévenin representations) leads to the incorrect estimate of the optimum load resistance (Figure 6) as well as to the incorrect optimum shape that provides the maximum power output in a beam optimization problem.

Finally, the variation of the power output (per squared based acceleration) with parameter Q and tip mass is shown

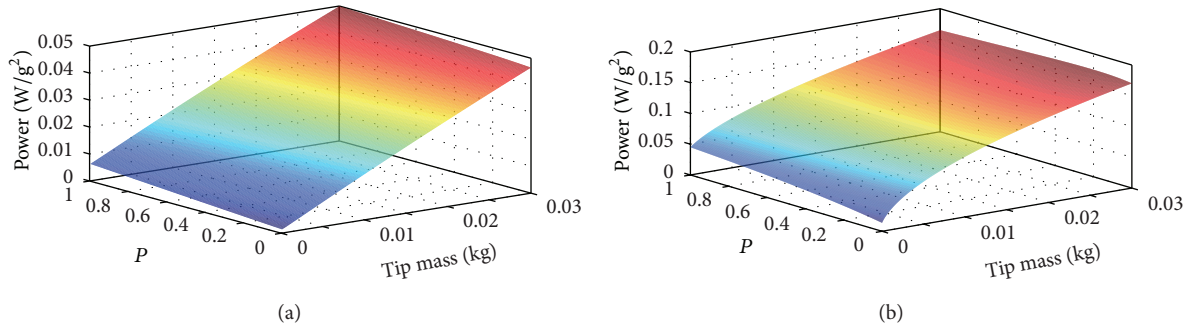

FIGURE 7: Variation of power output (per squared based acceleration) with parameter P and tip mass.

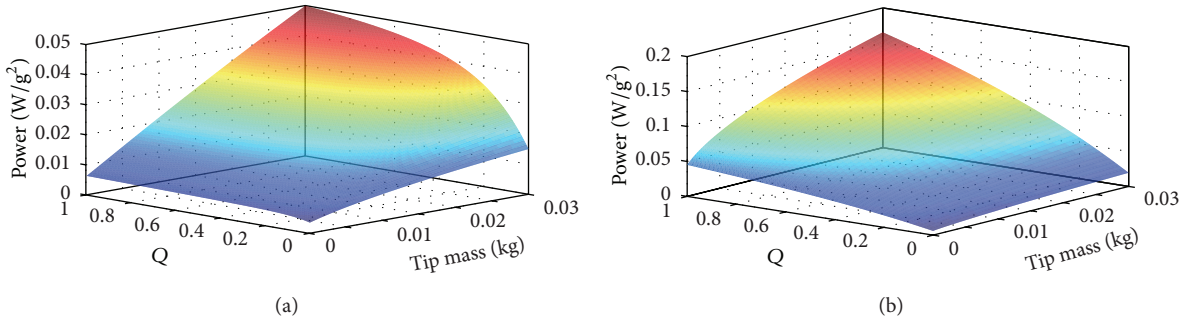

FIGURE 8: Variation of power output (per squared based acceleration) with parameter Q and tip mass.

in Figure 8. The system is excited at the short circuit resonant frequency of the first vibration mode of each configuration. The maximum power output displayed in Figure 8(a) is obtained by using the power FRF expression defined in Section 2 (obtained from the harmonic assumption in (9) and (10)) and the optimum load resistance (for each configuration) calculated by (23). Power increases with increasing tip mass for any geometric configuration (from rectangular to reversed tapered beam or $1 \leq Q \leq 0$). Power output increases with increasing Q for any tip mass considered in the simulations. Therefore, the maximum power output is obtained from the rectangular piezoelectric energy harvester. One should also note that power output dramatically drops (for any tip mass) with decreasing Q. In such a case, piezoelectric material is being removed from the region of maximum strain of a cantilever, which reduces the electromechanical coupling. The maximum power output displayed in Figure 8(b) is obtained from the power FRF defined from (9) and (10) with the electrical term in the mechanical domain (9) artificially set to zero. The optimum load resistance (for each configuration) is calculated with (22). The power output in Figure 8(b) is larger than that in Figure 8(a). The shunt damping effect is neglected in the simulations of Figure 8(b) (since electric feedback is neglected in (9)). The power output is quite similar in Figures 8(a) and 8(b) when $Q \rightarrow 0$. In this region, the electromechanical coupling decreases with decreasing Q and the effect of the electrical feedback in (9) is negligible. Therefore, for systems with small electromechanical coupling ($\boldsymbol{\theta}$), the optimum load resistances obtained from (22) and (23) are similar (or identical when $\boldsymbol{\theta} \rightarrow 0$ in (23)) and the effect on the power output is negligible.

4. Conclusions

The modeling and experimental verification of electromechanically coupled beams with uniform and varying cross-sectional areas have been reported for energy harvesting. The combination of Hamilton's principle and the Rayleigh-Ritz method based on the Euler-Bernoulli beam assumptions is used in the modeling approach. The electromechanical model was first verified against the analytical and experimental results for a rectangular bimorph under base excitation reported in the literature. The electromechanical vibration and voltage FRFs obtained from the presented model are in a very good agreement with those obtained from the analytical solution and experiments. In the second case, the model was successfully verified against the experimental results of a tapered bimorph with tip mass.

The effects of a varying cross-sectional area and tip mass on the electromechanical behavior of piezoelectric energy harvesters were also discussed for two conditions—tapered and reversed tapered beams. Issues related to the determination of the optimum load resistance and the consequences on beam shape optimization problems have also been addressed. When the electric term is neglected in the mechanical equation, the resulting expression for the optimum load resistance (for maximum power) is inaccurate, especially for

systems with large electromechanical coupling. Moreover, the power output is overestimated, since the shunt damping effect is not present, and an incorrect optimum shape that gives the maximum power output is obtained in a beam shape optimization problem.

Conflict of Interests

The authors declare that there is no conflict of interests regarding the publication of this paper.

Acknowledgments

The authors gratefully acknowledge CNPQ and FAPEMIG for partially funding the present research work through INCT-EIE and the support of the Sao Paulo Research Foundation (FAPESP) (2011/11711-0).

References

[1] H. A. Sodano, D. J. Inman, and G. Park, "A review of power harvesting from vibration using piezoelectric materials," *Shock and Vibration Digest*, vol. 36, no. 3, pp. 197–205, 2004.

[2] S. P. Beeby, M. J. Tudor, and N. M. White, "Energy harvesting vibration sources for microsystems applications," *Measurement Science and Technology*, vol. 17, no. 12, pp. R175–R195, 2006.

[3] S. Priya, "Advances in energy harvesting using low profile piezoelectric transducers," *Journal of Electroceramics*, vol. 19, no. 1, pp. 165–182, 2007.

[4] S. R. Anton and H. A. Sodano, "A review of power harvesting using piezoelectric materials (2003–2006)," *Smart Materials and Structures*, vol. 16, no. 3, pp. R1–R21, 2007.

[5] K. A. Cook-Chennault, N. Thambi, and A. M. Sastry, "Powering MEMS portable devices—a review of non-regenerative and regenerative power supply systems with special emphasis on piezoelectric energy harvesting systems," *Smart Materials and Structures*, vol. 17, no. 4, Article ID 043001, 2008.

[6] S. Roundy, P. K. Wright, and J. Rabaey, "A study of low level vibrations as a power source for wireless sensor nodes," *Computer Communications*, vol. 26, no. 11, pp. 1131–1144, 2003.

[7] N. E. duToit, B. L. Wardle, and S. G. Kim, "Design considerations for MEMS-scale piezoelectric mechanical vibration energy harvesters," *Integrated Ferroelectrics*, vol. 71, pp. 121–160, 2005.

[8] H. A. Sodano, G. Park, and D. J. Inman, "Estimation of electric charge output for piezoelectric energy harvesting," *Strain*, vol. 40, no. 2, pp. 49–58, 2004.

[9] N. E. duToit and B. L. Wardle, "Experimental verification of models for microfabricated piezoelectric vibration energy harvesters," *AIAA Journal*, vol. 45, no. 5, pp. 1126–1137, 2007.

[10] S.-N. Chen, G.-J. Wang, and M.-C. Chien, "Analytical modeling of piezoelectric vibration-induced micro power generator," *Mechatronics*, vol. 16, no. 7, pp. 379–387, 2006.

[11] J. H. Lin, X. M. Wu, T. L. Ren, and L. T. Liu, "Modeling and simulation of piezoelectric MEMS energy harvesting device," *Integrated Ferroelectrics*, vol. 95, no. 1, pp. 128–141, 2007.

[12] A. Erturk and D. J. Inman, "A distributed parameter electromechanical model for cantilevered piezoelectric energy harvesters," *Journal of Vibration and Acoustics, Transactions of the ASME*, vol. 130, no. 4, Article ID 041002, 2008.

[13] A. Erturk and D. J. Inman, "An experimentally validated bimorph cantilever model for piezoelectric energy harvesting from base excitations," *Smart Materials and Structures*, vol. 18, Article ID 025009, 2009.

[14] N. G. Elvin and A. A. Elvin, "A general equivalent circuit model for piezoelectric generators," *Journal of Intelligent Material Systems and Structures*, vol. 20, no. 1, pp. 3–9, 2009.

[15] A. Erturk, J. M. Renno, and D. J. Inman, "Modeling of piezoelectric energy harvesting from an L-shaped beam-mass structure with an application to UAVs," *Journal of Intelligent Material Systems and Structures*, vol. 20, no. 5, pp. 529–544, 2009.

[16] S. P. Matova, M. Renaud, M. Jambunathan, M. Goedbloed, and R. Van Schaijk, "Effect of length/width ratio of tapered beams on the performance of piezoelectric energy harvesters," *Smart Materials and Structures*, vol. 22, no. 7, Article ID 075015, 2013.

[17] S. Roundy, E. S. Leland, J. Baker et al., "Improving power output for vibration-based energy scavengers," *IEEE Pervasive Computing*, vol. 4, no. 1, pp. 28–36, 2005.

[18] F. Goldschmidtboeing and P. Woias, "Characterization of different beam shapes for piezoelectric energy harvesting," *Journal of Micromechanics and Microengineering*, vol. 18, no. 10, Article ID 104013, 2008.

[19] L. Mateu and F. Moll, "Optimum piezoelectric bending beam structures for energy harvesting using shoe inserts," *Journal of Intelligent Material Systems and Structures*, vol. 16, no. 10, pp. 835–845, 2005.

[20] D. Benasciutti, L. Moro, S. Zelenika, and E. Brusa, "Vibration energy scavenging via piezoelectric bimorphs of optimized shapes," *Microsystem Technologies*, vol. 16, no. 5, pp. 657–668, 2010.

[21] J. M. Dietl and E. Garcia, "Beam shape optimization for power harvesting," *Journal of Intelligent Material Systems and Structures*, vol. 21, no. 6, pp. 633–646, 2010.

[22] F. Lu, H. P. Lee, and S. P. Lim, "Modeling and analysis of micro piezoelectric power generators for micro-electromechanical-systems applications," *Smart Materials and Structures*, vol. 13, no. 1, pp. 57–63, 2004.

[23] S. B. Ayed, A. Abdelkefi, F. Najar, and M. R. Hajj, "Design and performance of variable-shaped piezoelectric energy harvesters," *Journal of Intelligent Material Systems and Structures*, 2014.

[24] A. Erturk, *Electromechanical modeling of piezoelectric energy harvesters [Ph.D. dissertation]*, Department of Engineering Science and Mechanics, Virginia Polytechnic Institute and State University, , Blacksburg, Va, USA, 2009.

[25] C. De Marqui Junior Jr., A. Erturk, and D. J. Inman, "An electromechanical finite element model for piezoelectric energy harvester plates," *Journal of Sound and Vibration*, vol. 327, no. 1-2, pp. 9–25, 2009.

[26] S. H. Crandall, D. C. Karnopp, E. F. Kurtz Jr., and D. C. Pridmore-Brown, *Dynamics of Mechanical and Electromechanical Systems*, McGraw-Hill, New York, NY, USA, 1968.

[27] N. W. Hagood, W. H. Chung, and A. von Flotow, "Modeling of piezoelectric actuator dynamics for active structural control," *Journal of Intelligent Material Systems and Structures*, vol. 1, pp. 327–354, 1990.

Hindawi Publishing Corporation
Shock and Vibration
Volume 2014, Article ID 656212, 10 pages
http://dx.doi.org/10.1155/2014/656212

Research Article

Dynamical Jumps in a Shape Memory Alloy Oscillator

H. S. Oliveira,[1] A. S. de Paula,[1] and M. A. Savi[2]

[1] *Department of Mechanical Engineering, Universidade de Brasília, 70910-900 Brasília, DF, Brazil*
[2] *Department of Mechanical Engineering, COPPE, Universidade Federal do Rio de Janeiro, P.O. Box 68.503, 21941-972 Rio de Janeiro, RJ, Brazil*

Correspondence should be addressed to A. S. de Paula; alinedepaula@unb.br

Received 26 June 2013; Accepted 10 March 2014; Published 18 August 2014

Academic Editor: Miguel Neves

Copyright © 2014 H. S. Oliveira et al. This is an open access article distributed under the Creative Commons Attribution License, which permits unrestricted use, distribution, and reproduction in any medium, provided the original work is properly cited.

The dynamical response of systems with shape memory alloy (SMA) elements presents a rich behavior due to their intrinsic nonlinear characteristic. SMA's nonlinear response is associated with both adaptive dissipation related to hysteretic behavior and huge changes in properties caused by phase transformations. These characteristics are attracting much technological interest in several scientific and engineering fields, varying from medical to aerospace applications. An important characteristic associated with dynamical response of SMA system is the jump phenomenon. Dynamical jumps result in abrupt changes in system behavior and its analysis is essential for a proper design of SMA systems. This paper discusses the nonlinear dynamics of a one degree of freedom SMA oscillator presenting pseudoelastic behavior and dynamical jumps. Numerical simulations show different aspects of this kind of behavior, illustrating its importance for a proper understanding of nonlinear dynamics of SMA systems.

1. Introduction

Shape memory alloys (SMAs) have unique thermomechanical properties responsible for their use in several applications. These remarkable properties are attracting technological interest in science and engineering fields [1–3]. In terms of applied dynamics, SMAs are being used in order to explore adaptive dissipation associated with hysteresis loop and the mechanical property changes due to phase transformation [4, 5]. Moreover, the dynamical response of systems with SMA actuators presents a unique dynamical behavior due to their intrinsic nonlinear characteristic, presenting periodic, quasiperiodic, and chaotic responses [4, 6–8]. Recently, SMA constraints have been used for vibration reduction since it is expected that the high dissipation capacity of SMAs changes the system response producing less complex behaviors [9–11]. Another important application of SMA related to dynamical system is the adaptive tuned vibration absorbers. The main idea related to tuned vibration absorbers is the use of a secondary system connected to a main system in order to dissipate energy. In general, this idea has been used in electrical transmission lines and structural systems. Although this is very effective in tuned frequencies, it is difficult to be applied when frequency variations occur. SMA can be employed in order to confer adaptive behavior to this tuned system, allowing its application when frequency variations are expected [12].

Although SMA systems have interesting behaviors to be exploited in dynamical applications, some characteristics may be critical for practical situations. In this regard, the design of SMA system has a huge importance, being necessary in a deep investigation of the dynamical aspects of the system. Besides chaos and multistability aspects that are present in SMA dynamical systems, an important aspect is the dynamical jump. Basically, dynamical jumps are associated with nonlinear resonant response, causing abrupt changes in system behavior, introducing unstable regions on system response.

Bernardini and Rega [8] presented several aspects related to dynamical jumps in SMA systems. Basically, the authors investigated a one degree of freedom oscillator considering both isothermal and anisothermal systems. It is shown that nonregular responses occur around the jumps. In general, multicomponent harmonic-balance method, path-following technique, and Adams-Moulton algorithm were employed to investigate the system response.

This paper revisits the dynamical jumps in a one degree of freedom SMA oscillator harmonically excited. The restitution force is provided by an SMA element described by a constitutive model with internal constraints [13]. Numerical simulations are carried out showing different aspects of the dynamical response of the system. Conclusions of this investigation establish a relationship between dynamical jumps and stress-strain relation of the SMA element.

2. Constitutive Model

The thermomechanical description of shape memory alloys is the objective of numerous research efforts that try to contemplate all behavior details [1, 2]. Here, a constitutive model that is built upon Fremond's model that was previously presented in some studies [6, 13–17] is employed. This model considers different material properties for each phase and four macroscopic phases for the description of the SMA behavior.

Therefore, besides the total strain, ε, and temperature, T, it is necessary to define four internal variables that represent volume fraction of each macroscopic phase: β_1 and β_2, related to detwinned martensites, respectively, associated with tension and compression; β_3 that represents the austenitic volume fraction; and β_4 that represents the volume fraction of twinned martensite. Since there is a constraint based on phase coexistence, $\beta_1+\beta_2+\beta_3+\beta_4 = 1$, it is possible to use only three volume fractions and the thermomechanical behavior of the SMA is described by the following set of equations [13, 18]:

$$\begin{aligned}
\sigma &= E\varepsilon + \left[E\alpha_h + \alpha\right](\beta_2 - \beta_1) - \Omega\,(T - T_0)\,,\\
\dot{\beta}_1 &= \frac{1}{\eta_1}\left\{\alpha\varepsilon + \Lambda_1\,(T) + \left(2\alpha\alpha_h + E\alpha_h^2\right)(\beta_2 - \beta_1)\right.\\
&\qquad \left. + \alpha_h\left[E\varepsilon - \Omega\,(T - T_0)\right] - \partial_{\beta_1} J_\pi\right\} + \partial_{\dot{\beta}_1} J_\chi,\\
\dot{\beta}_2 &= \frac{1}{\eta_2}\left\{-\alpha\varepsilon + \Lambda_2\,(T) - \left(2\alpha\alpha_h + E\alpha_h^2\right)(\beta_2 - \beta_1)\right.\\
&\qquad \left. - \alpha_h\left[E\varepsilon - \Omega\,(T - T_0)\right] - \partial_{\beta_2} J_\pi\right\} + \partial_{\dot{\beta}_2} J_\chi,\\
\dot{\beta}_3 &= \frac{1}{\eta_3}\left\{-\frac{1}{2}\left(E_A - E_M\right)\left[\varepsilon + \alpha_h(\beta_2 - \beta_1)\right]^2 + \Lambda_3\,(T)\right.\\
&\qquad + \left(\Omega_A - \Omega_M\right)(T - T_0)\left[\varepsilon + \alpha_h\,(\beta_2 - \beta_1)\right]\\
&\qquad \left. - \partial_{\beta_3} J_\pi\right\} + \partial_{\dot{\beta}_3} J_\chi,
\end{aligned} \tag{1}$$

where σ is the stress and $E = E_M + \beta_3(E_A - E_M)$ is the elastic modulus while $\Omega = \Omega_M + \beta_3(\Omega_A - \Omega_M)$ is related to thermal expansion coefficient. Note that subscript A refers to austenitic phase, while M refers to martensite. Parameters $\Lambda_1 = \Lambda_2 = \Lambda = \Lambda(T)$ and $\Lambda_3 = \Lambda_3(T)$ are associated with phase transformation stress levels. Parameter α_h defines the horizontal width of the stress-strain hysteresis loop, while α controls the height of the same hysteresis loop. The terms $\partial_n J_\pi$ ($n = \beta_1, \beta_2, \beta_3$) are subdifferentials of the indicator function J_π with respect to n. This indicator function is related to a convex set π, which provides the internal constraints related to the phase coexistence. With respect to evolution equations of volume fractions, $\eta_1 = \eta_2 = \eta$ and η_3 represent the internal dissipation related to phase transformations. Moreover $\partial_n J_\chi$ ($n = \beta_1, \beta_2, \beta_3$) are subdifferentials of the indicator function J_χ with respect to n. This indicator function is associated with the convex set χ, which establishes conditions for the correct description of internal subloops due to incomplete phase transformations. These subdifferentials may be replaced by Lagrange multipliers associated with the mentioned constraints [19].

Concerning parameter definitions, temperature-dependent relations are adopted for Λ and Λ_3 as follows:

$$\begin{aligned}
\Lambda &= \begin{cases} -L_0 + \dfrac{L}{T_M}\,(T - T_M)\,, & \text{if } T > T_M \\ -L_0, & \text{if } T \le T_M; \end{cases}\\
\Lambda_3 &= \begin{cases} -L_0^A + \dfrac{L^A}{T_M}\,(T - T_M)\,, & \text{if } T > T_M \\ -L_0^A, & \text{if } T \le T_M, \end{cases}
\end{aligned} \tag{2}$$

where T_M is the temperature below where the martensitic phase becomes stable. Usually, experimental tests provide information of M_s and M_f, temperatures of the start and finish of the martensitic formation. This model uses only one temperature that could be an average value or, alternatively, the M_f value. Moreover, L_0, L, L_0^A, and L^A are parameters related to critical stress for phase transformation.

In order to describe the characteristics of phase transformation kinetics, different values of η and η_3 might be considered during loading, η^L and η_3^L, and unloading processes, η^U and η_3^U. For more details about the constitutive model, see [13, 16]. All constitutive parameters can be matched from stress-strain tests.

As it is well known, SMA devices demonstrate time-dependent characteristics which means that their thermomechanical response depends on the loading rate; see, for example, [20, 21]. The proper modeling of this time dependency can be performed by considering the thermomechanical coupling terms in the energy equation. Reference [22] discusses the thermomechanical coupling and rate dependency in SMAs.

The considered constitutive model has viscous characteristic that allows the description of the thermomechanical coupling avoiding the integration of the energy equation, presenting useful results [15]. Reference [22] explores the same idea showing the difference between a viscous model and a rate-independent model with thermomechanical coupling. Both models have the ability to describe pseudoelastic behavior in SMA wires. This time-dependent aspect can be controlled by the proper choice of model parameters.

3. Single Degree of Freedom Shape Memory Oscillator

The dynamical behavior of SMAs is analyzed by considering a single degree of freedom oscillator (1DOF) with two different forcing possibilities. Initially, a harmonic base

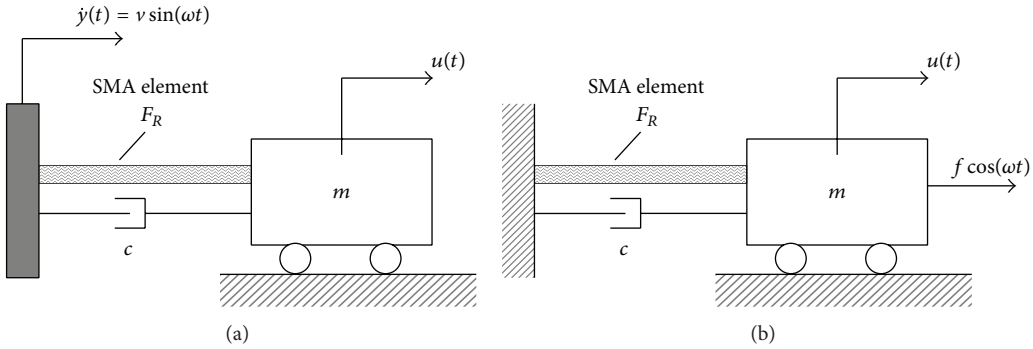

Figure 1: Single degree of freedom oscillator: (a) harmonic base excitation and (b) harmonic force applied to the mass.

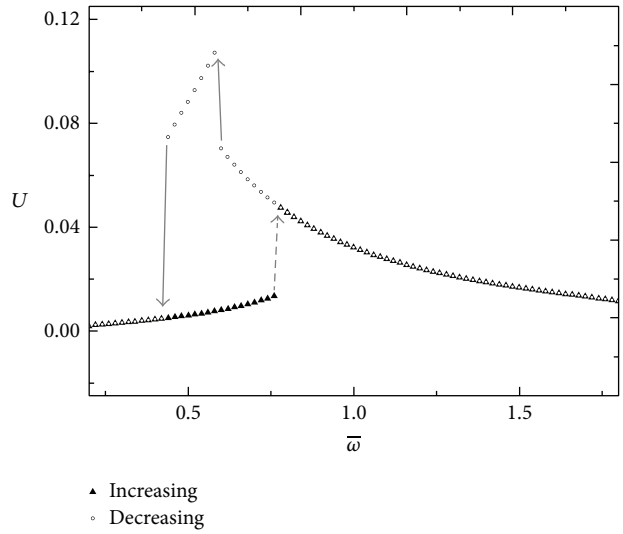

Figure 2: Maximum system amplitude with $v = 0.025$ m/s and a sine sweep of the forcing frequency.

excitation with prescribed velocity $\dot{y}(t) = v\sin(\omega t)$, as shown in Figure 1(a), is considered. Then, a harmonic excitation $F_0(t) = f\cos(\omega t)$ applied directly to the oscillator mass, as presented in Figure 1(b), is analyzed. The motivation of studying these two situations is the development of SMA vibration absorbers and isolators. The oscillator presented in Figure 1(a), for example, can be used to analyze classical dynamical absorbers, which are attached to a primary system that presents a harmonic response that must have its response amplitude reduced. The oscillator of Figure 1(b), on the other hand, can be used to analyze vibration reduction of systems harmonically excited, which occurs in rotating machines due to unavoidable unbalance. Therefore, the dynamical analysis of these systems is an important start for the design of SMA devices.

The SMA oscillator consists of a mass m attached to a shape memory element of length l and cross-sectional area A and restitution force F_R (Figure 1). A linear viscous damper, characterized by a viscous coefficient c, is also considered in order to represent dissipations different from the dissipation associated with the SMA element.

The equation of motion of this oscillator may be formulated by considering the balance of forces acting on the mass as follows:

$$m\ddot{u} + c\dot{u} + F_R = F_0\cos(\omega t), \tag{3}$$

where $F_R = \sigma A$, $u = (x - y)$, $F_0 = -mv\omega$ in the case of base excitation and $F_0 = f$ when the force is applied directly to the oscillator. The restitution force of the oscillator is provided by an SMA element described by the constitutive equations presented in the previous section [13]. Therefore, the following equation of motion is obtained [4]:

$$\begin{aligned} m\ddot{u} + c\dot{u} + \frac{EA}{l}u + \left(A\alpha + EA\alpha_h\right)\left(\beta_2 - \beta_1\right) \\ - \Omega A\left(T - T_0\right) = F_0\cos(\omega t), \end{aligned} \tag{4}$$

where volume fractions of evolution β_1 and β_2 are described by the constitutive model presented in the preceding section

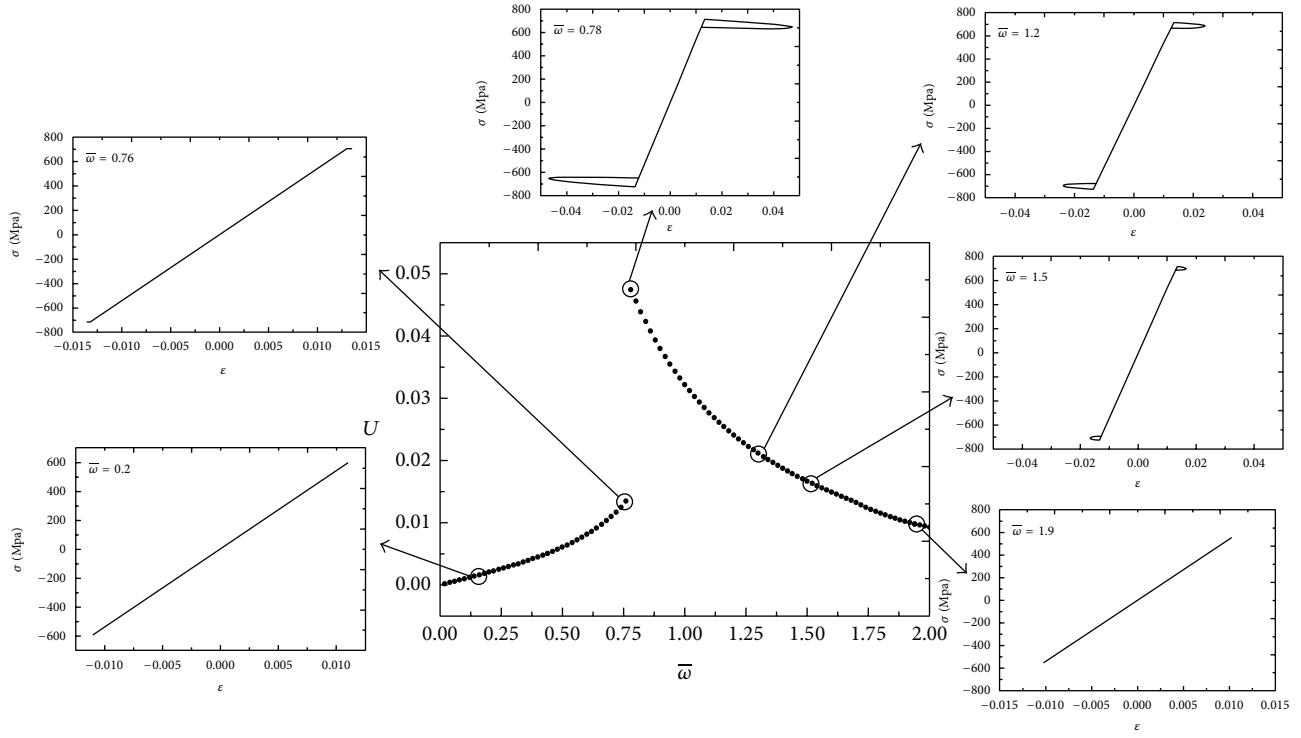

Figure 3: Up-sweep jumps with $\nu = 0.025$ m/s: comparison between frequency response and stress-strain curves.

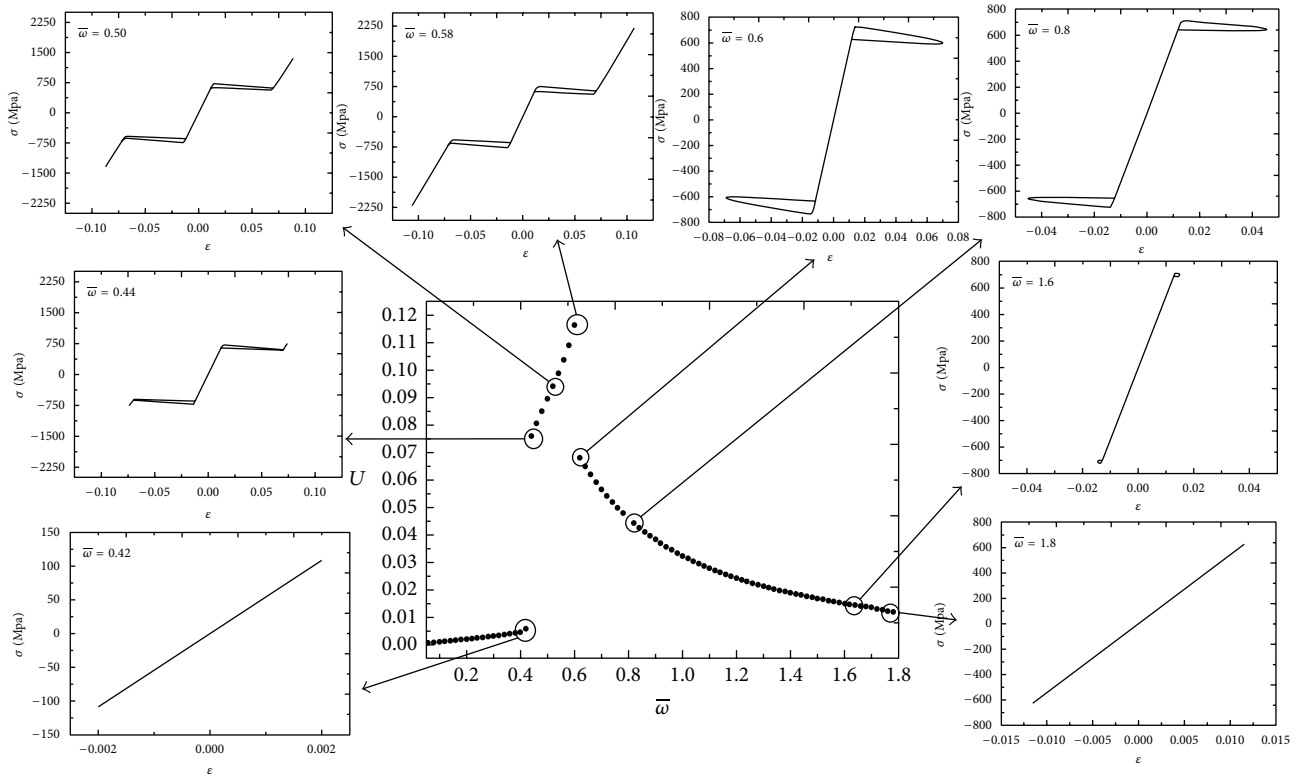

Figure 4: Down-sweep jumps with $\nu = 0.025$ m/s: comparison between frequency response and stress-strain curves.

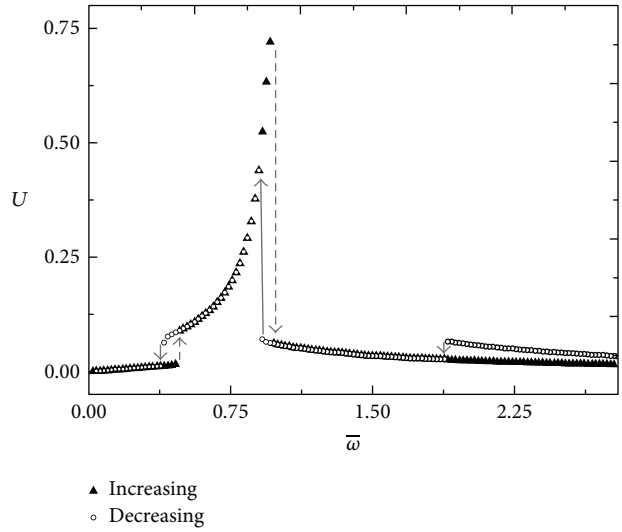

Figure 5: Maximum system amplitude with $v = 0.075$ m/s and increasing the forcing frequency.

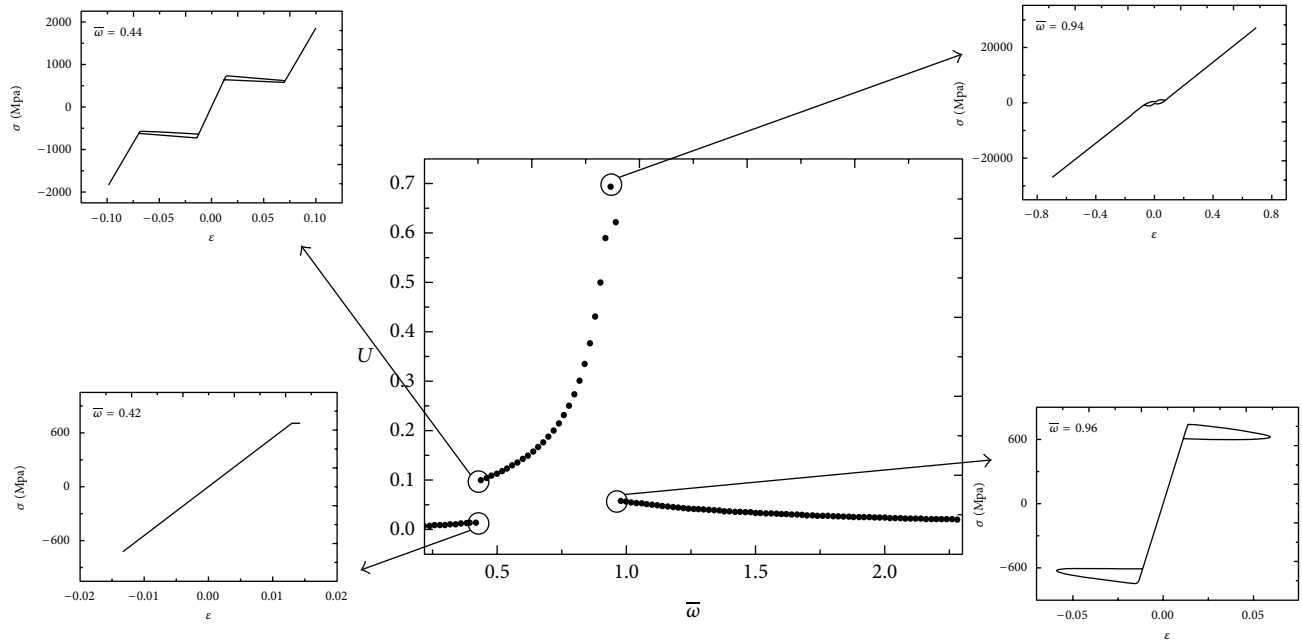

Figure 6: Up-sweep jumps with $v = 0.075$ m/s: comparison between frequency response and stress-strain curves.

and $\varepsilon = u/l$. In order to obtain a dimensionless equation of motion, the system's parameters are defined as follows:

$$\overline{\Omega} = \frac{\Omega_R A T_R}{ml\omega_0^2} = \frac{\Omega_R T_R}{E_R}; \qquad \overline{\alpha} = \frac{\alpha A}{ml\omega_0^2} = \frac{\alpha}{E_R};$$
$$\overline{\alpha}_h = \frac{\alpha_h E_R A}{ml\omega_0^2}; \qquad \omega_0^2 = \frac{E_R A}{ml};$$
$$\xi = \frac{c}{c\omega_0}; \qquad \mu_E = \frac{E}{E_R};$$
$$V = \frac{v}{\omega_0 l}; \qquad \mu_\Omega = \frac{\Omega}{\Omega_R}; \qquad \overline{\omega} = \frac{\omega}{\omega_0}. \tag{5}$$

Note that dimensionless parameters and variables are defined considering some reference values for temperature-dependent parameters. This is done by assuming a reference temperature, T_R, where these parameters are evaluated. Therefore, parameters with subscript R are evaluated at this reference temperature. These definitions allow one to define the following dimensionless variables, respectively, related to mass displacement (U), temperature (θ), and time (τ):

$$U = \frac{u}{l}; \qquad \theta = \frac{T}{T_R}; \qquad \tau = \omega_0 t. \tag{6}$$

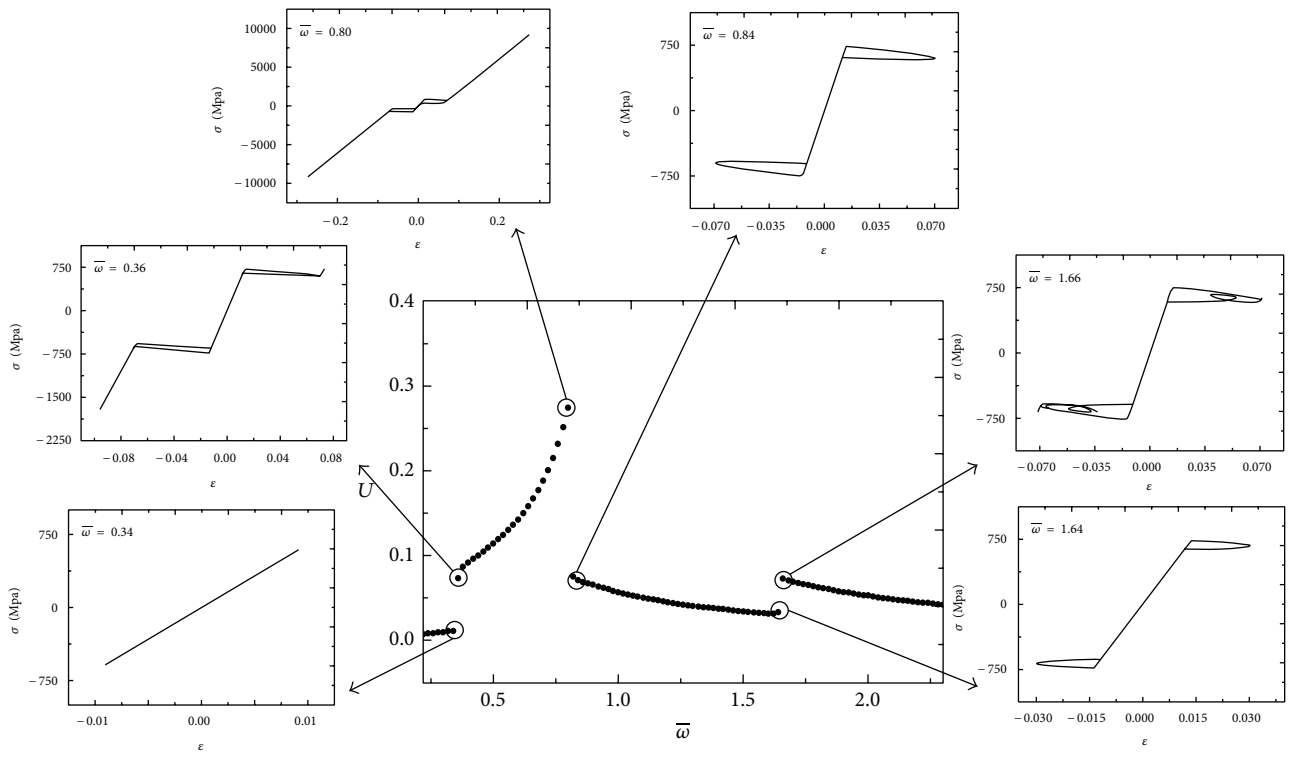

Figure 7: Down-sweep jumps with $v = 0.075$ m/s: comparison between frequency response and stress-strain curves.

Therefore, the dimensionless equation of motion has the following form:

$$
\begin{aligned}
&U'' + \xi U' + \mu_E U + \left(\overline{\alpha} + \mu_E \overline{\alpha}_h\right)\left(\beta_2 - \beta_1\right) \\
&\quad - \mu_\Omega \overline{\Omega}\left(\theta - \theta_0\right) = \delta \cos\left(\overline{\omega} t\right), \\
&\beta_1' = \frac{1}{\overline{\eta}_1}\left\{\alpha\varepsilon + \Lambda_1(T) + \left(2\alpha\alpha_h + E\alpha_h^2\right)\left(\beta_2 - \beta_1\right)\right. \\
&\qquad \left. + \alpha_h\left[E\varepsilon - \Omega\left(T - T_0\right)\right] - \partial_{\beta_1} J_\pi\right\} + \partial_{\dot{\beta}_1} J_\chi, \\
&\beta_2' = \frac{1}{\overline{\eta}_2}\left\{-\alpha\varepsilon + \Lambda_2(T) - \left(2\alpha\alpha_h + E\alpha_h^2\right)\left(\beta_2 - \beta_1\right)\right. \\
&\qquad \left. - \alpha_h\left[E\varepsilon - \Omega\left(T - T_0\right)\right] - \partial_{\beta_2} J_\pi\right\} + \partial_{\dot{\beta}_2} J_\chi, \\
&\beta_3' = \frac{1}{\overline{\eta}_3}\left\{-\frac{1}{2}\left(E_A - E_M\right)\left[\varepsilon + \alpha_h(\beta_2 - \beta_1)\right]^2 + \Lambda_3(T)\right. \\
&\qquad + \left(\Omega_A - \Omega_M\right)\left(T - T_0\right)\left[\varepsilon + \alpha_h\left(\beta_2 - \beta_1\right)\right] \\
&\qquad \left. - \partial_{\beta_3} J_\pi\right\} + \partial_{\dot{\beta}_3},
\end{aligned}
\tag{7}
$$

where derivatives with respect to dimensionless time are represented by $()' = d()/d\tau$, $\overline{\eta}_i = \eta_i/\omega_0$, and $\delta = -mv\omega/ml\omega_0^2 = -mv\omega/E_R A$ in the case of base excitation and $\delta = f/ml\omega_0^2 = f/E_R A$ when the force is applied directly to the oscillator.

4. Numerical Simulation

This section presents a numerical investigation of the 1DOF SMA oscillator. In order to deal with nonlinearities of the SMA oscillator equations of motion, an iterative procedure based on the operator split technique [23] is employed. Under this assumption, the fourth-order Runge-Kutta method is used together with the projection algorithm proposed in [6] to solve the constitutive equations. The solution of the constitutive equations also employs the operator split technique together with an implicit Euler method. The calculation of β_n ($n = 1, 2, 3$) considers that the evolution equations are solved in a decoupled way. At first, the equations (except for the subdifferentials) are solved using an iterative implicit Euler method. If the estimated results obtained for β_n do not satisfy the imposed constraints, an orthogonal projection algorithm pulls their value to the nearest point on the domain's surface [19]. On the other hand, the numerical integration of the dynamical system uses the classical Runge-Kutta method.

Parameters used in the numerical simulations, presented in Table 1, are the same used by Savi et al. [4]. These parameters are obtained by calibrating the model to experimental results of a NiTi alloy. Simulations are carried out at a temperature of 372 K, where only austenitic phase is stable at stress-free state.

The dynamical analysis of the SMA oscillator is mainly focused on the investigation of the dynamical jumps. The idea is to investigate numerical simulations related to sine-sweep tests of the forcing frequency. In this test, system response is investigated when the forcing frequency is increased

Table 1: SMA parameters.

E_R (GPa)	E_M (GPa)	α (MPa)	α_h	L_0 (MPa)	L (MPa)	${L_0}^A$ (MPa)	L^A (MPa)
54	42	330	0.048	0.015	41.5	0.63	185
Ω_A (MPa/K)	Ω_M (MPa/K)	T_M (K)	η^L (Mpa·s)	η^U (Mpa·s)	${\eta_3}^L$ (Mpa·s)	${\eta_3}^U$ (Mpa·s)	
0.74	0.17	291.4	1.0	2.7	1.0	2.7	

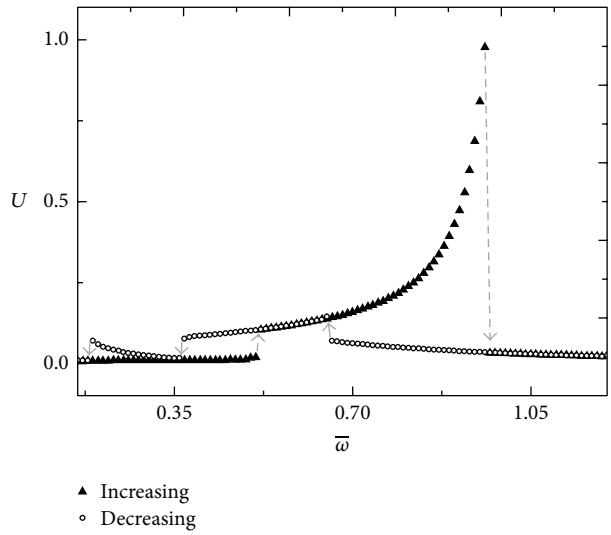

Figure 8: Maximum system amplitude with $\delta = 0.012$ and increasing the forcing frequency.

(up-sweep) or decreased (down-sweep) by some increment value. For each forcing frequency, the system is numerically integrated and the maximum amplitude in steady state is considered. When the frequency is changed, the last state at the previous forcing frequency is considered as the initial condition for the new frequency. This brute-force procedure is enough to identify dynamical jumps although it does not allow the identification of unstable paths related to the system response.

4.1. Harmonic Base Excitation. Initially, the SMA oscillator subjected to base excitation is of concern with $\xi = 0.05$. Figure 2 presents the system response considering the sine-sweep test of the frequency for $v = 0.025$ m/s. It is noticeable that there is one jump during the up-sweep while the down-sweep presents two jumps. This behavior is caused by system nonlinearities, specifically, hysteretic behavior. During the up-sweep, dynamical jump occurs around $\overline{\omega} = 0.77$. During the down-sweep, the first one occurs around $\overline{\omega} = 0.59$ and the second one occurs around $\overline{\omega} = 0.43$. Bernardini and Rega [8] identified similar situations with different approaches and a different constitutive model.

In order to have a better understanding about the dynamical jumps, an investigation is carried out establishing a relation between jumps and phase transformations. Figure 3 shows up-sweep frequency response curves highlighting the stress-strain curves for different forcing frequencies. It can be observed that the jump occurs when phase transformations start to occur. Therefore, linear stress-strain curve is changed to a hysteretic behavior associated with incomplete phase transformations. Note that, for frequencies smaller than $\overline{\omega} = 0.76$, the system has a linear behavior. By slightly increasing the forcing frequency, the system presents a hysteretic behavior. The hysteresis loop causes a significant increase of the strain, which produces a dynamical jump. By continuing to increase the forcing frequency the hysteresis loop starts to become smaller until it disappears and the system presents a linear behavior again.

Figure 4 shows the same analysis related to down-sweep test. The first jump occurs when the system changes from a situation where incomplete phase transformations are in course to a new one where complete phase transformations are occurring. This is noticeable by observing the presence of the elastic response related to martensitic phase in the stress-strain curve. Note that a very slight change around $\overline{\omega} = 0.6$ changes the stress level promoting complete phase transformations, presenting an elastic response on the martensitic phase. The second jump, on the other hand, occurs where phase transformation is not occurring anymore. Note that, near $\overline{\omega} = 0.44$, phase transformations are not occurring anymore causing an abrupt change from full loop to linear case.

It should be pointed out that, for the analyzed range, Figures 2–4 present a linear evolution of the frequency response when system has a linear response, without reaching the hysteretic behavior. Afterward, when the system presents a hysteretic response related to incomplete phase transformation, the response is associated with a nonlinear curve. The transition between one behavior and the other modifies the frequency response.

Now, the same analysis is carried out with a higher velocity $v = 0.075$ m/s. Figure 5 shows sine-sweep maximum amplitudes of the SMA oscillator. Under this new condition, the system presents two jumps during the up-sweep while the down-sweep presents three jumps. During the up-sweep (Figure 6), the first jump occurs when the response shifts from a linear behavior to a nonlinear behavior with the complete hysteresis loop. The second jump is related to the transition from the complete phase transformations to incomplete ones. Although the jumps are being caused by changes in stress-strain curves, it should be highlighted that the first jump, where the system goes from a complete hysteresis loop to a linear behavior, is different from the previous case.

Figure 7 establishes the comparison between jumps and phase transformation for the down-sweep case. The first one occurs around $\overline{\omega} = 1.66$, where the maximum amplitude decreases slightly. It is noticeable that incomplete phase transformation changes from a situation where internal

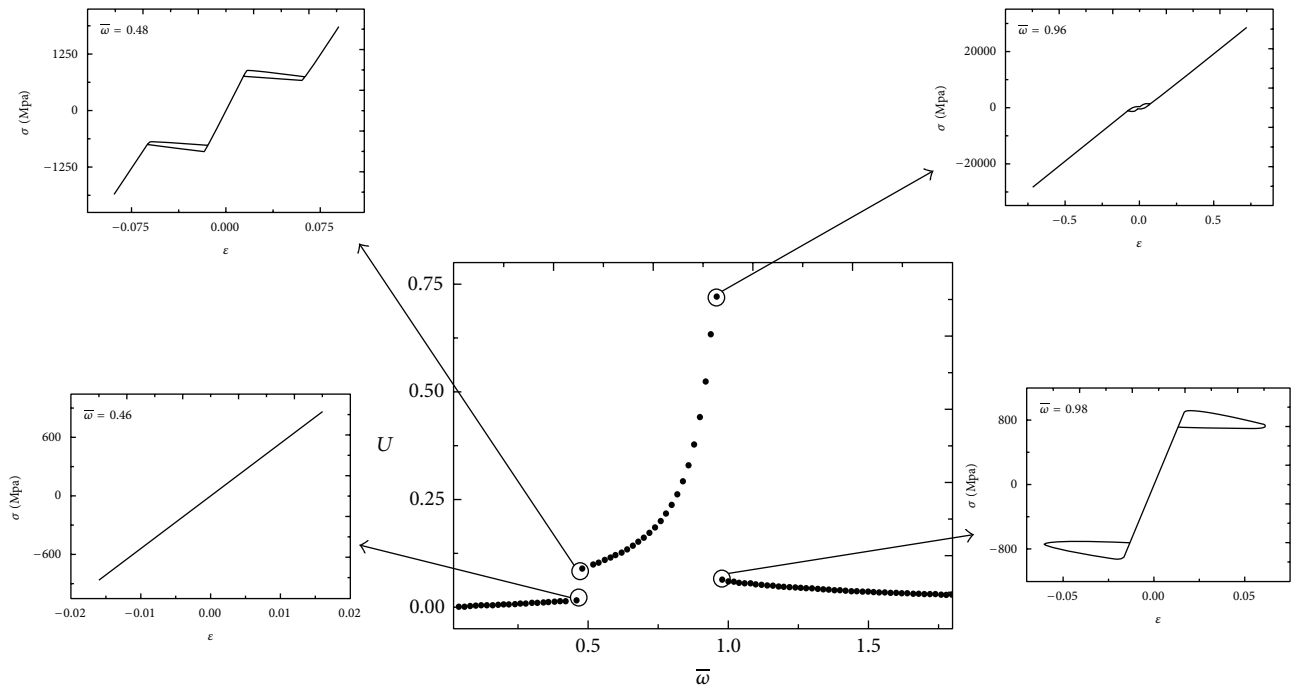

Figure 9: Up-sweep jumps with $\delta = 0.012$: comparison between frequency response and stress-strain curves.

subloops appear in stress-strain curves to a behavior without internal subloops. The second jump takes place at $\overline{\omega} = 0.8$, where no transition in stress-strain curve is observed. The last dynamical jump occurs when the material shifts from nonlinear behavior related to an incomplete hysteresis loop to a linear behavior.

It is important to mention that when a dynamical jump occurs, it is possible to have the transition between the behaviors in stress-strain diagram immediately before the dynamical jump. In Figure 7, for example, between the stress-strain diagrams presented at $\overline{\omega} = 0.84$ (incomplete hysteresis loop) and $\overline{\omega} = 0.80$ (complete hysteresis loop), there is a complete hysteresis loop at $\overline{\omega} = 0.82$, where the response amplitude is still low. This happens because the frequency variation is very small and the amount of the energy that increases from $\overline{\omega} = 0.84$ to $\overline{\omega} = 0.92$ is only sufficient to complete the hysteresis loop. After the loop is complete, even a very small increase of energy is enough to lead to the dynamical jump. Probably, this behavior occurs only in numerical simulations where a quasistatic variation of the forcing frequency is possible. In experimental tests, this subtle transition is probably not possible to be reached and only the response after the jump is captured.

4.2. Harmonic Force Applied to the Mass. At this point, the case where harmonic excitation is applied directly to SMA oscillator mass is analyzed, with $\xi = 0.01$. The main idea is to establish a qualitative comparison between the responses of both oscillators. The same order of magnitude for the forcing parameters and viscous damping coefficient is considered. Nevertheless, the forcing amplitude depends on the forcing frequency in the case of base excitation while in the other case the forcing amplitude is constant. Therefore, the qualitative comparison tries to show different possibilities when each forcing condition is considered.

Figure 8 presents system response considering the sine-sweep of the frequency with $\delta = 0.012$. During the up-sweep test two jumps are observed while in down-sweep three jumps are observed. In the up-sweep, presented in Figure 9, the first jump occurs when the response shifts from an incomplete hysteresis to a complete one. This jump consists in a different situation compared with the equivalent base excitation cases, where the transition related to the first dynamical jumps is from linear behavior to nonlinear behavior with complete hysteresis loop. The second jump is related to the inverse transition, from complete to incomplete loop.

Figure 10 establishes the comparison between jumps and phase transformation for the down-sweep case with $\delta = 0.012$. The first dynamical jump, which happens around $\overline{\omega} = 0.65$, is similar to the first jump of the down-sweep with base excitation with $v = 0.025$ m/s, when the transition from incomplete to complete hysteresis loop occurs. The second one occurs around $\overline{\omega} = 0.36$ in a transition from complete to incomplete hysteresis loop. This situation is also verified in the previous cases. The last dynamical jump, around $\overline{\omega} = 0.18$, occurs when the system goes from incomplete hysteresis loop to linear behavior. This jump, with a transition from incomplete hysteresis loop to linear behavior, consists in a different situation compared with the equivalent base excitation case.

It is important to mention that all regions related to dynamical jumps are associated with coexistence of attractors, due to the different possibilities of response when

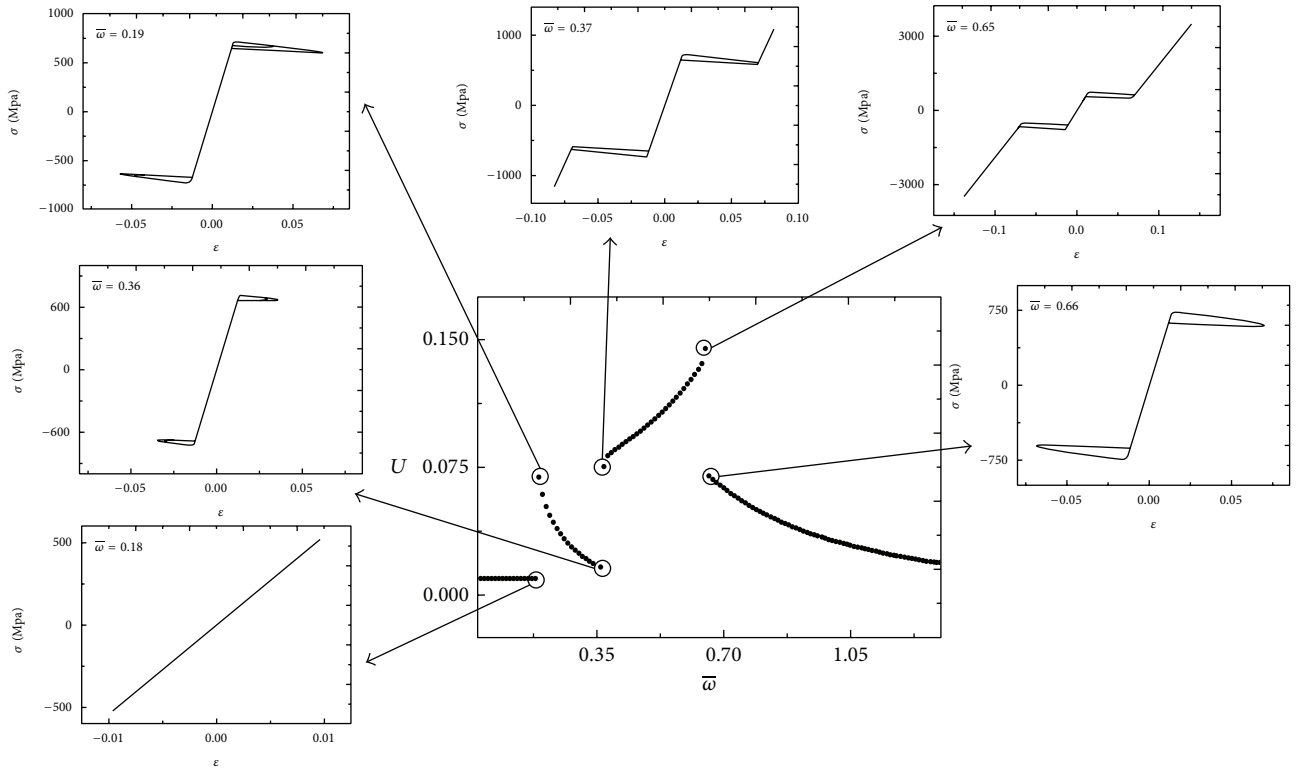

Figure 10: Up-sweep jumps with $\delta = 0.012$: comparison between frequency response and stress-strain curves.

increasing and decreasing the forcing frequency. This coexistence is associated with dynamical instability since small perturbations can cause the system to jump from one behavior to the other which is completely different. This kind of behavior is critical to system response and is important to be investigated.

5. Conclusions

This paper deals with the analysis of dynamical jumps in a shape memory alloy system. Basically, a nonlinear one degree of freedom oscillator with harmonic excitation is of concern. Two different situations are treated: base excitation and excitation applied directly to the oscillator mass. This system presents several dynamical jumps and their occurrence depends not only on the forcing amplitude—which depends on the velocity in the case of base excitation—but also on the way the forcing frequency is modified. Numerical simulations of the sine-sweep test are carried out showing that down-sweep causes more dynamical jumps than up-sweep. These jumps can be explained by phase transformation arguments, observing stress-strain curves. In this regard, three possible behaviors can be observed: linear behavior, minor hysteresis loops related to incomplete phase transformation, and major hysteresis loops related to complete phase transformation. The transition between these three behaviors leads to changes in system response, which can be a dynamical jump or a modification in the frequency response of the system. It is observed that the transition between linear and incomplete hysteresis loops can lead to dynamical jumps or modifications in the frequency response of the system. All other transitions lead to dynamical jumps.

Conflict of Interests

The authors declare that there is no conflict of interests regarding the publication of this paper.

Acknowledgments

The authors would like to acknowledge the support of the Brazilian Research Agencies CNPq, CAPES, and FAPERJ and through the INCT-EIE (National Institute of Science and Technology—Smart Structures in Engineering) the CNPq and FAPEMIG. The Air Force Office of Scientific Research (AFOSR) is also acknowledged.

References

[1] D. C. Lagoudas, *Shape Memory Alloys: Modeling and Engineering Applications*, Springer, New York, NY, USA, 2008.

[2] A. Paiva and M. A. Savi, "An overview of constitutive models for shape memory alloys," *Mathematical Problems in Engineering*, vol. 2006, Article ID 56876, 30 pages, 2006.

[3] L. G. Machado and M. A. Savi, "Medical applications of shape memory alloys," *Brazilian Journal of Medical and Biological Research*, vol. 36, no. 6, pp. 683–691, 2003.

[4] M. A. Savi, M. A. N. Sá, A. Paiva, and P. M. C. L. Pacheco, "Tensile-compressive asymmetry influence on shape memory

alloy system dynamics," *Chaos, Solitons and Fractals*, vol. 36, no. 4, pp. 828–842, 2008.

[5] J. Van Humbeeck, "Damping capacity of thermoelastic martensite in shape memory alloys," *Journal of Alloys and Compounds*, vol. 355, no. 1-2, pp. 58–64, 2003.

[6] M. A. Savi and P. M. C. L. Pacheco, "Chaos and hyperchaos in shape memory systems," *International Journal of Bifurcation and Chaos*, vol. 12, no. 3, pp. 645–657, 2002.

[7] L. G. Machado, M. A. Savi, and P. M. C. L. Pacheco, "Nonlinear dynamics and chaos in coupled shape memory oscillators," *International Journal of Solids and Structures*, vol. 40, no. 19, pp. 5139–5156, 2003.

[8] D. Bernardini and G. Rega, "Thermomechanical modelling, nonlinear dynamics and chaos in shape memory oscillators," *Mathematical and Computer Modelling of Dynamical Systems*, vol. 11, no. 3, pp. 291–314, 2005.

[9] E. Sitnikova, E. Pavlovskaia, and M. Wiercigroch, "Dynamics of an impact oscillator with SMA constraint," *The European Physical Journal Special Topics*, vol. 165, no. 1, pp. 229–238, 2008.

[10] E. Sitnikova, E. Pavlovskaia, M. Wiercigroch, and M. A. Savi, "Vibration reduction of the impact system by an SMA restraint: numerical studies," *International Journal of Non-Linear Mechanics*, vol. 45, no. 9, pp. 837–849, 2010.

[11] B. C. dos Santos and M. A. Savi, "Nonlinear dynamics of a nonsmooth shape memory alloy oscillator," *Chaos, Solitons and Fractals*, vol. 40, no. 1, pp. 197–209, 2009.

[12] M. A. Savi, A. S. de Paula, and D. C. Lagoudas, "Numerical investigation of an adaptive vibration absorber using shape memory alloys," *Journal of Intelligent Material Systems and Structures*, vol. 22, no. 1, pp. 67–80, 2011.

[13] A. Paiva, M. A. Savi, A. M. B. Braga, and P. M. C. L. Pacheco, "A constitutive model for shape memory alloys considering tensile-compressive asymmetry and plasticity," *International Journal of Solids and Structures*, vol. 42, no. 11-12, pp. 3439–3457, 2005.

[14] S. A. Oliveira, M. A. Savi, and A. L. Kalamkarov, "A three-dimensional constitutive model for shape memory alloys," *Archive of Applied Mechanics*, vol. 80, no. 10, pp. 1163–1175, 2010.

[15] R. A. A. Aguiar, M. A. Savi, and P. M. C. L. Pacheco, "Experimental and numerical investigations of shape memory alloy helical springs," *Smart Materials and Structures*, vol. 19, no. 2, Article ID 025008, 9 pages, 2010.

[16] M. A. Savi and A. Paiva, "Describing internal subloops due to incomplete phase transformations in shape memory alloys," *Archive of Applied Mechanics*, vol. 74, no. 9, pp. 637–647, 2005.

[17] A. P. Baêta-Neves, M. A. Savi, and P. M. C. L. Pacheco, "On the Fremond's constitutive model for shape memory alloys," *Mechanics Research Communications*, vol. 31, no. 6, pp. 677–688, 2004.

[18] J. Lemaitre and J. L. Charboche, *Mechanics of Solid Materials*, Cambridge University Press, Cambridge, UK, 1990.

[19] M. A. Savi, A. Paiva, A. P. Baêta-Neves, and P. M. C. L. Pacheco, "Phenomenological modeling and numerical simulation of shape memory alloys: a thermo-plastic-phase transformation coupled model," *Journal of Intelligent Material Systems and Structures*, vol. 13, no. 5, pp. 261–273, 2002.

[20] J. A. Shaw and S. Kyriakides, "Thermomechanical aspects of NiTi," *Journal of the Mechanics and Physics of Solids*, vol. 43, no. 8, pp. 1243–1281, 1995.

[21] S. H. Yoon and D. J. Yeo, "Experimental investigation of thermomechanical behaviors in Ni-Ti shape memory alloy," *Journal of Intelligent Material Systems and Structures*, vol. 19, no. 3, pp. 283–289, 2008.

[22] P. C. C. Monteiro Jr., M. A. Savi, T. A. Netto, and P. M. C. L. Pacheco, "A phenomenological description of the thermomechanical coupling and the rate-dependent behavior of shape memory alloys," *Journal of Intelligent Material Systems and Structures*, vol. 20, no. 14, pp. 1675–1687, 2009.

[23] M. Ortiz, P. M. Pinsky, and R. L. Taylor, "Operator split methods for the numerical solution of the elastoplastic dynamic problem," *Computer Methods in Applied Mechanics and Engineering*, vol. 39, no. 2, pp. 137–157, 1983.

Hindawi Publishing Corporation
Shock and Vibration
Volume 2014, Article ID 135767, 14 pages
http://dx.doi.org/10.1155/2014/135767

Research Article

Vibration Mitigation without Dissipative Devices: First Large-Scale Testing of a State Switched Inducer

Daniel Tirelli

European Laboratory for Structural Assessment (ELSA), Joint Research Centre of the European Commission, Italy

Correspondence should be addressed to Daniel Tirelli; daniel.tirelli@jrc.ec.europa.eu

Received 15 July 2013; Accepted 10 March 2014; Published 12 August 2014

Academic Editor: Miguel M. Neves

Copyright © 2014 Daniel Tirelli. This is an open access article distributed under the Creative Commons Attribution License, which permits unrestricted use, distribution, and reproduction in any medium, provided the original work is properly cited.

A new passive device for mitigating cable vibrations is proposed and its efficiency is assessed on 45-meter long taut cables through a series of free and forced vibration tests. It consists of a unilateral spring attached perpendicularly to the cable near the anchorage. Because of its ability to change the cable dynamic behaviour through intermittent activation, the device has been called state switched inducer (SSI). The cable behaviour is shown to be deeply modified by the SSI: the forced vibration response is anharmonicc and substantially reduced in amplitude whereas the free vibration decay is largely sped up through a beating phenomenon. The vibration mitigation effect is mainly due to the activation and coupling of various vibration modes, as evidenced in the response spectra of the equipped cable. This first large-scale experimental campaign shows that the SSI outperforms classical passive devices, thus paving the way to a new kind of low-cost vibration mitigation systems which do not rely on dissipation.

1. Introduction

Resonances of slender structures such as bridges, towers, or cables are usually mitigated by dampers of various types or/and dynamic absorbers [1–7]. In the case of cables, also crossties are sometimes used, but they totally change the original characteristics of the system [8]. Occasionally, these passive devices may not be sufficient and are then substituted by active or semiactive devices. All existing passive devices, including nonlinear energy sinks (NES) [9–13], are based on the same principle: part of the kinetic energy is transferred from the structure to the device where it is dissipated.

An original strategy of vibration mitigation is proposed which consists in attaching a unilateral spring perpendicularly to the cable near the anchorage. Because of its ability to change the cable dynamic behaviour through intermittent activation, this new passive device has been called state switched inducer (SSI). The scope of the present work is to assess the efficiency of the proposed device through large-scale testing and to understand how it operates. In fact, unlike existing passive devices, the SSI cannot mitigate vibrations through energy dissipation since it is purely elastic. A good understanding of the phenomena involved is essential for optimizing the device and identifying its limitations.

This paper is organised as follows. In Section 2, the SSI concept is explained and its effect on the cable behaviour is anticipated by using some established properties of nonlinear dynamic systems. Then, the experimental campaign is described with special emphasis on the difficulties arising from the very nature of the system. In Sections 4 and 5, a few representative free and forced vibration tests are presented and analysed. The observed behaviour of the equipped cable is tentatively interpreted in Section 6, by means of an "equivalent" SDoF bilinear oscillator. Finally, the SSI optimisation is addressed in Section 7 where an empirical formula for the most efficient switching position is proposed and fairly verified experimentally.

2. The State Switched Inducer (SSI)

2.1. Basic Concept. Structural resonances are due to the superposition of travelling waves. In the case of linear structures, this superposition results in a stationary wave. Since travelling waves are symmetric, each reflected wave, at the anchor of a cable, for example, superposes perfectly with the incident one, giving a linear increment of the resonant amplitude (Figure 1(a)). This is why any resonance needs

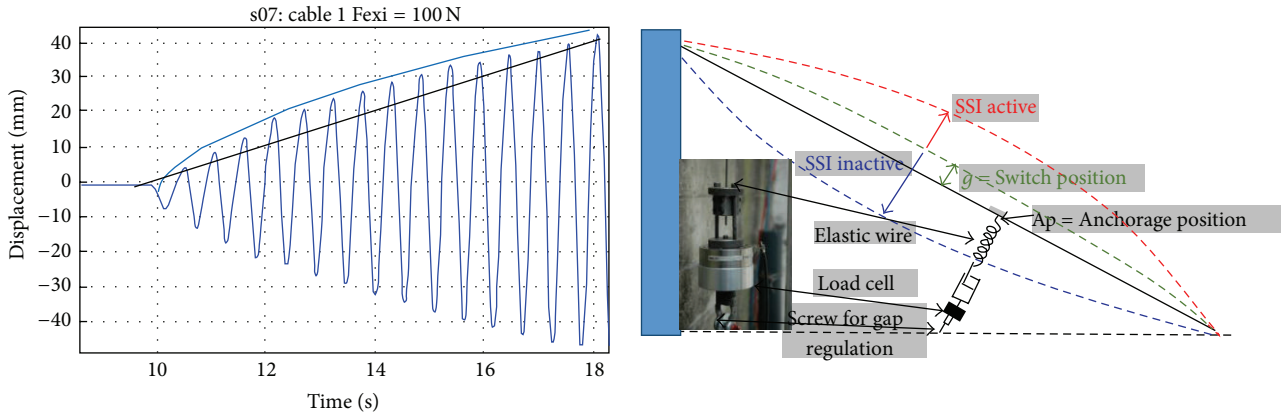

(a) (b)

Figure 1: (a) Cable resonance with low damping (blue curve fitting); (b) SSI principle.

a minimum number of excitation cycles to develop, possibly up to a dangerous level.

Now, if travelling waves are not perfectly symmetric, incident and reflected waves will not perfectly superpose. The amplitude increment will be smaller and the resonance phenomenon is reduced. Asymmetric travelling waves can be obtained if the structure is in one dynamic state S (stiffness K and mass M) for half a period and in another dynamic state S' (stiffness K' and possibly mass M') for the successive (nearly) half of the period. In a cable, this state switching can be easily achieved by attaching a unilateral spring of stiffness K_s between the cable and the ground or the deck (Figure 1(b)). This explains the name given to the proposed device: state switched inducer (SSI).

A linear structure equipped with a SSI becomes a bilinear oscillator, a system extensively studied in the literature. A bilinear oscillator admits more basins of energy (peaks) in the high frequency range than the corresponding linear oscillator. This property naturally yields a positive effect of the SSI: according to the Parseval theorem, conservative systems receiving the same input energy have the same integral in the frequency domain; thus, if peaks are more numerous for the nonlinear oscillator, their amplitude and thus the resonances are smaller than those for the corresponding linear oscillator.

Another interesting property of the SSI is the sudden change of dynamic state at the switch time. Any such nonlinear behaviour (in electricity, acoustics, mechanics, etc.) is known to generate harmonics. The amplitude of these harmonics depends on the degree of nonlinearity introduced in the system, but it is generally very small with respect to the excited frequency. Thus, the proportion of energy subtracted to the main resonant mode is usually insignificant. However, if these harmonics are closed to natural modes of the structure, a substantial proportion of the energy can be transferred to them: this phenomenon is called internal resonance. Taut cables are good candidates to internal resonance since their natural modal distribution is harmonic (nth frequency = $n *$ 1st frequency) at least for the first ten modes. Internal resonances have been observed in other types of (geometrically) nonlinear system with symmetric section when the symmetry is broken [14, 15]. In particular, the energy is then shown to be distributed among several modes even if only one of them is excited.

2.2. Expected Effects. A cable equipped with a SSI is a continuous (MDoF) structure combining two nonlinearities namely, a second-order effect in the cable (smooth nonlinearity) and a unilateral contact in the SSI (piecewise nonlinearity). The dynamic behaviour of nonlinear systems is known to be complex even in the simplest case of the SDoF bilinear oscillator. In fact, depending on the time variation and amplitude of the loading, different kinds of motions, periodic, quasiperiodic, chaotic, stable, or unstable, may coexist with bifurcations leading to them. Through approximated methods, closed form solutions have occasionally been derived but only for one or two DoF systems submitted to harmonic or impulsive loading [16, 17]. In the present case, even numerical models could easily fail to produce reliable solutions since there is a huge uncertainty on the loading.

This explains why the design and assessment of the SSI have initially been addressed in a purely experimental way, taking into account the practical aspects and limitations of this type of device. Essentially, the stiffness increment due to the SSI should be acceptable for the cable anchorage. In particular, this excludes the case of an impact oscillator and leads to a weakly bilinear system ($\Delta K \ll K_c$, with K_c = Cable stiffness, and $\Delta K = (K_s + K_c)/K_c$), also extensively studied in the literature.

Cable resonances are mainly due to parametric excitations through the anchorage motion or to direct excitations by a combination of wind and rain. In both cases, the loading, usually assumed harmonic, can last from some seconds to one minute and is followed by a free decay period.

The effect of the SSI on the cable response can be inferred from published experimental and/or numerical analyses of other nonlinear systems submitted to comparable inputs. Nonlinear responses are remarkably well processed in [18–20] mainly through wavelet analysis. For the same input, while energy concentrates on one mode/frequency in linear

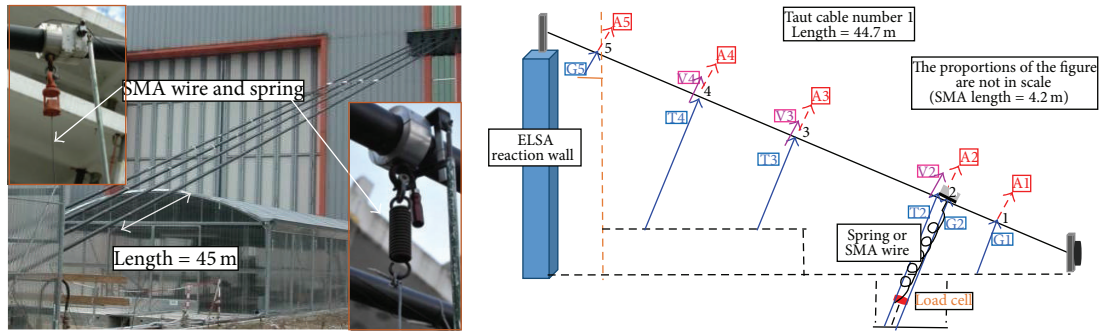

(a) (b)

Figure 2: (a) ELSA cable facility with zoomed views of the SSI attachments. (b) Transducers type and positions on the cable no. 1.

systems, the same energy is spread over different frequencies in bilinear oscillators and most other nonlinear systems. This distribution may occur contemporaneously (different frequencies at the same time) or in cascade (different frequencies at successive times). In both cases, resonances are mitigated since the highest peak in the response spectrum is capped. The energy transfer to higher modes has been evidenced in structures with nonlinear attachment [11] or presenting geometrical symmetry and light nonlinearity (e.g., plates, shells, and cymbals) and when this symmetry is slightly broken [14, 15]. A very good agreement has been found between computed and measured energy flow, even if the significance of this transfer is somehow hidden in the log graphs. This energy transfer is however essential from a vibration mitigation point of view since, at equivalent energy, vibration amplitudes are lower at higher frequency.

Whether and to which extent the SSI triggers the above-mentioned effects in the cable can be assessed by comparing the cable responses in different configurations: with SSI, without SSI (free cable) and, possibly, with the SSI spring attached permanently. In the sequel, these three cable configurations are, respectively, referred to as "SSI cable," "free cable," and "restraint cable."

3. The Test Campaign

3.1. Description of the Specimens. In the ELSA facility, four real cables of 45 meters and mass ~450 kg each are installed (Figure 2(a)). The performance of the SSI has been assessed on two of them.

(i) Cable no. 1, grouted with wax and under a tension of 250 KN, was instrumented with in-plane (vertical plane containing the cable) displacement transducers and accelerometers located at midspan, at the attachment of the SSI and in three other locations (Figure 2(b)). Since the SSI was expected to modify the modal content of the cable, the output locations were chosen on or nearby the antinodes of the first three modes. An out-of-plane accelerometer was located on the cable at the same point of the SSI attachment (7.2 m) to measure the variation of the ratio in-plane/out-of-plane acceleration (and displacement deduced).

(ii) Cable no. 2, grouted with cement and under a tension of 500 KN, was instrumented at 11 m from the bottom anchorage with one in-plane displacement transducer and four accelerometers, two in-plane and two out-of-plane. In fact, the tests performed on cable no. 1 showed that the contribution of the first three modes could be adequately measured at this particular position and that the out-of-plane cable motions were substantial. An in-plane displacement transducer was maintained at the attachment of the SSI.

In both cases, the SSI was attached to the cable at 7.2 m from the bottom anchorage and, at the other end, to a fixed foundation or to a movable steel mass of 1300 kg so that the attachment position could be changed easily along the cable. The tension in the SSI was recorded by a load cell so as to detect the switching times. The input force was applied at 10 m from the bottom anchorage and measured with a dynamometer. It is worth underlining that such an input location allows the effective excitation of any mode until the 3rd one at least.

As mentioned earlier, the SSI is a unilateral spring. In practice, it is made of a linear spring and a unilateral contact system connected in series. The unilateral contact system is shown in Figure 1(b). The load cell and the screw are required to regulate the gap (switching position) which can be set to a positive or negative value. For positive gaps (clearance), the spring is unloaded at equilibrium whereas, for negative gaps (interference), the spring is in tension at equilibrium.

Two different SSI have been tested. On cable no. 1, the SSI spring was a nitinol (nickel-titanium alloy) wire of diameter 2.5 mm and length 4.2 m (Figure 2(a), left). Initially, the wire was intended to work as a shape memory alloy (SMA) and had therefore been characterized and stabilized (Figures 3(a) and 3(b)). However, during the cable tests, the wire turned out to work simply as a super elastic spring (Figure 3(c)). Nevertheless, it is not excluded that the hysteretic behaviour of the SMA could be activated in the SSI in case of exceptional excitation (e.g., tornado or heavy storm) so that the SMA damping property at high strain (2% to 6%) could then also contribute to mitigate large amplitude vibrations. In our case, the SMA wire used was not adapted at the "high" frequencies of cables oscillations. In order to fulfil the condition of

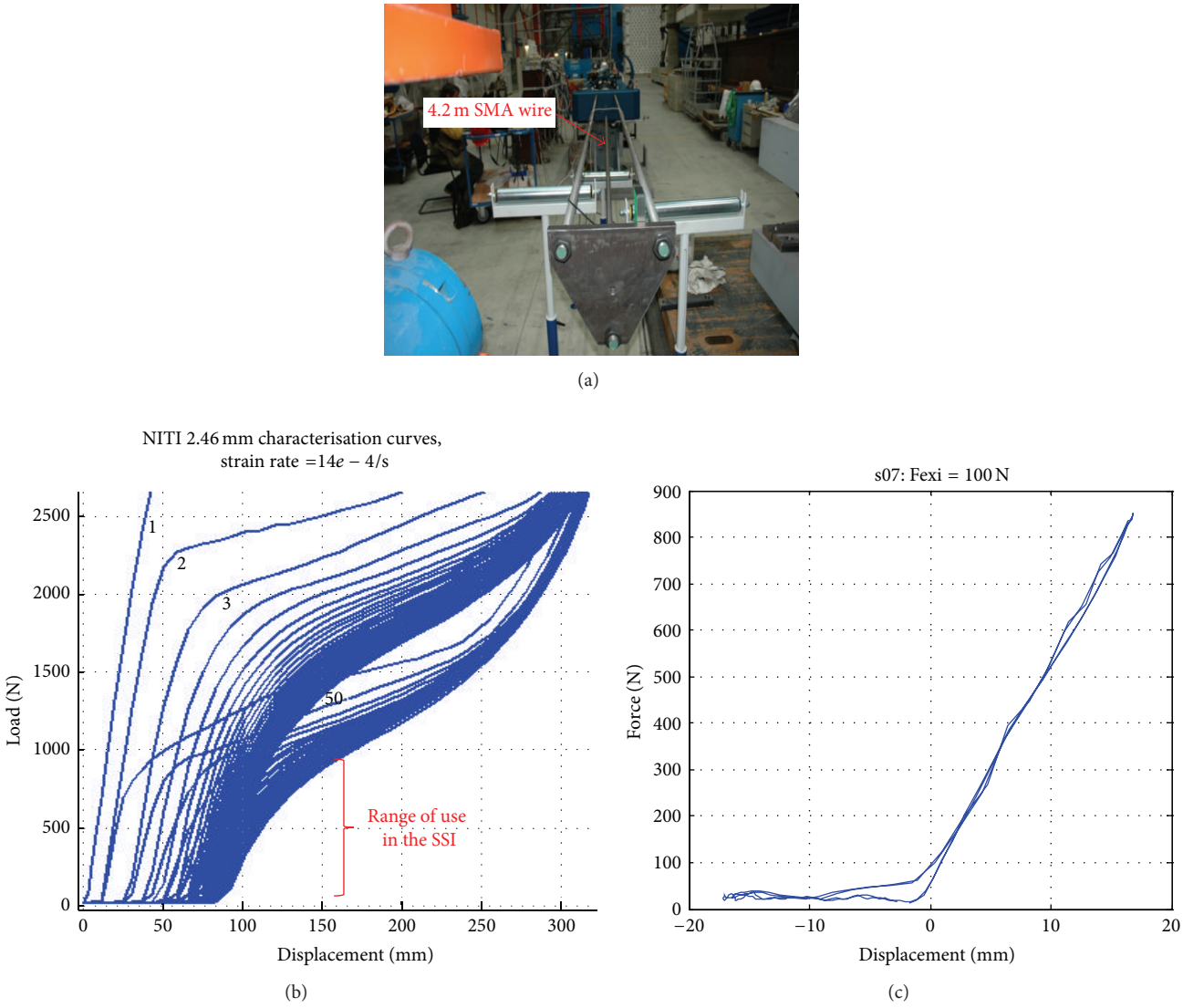

FIGURE 3: (a) SMA characterisation setup; (b) SMA training curve; (c) SMA behaviour during a cable dynamic test.

significant hysteretic dissipation, the wire type and setup must be optimized as described in [21], but it was not the aim of this work.

On cable no. 2, a classical steel spring was used in the SSI (Figure 2(a), right). Initially, the spring was connected to the unilateral system through a steel bar which had however a substantial mass likely to perturb the behaviour of the SSI. It has been subsequently replaced by a much lighter steel cable of diameter 4 mm.

Whether based on a nitinol wire or a steel spring, the SSI has a negligible mass; thus, unlike TMD and NES, it does not represent an additional DoF. Each SSI is defined by two parameters, spring stiffness and unilateral gap. Once installed on a cable, the attachment position constitutes a third parameter.

The stiffness increase induced in the cable by the SSI may be characterised by the transversal force/displacement relationship at the attachment point. It can be computed and/or measured on the equipped cable. In this latter case, the attachment point can be lifted up with a crane (Figure 4(a)) or pulled down with the gap regulation screw. The force displacement curve is directly given by the load cell and displacement transducer installed on the SSI. In Figure 4(b), the difference between the lift-up and pull-down slopes reveals a substantial relative stiffness increase for cable no. 1 ($\Delta K/K_c \approx 60\%$) which seems inconsistent with the weak bilinearity hypothesis, but this is a merely static (and local) value. In fact, static and dynamic stiffness generally differ for systems with more than one DoF. In dynamics, a more appropriate measure of the (global) stiffness increase is given by the increase of the squared fundamental frequency, which can be computed and/or measured between the free and the restraint configurations. For cable no. 1, the fundamental frequency is found to increase by 11% between the free and restraint configurations, which corresponds to a dynamic stiffness increase of 23%. For cable no. 2, the increase is

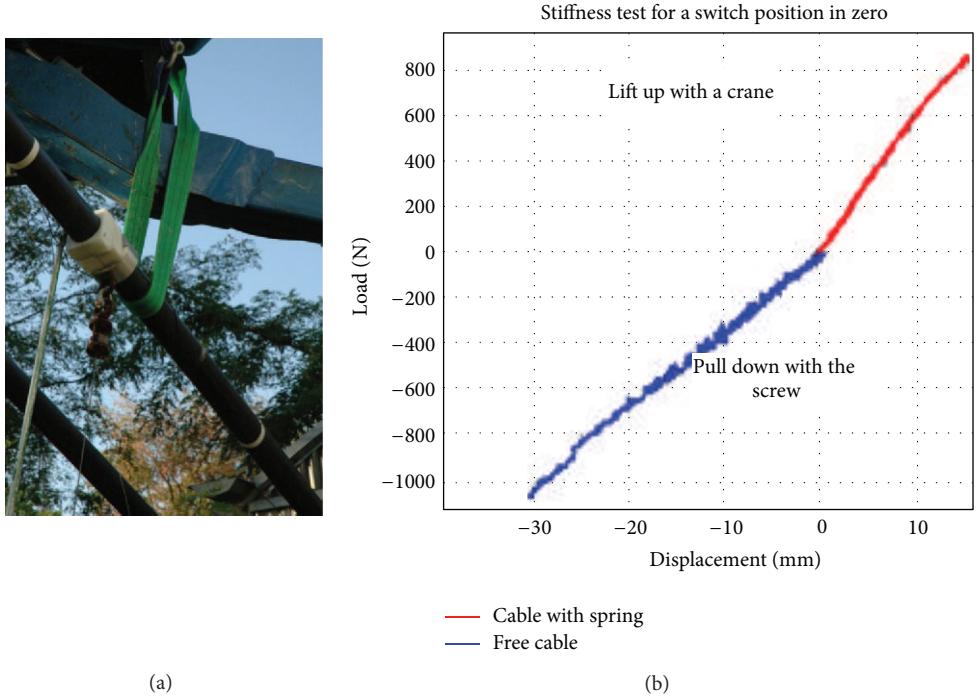

Figure 4: (a) Measurement of the static stiffness increase in cable no. 1. (b) Measured force/displacement curve.

approximately the same (+10% in frequency and thus +21% in dynamic stiffness). The weak nonlinearity hypothesis is thus reasonably verified.

3.2. Description of the Approach. The dynamic testing of the SSI cable presents specific difficulties which are absent in the other two configurations (free and restraint).

The first difficulty is to apply the most critical excitation that is to say the input inducing the largest response of the nonlinear structure and thus revealing the efficiency limit of the SSI. Since such a critical input is asymmetric (frequency alternatively tuned to each dynamic state), it is difficult to use an electrodynamic actuator also because the cable response has not the same frequency content as the input. Two types of excitation have therefore been chosen: a snap-back test which corresponds to an "autotuned" input and a manual shaking inducing resonance, a technique commonly used even for very long cables (up to 350 m) as mentioned in [22]. The loading and all cable displacements and accelerations are recorded by a dynamic data recorder (TEAC) so that critical excitations and corresponding anharmonic cable responses can be identified. During manual shaking, the input force is also processed online by a dynamic signal spectrum analyser (HP): different parameters (load frequency, maximum load per cycle, and load integration on cycles) can be checked to ensure immediately that the manual shaking is unbiased.

The second difficulty is to process and compare nonlinear outputs (SSI cable) and linear ones (free and restraint cables). The signals are processed mainly by Fourier transform with an automatic modal extraction toolbox described in [23] implemented under MATLAB. Even if some peaks in the Fourier transform of a nonlinear response do not necessarily represent actual modes, they nevertheless quantify the resonances of a fictitious linear system having the same response. Comparing the Fourier coefficients (frequencies, damping ratios) and the amplitude of the cable response in different configurations allows a better understanding of how and how much the cable vibrations are mitigated by the SSI. The SSI cable outputs are also processed in the time domain. From the recorded switching times, any SSI cable signal can be split up into two intermittent subsignals corresponding to each dynamic state. The frequency and damping evolution of each subsignal are then computed by a particular implementation of the logarithmic decrement method allowing processing asymmetric signals as described in [24].

The third difficulty is to deal with tricky phenomena inherent to nonlinear dynamics such as instabilities and bifurcations. To avoid experimental errors, spurious effects, and misinterpretations, the tests have been repeated for many different configurations (cable tension and grouting, SSI device, input/output locations, loading intensity, etc.) and, as mentioned before, the nonlinear outputs have also been processed with different methods, both in the time and frequency domains. Since all results were checked to be consistent, only a few selected tests are presented to support the drawn conclusions.

4. Free Vibration Tests

4.1. Effect of the SSI. The same snap-back test (sudden release of 700 N at 10 m from the lower anchorage) has been repeated in the three configurations of cable no. 1. The displacement

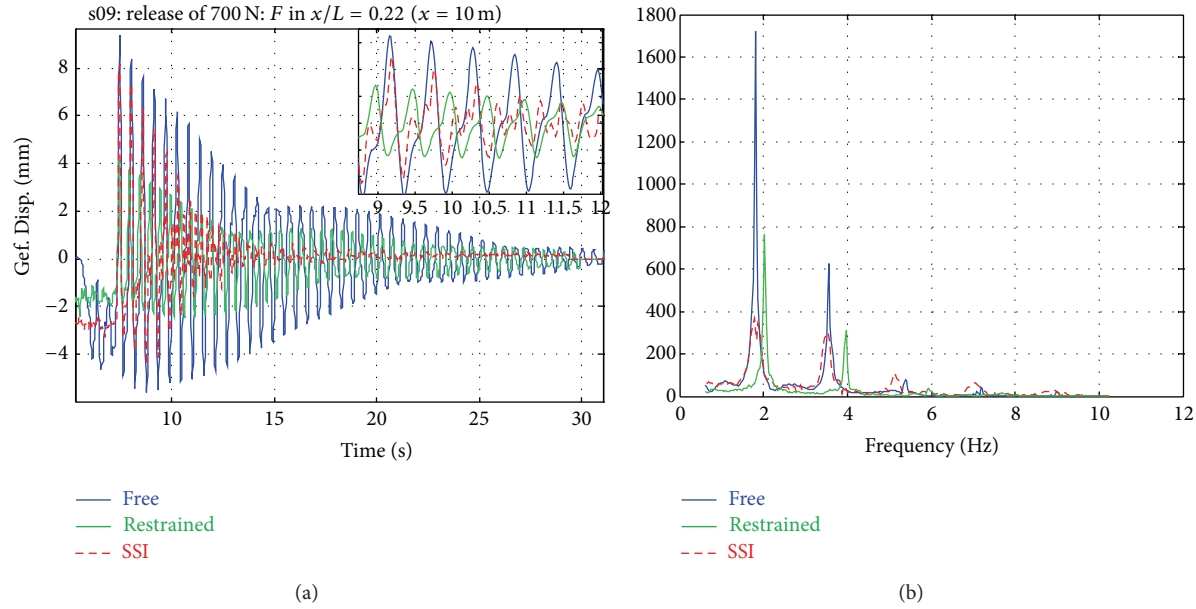

FIGURE 5: (a) Displacement and (b) associated spectrum at 37.8 m on the free, constraint, and SSI cable no. 1.

signals recorded at 37.8 m of the lower anchorage (~30 m from the SSI attachment) and the corresponding displacement spectra are displayed in Figure 5.

The initial displacement is the same for the free (blue) and SSI (green) cables because the spring is then inactive while it is lower for the constraint (red) cable because the spring is always active. In the free and restraint cables, the vibrations fade out very slowly but at a similar rate whereas, in the SSI cable, they fade out much faster especially at the beginning. In fact, after only 7 to 8 seconds, the vibrations of the SSI cable are already damped (more than 25 s for free and restraint cables) and remain the lowest in amplitude. The response spectra for the free and restraint cables are more or less proportional. In both cases, the first mode is largely dominant, but the higher modes are also visible. However, because of its higher dynamic stiffness (+23%) and fundamental frequency (+11%), the restraint cable exhibits a reduced spectrum with a shift to the right. Conversely, the response spectrum for the SSI cable is markedly different in amplitude: the first and second modes are substantially lower in amplitude and are approximately at the same level. This confirms the capping of the fundamental frequency through energy transfer towards the higher modes, mainly from the first to the second. In the time domain, this effect looks like a strong damping enhancement, but a closer look at the signals (zooming view in Figure 5(a)) confirms that the vibration reduction is actually due to the strong activation of higher modes, mainly the second one.

Tests repeated on cable no. 2 (Figure 6) are similar but show a slightly weaker effect of the SSI which might be due to the lower relative stiffness of the SSI or to less suitable value of the switch position. Nevertheless, the principle is confirmed: SMA hysteretic behaviour is not required at all in opposition to what is reported in [25].

4.2. Importance of the Output Location. The test of Figure 5 is now represented at midspan (22.5 m) in Figure 7. The SSI effect (apparent damping enhancement) is also visible and, more generally, is visible along the entire cable, as confirmed by the other three output locations installed on cable no. 1. However, the amplitude and frequency content of the cable motion are known to vary along the cable in relation to the nodes and antinodes of the activated modes. At 37.8 m from the lower anchorage, the four first modes are well detectable whereas, at midspan, only odd modes can be detected. This explains the difference observed between the two sets of signals of Figures 5 and 7.

4.3. Equivalent Stiffening and Damping of the SSI. Since the SSI appears to both reduce the vibration amplitude and increase the damping, its effect can be quantified by computing and comparing the equivalent dynamic stiffness and damping ratio of the cable in the different configurations. The equivalent dynamic stiffness is computed as a mean of the modal stiffness weighted by the modal participation. Likewise, the equivalent damping ratio is computed as a mean of the modal damping ratios weighted by the modal participation.

In practice, the modal parameters are extracted from acceleration signals because of their quality at high frequency. Free vibration tests are particularly suitable for this task because the results are not perturbed by input irregularities.

In Figure 8, the results are shown for the snap-back test carried out on cable no. 2 in the restrained and SSI configurations. The equivalent stiffness and damping have been derived from the in-plane acceleration signal recorded at 11.1 m from the lower anchorage, that is, between nodes of modes 4 and 5. The modal parameters have been extracted for 18 peaks in a frequency range of 0–45 Hz with a software of

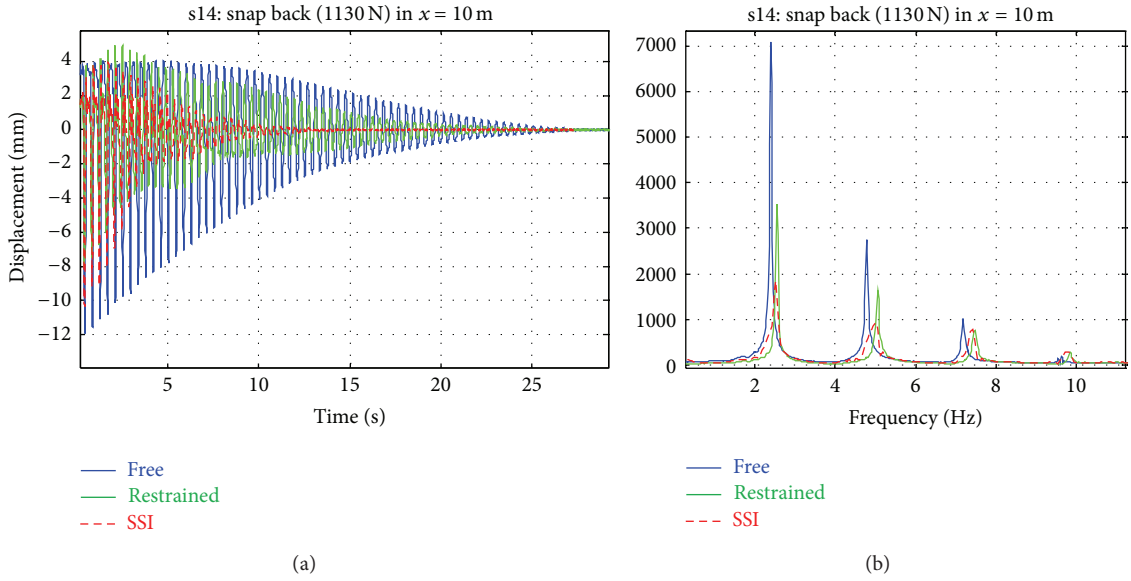

FIGURE 6: (a) Displacement and (b) associated spectrum at 7.2 m on the free, constraint, and SSI cable no. 2.

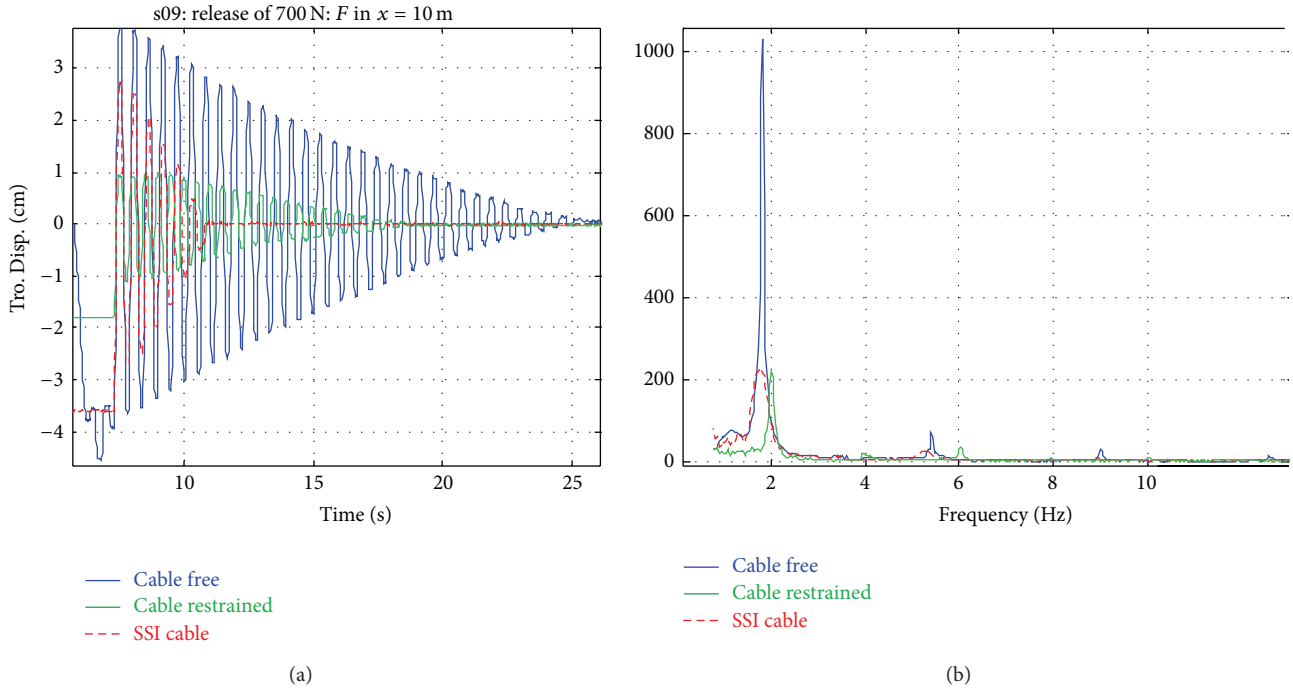

FIGURE 7: (a) Displacement and (b) associated spectrum at 22.5 (midspan) on the free, constraint, and SSI cable no. 1.

automatic modal extraction implemented for the fast impact hammer testing method (FIHT) described in [23] under MATLAB. The positive effect of the SSI is substantial even if it refers to the less favorable case since the difference between the restrained and SSI responses of cable no. 2 is the least one and the switch position is not optimized for this case.

5. Forced Vibration Tests

5.1. Effect of the SSI. Cable no. 1 has been submitted to forced vibration tests in the free, restrained, and SSI configurations. A rope was attached to the cable at 10 m from the anchorage and was manually pulled down, initially at the estimated frequency of the fundamental mode or of a higher mode.

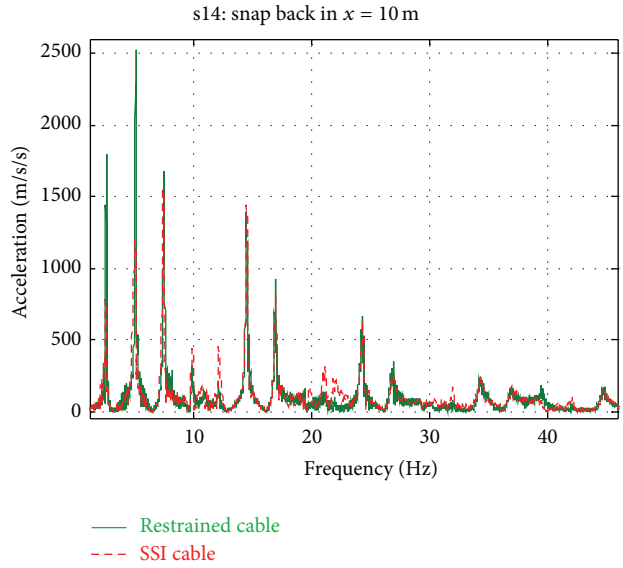

Mean values for 18 freq. peaks	Equivalent stiffness	Equivalent damping
Restrained cable	1.63	0.37%
SSI cable	2.69	0.98%
Ratio = SSI/restrained	165%	264%

Figure 8: Equivalent stiffness and damping for the SSI cable no. 2 as compared to the restrained configuration.

Then, the shaking was adapted so as to fit the response frequency; that is, the pulling force was applied only during the downward motion of the rope. The pulling force, measured with a dynamometer, could be 100 N or 200 N and was applied for either a short (5 s) or a long period (40 s). In the latter case, the steady state response could be reached.

The effect of the SSI is again assessed by comparing the cable responses under forced vibrations in the free, restrained, and SSI configurations. Of particular interest are the amplitude and frequency of the steady state response. In Figure 9, the responses of the free and SSI cable no. 1 are compared for a 40 s loading period at 100 N on the first mode. The amplitude of the steady state response is drastically reduced by the SSI but only in displacement whereas the response in acceleration is increased by the SSI, especially for negative values, that is, when the SSI is activated. Again, this is due to a transfer of energy from the fundamental mode to the higher modes as evidenced on the acceleration spectrum in Figure 9; the first mode is tremendously reduced while the 2nd and 3rd modes are enhanced. Similar results obtained with an input on the 2nd mode prove the robustness of the device: energy is always transferred from the excited mode to the higher modes with however different sharing among the modes.

5.2. Equivalent Damping Estimate. After the shaking period, the response of the cable was still recorded. This free decay test differs from the snap-back test by the initial conditions: the snap-back test starts from a static configuration under a given load while the free decay test starts from the dynamic (modal) configuration. However, it can be processed as in Section 4.3 to derive another equivalent stiffness and damping.

The SSI operates as long as the displacement amplitude is higher than the absolute value of the gap. For smaller displacement amplitudes, the SSI cable oscillates as the free cable (resp., restrained cable) if the gap is positive (resp., negative). In Figure 10, the first graph shows the output of a short period of shaking on cable no. 1 in the free, restrained, and SSI configurations. The input force is 100 N, the mode excited is the first one, and the output position is at midspan. Since the SSI gap was set to zero, the device works during all the decay period but is not very efficient. The second graph refers to the free decay following a long period of shaking and an output position at 7.2 m. The SSI gap was set to 1.6 mm. For clarity, only envelopes of displacements are reported in the amplitude range 10–35 mm. The SSI is particularly efficient in damping the vibrations as long as the amplitude is higher than 15 mm. Below this amplitude value, the damping is less important and when the amplitude falls below the gap position, the damping is the same as that for the restrained cable for this switch position chosen.

6. Tentative Explanation of the SSI Effect

The SSI concept relies on the mismatch (detuning) between the excitation and the response. In fact, a sinusoidal input force at a given frequency induces an unharmonic response of a cable equipped with a SSI device, owing to the sudden stiffness change at the switching times. Hereafter, this detuning effect is tentatively explained and quantified on the basis of a SDoF bilinear model of the equipped cable.

A cable equipped with a SSI device is a MDoF bilinear system. According to [16, 26], the most critical sinusoidal inputs for such systems are obtained for the so-called bilinear frequencies. The ith bilinear frequency f_i^b is approximately the harmonic average of the ith free and restrained frequencies, f_i^- and f_i^+; that is,

$$f_i^b = \frac{2 f_i^- f_i^+}{f_i^- + f_i^+}. \quad (1)$$

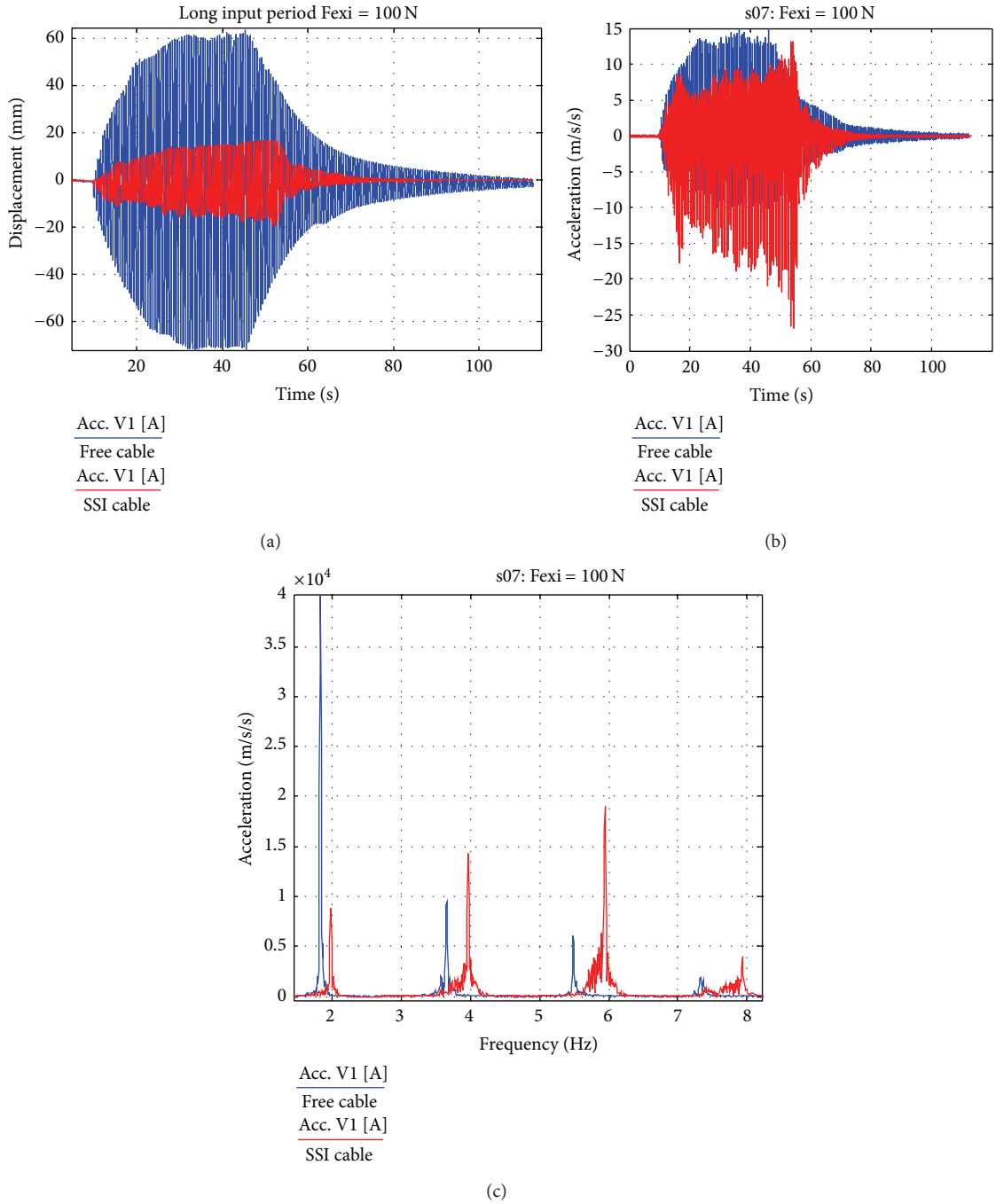

FIGURE 9: Displacement (a), acceleration (b), and acceleration spectrum (c) for the free and SSI cable no. 1 ($F = 100$ N on 1st mode).

This formulation is available for a zero clearance; the exact formulation for a nonzero clearance is more complex and can be found in [26]. However, depending on the switch position, f_i^b may vary in the $[f_i^-, f_i^+]$ range. Similarly, the ith mode shape is a combination of the ith free and restrained mode shapes and varies with the switch position. Basically, bilinear frequencies/modes are to bilinear systems what eigenfrequencies are to linear systems. However, bilinear frequencies/modes depend not only on the system characteristics (masses, stiffness, and switching position) but also on the input amplitude. Moreover, for increasing amplitude, completely different mode shapes may appear by bifurcation for the same value of the bilinear frequency. These mode shapes combine free and restrained mode shapes of different order (e.g., f_i^- and f_{i+1}^+). This phenomenon, called internal resonance, is typical of nonlinear systems.

During any type of test with varying amplitude (e.g., free decay after a snap-back or forced vibrations), the response of a MDoF bilinear system is therefore extremely complex since it is a varying combination of varying frequencies/modes.

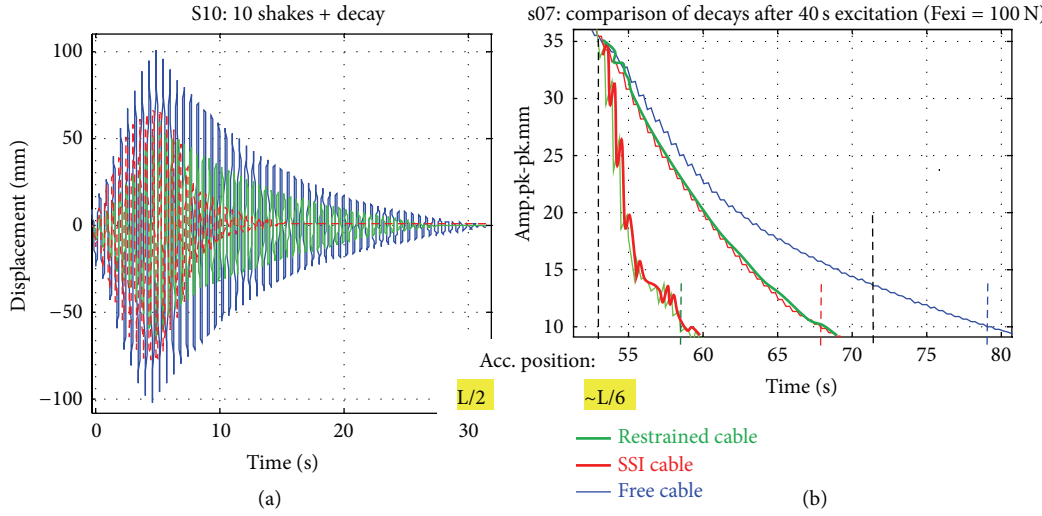

Figure 10: SSI damping effect during a free decay after a short (a) or long (b) loading period on mode number 1.

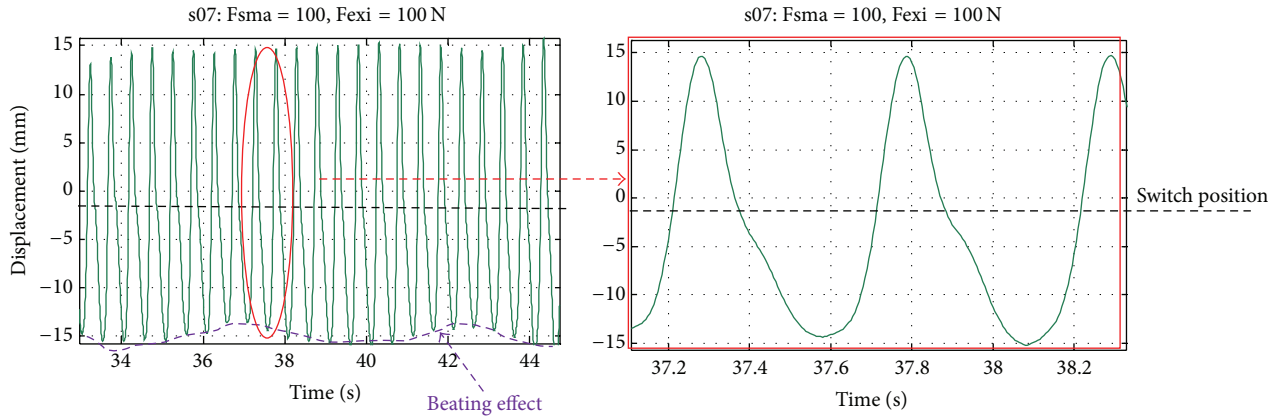

Figure 11: Nearly steady state response of SSI cable no. 1 at 7.2 m during a long shaking period.

In particular, the influence of the switching position evolves constantly, which makes any optimisation attempt difficult. The task is much easier in the case of a test (or test period) at nearly constant amplitude as the one shown in Figure 11 where, despite a slight beating, the cable displacement at the SSI attachment can be considered periodic of period close to f_1^b (~2 Hz in our case). During a period, the displacement appears distinctly composed of two parts separated by the switching position: the bottom part (SSI spring inactivated) recalls a sinusoidal curve of frequency f_1^- (=1.83 Hz in our case) whereas the upper displacement (SSI spring activated) is rather close to a sinusoidal curve of frequency f_2^+ (=4.07 Hz in our case). Therefore, the steady state response is actually an internal resonance of the mode no. 1 (free) and of the mode no. 2 (restrained). Its shape is not the composition of two half sines but the superposition of several harmonics giving a non sinusoidal and asymetric wave.

To quantify the detuning effect due to this internal resonance, a bilinear SDoF system is considered which is supposed to reproduce the observed steady state response of the SSI cable under forced vibrations. To this end, the SDoF system includes the main "ingredients" of the observed response that is to say the free mode 1 and restrained mode 2. The characteristics (mass, main stiffness, spring stiffness, and switch position) are thus chosen so that

(i) the SDoF free frequency coincides with the first free cable frequency f_1^-;

(ii) the SDoF restrained frequency coincides with the second restrained cable frequency f_2^+;

(iii) a small damping ratio (measured on the first free mode) is added through a linear dashpot;

(iv) the switching position measured from the equilibrium position can be varied.

The steady state response of this SDoF under a sinusoidal input force of 100 N has been computed for switching positions ranging from −4 cm to +4 cm and for input frequencies ranging from 1.5 Hz to 4.5 Hz, thus including the free and restrained mode frequencies. The numerical detuning effect

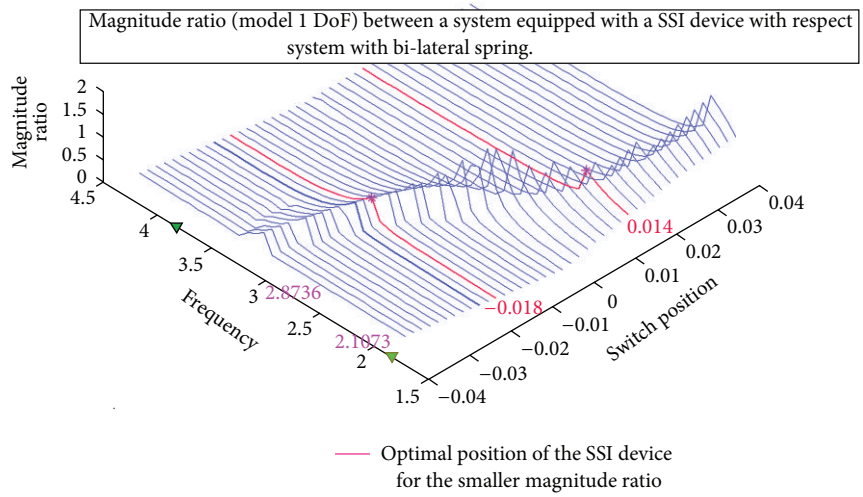

Figure 12: Detuning effect computed on a SDoF model in function of the switch position and input frequency.

is then computed by dividing the amplitude of this response by the amplitude of the restrained SDoF response under the same input. A 3D plot of the results obtained is shown in Figure 12.

The computed detuning effect is substantial for the chosen free and restrained frequencies. Other computations performed for closer free and restrained frequencies (e.g., first free and first restrained) lead to much lower detuning effects. It can be noticed that very small increment in frequency and chiefly in time (>20000 iterations/points of the curve) must be used to obtain accurate results.

The largest detuning effect is obtained for two particular switching positions of opposite sign: the negative one is slightly more effective than the positive one and, for the most critical frequency, gives a reduction of 18% with respect to the restrained system and a much higher reduction with respect to the free system. However, both computed values underestimate the experimental measurements on the cable. A possible explanation could be that the SDoF system does combine the appropriate modes in a nonlinear way but inappropriately: the mode shape associated with the bilinear frequency does not result from an internal resonance phenomenon. This is why the resonant frequency varies continuously with the switching position whereas, in the experiment, it remains almost constant for a wide range of switching positions.

7. Optimisation of the Switch Position

Independent of the input frequency, the proposed SSI device has always been found to mitigate the cable vibrations in a more or less effective way though. In particular, the SSI efficiency appears to depend on the form and amplitude of the input signal. The problem thus remains to design the SSI device that is to say to determine its most appropriate characteristics to mitigate potentially dangerous vibrations induced in a given cable by a set of possible excitations. In the following, an empirical design formula is proposed which gives the best switching position, once all other parameters (cable characteristics, SSI stiffness, and maximum vibration amplitude) are fixed.

From the experimental results obtained so far, the following conclusions can be drawn.

(i) A stiffening of the cable is noticeable mainly during the excitation phase and occurs through energy transfer from the excited mode to higher modes. The cable motions are reduced in displacement but not in acceleration.

(ii) An increase of the cable damping ratio is noticeable during the free decay phase and occurs through the similar energy transfer phenomenon.

(iii) In weakly bilinear MDoF systems, the ith bilinear frequency resulting from the combination of the ith free and restrained modes is accompanied by sub- and superharmonics which may activate higher bilinear frequencies and trigger internal resonances between free and restrained modes of different orders.

(iv) Under sinusoidal input, the detuning effect is substantial if internal resonances are activated.

The aforementioned effects increase with the increasing nonlinearity and also with the increasing velocity at the switch time. For a given spring stiffness K_s and a given SSI attachment position d (far from the nodes of the first cable modes), the increase ΔK_i of the dynamic stiffness K_i for the ith mode can be derived from a Galerkin approximation [27] as follows:

$$\Delta K_i = K_s \cdot \sin^2\left(\frac{i\pi x_d}{L}\right), \tag{2}$$

where L is the cable length and x_d is the distance of the device attachment from the lower anchorage. However, this stiffness increase should remain small to avoid excessive energy transfer to the cable anchorages. The design of the SSI device thus reduces to the optimisation of the switch position SP for the maximum amplitude A_i allowable on the ith cable

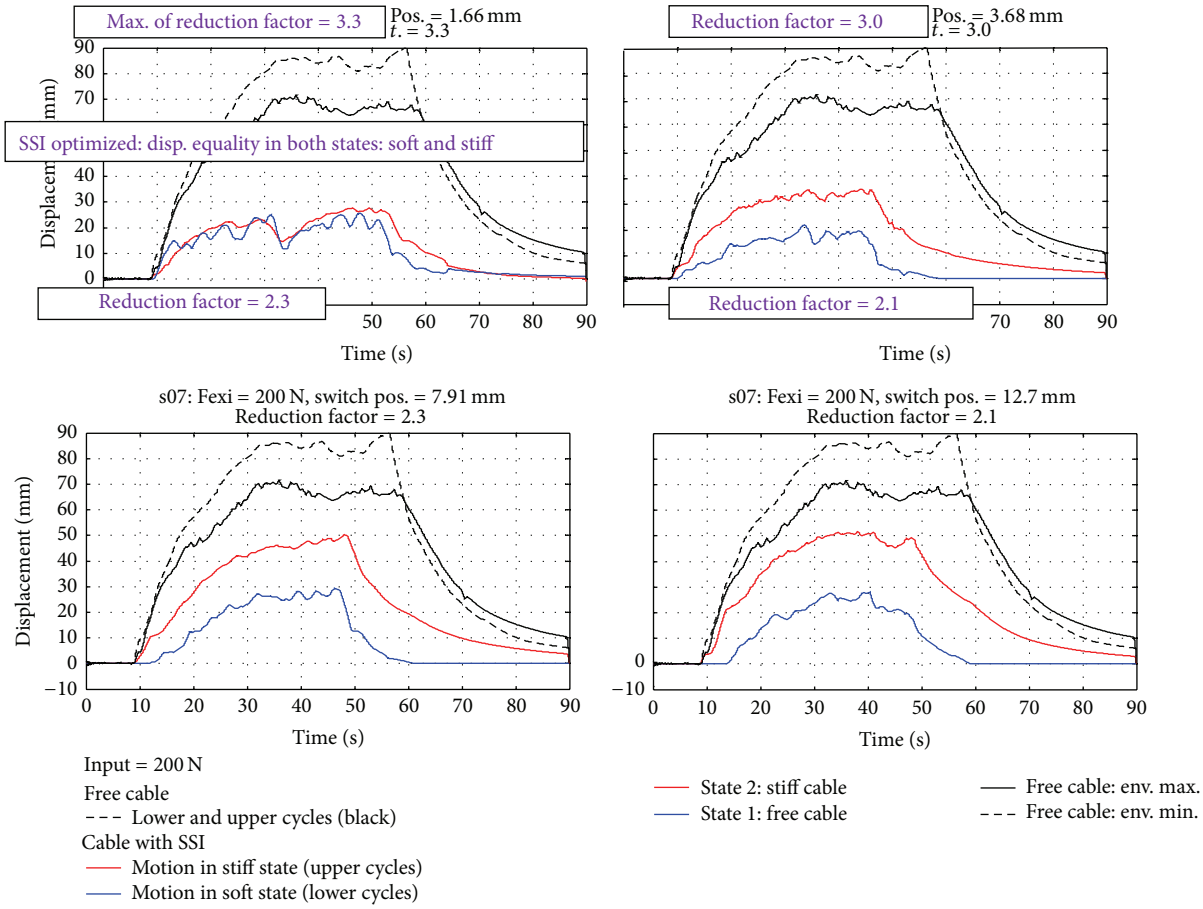

FIGURE 13: Variation of the reduction factor with respect to the switch position (4 different tensions of the spring).

mode (provided by the bridge designer) and a given stiffness increase ΔK_i. For a given spring (ΔK_i) and a given amplitude total A_i, the amplitude is distributed between the two states ($s1$: soft, $s2$: stiff) of the cable and it reads as follows:

$$A_i = A_{s1} + A_{s2}. \tag{3}$$

Two effects contribute to obtain a smaller displacement:

(1) the maximum transfer of energy to higher harmonics: to transfer the maximum of energy on the harmonics of the mode governing the motion, the velocity of the cable has to be the maximum at the switch event (impulse dF/.dt maximum). The velocity at the switching time is the highest when the switch position is at equilibrium of the cable (SP = 0). It means that the displacement in the stiff state ($s2$) is lightly (because ΔK_i is small) smaller than in the soft state ($s1$);

(2) the critical sinusoidal input produces an increment of displacement by resonance effect in each of the states of the cables. To obtain the smaller increment of the displacement in both states, the amplitudes A_{s1} and A_{s2} of the signal in each state must be equal. If the stiffness is lightly different in each state, the switch position must be an interference [26] which means that the spring will have a small tension (SP = $-x$) at the equilibrium position. To calculate it, we start from the switch position in zero; if we applied the same force on the cable in each direction (or each state), we have

$$K_i A_{s1} = (K_i + \Delta K_i) \cdot A_{s2}. \tag{4}$$

It appears clearly that the displacement amplitude A_{s1} is greater than A_{s2} of the quantity 2.SP = $(\Delta K_i/K_i) \cdot A_{s2}$. To obtain the same amplitude in each state, it is sufficient to stretch the spring of a value equal to the switch position:

$$\text{SP} = \frac{\Delta K_i}{2K_i} \cdot A_{s2}. \tag{5}$$

Then, using (3) and (4) to substitute A_{s2}, we obtain the switch position which gives the equal displacement in each state:

$$\text{SP} = \frac{\Delta K_i}{2K_i + \Delta K_i} \cdot A_i. \tag{6}$$

It is clear from (6) that the switch position SP is amplitude dependent for this second effect. Now, to reach the best

efficiency of the device, we should respect the optima of the two effects. Equation (6) shows that SP is a small proportion of the amplitude maximum A_i.

In the example of Figure 11, the amplitude A_i is about 30 mm for an increment of stiffness ΔK_i equal to 23%. The switch position is therefore equal to 10% of the amplitude which is about 3 mm. It is a small value and in that case it could be adjusted with the value of SP = 0 of the first effect (energy transfer) to benefit of both optima, at the half sum (3 and 0) =1.5 mm.

This value gives the best SSI effect only on the given amplitude of a given mode. For other modes and/or other amplitudes of the same mode, the SSI effect is lower but remains positive.

The validity of these two assumptions has been checked by repeating the same forced vibration test with four different values of the switching position. In Figure 13, the results confirm that the greater displacement reductions with input on mode 1 are obtained for the switch position SP given by (6) and SP = 0.

The optimum is for SP = 1.6 mm. The same tests were conducted with a different level of excitation, not included in this paper, showing again that when the two displacements in each state are equal the reduction is optimal.

Even these results are in agreement with the previous assumptions; much more cases should be studied to better understand the behaviour of the cable equipped with the SSI device.

8. Conclusion

The state switched inducer (SSI) is a unilateral spring which slightly stiffens in an intermittent way the structure it is connected to. The equipped structure thus becomes a bilinear oscillator. An experimental campaign conducted on two full-scale cables has shown that SSI devices reduce significantly the steady state vibration amplitude under forced vibrations and shorten drastically the free decay period. To the author's best knowledge, it is the first time that cable resonances could be mitigated by a passive device without involving any dissipation process but relying exclusively on some established properties of nonlinear dynamic systems. Thanks to the specific harmonic modal distribution of cables, SSI devices trigger a substantial transfer of energy from the excited mode to the higher modes through the so-called internal resonances.

The SSI efficiency depends on the expected vibration amplitude. An empirical formula for optimising the SSI switching position for a given vibration amplitude has been proposed and fairly verified experimentally. However, further work based on numerical models with two or more DoFs is needed to characterize more accurately the SSI behaviour and to improve its efficiency.

This first large-scale experimental campaign shows that the SSI outperforms classical passive devices and opens the way to a new kind of vibration mitigation systems. Last but not least, SSI devices are cheap, very simple to install, and easy to maintain. However, before any commercial used, further testing is recommended so as to exclude undesirable effects such as unexpected response to irregular excitation (wind/rain) or large out-of-plane vibrations or whirling amplitudes.

Conflict of Interests

The author declares that there is no conflict of interests regarding the publication of this paper.

Acknowledgments

The research leading to these results has received funding from the European Community's Seventh Framework Program (FP7/2007–2013). The author expresses his gratitude to the Scientific Committee of the Institute for the Protection and the Security of the Citizen (IPSC) for supporting this exploratory research project and to the European Science Foundation (ESF) for supporting the Project Shape Memory Alloys to Regulate Transient Responses in Civil Engineering (SMARTER) during which the first experiments of this paper were carried out. The author thanks several colleagues of the ELSA Laboratory for the discussions and the different point of views of this complex mechanical oscillator. The author is grateful to Pr. V. Torra (Universitat Politècnica de Catalunya, Barcelona, Spain) for the collaboration during the Project SMARTER from which the first idea of a SSI device was born.

References

[1] F. Weber, J. Hogsberg, and S. Krenk, "Optimal tuning of amplitude proportional Coulomb friction damper for maximum cable damping," *Journal of Structural Engineering*, vol. 136, no. 2, pp. 123–134, 2010.

[2] F. Casciati, L. Faravelli, and C. Fuggini, "Cable vibration mitigation by added SMA wires," *Acta Mechanica*, vol. 195, no. 1–4, pp. 141–155, 2008.

[3] X. Y. Wang, Y. Q. Ni, J. M. Ko, and Z. Q. Chen, "Optimal design of viscous dampers for multi-mode vibration control of bridge cables," *Engineering Structures*, vol. 27, no. 5, pp. 792–800, 2005.

[4] G. Cazzulani, F. Resta, and F. Ripamonti, "Active modal tuned mass damper for smart structures," *Engineering Letters*, vol. 19, no. 4, p. 297, 2011.

[5] J. P. Ou and H. Li, "The state-of-the-art and practice of structural control of civil structures for hazard mitigation in mainland," in *Proceedings of the 14th World Conference on Earthquake Engineering*, Beijing, China, 2008.

[6] H. Yamaguchi and Md. Alauddin, "Control of cable vibrations using secondary cable with special reference to nonlinearity and interaction," *Engineering Structures*, vol. 25, no. 6, pp. 801–816, 2003.

[7] B. F. Spencer and S. Nagarajaiah, "State of the art of structural control," *Journal of Structural Engineering*, vol. 129, no. 7, pp. 845–856, 2003.

[8] L. Caracoglia and N. P. Jones, "Passive hybrid technique for the vibration mitigation of systems of interconnected stays," *Journal of Sound and Vibration*, vol. 307, no. 3–5, pp. 849–864, 2007.

[9] A. Y. Koz'min, Y. V. Mikhlin, and C. Pierre, "Localization of energy in nonlinear systems with two degrees of freedom," *International Applied Mechanics*, vol. 43, no. 5, pp. 568–576, 2007.

[10] G. Kerschen, D. M. McFarland, J. J. Kowtko, Y. S. Lee, L. A. Bergman, and A. F. Vakakis, "Experimental demonstration of

transient resonance capture in a system of two coupled oscillators with essential stiffness nonlinearity," *Journal of Sound and Vibration*, vol. 299, no. 4-5, pp. 822–838, 2007.

[11] T. P. Sapsis, D. D. Quinn, A. F. Vakakis, and L. A. Bergman, "Effective stiffening and damping enhancement of structures with strongly nonlinear local attachments," *Journal of Vibration and Acoustics*, vol. 134, no. 1, Article ID 011016, 12 pages, 2012.

[12] B. Vaurigaud, A. T. Savadkoohi, and C.-H. Lamarque, "Targeted energy transfer with parallel nonlinear energy sinks. Part I: design theory and numerical results," *Nonlinear Dynamics*, vol. 66, no. 4, pp. 763–780, 2011.

[13] B. Vaurigaud, L. I. Manevitch, and C.-H. Lamarque, "Passive control of aeroelastic instability in a long span bridge model prone to coupled flutter using targeted energy transfer," *Journal of Sound and Vibration*, vol. 330, no. 11, pp. 2580–2595, 2011.

[14] C. Touzé, O. Thomas, and M. Amabili, "Transition to chaotic vibrations for harmonically forced perfect and imperfect circular plates," *International Journal of Non-Linear Mechanics*, vol. 46, no. 1, pp. 234–246, 2011.

[15] E. C. Carvalho, P. B. Gonçalves, J. G. N. Del Prado Zenon, and G. Rega, "The influence of symmetry breaking on the non-planar vibrations of slender beams," in *Proceedings of the 15th International Symposium on Dynamic Problems of Mechanics (DINAME '13)*, M. A. Savi, Ed., ABCM, Rio de Janeiro, Brazil, February 2013.

[16] A. V. Dyskin, E. Pasternak, and E. Pelinovsky, "Periodic motions and resonances of impact oscillators," *Journal of Sound and Vibration*, vol. 331, no. 12, pp. 2856–2873, 2012.

[17] Z. K. Peng, Z. Q. Lang, S. A. Billings, and Y. Lu, "Analysis of bilinear oscillators under harmonic loading using nonlinear output frequency response functions," *International Journal of Mechanical Sciences*, vol. 49, no. 11, pp. 1213–1225, 2007.

[18] S. Tsakirtzis, G. Kerschen, P. N. Panagopoulos, and A. F. Vakakis, "Multi-frequency nonlinear energy transfer from linear oscillators to mdof essentially nonlinear attachments," *Journal of Sound and Vibration*, vol. 285, no. 1-2, pp. 483–490, 2005.

[19] T. M. Nguyen, *Non-linear dynamics of coupled mechanical systems: model reduction and identification [Ph.D. thesis]*, Ecole Nationale des Ponts et Chaussees, 2007, (French).

[20] F. Nucera, D. M. McFarland, L. A. Bergman, and A. F. Vakakis, "Application of broadband nonlinear targeted energy transfers for seismic mitigation of a shear frame: computational results," *Journal of Sound and Vibration*, vol. 329, no. 15, pp. 2973–2994, 2010.

[21] D. Tirelli and S. Mascelloni, "Characterisation and optimization of shape memory alloys for seismic applications," *Journal de Physique IV France*, vol. 10, 2000.

[22] Federal Highway Administration (FHWA), "Chapter 3. Analysis, evaluation, and testing, wind-induced vibration of stay cables," Tech. Rep. FHWA-HRT-05-083, United States Department of Transportation, 2007.

[23] D. Tirelli, "Modal analysis of small & medium structures by fast impact hammer testing method," Tech. Rep. EUR, 24964 EN, Joint Research Centre, Publications Office of the European Union, Luxembourg, 2010.

[24] D. Tirelli, "A fast automated impact hammer test method for modal parameter extraction (FIHT) implementation on a composite bridge beam," in *Proceedings of the International Symposium on Nondestructive Testing of Materials and Structures (NDTMS '11)*, Istanbul, Turkey, May 2011.

[25] V. Torra, C. Auguet, A. Isalgue, G. Carreras, P. Terriault, and F. C. Lovey, "Built in dampers for stayed cables in bridges via SMA. The SMARTeR-ESF project: a mesoscopic and macroscopic experimental analysis with numerical simulations," *Engineering Structures*, vol. 49, pp. 43–57, 2013.

[26] E. A. Butcher, "Clearance effects on bilinear normal mode frequencies," *Journal of Sound and Vibration*, vol. 224, no. 2, pp. 305–328, 1999.

[27] H. Li, M. Liu, and J. Ou, "Vibration mitigation of a stay cable with one shape memory alloy damper," *Structural Control and Health Monitoring*, vol. 11, no. 1, pp. 21–36, 2004.

Hindawi Publishing Corporation
Shock and Vibration
Volume 2014, Article ID 870564, 7 pages
http://dx.doi.org/10.1155/2014/870564

Research Article

Reduction of Structural Vibrations by Passive and Semiactively Controlled Friction Dampers

L. Gaul and J. Becker

Institute of Applied and Experimental Mechanics, University of Stuttgart, Germany

Correspondence should be addressed to L. Gaul; gaul@iam.uni-stuttgart.de

Received 26 July 2013; Accepted 24 February 2014; Published 17 July 2014

Academic Editor: Nuno Maia

Copyright © 2014 L. Gaul and J. Becker. This is an open access article distributed under the Creative Commons Attribution License, which permits unrestricted use, distribution, and reproduction in any medium, provided the original work is properly cited.

Reduction of structural vibrations is of major interest in mechanical engineering for lowering sound emission of vibrating structures, improving accuracy of machines, and increasing structure durability. Besides optimization of the mechanical design or various types of passive damping treatments, active structural vibration control concepts are efficient means to reduce unwanted vibrations. In this contribution, two different semiactive control concepts for vibration reduction are proposed that adapt to the normal force of attached friction dampers. Thereby, semiactive control concepts generally possess the advantage over active control in that the closed loop is intrinsically stable and that less energy is required for the actuation than in active control. In the chosen experimental implementation, a piezoelectric stack actuator is used to apply adjustable normal forces between a structure and an attached friction damper. Simulation and experimental results of a benchmark structure with passive and semiactively controlled friction dampers are compared for stationary narrowband excitation. For simulations of the control performance, transient simulations must be employed to predict the achieved vibration damping. It is well known that transient simulation of systems with friction and normal contact requires excessive computational power due to the nonlinear constitutive laws and the high contact stiffnesses involved. However, commercial finite-element codes do not allow simulating feedback control in a general way. As a remedy, a special simulation framework is developed which allows efficiently modeling interfaces with friction and normal contact by appropriate constitutive laws which are implemented by contact elements in a finite-element model. Furthermore, special model reduction techniques using a substructuring approach are employed for faster simulation.

1. Introduction

Semiactive control strategies for vibration reduction offer interesting alternatives to passive means of damping enhancement or fully active vibration control (AVC). Hereby, the term semiactive means that passive system properties, such as friction, material damping, or fluid viscosity, are actively controlled. This intrinsically eliminates the problem of system destabilization due to spillover effects encountered in AVC applied to flexible structures [1, 2]. Furthermore, semiactive control is more energy-efficient than fully active ones in general which is an important aspect from an application point of view. In exchange of these advantages, the achievable performance is limited by the effectiveness of the underlying passive damping mechanism. Though, they outperform passive vibration reduction means due to their ability to adapt to the instantaneous vibration state of the structure, this property links semiactive control concepts to the research area of smart/adaptive structures and adaptronics. Advantages over fully active control are that semiactive control is inherently fail-safe, guarantees stability, and introduces significant passive damping into the mechanical system, for example, by the attached friction damper in this contribution. Semiactive control concepts are probably most often applied to magneto- or electrorheological dampers, friction damping devices, or actively tuned absorbers with variable-stiffness dampers; see [3–11] for some examples. In this contribution, a semiactive control concept for a friction damper which is able to reduce structural vibrations of multiple modes is presented. The specific idea of using friction in joints for vibration damping by normal force control is reported first in [12], which subsequently inspired several researchers; see, for example, [13]. Two control algorithms for the semiactive vibration

control of the normal force between a main structure and attached damper exploiting dry friction damping are investigated. The focus of this contribution is to damp several structural modes of beam.

2. System Representation

2.1. Beam Structure. A beam-like friction damper element is attached to a beam-like metal benchmark structure by a normal screw and an adaptive screw. The principle is depicted schematically in Figure 1; a picture of the experimental realization is shown in Figure 2. One screw is strongly tightened with a normal force of $F_{N,2} = 6000\,\mathrm{N}$ whereas the normal force $F_{N,1}$ of the adaptive screw can be controlled by means of a piezoelectric ring stack actuator. For that purpose, the control measures the acceleration close to the tip.

2.2. Finite-Element Modeling. The structure is discretized by the finite-element (FE) method using ANSYS (Figure 3). The beam and the friction damper are modeled as independent substructures with solid elements having quadratic shape functions. The mesh size is chosen in accordance with Shannon's theorem. At the interface identical meshes are used to enable the application of a node-to-node contact formulation. After assembly the established system matrices in terms of mass and stiffness are transferred to MATLAB using the Structural Dynamics Toolbox. This procedure offers flexibility for applying different model reduction as well as applying control techniques. Reduced models with a minimal truncation error were found in a previous investigation and for more details it is referred to [14, 15] at this point.

In a generic way, the discretized structural dynamics of the two substructures, namely, the main structure and the attached friction damper beam, are given by

$$\begin{bmatrix} M^{(1)} & 0 \\ 0 & M^{(2)} \end{bmatrix} \ddot{x} + \begin{bmatrix} K^{(1)} & 0 \\ 0 & K^{(2)} \end{bmatrix} x + \begin{bmatrix} B_T^{(1)} \\ B_T^{(2)} \end{bmatrix} F_T^c + \begin{bmatrix} B_N^{(1)} \\ B_N^{(2)} \end{bmatrix} F_N^c = B \begin{bmatrix} F_{N,1} \\ F_{N,2} \end{bmatrix} + F_{\mathrm{exc}}, \tag{1}$$

where the nodal normal contact forces F_N^c and tangential friction forces F_T^c act as internal forces on the contact interface between main structure and damper beam. On the right-hand side, the external forces appear, namely, the two pairs of clamping forces $F_{N,1}$, $F_{N,2}$ and dynamic excitation loads F_{exc} (later, $F_{N,1}$ is controlled).

Constitutive equations are implemented for the normal contact and the tangential contact in the interface by node-to-node contact elements. The former is a bilinear stiffness relationship (Figure 4) that allows separation for a gap $g > g_0$ but penalizes penetration in two steps for $g < g_0$ and $g < g_1$. For the friction an elastoplastic model is used, which can be seen as two-dimensional version of a Jenkins element model depicted in Figure 4 for the one-dimensional case, that is, a series combination of a spring and a Coulomb element.

The nonlinear system of (1) is solved with the Newmark scheme and Newton equilibrium iterations at each fixed time step. Beforehand, substructure model reduction techniques are employed to reduce the dimensions of the system. For that purpose, an in-house simulation tool [14] is developed to facilitate general feedback control simulation, which is not supported by commercial FE codes. The model parameters including the contact parameters are updated by comparison of experimentally and numerically obtained FRFs (frequency response function) with impulse hammer excitation that cover a large range of constant clamping forces. An exemplary FRF is shown in Figure 5 where the nonlinear effects become visible by some unsymmetric peak forms (e.g., at 230 Hz) and some higher harmonics peaks. From the FRF, the damping ratios are identified for the bending modes; see Figure 5. They show good agreement between simulation and experiment and significant damping is introduced by the friction damper if they are compared to the modal damping ratios of less than 0.15% found without attached damper.

3. Semiactive Vibration Control

Two controllers each consisting of an appropriate nonlinear control law plus an observer to estimate nonmeasurable variables required by the control are introduced in the following. The first control is denoted by hysteresis-optimal control and is motivated by experimental investigations. They show that relatively simple dynamical friction models are often capable of modeling the most dominant friction effects in structures with local joints [16]. Among others, the Jenkins element, as depicted in Figure 4, has proven its usability for that purpose and serves as base for the control derivation.

3.1. Hysteresis-Optimal Control. For that, it is assumed that the dominant damping effects are located in the contact area close to the adaptive screw and can be modeled by a discrete friction model. Then, the dissipated work W_d due to friction during one vibration cycle is maximized to find the control. For the chosen model, the dissipated energy

$$W_d = 4\left(u_{\mathrm{rel},0} - \frac{F_C}{k_T}\right) F_C \quad \text{with } F_C = \mu F_N \tag{2}$$

is maximized to yield the optimal normal force F_N as a function to the tangential contact stiffness k_T, the friction coefficient μ, and the relative sliding oscillation amplitude $u_{\mathrm{rel},0}$:

$$F_N = f\left(u_{\mathrm{rel},0}\right) = \frac{k_T u_{\mathrm{rel},0}}{2\mu} = k_T^* u_{\mathrm{rel},0}. \tag{3}$$

Note that similar algebraic expressions could be derived also based on hysteresis loops of more complex friction models involving more parameters. Equation (3) is interpreted as control law to adjust the normal force $F_N = F_{N,1}$ according to Figure 1 to the structural vibration tangential amplitude. The required actual vibration displacement amplitude $u_{\mathrm{rel},0}$ can be found under the assumption of monofrequent displacement (with zero mean) by $u_{\mathrm{rel},0} \approx (\pi/2T)\int_{t-T}^{t} |u_{\mathrm{rel}}| d\tau$ from

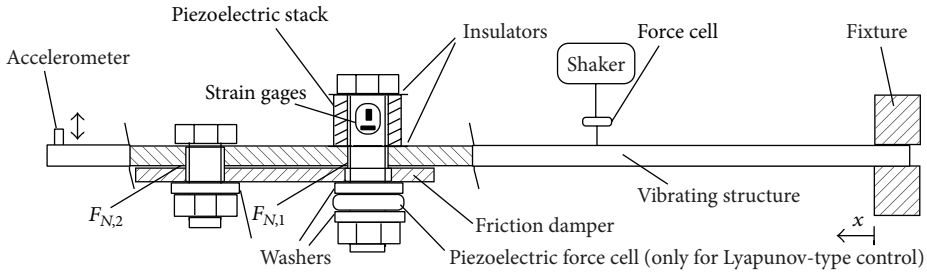

Figure 1: Sketch of the benchmark structure (steel, 775 mm length, 40 mm width, and 3 mm thickness) with adaptive friction damper beam (steel, 160 mm length, 40 mm width, and 3 mm thickness).

Figure 2: Photograph of the experimental setup with structure, damper beam, piezoelectric stack, force cell, accelerometers, and attached shaker stinger (cf. Figure 1).

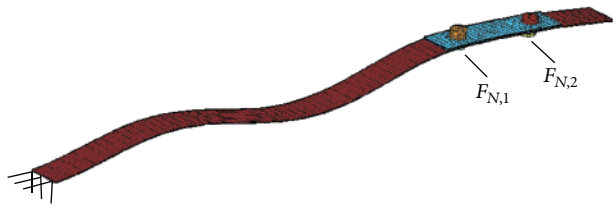

Figure 3: Finite-element model (≈30000 DOFs and 632 nodes in contact) in typical bending deformation with the two screws that impose the external clamping force pairs $F_{N,1}$ and $F_{N,2}$.

the estimated signal u_{rel}. The evaluation of the integral would need large memory storage for the required integration time much larger than the largest vibration period of interest; hence it is efficiently approximated by a first-order lag element (PT_1), where the time constant T_1 prescribes how fast the signal $u_{\text{rel},0}$ follows a change in the vibration amplitude:

$$T_1 \dot{u}_{\text{rel},0} + u_{\text{rel},0} = \frac{\pi}{2} \left| u_{\text{rel}} \right|. \tag{4}$$

3.2. Model-Based Design of Nonlinear Observer. In general, the required tangential displacement u_{rel} at the adaptive screw cannot be measured which makes the design of a nonlinear observer necessary which estimates it from available measurements such as displacements, strains, or accelerations and a simplified approximate simulation model without having any information about the excitation forces.

This model is derived by rigid connection of the damper beam at one end ($F_{N,2}$) and neglect of the normal contact between damper and base structure; instead appropriate spring elements are introduced in normal direction in some distance around the adaptive screw. The relative motion at the adaptive screw is used for the output definition of $\hat{u}_{\text{rel}}$. The nonlinear observer is of the form

$$\begin{aligned} \dot{\hat{z}} &= A\hat{z} + B_T f_{\text{friction}} \left(\hat{F}_T, \dot{\hat{u}}_{\text{rel}}, F_N \right) + B_{\text{exc}} F_{\text{exc}} \\ &\quad + l \left(y_{\text{meas}} - \hat{y}_{\text{meas}} \right), \\ &\text{with } \hat{y}_{\text{meas}} = C\hat{z}, \qquad \hat{u}_{\text{rel}} = C_{\text{rel}}\hat{z}. \end{aligned} \tag{5}$$

Hereby, the measurement output y_{meas} denotes the velocity measurement obtained by integration of the acceleration in the experiment. The estimated output $\hat{u}_{\text{rel}}$ replaces the required variable u_{rel} by the nonlinear control law (3). A simple dynamic friction model $f_{\text{friction}}(\cdot)$ is used to model the friction F_T at the adaptive screw, namely, a regularized Coulomb friction model:

$$F_T = f_{\text{friction}} \left(\dot{\hat{u}}_{\text{rel}}, F_N \right) = \mu F_N \frac{2}{\pi} \arctan \left(\alpha \dot{\hat{u}}_{\text{rel}} \right), \tag{6}$$

which depends on the relative velocity $\dot{\hat{u}}_{\text{rel}}$ with the regularization parameter α determined by simulation studies. Theoretically, the use of more complex dynamic friction models would be of interest; the hard real-time limitations imposed by the fixed-step time-integration in the experiment and the considered high frequencies forbid their application for the investigated problem. The obtained estimation accuracy has been verified in simulations that are also used to optimize the observer. The linear system parts in (5) are obtained from a simplified, linear FE model after modal truncation plus a static correction step. With the required output variables, mass and stiffness matrices M, K and load vector F_{exc}, this simplified model reads with nonlinear inner force vector F_I consisting of normal contact and friction forces

$$\begin{aligned} M\ddot{x} + Kx + F_I = \beta_{\text{exc}} F_{\text{exc}}, \qquad y_{\text{meas}} = \gamma_{\text{meas}} x, \\ u_{\text{rel}} = \gamma_{\text{rel}} x. \end{aligned} \tag{7}$$

Solving the associated eigenvalue problem $(K - \omega^2 M)\phi = 0$ yields the eigenfrequencies ω_k and eigenvectors ϕ_k ($k \in \mathbb{N}^+$) which allows a modal truncation to the first N important bending modes by the transformation $x = Tx^*$ with $T = [\phi_1, \phi_2, \ldots, \phi_N]$. For a real-time application, an observer of low order is aspired. Additional information to identify important bending modes which are observable can be obtained by modal Gramians; see [15, 17]. This transforms

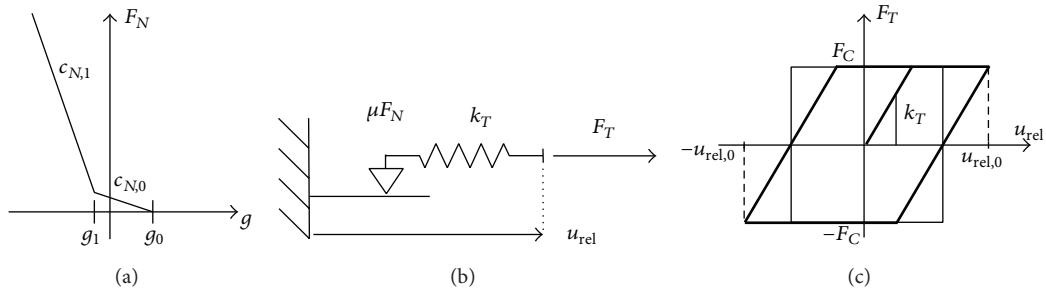

Figure 4: (a) Normal force stiffness relation. (b) 1D Jenkins friction model. (c) Jenkins model hysteresis loop (thick) in comparison to the Coulomb friction hysteresis (thin). Note, that for increasing tangential stiffness, the hysteresis approximates the Coulomb model hysteresis.

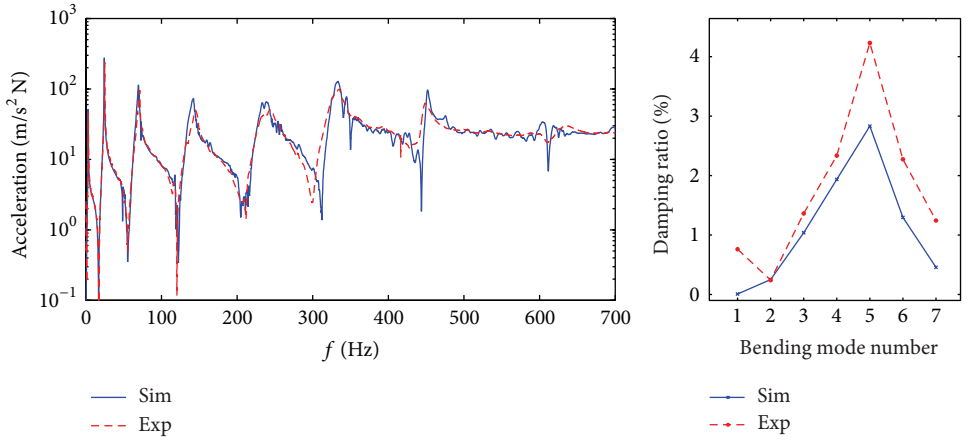

Figure 5: Measured and simulated FRFs for impulse excitation and $F_{N,1} = 100$ N, $F_{N,2} = 6000$ N (excitation and measurement close to tip on the mid-axis) and determined modal damping ratios.

the system matrices, $I = T^T M T$ and $\Omega = T^T K T = \text{diag}\{\omega_1^2, \omega_2^2, \ldots, \omega_N^2\}$, as well as the other matrices in (5). With the state vector $z^T = [\dot{x}^{*T}, x^{*T}]$ and some damping matrix Δ, these linear system parts read

$$A = \begin{bmatrix} -\Delta & -\Omega \\ I & 0 \end{bmatrix}, \qquad B_T = \begin{bmatrix} -\Theta^T \gamma_{\text{rel}}^T \\ 0 \end{bmatrix},$$
$$B_{\text{exc}} = \begin{bmatrix} \Theta^T \beta_{\text{exc}} \\ 0 \end{bmatrix}, \qquad C_{\text{rel}} = [0, \gamma_{\text{rel}}\Theta], \tag{8}$$
$$C_{\text{meas}} = [0, \gamma_{\text{meas}}\Theta].$$

After linearization around $u_{\text{rel}} = 0, F_N = 0$, the observer gains l in (5) are determined by a Kalman design procedure from the solution of the associated Riccati equation for appropriate state and measurement noise variance matrices. The obtained control loop is shown in Figure 6.

3.3. Lyapunov-Type Control. For the second proposed control law, Lyapunov's direct method is applied by choosing the mechanical system energy as Lyapunov function $V(x)$ and under the assumption of a discrete friction model with controlled normal force [13]. It is imposed that its time derivative $\dot{V}(x)$ must be seminegative, which is directly related to the differential form of the passivity condition. Its absolute value is furthermore maximized for optimality in the Lyapunov sense. Recalling the dynamics of a 1-DOF system

$$m\ddot{u}_{\text{rel}} + k u_{\text{rel}} + F_T = 0, \tag{9}$$

the passivity condition in terms of the friction force F_T and the relative velocity $\dot{u}_{\text{rel}}$

$$F_T \dot{u}_{\text{rel}} \geq 0 \quad \forall t \tag{10}$$

ensures a power flow outwards of the controlled structure. To enforce (10), a control law based on a Jenkins friction model must depend on the actual friction force F_T. However, in practice, for structures as the investigated one, it is almost impossible to measure or estimate this force because of the distributed friction interface and the high stiffnesses in combination with the hard real-time constraints. Hence, the Coulomb friction model according to $F_T = \mu F_N \,\text{sign}(\dot{u}_{\text{rel}})$ is assumed as a good approximation instead. For this, it can be shown that a velocity-dependent bang-bang controller, which switches continuously between the two possible states, is optimal in the Lyapunov sense [13]; $F_N = 0$ for $|\dot{u}_{\text{rel}}| = 0$ and $F_N = F_{N,\max}$ for $|\dot{u}_{\text{rel}}| \geq 0$. This approach is appropriate in view of the high values for the tangential stiffness k_T found in the model updating before. Additional regularization with a boundary layer ε to avoid chattering

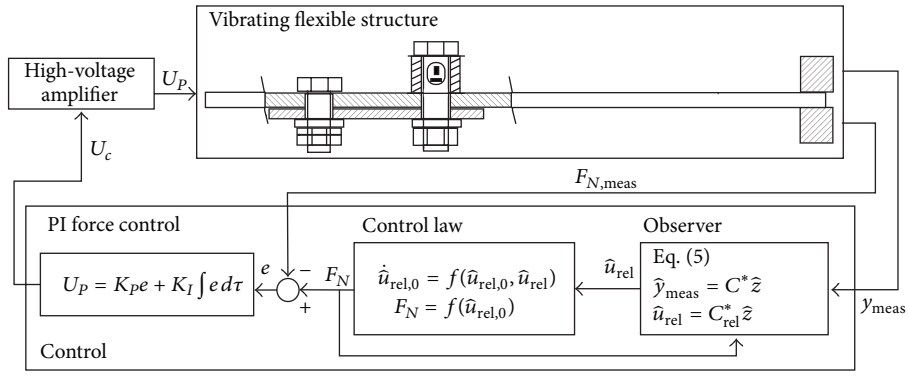

FIGURE 6: Closed control loop with hysteresis-optimal control law.

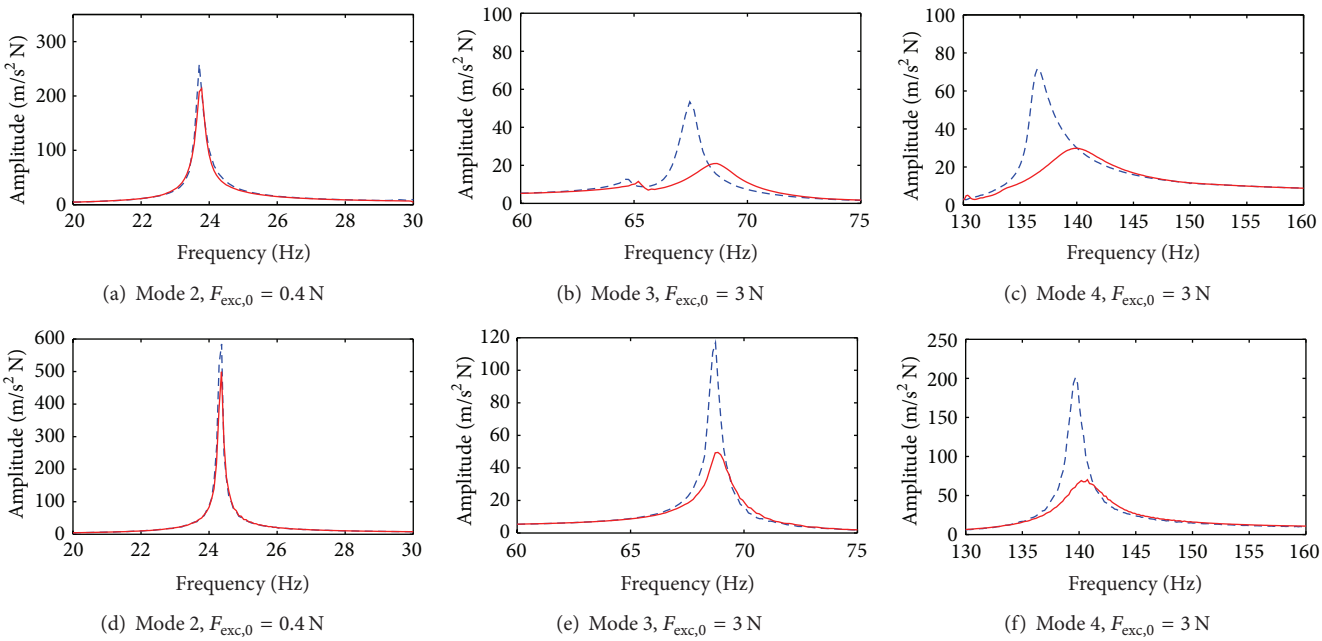

(a) Mode 2, $F_{\text{exc},0} = 0.4$ N (b) Mode 3, $F_{\text{exc},0} = 3$ N (c) Mode 4, $F_{\text{exc},0} = 3$ N

(d) Mode 2, $F_{\text{exc},0} = 0.4$ N (e) Mode 3, $F_{\text{exc},0} = 3$ N (f) Mode 4, $F_{\text{exc},0} = 3$ N

FIGURE 7: Hysteresis-optimal control: measured (top) and simulated (bottom) accelerance FRFs for controlled sine-sweep excitation with (solid) and without (dashed) control ($k_T^* = 2.5 \cdot 10^7$ N/m).

effects and introduction of the minimal normal force yields the suboptimal law:

$$F_N = \begin{cases} \max\left\{ \dfrac{|\dot{u}_{\text{rel}}|}{\varepsilon} F_{N,\max}, F_{N,\min} \right\} & \text{for } |\dot{u}_{\text{rel}}| < \varepsilon \\ F_{N,\max} & \text{for } |\dot{u}_{\text{rel}}| \geq \varepsilon. \end{cases} \quad (11)$$

Again, the required tangential relative motion must be estimated by the previously introduced observer which now estimated the relative velocity $\dot{u}_{\text{rel}}$ instead of the displacement u_{rel}. Note that the minimal and maximal normal forces $F_{N,\min}$ and $F_{N,\max}$ are determined by the mechanical properties of the adaptive screw.

4. Experiments and Simulation Results

The proposed controls are investigated for the benchmark structure with a damper beam at $x_d = 0.545$ m away from the fixture. For this position, significant relative displacement between structure and damper is expected for the bending modes 3, 4 and higher. For mode 2, much less relative motion is expected which explains the small damping values obtained in the experiment and simulations, for example, for the passive results in Figure 5. The first mode is not considered because it cannot be excited by the available shaker. For evaluation, accelerated FRFs from the excitation force (at $x = 0.325$ m) to the measured acceleration (at $x = 0.45$ m) are compared.

4.1. Controller Implementation. A *dSpace* system running at 21 kHz sampling frequency is used for the real-time implementation. The observer is designed based on 7 normal modes and uses the out-of-plane tip acceleration at $x = 0.765$ m as measurement variable y_{meas}. In the experiment, the prescribed force F_N for the adaptive screw from (3) or

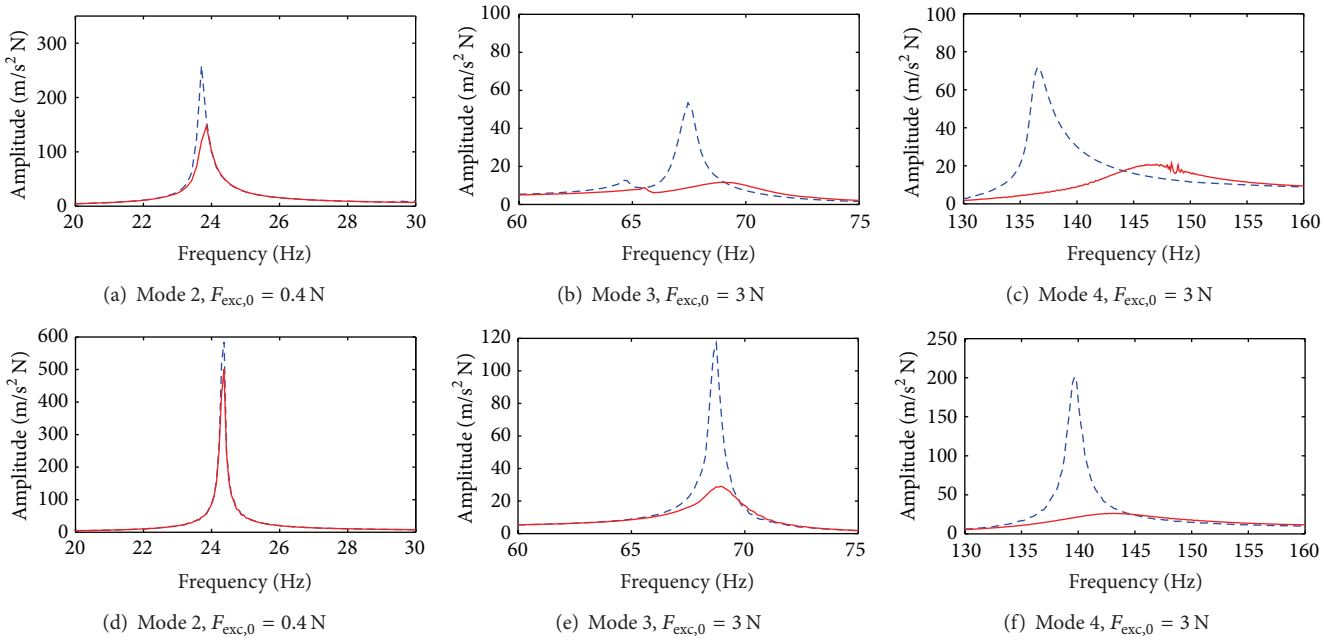

FIGURE 8: Lyapunov-type control: measured (top) and simulated (bottom) accelerance FRFs for controlled sine-sweep excitation with (solid) and without (dashed) control ($\varepsilon = 1/200$ m/s).

(11) must be tracked by an underlying force feedback control loop to compensate nonlinearities, large-signal piezoelectric effects, and creep effects in the screw threads as well as decrease the inertia forces of the actuator and sensor masses due to the structural vibrations. For that, a tracking controller is employed which is combined from a feedforward term derived from the static actuator voltage-force relationship and a PID feedback control of the measured force. The obtained actuator signal U_P is filtered by a 30 kHz low-pass filter to decrease the digitization noise before it is amplified for the piezoelectric stack actuator. To maximize the stiffness of the clamping of the piezoelectric actuators determining the achievable stroke [2], strain gages directly embedded in the bolt shaft (see Figure 6) measure the actual force instead of strain-gage based ring force cells that would significantly weaken the configuration. The applicable actuator stroke lies between $F_{N,\min} = 40$ N and $F_{N,\max} \approx 600$ N.

For the Lyapunov-type control, a piezoelectric force cell of high sensitivity and bandwidth is added (cf. Figure 2) because its high actuation dynamics requires a very high control bandwidth which is difficult to realize with strain-gage based force measurements due to the found signal-to-noise ratio and delays originating from the necessary amplifiers.

4.2. Shaker Test Setup with Excitation Force Control. For nonlinear mechanical structures, comparing FRFs requires special care because the obtained FRFs are nonlinear. More specifically, their resonance frequencies, peak amplitudes, and peak forms depend on the excitation signal as well as amplitudes. Consequently, the amplitude is controlled during sine sweep measurements to make the excitation independent of the structural impedance for consistent comparisons. Very low sweep velocities (0.1 Hz/s) are employed to obtain steady-state conditions which approximate step-sine testing and to avoid interaction between the interesting effects of the semiactive structural control and the shaker control. Due to the very small relative displacements outside resonances, the control is only effective close to resonances which allows restricting the evaluation around the resonance frequencies to save simulation and measurement time.

In Figures 7 and 8, FRFs with and without semiactive control are shown for some typical excitation amplitudes for the two control concepts. Similar results are obtained for other amplitudes. It can always be seen that the control strongly reduces the resonance amplitudes of multiple modes. However, for the second mode the obtained damping is quite small in the active as well as the passive case. This is due to the slight curvature of the beam at the lower modes which results in a small relative motion in the interface. Additionally, this fact implies that the obtained efficiency of the damper is dependent on its position.

In the passive case, the minimal possible force $F_N = F_{N,\min}$ is applied to the adaptive screw which still introduces significant structural damping compared to the case without attached damper. Experiments and simulation additionally prove that the semiactive control never decreases the passive damping effect at lower excitation amplitudes. Generally, the agreement obtained between experiment and simulations is rated very good in view of the well-known difficulties encountered in the prediction of nonlinear damping of structures, especially for distributed friction with inhomogeneous normal contact pressure distribution. Furthermore, some imperfections of the excitation control cannot be avoided as well as some changes in the contact parameters. The Lyapunov-type control achieves higher vibration reduction

than the hysteresis-optimal one in both experiments and simulations, especially at smaller vibration amplitudes. It is also suited to suppress broadband vibrations and relatively robust to errors in the estimation, but, as a drawback, its high dynamical actuation requires more power. Advantageously, the hysteresis-optimal control could be implemented with low dynamical actuators, for example, of different actuation principles.

5. Conclusion

Multimodal, semiactive vibration controllers that adapt the normal force applied to friction damper beams by piezoelectric stack actuators are investigated for a generic benchmark structure in experiments and simulations. They are shown to efficiently damp structural resonances for different excitation amplitudes and vibration modes. Which of the investigated controller concepts suits best for a certain application depends mainly on the actuator principle, the power considerations, and whether the excitation being rather broadband or narrowband. Based on the results of the beam experiment, the proposed friction damper is used to reduce the vibrations of machine tools [18].

Conflict of Interests

The authors declare that there is no conflict of interests regarding the publication of this paper.

Acknowledgment

The support of the DFG (German Research Foundation) with Project SPP 1156 is gratefully acknowledged.

References

[1] M. J. Balas, "Feedback control of flexible systems," *IEEE Transactions on Automatic Control*, vol. AC-23, no. 4, pp. 673–679, 1978.

[2] C. Fuller, S. Elliott, and P. Nelson, *Active Control of Vibration*, Academic Press, New York, NY, USA, 1996.

[3] P. Dupont, P. Kasturi, and A. Stokes, "Semi-active control of friction dampers," *Journal of Sound and Vibration*, vol. 202, no. 2, pp. 203–218, 1997.

[4] L. M. Jansen and S. J. Dyke, "Semiactive control strategies for MR dampers: a comparative study," *Journal of Engineering Mechanics*, vol. 126, no. 8, pp. 795–803, 2000.

[5] O. E. Ozbulut, M. Bitaraf, and S. Hurlebaus, "Adaptive control of base-isolated structures against near-field earthquakes using variable friction dampers," *Engineering Structures*, vol. 33, no. 12, pp. 3143–3154, 2011.

[6] S. Nagarajaiah, S. Narasimhan, A. Agrawal, and P. Tan, "Semiactive Lyapunov controller for phase II seismic isolated highway bridge benchmark," in *Proceedings of the Structures Congress*, pp. 1–10, 2006.

[7] F. Nitzsche, D. G. Zimcik, V. K. Wickramasinghe, and C. Yong, "Control laws for an active tunable vibration absorber designed for rotor blade damping augmentation," *Aeronautical Journal*, vol. 108, no. 1079, pp. 35–42, 2004.

[8] W. N. Patten, C. Mo, J. Kuehn, and J. Lee, "A primer on design of semiactive vibration absorbers (SAVA)," *Journal of Engineering Mechanics*, vol. 124, no. 1, pp. 61–67, 1998.

[9] H. Li, J. Li, and G. Song, "Improved suboptimal Bang-Bang control of aseismic buildings with variable friction dampers," *Acta Mechanica Sinica*, vol. 23, no. 1, pp. 101–109, 2007.

[10] M. D. Symans and M. C. Constantinou, "Seismic testing of a building structure with a semi-active fluid damper control system," *Earthquake Engineering and Structural Dynamics*, vol. 26, no. 7, pp. 759–777, 1997.

[11] M. Unsal, C. Niezrecki, and C. Crane III, *A New Semi-Active Piezoelectric-Based Friction Damper*, Department of Mechanical Engineering, University of Florida, 2007.

[12] J. S. Lane, A. A. Ferri, and B. S. Heck, "Vibration control using semi-active friction damping," in *Proceedings of the Winter Annual Meeting of the American Society of Mechanical Engineers (ASME '92)*, vol. 49, pp. 165–171, November 1992.

[13] R. Nitsche and L. Gaul, "Lyapunov design of damping controllers," *Archive of Applied Mechanics*, vol. 72, no. 11-12, pp. 865–874, 2003.

[14] J. Becker and L. Gaul, "CMS methods for efficient damping prediction for structures with friction," in *Proceedings of the 26th Conference and Exposition on Structural Dynamics (IMAC-XXVI '08)*, Orlando, Fla, USA, February 2008.

[15] J. Becker, *Semi-active control of friction dampers and feedforward tracking control design for structural vibration reduction [Ph.D. thesis]*, University of Stuttgart, Der Andere, 2009.

[16] L. Gaul and R. Nitsche, "The role of friction in mechanical joints," *Applied Mechanics Reviews*, vol. 54, no. 2, pp. 93–105, 2001.

[17] W. K. Gawronski, *Dynamics and Control of Structures*, Mechanical Engineering Series, Springer, New York, NY, USA, 1998.

[18] J. Hesselbach, *Adaptronik für Werkzeugmaschinen: Forschung in Deutschland*, Shaker, 2011.

Hindawi Publishing Corporation
Shock and Vibration
Volume 2014, Article ID 404132, 12 pages
http://dx.doi.org/10.1155/2014/404132

Research Article

Spatial Information in Autonomous Modal Parameter Estimation

Randall J. Allemang and Allyn W. Phillips

Department of Mechanical and Materials Engineering, College of Engineering and Applied Science, University of Cincinnati, Cincinnati, OH 45221-0072, USA

Correspondence should be addressed to Randall J. Allemang; randall.allemang@uc.edu

Received 13 July 2013; Accepted 20 January 2014; Published 17 July 2014

Academic Editor: Nuno Maia

Copyright © 2014 R. J. Allemang and A. W. Phillips. This is an open access article distributed under the Creative Commons Attribution License, which permits unrestricted use, distribution, and reproduction in any medium, provided the original work is properly cited.

Recent work with autonomous modal parameter estimation has shown great promise in the quality of the modal parameter estimation results when compared to results from traditional methods by experienced users. While autonomous modal parameter estimation means slightly different things to different researchers and practitioners, for the purpose of this discussion, autonomous will require an automated procedure which sorts and processes a large number of possible modal parameter solutions to yield one consistent estimate with no user interaction after initial thresholds are chosen. In the work discussed, this final, consistent set of modal parameters is identifiable due to the combination of temporal and spatial information in a z domain state vector of relatively high order (5–10). Since this z domain state vector has both complex modal frequency and modal vector information as embedded content, sorting consistent estimates from the multitude of possible solutions is relatively trivial. Because this z domain state vector can be developed from the results of any modal parameter estimation method, possible solutions from different traditional methods can be utilized in the autonomous procedure to yield one consistent set of modal parameters.

1. Introduction

The desire to estimate modal parameters automatically, once a set or multiple sets of test data are acquired, has been a subject of great interest for more than 40 years. In the 1960s, when modal testing was limited to analog test methods, several researchers were exploring the idea of an automated test procedure for determining modal parameters [1–3]. Today, with the increased memory and compute power of current computers used to process test data, an automated or autonomous, modal parameter estimation procedure is entirely possible and is being evaluated by numerous researchers and users.

Before proceeding with a discussion of the use and impact of spatial information in autonomous modal parameter estimation, some philosophy and definitions regarding what is considered autonomous is required. In general, autonomous modal parameter estimation refers to an automated procedure that is applied to a modal parameter estimation algorithm so that no user interaction is required once the process is initiated. This typically involves setting a number of parameters or thresholds that are used to guide the process in order to exclude solutions that are not acceptable to the user. When the procedure finishes, a set of modal parameters is identified that can then be reduced or expanded if necessary. The goal is that no further reduction, expansion, or interaction with the process will be required.

For the purposes of further discussion, the autonomous modal parameter estimation procedure is simply an efficient mechanism for sorting a very large number of solutions into a final set of solutions that satisfies a set of criteria and thresholds that are acceptable to the user. This user is assumed to be very experienced and uses autonomous modal parameter estimation as a sophisticated tool to highlight the most likely solutions based upon statistics. The experienced user will realize that the final solutions may include unrealistic solutions or nonoptimal solutions and further evaluation will be required.

2. Background

In order to discuss the impact and use of spatial information in autonomous modal parameter estimation, some background is needed to clarify terminology and methodology. This background has been provided in previous papers and will only be highlighted here in terms of spatial information, modal parameter estimation, and autonomous modal parameter estimation.

2.1. Spatial Information. Spatial information, with respect to experimental modal parameter estimation, refers to the vector information and dimension associated with the inputs and outputs of the experimental test. Essentially, this represents the locations of the sensors in the experimental test. It is important to recognize that an experimental test should always include multiple inputs and outputs in order to clearly estimate different modal vectors and to resolve modal vectors when the complex natural frequencies are close, what is called repeated or pseudorepeated roots.

Since the data matrix, normally involving frequency response functions (FRF) or impulse response functions (IRF), is considered to be symmetric or reciprocal, the data matrix can be transposed, switching the effective meaning of the row and column index with respect to the physical inputs and outputs. Consider

$$\left[H\left(\omega_i\right)\right]_{N_o\times N_i} = \left[H\left(\omega_i\right)\right]^T_{N_i\times N_o}. \quad (1)$$

Since many modal parameter estimation algorithms are developed on the basis of either the number of inputs (N_i) or the number of outputs (N_o), assuming that one or the other is larger based upon test method, some nomenclature conventions are required for ease of further discussion. In terms of the modal parameter estimation algorithms, it is more important to recognize whether the algorithm develops the solution on the basis of the larger (N_L) of N_i or N_o or the smaller (N_S) of N_i or N_o, dimension of the experimental data. For this reason, the terminology of *long* (larger of N_i or N_o) dimension or *short* (smaller of N_i or N_o) dimension is easier to understand without confusion.

Therefore, the nomenclature of the number of outputs (N_o) and number of inputs (N_i) has been replaced by the length of the long dimension of the data matrix (N_L) and the length of the short dimension (N_S) regardless of which dimension refers to the physical output or input. This means that the above reciprocity relationship can be restated as

$$\left[H\left(\omega_i\right)\right]_{N_L\times N_S} = \left[H\left(\omega_i\right)\right]^T_{N_S\times N_L}. \quad (2)$$

Note that the reciprocity relationships embedded in (1) and (2) are a function of the common degrees of freedom (DOFs) in the short and long dimensions. If there are no common DOFs, there are no reciprocity relationships and the data requirement for modern modal parameter estimation algorithms (multiple references) will not be met. Nevertheless, the importance of (1) and (2) is that the dimensions of the FRF matrix can be transposed as needed to fit the requirement of specific modal parameter estimation algorithms. This impacts the size of the square matrix coefficients in the matrix coefficient, polynomial equation, and the length of the associated modal (base) vector.

2.2. Modal Parameter Estimation. All modern, commercial algorithms for estimating modal parameters from experimental input-output data utilize matrix coefficient, polynomial models. This general matrix coefficient, polynomial formulation yields essentially the same polynomial form for both time and frequency domain data. Note, however, that this notation does not mean that, for an equivalent model order, the associated matrix coefficients are numerically equal.

For the frequency domain data case, this is

$$\left|\left[\alpha_m\right] s^m + \left[\alpha_{m-1}\right] s^{m-1} + \left[\alpha_{m-2}\right] s^{m-2} + \cdots + \left[\alpha_0\right]\right| = 0, \quad (3)$$

where

$$s_r = \lambda_r, \qquad \lambda_r = \sigma_r + j\omega_r. \quad (4)$$

For the time domain data case, this is

$$\left|\left[\alpha_m\right] z^m + \left[\alpha_{m-1}\right] z^{m-1} + \left[\alpha_{m-2}\right] z^{m-2} + \cdots + \left[\alpha_0\right]\right| = 0, \quad (5)$$

where

$$z_r = e^{\lambda_r \Delta t}, \qquad \lambda_r = \sigma_r + j\omega_r,$$
$$\sigma_r = \mathrm{Re}\left[\frac{\ln z_r}{\Delta t}\right], \qquad \omega_r = \mathrm{Im}\left[\frac{\ln z_r}{\Delta t}\right]. \quad (6)$$

The size of the square, matrix coefficients ($[\alpha]$), and the order of the polynomial (m) vary with the algorithm. Once the matrix coefficients ($[\alpha]$) have been found, the modal frequencies (λ_r or z_r) can be found as the roots of the matrix coefficient polynomial (see (3) or (5)) using any one of a number of numerical techniques, normally involving an eigenvalue problem of the companion matrix associated with the matrix coefficient polynomial.

When the modal frequencies are estimated from this eigenvalue problem, a unique estimate of the unscaled modal vector is identified from the associated eigenvector at the same time. The length or dimension of this unscaled modal vector is equal to the dimension of the square, alpha coefficients which, in general, is equal to N_S or N_L.

In all cases, the size of the square, alpha coefficient matrices ($[\alpha]$), and/or the size of the model order (m) can be varied to estimate multiple sets of solutions from the same data. These multiple sets of solutions are generally presented graphically in terms of consistency diagrams to identify a final set of realistic solutions. For this reason, with minor implementation differences, all of these algorithms can take advantage of the consistency diagram as an aid in identifying the correct complex modal frequencies from the large number of estimates that are found.

The most commonly used modal identification methods can be summarized as shown in Table 1.

All of the methods summarized in Table 1 have a common characteristic in that they involve a matrix coefficient, characteristic polynomial of the form in (3) and (5). Once

Table 1: Summary of modal parameter estimation algorithms.

Algorithm	Domain		Matrix polynomial order			Coefficients	
	Time	Freq.	Zero	Low	High	Scalar	Matrix
Complex Exponential Algorithm (CEA)	•				•	•	
Least Squares Complex Exponential (LSCE)	•				•	•	
Polyreference Time Domain (PTD)	•				•		$N_S \times N_S$
Ibrahim Time Domain (ITD)	•			•			$N_L \times N_L$
Multireference Ibrahim Time Domain (MRITD)	•			•			$N_L \times N_L$
Eigensystem Realization Algorithm (ERA)	•			•			$N_L \times N_L$
Polyreference Frequency Domain (PFD)		•		•			$N_L \times N_L$
Simultaneous Frequency Domain (SFD)		•		•			$N_L \times N_L$
Multireference Frequency Domain (MRFD)		•		•			$N_L \times N_L$
Rational Fraction Polynomial (RFP)		•			•	•	$N_S \times N_S$
Orthogonal Polynomial (OP)		•			•	•	$N_S \times N_S$
Polyreference Least Squares Complex Frequency (PLSCF)		•			•	•	$N_S \times N_S$
Rational Fraction Polynomial-Z Domain (RFP-Z)		•			•	•	$N_S \times N_S$
Complex Mode Indication Function (CMIF)		•	•				$N_L \times N_S$

this is noted, all of these methods can be explained with a common mathematical form. In previous papers, this has been referred to as the Unified Matrix Polynomial Algorithm (UMPA) model [4–7]. Since both the frequency and time domain models are based upon functionally similar matrix coefficient, characteristic polynomials, the UMPA (m, n, v) terminology can be used for models in both domains to reflect the order of the denominator polynomial (m), the order of the numerator polynomial (n), and the order of the base vector (v) involved in the basic UMPA formulation. This common approach to all algorithms is particularly useful in autonomous modal parameter estimation procedures in that multiple, different algorithms can be more easily combined into a single solution approach. This is an extremely useful concept when developing autonomous modal parameter estimation procedures and bringing solutions from all methods together in one autonomous procedure. If the interested reader is unfamiliar with any of the modal parameter estimation algorithms cited in Table 1, the complete list of references for each modal parameter estimation algorithm can be found in one of the cited UMPA references [4–7].

Table 2 organizes the modal parameter estimation algorithms from Table 1 into one of four categories. Algorithms in each category have similar numerical structure and performance characteristics. The methods highlighted in bold font text in both tables are used together in a single autonomous modal parameter estimation procedure throughout the remainder of this paper. The highlighted methods are chosen as representative of the characteristics of all of the methods in their respective category in Table 2 and are representative of methods used by most practitioners in both research and commercial implementations.

As a matter of further clarification, two different Polyreference Frequency Domain (PFD) algorithms were developed independently in the 1980s. Both methods are low order, frequency domain methods. PFD-1 is the designation for the first order form and PFD-2 is the designation for the second order form. A recent paper explains that the two methods are theoretically equivalent [8].

Table 2: Four corners of modal parameter estimation.

	Time domain	Frequency domain
Low order models	ITD MRITD **ERA**	**PFD-1** PFD-2 PFD-Z SFD MRFD
High order models	CEA LSCE **PTD**	RFP OP PLSCF **RFP-Z** PolyMAX AF-Poly

2.3. Autonomous Modal Parameter Estimation. The interest in automatic modal parameter estimation methods has been documented in the literature since at least the mid-1960s when the primary modal method was the analog, force appropriation method [1–3]. Following that early work, there has been a continuing interest in autonomous methods that, in most cases, have been procedures that are formulated based upon a specific modal parameter estimation algorithm like the Eigensystem Realization Algorithm (ERA), the Polyreference Time Domain (PTD) algorithm, or more recently the Polyreference Least Squares Complex Frequency (PLSCF) algorithm or the commercial version of the PLSCF, the PolyMAX method [4–7]. A relatively complete list of autonomous and semiautonomous methods that have been reported prior to 2010 can be found in a recent paper [9]. The interested reader should also review other similar methods in more recent references [10–13].

Each of these past procedures has shown some promise but has not yet been widely adopted. In many cases, the procedure focussed on a single modal parameter estimation algorithm and did not develop a general procedure. Most of

the past procedural methods focussed on modal frequency (pole) density but depended on limited modal vector data to identify correlated solutions. Currently, due to increased computational speed and availability of memory, procedural methods can be developed that were beyond the computational scope of available hardware only a few years ago. These methods do not require any initial thresholding of the solution sets and rely upon correlation of the vector space of hundreds or thousands of potential solutions as the primary identification tool.

The discussion in the following sections of the use and impact of spatial information in autonomous modal parameter estimation is based upon recent implementation and experience with an autonomous modal parameter estimation procedure referred to as the common statistical subspace autonomous mode identification (CSSAMI) method [9, 14–16]. The strategy of the CSSAMI autonomous method is to use a default set of parameters and thresholds to allow for all possible solutions from a given data set. This strategy allows for some poor estimates to be identified as well as the good estimates. The philosophy of this approach is that it is easier for the user to evaluate and eliminate poor estimates compared to trying to find additional solutions. The reader is directed to a series of previous papers in order to get an overview of the methodology and to view application results for several cases [9, 14–16].

Note that much of the background of the CSSAMI method is based upon the Unified Matrix Polynomial Algorithm (UMPA) described in the previous section. This means that this method can be applied to both low and high order methods with short or long dimension modal (base) vectors. This also means that most commercial algorithms could take advantage of this procedure. Note that high order matrix coefficient polynomials normally have coefficient matrices of a dimension that is based upon the short dimension of the data matrix (N_S). In these cases, it may be useful to solve for the complete, unscaled, or scaled, modal vector of the large dimension (N_L). This will extend the temporal-spatial information in the modal (base) vector so that the vector will be more sensitive to change. This characteristic is what gives the CSSAMI autonomous method a robust ability to distinguish between computational and structural modal parameters.

3. Pole-Weighted Modal Vectors

When comparing modal (base) vectors, at either the short or the long dimension, a pole-weighted vector can be constructed independent of the original algorithm used to estimate the poles and modal (base) vectors. For a given order k of the pole-weighted vector, the modal (base) vector and the associated pole can be used to formulate the pole-weighted vector as follows:

$$\{\phi\}_r = \begin{Bmatrix} \lambda_r^k\{\psi\}_r \\ \vdots \\ \lambda_r^2\{\psi\}_r \\ \lambda_r^1\{\psi\}_r \\ \lambda_r^0\{\psi\}_r \end{Bmatrix}_r, \qquad \{\phi\}_r = \begin{Bmatrix} z_r^k\{\psi\}_r \\ \vdots \\ z_r^2\{\psi\}_r \\ z_r^1\{\psi\}_r \\ z_r^0\{\psi\}_r \end{Bmatrix}_r. \tag{7}$$

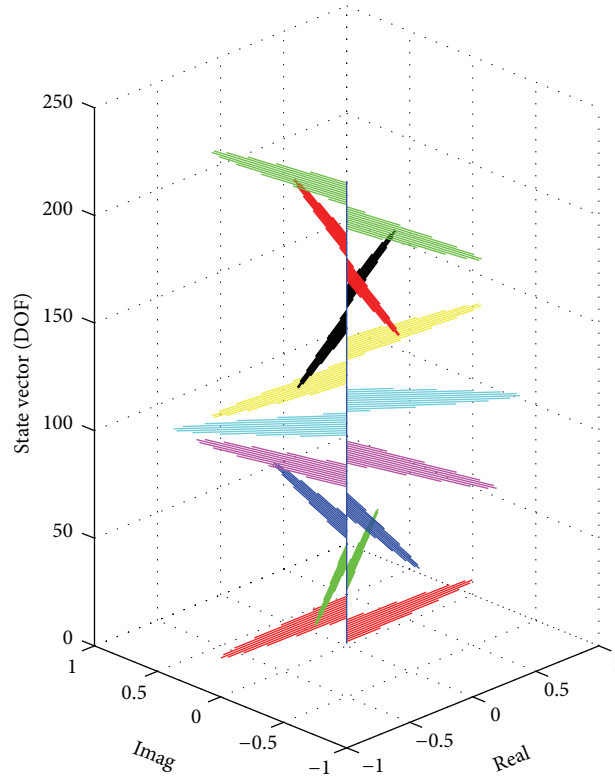

Figure 1: Eighth order, pole-weighted vector (state vector) example.

While the above formulation (on the left) is possible, this form would be dominated by the high order terms if actual frequency units are utilized. Generalized frequency concepts (frequency normalization or z domain mapping) are normally used to minimize this issue by using the z domain form (z_r) of the complex modal frequency (λ_r) as shown above (on the right). The z domain form of the complex natural frequency is developed as follows:

$$z_r = e^{\pi*(\lambda_r/\Omega_{\max})}, \qquad z_r^m = e^{m*\pi*(\lambda_r/\Omega_{\max})}. \tag{8}$$

In the above equations, $\Omega_{\max}$ can be chosen as needed to cause the positive and negative roots to wrap around the unit circle in the z domain without overlapping (aliasing). Normally, $\Omega_{\max}$ is taken to be five percent larger than the largest frequency (absolute value of the complex frequency) identified in the roots of the matrix coefficient polynomial.

Figures 1 and 2 are graphical representations of the pole-weighted vector (state vector) defined in (7). In this representative example, the modal (base) vector (at the bottom of Figure 1) is a real-valued, normal mode that looks like one period of a sine wave. The successive higher orders, up to order eight, are shown in different colors moving up the vertical axis of this figure. The effect of scaling of the modal (base) vector by the higher powers of the z domain frequency value causes the base vector to rotate in the real and imaginary space. Figure 2 shows the rotation effect clearly. Note that the choice of the order (k) of the pole-weighted

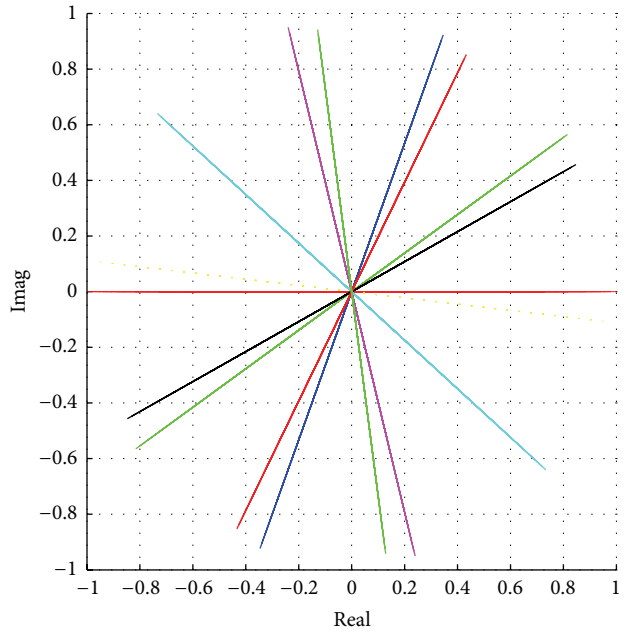

FIGURE 2: Eighth order, pole-weighted vector (state vector) example, top view.

vector, therefore, just generates additional length and rotation in the pole-weighted vector and gives varying sensitivity to comparisons between estimates. Furthermore, note that the choice of order (k) is independent of the modal parameter estimation algorithm and the order of the matrix polynomial used in the algorithm. State vectors are a natural part of the numerical formulation for all modal parameter estimation algorithms, but this pole-weighted vector (state vector) which looks similar is not constrained by the algorithm. Note that if the base vector is complex-valued, rather than real-valued, each vector contribution to the pole-weighted vector will contain this real versus imaginary scatter and Figure 2 will present rotated, banded areas rather than the rotated lines in this example.

The order (k) of the pole-weighted vector (state vector) is up to the user. Generally, if spatial dimension used to generate the pole-weighted vector (N_S and/or N_L) is small, a higher order will be required to discriminate between modal vectors that have similar spatial characteristics, maybe as high as 50 or 60. As the spatial dimension gets bigger, the model order (k) can be chosen more modestly. Essentially, the order (k) of the pole-weighted vector is inversely proportional to the dimension of the base vector. Experience has shown that an order of four or five is probably the minimum and that larger choices for model order (k) do not appear to cause any issues. For the purposes of the examples used in this paper, the order has been chosen to be ten, meaning orders of zero to ten (eleven times the base vector) have been used to generate the pole-weighted vectors.

While the order (k) of the pole-weighted vector (state vector) can be raised ($k = 50$ or $k = 60$, e.g.) for a case with minimal base vector dimension (two or three, e.g.), this is generally not as desirable as using a larger base vector (thirty, e.g.) raised to a more modest order ($k = 5$ or $k = 6$, e.g.). In this example, the longer base vector would have more independent spatial information contributing to the pole-weighted vector. While this is intuitive and has been observed to be the case, no formal study has taken place concerning this issue. Using the longest base vector seems to be the prudent approach, assuming that the data is representative of the DOF space.

Since the magnitude of the z domain frequency value is unity, there is no magnitude weighting involved. This rotation gives a method for a single vector to represent the modal (base) vector shape together with the complex-valued frequency. With respect to sorting and separating modal vectors that have similar shapes but different frequencies or similar frequencies but different modal vector shapes, this becomes a powerful parameter, together with modal vector correlation tools like the modal assurance criterion (MAC) [17, 18], for modal parameter estimation and for autonomous modal parameter estimation.

4. Multialgorithm, Extended Consistency Diagrams

Consistency diagrams have historically been developed for a specific modal parameter estimation algorithm. As such the numerical implementation can be different as a function of basis dimension (N_S or N_L), model order, and/or subspace iteration. This would make it very hard to combine different algorithms into a single consistency diagram. However, every algorithm, at the point of the numerical implementation of the consistency diagram, has multiple sets of complex modal frequency and complex-valued modal vectors. The modal vectors may be of different length (N_S or N_L) as a function of algorithm. This potential mismatch in modal (base) vector length can be solved by restricting the long dimension to the DOFs of the short dimension or, more preferably, adding an extra step in the solution procedure to estimate the missing portion of the short dimension vectors, extending them to the long dimension DOFs. The latter approach is used in the following two figures as an example of *extended consistency diagrams* based upon multiple modal parameter estimation algorithms. In these examples, the results from the individual algorithms are simply stacked into the extended consistency diagram with common sorting and evaluation settings.

The data used for this, and all following examples in this paper, is FRF data taken from an impact test of a steel disc supported in a pseudo-free-free boundary condition. The steel disc is approximately 2 cm. thick and 86 cm. in diameter with several small holes through the disc. The center area of the disc (diameter of approximately 25 cm.) has a thickness of approximately 6 cm. There are seven reference accelerometers and measured force inputs from an impact hammer are applied to thirty-six locations, including next to the seven reference accelerometers. The frequency resolution of the data is 5 Hertz. While the disc is not as challenging as some industrial data situations that contain more noise or other complicating factors like small nonlinearities, the disc has a number of pseudorepeated roots spaced well within the 5 Hertz frequency resolution and a mix of close modes involving repeated and nonrepeated roots which are very

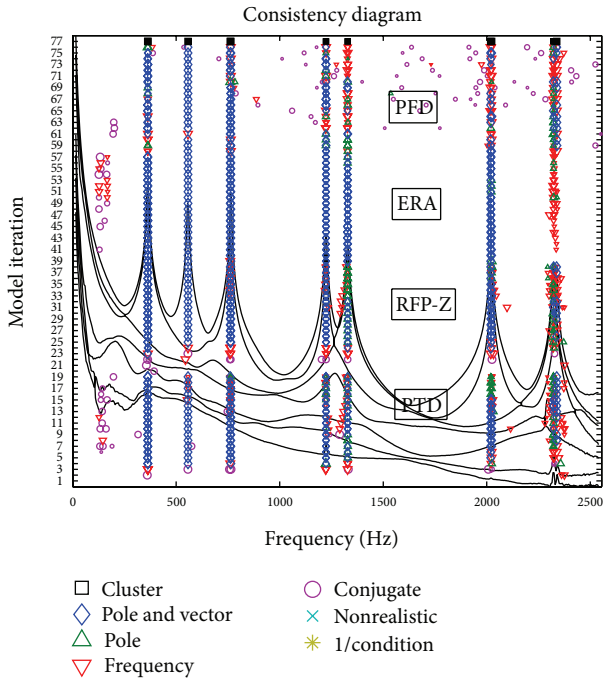

Figure 3: Extended consistency diagram, conventional version.

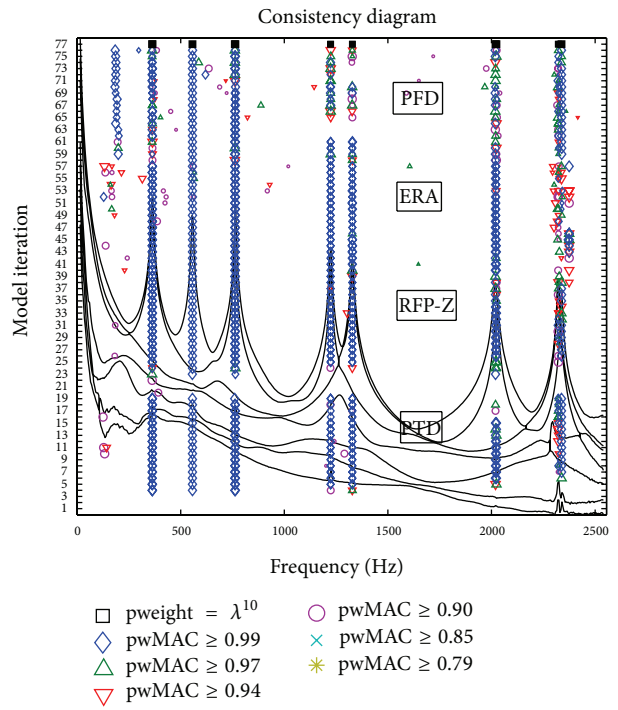

Figure 4: Extended consistency diagram, pole-weighted MAC version.

challenging. Based upon the construction of the disc, real-valued, normal modes can be expected and the inability to resolve these modes can be instructive relative to both modal parameter estimation algorithm and autonomous procedure performance. For the interested reader, a number of realistic examples are shown in other past papers including FRF data from an automotive structure and a bridge structure [9, 16].

Figure 3 is an example of using a conventional, sequential sorting procedure involving criteria for frequency, damping, and modal vector consistency. The symbol designations in the legend box identify consistency based upon separate user definitions regarding frequency; frequency and damping (pole); and frequency, damping, and modal vector closeness. Modal vector consistency is determined by using typical vector correlation methods (MAC) [17, 18] to identify consistency. In this type of consistency diagram, the only consistency comparisons that are made compare the current model order values to the previous model order values. This sequential estimation of consistency allows for some parameter drift as model order or algorithm is changed.

The figure includes a complex mode indicator function (CMIF) for the FRF dataset in the background. The blue diamond symbols indicate that modes have been identified with consistent frequency, damping and modal vector estimates as both model order and algorithm are changed. From the CMIF plot in the background, it is clear that most of the identified modes are closely spaced, repeated roots. For these cases, there are two blue diamonds at each solution on top of one another. The multialgorithm approach is sensitive to the transitions between algorithms as the modal parameter estimates and symbol designations are estimated sequentially across these transitions.

Figure 4 is an example using a pole-weighted vector (state vector) method of producing a similar consistency diagram. This approach is easier to implement numerically and provides equal or better results when compared to the conventional approach for almost all cases. In this example, every estimate from every matrix coefficient polynomial solution from every algorithm is converted into a pole-weighted vector of a specific order, in this case tenth order. Then, the consistency diagram is developed by using the same vector correlation methods (MAC) [17, 18] to identify consistency without a need for a separate consistency comparison for frequency and damping (since the modal frequency is included in the pole-weighted vector). A similar set of symbols, as those used in Figure 3, are used to define increased levels of vector consistency in terms of the MAC value between all pole-weighted vectors.

Both methods work very well but the implementation of Figure 4 is computationally easier and not subject to a frequency drift in the symbol path that can occur in the conventional implementation, shown in Figure 3, that is due to frequency and damping variation with model order for each algorithm. Note that the solid square symbols at the top of both consistency diagrams represent the solution found from the CSSAMI autonomous modal parameter estimation procedure applied to the information represented by each consistency diagram.

5. Autonomous Modal Parameter Estimation with Extended Consistency Diagrams

The CSSAMI autonomous procedure utilizes all solutions indicated by a symbol in the consistency diagram. If some

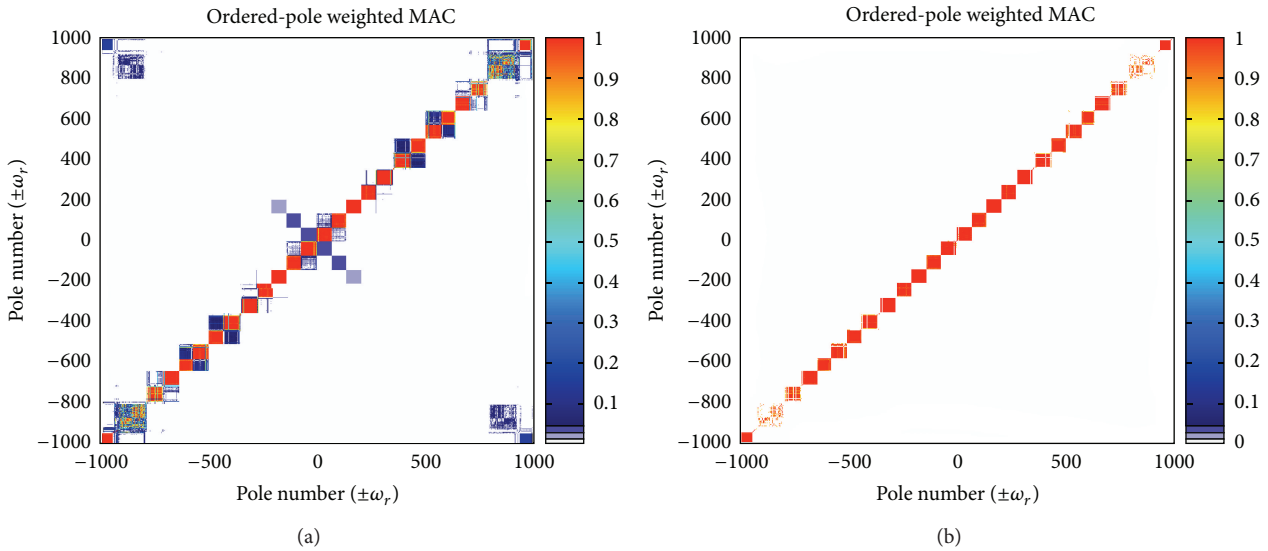

Figure 5: Pole-weighted MAC of all consistency diagram solutions, before and after threshold applied.

symbols are not present, it means that the user has decided not to view solutions identified by those symbols. This provides a way to remove solutions from the autonomous procedure that are clearly not reasonable. However, experience with the CSSAMI autonomous procedure has shown that some solutions that are often eliminated by users in an attempt to have a clear consistency diagram are often statistically consistent and useful.

Figure 5 shows the solutions that are included in the autonomous procedure. The graphical representation on the left represents an auto-MAC matrix involving the pole-weighted vectors for all possible solutions from Figure 3 compared to themselves. Naturally, the diagonal will be 1.0 but when the off-diagonal terms are 1.0 or nearly 1.0, this means that the pole-weighted vectors are consistent and represent a cluster. The graphical representation on the right represents the pole-weighted vectors that remain after a MAC threshold (0.9) and minimum cluster size (4) limitations are imposed. Each cluster that remains is evaluated, cluster by cluster, independently to estimate the best modal frequency and modal vector from that cluster. Note that both the positive frequency and negative frequency (complex conjugate) roots are included and identified separately as clusters. Figure 5 represents nearly 1000 solution estimates spanning four different algorithms and 19 different solutions from each algorithm.

For the examples used in this paper, a minimum cluster size is chosen to be four. This choice is up to the user and generally should not be chosen too large. The philosophy is to allow the autonomous procedure to identify all possible clusters and then have the experienced user make the final decision if some of the clusters yield nonphysical results. These decisions can be made based upon statistics associated with the cluster or physical characteristics of the modal parameters. If the cluster size is too small, some modal vectors might be excluded. This would require the user to reprocess the data looking for a missing modal vector. It is far easier for the user to remove unwanted or nonphysical modes than to try to find modes that have been marginally excited in the data. The first column of Table 3 shows the cluster size for each mode estimated from the autonomous procedure.

Once the final set of modal parameters, along with their associated statistics, is obtained, quality can be assessed by many methods that have been used in the past. The most common example is to perform comparisons between the original measurements and measurements synthesized from the modal parameters. Another common example is to look at physical characteristics of the identified parameters such as reasonableness of frequency and damping values, normal mode characteristics in the modal vectors, and appropriate magnitude and phasing in the modal scaling. Other evaluations that may be helpful are modal assurance criterion (MAC) evaluation of the independence of the complete modal vector set, mean phase correlation (MPC) of each vector, or any other method available. Naturally, since a significant number of pole-weighted vectors are used in a cluster to identify the final modal parameters, traditional statistics involving mean and standard deviation are now available. Some of these statistical methods are discussed in the next section.

6. Statistical Evaluation Parameters

Statistical evaluation parameters can be estimated for each common cluster of pole-weighted vectors on the basis of the complex modal frequency, the modal vector, and the modal scaling. The number of pole-weighted vectors will in general be different in each cluster so the statistics will be based upon the number of estimates available (sample size N). Examples of the statistics currently computed for each modal parameter are described in the following sections.

6.1. Modal Frequency Statistics. The weighted modal frequency for the cluster is found by constructing the pole-weighted vector (typically 10th order) for each pole retained

Table 3: Summary of autonomous modal parameter estimation statistics.

N	Freq. (SV)	Damp (SV)	% Zeta	MPC	Freq. (Mean)	Damp (Mean)	Std. Dev.	$NMVR_1$%	$NMVR_2$%	$NSVR_1$%	$NSVR_2$%
69	362.356	−3.128	0.8633	0.9199	362.356	−3.128	0.1049	0.7686	6.3402	0.7686	6.3402
69	363.696	−3.403	0.9358	0.8915	363.696	−3.403	0.1112	1.2308	10.2036	1.2312	10.2062
71	557.008	−2.888	0.5184	0.9926	557.008	−2.888	0.1144	0.0810	0.6281	0.0812	0.6281
69	761.172	−5.091	0.6688	0.9701	761.172	−5.091	0.1345	0.8888	7.1128	0.8889	7.1129
70	764.175	−2.581	0.3377	0.9862	764.175	−2.581	0.0865	0.3335	2.2550	0.3337	2.2566
64	1222.940	−4.074	0.3332	0.8286	1222.940	−4.074	0.0855	0.9708	6.4450	0.9712	6.4492
67	1224.080	−3.962	0.3236	0.8316	1224.079	−3.962	0.1645	1.0343	8.3785	1.0338	8.3748
68	1327.955	−6.704	0.5048	0.8264	1327.953	−6.705	0.3577	1.2250	9.9197	1.2248	9.9176
57	1328.699	−5.421	0.4080	0.8169	1328.698	−5.421	0.1400	0.8649	6.3990	0.8645	6.3960
69	2019.161	−8.153	0.4038	0.9655	2019.163	−8.159	1.0262	1.0610	7.3389	1.0623	7.3411
56	2023.589	−7.525	0.3719	0.9481	2023.590	−7.525	0.5596	1.8525	11.7555	1.8518	11.7490
18	*2321.822*	*−3.947*	*0.1697*	*0.7848*	*2321.819*	*−3.947*	*0.5460*	*3.3706*	*14.0340*	*3.3657*	*14.0137*
4	*2324.280*	*−3.537*	*0.1522*	*0.8555*	*2324.271*	*−3.537*	*1.3115*	*7.3179*	*13.3856*	*7.3251*	*13.3951*
47	2337.946	−4.194	0.1794	0.9654	2337.945	−4.201	0.9058	0.9132	4.5838	0.9129	4.5811

in a cluster, then taking the SVD of the group of pole-weighted vectors and selecting the singular vector associated with the largest singular value. This chosen singular vector contains both the shape and the modal frequency information. The modal frequency is identified by dividing the first order portion by the zeroth order portion of the vector in a least squares sense. (Note that it is also possible to solve the frequency polynomial which would result from using the complete vector.) Also, for numerical reasons, the pole-weighted vector is actually computed in the z domain.

For comparison purposes, the actual mean value and standard deviation of the poles (as well as the separate frequency and damping means and standard deviations) which were used in the computation of the weighted solution are computed. Since these results are unweighted by the vector characteristics, they may be somewhat different from the vector weighted solution and provide comparative feedback about the pole.

6.2. Modal Vector Statistics. In order to evaluate the quality of the resulting modal vectors, several different parameters (representing noise to signal ratios) are calculated. These ratios are evaluated for both the original normalized vectors and the pole-weighted (state extended) vectors and are computed using the singular value decomposition of each of the set of vectors.

6.2.1. Normalized Modal Vector Residual (NMVR). The first modal vector parameter is evaluated by taking the total residual magnitude (the Frobenius norm of the residuals) divided by the magnitude of the principal vector magnitude. In other words, the square root of the sum of the squares of the residual singular values divides by the first (largest) singular value. This provides an indication of the consistency of the original contributing vectors. Small values tend to indicate greater consistency. Large values indicate greater variance or the possibility that more than one mode has been included in a cluster. Consider

$$\lceil \sigma \rfloor = \mathrm{SVD}\left(\left[\psi_1 \psi_2 \cdots \psi_N\right]\right),$$
$$\mathrm{NMVR}_1 = \frac{1}{\sigma_1}\left(\frac{\sum_{k=2}^{N} \sigma_k^2}{N}\right)^{1/2}. \tag{9}$$

The second modal vector parameter is evaluated by taking the largest residual magnitude divided by the magnitude of the principal vector magnitude. In other words, the second singular value divided by the first singular value. This provides an indication of the consistency of the original contributing vectors. A small value tends to indicate random variance. A larger value can indicate a consistent modal contamination of the original vectors, possibly caused by a second mode included in the cluster:

$$\mathrm{NMVR}_2 = \frac{\sigma_2}{\sigma_1}. \tag{10}$$

6.2.2. Normalized State Vector Residual (NSVR). The associated state vector parameters are calculated analogous to the above except that the complete pole-weighted vector (state vector) is used:

$$\lceil \sigma \rfloor = \mathrm{SVD}\left(\left[\phi_1 \phi_2 \cdots \phi_N\right]\right),$$
$$\mathrm{NMVR}_1 = \frac{1}{\sigma_1}\left(\frac{\sum_{k=2}^{N} \sigma_k^2}{N}\right)^{1/2}, \tag{11}$$
$$\mathrm{NSVR}_2 = \frac{\sigma_2}{\sigma_1}.$$

6.3. Modal Scaling Statistics. If modal scaling (residue) information is available in the original vectors, it can be

applied to the principal pole-weighted vector such that the consistency of modal scaling (Modal A) can also be evaluated. By scaling the largest driving point response to unity, a uniform, comparable value for Modal A is chosen. Since the modal scaling parameter (Modal A) contains the physical units and hence the relative contribution of each pole/vector combination to the original data set, a means of evaluating the significance and confidence in each estimate is possible. Because the original vectors represent multiple scaled solutions and since Modal A is a single scalar complex value for each pole/vector combination, the statistical distribution of Modal A (mean and standard deviation) of the original cluster can be compared with the scaling estimated from the pole-weighted (state extended) vector. The magnitude of Modal A can be used to evaluate the contribution of this vector to the total set of identified vectors. When the user believes that the identified vectors should be normal modes, the phase of the Modal A can be used to evaluate the closeness to a normal mode.

6.4. Example: Statistical Evaluation. Table 3 represents a tabulation of the modal parameters found along with some of the statistical information described in the previous sections. Most of the indicators are quite good with the exception of the modes in the region around 2320 Hertz. The fact that the size of the clusters is much smaller (18 and 4) than all of the other clusters is a quick way to identify possible problems.

Figure 6 shows the location of the complex modal frequency estimates in the second quadrant of the S plane. The scatter in the modal frequency estimates is clearly identifiable. However, the exact cause of the scatter is not definitive.

The two modes in this region, within one Δf, plus a third mode within four Δf, are providing a difficult identification problem. The spatial resolution of the sensors is also nearly at a limit due to the complexity of the motion in the modal vector. This contamination of the modal vectors, when resolving close modal frequencies, will be discussed briefly in the next section using some variations of the modal assurance criterion (MAC).

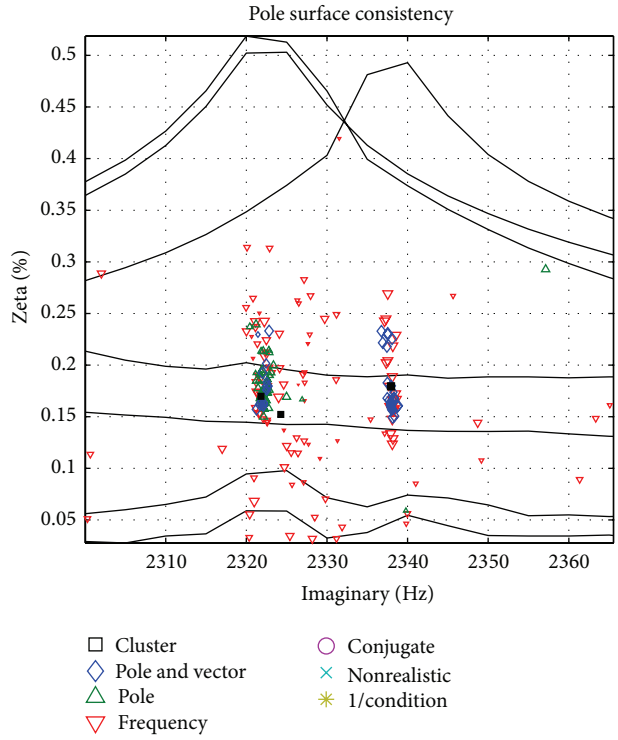

Figure 6: Pole surface consistency, 2320 Hertz region.

7. Future Work: Resolving Modal Vector Contamination

Much of the CSSAMI autonomous procedure, as well as most commonly used modal parameter estimation methods, utilize the traditional modal assurance criterion (MAC) computation, restated in (12), to sort the numerous possible solutions into clusters related to different modes or to identify contamination between modal vectors:

$$\mathrm{MAC}_{cd} = \frac{\left|\{\psi_c\}^H \{\psi_d\}\right|^2}{\{\psi_c\}^H \{\psi_c\} \{\psi_d\}^H \{\psi_d\}} = \frac{\{\psi_c\}^H \{\psi_d\} \{\psi_d\}^H \{\psi_c\}}{\{\psi_c\}^H \{\psi_c\} \{\psi_d\}^H \{\psi_d\}}. \quad (12)$$

The only difference in the CSSAMI autonomous modal parameter estimation procedure is that the pole-weighted vectors of an arbitrarily (user defined) order are constructed and used in the MAC calculation so that the dimension of each vector is much larger. In this way, the clusters for spatially undersampled modal vectors can be separated from one another. Likewise, modal vectors associated with close frequencies will be separated into distinct clusters. This is done automatically once (1) the order of the pole-weighted vector is chosen and (2) the lowest acceptable threshold for MAC correlation is chosen. A third parameter is also needed (3) to define the minimum number of modal vector estimates required to define a cluster (otherwise clusters of one or two will be identified that generally represent spurious estimates based upon noise on the data). Normally this minimum number of modal vectors to define a cluster is greater when more estimates are available, as in the case where multiple modal parameter estimation algorithms are incorporated into the autonomous procedure. Figure 5 is a graphical representation of the before and after information gained from this MAC procedure.

Note that the CSSAMI autonomous procedure treats each cluster of estimates independently and does not constrain the final set of modal vector estimates in any way. At this point in the autonomous procedure, the MAC computation is again utilized to evaluate the quality of the solutions. This begins with an evaluation of the MAC between all of the modal vectors in the final set to ascertain whether the modal set is an independent set of vectors. This often involves including the estimates of the modal vectors associated with the conjugate poles. Since the conjugate poles and vectors are estimated separately, if nonconjugate relationships exist between the associated modal vector estimates (between the modal vector for pole and the modal vector of the conjugate

pole), the MAC between these two associated vectors will not be unity as expected. A number of users have noted that this often correlates with modal vectors that are exhibiting some unexpected, nonphysical characteristics.

Since much of the autonomous procedure is based upon numerical processing methods like singular value decomposition (SVD), solutions that are identified, based upon the data associated with a cluster of estimates, have no physical or causal constraint. An example of a physical or causal constraint would be the expectation of real-valued, normal modes for systems where no expectation of nonproportional damping is likely. SVD methods will identify the most dominant unitary (orthogonal and unit length) vectors in a cluster, yielding a complex-valued vector. Experience has shown that when modes are very close in frequency with minimal spatial resolution, the complex-valued vectors will still show significant dependence or correlation.

However, when these complex-valued vectors are examined closely, the nondominant portion of the complex-valued vector often correlates very highly with one or more nearby modal vectors. This can be examined by the MAC calculation or several variants of the MAC calculation (like the weighted MAC calculation defined in (14)). Identifying the potential contamination of modal vectors is helpful to the thorough understanding of the modal parameter estimation algorithms and autonomous procedure as well as being instructive for potential removal of the contamination. If some sort of real normalization is desirable (to match up well with an undamped analytical model, e.g.), understanding of the contamination that is being removed is a prerequisite to any procedure. Random contamination may simply be ignored, smoothed, or averaged out, but if the contamination is related to nearby modes, it may indicate that the modal parameter estimation may need further evaluation or that more data is required.

For this evaluation of the modal vector contamination, it will be easiest to first rotate each complex-valued modal vector to a real (or imaginary) dominant vector. This is done by using a least squares method to identify the rotation of the modal vector away from the real or imaginary axis and then using the associated complex phasor to rotate each original complex-valued modal vector to a new complex-valued modal vector that aligns with the real or imaginary axis. For all following discussions, the original complex-valued modal vectors are rotated to be dominantly real-valued. It is convenient, for display reasons, to also normalize the new complex-valued modal vector to a unity maximum or unity vector length. Naturally, this rotation and rescaling must be considered in any final estimates of modal scaling.

To understand the nature of the possible modal vector contamination in a complex-valued modal vector, three conventional MAC calculations can be performed (1) between the real parts of the modal vectors and the complex-valued modal vectors (rMAC), (2) between the imaginary parts of the modal vectors and the complex-valued modal vectors (iMAC), and (3) between the real parts of the modal vectors and the imaginary parts of the modal vectors (riMAC). These three MAC calculations and the interpretation of these MAC values will be sensitive to the rotation and normalization of the complex-valued modal vector estimates. The following use and discussion assumes that the complex-valued modal vectors have been rotated so that the central axis of the complex-valued modal vector is centered on the real axis. These three MAC computations identify (1) that the real part of the modal vector is the dominant part of the complex-valued modal vector (rMAC), (2) that the imaginary part of the modal vector is the dominant part of the complex-valued modal vector (iMAC), and (3) that the real and imaginary parts of the modal vector are, or not, related to one another. All MAC computations in this case are, as always, bounded from zero to one. If near normal modes are expected, (1) the rMAC should be close to one, (2) the iMAC should be close to zero, and (3) the riMAC should also be close to zero. Note in the following definitions, complex-valued modal vectors c and d can again be any of the modal vectors that the user wishes to include in the evaluation:

$$\mathrm{rMAC}_{cd} = \frac{\left(\mathrm{Re}\left\{\psi_c\right\}^H\right)\left\{\psi_d\right\}\left\{\psi_d\right\}^H\left(\mathrm{Re}\left\{\psi_c\right\}\right)}{\left(\mathrm{Re}\left\{\psi_c\right\}^H\right)\left(\mathrm{Re}\left\{\psi_c\right\}\right)\left\{\psi_d\right\}^H\left\{\psi_d\right\}},$$

$$\mathrm{iMAC}_{cd} = \frac{\left(\mathrm{Im}\left\{\psi_c\right\}^H\right)\left\{\psi_d\right\}\left\{\psi_d\right\}^H\left(\mathrm{Im}\left\{\psi_c\right\}\right)}{\left(\mathrm{Im}\left\{\psi_c\right\}^H\right)\left(\mathrm{Im}\left\{\psi_c\right\}\right)\left\{\psi_d\right\}^H\left\{\psi_d\right\}},$$

$$\mathrm{riMAC}_{cd} = \frac{\left(\mathrm{Re}\left\{\psi_c\right\}^H\right)\left(\mathrm{Im}\left\{\psi_d\right\}\right)\left(\mathrm{Im}\left\{\psi_d\right\}^H\right)\left(\mathrm{Re}\left\{\psi_c\right\}\right)}{\left(\mathrm{Re}\left\{\psi_c\right\}^H\right)\left(\mathrm{Re}\left\{\psi_c\right\}\right)\left(\mathrm{Im}\left\{\psi_d\right\}^H\right)\left(\mathrm{Im}\left\{\psi_d\right\}\right)}. \tag{13}$$

Use of the above modified MAC evaluations indicate that the imaginary part (contamination) of a given mode is strongly related to the real part (dominant) of the modal vector associated with its pseudorepeated root companion. This is consistent with theory that explains the cause of a complex-valued modal vector when two real-valued modal vectors are close in frequency and misidentified as a single modal vector [19].

The above MAC evaluations identify whether, and how, the contamination of a complex-valued modal vector is related to another of the identified modal vectors. However, the MAC computation is normalized to vector length, vector by vector, for the vectors used in the calculation. A weighted MAC can be used to determine the scale of the contamination. The following three definitions of the weighting for each of the above MAC calculations limit the associated MAC value to a fraction of the zero to one scale. If near normal modes are expected, (1) the weighting and rwMAC should be close to one, (2) the weighting and iwMAC should be close to zero, and (3) the combined weighting and riwMAC should also be close to zero. Note in the following definitions, complex-valued modal vectors c and d can again be any of the modal vectors that the user wishes to include in the evaluation:

$$\mathrm{rwMAC}_{cd} = rW_c \times \mathrm{rMAC}_{cd}$$

$$\text{where } rW_c = \frac{\left(\mathrm{Re}\left\{\psi_c\right\}^H\right)\left(\mathrm{Re}\left\{\psi_c\right\}\right)}{\left\{\psi_c\right\}^H\left\{\psi_c\right\}},$$

$$\text{iwMAC}_{cd} = iW_c \times \text{iMAC}_{cd}$$
$$\text{where } iW_c = \frac{\left(\text{Im}\{\psi_c\}^H\right)\left(\text{Im}\{\psi_c\}\right)}{\{\psi_c\}^H\{\psi_c\}},$$
$$\text{riwMAC}_{cd} = rW_c \times iW_d \times \text{riMAC}_{cd}. \tag{14}$$

At this point, now that the contamination of the complex-valued modal vectors can be confirmed to be from the dominant portion (real part) of other complex-valued modal vectors and that the contamination is not significant, a strategy for determining the best set of real-valued modal vectors can be identified. One reasonable option would be to place the real parts and imaginary parts of each complex-valued modal vector into a matrix as separate real-valued vectors. A singular value decomposition of this real-valued matrix will yield real-valued singular vectors and the most significant singular vectors, equal to the original number of complex-valued modal vectors, associated with the largest singular values can be utilized as the final set of real-valued, normal modes. A simpler solution would be to eliminate the imaginary parts since the scale of the contamination is shown to be small.

8. Summary

With the advent of more computationally powerful computers and sufficient memory, it has become practical to evaluate sets of solutions involving hundreds or thousands of modal parameter estimates and to extract the common information from those sets. In many cases, autonomous procedures give very acceptable results, in some cases superior results, in a fraction of the time required for an experienced user to get the same result. However, it is important to reiterate that the use of these autonomous procedures or *wizard* tools by users with limited experience is probably not yet appropriate. Such tools are most appropriately used by users with the experience to accurately judge the quality of the parameter solutions identified.

Future work will involve better numerical methods for combining algorithms into single consistency diagrams and autonomous methods for identifying the best causal (physical) solution are still needed. The application of MAC and related weighted MAC estimates is helpful for detecting contaminated modal vector solutions but numerical solution methods that identify both real-valued modal vectors (normal modes) and complex-valued modal vectors, when appropriate, are still needed. Initial positive results have been obtained, with respect to removing this close mode contamination, by constraining the modal participation factors via real normalization [20]. If this problem can be resolved, this would truly yield an autonomous modal parameter estimation procedure.

Nomenclature

N_i: Number of inputs
N_o: Number of outputs
N_S: Short dimension size
N_L: Long dimension size
N: Number of vectors in cluster
λ_r: S domain polynomial root
λ_r: Complex modal frequency (rad/sec)
λ_r: $\sigma_r + j\omega_r$
σ_r: Modal damping
ω_r: Damped natural frequency
z_r: z domain polynomial root
$\{\psi_r\}$: Base vector (modal vector)
$\{\phi_r\}$: Pole-weighted vector (state vector)
r: Mode number
ω_i: Discrete frequency (rad/sec)
$[H(\omega_i)]$: FRF matrix ($N_o \times N_i$)
$[\alpha]$: Numerator polynomial matrix coefficient
$[\beta]$: Denominator polynomial matrix coefficient
m: Model order for denominator polynomial
n: Model order for numerator polynomial
v: Model order for base vector
Std. Dev.: Standard deviation
NMVR_1: Normalized modal vector residual 1
NMVR_2: Normalized modal vector residual 2
NSVR_1: Normalized state vector residual 1
NSVR_2: Normalized state vector residual 2
σ_r: Singular value r from cluster
MAC: Modal assurance criterion
wMAC: Weighted modal assurance criterion.

Conflict of Interests

The authors declare that there is no conflict of interests regarding the publication of this paper.

Acknowledgments

The authors would like to acknowledge the collaboration and assistance from the graduate students and faculty of the Structural Dynamics Research Lab at the University of Cincinnati. In particular, the discussions and collaborations with Dr. David L. Brown have been instrumental in the progress made to this point.

References

[1] F. J. Hawkins, "An automatic resonance testing technique for exciting norma l modes of vibration of complex structures," in *Symposium IUTAM, Progres Recents de la Mecanique des Vibrations Lineaires*, pp. 37–41, 1965.

[2] F. J. Hawkins, "GRAMPA—an automatic technique for exciting the principal modes of vibration of complex structures," Royal Aircraft Establishment RAE-TR-67-211, 1967.

[3] G. A. Taylor, D. R. Gaukroger, and C. W. Skingle, "MAMA—a aemi-automatic technique for exciting the principal modes of vibration of complex structures," Tech. Rep. ARC-R/M-3590, Aeronautical Research Council, 1967.

[4] R. J. Allemang, D. L. Brown, and W. Fladung, "Modal parameter estimation: a unified matrix polynomial approach," in *Proceedings of the 1994 International Modal Analysis Conference*, pp. 501–514, 1994.

[5] R. J. Allemang and D. L. Brown, "A unified matrix polynomial approach to modal identification," in *Proceedings of the Indo-US Symposium on Emerging Trends in Vibration and Noise Engineering*, pp. 379–390, Indian Institute of Technology, Allied Publishers Limited, New Delhi, India, March 1996.

[6] R. J. Allemang and D. L. Brown, "A unified matrix polynomial approach to modal identification," *Journal of Sound and Vibration*, vol. 211, no. 3, pp. 301–318, 1998.

[7] R. J. Allemang and A. W. Phillips, "The unified matrix polynomial approach to understanding modal parameter estimation: an update," in *Proceedings of the 2004 International Conference on Noise and Vibration Engineering (ISMA '04)*, pp. 2373–2401, September 2004.

[8] R. J. Allemang, A. W. Phillips, and D. L. Brown, "Combined state order and model order formulations in the unified matrix polynomial method (UMPA)," in *Proceedings of the 29th IMAC, a Conference on Structural Dynamics*, pp. 429–443, February 2011.

[9] R. J. Allemang, D. L. Brown, and A. W. Phillips, "Survey of modal techniques applicable to autonomous/semi-autonomous parameter identification," in *Proceedings of the International Conference on Noise and Vibration Engineering (ISMA '10)*, p. 42, Katholieke Universiteit Leuven, Leuven, Belgium, 2010.

[10] P. Verboven, B. Cauberghe, E. Parloo, S. Vanlanduit, and P. Guillaume, "User-assisting tools for a fast frequency-domain modal parameter estimation method," *Mechanical Systems and Signal Processing*, vol. 18, no. 4, pp. 759–780, 2004.

[11] F. Magalhães, Á. Cunha, and E. Caetano, "Online automatic identification of the modal parameters of a long span arch bridge," *Mechanical Systems and Signal Processing*, vol. 23, no. 2, pp. 316–329, 2009.

[12] F. Magalhães, A. Cunha, and E. Caetano, "Vibration based structural health monitoring of an arch bridge: from automated OMA to damage detection," *Mechanical Systems and Signal Processing*, vol. 28, pp. 212–228, 2012.

[13] E. Reynders, J. Houbrechts, and G. de Roeck, "Fully automated (operational) modal analysis," *Mechanical Systems and Signal Processing*, vol. 29, pp. 228–250, 2012.

[14] A. W. Phillips, R. J. Allemang, and D. L. Brown, "Autonomous modal parameter estimation: methodology," in *Proceedings of the International Modal Analysis Conference (IMAC '11)*, 2011.

[15] R. J. Allemang, A. W. Phillips, and D. L. Brown, "Autonomous modal parameter estimation: statisical considerations," in *Proceedings of the 29th IMAC, a Conference on Structural Dynamics (IMAC '11)*, pp. 385–401, February 2011.

[16] D. L. Brown, R. J. Allemang, and A. W. Phillips, "Autonomous modal parameter estimation: application examples," in *Modal Analysis Topics* , vol. 3 of *Conference Proceedings of the Society for Experimental Mechanics Series*, pp. 403–428, 2011.

[17] R. J. Allemang and D. L. Brown, "A correlation coefficient for modal vector analysis," in *Proceedings of the International Modal Analysis Conference*, pp. 110–116, 1982.

[18] R. J. Allemang, "The modal assurance criterion (MAC): twenty years of use and abuse," *Sound and Vibration Magazine*, vol. 37, no. 8, pp. 14–23, 2003.

[19] F. Deblauwe and R. J. Allemang, "A possible origin of complex modal vectors," in *Proceedings of the 11th International Seminar on Modal Analysis*, p. 10, Katholieke Universiteit Leuven, Leuven, Belgium, 1986.

[20] A. W. Phillips and R. J. Allemang, "Normalization of experimental modal vectors to remove modal vector contamination," in *Proceedings of International Modal Analysis Conference (IMAC '14)*, 2014.

Hindawi Publishing Corporation
Shock and Vibration
Volume 2014, Article ID 201952, 9 pages
http://dx.doi.org/10.1155/2014/201952

Research Article

Fully Equipped Dynamic Model of a Bus

I. Kowarska,[1] J. Korta,[1] K. Kuczek,[2] and T. Uhl[1]

[1] *Department of Robotics and Mechatronics, AGH University of Science and Technology, Aleja Mickiewicza 30, 30-059 Krakow, Poland*
[2] *EC Engineering Sp. z o.o., Ulica Opolska 100, 31-323 Krakow, Poland*

Correspondence should be addressed to T. Uhl; tuhl@agh.edu.pl

Received 26 June 2013; Accepted 5 February 2014; Published 15 July 2014

Academic Editor: Nuno Maia

Copyright © 2014 I. Kowarska et al. This is an open access article distributed under the Creative Commons Attribution License, which permits unrestricted use, distribution, and reproduction in any medium, provided the original work is properly cited.

Nowadays, the time to market a new vehicle is crucial for every company as it is easier to meet the customers' needs and expectations. However, designing a new vehicle is a long process which needs to take into account different performances. The most difficult is to predict a dynamic behavior of a vehicle especially when such a big vehicles as urban buses are considered. Therefore, there is a necessity to use a virtual model to investigate different performances. However, there is a lack of urban bus models that can fully reflect a dynamic behavior of the bus. This paper presents a fully equipped urban bus model which can be used to study a dynamic behavior of such vehicles. The model is based on innovative technique called cosimulation, which connects different modeling techniques (3D and 1D). Such a technique allows performing different analyses that require small deformations and large translations and rotations in shorter time and automatic way. The work has been carried out in a project EUREKA CHASING.

1. Introduction

In nowadays vehicle industry, time to market is a crucial parameter. It is caused by an increasing number of customers' needs and expectations to be met. However, vehicle design is a long process, during which engineers need to take into account many guidelines and fulfill all the requirements connected to safety and comfort of the occupants. Predicting the structural dynamic behavior is one of the most difficult tasks, especially when such big vehicles as urban buses are considered. Due to their size and complexity, experimental derivation of comprehensive dynamic performances can be very difficult and economically unjustified. However, as vehicle dynamics is a very important performance, it cannot be neglected in vehicle analyses. Therefore, there is an opportunity to take advantage of numerical modeling and simulations, to investigate structural performances under different operational conditions. However, despite that fact, there is a lack of engineering literature describing urban bus virtual prototyping projects. Such a literature would have been of help in understanding how to create models that allow accurately predicting the dynamic behavior of the bus. Standard vehicle design process provides short concept design phase and very long prototype testing stage. However, following van der Auweraer and Leuridan [1, 2], modern product development is often based on virtual prototyping according to the rule "Design Right First Time" [3]. It is caused by the need for decreasing production costs and time to market of new vehicle and improving the product quality at the same time.

The main objective for the engineering design of passenger vehicles is to develop models that perfectly reflect the behavior of a real construction. Typically, to obtain trustworthy structural dynamic response, modal analysis of a real structure has to be performed [4, 5]. Modal analysis is carried out to extract structural resonance frequencies and spatial description of vibration patterns, called normal modes frequencies and shapes, respectively. Classical modal analysis is based on a controlled excitation of a system vibration and measurement of a structure response. This can be easily simulated with a standard finite element approach. However, due to the necessity of input forces measurements, classical formulation has a limited use for a lot of large structures like an urban bus, and it is more convenient to use a method based on operational excitation, called operational modal analysis [6]. Therefore, during the simulations, engineers try

to recreate vehicle operating conditions to obtain the most accurate results.

Virtual test rides can be modeled with multibody techniques. Multibody models are used to model the dynamic behavior of a vehicle, which may undergo large translational and rotational displacements. For this reason, those models can be used to simulate vehicles rides. Unfortunately, many problems connected to dynamics cannot be solved by using rigid body approximation of the structure. The necessity for more reliable models describing the complex behavior of mechanical systems undergoing large motions with small elastic deformations forced the development of many powerful analysis techniques. One of the most popular is coupling of rigid multibody systems and flexible components (mostly finite element models), supplemented by auxiliary 1D systems [7].

For this reason, the authors decided to build a hybrid urban bus model that was composed of a rigid-flexible structural multibody model, equipped with on-board intelligent systems that have an influence on riding conditions and, consequently, on the results of dynamic analyses.

The developed model can be used to evaluate a structure's behavior during virtual test rides, which can be carried out on test lanes providing desired dynamic excitations and forcing different maneuvers.

In this paper, an introduction to rigid-flexible body coupling is provided in the beginning. The subsequent parts describe the link between 3D spatial model and block 1D modeling of the on-board systems and the model itself. Such a link is called cosimulation and is an innovative technique that allows performing simulations from different engineering domains (from vehicle dynamics to NVH analysis) in shorter time and in automatic way. The paper describes hybrid urban bus modeling process with underlined base model parts like suspension, structure, and on-board systems. Simulation results are then correlated with experimental data showing correctness of the technique. Those chapters are then followed by the discussion and conclusions.

2. Coupled Rigid-Flexible Multibody Model

Due to the fact that the full model has been developed with LMS Virtual.Lab software, rigid and flexible equations of motion are provided based on [8].

Multibody modeling technique has been developed to simulate industrial and technological applications that are made of interconnected components which exhibit relative movement. These components are represented by sets of bodies linked together by joints and coupling elements like springs, dampers conjugated with constraints, and external force components. The system has to be prepared in order to allow motion in the desired direction to ensure required operating conditions (Figure 1).

Rigid multibody systems are considered to have a fixed frame of reference in which motion of the chosen points is observed.

To describe rigid multibody motion as a function of time, generation of equations of motion is needed. However, for large systems, it is a nontrivial task. For this reason, a lot of formalisms have been developed. Numerical formalisms especially play a significant role as they are used in computer multibody codes which becomes more and more popular and sophisticated [9].

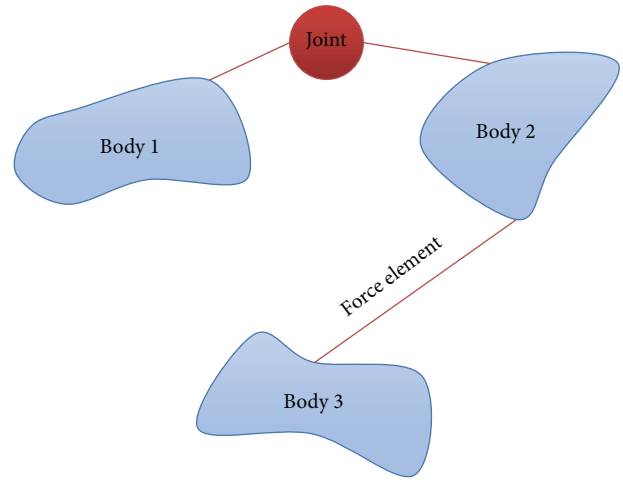

Figure 1: Multibody system.

The most popular formalism is one based on Newton-Euler equations rewritten in the matrix form and used in LMS Virtual.Lab [8]:

$$\begin{bmatrix} M & \Phi_q^T \\ \Phi_q & 0 \end{bmatrix} \cdot \begin{bmatrix} \ddot{q} \\ 1 \end{bmatrix} = \begin{bmatrix} Q \\ g \end{bmatrix}, \quad (1)$$

where Mrepresents a multibody mass matrix, Φ_q is a Jacobian matrix of the vector of constrains relative to the generalized coordinates q, and Q is a vector of applied forces while g is the constraint acceleration *gamma* term and λ is the vector of Lagrange multipliers of the constraints. Equation (1) is then solved inside Virtual.Lab with special integration codes.

Unfortunately, many dynamic problems cannot be solved using only rigid body formulations. In case of small deformations, especially, to calculate structural dynamics, the linear finite element modeling (FEM) method is employed. For this reason coupling between multibody systems and finite element models has become an issue. Finite element models represent linear elastic deformation and can be integrated with nonlinear, large rotations and translations (multibody models). Different solutions for flexible multibody systems can be found in [10].

In Virtual.Lab formulation, the coupled flexible-rigid multibody models require a finite element analysis. The flexibility is represented with a set of flexible body modes which is a combination of normal modes (to represent natural vibration) and static ones (to represent loading and coupling between bodies).

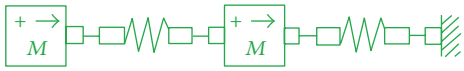

Figure 2: Example of 1D model (block-diagram).

Equation of motion with applied flexibility leads to

$$\begin{bmatrix} M_r & M_{rf} & \Phi_{qr}^T \\ M_{fr} & M_f & \Phi_{qf}^T \\ \Phi_{qr} & \Phi_{qf} & 0 \end{bmatrix} \cdot \begin{bmatrix} \ddot{q}_r \\ \ddot{u} \\ \lambda \end{bmatrix} = \begin{bmatrix} Q_r \\ Q_f \\ g \end{bmatrix}. \quad (2)$$

Mass matrix M is divided into r-rigid part and f-flexible part; the same applies for Jacobian matrix Φ of the constraint equations. Apart from rigid generalized coordinates q, a vector of modal coordinates u appeared; λ represents Lagrange multiplier. On the right-hand side, vector of applied forces Q divided into Q_r forces applied on a rigid body and Q_f forces applied on a flexible body (including body stiffness matrix) and general constrain force g are shown.

The mentioned set of flexible body modes can be obtained in a large number of methods [8]. One of them is the Craig-Bampton dynamic reduction [11]. This method combines normal modes with static-constraint modes (q, u_b) by Craig-Bampton transformation matrix Φ_{CB} which contains a fixed base modeshape Φ_L and a rigid body vector Φ_R:

$$u = \Phi_{\mathrm{CB}} \cdot \begin{Bmatrix} u_b \\ q \end{Bmatrix} = \begin{bmatrix} I & 0 \\ \Phi_R & \Phi_L \end{bmatrix} \cdot \begin{Bmatrix} u_b \\ q \end{Bmatrix}. \quad (3)$$

Modern coupling techniques are still under investigation.

3. 1D System Simulation

The one-dimensional modeling is a mathematical approach in representation of components. In contrast to 3D CAE modeling, this approach gives the capability to simulate the behavior of systems before detailed CAD geometry is available. Model components are described using validated analytical models that represent the systems behavior. This technique of modeling is also referred to as a block modeling or a multiport modeling technique [12]. 1D models are physical models of real systems that are described with mathematical models (systems equation of motion).

One-dimensional models are created by linking individual physical elements together, creating a block diagram of full system (Figure 2). In such a system, the signal flows between individual components. Due to different mathematical representations of individual elements, the input signal is transformed in a predefined manner, to form an output. Those 1D models can be treated separately (solving their equations of motion) or can be linked with 3D models by cosimulation method linking the two solvers (1D and 3D) that can run separately by embedding one set of equations into the other, using only one single solver.

This solution is widely used among automotive engineers especially to simulate electronic systems inside a vehicle [13].

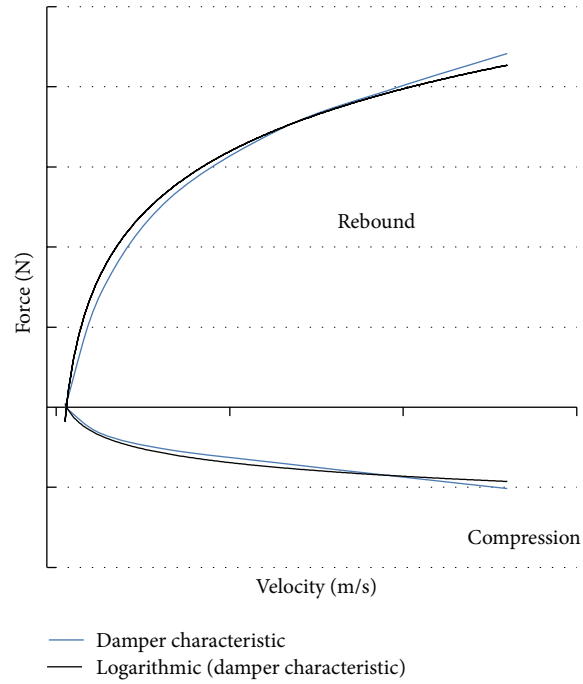

Figure 3: Typical damper characteristic and its logarithmic approximation.

One platform that provides a possibility to build 1D models is LMS Imagine.Lab AMESim that is used in this work.

4. Hybrid Urban Bus Model

4.1. Coupled Bus Multibody Model. The urban bus model developed at AGH UST has been based on a real city bus construction. Individual components have been modeled using CAD geometry and characteristics and additional information provided by the manufacturer. The model contains about 70 individual parts and about 90 kinematic joins. The number of general coordinates (including modal coordinates) is less than 500.

In case of structural dynamics behavior, the suspension is used only as a filter between the track and the bus superstructure. Because of a high rigidity of the suspension structural elements and the frequency band of interest, their deformations were neglected. For this reason, all suspension elements, excluding tires, have been prepared as rigid bodies. Only coupling elements (dampers and bushings) have been described with original characteristics to incorporate proper stiffness and damping characteristics to the model. To obtain accurate damping elements characteristics for the front and the rear suspension, a logarithmic approximation has been performed according to the following (Figure 3):

$$F = c \cdot \ln(v). \quad (4)$$

F represents a rebound/compression damper force, c is a constant (depends on damper type), and v is a car body vibration velocity relative to the wheels.

To connect bus suspension elements, based on supplier technical data, bushing elements are used. Those elements provide an interface between two parts, damping the energy transmitted through the bushing. Bus suspension bushings are made of rubber separating the faces of two metal objects while allowing a certain amount of movement.

To provide good simulation results, bus suspension bushings have been modelled inside Virtual.Lab Motion software as special connector element called bushing. This element allows providing real bushing characteristics to the virtual model as an excel file.

Such connectors minimize vibrations through the chassis of the vehicle in virtual simulations like in the real vehicle.

Another important element that provides traction between the vehicle and the road and absorbs shock is the tire. Based on available information about tire characteristics from the bus manufacturer, those components have been modeled using a Virtual.Lab special tire module called Complex Tire, which permits inputting tire parameters like diameter, stiffness, damping, and so forth, in terms of providing real ride conditions. Parameters values have been taken from supplier data and adjusted to the values that provide good correlation between real experiment and simulation.

Unfortunately, because of missing measurement of real bushing and tires, no correlation directly for those elements has been done.

Urban buses are often equipped with a pneumatic suspension where standard steal springs are replaced with air cushions, filled with pressurized air. The main advantages of using air springs over the standard steel-spring suspensions in an urban bus are

(i) high comfort expressed by small deflections and lower natural frequencies,

(ii) possibility of controlling the operation conditions, by modifying the internal pressure value,

(iii) kneeling function—in case of buses this function eases getting on and off the vehicle on stops [14].

Air springs have been modeled as combined damping and stiffness forces elements controlled by ECAS (electronically controlled air suspension) system. Such a configuration provided a possibility of applying real air spring characteristics to the model.

Due to the fact that the scope of the investigations was to measure bus driver's comfort by means of structure vibration level, the bus superstructure has been modeled as a deformable element. Nastran finite element coding was used to create a FE model based on CAD geometry. To simplify the model, some of the elements like engine or gear have been substituted with concentrated mass elements. Figure 4(a) presents an urban bus suspension multibody model and Figure 4(b) presents a coupled flexible-rigid urban bus model.

4.2. Bus On-Board Systems. To ensure the most realistic simulation conditions and obtain the most accurate response of the analyzed urban bus, electronic auxiliary systems have also been taken into consideration. Nowadays, vehicles are equipped with electronic devices which improve ride quality and safety. For a regular urban bus, the most important are ABS/ASR and EBD (i.e., anti-lock braking system/anti-slip regulation and electronic breaking force distribution) to maintain safety during breaking maneuvers and ECAS (i.e., electronically controlled air suspension) system which controls the work of a pneumatic suspension [15]. To assure a realistic prediction of the behavior of the bus in operating conditions, the abovementioned systems have been applied to the coupled multibody model.

As it was mentioned before, bus structure and suspension have been modeled with 3D models (multibody and FE models), which is necessary to simulate its dynamic behavior. In case of on-board systems, it is not necessary to create 3D models of electronic devices as the most important thing is signal flow from the bus to the electronic units and vice versa. For this reason, on-board systems have been modeled with 1D block diagram method in Imagine.Lab AMESim software. To integrate 3D bus model and 1D electronic devices, a cosimulation between Virtual.Lab and AMESim has been used to exchange information between 3D and 1D models.

Such a cosimulation technique allows reducing simulation time, increasing the realism of the virtual bus.

A brake assist (ABS/ASR and EBD) block diagram, coupled with other parts of the model, is shown in Figure 5. In this circuit, predefined ABS/ASR and EBD elements have been used. The characteristic parameters have been elaborated according to the data provided by the systems manufacturers. The principles of the breaking maneuver, used for the simulation of the model equipped with electronic elements, are similar to realistic driver behavior. Multibody solver sends a signal to AMESim, which contains information about bus actual travelling velocity and angular velocities of each wheel. Based on those, breaking torque for each wheel is evaluated and resent to the leading model. Figure 6 shows that, with break assistant system, the angular velocity of the wheels is a nonzero value, while, without it, axes are blocked in slippage. This underlines the importance of this system for the passenger's safety.

The second system applied to a coupled multibody model was ECAS. Figure 7 presents the ECAS numerical model. This circuit has been fully developed at AGH UST. The investigated system has been equipped with 6 air cushions, two connected to the front axle and four supporting the rear one. This asymmetry is due to the unequal mass distribution—that is, engine, gearbox, and auxiliary systems are located at the back of the vehicle.

The ECAS system has been modeled using the inputs provided by the bus manufacturer. By virtue of submitted data, there was a need for approximation of the received numbers. The derivation of the mathematical models describing the dynamical behavior of the air spring can be found in [16–20]. In general, if isothermal process is assumed inside the air spring, its static stiffness can be described by the following [18]:

$$k_s = \frac{dF}{dx} = P\frac{A_e^2}{V} + \left(P - P_a\right)\frac{dA_e}{dx}, \tag{5}$$

(a) (b)

Figure 4: (a) Multibody bus suspension system; (b) rigid-flexible multibody bus model.

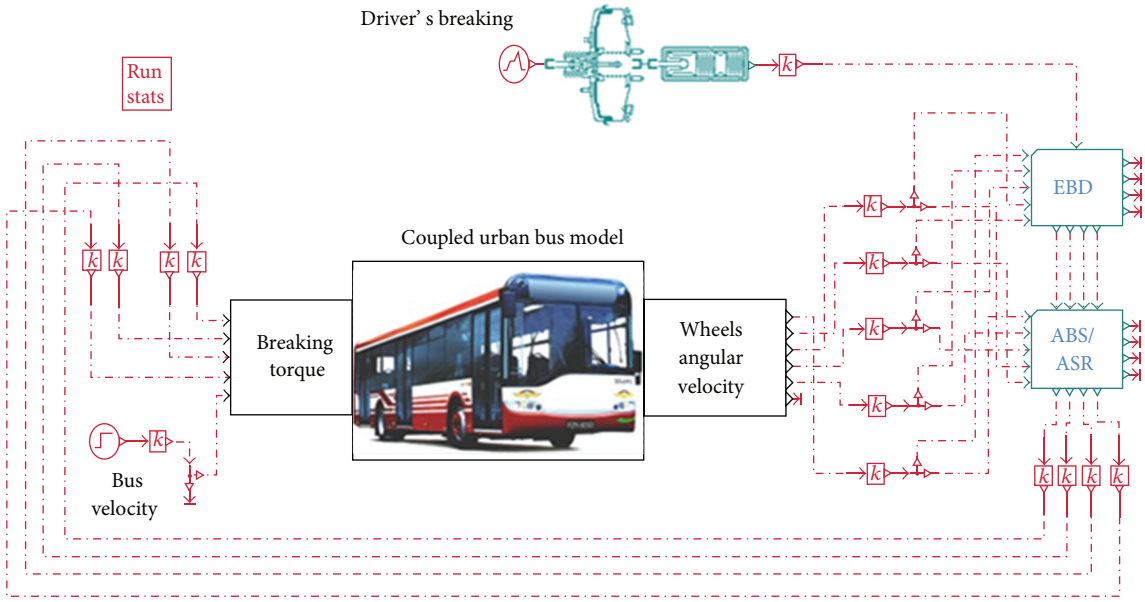

Figure 5: ABS/ASR/EBD signal circuit.

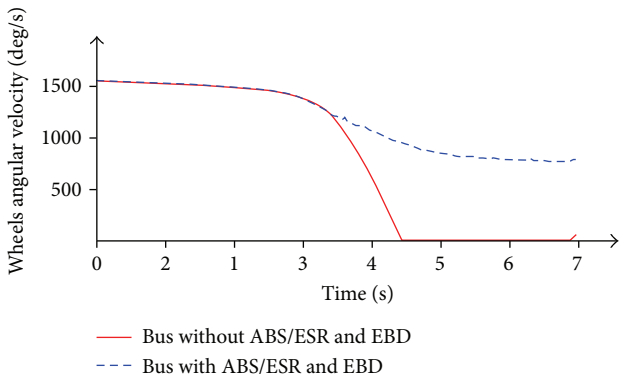

Figure 6: Virtual breaking performance on a slippery road. Comparison of angular velocity of the left wheel: with and without break assist.

where F is an applied force, x is an air sprig deflection (difference between nominal and compressed air spring height), P is the absolute pressure inside the air spring, P_a is the atmospheric pressure, V denotes internal bellows volume, and A_e is an effective area of an air spring (i.e., supported load value divided by P).

Based on a manufacturer's technical data, a regression model approximating the static response of each air spring was developed. To fit a curve on the obtained measurement points, linear robust least squares method has been employed. Standard least squares method tends to minimize the squared distance between the regression curve and the provided data points; thus, it is sensitive to outliers. To omit that problem, algorithm described by (6) [17] was implemented which assigns a weighting factor to every measurement point. The value is inversely proportional to the distance of the measured

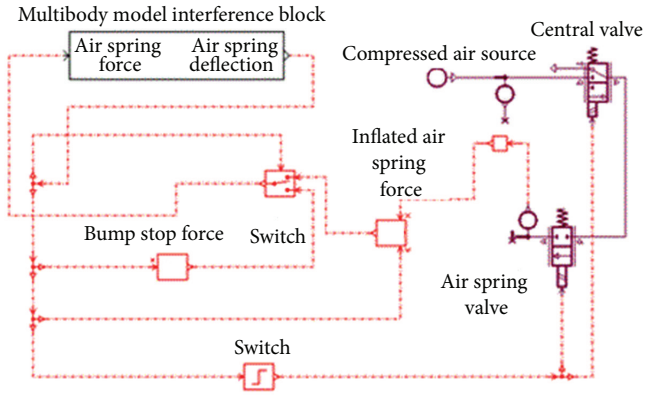

Figure 7: One-quarter of an ECAS model.

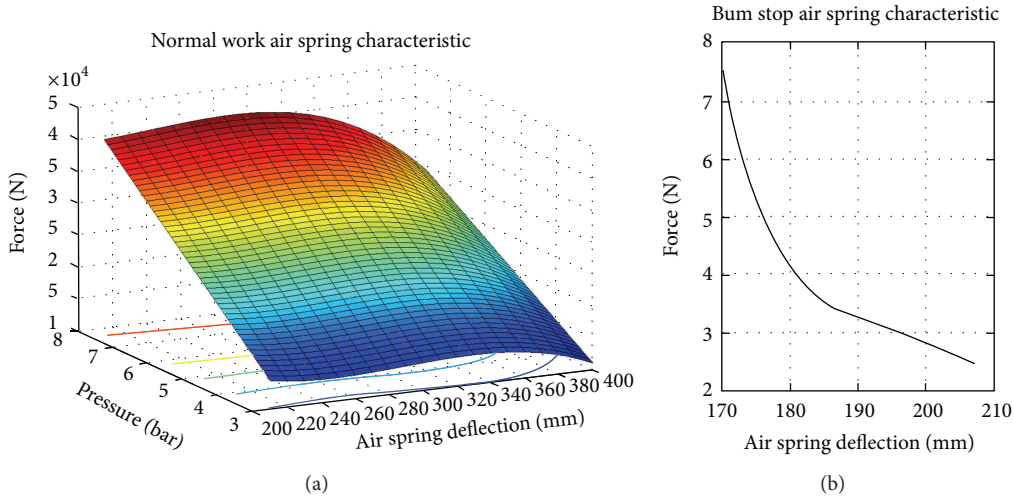

Figure 8: Measurement data approximation: the inflated air spring (a) and the bump stop (b) characteristics.

points from the fitted polynomial curve; thus, the influence of the outliers can be minimized. Furthermore, points which are further than would be expected are ignored during the regression process. Consider

$$S = \sum_{i=1}^{n} w_i \left(y_i - \widehat{y_i}\right)^2, \tag{6}$$

where w_i is the weighting factor for the squared distance between measured y_i and fitted $\widehat{y_i}$ values. Measuring equipment inaccuracies are supposed to be invariant in time; hence, the variance of the acquired data should be constant. If this assumption is violated, it is highly probable that input data set contains some elements of poor quality. The weights w_i are then applied to transform the variances to a constant value. Results of approximation are visible in Figure 8. Because of a strong nonlinearity of the abovementioned characteristic and for simplification, the characteristic was split into two separate regions: force generated by an inflated air spring and force generated by a bump stop, after reaching a critical deflection. The latter is expressed only as a function of bump stop material stiffness.

Consistent with a measured air spring deflection (received from a multibody model) and desired pressure, corresponding force value is sent back to the base structure. If the deflection falls below the specified value, the signal is switched to the bump stop characteristics. If, on the other hand, operational height is within the allowable tolerances, compressed air flow is cut off and the air spring is working as an inflated cushion.

Based on [18], the authors have introduced also an appropriate damping coefficient to the analyzed bus model to simulate not only air spring stiffness but also its damping behavior.

Coupling between flexible and rigid bodies and link with on-board systems block diagrams ensures real ride conditions. Because of a juncture between different modeling techniques, such a structure is called a hybrid model.

5. Simulations

The hybrid model described in a previous chapter has been developed to perform structural dynamics analyses under operational conditions.

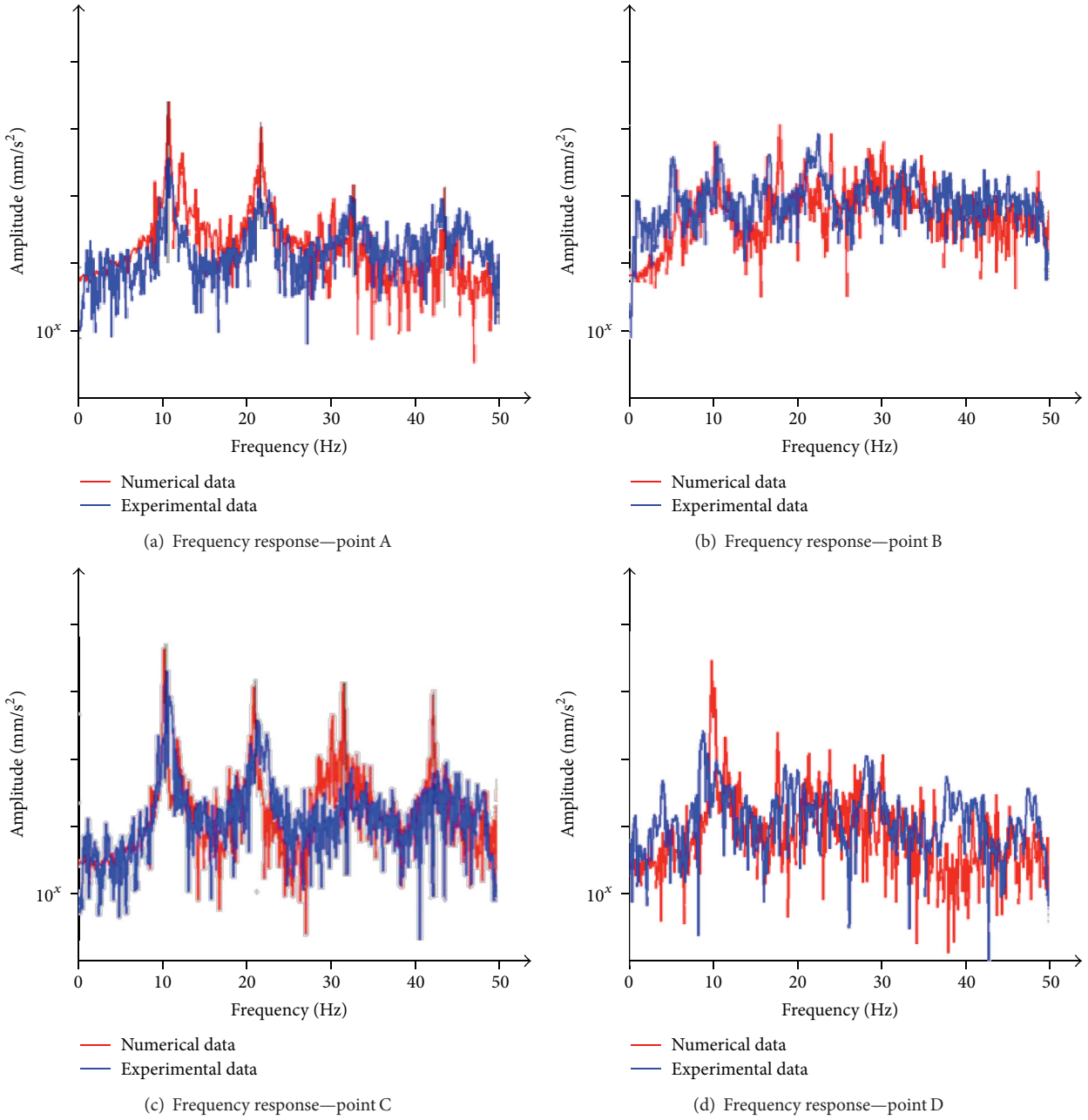

Figure 9: Comparison between numerical and experimental vibration acceleration as a function of frequency: (a) point A; (b) point B; (c) point C; (d) point D.

In order to examine a usefulness of the developed model for the structural measurements, virtual test has been performed and compared with the real test ride on a test track, which was combined from two different surfaces on its left and right side. To obtain the needed data, the conditions of the analysis were set the same as in the case of experiment; that is, the traveling speed was set to 30 km/h. During the experiment, the driver was obliged to keep the velocity constant, but, because of many factors (e.g., speedometer inaccuracy, irregular pavement conditions, etc.), this was only a rough value. Nevertheless, as can be seen in Figure 9, the results of numerical computations are in great correlation with the data obtained experimentally. The peaks at 11 Hz and their harmonics are the consequence of the form of the test track surface, which was covered by regularly distributed curbstones, and the vehicle's speed. Other peaks are caused by structural dynamic response.

Several measurement points located near the suspension mountings (points A (Figure 9(a)) and B (Figure 9(b))) and near the driver seat (points C (Figure 9(c)) and D (Figure 9(d))) were chosen to collect the experimental data during the tests. The obtained results were compared with the output from the numerical computations, which is shown in the examples in Figure 9.

Figure 10: Hybrid urban bus model-stress Von Mises's measurement.

The differences are results of imprecise mapping of the road due to its complicated shape. Inaccuracies can also result from differences in placing the accelerometers on real and virtual structures, which affects the output data strongly. Another reason of the numerical and experimental data variations can arise from the tire modelling technique. As mentioned before, the tires have been modelled with the specialized Virtual.Lab module, including proper features like stiffness and damping. However, due to the complexity of tire dynamic characteristics and the difficulties in modelling the contact between the track and the wheels, those important parameters can be only roughly approximated.

However, the developed model is precise enough to be used for different measurements. For instance, the described model can be used for stress and strain evaluation; hence, the weakest regions can be pointed out. Figure 10 shows an example of a stress distribution map. Such analyses are extremely useful because they can reveal structural defects in the very first phase and, hence, the problem can be solved before the first prototype is released.

6. Conclusions

Urban buses have not yet been investigated thoroughly which opens the way to many improvements that can be obtained cheaply, by means of numerical methods. The presented hybrid urban bus model is a link between different modeling techniques which takes advantage of them in order to solve complex structural dynamics problems. Utilization of coupled flexible-rigid multibody model instead of dynamic loads on finite element model only gives more reliable representation of reality. Buses work on the streets and theirs structures are extorted with road irregularities. Applying such load conditions to a pure FE model is not a trivial task. However, with the proposed model, it can be achieved using an arbitrary track model and a contact connection with tires. Hybrid urban bus model has been developed, linking FE structure model (to make stress calculation on it possible), rigid suspension multibody model (for vehicle dynamics simulations with large translations and rotations), and 1D modeling techniques of on-board electronic devices (where time-consuming 3D modeling is not necessary). Such a model is useful for analyses of structure behavior under real, operational loads and optimizing in terms of vehicle parameters.

Such a model has been simulated in terms of operational conditions from real bus test on test truck. Results of simulation and real experiments have been compared. The comparison presented good correlation between data, which means that model can be used for virtual prototyping of urban buses.

The proposed multibody hybrid model can be used instead of FE representation, ensuring more precise results; due to application of realistic operating conditions, the usage of commercial software ensures the availability of the method.

The elaborated modeling technique can be also used in the optimization problems, combining both structural and vehicle dynamics, which is planned for the future.

Conflict of Interests

The authors declare that there is no conflict of interests regarding the publication of this paper.

Acknowledgments

This work is a part of international project EUREKA E! 4907 done at AGH University of Science and Technology from Poland with consortium from Belgium LMS International and Poland including EC Engineering and Solaris Bus & Coach. The authors would like to gratefully acknowledge the support from the Polish National Centre of Research and Development. The authors kindly acknowledge also the other researchers at LMS International, EC Engineering, and SOLARIS Bus & Coach, who have contributed to the CHASING R&D activities and results reported in this paper.

References

[1] H. van der Auweraer and J. Leuridan, "A new testing paradigm for today's product development process-part 1," *Sound and Vibration*, vol. 39, no. 9, pp. 14–18, 2005.

[2] H. van der Auweraer and J. Leuridan, "A new testing paradigm for today's product development process—part 2," *Sound and Vibration*, vol. 39, no. 11, pp. 18–22, 2005.

[3] S. Donders, *Computer-aided engineering methodologies for robust automotive NVH design [Ph.D. dissertation]*, KU Leuven, 2008.

[4] T. Uhl, "Computer aided model identification of mechanical systems," WNT, 1997.

[5] R. Craig, *Structural Dynamic*, John Wiley & Sons, 1981.

[6] T. Uhl and W. Lisowski, "Operational modal analysis," Wydawnictwo Katedry Dynamiki Maszyn i Robotyki AGH w Krakowie, 1999 (Polish).

[7] A. Shabana, *Dynamic Analysis of Large-Scale Inertia Variant Flexible Systems [Ph.D. dissertation]*, University of Iowa, 1982.

[8] LMS, Virtual.Lab online help, 2012.

[9] W. Schiehlen, *Multibody Systems Handbook*, Springer, 1990.

[10] A. Shabana, *Dynamics of Multibody Systems*, Cambridge University Press, 2005.

[11] MSC.Software, *MSC.Nastran 2001: Superelement User's Guide*, 2001.

[12] LMS, "AMESim platform," 2012, http://www.lmsintl.com.

[13] A. Sarniotti and G. Repici, "A simulation based approach to failsafe systems in automotive design," in *WSEAS International Conferences*, Miami, Fla, USA, January 2004.

[14] WABCO, Electronic level control (ECAS) for buses with pneumatic suspension system, 1997, (Polish), http://inform.wabco-auto.com.

[15] L. Prochowski and A. Żuchowski, *Trucks and Buses*, Wydawnictwo Komunikacji i Lacznosci, 2004.

[16] D. Ha, H. Kim, and H. Lee, "Height sensor fault diagnosis for electronic air suspension (EAS) system," in *Proceedings of the IEEE International Symposium on Industrial Electronics (ISIE '09)*, pp. 211–216, Seoul, Republic of Korea, July 2009.

[17] *Engineering Statistic Handbook*, http://www.itl.nist.gov/div898/handbook/pmd/section1/pmd143.htm.

[18] H. Liu and J. Lee, "Model development of automotive air spring based on experimental research," in *Proceedings of the 3rd International Conference on Measuring Technology and Mechatronics Automation (ICMTMA '11)*, vol. 2, pp. 585–590, Shanghai, China, January 2011.

[19] H. Kim and H. Lee, "Height and leveling control of automotive air suspension system using sliding mode approach," *IEEE Transactions on Vehicular Technology*, vol. 60, no. 5, pp. 2027–2041, 2011.

[20] I. Jang, H. Kim, H. Lee, and S. Han, "Height control and failsafe algorithm for closed loop air suspension control system," in *Proceedings of the International Conference on Control, Automation and Systems (ICCAS '07)*, pp. 373–378, Seoul, Republic of Korea, October 2007.

Hindawi Publishing Corporation
Shock and Vibration
Volume 2014, Article ID 684786, 12 pages
http://dx.doi.org/10.1155/2014/684786

Research Article

Updating Finite Element Model of a Wind Turbine Blade Section Using Experimental Modal Analysis Results

Marcin Luczak,[1] Simone Manzato,[2] Bart Peeters,[2] Kim Branner,[3] Peter Berring,[3] and Maciej Kahsin[4]

[1] *Institute of Fluid-Flow Machinery Polish Academy of Sciences, Gdansk, Poland*
[2] *LMS International, Leuven, Belgium*
[3] *Department of Wind Energy, Technical University of Denmark, Denmark*
[4] *Gdansk University of Technology, Gdansk, Poland*

Correspondence should be addressed to Simone Manzato; simone.manzato@lmsintl.com

Received 3 March 2014; Accepted 3 March 2014; Published 15 July 2014

Academic Editor: Miguel M. Neves

Copyright © 2014 Marcin Luczak et al. This is an open access article distributed under the Creative Commons Attribution License, which permits unrestricted use, distribution, and reproduction in any medium, provided the original work is properly cited.

This paper presents selected results and aspects of the multidisciplinary and interdisciplinary research oriented for the experimental and numerical study of the structural dynamics of a bend-twist coupled full scale section of a wind turbine blade structure. The main goal of the conducted research is to validate finite element model of the modified wind turbine blade section mounted in the flexible support structure accordingly to the experimental results. Bend-twist coupling was implemented by adding angled unidirectional layers on the suction and pressure side of the blade. Dynamic test and simulations were performed on a section of a full scale wind turbine blade provided by Vestas Wind Systems A/S. The numerical results are compared to the experimental measurements and the discrepancies are assessed by natural frequency difference and modal assurance criterion. Based on sensitivity analysis, set of model parameters was selected for the model updating process. Design of experiment and response surface method was implemented to find values of model parameters yielding results closest to the experimental. The updated finite element model is producing results more consistent with the measurement outcomes.

1. Introduction

Wind turbine blades must be designed to resist the extreme load cases and fatigue loads from normal operation. Sudden wind gusts are often too quick for the active pitch control system to react and may shorten the fatigue life substantially. This problem may be overcome by an aeroelastic tailoring of the blades. Particular implementation of the anisotropic composite material can introduce the bend-twist coupling in the blade [1–4]. In [5] a new beam element, which is able to take the behavior of anisotropic materials into account, is developed and implemented into the aeroelastic code HAWC2. This makes it possible to simulate wind turbines with structural couplings in the blades. The coupling causes the feathering blade to twist under the bending load and as a result decreases the angle of attack. The original wind turbine blade section made of composite material was statically tested and modeled with model validation analysis [6, 7]. Based on the analysis outcomes the bend-twist coupling design of existing blade was modified by means of additional composite material layers. In [8] an overview of the statistical and modal analysis experiments on the original and modified blade section is presented. In this paper the updating of the modified wind turbine blade section's finite element model using experimental modal analysis is presented. Finite element (FE) model updating has become an important tool used in structural dynamics [9, 10]. A number of FE model updating procedures have been proposed [11–13]. Direct, noniterative methods update the FE model properties in one-step procedure [14]. The methods based on sensitivity of the parameters solve the optimization problem in an iterative procedure. Examples of application of static strain measurements for FE model updating are noted [15]. Multiobjective optimization technique applied

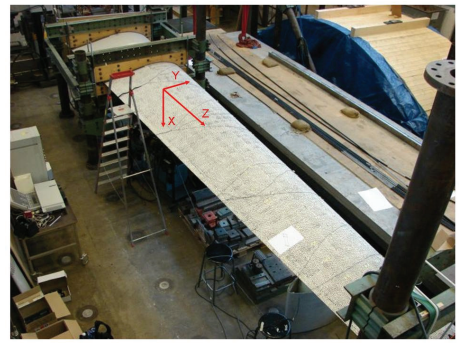

Figure 1: Experimental set-up showing the wind turbine blade section mounted on the test rig with the coordinate system.

Table 1: Basic information about geometry and material properties used for modeling of supporting structure.

Geometry [mm]	Pipes Inner radius 170 Outer radius 160	C-Shapes Standard UPN 200	I-Shapes Two bolted standard UPN 200	Plywood Thickness 180
E modulus [GPa]	200	200	200	13.2
Density [kg/m^3]	7890	7890	7890	736
Poisson's Ratio	0.3	0.3	0.3	0.01

to update the FE models of civil engineering structures in structural dynamics is reported [16–18]. Iterative updating using sensitivity based methods requires large number of computations of FE models with modified parameter values [9, 19, 20]. Response surface method (RSM) based meta-model is an approximation of the FE model which could be replaced in the updating procedure [21, 22]. RSM method is widely used in engineering applications [19, 23, 24]. Sections 2 and 3 of this paper present the structural dynamics identification, which was performed by means of experimental modal analysis. The RSM based FE model updating procedure using design of experiment (DOE) to estimate the structural parameters based on measured natural frequencies and mode shapes is presented in Section 4. The FE model was updated and validated against experimentally identified dynamic behavior of the modified blade section with support structure. The influence of the support structure dynamics on the test specimen is discussed.

2. Object of the Investigations

The object of investigation is an 8-meter long section cut from a 23-meter wind turbine blade. Blade section is mounted in the two root clamps (Figure 1).

The blade is a hollow structure with two shells. The two shells form the suction and pressure side of the blade. To join the two shells together the structural web is incorporated. Investigated blade designed by Vestas has a load carrying box girder. The original blade section was modified with four layers of UD1200, which were laminated on the pressure and suction side of the blade with the fibers angle of 25° to create a measurable flapwise bend-twist coupling. The additional layers were laminated as indicated in [6, 7]. Support structure is built with use of cylindrical beams (steel pipes), "I" and "C" shaped UNP-profiles, and airfoil contour-cut plywood clamps. Geometry and material properties are presented in Table 1.

3. Experimental and Numerical Investigation of Structural Dynamics of Modified Blade Section

The modified blade section was investigated by means of experimental modal analysis. Particular focus was on the influence of the support structure in the correlation analysis between numerical and experimental modal models [25, 26].

3.1. Experimental Campaign and Results. Blade section was excited with two electrodynamic shakers attached at the tip end in the flapwise and edgewise directions. Frequency response functions were measured and stored within 0 and 120 Hz frequency range.

For adequate identification of the blade dynamic displacement, accelerations of the vibrations were measured in 130 points. Thirteen equidistant measurement cross-sections were defined along the span-wise direction (Z) every 0.5 (m). Each cross-section contains five measurement points in which accelerations were acquired along the flapwise (X) and edgewise (Y) direction. These points are located at the leading edge, trailing edge, on the line of airfoil maximum thickness, and in the midpoints between the previous three. Measurement directions were precisely defined based on the CAD geometry of the blade section.

Model quality assessment was an integrated part of the investigation. Except time invariance another condition must be observed to satisfy of modal analysis assumptions: linearity, Maxwell's reciprocity principle, and observability. Possible sources of nonlinearities within investigated structure are material properties, geometrical properties, and the existence

of bond connections verification of a superposition rule is one of the methods of detecting nonlinearities. Linearity check was done for the level of driving voltage ranging from 0.5 (V) to 2 (V) with a step of 0.5 (V). Results are presented in Figure 2. Frequency response function (FRF) between input signal and output spectrum defined as acceleration over force remains constant independently of excitation voltage level. This proves that the structure dynamic behavior is linear within bandwidth of interest.

The reciprocity check is based on Maxwell's principle, which states that the FRFs obtained by applying the force on point 1 and measuring the response in 2 and vice versa should be the same. The results for the two checks performed confirmed applicability of the reciprocity rule.

During the processing of the data, some significant noise was observed in the acquired FRFs in the low frequency region. The driving point coherence functions show a small drop in this region, meaning a nonideal excitation (Figure 3).

The modal parameter identification technique was not able to clearly stabilize modes in this region, possibly resulting in some local errors in the mode shapes below 7 Hz. The estimation provided natural frequencies, mode shapes, and corresponding damping ratios in the frequency bandwidth 0–60 Hz. First five out of 12 identified mode shapes are provided in Figure 4. MAC (modal assurance criterion) can be used to compare two modal models [27]. If a linear relationship exists between the two complex vectors, the MAC value will be near to 1. If they are linearly independent, the MAC value will be small (near zero). Figure 5 shows a comparison between the AutoMAC of the modal model obtained by considering only the sensors on the blade and the one where also the response of the supporting structure is included.

Low valued off-diagonal terms for the blade only model ensure linear independence of estimated modal vectors. The correlation between off-diagonal terms is increased when including the supporting structure in the analysis. This is due to the fact that the clamping is not perfectly rigid and the support has its own dynamic behavior which influences the measured response of the blade.

In Figure 5, red color corresponds to MAC value equal 100. Light green color reflects the MAC value 0. Modes corresponding to frequencies 8 Hz, 28 Hz, 31 Hz, and 33 Hz are related to dynamic properties of the supporting structure. Additionally, appraisal of (a) and (c) in Figure 5 shows that the numerical model basing solely on blade geometry yields less distinctive mode shapes. Comparing Figures 5(a) and 5(c), the correlation of the off-main diagonal terms of the AutoMAC is lower which is a desired situation due to distinction of mode shapes. The model producing undistinguished mode shapes is not suitable for model updating.

3.2. FE Model of the Blade Section with Support Structure. The numerical model adopts MSC.Patran/Nastran blade FE model (Figure 6). It is comprised of 8-noded shell elements (Quad8) and the 20-noded solid elements (Hex20). This model has approximately 600 000 degrees of freedom [6]. The original FE model of the blade was developed to study the static response. The blade section was fully fixed at the chosen

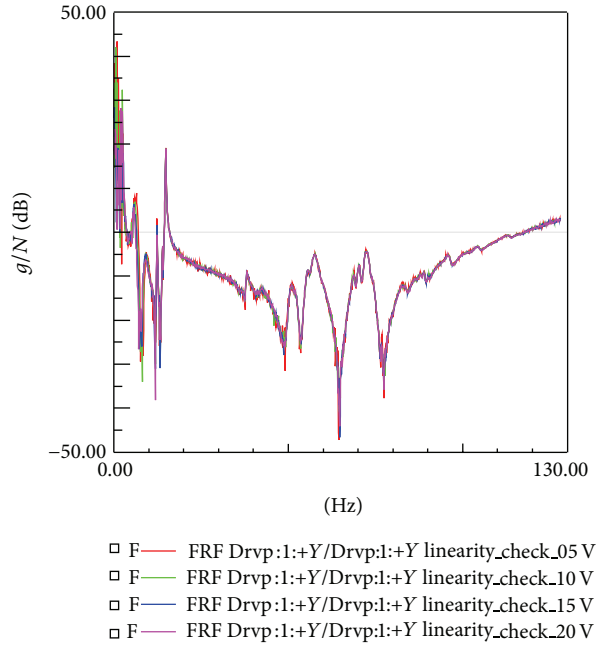

Figure 2: Linearity check for one of the points on the blade. Voltage values = 0.5 V, 1 V, 1, 5 V, and 2 V.

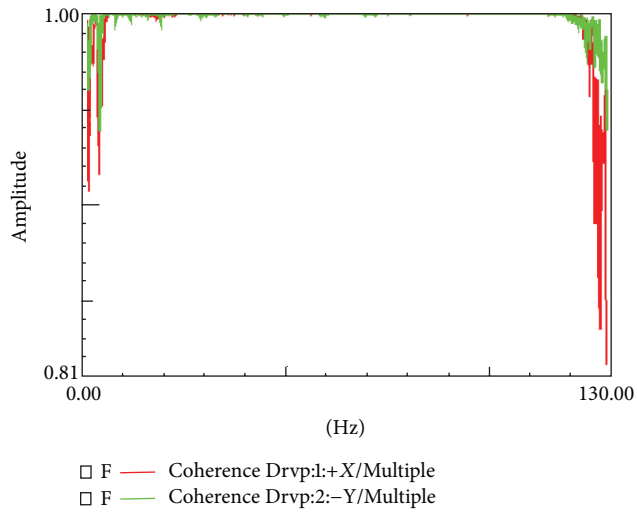

Figure 3: Coherence functions for the two driving points. It is used as measure of the FRF quality. Ideally it should take value equal to 1.

cross-section near the boundary to represent the clamped configuration of the test rig.

The boundary conditions which were adequately representing support structure in static analysis [6, 7, 28] were used in the initial theoretical modal analysis. In the correlation analysis of the test and FE modal models it turned out that a nonnegligible discrepancy in mode shapes occurs. Relatively light and flexible support (Figure 5(b)) has significant contribution on the mode shapes of studied structure which can be observed in the MAC values (Figure 5(c)). In order to eliminate abovementioned problem, an additional support structure model had to be introduced into the blade

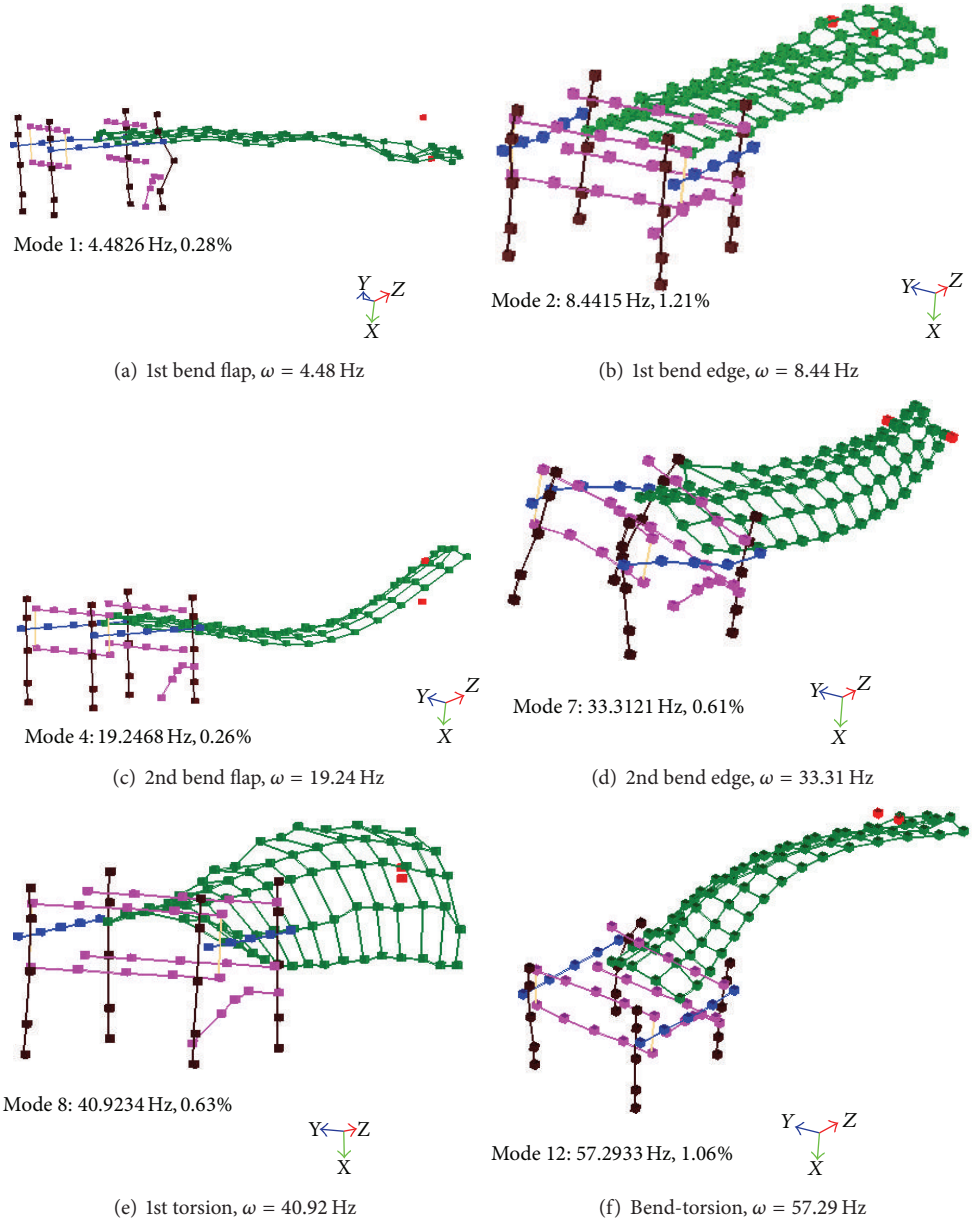

Figure 4: Estimated experimental mode shapes of the modified blade section and support structure.

section test set-up FE model. The main assumption prior modification of original FE model was to keep additional FE model as simple as possible, due to the fact that numerical model was yet relatively large, while making it possible to correlate simulation results with measured data in all points used in the test phase.

As it can be seen in Figure 6 left, the real supporting structure comprises of pipes, UNP-profiles, and support clams of contour-cut plywood. Basic information about geometry and material properties exploited in derived additional FE model are presented in Table 1.

The additional FE model consists of beam elements (CBEAM in Nastran notation), shell elements representing plywood (QUAD8), elastic springs representing mountings between beam elements (CELAS1), rigid bars connecting plywood and I shape clamp beams (RBE2 and), and additional rigid bars with ends at position corresponding to the position of measuring points from test setup (RBAR). Rigid connection between plywood and I shapes is justified because of the large difference in E modules of both materials. Representation of FE-to-test matching with rigid bars does not introduce additional stiffness to the system and is acceptable as long as global mode shapes of support are of interest only. After preparation of support FE model, both additional and the original FE models were merged. Nodes at the interface between blade and supporting structure, that is, between plywood and outer surface of the blade, have restrained rotational DOFs. Such an approach was taken because in the

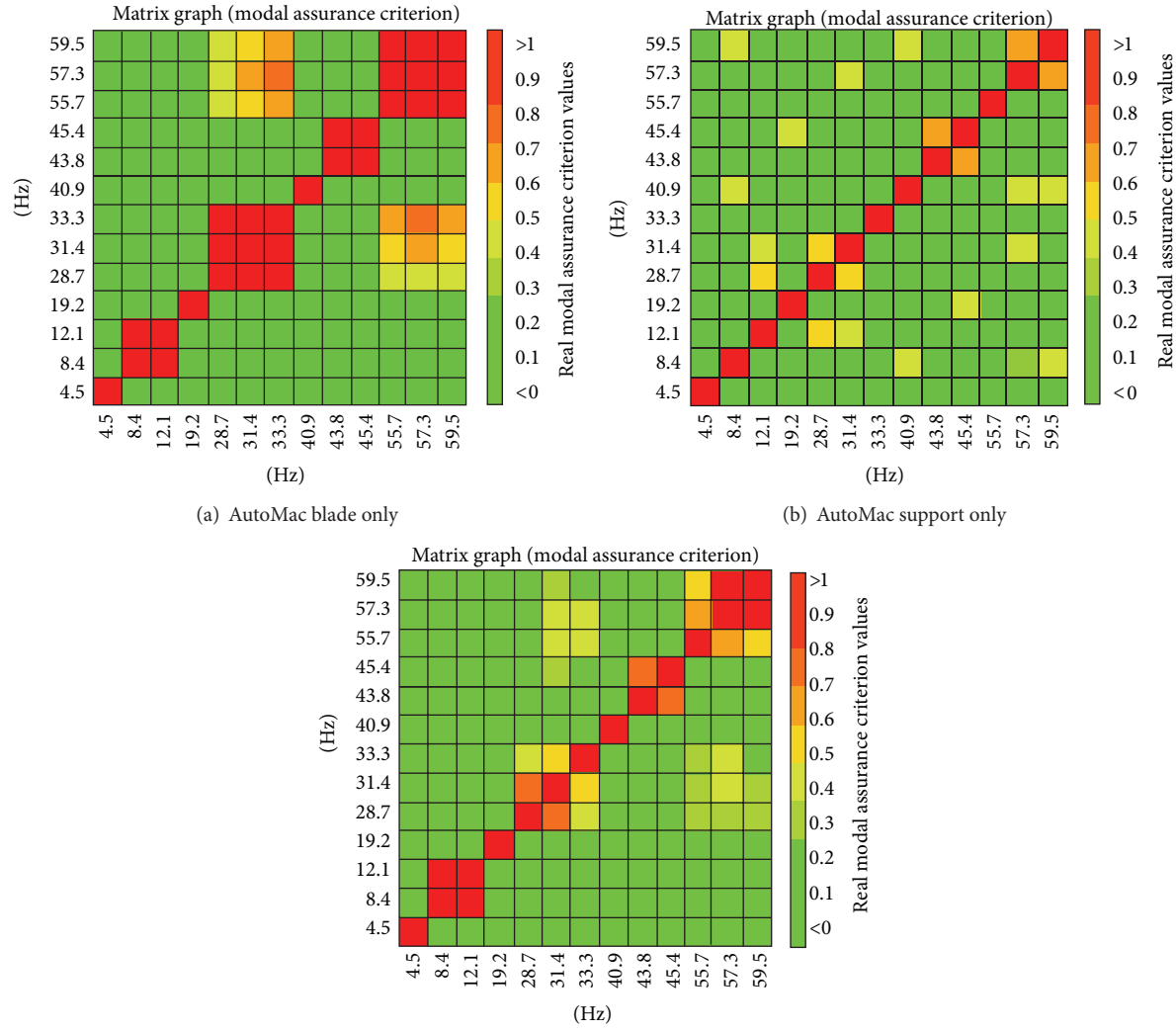

(a) AutoMac blade only

(b) AutoMac support only

(c) AutoMac complete structure

Figure 5: AutoMAC matrices for experimental modal models with sensors only on the modified blade section (a), support structure (b), and blade section with support structure (c).

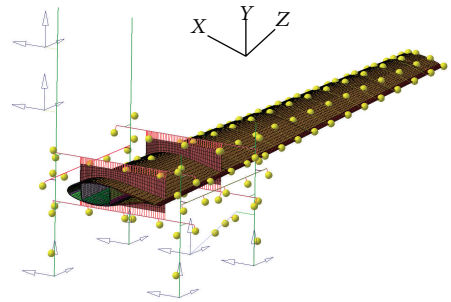

Figure 6: FE model of the blade section clamped to the support structure. Yellow bulbs denote test and FE geometry correlation node mapping.

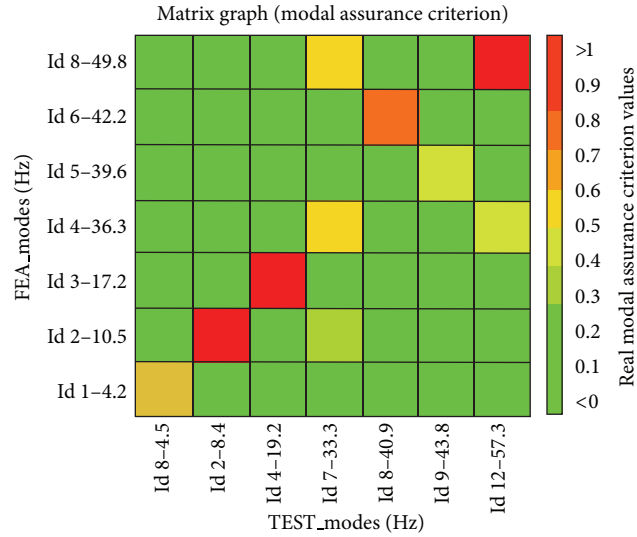

Figure 7: MAC matrix for test and FE simulation modal vectors of modified blade without support structure.

real structure interface between profile-cut plywood and the blade is realized on approximately 200 mm of width, while in the numerical model only single row of nodes is used.

3.3. Correlation Analysis for the Simulation and Test Results. Based on the estimated experimental modal model and modified blade FEM analysis models the correlation analysis can be applied. The FE model should yield natural frequencies values and mode shapes conforming to the measured. Modal assurance criterion is used as the original-modified blade simulation and also test-simulation correlation metrics.

The global coordinate system used to define the test model differs from that used for the FE model. In order to make the models match it is necessary to apply geometric correlation by translation and rotation of the test model (Figure 6). Next step is node mapping. The number of measurement nodes is much less than the FE nodes. Modal vectors are compared only for the nodes from FE which are located closest to the measurement points. Only the portion of the blade after the clamp is considered.

The blade section model was solved to compute mode shapes in the 0–60 Hz frequency bandwidth. Calculations were carried out at the CI TASK, Academic Computer Center in Gdańsk on a 50 Tflop cluster. Modal assurance criterion was calculated for the corresponding modes in order to associate the closest numerical and experimental mode shapes The procedure accounted for both natural frequency value and the mode shape consistency (Table 2).

The following modes were investigated: 1st and 2nd flapwise bending, 1st and 2nd edgewise bending, and 1st torsional (Figure 4). The MAC matrix in Figure 7 clearly shows that the off-diagonal terms are low valued which confirms linear independence of estimated modal vectors. The best test and simulation modal vectors consistency can be observed for the 2nd flapwise mode (Table 2).

The consistency of the results can be recognized as satisfactory; however the present differences need to be further investigated. Observing the values of the MAC criterion between test and simulation modes (Figure 7), differences can be notified. They are caused by the influence of the support structure and not perfectly excited 1st bending mode. Further investigation of observed differences is presented in Section 4.

Table 2: Initial consistency of the modal model parameters.

Initial WT blade				
TEST	FE			
Freq. 1	Freq. 2	MAC value	Freq. 2–Freq. 1 (Hz)	Freq. 2–Freq. 1 (% of Freq. 1)
4.5	4.2	0.636	−0.24	−5.4
8.4	10.5	0.94	2.1	24.9
19.2	17.2	0.963	−2.03	−10.5
33.3	36.3	0.503	3.02	9.1
40.9	42.2	0.76	1.33	3.3
43.8	39.6	0.479	−4.2	−9.6
57.3	49.8	0.857	−7.5	−13.1

4. Updating of the Numerical Model to the Test Results

Satisfactory conformity of the static tests and simulations results has proven the validity of the FE model of modified blade section. Structural dynamics analysis revealed the unsatisfactorily large difference in between tests and simulations. The main reason for these differences is associated to the influence of the flexibility of the support structure. It is complex structure constructed with numerous pipes clamping rings, screwed I beams, and plywood. Part of the structure is constrained to the next structure. For the improvement of the FE model the three-step routine was realized. In the first step sensitivity analysis of the model was

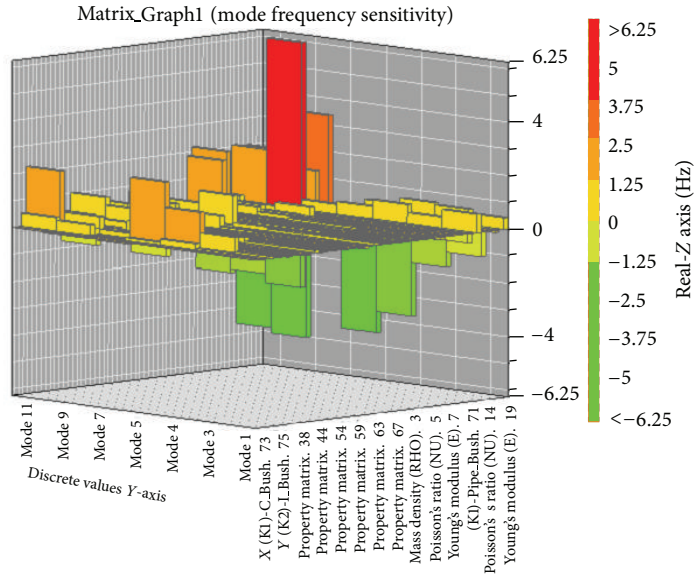

Figure 8: Frequency sensitivity matrix graphically presenting normalized magnitude of the impact of selected design variables (inputs) on the modes frequencies of interest (outputs).

computed in order to determine model parameters which are most influential on the investigated modes. In the second step the design of experiment (DOE) procedure to produce statistical data tabulating input-output relationships. In the third step the response surface model (RSM) is calculated to determine how model parameters influences on the natural frequencies. Study of responses obtained from particular values of the model parameters allows to update the FE model of support structure.

4.1. Sensitivity Analysis. Parameters of the original blade section model were assumed to be constant and were not a subject of updating analysis. 56 parameters characterizing the support structure and additional composite unidirectional layers model were defined as a design variable for the preliminary sensitivity analysis. They comprised material properties such as elasticity modulus, shear modulus and density of the additional composite unidirectional layers, plywood clamps, the rubber pads, the steel pipes, and the bushings. This study was realized to:

(i) identify parameters (inputs) which have no impact on the mode frequencies of interest (outputs);

(ii) identify inputs that cause significant change in the outputs.

Outcome of the frequency sensitivity analysis is presented in Figure 8. The total mass of the system was not known therefore the mass sensitivity was not computed. Based on the outcomes of the analysis the set of 7 parameters was selected as input variables for the design of experiment (Table 3).

Frequency sensitivity analysis provided information about most influential material properties of the supporting structure and additional composite layers. There are several uncertainties related to unknown properties of support structure construction components (Figure 9). C shape beams are drilled; I shape clamp beams consist of two bolted C shape beams, plywood properties, and connections of components. Based on the frequency sensitivity analysis outcomes the material properties of the supporting structure and additional composite layers were selected to be updated parameters.

Table 3: Updated parameters as variables in the model and their initial values.

Name	Initial
I Bush K1	$2.96E7$
Steel pipes E	$2.09E11$
Steel E	$1.99E11$
MAT9_7_G13	$2.49E10$
MAT9_7_G14	$-1.57E10$
MAT9_7_G24	$-7.32E9$
MAT9_7_G34	$-6.85E9$
MAT9_8_G56	$-2.65E8$

4.2. Design of Experiment. Computation of the FE model of the system under investigation takes large number of hours for a single run. Therefore applying optimization analysis which would require large number of runs is not a best available method of model updating. In the system with numerous variable inputs (factors) which affect the outputs (responses) the design of experiment procedure can be used to gather data. The result data is used to develop an approximate model (such as response surface method) linking outputs and inputs. Experimental design which was used is full factorial. It required computation of 2^k combinations where k is a number of factors. With 7 factors (Table 3) applied number of runs was 128. It yielded 21 terms present in quadratic model.

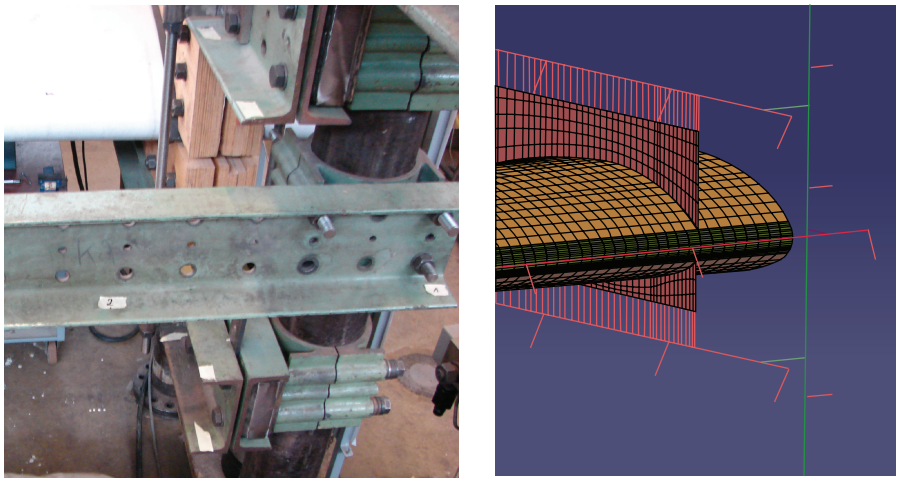

I and C type beams connections with pipes

Connection model with bush type properties

FIGURE 9: Mountings of supporting structure modeled with steel pipes, steel, and bushing properties.

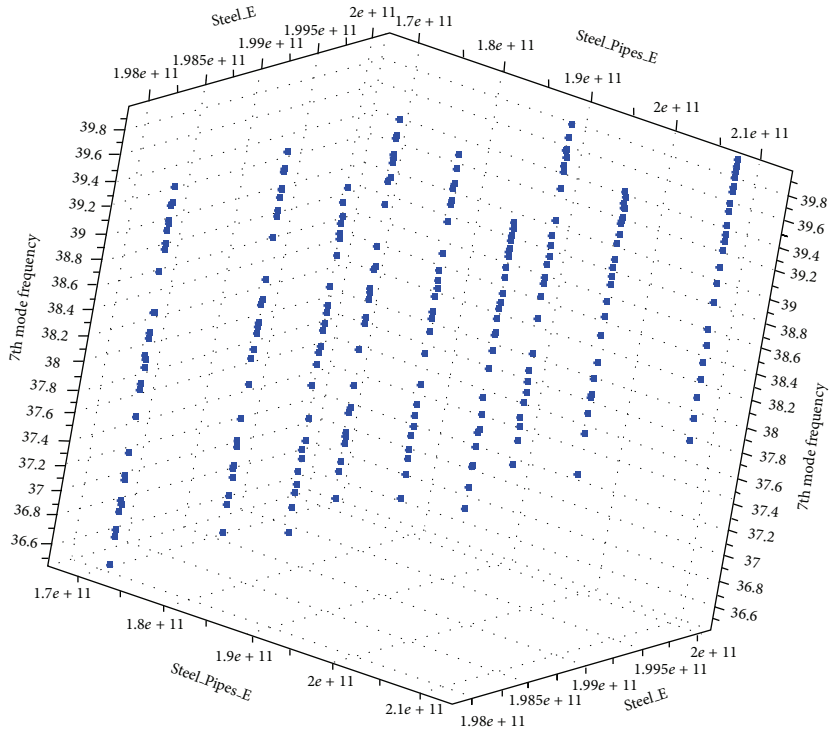

FIGURE 10: Example of 3D scatter plot of two inputs (factors) impact on the output (response) 7th mode frequency.

Analysis of DOE data was performed to identify inputs (factors) which introduce significant change in output (response). For this purpose numerous scatter plots were drawn and analyzed. Example of 3D scatter plot is shown in Figure 10. It also allows to screen for response values computed from model which are closest to the values obtained from measurement. The DOE scatter plot shows the output (response) values for each level of each input (factor) variable. It can be observed that the location and scale vary for both within a factor variable (nominal, minimum, and maximum) and between different factor variables (Young modulus of steel pipes and Young modulus of steel bars). Review of the scatter plots for number of variables allows to identify important factors (inputs) and provides a ranked list of important factors from a results of design of experiment.

Next to the scatter plot the histogram plots were drawn to present the distribution of the computed responses. It is possible to identify the center, spread, and outliers. Example of the histogram plot for the 9th mode frequency is presented in Figure 11. Vertical axis shows number of runs corresponding to the response on horizontal axis.

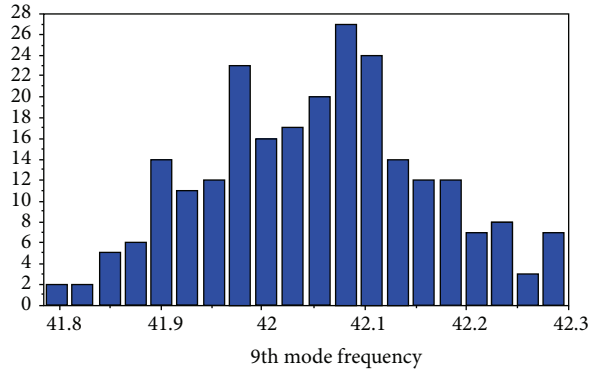

Figure 11: Histogram plot of 9th mode frequency distribution.

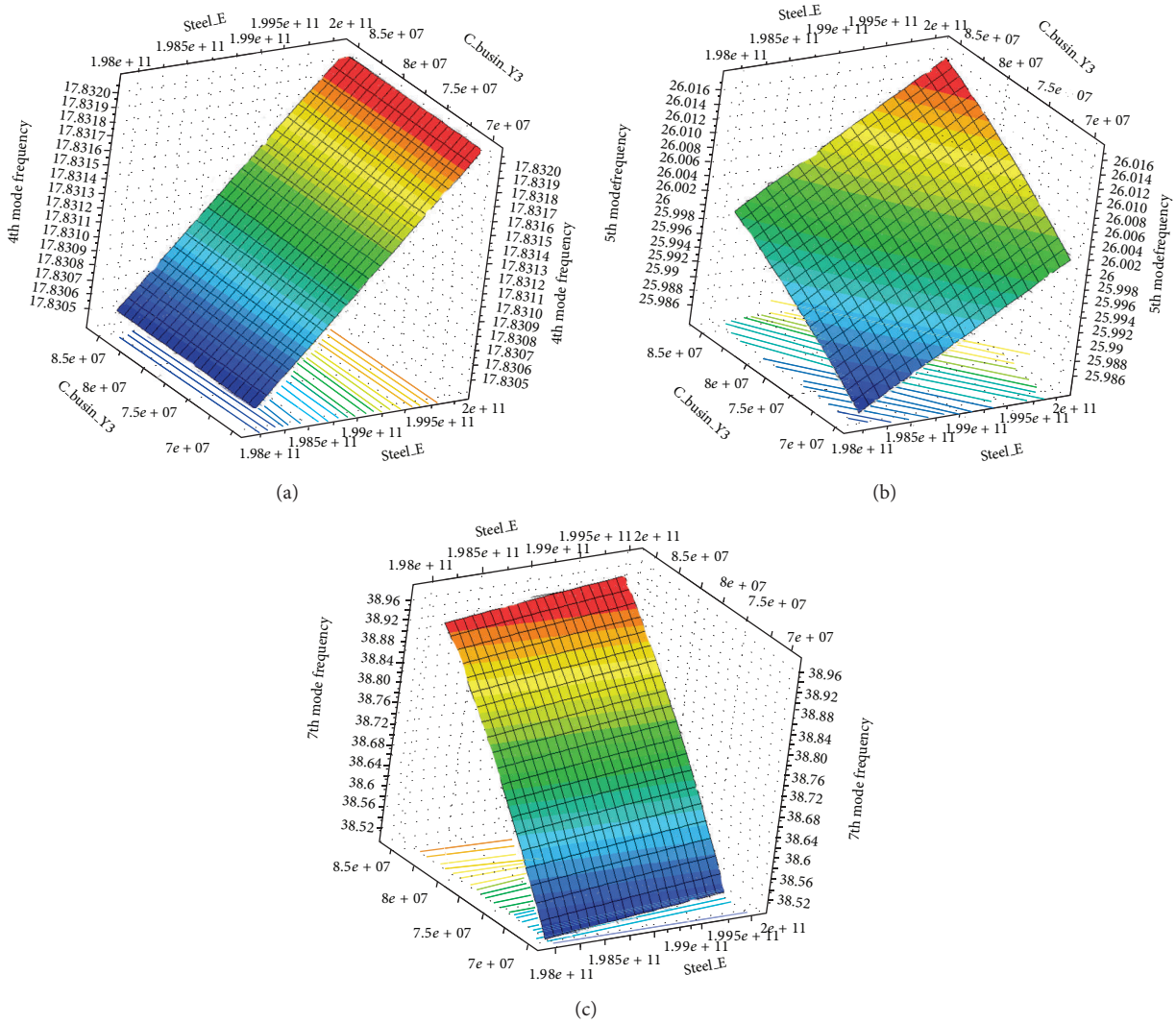

Figure 12: Quadratic response surface models 3D perspective plot for the same input variables and (a) 4th mode, (b) 5th mode, and (c) 7th mode frequency.

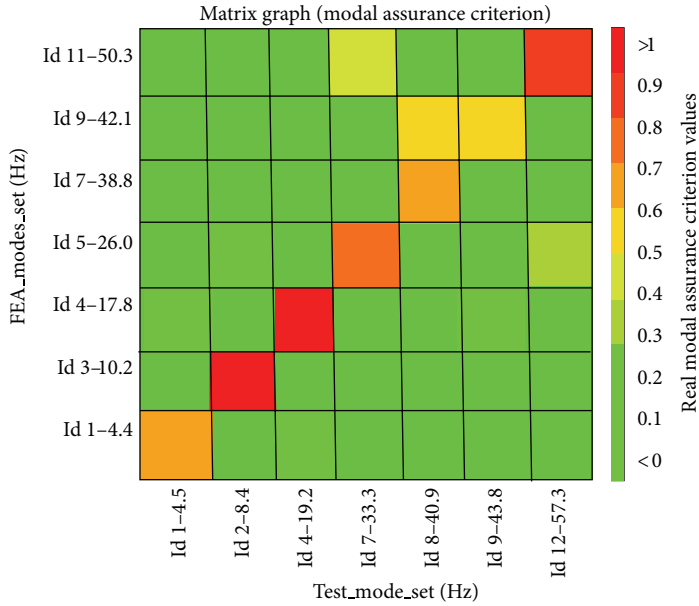

Figure 13: MAC matrix, test versus updated FE model of the blade with flexible support.

Table 4: Updated parameters and their final values.

Name	Final
I Bush K1	$3.289E7$
Steel pipes E	$1.9E11$
Steel E	$2.0E11$
MAT9_7_G13	$1.122E10$
MAT9_7_G14	$-1.424E10$
MAT9_7_G24	$-6.644E9$
MAT9_7_G34	$-6.225E9$
MAT9_8_G56	$-2.413E8$

Histogram of 9th mode frequency shows the results distribution is almost symmetric with most of the results located in the proximity of nominal value. Data is not skewed nor contains outliers and the distribution is moderate tailed—the number of runs is dying off out in the tails of the histogram.

4.3. Response Surface Model. Based on design of experiment, response surface method was computed using polynomial model of several factors, including terms for quadratic cross-products displayed in Figure 12.

The RSM methodology allows for further processing of the DOE results. 3D graphs are plotted based on the available design variables contributions. The inherent trend of the factor-response multidimensional relationship was computed for selected inputs applying Taylor polynomial. Statistical model allows to approximate data and correctly predicts the response without lengthy and costly simulation runs.

Based on the analysis of the RSM model the values of the FE model parameters (factors/inputs) were selected (Table 4).

As a result a correlation analysis of updated and validated FE model shows significant improvement in comparison to the results from original FE model (Figure 13). Test modes of 40.9 (Hz) and 43.8 (Hz) correspond better with the FE modes.

Comparison of frequency value differences of initial (Table 2) and final models (Table 5) shows that the highest discrepancy between simulation and experimental frequencies could be observed for torsional mode for both initial and final model. Frequency difference between FE initial and final model for Test modes 4.5 (Hz) has decreased from −5.4% to −2.2% and for 19.2 (Hz) mode from −10.5% to −7.3%.

5. Conclusions

This paper presents some results and aspects of the multidisciplinary and interdisciplinary research oriented for the numerical study in updating of the finite element model of a wind turbine blade section using experimental modal analysis results.

Experimental test data examples were shown and used for two purposes: firstly to evaluate the influence of the flexible support structure onto measurement results of the bend-twist coupled blade section and secondly to use the test results for FE models updating. The common observation from displayed investigations is that the blade section model accuracy strongly depends on the boundary conditions represented in the model. Simple approaches based on constraining degrees of freedom led to discrepancies in between experimental and numerical results. Presented research introduced complex parametric model of the flexible support structure which led to more realistic structural behavior of the object-support system. In detail the plywood plates and steel profiles were included and contact elements were applied to model the contact between the clamps and the blade section. As expected that the more sophisticated support structure FE

Table 5: Final consistency of the modal model parameters.

Final WT blade (versus initial)				
TEST Freq. 1	FE Freq. 2	MAC value	Freq. 2−Freq. 1 (Hz)	Freq. 2−Freq. 1 (% of Freq. 1)
4.5	4.4	0.634 (0.636)	−0.1 (−0.24)	−2.2 (−5.4)
8.4	10.2	0.942 (0.94)	1.73 (2.1)	20.6 (24.9)
19.2	17.8	0.962 (0.963)	−1.41 (−2.03)	−7.3 (−10.5)
33.3	26	0.722 (0.503)	−7.3 (3.02)	−21.9 (9.1)
40.9	38.8	0.602 (0.76)	−2.11 (1.33)	−5.2 (3.3)
43.8	42.1	0.538 (0.479)	−1.72 (−4.2)	−3.9 (−9.6)
57.3	50.3	0.802 (0.857)	−7.03 (−7.5)	−12.3 (−13.1)

representation has improved the consistency in between test and simulations. Design of experiment with response surface model study allowed successful updating of the FE model confirmed by modal assurance criterion. The comparison of experimental and numerical models clearly shows the influence of support structure flexibility.

Conflict of Interests

The authors declare that there is no conflict of interests regarding the publication of this paper.

Acknowledgments

Vestas Wind Systems A/S has provided and modified the blade sections presented in this study. The work is partly supported by the Danish Energy Authority through the 2007 Energy Research Programme (EFP 2007). The supported EFP-Project is titled "Anisotropic beam model for analysis and design of passive controlled wind turbine blades" and has journal no. 33033-0075. The support is gratefully acknowledged and highly appreciated. Authors would like to acknowledge the assistance of Mr. Philipp Haselbach. Research presented in Section 5 was conducted in the context of the FP7 project STA-DY-WI-CO Ref. no. 251309, IMESCON Ref. no. 264672, and MARE-WINT Ref. no. 309395. Computations were performed on a 50Tflop cluster in TASK Academic Computer Centre in Gdansk, Poland. This research was supported in part by PL-Grid Infrastructure.

References

[1] C. Ong and S. W. Tsai, *Design, Manufacture and Testing of a Bend-Twist D-spar*, Sandia National Laboratories, SAND, 1999.

[2] D. W. Lobitz, P. S. Veers, and G. R. Eisler, "The use of twisted-coupled blades to enhance the performance of horizontal axis wind turbines," Sandia National Laboratories SAND01-1303, Sandia National Laboratories, 2001.

[3] J. Locke and I. C. Hildago, *The Implementation of Braided Composite Materials in the Design of a Bend-Twist Coupled Blade*, Sandia National Laboratories, SAND02-2425, Sandia National Laboratories, 2002.

[4] J. M. Walsh, *Composite Material Bend-Twist Coupling for Wind Turbine Blade Applications*, AAT 1470715, University of Wyoming, Laramie, Wyo, USA, 2009.

[5] T. Kim, A. M. Hansen, and K. Branner, "Development of an anisotropic beam finite element for composite wind turbine blades in multibody system," *Renewable Energy*, vol. 59, pp. 172–183, 2013.

[6] P. Berring, K. Branner, C. Berggreen, and H. W. Knudsen, "Torsional performance of wind turbine blades—part I: experimental investigation," in *Proceedings of the 16th International Conference of Composite Materials*, Kyoto, Japan, July 2007.

[7] K. Branner, P. Berring, C. Berggreen, and H. W. Knudsen, "Torsional performance of wind turbine blades—part II: numerical verification," in *Proceedings of the 16th International Conference of Composite Materials*, Kyoto, Japan, July 2007.

[8] M. Luczak, S. Manzato, B. Peeters, K. Branner, P. Berring, and M. Kahsin, "Dynamic investigation of twist-bend coupling in a wind turbine blade," *Journal of Theoretical and Applied Mechanics*, vol. 49, no. 3, pp. 765–789, 2011.

[9] T. Marwala, *Finite-Element-Model Updating Using Computational Intelligence Techniques: Applications to Structural Dynamics*, Springer, New York, NY, USA, 2010.

[10] M. Friswell and J. E. Mottershead, *Finite Element Model Updating in Structural Dynamics*, Springer, New York, NY, USA, 1995.

[11] M. Link, "Updating of analytical models—review of numerical procedures and application aspects," in *Proceedings of the Structural Dynamics Forum SD2000*, 1999.

[12] S. Manzato, B. Peeters, and A. Toso, *Linking Models and Experiments*, vol. 2, Springer, 2011.

[13] C. Soize, "Stochastic modeling of uncertainties in computational structural dynamics—recent theoretical advances," *Journal of Sound and Vibration*, vol. 332, no. 10, pp. 2379–2395, 2013.

[14] A. Berman and E. J. Nagy, "Improvement of a large analytical model using test data," *AIAA journal*, vol. 21, no. 8, pp. 1168–1173, 1983.

[15] M. Sanayei, G. R. Imbaro, J. A. S. McClain, and L. C. Brown, "Structural model updating using experimental static measurements," *Journal of Structural Engineering*, vol. 123, no. 6, pp. 792–798, 1997.

[16] B. Jaishi and W. Ren, "Finite element model updating based on eigenvalue and strain energy residuals using multiobjective optimisation technique," *Mechanical Systems and Signal Processing*, vol. 21, no. 5, pp. 2295–2317, 2007.

[17] D. Foti, M. Diaferio, N. I. Giannoccaro, and M. Mongelli, "Ambient vibration testing, dynamic identification and model

updating of a historic tower," *NDT & E International*, vol. 47, pp. 88–95, 2012.

[18] D. Ribeiro, R. Calçada, R. Delgado, M. Brehm, and V. Zabel, "Finite element model updating of a bowstring-arch railway bridge based on experimental modal parameters," *Engineering Structures*, vol. 40, pp. 413–435, 2012.

[19] R. H. Myers, D. C. Montgomery, and C. M. Anderson-Cook, *Response Surface Methodology: Process and Product Optimization Using Designed Experiments*, Wiley Series in Probability and Statistics, Wiley, Hoboken, NJ, USA, 3rd edition, 2009.

[20] B. Goller, M. Broggi, A. Calvi, and G. I. Schuëller, "A stochastic model updating technique for complex aerospace structures," *Finite Elements in Analysis and Design*, vol. 47, no. 7, pp. 739–752, 2011.

[21] İ. Batmaz and S. Tunali, "Small response surface designs for metamodel estimation," *European Journal of Operational Research*, vol. 145, no. 2, pp. 455–470, 2003.

[22] V. J. Romero, L. P. Swiler, and A. A. Giunta, "Construction of response surfaces based on progressive-lattice-sampling experimental designs with application to uncertainty propagation," *Structural Safety*, vol. 26, no. 2, pp. 201–219, 2004.

[23] S. Chakraborty and A. Sen, "Adaptive response surface based efficient finite element model updating," *Finite Elements in Analysis and Design*, vol. 80, pp. 33–40, 2014.

[24] W. Ren and H. Chen, "Finite element model updating in structural dynamics by using the response surface method," *Engineering Structures*, vol. 32, no. 8, pp. 2455–2465, 2010.

[25] M. Luczak, K. Dziedziech, and M. Vivolo, "Contact versus non-contact measurement of a helicopter main rotor composite blade," in *Proceedings of the 9th International Conference on Vibration Measurements by Laser and Noncontact Techniques (AIVELA '10)*, vol. 1253 of *AIP Conference Proceedings*, p. 352, Ancona, Italy, June 2010.

[26] B. Peeters, H. Van Der Auweraer, P. Guillaume, and J. Leuridan, "The PolyMAX frequency-domain method: a new standard for modal parameter estimation?" *Shock and Vibration*, vol. 11, no. 3-4, pp. 395–409, 2004.

[27] D. J. Ewins, *Modal Testing: Theory, Practice, and Application*, Research Studies Press, Baldock, UK, 2000.

[28] V. A. Fedorov, N. Dimitrov, C. Berggreen, S. Krenk, K. Branner, and P. Berring, "Investigation of structural behaviour due to bend-twist couplings in wind turbine blades," in *Proceedings of the NAFEMS Nordic Seminar of Simulating Composite Materials and Structures*, NAFEMS, Esbjerg, Denmark, 2010.

Hindawi Publishing Corporation
Shock and Vibration
Volume 2014, Article ID 670683, 14 pages
http://dx.doi.org/10.1155/2014/670683

Research Article

Predictive Control for Earthquake Response Mitigation of Buildings Using Semiactive Fluid Dampers

F. Oliveira,[1] P. Morais,[1] and A. Suleman[2,3]

[1] *Laboratório Nacional de Engenharia Civil (LNEC), Avenida do Brasil 101, 1700-066 Lisboa, Portugal*
[2] *Department of Mechanical Engineering, University of Victoria, P.O. Box 1700 STN CSC, Victoria, BC, Canada V8W 2Y2*
[3] *Institute of Mechanical Engineering (IDMEC/IST), Avenida Rovisco Pais 1, 1049-001 Lisbon, Portugal*

Correspondence should be addressed to F. Oliveira; fvoliveira@lnec.pt

Received 12 July 2013; Accepted 5 February 2014; Published 7 July 2014

Academic Editor: Nuno Maia

Copyright © 2014 F. Oliveira et al. This is an open access article distributed under the Creative Commons Attribution License, which permits unrestricted use, distribution, and reproduction in any medium, provided the original work is properly cited.

A predictive control strategy in conjunction with semiactive control algorithms is proposed for damping control of base-isolated structures employing semiactive fluid dampers when subjected to earthquake loads. The controller considers the delays resulting from the device's dynamics and an observer for state estimation. Twenty artificial accelerograms were generated according to the Eurocode 8 for the Portuguese territory and considered for the numerical simulations of the base-isolated structure representative model. The results of a parametric study on a single degree of freedom model provide an indication for controller design in this type of problems. To evaluate the effectiveness of the proposed strategies, the response of a 10-storey base-isolated dual frame-wall building employing semiactive systems is compared with the original, passive solution and with an earlier proposed optimal controller for this type of problems. It is shown that a well-tuned controller could outperform the original structure, the structural system with a passive device (optimized) as well as with the semiactive optimal controller, in terms of relative displacement and absolute acceleration reductions.

1. Introduction

Civil engineering structures are usually built as passive structures with no adaptability to uncertain dynamic loads like earthquakes [1]. For structures that should be operational during and immediately after the occurrence of those events, such as hospitals, energy power stations, communication centres, civil protection, and fire station buildings, among others, special precautions should be taken. It is intended that structural relative displacements (interstorey drifts) and accelerations are small in order to avoid damage and protect sensitive equipments from induced vibrations [2, 3]. New systems integrated in structures have been proposed to protect them against earthquakes with passive, semiactive, and active control technologies [4].

Semiactive (SA) control systems have received much attention in recent years due to some notable advantages: capacity of adapting its characteristics in real time, better overall performance when compared with passive devices, and lower operational power requirements, thus allowing for battery operation. Semiactive devices are seen as controllable passive devices that allow for adjustment of its mechanical characteristics (damping, stiffness) in real time [5]. Magnetorheological (MR) and fluid viscous dampers (FVD) are typical examples of semiactive devices. MR fluids consist of micron-sized particles in a carrier fluid (usually oil) whose characteristics can be reversibly changed from a free-flowing to a semisolid in milliseconds when subjected to a magnetic field [5, 6]. A lot of investigations on this subject have been done in the last years and several applications can be found today [7–14]. The second type of devices (FVD) consists typically of a hydraulic cylinder filled with oil with a piston head separating its two chambers. A hydraulic link with a control valve is used to control the amount of fluid that flows from one chamber to the other [5, 6]. Research projects and investigation with semiactive oil dampers are being made since the 1990s and many applications with these devices can be found all around the world, and especially in Japan [7, 15–21]. In order to control the device's behaviour several control strategies have been proposed: (i) sky-hook control [6],

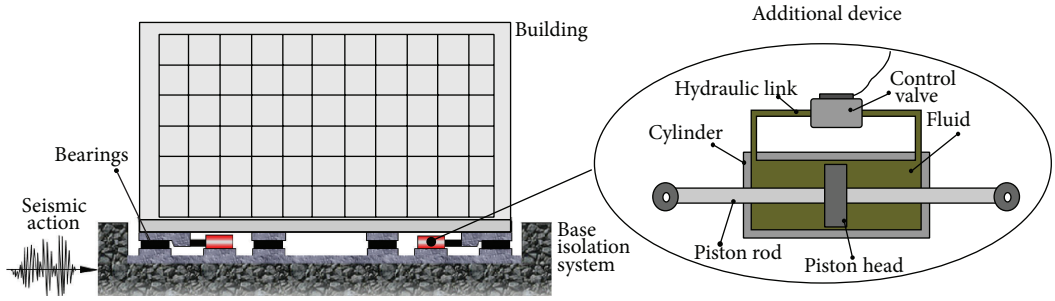

Figure 1: Hybrid system: base-isolated structure with semiactive fluid viscous damper.

(ii) optimal control [8, 9, 15, 16], (iii) control based on the Lyapunov stability theory [8], (iv) bang-bang control [8], (v) modulated homogeneous friction control algorithm [8], (vi) sliding mode control [15, 17], (vii) fuzzy logic [9], (viii) neural-network-based control [9], (ix) proportional plus integral control [10], (x) force derivative feedback control [11], quantitative feedback theory [12], and backstepping control technique [12].

In order to accomplish those goals (reduce both accelerations and interstorey drifts) the base isolation concept has been considered [2, 3]. However, under near field seismic actions, base-isolated structures could face large displacements at the base due to pulse-like ground motions which make them vulnerable to structural damage [3]. An alternative solution would be the use of hybrid systems. Base isolation systems with passive devices like fluid viscous dampers have been proposed and experimentally verified to meet those goals [3, 22, 23]. Other approaches consisting of base isolation with semiactive devices have also been proposed to further improve more the system performance [9, 11, 16, 17].

Predictive control is a strategy that has been successfully implemented in petrochemical and process industry [24] and is considered here for an application in semiactive control. In this communication a variable fluid viscous damper is studied for reducing vibrations in civil engineering structures subjected to earthquakes using a predictive control strategy. The results of numerical simulations using representative models (single and multidegree of freedom models—SDOF and MDOF) of typical building structures employing a semiactive device excited by seismic actions at the base are presented. Comparisons with the original structure, with passive control and the optimal controller, show the potential of using this strategy.

2. Problem Formulation

The reduction of vibrations induced by earthquakes in structures consists in adding damping by means of variable damping devices whose damping characteristics are controlled by a predictive control strategy. Although several ways for installation of these devices can be found [5], we will consider a hybrid system consisting of SA devices in conjunction with base isolation systems (Figure 1).

A satisfactory approach usually considered in the building's modelling is that (i) each floor has very high stiffness where the mass is concentrated; (ii) the connections between floors are massless elements where the stiffness and damping are concentrated. In base-isolated structures the superstructure is constructed over a base floor which in turn is supported by bearings. For the purpose of this study bearings are modelled as linear elastic and viscous damping elements. A simple model that represents the key responses of civil engineering structures including the base isolation system can be described by the mass $\mathbf{M}_s$, stiffness $\mathbf{K}_s$, and damping $\mathbf{C}_s$ matrices. Considering the input ground motion (acceleration) $\ddot{x}_g$ and the force f developed by the additional devices at the base, then the mechanical behaviour can be represented by a n degree of freedom model (base plus $n-1$ floors):

$$\mathbf{M}_s \cdot \ddot{\mathbf{x}}_{rg} + \mathbf{C}_s \cdot \dot{\mathbf{x}}_{rg} + \mathbf{K}_s \cdot \mathbf{x}_{rg} = -\mathbf{M}_s \cdot \mathbf{1} \cdot \ddot{x}_g + \mathbf{G} \cdot f, \quad (1)$$

where $\mathbf{1}$ is a unitary column vector; $\mathbf{G}$ is the matrix that defines the input force location (for the present case $\mathbf{G} = [-1 \;\; 0 \;\; \cdots \;\; 0]^T$, where the minus sign means that the force is dissipative); and $\mathbf{x}_{rg}$ is the vector of relative displacements to the ground. Additional damping is added at the base level by additional devices, which can be passive, active, or semiactive. The semiactive fluid viscous damper was considered and its behaviour was described by the viscous dashpot model with a variable damping coefficient [4, 15]. However, to include the dynamic behaviour of the damper one must account the time response associated with its operation (the time to develop the damping force after the command to change the damping coefficient) [15, 17]. In this type of devices the time response results in both valve dynamics and hydraulic system dynamics. The total response time can be described as the sum of pure time delays (or dead time) and lag (or phase delay), which are designated in [15] as static and dynamic response time, respectively. In [17] the total time response is treated as time lag. Time delays can change during operation (as damping increases or decreases) and an average time delay considering both operation processes is usually taken. In this work the device total time response (or delay) is accounted as lag and thus the viscous model is complemented with a first-order dynamic system which results in the Maxwell model:

$$T_d \cdot \dot{f} + f = c_v \cdot \dot{x}_r, \quad c_{\min} \le c_v \le c_{\max}, \quad (2)$$

where T_d is the relaxation time, or time constant representing an average of the device time response; f is the damping force; c_v is the damping coefficient which can be changed between a minimum and a maximum value; and $\dot{x}_r$ is the relative velocity between the cylinder case and the piston head of the damper.

The system described by (1) can be represented in the state-space form by

$$\begin{aligned}
\dot{\mathbf{z}} &= \mathbf{A}\cdot\mathbf{z} + \mathbf{B}\cdot f + \mathbf{E}\cdot\ddot{x}_g,\\
\mathbf{y} &= \mathbf{C}\cdot\mathbf{z} + \mathbf{D}\cdot f,\\
\mathbf{A} &= \begin{bmatrix} \mathbf{0}_{n\times n} & \mathbf{I} \\ -\mathbf{M}_s^{-1}\cdot\mathbf{K}_s & -\mathbf{M}_s^{-1}\cdot\mathbf{C}_s \end{bmatrix},\\
\mathbf{B} &= \begin{bmatrix} \mathbf{0}_{n\times 1} \\ -\mathbf{M}_s^{-1}\cdot\mathbf{G} \end{bmatrix}, \qquad \mathbf{E} = \begin{bmatrix} \mathbf{0}_{n\times 1} \\ -\mathbf{1} \end{bmatrix},
\end{aligned} \tag{3}$$

where $\mathbf{z} = \{\mathbf{x}_{rg}, \dot{\mathbf{x}}_{rg}\}^T$ is the state vector; $\mathbf{C}$ and $\mathbf{D}$ are defined according to the quantities for output; for instance, if $\mathbf{C} = \mathbf{A}$ and $\mathbf{D} = \mathbf{B}$ the outputs will be the relative velocities and absolute accelerations; $\mathbf{0}$, $\mathbf{I}$, and $\mathbf{1}$ are a null matrix, identity matrix, and unitary vector, respectively.

3. Vibration Control

Figure 2 depicts the control loop considered in this work. The force tracking control scheme makes use of a controller and an algorithm to find the desired damping coefficient. The idea is that the device's force f follows the desired force f_d evaluated by the controller. A model predictive controller (MPC) is used to find the desired control force. According to the nature of the device, the algorithm assumes that it is only possible to dissipate energy, and thus the damping coefficient will be changed only when the desired force and damper force have the same sign. With this strategy a linear model of the plant (3) can be used and thus the calculation of the desired force is relatively straightforward [24]. In Figure 2 SW determines the algorithm considered: with or without feedback from the measured force.

3.1. Model Predictive Control Formulation. The MPC block in Figure 2 uses the predictive control strategy based on a linear model of the plant. The controller is formulated in the discrete domain and the idea consists in predicting future outputs from actual measurements and past inputs using the plant's model (predictor), comparing those outputs with the reference values, and determining a sequence of input trajectories that result from the solution of an optimization problem (optimizer). Only the first input is applied to the plant, and then the whole cycle of measurement, prediction, and input calculation is repeated in the next sampling interval (receding horizon). Since the states are not always available, this strategy uses an observer to estimate the remaining states (observer).

In the control loop of Figure 2 time delays can result from the process of measurement, input computation, and input application. The prediction model used in the MPC block considers input delays since input action f generated at time $t - T_d$ (T_d is the device time delay) only takes effect at time t, due to delays resulting from the force application (device). In the present case, the MPC block will generate a desired force $f_d(k-d)$ that will result in a force $f(k)$ applied by the device $d = T_d/T_s$ instants later (T_s is the sampling time), mainly due to the time response of the SA device. Thus, the following relationship is considered in the controller formulation: $f(k) = f_d(k-d)$. Measurement delays are assumed to be small when compared to the input application delays and thus are not considered in the formulation. Moreover, the computations are assumed to occur during the control interval T_s (or sampling period). When converting this model to the discrete domain additional states are added. Then the MPC block internal model in the state-space discrete-time form is given by

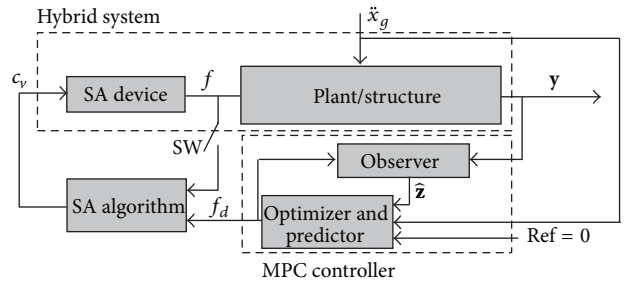

Figure 2: Proposed control loop: force tracking scheme using a MPC controller with a semiactive (SA) algorithm.

$$\begin{aligned}
\mathbf{z}_a(k+1) &= \mathbf{A}_a\cdot\mathbf{z}_a(k) + \mathbf{B}_a\cdot f_d(k) + \mathbf{E}_a\cdot a_g(k),\\
\mathbf{y}(k) &= \mathbf{C}_a\cdot\mathbf{z}_a(k),
\end{aligned} \tag{4}$$

where k is the time step derived from the discretisation process with a sampling time T_s; $\mathbf{z}_a(k) = \{(\mathbf{z}(k))^T, f_d(k-d), \ldots, f_d(k-1)\}^T$ is the state vector (dimension $n_a \times 1$) including relative displacements and velocities, and the past instant desired forces $f_d(k-i)$, $i = 1, 2, \ldots, d$; $f_d(k)$ is the actual desired force (scalar); $a_g(k)$ is the input ground motion (scalar); $\mathbf{y}(k)$ is the output vector (dimension $m_a \times 1$); and $\mathbf{A}_a$, $\mathbf{B}_a$, $\mathbf{E}_a$, and $\mathbf{C}_a$ are the discretized state-space model matrices. Using this model to predict the behaviour of the system for a specific prediction horizon (HP steps) and considering that the input force remains constant after a specific control horizon (HC steps), then the output predictions are given by the following equation [24]:

$$\begin{aligned}
\mathbf{Y}(k) = {} & \boldsymbol{\Psi}\cdot\hat{\mathbf{z}}_a(k\mid k) + \mathbf{T}\cdot f_d(k-1)\\
& + \boldsymbol{\Theta}\cdot\Delta\mathbf{F}_d(k) + \boldsymbol{\Xi}\cdot\mathbf{A}(k),
\end{aligned} \tag{5}$$

where $\mathbf{Y}(k) = \{(\hat{\mathbf{y}}(k+1k))^T, \ldots, (\hat{\mathbf{y}}(k+\mathrm{HP}k))^T\}^T$ is the vector (dimension $m_a \cdot \mathrm{HP} \times 1$) of output predictions at instant k for instant $k+1$ to $k+\mathrm{HP}$; $\hat{\mathbf{z}}_a(k\mid k)$ is the estimated state vector at instant k (when the full state vector is not available); $\Delta\mathbf{F}_d(k) = \{\Delta\widehat{f}_d(k\mid k), \ldots, \Delta\widehat{f}_d(k+\mathrm{HC}-1\mid k)\}^T$ is the vector (dimension $\mathrm{HC} \times 1$) of future force input moves;

$\Delta f_d(k) = f_d(k) - f_d(k-1)$; $\mathbf{A}(k) = \{a_g(k), \hat{a}_g(k \mid k), \ldots, \hat{a}_g(k+\mathrm{HP}-1 \mid k)\}^T$ is the vector (dimension HP × 1) of measured and future disturbances (commonly assumed as constant and equal to the last measured value $a_g(k)$); and $\boldsymbol{\Psi}$, $\mathbf{T}$, $\boldsymbol{\Theta}$, and $\boldsymbol{\Xi}$ are constant matrices derived from the plant's model: $\boldsymbol{\Psi} = \mathscr{C}_a \cdot \mathscr{A}$; $\mathbf{T} = \mathscr{C}_a \cdot \mathscr{B}$; $\boldsymbol{\Theta} = \mathscr{C}_a \cdot \mathscr{H}$; $\boldsymbol{\Xi} = \mathscr{C}_a \cdot \mathscr{E}$; with

$$\mathscr{A} = \left[(\mathbf{A}_a)^T \cdots (\mathbf{A}_a^{\mathrm{HP}})^T \right]^T$$

$$\mathscr{B} = \left[(\mathbf{B}_a)^T \cdots \left(\sum_{j=0}^{j=\mathrm{HP}-1} \mathbf{A}_a^j \cdot \mathbf{B}_a \right)^T \right]^T$$

$$\mathscr{C}_a = \mathrm{diag}(\mathbf{C}_a \quad \cdots \quad \mathbf{C}_a);$$

$$\mathscr{C} = \begin{bmatrix} \mathbf{E}_a & \mathbf{0} & \cdots & \mathbf{0} \\ \mathbf{A}_a \cdot \mathbf{E}_a & \mathbf{E}_a & \cdots & \mathbf{0} \\ \vdots & \vdots & \ddots & \vdots \\ \mathbf{A}_a^{\mathrm{HP}-1} \cdot \mathbf{E}_a & \mathbf{A}_a^{\mathrm{HP}-2} \cdot \mathbf{E}_a & \cdots & \mathbf{E}_a \end{bmatrix}$$

$$\mathscr{H} = \begin{bmatrix} \mathbf{B}_a & \cdots & \mathbf{0} \\ \vdots & \ddots & \vdots \\ \sum_{j=0}^{j=\mathrm{HC}-1} \mathbf{A}_a^j \cdot \mathbf{B}_a & \cdots & \mathbf{B}_a \\ \sum_{j=0}^{j=\mathrm{HC}} \mathbf{A}_a^j \cdot \mathbf{B}_a & \cdots & \mathbf{A}_a \cdot \mathbf{B}_a + \cdot \mathbf{B}_a \\ \vdots & \ddots & \vdots \\ \sum_{j=0}^{j=\mathrm{Hp}-1} \mathbf{A}_a^j \cdot \mathbf{B}_a & \cdots & \sum_{j=0}^{j=\mathrm{HP}-\mathrm{HC}} \mathbf{A}_a^j \cdot \mathbf{B}_a \end{bmatrix}. \tag{6}$$

The optimal input force moves can be obtained as the solution of an unconstrained optimization problem (minimization) with the following cost function [24]:

$$V(k) = \sum_{i=1}^{\mathrm{HP}} \left\| \hat{\mathbf{y}}(k+i \mid k) \right\|_Q^2 + \sum_{i=0}^{\mathrm{HC}-1} \left\| \Delta \widehat{f}_d(k+i \mid k) \right\|_R^2 = \left\| \mathbf{Y}(k) \right\|_{\mathscr{Q}}^2 + \left\| \Delta \mathbf{F}_d(k) \right\|_{\mathscr{R}}^2, \tag{7}$$

where Q is the matrix (dimension $m_a \times m_a$) that weights the outputs and R (dimension 1×1) weights the input moves; $\mathscr{Q}$ is the compound weight matrix (dimension $m_a \cdot \mathrm{HP} \times m_a \cdot \mathrm{HP}$) with the weighting matrices Q in the diagonal; and $\mathscr{R}$ is the compound weight matrix (dimension HC × HC) with R in the diagonal. The solution of this optimization problem can be obtained by finding the gradient of the cost function and set it to zero:

$$\Delta \mathbf{F}_d(k) = \frac{1}{2} \mathscr{H}_{\mathrm{term}}^{-1} \cdot \mathscr{G}_{\mathrm{term}}, \quad \text{with } \mathscr{H}_{\mathrm{term}} = \boldsymbol{\Theta}^T \cdot \mathscr{Q} \cdot \boldsymbol{\Theta} + \mathscr{R}, \quad \mathscr{G}_{\mathrm{term}} = 2 \cdot \boldsymbol{\Theta}^T \cdot \mathscr{Q} \cdot \mathbf{E}(k), \tag{8}$$

where $\mathbf{E}(k) = -\boldsymbol{\Psi} \cdot \hat{\mathbf{z}}_a(k \mid k) - \mathbf{T} \cdot f(k-1) - \boldsymbol{\Xi} \cdot \mathbf{A}(k)$ is the tracking error (difference between the future target, which in this case is zero, and the free response, $\Delta \mathbf{F}_d(k) = \mathbf{0}$). In order to guarantee the minimum solution the second derivative, or the Hessian matrix of $V(k)$, should be positive definite. This condition is verified if the weighting matrices are positive definite or at least one is positive definite and the other is semipositive definite.

If one cannot have access to the full state vector an observer has to be used to estimate the state vector $\hat{\mathbf{z}}_a(k \mid k)$. The observer is designed using the Kalman filter technique: assuming that the plant is subjected to white noise disturbances (process noise $a_g(k)$ and measurement noise $v(k)$) with zero mean and known covariance matrices, $E[a_g(k) \cdot a_g(k)^T] = Q_o$, $E[v(k) \cdot v(k)^T] = R_o$, then the observer gain $\mathbf{K}$ can be chosen to minimize the mean square state estimation error [25]. The observer equations include the time and measurement update and are given by

$$\begin{aligned} \hat{\mathbf{z}}_a(k+1 \mid k) &= \mathbf{A}_a \cdot \hat{\mathbf{z}}_a(k \mid k) + \mathbf{B}_a \cdot f_d(k), \\ \hat{\mathbf{y}}(k \mid k-1) &= \mathbf{C}_a \cdot \hat{\mathbf{z}}_a(k \mid k-1), \\ \hat{\mathbf{z}}_a(k \mid k) &= \hat{\mathbf{z}}_a(k \mid k-1) + \mathbf{K} \cdot \left[y(k) - \hat{y}(k \mid k-1) \right]. \end{aligned} \tag{9}$$

Manipulating the expressions of (9), the Kalman filter with a stationary gain is obtained by solving the corresponding *Riccati* equation with adequate covariance matrices:

$$\begin{aligned} \hat{\mathbf{z}}_a(k+1 \mid k) &= \mathbf{A}_a \left(\mathbf{I} - \mathbf{K} \cdot \mathbf{C}_a \right) \cdot \hat{\mathbf{z}}_a(k \mid k-1) + \mathbf{B}_a \cdot f_d(k) + \mathbf{A}_a \cdot \mathbf{K} \cdot \mathbf{y}(k), \\ \mathbf{K} &= P_o \cdot \mathbf{C}_a^T \cdot \left[R_o + \mathbf{C}_a \cdot P_o \cdot \mathbf{C}_a^T \right]^{-1}, \\ P_o &= \mathbf{E}_a \cdot Q_o \cdot \mathbf{E}_a^T + \mathbf{A}_a \cdot P_o \cdot \mathbf{A}_a^T - \mathbf{A}_a \cdot P_o \cdot \mathbf{C}_a^T \left[R_o + \mathbf{C}_a \cdot P_o \cdot \mathbf{C}_a^T \right]^{-1} \cdot \mathbf{C}_a \cdot P_o \cdot \mathbf{A}_a^T. \end{aligned} \tag{10}$$

In order to find adequate MPC controller solutions, stable closed-loop systems (linear counterpart, blocks SA device, and algorithm with unitary transfer functions) should be

chosen. The closed-loop system equations can be found using the system's expressions (4), observer expressions (9), and the solution of the optimization problem (8). Only the first term of the $\Delta\mathbf{F}_d(k)$ will be used:

$$\Delta f_d(k) = \mathbf{C}_1 \cdot \hat{\mathbf{z}}_a(k \mid k) + \mathbf{C}_2 \cdot f_d(k-1) + \mathbf{C}_3 \cdot a_g(k)$$
$$\text{with } \mathbf{C}_1 = \text{fr}\left(-\mathbf{T}_{\text{term}} \cdot \boldsymbol{\Psi}\right),$$
$$\mathbf{C}_2 = \text{fr}\left(-\mathbf{T}_{\text{term}} \cdot \mathbf{T}\right),$$
$$\mathbf{C}_3 = \text{fr}\left(-\mathbf{T}_{\text{term}} \cdot \boldsymbol{\Xi} \cdot \mathbf{1}\right),$$
$$\mathbf{T}_{\text{term}} = \left(\boldsymbol{\Theta}^T \cdot \mathcal{Q} \cdot \boldsymbol{\Theta} + \mathcal{R}\right)^{-1} \cdot \boldsymbol{\Theta}^T \cdot \mathcal{Q}, \tag{11}$$

where $\mathbf{1}$ is a unitary column vector and fr(·) denotes the matrix first row. The closed-loop system is given by

$$\begin{bmatrix} \mathbf{z}_a(k+1) \\ \hat{\mathbf{z}}_a(k+1 \mid k) \end{bmatrix} = \begin{bmatrix} \mathbf{A}_a + \mathbf{B}_a \cdot \left(\mathbf{C}_1 \cdot \mathbf{K} \cdot \mathbf{C}_a + \left(\mathbf{C}_2 + 1\right) \cdot \mathbf{M}_{01}\right) & \mathbf{B}_a \cdot \mathbf{C}_1 \cdot \left(\mathbf{I} - \mathbf{K} \cdot \mathbf{C}_a\right) \\ \mathbf{A}_a \cdot \mathbf{K} \cdot \mathbf{C}_a + \mathbf{B}_a \cdot \left(\mathbf{C}_1 \cdot \mathbf{K} \cdot \mathbf{C}_a + \left(\mathbf{C}_2 + 1\right) \cdot \mathbf{M}_{01}\right) & \left(\mathbf{A}_a + \mathbf{B}_a \cdot \mathbf{C}_1\right) \cdot \left(\mathbf{I} - \mathbf{K} \cdot \mathbf{C}_a\right) \end{bmatrix}$$
$$\cdot \begin{bmatrix} \mathbf{z}_a(k) \\ \hat{\mathbf{z}}_a(k \mid k-1) \end{bmatrix} + \begin{bmatrix} \mathbf{E}_a + \mathbf{B}_a \cdot \mathbf{C}_3 \\ \mathbf{B}_a \cdot \mathbf{C}_3 \end{bmatrix} \cdot a_g(k), \tag{12}$$

where $\mathbf{I}$ is the identity matrix and $\mathbf{M}_{01}$ is the matrix that satisfies $f_d(k-1) = \mathbf{M}_{01} \cdot \mathbf{z}_a(k)$. A stable system must have the dynamic matrix eigenvalues inside the unit circle. If all the states are available, the estimated state will be substituted by $\hat{\mathbf{z}}_a(k \mid k) = \hat{\mathbf{z}}_a(k \mid k-1) = \mathbf{z}_a(k)$ and the terms involving the observer gain $\mathbf{K}$ will cancel out in the above equations.

3.2. Control Algorithms. In the "SA Algorithm" block (see Figure 2) two different control algorithms were considered:

(1) *variable damping* (VD) is adequate for use with proportional valves since the damping can be changed continuously between the minimum and the maximum values; the inverse of the device's model (2) is used to convert the desired force (f_d) into a damping value; to compute this value the algorithm also needs access to the relative velocity $\dot{x}_r$, the force derivative, and the device's physical limits ($c_{\min} \le c_v \le c_{\max}$);

(2) the *clipped on-off* (COO) is the other control algorithm tested and this is a bang-bang control algorithm adequate for use with dampers employing on-off valves; this algorithm consists in applying the maximum damping when the device's force is smaller than the desired one and both have the same sign; otherwise the damping coefficient is set to the minimum value; this algorithm is implemented according to the following law [6, 8]:

$$c_v = c_{\min} + \left(c_{\max} - c_{\min}\right) \cdot H\left[\left(f_d - f\right) \cdot f\right], \tag{13}$$

where $H[\cdot]$ is the Heaviside step function. To implement this algorithm the device's force must be measured.

4. Numerical Simulations

4.1. Structural Systems. In this section a model of the structure subjected to typical Portuguese seismic actions will be used to test the effectiveness of the proposed control strategies. Only the acceleration (base floor acceleration for the MDOF system) will be used for feedback in the controller. Comparisons with the original structure (without any additional device), with the passive cases (the best one and the one with the maximum damping considered for the SA device), and with the semiactive case using and optimal controller will be presented. A nonlinear fluid viscous damper following the law $f_P = c_p \cdot \dot{x}_r^{\alpha}$ was considered for the best passive case. f_P is the passive damper force, c_p is the damping coefficient, $\dot{x}_r$ is the relative velocity, and α is the velocity exponent (it was found that $\alpha = 0.15$ for the SDOF model and $\alpha = 1$ for the MDOF model as the exponents that lead to the best passive cases performance). The best passive case is identified as the one having a damping coefficient that provides the lowest mean peak acceleration (top floor acceleration for the MDOF model). Figure 3 shows the typical plot of the evolution of the responses with the device damping values (a) and the identified damping values for type 1 and type 2 seismic actions corresponding to the best passive cases (b).

A semiactive solution employing an optimal controller (stochastic linear quadratic regulator [6]) with a unitary input weight and an output weight on the base acceleration that minimizes the mean peak acceleration for each set of seismic actions [16] (referred as SALQRVD) was also considered for comparison. Relative displacement and absolute accelerations will be considered to evaluate the systems' performance.

At first a SDOF system is used to model the first vibration mode of base-isolated structures (building supported by bearings) considering that the base isolation system is flexible and the superstructure (building structure) is rigid enough as to be modelled as a rigid mass (base mass plus superstructure's mass). Base isolation systems are used to reduce the structure's natural frequency and deviate it from the seismic input action frequency content. Common base isolation systems are designed to have natural frequencies bellow 1 Hz. In order to evaluate the performance of several base isolation systems the model's properties considered in

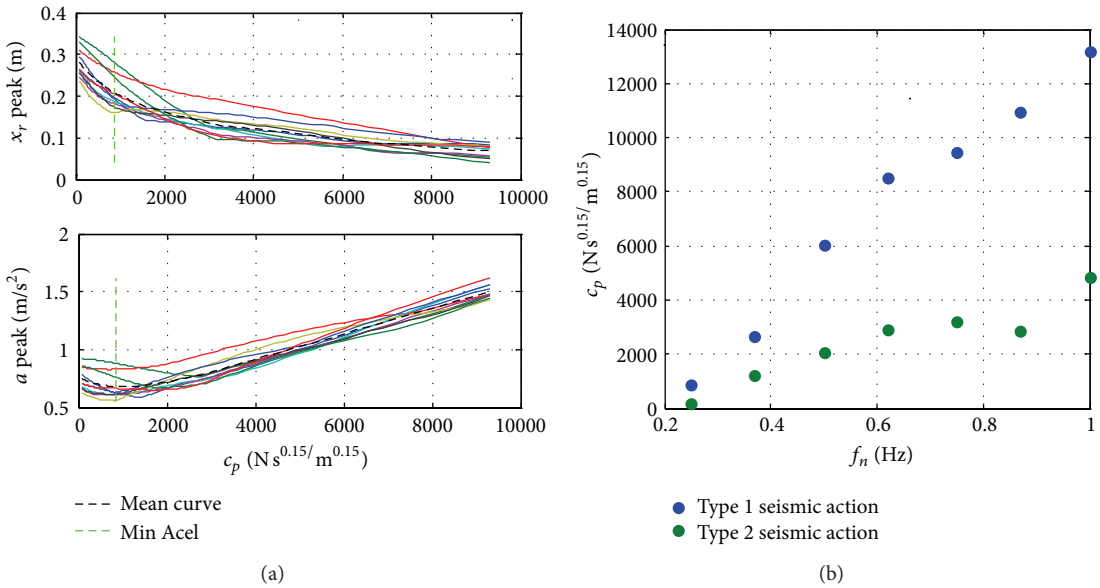

FIGURE 3: Simulation results for the SDOF model (f_n = 0.25 Hz; ξ = 10%) with a passive damper. (a) Evolution of responses versus passive device damping for 10 type 1 seismic actions and the correspondent mean curve; (b) damping coefficients (for α = 0.15) for the minimum mean peak acceleration response function of system natural frequencies under type 1 and 2 seismic actions.

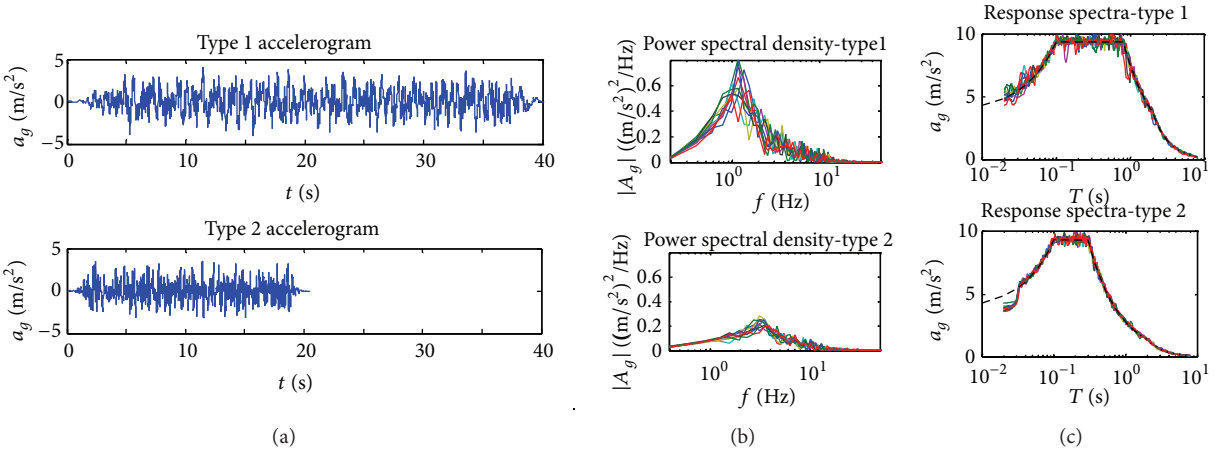

FIGURE 4: Input ground motions characteristic considered in the numerical simulations. (a) One of ten artificial accelerograms; (b) frequency spectra of 10 accelerograms; (c) response spectra of 10 accelerograms.

the simulations were m = 5750 kg (mass), f_n = 0.25 to 1 Hz (natural frequency), and ξ = 0.1 (damping ratio). The semiactive fluid damper can add additional damping between ξ_{min} = 0.05 and ξ_{max} = (1−ξ)/2 = 0.45. The device's dynamics is characterized by a time constant of T_d = 0.05 s which is an average of time delays found in [15, 17]. Two different semiactive control strategies were considered depending on the algorithm used, although both make use of the predictive controller: (i) SAMPCVD, for a variable damping algorithm; (ii) SAMPCCOO, when a clipped on-off algorithm is used. In the end, a 10-storey base-isolated building (MDOF model) is used to verify the effectiveness of the proposed strategies.

4.2. Input Action. The input actions considered in this work were artificial accelerograms generated using the extreme response spectrums provided in the Eurocode 8 for Portugal [26]: type 1 (far field) seismic action; type 2 (near field) seismic action. Ten accelerograms were generated for each spectrum. The accelerograms were generated for zone 1, soil type D, and structures of class II importance. The accelerograms and the spectrums are presented in Figure 4. It can be seen that type 1 input action has a longer duration, is richer in the lower frequencies (or higher periods), and has higher amplitudes. It must be referred that if other specifications were used, for example, ASCE 7 [27], the seismic hazard would be described in a different way, especially for near-fault applications.

4.3. SDOF Model Results. Numerical simulations were performed in the time domain considering the generated artificial accelerograms as inputs. MATLAB/Simulink environment was used to run the simulations.

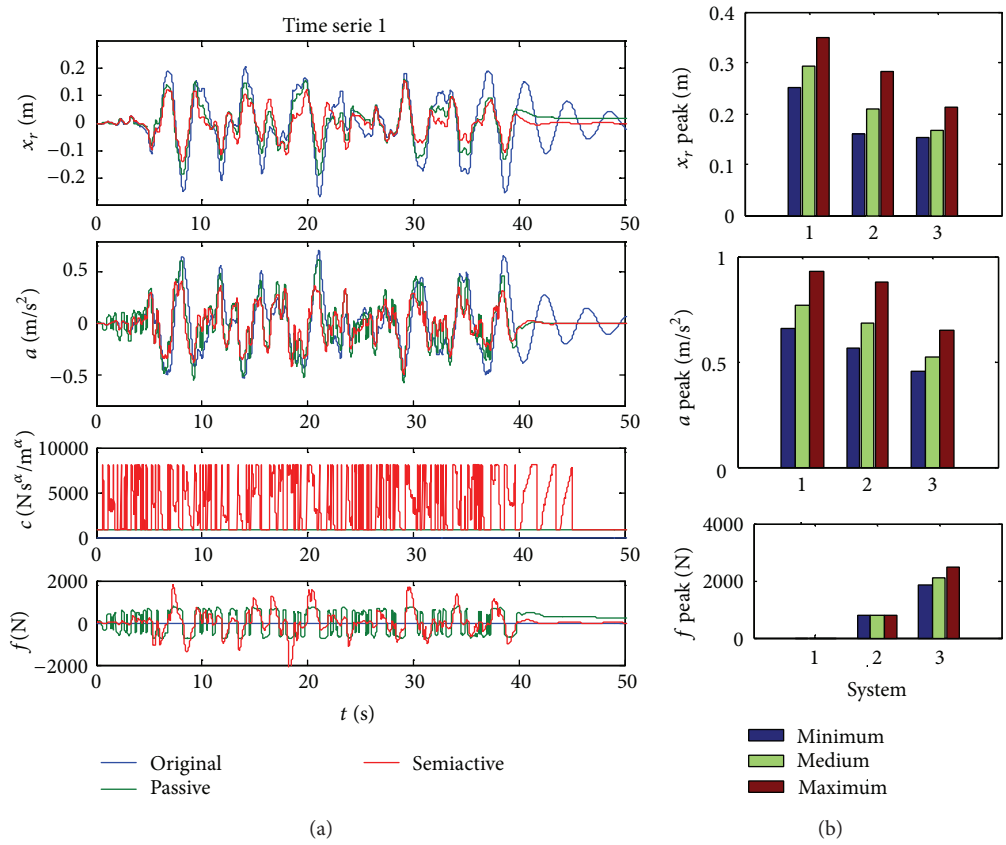

FIGURE 5: (a) Simulation results for the SDOF model (f_n = 0.25 Hz and ξ = 10%) subjected to one type 1 accelerogram without devices, with passive and SAMPCVD; (b) peak values' statistics for 10 type 1 input time series.

The predictive controller described has several adjustable parameters: weights (acceleration weight Q and input move weight R), horizons (HP and HC), control interval (T_s), and observer dynamics (covariance matrices Q_0 and R_0). The weights and covariance matrices are 1×1 dimension matrices since the controller's internal model is characterized by one input (desired force) and one output (acceleration); thus, $Q = q, R = r, Q_0 = q_0$, and $R_0 = r_0$. For nonlinear problems tuning these parameters is a question of applying a set of "rules of thumb" based on experience gained from simulations [24]. Following the methodology that will be described below, adequate parameters for this kind of problems were found. It will be shown that a well-tuned controller could improve the system's performance (relative displacement and absolute acceleration) even better than the best passive solution, only by changing the damping coefficient in "real time." Typical system's responses are shown in Figure 5.

The control interval (or sampling period) should be adequate to capture the system's dynamics. Its value is delimited by the time taken to solve the optimization problem and by the inverse of the Nyquist frequency, obtained from the smallest time constant of the system. It should also be small enough so that the control input (desired force or damping) responds quickly to the output changes. In contrast, the limit is the passive case where damping is constant. An example of the influence of this parameter on the system's performance (mean peak responses) can be found in Figure 6 where a comparison with different values of control interval and prediction horizons is presented for the SDOF case. It is shown that higher control intervals lead to poor performances (increases in relative displacements and absolute accelerations). Higher control intervals also have a negative impact on the evolution of responses with the prediction horizon. As the control interval increases the range of prediction horizons that lead to good performances gets smaller (see Figure 6(a)), and thus as the control interval increases smaller prediction horizons should be considered to achieve good responses. A control interval (or sampling time) of T_s = 5 ms was considered in this work.

The observer was designed with a Kalman filter with unitary covariance matrices. This solution is a compromise between observer response in estimating the state vector and control aggressiveness. A deadbeat observer would be preferable but it could lead to aggressive control actions which would compromise the overall performance of the system.

In order to identify the range of acceptable controllers the closed-loop linear system counterpart was analysed. The maximum moduli of the eigenvalues for the closed-loop system were used to identify the systems' stability: stable systems have their eigenvalues inside the unit circle and thus their moduli are less than one. Time delays d were considered on the simulations to compensate for the device dynamics T_d

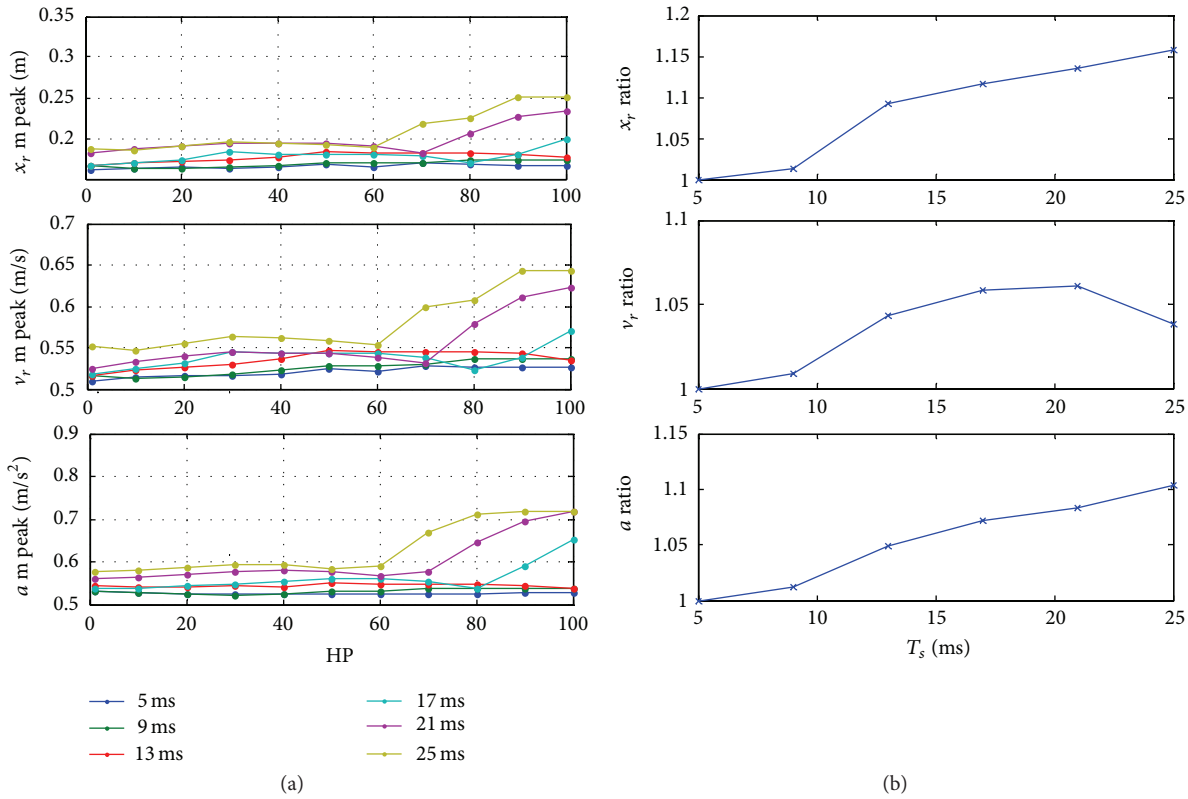

FIGURE 6: (a) SDOF system's mean peak responses ($f_n = 0.25$ Hz and $\xi = 10\%$ for SAMPCVD with HC $= 1$ and $r = 1$) evolutions with control interval T_s and prediction horizon HP, when subjected to type 1 seismic actions (10 accelerograms). (b) Ratios evolution with control interval (relative to $T_s = 5$ ms) for HP $= 50$.

(time response). Figure 7(a) shows an example of the maximum moduli evolution with the acceleration weight q. It can be seen that the desired solution lies in the range $q^{0.5} < 150$. After that, each structural system with an SA device was subjected to 10 accelerograms of each action type and the mean peak values were evaluated. Applying this procedure for different weights and horizons, combinations of these parameters that lead to the best system's response were found. Figure 7(b) shows the evolution of system's peak responses with the controller acceleration weight q for each accelerogram (with $r = 1$). The dashed vertical line indicates the minimum of the mean peak acceleration curve. Using this point as criteria to design the controller, reductions in relative displacement and velocity are also achieved, which leads also to reductions in base shear forces. Higher values for this weighting parameter lead to poor performances in terms of relative displacement and acceleration. In fact, for higher acceleration weights the closed-loop system becomes unstable as mentioned before, and the desired force resulting from the controller goes to infinity which leads to poor performance.

It was also found that an increase on the input move weight r slides those curves (responses versus acceleration weight) to the right, meaning that the acceleration weight that minimizes the acceleration response also increases. From the analysis of the cost function (7) increasing the input move weight relative to the output weights has the effect of reducing the control activity. In the present study a unitary weight in the input move was considered.

The results with different prediction and control horizons showed similar responses although for higher prediction horizons higher responses are obtained. Figure 7(c) shows the typical evolution of the responses (mean peak values) with this parameter. An almost constant evolution of relative displacements and absolute accelerations were found with the prediction horizon HP up to a value dependent on the system's natural frequency and control interval (HP $= 70$ for $f_n = 1$ Hz and $T_s = 5$ ms, and higher values of HP for lower natural frequencies). Above those values the responses increase (poor performances). Thus, prediction horizons inferior to 70 were found to be adequate for the studied cases. In fact, having found no significant influence of the prediction horizon on the results in that range, the smallest value is desired in order to reduce the order of the controller (matrices dimension, solution of the optimization problem). However, since the internal model has input delays to account for the device's response, one should assure that HP $> d$. In the present study the instant delays are $d = 10$ (50 ms) and thus the prediction horizon was set to HP $= 50$. In what concerns the influence of the control horizon HC in the results, no evidence of improvements was found for HC > 1,

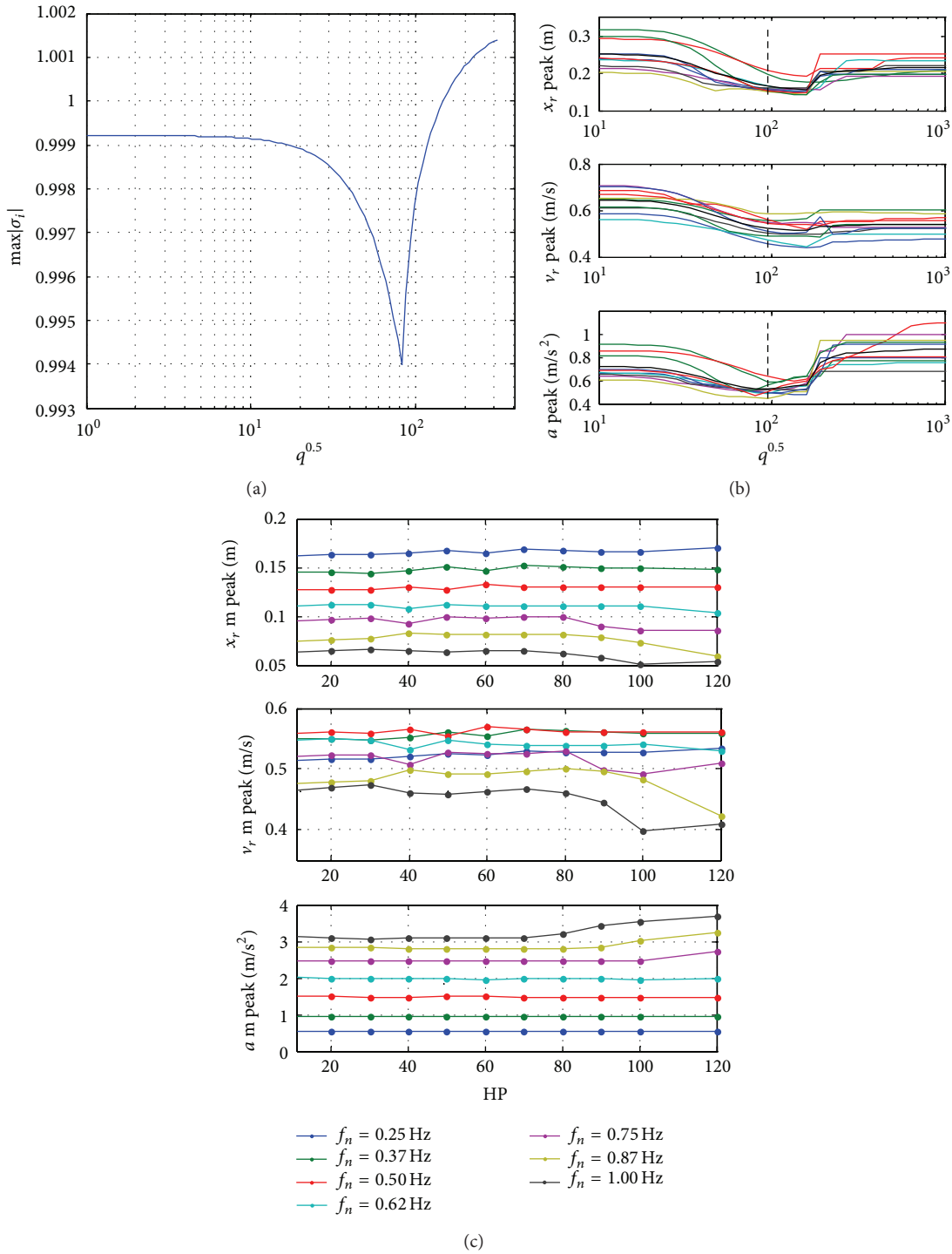

FIGURE 7: Result for system with $f_n = 0.25$ Hz and $\xi = 10\%$ considering $T_s = 5$ ms, HC = 1. $r = 1$ and $d = 10$. (a) System eigenvalues' moduli (maximum values) evolution with acceleration weight; (b) system responses' (peak values) evolution with acceleration weight when subjected to type 1 seismic actions; (c) system responses' (mean peak values) evolution with prediction horizon for different natural frequencies (f_n = 0.25 to 1.00 Hz) for SAMPCVD, when subjected to type 1 seismic actions (10 input time accelerograms).

and thus the unitary value was considered in the subsequent analysis.

Good performance is achieved with the parameterization previously indicated since the device force follows very closely the desired force, as is shown in Figure 8.

Having found the best parameters, the mean peak responses for each structural system (with different natural frequencies) were determined. Comparisons with the original, passive (with a damping coefficient for the lowest mean peak top floor acceleration), and semiactive with an optimal

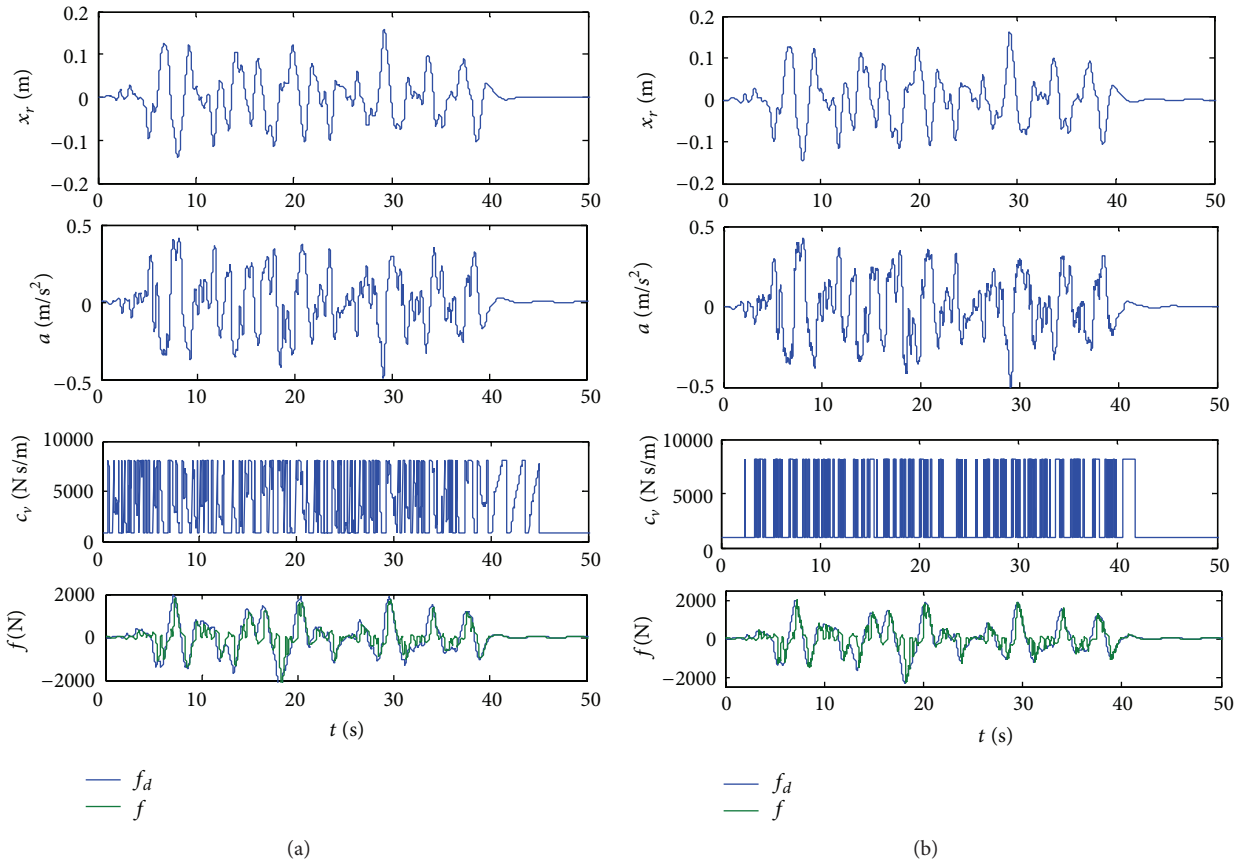

FIGURE 8: Simulation results for the SDOF model (f_n = 0.25 Hz and ξ = 10%) subjected to one type 1 accelerogram employing SA systems with T_s = 5 ms, HP = 50, HC = 1, r = 1, and d = 10, with both VD (a) and COO (b) control algorithms.

controller are presented in Figure 9. It is shown that any proposed system is better than the original one. In terms of accelerations the proposed semiactive systems show the best performance for structural systems with natural frequencies below 0.6 Hz for type 1 seismic actions, and below 1 Hz for type 2 seismic actions. This means that base isolation systems should employ semiactive devices in detriment of passive ones on such circumstances. It can also be seen that the SA device controlled by an on-off algorithm almost reaches the same performance of the variable damping algorithm. This result shows that a simple solenoid valve can be used instead of a proportional one, which in terms of practical implementation leads to a less expensive solution. It was also found that the proposed solution with an MPC controller is slightly better than the one with an optimal controller in terms of both relative displacements and accelerations. Thus, the SA systems presented can provide reductions in relative displacements (between 50 and 60%) when compared to the original structure, improve the acceleration responses better than the best passive case, and outperform the SA one with an optimal controller.

Other numerical simulations were performed with structural systems of different properties (m, k, and c). The main difference found was on the optimal acceleration weight q. Thus, for different structural systems this value should be determined (with the proposed values for the other parameters) under a numerical analysis by finding first a range of stable solutions and then considering a representative set of accelerograms of the site where the structure is to be installed to find the weight q that leads to the best performance.

4.4. MDOF Model Results. A ten-storey base-isolated structure was considered to evaluate the effectiveness of the presented strategies. The superstructure's fundamental frequency is f_{s1} = 1.6 Hz (representative of a 10-storey dual frame-wall structure), and a damping ratio of ξ_1 = 5% is assumed. Each floor has a mass of $m_f = 10^5$ kg. The stiffness and damping matrices were determined considering constant stiffness between floors and a stiffness proportional damping matrix ($\mathbf{C} = a_0 \cdot \mathbf{K}$), which correspond to stiffness and damping coefficients between floors of k_f = 452.43 kN/mm and c_f = 1.51 kN s/mm with a_0 = 0.0033 s. The superstructure is supported on a base isolation system with mass $m_i = 1.4 \cdot m_f$ and laminated rubber bearings made of natural rubber represented by a linear elastic and viscous model, with a target frequency f_i = 0.4 Hz and an equivalent damping ratio of ξ_i = 10%. The correspondent stiffness and damping coefficients were obtained assuming a rigid superstructure: k_i = 7.20 kN/mm and c_i = 0.57 kN s/mm. The base-isolated structure model is obtained after assembling the base isolation

Type 1 seismic action responses							
f_n (Hz)	0,25	0,37	0,50	0,62	0,75	0,87	1,00
x_r (m)	0,293	0,278	0,266	0,222	0,187	0,155	0,131
a (m/s^2)	0,765	1,554	2,694	3,457	4,253	4,742	5,298

Type 2 seismic action responses							
f_n (Hz)	0,25	0,37	0,50	0,62	0,75	0,87	1,00
x_r (m)	0,113	0,109	0,104	0,0845	0,0704	0,0602	0,0516
a (m/s^2)	0,300	0,623	1,062	0,62	1,618	1,848	2,088

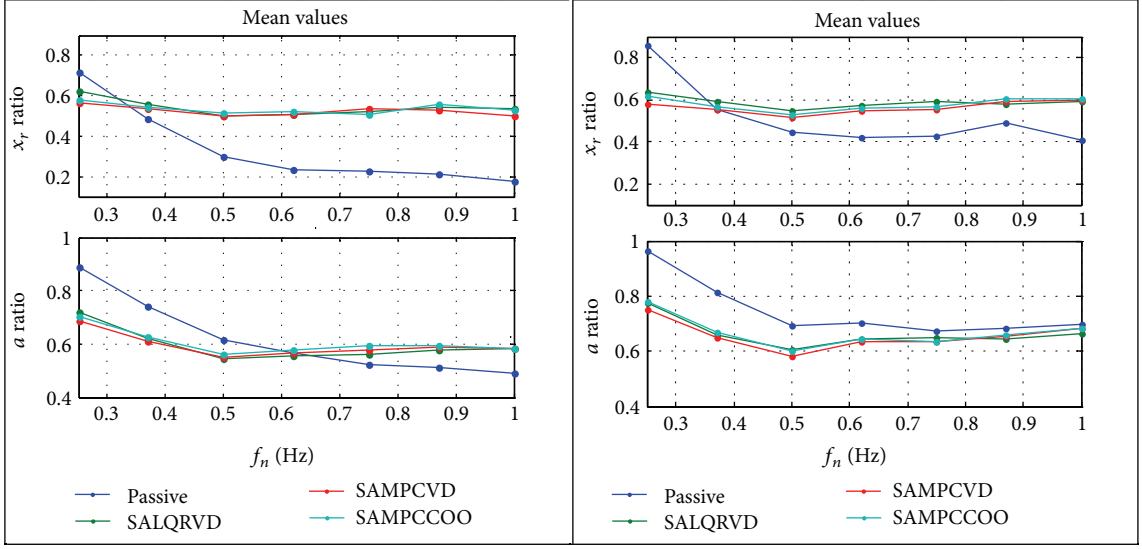

FIGURE 9: SDOF mean peak response values for the original system and ratios (relative to the original structure) for different system's natural frequencies.

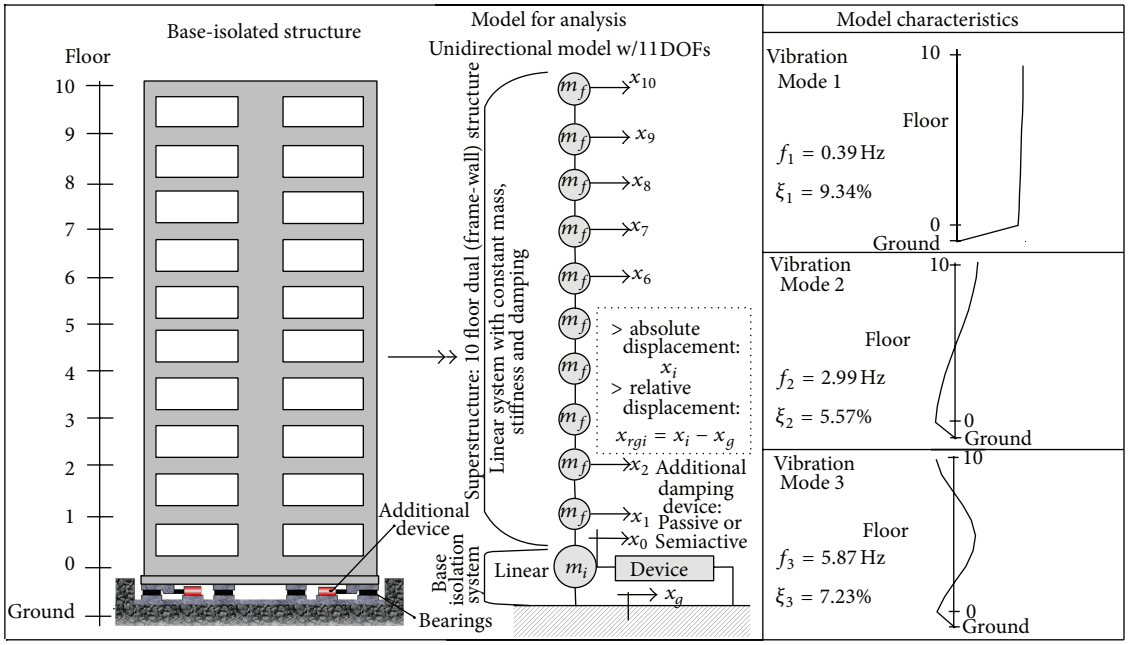

FIGURE 10: 10-storey base-isolated building and equivalent model for analysis.

system and the superstructure models together. Figure 10 depicts the model under study. Considering the controller parameters for the SDOF case, the MPC scheme was implemented assuming a rigid superstructure and thus only the base acceleration is used for feedback. After analysing the closed-loop system the acceleration weight $q^{0.5} = 10^4$ was chosen. Figure 11 and Table 1 show a comparison of results with the original structure, the best passive (with a damping coefficient for the lowest mean peak top floor acceleration, $c_{id} = 1.1$ kN s/mm, additional damping of $\xi = 0.19$) case, the passive with maximum damping, $c_{max} = 2.58$ kN s/mm (additional damping of $\xi = 0.45$), and with the semi-active manipulated by an optimal controller (controller implemented considering a rigid superstructure

Table 1: 10-storey base isolated building results. Comparison in terms of mean response peak values ratios: relative displacements, accelerations (at base and top) and base shear force V, in relation to the original structure; and peak device's force ratio f/W in relation to the structure's weight W.

System	Type 1 seismic action						Type 2 seismic action					
	$x_{r\,\text{base}}$	$x_{r\,\text{top}}$	a_{base}	a_{top}	V	f/W	$x_{r\,\text{base}}$	$x_{r\,\text{top}}$	a_{base}	a_{top}	V	f/W
Passive c_{id}	0.67	0.67	0.87	0.88	0.77	0.04	0.70	0.71	**1.14**	**1.09**	0.82	0.02
Passive c_{max}	0.40	0.41	**1.03**	**1.14**	0.78	0.10	0.42	0.44	**1.64**	**1.63**	0.93	0.05
SALQRVD	0.60	0.60	0.83	0.85	0.70	0.05	0.64	0.64	**1.07**	**1.07**	0.75	0.02
SAMPCVD	0.65	0.66	0.77	0.78	0.70	0.04	0.69	0.70	0.91	0.89	0.75	0.02
SAMPCCOO	0.66	0.66	0.81	0.81	0.71	0.04	0.69	0.70	0.98	0.93	0.75	0.02

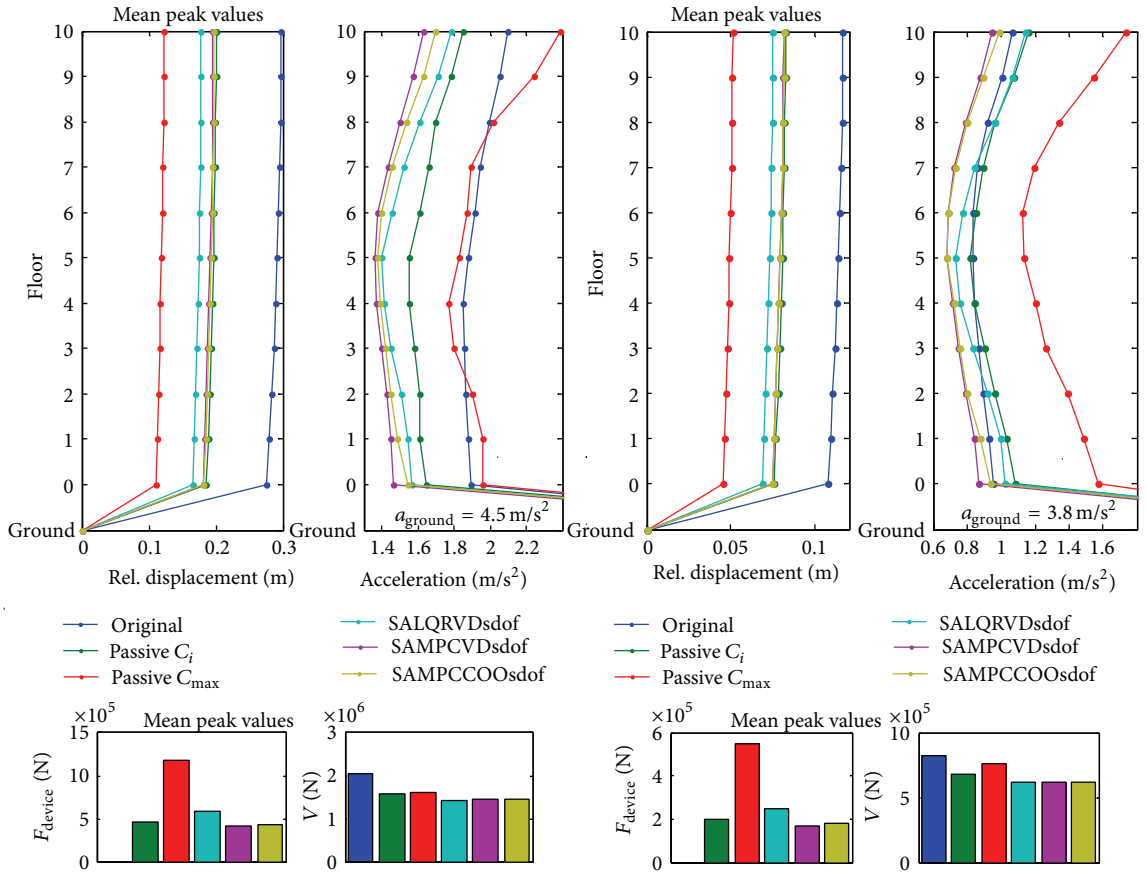

Figure 11: 10-storey base-isolated building responses to 10 type 1 and type 2 accelerograms. Mean peak values in terms of relative displacements, accelerations, base shear V, and device's force f for the systems under study.

with weighting values determined as for de SDOF case; see Section 4.1).

The results show that all solutions can improve the structure's relative displacements, with the maximum damping passive device having the best performance for this parameter. However, this solution has the disadvantage of increasing the acceleration responses, especially for type 2 seismic actions, with higher damper forces. The SA solutions appear as an attractive answer to the problem since it is possible to reduce the base relative displacements without compromising and even improving the acceleration responses. The proposed solutions perform also better in terms of acceleration than the one considering an optimal controller to manipulate the SA device. However, the last one has the disadvantage of slightly increasing the accelerations more than the original structure for type 2 seismic actions. In terms of displacement at the base level, the optimal controller solution performs better than the MPC-based ones. Even the best passive solution (passive c_{id}) has the inferior performance in terms of absolute accelerations. All the solutions can reduce the base shear forces transmitted to the structure at the base since part of the seismic force is dissipated by the devices. Thus, higher damper forces lead to lower base relative displacements. It is shown also that SA device control forces (mean peak values) are less than 5% of the structure's weight. The results also show that an SA device manipulated by an on-off algorithm (COO)

can achieve similar results to that of a variable damping algorithm (VD). Differences are less than 1% in terms of relative displacements but major differences are found in the accelerations, which can reach 7% for the base floor acceleration when type 2 seismic actions are considered.

5. Conclusions

A force tracking scheme comprising a predictive controller and a semiactive control algorithm is proposed for damping control of semiactive fluid dampers employed in base isolation systems subjected to earthquake loads. The controller formulation includes the input delays resulting from the device's behaviour. Moreover, assuming that all the system's variables are not always available, the controller was formulated using an embedded observer as well. The numerical simulations show that a well-tuned controller can improve the system's performance (peak of relative displacement and absolute acceleration) only by changing the damping in "real time." The proposed solution outperforms the original structure and the structural system with passive devices for natural frequencies below 0.6 Hz when subjected to several artificial accelerograms generated according to current codes for the Portuguese territory. The parametric study of a SDOF model provided some indicators to tune the controller. However, with the proposed tuning the acceleration weight always has to be determined by numerical simulations of the closed-loop system under several input accelerograms. Slightly better performance was found with the proposed strategy when compared with the solution provided by an optimal controller to manipulate the SA device. When applied to a MDOF system, a 10-storey base-isolated structure, better performance than the original and passive cases, was also found in terms of accelerations. The proposed solution also outperforms the SA solution manipulated by an optimal controller in terms of accelerations. In terms of relative displacements, the passive case with maximum damper and the SA device manipulated by an optimal controller provide better results but at the expense of increasing the absolute accelerations.

It has been demonstrated that a predictive controller with an adjusting damping rule can be effective in reducing earthquake induced responses using variable fluid dampers. The range of controller acceleration weights is first determined by the analysis of the closed-loop system and tuned through numerical simulations using a representative number of accelerograms (test functions) from the site of structures' installation. Thus, the proposed strategies have potential for future implementations in civil engineering structures located in active seismic zones.

Conflict of Interests

The authors declare that there is no conflict of interests regarding the publication of this paper.

Acknowledgments

The authors would like to thank the Portuguese Foundation for Science and Technology (FCT) for the Ph.D. scholarship provided (reference SFRH/BD/84769/2012) and to LNEC and IST for providing the resources needed to develop this work.

References

[1] T. T. Soong and G. F. Dargush, *Passive Energy Dissipation Systems in Structural Engineering*, John Wiley & Sons, New York, NY, USA, 1997.

[2] A. K. Chopra, *Dynamics of Structures: Theory and Applications to Earthquake Engineering*, Prentice Hall, New York, NY, USA, 2nd edition, 1995.

[3] J. M. Kelly, "The role of damping in seismic isolation," *Earthquake Engineering and Structural Dynamics*, vol. 28, no. 1, pp. 3–20, 1999.

[4] T. T. Soong and B. F. Spencer Jr., "Supplemental energy dissipation: state-of-the-art and state-of-the-practice," *Engineering Structures*, vol. 24, no. 3, pp. 243–259, 2002.

[5] M. D. Symans and M. C. Constantinou, "Semi-active control systems for seismic protection of structures: a state-of-the-art review," *Engineering Structures*, vol. 21, no. 6, pp. 469–487, 1999.

[6] A. Preumont, *Vibration Control of Active Structures—An Introduction*, Kluwer Academic, New York, NY, USA, 2nd edition, 2002.

[7] Y. Ikeda, "Active and semi-active vibration control of buildings in Japan-practical applications and verification," *Structural Control and Health Monitoring*, vol. 16, no. 7-8, pp. 703–723, 2009.

[8] S. J. Dyke and B. F. Spencer Jr., "A comparison of semi-active control strategies for the MR damper," in *Proceedings of the International Conference on Intelligent Information Systems (IIS '97)*, pp. 580–584, Grand Bahama Island, Bahamas, December 1997.

[9] D. Shook, P. Lin, T. Lin, and P. N. Roschke, "A comparative study in the semi-active control of isolated structures," *Smart Materials and Structures*, vol. 16, no. 4, pp. 1433–1446, 2007.

[10] N. Aguirre, F. Ikhouane, and J. Rodellar, "Proportional-plus-integral semiactive control using magnetorheological dampers," *Journal of Sound and Vibration*, vol. 330, no. 10, pp. 2185–2200, 2011.

[11] A. Rodríguez, F. Pozo, A. Bahar, L. Acho, Y. Vidal, and J. Rodellar, "Force-derivative feedback semi-active control of base-isolated buildings using large-scale MR fluid dampers," *Structural Control and Health Monitoring*, vol. 19, no. 1, pp. 120–145, 2012.

[12] M. Zapateiro, H. R. Karimi, N. Luo, and B. F. Spencer Jr., "Real-time hybrid testing of semiactive control strategies for vibration reduction in a structure with MR damper," *Structural Control and Health Monitoring*, vol. 17, no. 4, pp. 427–451, 2010.

[13] A. M. Aly, A. Zasso, and F. Resta, "On the dynamics of a very slender building under winds: response reduction using MR dampers with lever mechanism," *Structural Design of Tall and Special Buildings*, vol. 20, no. 5, pp. 539–551, 2011.

[14] A. M. Aly, "Vibration control of buildings using magnetorheological damper: a new control algorithm," *Journal of Engineering*, vol. 2013, Article ID 596078, 10 pages, 2013.

[15] M. D. Symans and M. C. Constantinou, "Development and experimental study of semi-active fluid damping devices for seismic protection of structures," Report No. NCEER 95-0011, National Center for Earthquake Engineering Research, Buffalo, NY, USA, 1995.

[16] F. Sadek and B. Mohraz, "Semiactive control algorithms for structures with variable dampers," *Journal of Engineering Mechanics*, vol. 124, no. 9, pp. 981–990, 1998.

[17] I. Nagashima, Y. Shinozaki, R. Maseki et al., "A building with semi-active base isolation using sliding mode control," in *Proceedings of the World Forum on Smart Materials and Smart Structures Technology (SMSST '07)*, pp. 523–524, May 2007.

[18] H. Kurino, J. Tagami, K. Shimizu, and T. Kobori, "Switching oil damper with built-in controller for structural control," *Journal of Structural Engineering*, vol. 129, no. 7, pp. 895–904, 2003.

[19] H. Kurino, Y. Matsunaga, T. Yamada, and J. Tagami, "High performance hydraulic damper with semi-active characteristics," in *Proceedings of the 13th World Conference on Earthquake Engineering*, paper no. 33, p. 12, Vancouver, Canada, August 2004.

[20] H. Kurino, S. Orui, and K. Shimizu, "Structural control by innovative oil damper with automatic on/off valve operation," *Journal of Disaster Research*, vol. 4, no. 3, pp. 253–260, 2009.

[21] A. Occhiuzzi and G. Serino, "A semi-active oleodynamic damper for earthquake control—part 2: evaluation of performance through shaking table tests," *Bulletin of Earthquake Engineering*, vol. 1, no. 2, pp. 241–273, 2003.

[22] J. F. Hall, "Discussion: the role of damping in seismic isolation," *Earthquake Engineering and Structural Dynamics*, vol. 28, no. 12, pp. 1717–1720, 1999.

[23] E. D. Wolff and M. C. Constantinou, "Experimental study of seismic isolation systems with emphasis on secondary system response and verification of accuracy of dynamic response history analysis methods," Report No. MCEER-04-0001, Multidisciplinary Center for Earthquake Engineering Research, Buffalo, NY, USA, 2004.

[24] J. M. Maciejowski, *Predictive Control with Constraints*, Pearson Education, Upper Saddle River, NJ, USA, 2002.

[25] F. L. Lewis, *Optimal Estimation: With an Introduction to Stochastic Control Theory*, John Wiley & Sons, New York, NY, USA, 1986.

[26] EN, 1998-1, "Eurocode 8-1: design of structures for earthquake resistance," Portuguese Version: Eurocodigo8, Projecto de Estruturas para Resistência aos Sismos—Parte 1: Regras Gerais, Acções Símicas e Regras para Edifícios, Instituto Português da Qualidade, NP EN, 1998-1, 2010, http://eurocodes.jrc.ec.europa.eu/showpage.php?id=138.

[27] ASCE/SEI 7, "Minimum design loads for buildings and other structures," ASCE Standard, American Society of Civil Engineers, 2010, http://www.asce.org/sei/Content.aspx?id=23622324319.

Hindawi Publishing Corporation
Shock and Vibration
Volume 2014, Article ID 325839, 11 pages
http://dx.doi.org/10.1155/2014/325839

Research Article

Some Elements of Operational Modal Analysis

Rune Brincker

Department of Engineering, Aarhus University, Edison Building, Finlandsgade 22, 8200 Aarhus N, Denmark

Correspondence should be addressed to Rune Brincker; rub@science.au.dk

Received 27 June 2013; Accepted 26 February 2014; Published 6 July 2014

Academic Editor: Nuno Maia

Copyright © 2014 Rune Brincker. This is an open access article distributed under the Creative Commons Attribution License, which permits unrestricted use, distribution, and reproduction in any medium, provided the original work is properly cited.

This paper gives an overview of the main components of operational modal analysis (OMA) and can serve as a tutorial for research oriented OMA applications. The paper gives a short introduction to the modeling of random responses and to the transforms often used in OMA such as the Fourier series, the Fourier integral, the Laplace transform, and the Z-transform. Then the paper introduces the spectral density matrix of the random responses and presents the theoretical solutions for correlation function and spectral density matrix under white noise loading. Some important guidelines for testing are mentioned and the most common techniques for signal processing of the operating signals are presented. The algorithms of some of the commonly used time domain and frequency domain identification techniques are presented and finally some issues are discussed such as mode shape scaling, and mode shape expansion. The different techniques are illustrated on the difficult case of identifying the three first closely spaced modes of the Heritage Court Tower building.

1. Introduction

While in traditional experimental modal analysis (EMA) the forces exciting the test specimen are controlled and normally the testing is carried out in the laboratory, in OMA the forces are just the ones that are naturally present during the operation of the structure and the test should be carried under the actual operating "in situ" conditions. For a civil engineering structure forces that might be ambient forces like wind and waves and for a mechanical structure that might be the operating forces on an engine or a gearbox, in both cases nothing is done to control temperature and other conditions that might influence the result.

In OMA all modal parameters are to be determined without knowing the excitation forces. Therefore it is normally assumed that the excitation forces are Gaussian white noise, or at least that spectral densities of these forces are all flat. It is not necessary to satisfy that assumption for the actual physical forces because the physical forces acting on the structure can be thought of as created by a linear filter loaded by white noise, Figure 1. In this case we maintain the assumption of white noise system input but add the properties of a linear filter to the system that is going to be identified. The properties of the filter do not change the properties of the structural system to be identified, Asmussem et al. [1], but of course we have to deal with the challenge of separating the "modes" of the loading system from the structural modes of interest.

In this paper we shall focus on the theories behind the OMA technology. The paper can serve as a short overview of the present knowledge of these theories and methods. Details, derivations, and more references and information related to the treated subjects can be found in Brincker and Ventura [2] and for a more broad description of the subject, in the literature on OMA from the IMAC and IOMAC proceedings, we refer the reader to [3, 4].

2. Random Modeling

Since in OMA we assume the forces to be unknown we need to treat everything from a probabilistic point of view. Any parameter that we are going to observe is considered as a stochastic variable, say X, and is in principle only known in terms of its probability density function $p(x)$. If we know the

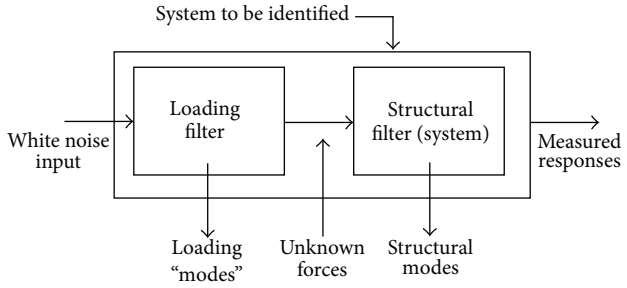

Figure 1: The commonly accepted assumption of white noise input should be thought of as loading an imaginary linear filter that produces the unknown forces. Thus the actual physical forces do not need to be white noise or have a flat spectrum.

density function we can find, for instance, the mean μ_x and variance σ_x^2 as follows:

$$\begin{aligned} \mu_x &= \int_{-\infty}^{\infty} x p(x)\, dx \\ \sigma_x^2 &= \mathrm{E}\left[(X-\mu_x)^2\right] = \int_{-\infty}^{\infty} (x-\mu_x)^2 p(x)\, dx. \end{aligned} \tag{1}$$

However, since we seldom will know the density function in OMA we use time averaging. If we have observed the signal $x(t)$, then we can calculate the mean and variance for that signal using time averaging as, Newland [5], follows:

$$\begin{aligned} \mu_x &= \frac{1}{T}\int_0^T x(t)\, dt \\ \sigma_x^2 &= \mathrm{E}\left[(x(t)-\mu_x)^2\right] = \frac{1}{T}\int_0^T (x(t)-\mu_x)^2 dt. \end{aligned} \tag{2}$$

As a main rule in OMA, we cannot use the mean values for much in practice due to large measurement errors in the low frequency region, and therefore normally we will remove the mean from the signals and calculate correlation based on the resulting zero mean signals as follows:

$$\mathrm{cor}\left[x(t), y(t)\right] = \mathrm{E}\left[x(t)\, y(t)\right] = \frac{1}{T}\int_0^T x(t)\, y(t)\, dt. \tag{3}$$

Since we are considering dynamic systems where the response is a linear combinations of the responses to many independent force impulses from the past, according to the central limit theorem, a random structural response is Gaussian or nearly Gaussian distributed. Therefore, since a Gaussian distribution is totally described by its second order properties (we discard the first order properties as explained above), we only need second order properties to describe random responses and in case of two signals $x(t)$ and $y(t)$ all information is contained in the correlation functions

$$\begin{aligned} R_{xy}(\tau) &= \mathrm{E}\left[x(t)\, y(t+\tau)\right] = \mathrm{E}\left[x(t-\tau)\, y(t)\right], \\ R_{yx}(\tau) &= \mathrm{E}\left[y(t)\, x(t+\tau)\right] = \mathrm{E}\left[y(t-\tau)\, x(t)\right]. \end{aligned} \tag{4}$$

The correlation functions possess the following symmetry properties that rely on the fact that we assume stationary signals and thus the time can be shifted arbitrarily so that $R_{xy}(\tau) = \mathrm{E}[x(t'-\tau)y(t')] = R_{yx}(-\tau)$. In the general case of a vector response containing the individual response channels similarly we estimate the correlation function matrix as follows:

$$\mathbf{R}(\tau) = \mathrm{E}\left[\mathbf{y}(t)\,\mathbf{y}^T(t+\tau)\right] = \frac{1}{T}\int_0^T \mathbf{y}(t)\,\mathbf{y}^T(t+\tau)\, dt. \tag{5}$$

Again we assume stationary conditions and we can also calculate the correlation function matrix as $\mathrm{E}[\mathbf{y}(t-\tau)\mathbf{y}^T(t)]$ and we get the symmetry relation for the correlation function matrix

$$\mathbf{R}(-\tau) = \mathbf{R}^T(\tau). \tag{6}$$

3. Transforms

The many transforms used in signal processing and development of methods and theories in OMA constitute a problem for an easy introduction to the field. However, all the transforms are closely related. The classical Fourier series

$$y(t) = a_0 + \sum_{k=1}^{\infty}\left(a_k \cos\frac{2\pi k t}{T} + b_k \sin\frac{2\pi k t}{T}\right) \tag{7}$$

is used to describe signals with the period T. However, it is normal to write the series in the complex form

$$y(t) = \sum_{k=-\infty}^{\infty} Y_k e^{i\Delta\omega k t} \tag{8}$$

that allows us to express the Fourier coefficients in the simple way

$$Y_k = \frac{1}{T}\int_{-T/2}^{T/2} y(t)\, e^{-i\Delta\omega k t} dt. \tag{9}$$

The Fourier coefficients Y_k are discrete functions of the frequency due to the limited period T. If we extend the period to infinity we then get the Fourier integral and its inverse

$$\begin{aligned} y(t) &= \int_{-\infty}^{\infty} Y(\omega)\, e^{i\omega t} d\omega, \\ Y(\omega) &= \frac{1}{2\pi}\int_{-\infty}^{\infty} y(t)\, e^{-i\omega t} dt. \end{aligned} \tag{10}$$

Just like periodic time functions result in discrete frequency, periodic frequency functions result in discrete time functions, thus assuming also periodic frequency functions introduce the discrete Fourier series and discrete Fourier transform

$$\begin{aligned} y_n &= \sum_{k=1}^{N} Y_k e^{i2\pi(k-1)(n-1)/N}; \\ Y_k &= \frac{1}{N}\sum_{n=1}^{N} y_n e^{-i2\pi(k-1)(n-1)/N} \end{aligned} \tag{11}$$

in this formulation with time and frequency shifted to comply with Matlab preferences. For the discrete time case it is important to note that according to the Shannon sampling theorem, we do not lose any information about the signal in between the sample points.

The Laplace transform can be seen as a generalization of the Fourier integral where we limit our time functions to the positive axis and multiply all time functions with an exponential term so that all time functions are damped like $y'(t) = e^{-\sigma t} y(t)$. We can then define the complex variable $s = \sigma + i\omega$ and the Laplace transform and its inverse

$$Y(s) = \int_0^\infty y(t)\, e^{-st} dt,$$
$$y(t) = \frac{1}{2\pi i} \int_{\sigma - i\infty}^{\sigma + i\infty} Y(s)\, e^{st} ds. \tag{12}$$

The Z-transform can be seen as the transform corresponding to the discrete series given by (8) and (9) but where we have swapped time and frequency, and thus we have continuous periodic frequency and discrete time

$$Y(z) = \sum_{n=-\infty}^{\infty} y_n z^{-n}. \tag{13}$$

Here we have introduced the periodicity in the frequency domain by defining the complex variable $z = e^{s\Delta t}$ and as before for the Laplace transform we are dealing with damped version of time functions using $s = \sigma + i\omega$.

The reason for using the transforms is their attractive properties that they all have in common, like, for instance, the convolution property (that convolution in the time domain corresponds to multiplication in the transform domain)

$$h(t) * g(t) \longleftrightarrow H(s)\, G(s) \tag{14}$$

here expressed for the Laplace transform.

4. Random Vibration

Random vibration is often characterized by the power spectral density (PSD) function that for a time series $x(t)$ is defined as the Fourier transform of the correlation function $R_x(\tau)$

$$G_{xy}(\omega) = \frac{1}{2\pi} \int_{-\infty}^{\infty} R_{xy}(\tau)\, e^{-i\omega\tau} d\tau. \tag{15}$$

The PSD is popular mainly because modes are clearly indicated by spectral peaks and according to the Parseval theorem; the area below a PSD for any frequency band is equal to the variance of the corresponding time signal (band-pass filtered to the same frequency band), and therefore the PSD has a simple physical interpretation of energy distribution (therefore the name "power" spectral density).

One of the most important equations in random vibrations is the fundamental theorem that is relating the product of the PSD matrix of the input and the FRF matrix of the system to the PSD matrix of the response

$$\begin{aligned} \mathbf{G}_y(\omega) &= \widetilde{\mathbf{H}}^*(i\omega)\, \mathbf{G}_x(\omega)\, \widetilde{\mathbf{H}}^T(i\omega) \\ &= \widetilde{\mathbf{H}}(-i\omega)\, \mathbf{G}_x(\omega)\, \widetilde{\mathbf{H}}(i\omega). \end{aligned} \tag{16}$$

The last equation follows from the identity $\widetilde{\mathbf{H}}^*(i\omega) = \widetilde{\mathbf{H}}(-i\omega)$ and from the fact that the transfer function is symmetric.

Other central relations in random vibrations are the modal decompositions of the correlation function and PSD function matrices. The modal decomposition of the correlation function matrix is due to James et al. [6]. Expressing a general response by its modal decomposition and assuming white noise input where the correlations functions all degenerate to the Dirac delta functions it can be shown that the correlation function matrix for negative times $\mathbf{R}_{y-}(\tau)$ and for positive times $\mathbf{R}_{y+}(\tau)$ is given by

$$\begin{aligned} \mathbf{R}_{y-}(\tau) &= 2\pi \sum_{n=1}^{N} \left(\mathbf{b}_n \gamma_n^T e^{-\lambda_n \tau} + \mathbf{b}_n^* \gamma_n^H e^{-\lambda_n^* \tau} \right), \\ \mathbf{R}_{y+}(\tau) &= 2\pi \sum_{n=1}^{N} \left(\gamma_n \mathbf{b}_n^T e^{\lambda_n \tau} + \gamma_n^* \mathbf{b}_n^H e^{\lambda_n^* \tau} \right), \end{aligned} \tag{17}$$

where $\mathbf{b}_n$ is the mode shape for mode n and γ_n is a vector describing the modal participation of the considered mode. It is important to note that the negative time part of the correlation function matrix $\mathbf{R}_{y-}(\tau)$ is in fact a free decay because it is written as a linear combination of modal contributions (terms proportional to the mode shape times a complex exponential), whereas the positive time part $\mathbf{R}_{y+}(\tau)$ is in fact only a free decay if it is used in its transposed form so the terms $\gamma_n \mathbf{b}_n^T$ turn into the form $\mathbf{b}_n \gamma_n^T$ and the response becomes proportional to the mode shapes. This means that whenever correlation functions are used as free decays, using the positive part of the correlation function matrix, the matrix must be used in its transposed form. It should also be noted that if we had not followed the definition given by (5) but instead defined the correlation matrix as $\mathbf{R}(\tau) = \mathrm{E}[\mathbf{y}(t+\tau)\mathbf{y}^T(t)]$ which is common in some presentations of random vibration theory, then because of stationarity this is equal to $\mathrm{E}[\mathbf{y}(t)\mathbf{y}^T(t-\tau)]$. So this swaps the time of the solutions for the correlation function matrix in (17), and thus in this case the positive part of the correlation function matrix can indeed be used as free decays without taking the transpose.

The decomposition in the frequency domain can be found by taking the Fourier transform of (17) or by assuming a white noise input and using the fundamental theorem (16), Brincker et al. [7, 8],

$$\mathbf{G}_y(\omega) = \sum_{n=1}^{N} \left(\frac{\mathbf{b}_n \gamma_n^T}{-i\omega - \lambda_n} + \frac{\mathbf{b}_n^* \gamma_n^H}{-i\omega - \lambda_n^*} + \frac{\gamma_n \mathbf{b}_n^T}{i\omega - \lambda_n} + \frac{\gamma_n^* \mathbf{b}_n^H}{i\omega - \lambda_n^*} \right). \tag{18}$$

As it appears, in the frequency domain we do not have a modal decomposition that can be considered as a linear combination of free decays from the system, because some

terms are proportional to the mode shapes and some terms are proportional to the modal participation vectors. This is due to the fact that when taking the Fourier transform of (17) the terms from the negative and the positive time axes get mixed so that the first two terms in (18) are from the negative time axis and the last two ones are from the positive time axis.

Including only the positive part of the correlation function matrix in the Fourier transform defines the so-called half spectrum matrix that consists only of the two last terms of (18), and, as we can see, the half spectrum matrix is a spectral representation of free decays, but again only in its transpose form.

It is important to note that by using the transposed correlation function matrix as free decays in any identification technique—or using its counterpart in the frequency domain as the corresponding half spectrum—we see that we have as many free decays as we have sensors. Therefore OMA is so to speak born as a multiple input technique. From (16) we can see that a reduced rank of the input spectral density matrix $\mathbf{G}_x(\omega)$ will reduce the rank of the output spectral density accordingly, so normally it is a common assumption in OMA that the excitation of the structure is also multiple input, that is, using many independent excitation sources.

5. Testing

The most important concerning the testing part is to make a clear plan for the test, to secure that all measurements are carried out well, all data have the required quality, and the testing is well documented. For each data set that is to be used for OMA it can be argued, see Brincker and Ventura [2], that the total length of the time series should not be shorter than

$$T_{\text{tot}} > \frac{20}{2\varsigma f_{\min}} = \frac{10}{\varsigma f_{\min}} \tag{19}$$

and the sampling frequency should not be smaller than

$$f_s > 2.4 f_{\max}, \tag{20}$$

where $f_{\min}$ is the smallest natural frequency that we are looking for and $f_{\max}$ is the largest. It is important to secure a reasonable signal-to-noise ratio. This is done by making sure that the noise floor of the sensors (and the total measurement system) is well below the expected response level. Using two sensors to measure the same signal, the PSD of the measurement noise can be estimated as, Brincker and Larsen [9], follows:

$$G_n(f) = (1 - \gamma_{12}(f)) \sqrt{G_1(f) G_2(f)}, \tag{21}$$

where y_1 and y_2 are the measured signals from the two sensors, G_1 and G_2 are the corresponding auto spectral densities, and γ_{12} is the ordinary coherence between the two signals.

6. Signal Processing

As we have concluded in Section 2, we extract the information from the random signals by calculating correlation functions. However before we do that we need to go through some initial preprocessing steps as follows.

(i) Validate data quality (check for clipping, dropouts, etc.).

(ii) Calibrate signals to refer to physical units.

(iii) Detrending (remove mean or slowly varying trend).

After this initial step the user might want to evaluate and classify the operating condition during the test (for instance one or many cars on a bridge), judge the stationarity of the signals (make a time-frequency analysis), and finally evaluate the presence of harmonics (if possible remove them). Some optional preprocessing steps often used in OMA are

(i) adjustments of the sampling frequency (upsampling and downsampling, also denoted decimation),

(ii) filtering to reduce the frequency band (low-pass, band-pass, or high-pass filters),

(iii) integration/differentiation of signals.

The different kinds of filtering can be carried out using digital FIR and IIR filters often used in electrical engineering. However, in OMA we do not need real-time filtering because common practice is to store the raw data during testing and to perform needed filtering afterwards. Because of this, FFT filters might be considered due to small phase and amplitude errors.

When the preprocessing has been performed the correlation function matrix can be estimated by direct calculation according to (6) adjusting the integration to fit the total time length of the data $T = N\Delta t$ and to take the sampling into account which lead to the following simple and unbiased estimator

$$\begin{aligned} \widehat{\mathbf{R}}(k) &= \frac{1}{(N-k)\,\Delta t} \sum_{n=1}^{N-k} \mathbf{y}(n)\,\mathbf{y}^T(n+k)\,\Delta t \\ &= \frac{1}{N-k} \sum_{n=1}^{N-k} \mathbf{y}(n)\,\mathbf{y}^T(n+k). \end{aligned} \tag{22}$$

The tradition is to calculate the spectral density first by segmenting the data and using Welsh method, Brandt [10]

$$\widehat{\mathbf{G}}(\omega) = \frac{1}{S} \sum_{s=1}^{S} \widetilde{\mathbf{y}}_s(\omega)^* \widetilde{\mathbf{y}}_s^T(\omega), \tag{23}$$

where $\widetilde{\mathbf{y}}_s(\omega)$ is the Fourier transformed response of segment s. The correlation function can then be found by inverse Fourier transform. In OMA one should be careful with possible bias on spectral function and correlation function estimates that eventually might result in large errors in the damping values. It is worth making some comments about bias and the Welch formula for spectral estimation given by (23) because in many software implementations the Welch technique is the basis of both spectral function and correlation function estimation.

It follows directly from (5) and the convolution property of the Fourier series, corresponding to (14), that (23) is

only a spectral density estimate under the assumption that each data segment is periodic. Applying this technique without any windowing on the data segments corresponds to estimating the so-called circular correlation function in the time domain, and this clearly will introduce bias on the estimates. This bias is often denoted as "wrap-around" bias due to the wrong correlation so introduced between the ends of the data segment. In the frequency domain this leads to blunting of the spectral peaks and since this can be seen as energy "leaking" from the peaks to adjacent frequencies, the phenomenon is also denoted as leakage bias. The bias can be reduced giving the end points of the data segment a smaller weight by applying a windowing function on the data segments. This will reduce the leakage error but will not completely remove it.

An alternative is to increase all data segments to double size by zero padding. This corresponds to assuming that the signal is zero outside of the data segment, which is also wrong and introduces a bias, but it can be shown that this bias is well defined and can be removed in the time domain by dividing the circular correlation function estimate with a triangular window. This correlation function estimate has been known since the seventies and is often denoted as the "unbiased" FFT estimate. The properties of this estimate are very close to the properties of the direct estimate given by (22).

Another unbiased alternative to the direct estimation given by (22) or to zero padding is to use the random decrement technique that allows for unbiased estimating of both the correlation function and its derivative. It might also be of interest to apply the random decrement technique in cases where the user wants to apply only one single response signal to check if modal parameters depend on the excitation level of the structure.

In the later years it has become popular to skip the negative part of the correlation functions so that according to (17) when taking the Fourier transform to get the spectral density the two first terms in (18) disappear and we obtain a so-called half spectrum that is a spectral representation of time domain free decays; see the discussion about this issue in Section 4. This allows for application of curve fitters known from traditional modal analysis.

7. Time Domain Identification

In time domain identification (TD-ID) it is normal to use parametric models obtained by least square (LS) fitting. In practice this is done by formulating an overdetermined set of equations that is solved using the pseudo inverse of the equation matrix. We will shortly summarize the ID recipes when using some popular ID algorithms like the polyreference (PR) technique, Ibrahim time domain (ITD), the eigensystem realization algorithm (ERA), and the stochastic subspace identification (SSI) technique.

In PR the free decays are established (taking columns from the transposed correlation function matrix) by the correlation functions and the free decays are then arranged in a Hankel matrix, Vold et al. [11, 12],

$$\mathbf{H}_1 = \begin{bmatrix} \mathbf{y}(1) & \mathbf{y}(2) & \cdots & \mathbf{y}(np-na) \\ \mathbf{y}(2) & \mathbf{y}(3) & & \mathbf{y}(np-(na-1)) \\ \vdots & \vdots & \ddots & \vdots \\ \mathbf{y}(na) & \mathbf{y}(na+1) & & \mathbf{y}(np-1) \end{bmatrix} \tag{24}$$

and a "Hankel matrix" with only a single block row

$$\mathbf{H}_2 = \begin{bmatrix} \mathbf{y}(na+1) & \mathbf{y}(na+2) & \cdots & \mathbf{y}(np) \end{bmatrix}. \tag{25}$$

Here the operating responses $\mathbf{y}(n)$ are given in terms of the discrete time $t_n = n\Delta t$. The matrix containing the AR matrices of the free decays

$$\mathbf{A} = \begin{bmatrix} \mathbf{A}_{na}, \mathbf{A}_{na-1}, \ldots, \mathbf{A}_1 \end{bmatrix} \tag{26}$$

is then found by the LS solution

$$\widehat{\mathbf{A}} = \mathbf{H}_2 \mathbf{H}_1^{+}, \tag{27}$$

where $\mathbf{H}_1^{+}$ is the pseudo inverse of $\mathbf{H}_1$. The modal parameters can then be found by forming the companion matrix and performing an eigenvalue decomposition. Thus PR is an AR model-based technique. The order na of the AR model determines the number of modes in the model. If the number of measurement channels is nc, then the number of rows and column of the companion matrix is $na \times nc$ and the number of eigenvalues is then also $na \times nc$ corresponding to $na \times nc/2$ modes.

ARMA models where the response data can be modeled directly have never become popular in OMA due to the large convergence problems when several modes and channels of data are present.

In ITD (in a modern formulation) a Hankel matrix is formed with four block rows, Ibrahim [13–15],

$$\mathbf{H} = \begin{bmatrix} \mathbf{y}(1) & \mathbf{y}(2) & \cdots & \mathbf{y}(np-3) \\ \mathbf{y}(2) & \mathbf{y}(3) & \cdots & \mathbf{y}(np-2) \\ \mathbf{y}(3) & \mathbf{y}(4) & \cdots & \mathbf{y}(np-1) \\ \mathbf{y}(4) & \mathbf{y}(5) & \cdots & \mathbf{y}(np) \end{bmatrix} = \begin{bmatrix} \mathbf{H}_1 \\ \mathbf{H}_2 \end{bmatrix} \tag{28}$$

that is split in the middle defining $\mathbf{H}_1$ and $\mathbf{H}_2$. The system matrix is then simply found by the LS solution

$$\widehat{\mathbf{A}} = \mathbf{H}_2 \mathbf{H}_1^T \left(\mathbf{H}_1 \mathbf{H}_1^T \right)^{-1}, \tag{29}$$

where $\mathbf{H}_1^T (\mathbf{H}_1 \mathbf{H}_1^T)^{-1}$ can be considered as the pseudo inverse of $\mathbf{H}_1$. The modal parameters are found performing the eigenvalue decomposition of the system matrix $\widehat{\mathbf{A}}$. This matrix defines the model order. With the previous defined variables, we see that the number of eigenvalues is $2 \times nc$, and the model has nc number of modes. This means that the ITD model has a fixed model order corresponding to $na = 2$ for the AR model.

In ERA two Hankel matrices are formed, Juang and Pappa [16] and Pappa et al. [17, 18],

$$\mathbf{H}(0) = \begin{bmatrix} \mathbf{Y}(0) & \mathbf{Y}(1) & \cdots \\ \mathbf{Y}(1) & \mathbf{Y}(2) & \cdots \\ \vdots & \vdots & \\ \mathbf{Y}(s-1) & \mathbf{Y}(s) & \cdots \end{bmatrix};$$
$$\mathbf{H}(1) = \begin{bmatrix} \mathbf{Y}(1) & \mathbf{Y}(2) & \cdots \\ \mathbf{Y}(2) & \mathbf{Y}(3) & \cdots \\ \vdots & \vdots & \\ \mathbf{Y}(s) & \mathbf{Y}(s+1) & \cdots \end{bmatrix} \tag{30}$$

and an SVD is performed on the first matrix

$$\mathbf{H}(0) = \mathbf{U}\mathbf{S}\mathbf{V}^T. \tag{31}$$

We can then estimate the observability and controllability matrices as follows:

$$\widehat{\mathbf{\Gamma}} = \mathbf{U}\sqrt{\mathbf{S}}$$
$$\widehat{\mathbf{\Lambda}} = \sqrt{\mathbf{S}}\mathbf{V}^T \tag{32}$$

and finally the discrete time system matrix is estimated as follows:

$$\widehat{\mathbf{D}} = \widehat{\mathbf{\Gamma}}^{+}\mathbf{H}(1)\widehat{\mathbf{\Lambda}}^{+}. \tag{33}$$

The modal parameters are found performing the eigenvalue decomposition of $\widehat{\mathbf{D}}$, but in this case the eigenvectors must be brought back to physical coordinates by the observation matrix. It should be noted that using the number of block rows of the block Hankel matrices equal to $s = na$, the ERA has the same number of modes as an AR model.

The above mentioned techniques are all based on using the correlation functions as free decays. In SSI we use a different approach and we use the responses to construct the block Hankel matrix with $2s$ block rows, Overschee and de Moor [19], Peeters [20], and Peeters and de Roeck [21]

$$\mathbf{H} = \begin{bmatrix} \mathbf{y}(1) & \mathbf{y}(2) & \cdots & \mathbf{y}(np-2s+1) \\ \mathbf{y}(2) & \mathbf{y}(3) & \cdots & \mathbf{y}(np-2s+2) \\ \vdots & \vdots & & \vdots \\ \mathbf{y}(2s) & \mathbf{y}(2s+1) & & \mathbf{y}(np) \end{bmatrix} = \begin{bmatrix} \mathbf{H}_1 \\ \mathbf{H}_2 \end{bmatrix} \tag{34}$$

that is split in the middle defining $\mathbf{H}_1$ and $\mathbf{H}_2$. A projection matrix is then formed by the LS solution

$$\mathbf{O} = \mathbf{H}_2\mathbf{H}_1^T\left(\mathbf{H}_1\mathbf{H}_1^T\right)^{+}\mathbf{H}_1. \tag{35}$$

Parallel to the solution idea in the ERA we now take the SVD of the projection matrix

$$\mathbf{O} = \mathbf{U}\mathbf{S}\mathbf{V}^T \tag{36}$$

and we estimate the observability and Kalman state matrix

$$\widehat{\mathbf{\Gamma}} = \mathbf{U}_n\sqrt{\mathbf{S}_n},$$
$$\widehat{\mathbf{X}} = \sqrt{\mathbf{S}_n}\mathbf{V}_n^T. \tag{37}$$

The last matrix can be thought of as containing the initial conditions of the free decays in the projection matrix. Finally the discrete time system matrix and the observation matrix can be found by solving a least squares problem and the modal parameters are found performing the eigenvalue decomposition of the system matrix. The number of eigenvalues of the SSI model is equal to $s \times nc$, and the number of modes in the model is then equal to $s \times nc/2$.

8. Frequency Domain Identification

Frequency domain (FD) methods are mainly popular due to their ability to appeal to our intuition by the nice plots where we can inspect spectral peaks and have an idea about modal participation by evaluating the height of each peak and the damping by evaluating its width. But they tend to suffer from bias problems due to leakage because even though the spectral density can be estimated so that it is asymptotically unbiased (bias is zero when information approaches infinity), in practice we need to deal with a limited amount of information, and thus the leakage bias will tend to lead to overestimation of the damping in the frequency domain. Also the missing modal (free decay) decomposition of the spectral density as given by (18) is a problem because no commonly known identification techniques are designed to deal with this form, but this problem can be solved by working with the half spectral density functions. Similar to what we did for time domain we shortly summarize the ID recipes when using some popular ID algorithms in FD like classical FD (also called basic FD), frequency domain decomposition (FDD), and frequency domain polyreference (FD-PR, also denoted Polymax).

In classical FD we have the simplest possible recipe, Bendat and Piersol [22] and Felber [23]:

(i) natural frequency is estimated from the location of the peak in the considered PSD;

(ii) damping is estimated from the width of the peak;

(iii) mode shape is estimated from any column or row in the PSD matrix.

This works well only in case of well-separated modes. Also it is a problem that the user has to deal with the large number of PSD plots. In case of closely spaced modes an alternative is the FDD recipe where the PSD matrix is decomposed using SVD, Brincker et al. [7],

$$\mathbf{G}_y(f) = \mathbf{U}\mathbf{S}\mathbf{U}^H = \mathbf{U}\left[s_n^2\right]\mathbf{U}^H. \tag{38}$$

In this case the application is even simpler for the user because he is only inspecting a single PSD plot, that is, a plot of the singular values taken from the diagonal matrix $\mathbf{S}$. These singular values can be considered as a combination of estimates of the modal coordinate auto-PSDs and the noise in the operational data. Just like in classical FD, the natural frequency can be estimated from the location of a peak in the plot, but in the FDD the mode shape is estimated as the first singular vector (first column in $\mathbf{U}$) at the same frequency line. A better frequency estimate of the natural frequency

(and damping) can be found by modal filtering of the PSD matrix isolating each modal coordinate in FD, taking the modal coordinate PSD to time domain and finally finding modal parameters from the 1DOF free decay, Brincker et al. [24].

In FD-PR where the idea is to take the polyreference to the frequency domain, we have the problem that we cannot consider "just free decays" like in the TD, because in the FD the whole time axis is transformed into every point in the FD. Therefore in principle we have to deal with a full ARMA model in the FD; that is, the free decay in the TD resulting in a homogeneous equation of motion becomes a nonhomogenous equation of motion in the FD, Parloo [25] and Peters et al. [26, 27]. The simplest possible case is achieved assuming that the right hand side is a constant matrix (this is of course only a reasonable assumption for a narrow band estimator), Brincker and Ventura [2], and in this case the corresponding recipe is quite simple. Taking the response to be equal to the half spectrum transposed $\mathbf{Y}(f) = \mathbf{G}_y^T(f)$ we form the two Hankel matrices

$$\begin{aligned}\mathbf{H}_1 &= \left[\mathbf{Y}_{na}\left(f\left(k_1\right)\right), \mathbf{Y}_{na}\left(f\left(k_1+1\right)\right), \ldots, \mathbf{Y}_{na}\left(f\left(k_2\right)\right)\right] \\ \mathbf{H}_2 &= \left[\mathbf{I}, \mathbf{I}, \ldots, \mathbf{I}\right].\end{aligned} \tag{39}$$

The matrix containing the autoregressive matrices given by (25) is found by the LS solution

$$\widehat{\mathbf{A}} = \mathbf{H}_2\mathbf{H}_1^{+}. \tag{40}$$

And finally the modal parameters are then found by forming the companion matrix based on the autoregressive coefficient matrices and performing an eigenvalue decomposition.

9. Example: The Heritage Court Tower Data

We will illustrate the OMA techniques on the well-known case of operational data from the Heritage Court Tower building. The case is described in detail in Dyck and Ventura, [28].

The operational data was obtained using four datasets measuring only horizontal acceleration; two sensors close to the top of the building were used as references and the remaining sensors were then roved down the building. The first dataset applies 6 sensors placed close to the top of the building, the second dataset applies 8 sensors, the six roving sensors now moved downwards, the third dataset is similar but the roving sensors again moved downwards the building, and finally the fourth dataset includes 8 sensors where the six roving sensors are now close to the bottom of the building. All datasets have a total measurement time of 328 s and a sampling frequency of 40 Hz. Three sensors were used on each measured floor.

The simplest way to graphically illustrate the operational data is to make an FDD plot. The results for the first dataset are shown in Figure 2 showing the lowest quarter of the frequency band. The figure is also showing the results of the FDD performing a modal filtering taking mode shapes as the first singular vector of (38) in the points indicated in Figure 2.

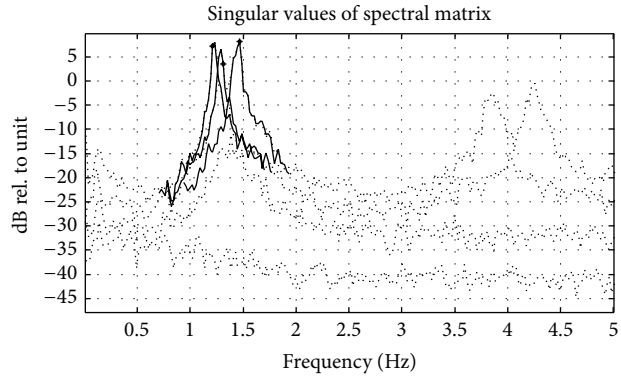

Figure 2: Results of using FDD to identify the first three modes on the first dataset of the HCT case. The singular values of the SD matrix are shown in dotted line. In the plot the frequency lines where the mode shape vectors are estimated are indicated by an asterisk and the corresponding modal decomposition is shown in solid line.

As it appears the first three modes are in the frequency band from 1.3 to 1.5 Hz.

The expected excitation of the building is a combination of wind, traffic, and excitation from people moving around in the building, so it seems reasonable to assume that the assumption of multiple input loading is fulfilled. The multiple input assumption is also supported by the fact that the SVD plot in Figure 2 shows a relatively good modal separation (sufficient rank of the spectral density matrix).

Since the lowest natural frequency is around 1.3 Hz, and if we assume the damping ratio to be around 1%, then the total length of each record according to (19) should be approximately 770 s. Thus the actual measurement time of 328 s is lower than the half of what is recommended by (19), and since the three first modes of this example are relatively closely spaced, it should be expected that we have some difficulties identifying the three first modes of this structure consistently. It, especially, should be expected that we have difficulties identifying the modes for the datasets where the roving sensors get close to the base of the building where the response is low and we have a decreasing signal-to-noise ratio in the measurements.

The results of the identification of the first three modes of dataset 1 are shown in Table 1 and the similar results for dataset 4 are shown in Table 2.

For all the time domain identifications the modal participation vectors γ_n in (17) are used to find the relative modal participation factor π_n as described in Brincker and Ventura [2]. Similarly in the frequency domain the modal participation vectors γ_n in (18) are obtained using the half spectral density matrix including only the two last terms in (18).

In the time domain the first three modes were isolated using a band-pass filter with a center frequency of 1.35 Hz, a flat characteristic in a band around the center frequency with a band width of 0.4 Hz, and a roll-off band on each side with a width of 0.4 Hz.

For the AR, ITD, and ERA techniques the correlation function matrices were estimated using the direct technique

Table 1: Modal identification on dataset 1 of the Heritage Court Tower case.

Modal quantity	Modal identification method					
	AR	ITD	ERA	SSI	FDD	FD-PR
Mode 1, f_n, (Hz)	**1.227**	**1.227**	**1.227**	**1.227**	**1.225**	**1.228**
Mode 1, ς_n, (%)	0.96	0.97	0.96	0.53	1.29	1.32
Mode 1, π_n, (%)	30.1	30.2	30.1	32.6	27.9	29.7
Mode 2, f_n, (Hz)	**1.285**	**1.285**	**1.285**	**1.284**	**1.287**	**1.290**
Mode 2, ς_n, (%)	1.19	1.20	1.19	0.58	1.41	1.46
Mode 2, π_n, (%)	19.2	19.3	19.3	18.5	17.4	19.0
Mode 3, f_n, (Hz)	**1.452**	**1.451**	**1.452**	**1.450**	**1.450**	**1.454**
Mode 3, ς_n, (%)	1.11	1.11	1.11	0.63	1.59	1.36
Mode 3, π_n, (%)	50.6	50.5	50.6	48.9	55.8	51.3

Table 2: Modal identification on dataset 4 of the Heritage Court Tower case.

Modal quantity	Modal identification method					
	AR	ITD	ERA	SSI	FDD	FD-PR
Mode 1, f_n, (Hz)	**1.246**	**1.246**	**1.246**	**1.215**	**1.235**	**1.213**
Mode 1, ς_n, (%)	1.12	1.05	1.12	1.92	2.72	2.52
Mode 1, π_n, (%)	23.4	26.0	23.4	16.3	35.5	31.8
Mode 2, f_n, (Hz)	**1.299**	**1.300**	**1.299**	**1.279**	**1.293**	**1.301**
Mode 2, ς_n, (%)	1.57	1.40	1.57	7.20	2.45	2.62
Mode 2, π_n, (%)	3.4	3.6	3.4	10.0	0.7	0.2
Mode 3, f_n, (Hz)	**1.441**	**1.442**	**1.441**	**1.443**	**1.450**	**1.446**
Mode 3, ς_n, (%)	0.33	0.31	0.33	0.89	1.27	1.08
Mode 3, π_n, (%)	58.6	34.1	58.6	69.0	63.8	63.6

according to (22); the full correlation function matrix was transposed as described in Section 4 and all columns (all free decays) in the transposed correlation function matrix were then used for the identification. For the first dataset 500 discrete time lags were used in the correlation function matrix; however, for the last dataset where the modes are somewhat more difficult to identify, 950 time lags were used. For the AR, ITD, and ERA techniques a low model (corresponding to $na = 2$) order was used including 6 modes for dataset 1 and 8 modes for dataset 4.

The PC algorithm using the stochastic algorithm 1 from Overschee and de Moor [19] was used for the SSI identification. In SSI the need for an oversized model is larger than for the previously mentioned techniques and therefore in this example a large model with $s = 80$ block rows was used for the estimation. This corresponds to a model with 240 modes for the first dataset and to a model with 320 modes for dataset 4. The SVD matrices in (37) were reduced to the first 6 singular values for the first dataset (corresponding to a reduced model with only three modes) and to 18 singular values for the last dataset (corresponding to a reduced model with nine modes). It was needed to use nine modes in the last dataset in order to obtain a model including the three modes with a reasonable participation factor.

In the frequency domain the modes were identified using the FDD and the FD-PR technique. In both cases the spectral density matrix was estimated taking the discrete Fourier transform of the directly estimated correlation function matrix.

As it is indicated earlier, it is good idea to start any OMA with the simple FDD analysis, just looking at the plot of the singular values; see Figure 2. As it appears three singular values are peaking inside the interval 1-2 Hz, while the fourth singular value is flat. Therefore the fourth singular value defines the noise floor; the first three singular values describe the physics of the system and it can be concluded that three modes are present in the considered frequency band. As mentioned earlier, the singular vectors at the three indicated points close to the three spectral peaks were chosen as mode shape estimates, and the modal coordinates were then found solving the equation $\mathbf{y}(t) = \mathbf{A}\mathbf{q}(t)$, where the matrix $\mathbf{A}$ contains the estimated mode shapes and $\mathbf{q}(t)$ are the modal coordinates. We can find the solution to this heavily overdetermined problem as the LS solution $\widehat{\mathbf{q}}(t) = \mathbf{A}^{+}\mathbf{y}(t)$. This can also be done in the frequency domain, and the modal coordinate estimates are indicated by the solid lines in Figure 2. The modal coordinates estimates in the frequency domain can then be taken back to time domain by inverse FFT and the frequency and damping can be found from the modal coordinate correlation function by simple means (in this case using simple ITD for one single channel of data).

The FD-PR identification was carried out based on the half spectrum matrix estimated with 1025 frequency lines in the whole frequency band up to 20 Hz. The autoregressive

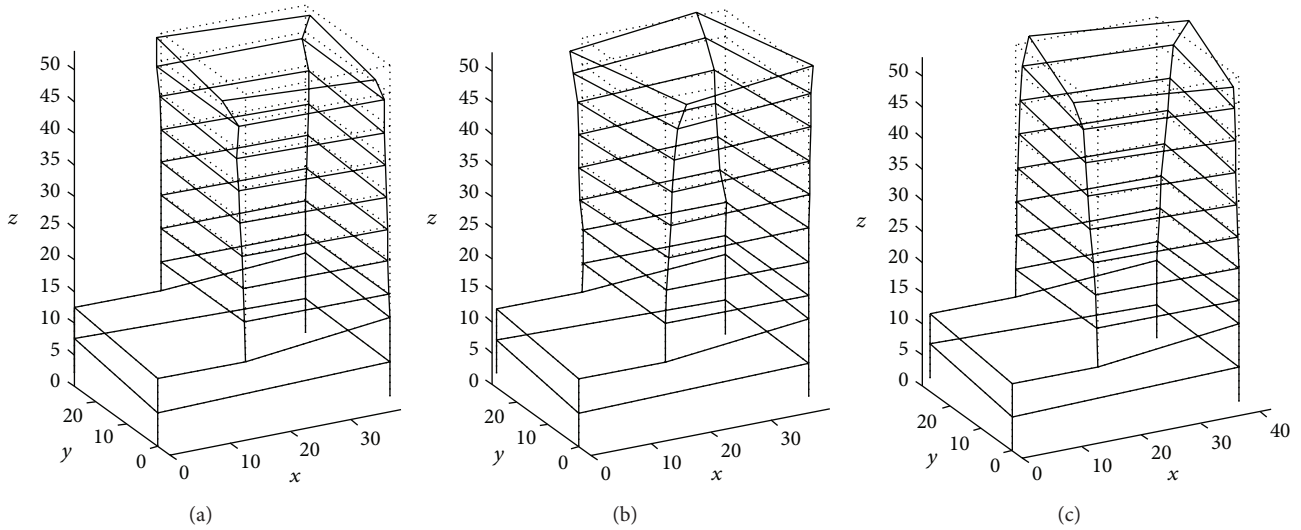

Figure 3: Mode shapes of the HCT building found by AR identification and merging the mode shapes from the 4 data using the reference DOFs. The units of the coordinate system are meters.

matrices were found using (40) over the frequency band centered at 1.35 Hz and with a band width of 0.6 Hz. The first dataset was identified using a model order of $na = 2$ (corresponding to 6 modes for the first dataset); however, for the last dataset in order to identify all three modes with a reasonable modal participation, a model order of $na = 8$ was used (corresponding to 32 modes).

Using that each floor in the building is moving like a ridged body in the horizontal plane the movements of all points of a given floor can be estimated using only the measured three horizontal components and the different parts of the mode shape can be merged using the common reference DOFs. The mode shapes of the three first modes obtained by the different techniques are quite similar. The mode shapes of the HCT building from the AR identification are shown in Figure 3.

The differences in the identification can be discussed on the basis of the results in Tables 1 and 2. For dataset 1 it is clear that all techniques identify nearly the same natural frequencies for all three modes. Concerning the damping we can see a somewhat higher estimation uncertainty (as expected), and we can see that frequency domain techniques have a tendency to provide higher damping values than the time domain techniques. The higher damping is most probably due to leakage errors introduced by the discrete Fourier transform of the correlation functions to frequency domain. All techniques also agree that the relative modal participation is around 30% for mode 1, it is around 19% for mode 2, and it is around 50% for mode 3. The high modal participation for all three modes secures the relatively consistent identification results.

Considering the results of Table 2 we clearly see that this case is somewhat more difficult. We have already mentioned that in order to identify all three modes we needed to adjust the identification; for instance, the time domain techniques needed more time lags in the correlation functions, and the SSI needed to include more singular values to have more modes in the model. Even doing these adjustments in order to improve identification accuracy, we clearly now see some deviations of the natural frequencies. For the first mode we see that SSI and FD-PR provide the value $f_1 = 1.215$ Hz, whereas the AR, ITD, and ERA agree on $f_1 = 1.246$ Hz, but we know from the results of dataset 1 that the right natural frequency is $f_1 = 1.227$. These deviations are quite large to what would normally be expected. Modes 2 and 3 show smaller, but similar, deviations that are also larger than normally expected. Larger deviations on the damping value are observed and, for instance, the SSI provides an unrealistic estimate of more than 7% damping. These difficulties are most probably due to a small amount of data combined with a smaller signal-to-noise ratio caused by having most of the sensors close to the ground where the response is small. Another important reason to the difficulties identifying dataset 4 is that we see from Table 2 that the modal participation of mode 2 is relatively weak.

This example stresses the need for good testing practice making sure that an appropriate amount of data is taken and that a good signal-to-noise ratio is present in all datasets. The analysis of this example was carried out using the MATLAB toolbox that comes with Brincker and Ventura [2].

10. Mode Shape Scaling and Expansion

The most commonly used method in mode shape scaling is to make a mass and/or stiffness perturbation of the test specimen and to use the corresponding change of natural frequencies and mode shape to estimate the scaling factor α that is defined as $\alpha = 1/\sqrt{m}$, where m is the modal

mass. Many formulas exist, but the most general one is the following, López-Aenlle et al. [29]:

$$\alpha_j^2 = \frac{\left(\omega_{0j}^2 - \omega_{Ii}^2\right) t_{ji}}{\mathbf{a}_{0j}^T \left(\omega_{Ii}^2 \Delta\mathbf{M} + \Delta\mathbf{K}\right) \mathbf{a}_{Ii}}, \tag{41}$$

where the natural frequency ω_{0j} of mode j in its unperturbed state and the corresponding mode shape $\mathbf{a}_{0j}$ and the natural frequency ω_{Ii} of mode i in its perturbed state and the corresponding mode shape $\mathbf{a}_{Ii}$ are used to find an estimate of the scaling factor so that the corresponding mass scaled mode shape $\boldsymbol{\alpha}_j = \alpha_j \mathbf{a}_j$ can be defined. The terms t_{ji} are found from the LS solution

$$\mathbf{T} = \left[t_{ji}\right] = \mathbf{A}_0^+ \mathbf{A}_I, \tag{42}$$

where $\mathbf{A}_0$ contains the unperturbed mode shapes and $\mathbf{A}_I$ contains the perturbed mode shapes. In principle this equation is exact and the only approximation is due to the estimation of the projection terms in (42). The first formulation of this kind of equation is due to Bernal [30]. However, because of the small changes of mass and stiffness that are often used due to practical reasons and because of the problems of detecting these small changes due to measurement and ID noise, the uncertainty on the scaling factor is often large and therefore it might in many cases be more accurate to expand the mode shapes and perform the scaling using the expanded mode shapes on the FE mass matrix, López-Aenlle and Brincker [31].

Mode shape expansion is based on the idea of fitting a measured mode shape $\mathbf{a}$ with a limited number of mode shapes (subspace) from an FE model. Given a fixed subspace from the FE model with mode shapes arranged in mode shape matrix

$$\mathbf{B} = \begin{bmatrix} \mathbf{B}_a \\ \mathbf{B}_d \end{bmatrix}, \tag{43}$$

where $\mathbf{B}_a$ contains the DOFs corresponding to the experiment (active DOF's) and $\mathbf{B}_d$ contains the remaining DOFs in the FE model (deleted DOFs), we then have the classical fitting problem

$$\mathbf{a} \cong \mathbf{B}_a \mathbf{p} \tag{44}$$

that can only be approximately fulfilled since we are dealing with overdetermined problem. We find the classical LS estimate for the parameter vector

$$\hat{\mathbf{p}} = \mathbf{B}_a^+ \mathbf{a} \tag{45}$$

and we have now a smoothed version of the experimental mode shape

$$\hat{\mathbf{a}} = \mathbf{B}_a \hat{\mathbf{p}}. \tag{46}$$

The smoothed version can be expanded to all DOFs in the FE model just by including all DOFs in the FE mode shapes

$$\hat{\mathbf{a}} = \mathbf{B} \hat{\mathbf{p}}. \tag{47}$$

The expanded version can be used for scaling as mentioned above and in damage detection and updating. If the expanded mode shapes are used for scaling together with the mass matrix of the finite element model as mentioned above, this provides a simple procedure for the scaling of OMA mode shapes. Assuming that the mode shapes from the finite element model are mass scaled, the modal mass is obtained as the inner product of the expanded experimental mode shape over the mass matrix of the finite element model

$$m = \hat{\mathbf{a}}^T \mathbf{M} \hat{\mathbf{a}} = \hat{\mathbf{p}}^T \mathbf{B}^T \mathbf{M} \mathbf{B} \hat{\mathbf{p}} = \hat{\mathbf{p}}^T \hat{\mathbf{p}}. \tag{48}$$

The result follows from (47), the well-known orthogonality principle, and the assumption of mass scaled FE modes so that the inner product $\mathbf{B}^T \mathbf{M} \mathbf{B}$ is equal to the identify matrix, Aenlle and Brincker, [32].

Using the above mentioned expansion assuming a fixed subspace is equivalent to expansion using SEREP, O'Callahan et al. [33]. One of the problems of the expansion as outlined above is to know which modes should be included in the subspace matrix $\mathbf{B}$. It is obvious that the subspace should be chosen minimal in order to obtain the best solution, (45), and thus that the optimal choice of subspace must change from mode to mode. This problem can be solved by the local correspondence (LC) principle, Brincker et al. [34], that states that any perturbed mode shape can be written as a linear combination of modes of the unperturbed system including only a few mode shapes around the corresponding unperturbed mode.

11. Conclusions

Some of the main elements of operational modal analysis (OMA) have been considered. It is argued that it is not necessary to assume a white noise input in order to use OMA; however, it is a central assumption in OMA that only second order information is considered (correlation and spectral density functions) and that the excitation is multiple input. The theoretical solutions for the correlation function matrix and the spectral density matrix are discussed and it is pointed out that care should be taken in order to use the second order information in a form that in fact represents free decays of the system. The identification recipes for some commonly used time domain and frequency domain techniques are presented and their ability to identify the first three closely spaced modes of the Heritage Court Tower building is illustrated. Finally the important issues of mode shape scaling and mode shape expansion are presented.

Conflict of Interests

The author declares that there is no conflict of interests regarding the publication of this paper.

References

[1] J. C. Asmussen, S. R. Ibrahim, and R. Brincker, "Modal parameter identification from responses of general unknown random inputs," in *Proceedings of the 14th International Modal Analysis Conference (IMAC '96)*, 1996.

[2] R. Brincker and C. E. Ventura, *Introduction to Operational Modal Analysis*, Wiley, 2014.

[3] https://www.sem.org/Proceedings/ConferencePapers-Home.cfm.

[4] http://www.iomac.dk/iomac-proceedings.

[5] D. E. Newland, *An Introduction to Random Vibrations, Spectral & Wavelet Analysis*, Longman, 3rd edition, 1997.

[6] G. H. James, T. G. Carne, and J. P. Lauffer, "The natural excitation technique (NExT) for modal parameter extraction from operating structures," *The International Journal of Analytical and Experimental Modal Analysis*, vol. 10, no. 4, pp. 260–277, 1995.

[7] R. Brincker, L. Zhang, and P. Andersen, "Modal identification of output-only systems using frequency domain decomposition," *Smart Materials and Structures*, vol. 10, no. 3, pp. 441–445, 2000.

[8] R. Brincker and L. Zhang, "Frequency domain decomposition revisited," in *Proceedings of the International Operational Modal Analysis Conference (IOMAC '09)*, pp. 615–626, 2009.

[9] R. Brincker and J. A. Larsen, "Obtaining and estimating low noise floors in vibration sensors," in *Proceedings of the 25th Conference and Exposition on Structural Dynamics (IMAC '07)*, Bethel, Conn, USA, February 2007.

[10] A. Brandt, *Noise and Vibration Analysis. Signal Analysis and Experimental Procedures*, Wiley, 2011.

[11] H. Vold, J. Kundrat, G. T. Rocklin, and R. Russell, "A multi-input modal estimation algorithm for mini-computers," SAE Paper 820194, SAE, 1982.

[12] H. Vold and G. T. Rocklin, "The numerical implementation of a multi-input modal estimation method for mini-computers," in *Proceedings of the International Modal Analysis Conference (IMAC '82)*, pp. 542–548, 1982.

[13] S. R. Ibrahim and E. C. Mikulcik, "A method for direct identification of vibration parameters from the free response," *The Shock and Vibration Bulletin*, vol. 47, pp. 183–196, 1977.

[14] S. R. Ibrahim, "Random decrement technique for modal identification of structures," *Journal of Spacecraft and Rockets*, vol. 14, no. 11, pp. 696–700, 1977.

[15] S. R. Ibrahim, "Modal confidence factor in vibration testing," *Journal of Spacecraft and Rockets*, vol. 15, no. 5, pp. 313–316, 1978.

[16] J. Juang and R. S. Pappa, "An eigen system realization algorithm for modal parameter identification and modal reduction," *Journal of Guidance, Control, and Dynamics*, vol. 8, no. 5, pp. 620–627, 1985.

[17] R. S. Pappa, K. B. Elliott, and A. Schenk, "Consistent-mode indicator for the eigensystem realization algorithm," *Journal of Guidance, Control, and Dynamics*, vol. 16, no. 5, pp. 852–858, 1993.

[18] R. S. Pappa, "Eigensystem realization algorithm, user's guide for VAX/VMS computers," NASA Technical Memorandum 109066, NASA, 1994.

[19] P. Overschee and B. de Moor, *Subspace Identication for Linear Systems, Theory, Implementation, Application*, Kluwer Academic Publishers, 1996.

[20] B. Peeters, *System identification and damage detection in civil engineering [Ph.D. thesis]*, Faculteit Toegepaste Wetenschapen, Katholieke Universiteir Leuven, 2000.

[21] B. Peeters and G. de Roeck, "Reference-based stochastic subspace identification for output-only modal analysis," *Mechanical Systems and Signal Processing*, vol. 13, no. 6, pp. 855–878, 1999.

[22] J. S. Bendat and A. G. Piersol, *Engineering Applications of Correlation and Spectral Analysis*, John Wiley & Sons, 2nd edition, 1993.

[23] A. J. Felber, *Development of a hybrid bridge evaluation system [Ph.D. thesis]*, University of British Colombia, 1993.

[24] R. Brincker, C. E. Ventura, and P. Andersen, "Damping estimation by frequency domain decomposition," in *Proceedings of the 19th International Modal Analysis Conference (IMAC '01)*, pp. 698–703, Kissimmee, Fla, USA, February 2001.

[25] E. Parloo, *Application of frequency-domain system identification techniques in the field of operational modal analysis [Ph.D. thesis]*, Department of Mechanical Engineering, Vrije Universiteit Brussel, Brussel, Belgium, 2003.

[26] B. Peeters, H. van der Auweraer, P. Guillaume, and J. Leuridan, "The PolyMAX frequency-domain method: a new standard for modal parameter estimation?" *Shock and Vibration*, vol. 11, no. 3-4, pp. 395–409, 2004.

[27] B. Peeters, H. van der Auweraer, F. Vanhollebeke, and P. Guillaume, "Operational modal analysis for estimating the dynamic properties of a stadium structure during a football game," *Shock and Vibration*, vol. 14, no. 4, pp. 283–303, 2007.

[28] C. Dyck and C. E. Ventura, *Ambient Vibration Measurements of the Heritage Court Tower*, EQ LAB, University of British Columbia, Earthquake Engineering Reserach, 1998.

[29] M. López-Aenlle, R. Brincker, F. Pelayo, and A. F. Canteli, "On exact and approximated formulations for scaling-mode shapes in operational modal analysis by mass and stiffness change," *Journal of Sound and Vibration*, vol. 331, no. 3, pp. 622–637, 2012.

[30] D. Bernal, "Modal scaling from known mass perturbations," *Journal of Engineering Mechanics*, vol. 130, no. 9, pp. 1083–1088, 2004.

[31] M. López-Aenlle and R. Brincker, "Scaling mode shapes in operational modal analysis using the finite element model mass matrix," *International Journal of Mechanical Sciences*, vol. 76, pp. 86–101, 2013.

[32] M. L. Aenlle and R. Brincker, "Modal scaling in OMA using the mass matrix of a finite element model," in *Proceedings of the 32nd International Modal Analysis Conference (IMAC '14)*, Orlando, Fla, USA, February 2014.

[33] J. O'Callahan, P. Avitabile, and R. Riemer, "System equivalent reduction expansion process," in *Proceedings of the 7th International Modal Analysis Conference (IMAC '89)*, SEM, Las Vegas, Nev, USA, February 1989.

[34] R. Brincker, A. Skafte, M. López-Aenlle, A. Sestieri, W. D'Ambrogio, and A. Canteli, "A local correspondence principle for mode shapes in structural dynamics," *Mechanical Systems and Signal Processing*, vol. 45, no. 1–3, pp. 91–104, 2014.

Hindawi Publishing Corporation
Shock and Vibration
Volume 2014, Article ID 303567, 9 pages
http://dx.doi.org/10.1155/2014/303567

Research Article

Concept Modelling of Vehicle Joints and Beam-Like Structures through Dynamic FE-Based Methods

G. De Gaetano,[1,2] D. Mundo,[1] F. I. Cosco,[2] C. Maletta,[1] and S. Donders[3]

[1] *Department of Mechanical, Energy and Management Engineering, University of Calabria, Ponte Pietro Bucci, 46/C, 87036 Rende, Italy*
[2] *G&G Design and Engineering, Via Gabriele Barrio, 87100 Cosenza, Italy*
[3] *Simulation Division-LMS International, Interleuvenlaan 68, 3001 Leuven, Belgium*

Correspondence should be addressed to D. Mundo; domenico.mundo@unical.it

Received 28 June 2013; Accepted 7 March 2014; Published 6 July 2014

Academic Editor: Miguel M. Neves

Copyright © 2014 G. De Gaetano et al. This is an open access article distributed under the Creative Commons Attribution License, which permits unrestricted use, distribution, and reproduction in any medium, provided the original work is properly cited.

This paper presents dynamic methodologies able to obtain concept models of automotive beams and joints, which compare favourably with the existing literature methods, in terms of accuracy, easiness of implementation, and computational loads. For the concept beams, the proposed method is based on a dynamic finite element (FE) approach, which estimates the stiffness characteristics of equivalent 1D beam elements using the natural frequencies, computed by a modal analysis of the detailed 3D FE model of the structure. Concept beams are then connected to each other by a concept joint, which is obtained through a dynamic reduction technique that makes use of its vibration normal modes. The joint reduction is improved through the application of a new interface beam-to-joint element, able to interpolate accurately the nodal displacements of the outer contour of the section, to obtain displacements and rotations of the central connection node. The proposed approach is validated through an application case that is typical in vehicle body engineering: the analysis of a structure formed by three spot-welded thin-walled beams, connected by a joint.

1. Introduction

The virtual models obtained by computer-aided engineering (CAE) tools play a fundamental role in the development process of complex products, because they enable engineers to predict various performance attributes, avoiding the use of expensive physical prototypes and thus reducing the time of design process. Particularly in the field of automotive industry, the performances related to noise, vibration, and harshness (NVH) are hard to improve in the last steps of the development process without raising conflicts with others vehicle requirements. For this reason, many researchers have developed predictive concept modelling methodologies, which can be used to predict and improve the vehicle design from the concept phase onwards.

This paper focuses its attention on concept modelling techniques concerning the reduction in an equivalent simplified model of the detailed vehicle body in white (BIW) model, allowing to drastically reduce the required computational resources and the time needed for its modifications.

The reduction of detailed 3D FE models can rely on different commercial FE solvers available today (such as Nastran, Abaqus, and Ansys), which provide libraries of simplified elements (1D beam elements, superelements, etc.). In the literature, there are several approaches able to simplify the principal structural elements of a BIW, such as beam-like structures and joints.

Regarding element models having beam-like global behaviour, main methodologies to reduce a 3D element into a 1D element with equivalent characteristics can be grouped in three categories: *geometric*, *static FE-based,* and *dynamic FE-based* approaches. The geometric concept modelling methods rely on a geometric analysis of the beam cross-sections [1–3]. The mass and stiffness properties of the equivalent 1D beam element are computed by analysing the mass distribution along the section and considering whether the section has a single or a multiconnected closed shape.

Instead, in the static FE-based methods [4, 5], a set of static load cases is generated by applying bending, torsion,

and axial loads at the end sections of each beam segment. For some beam cross-sections, central nodes are created and connected to the other nodes at the same cross-sections, by means of multipoint constraint (MPC) elements, which are of rigid type for the two end sections and of interpolation type for the intermediate sections. In this way, external and reaction loads are applied directly to the central node of the end sections, and the rigid elements transfer them to the rest of the structure, while the interpolating elements allow estimating the linear elastic deformation of the beam central line. Finally, the stiffness properties of the equivalent 1D beam are estimated by applying the linear elastic load-deformation relationships of the beam structure, starting from the static deformations predicted by analysing the detailed 3D model. A scheme illustrating the static FE-based method is shown in Figure 1.

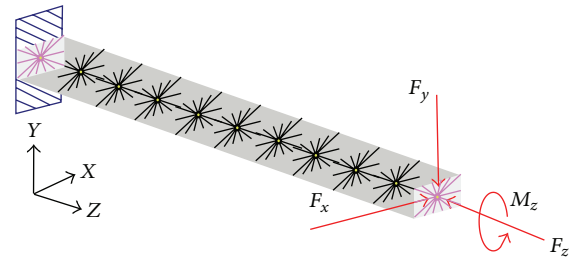

Figure 1: Application of static FE-based method: loads, constraint, and connection elements applied to the detailed 3D beam model.

This work discusses an original method pertaining to the last category, the dynamic FE-based approach [6], through which the stiffness characteristics (e.g., quadratic moments of inertia, torsional modulus, etc.) of equivalent 1D beam elements are estimated using the natural frequencies computed by a modal analysis of the detailed 3D FE model of the structure. Its main advantages came from the fact that any possible discontinuities and variations that may occur along a beam and that affect its stiffness are taken into account during the computation, so that the proposed method results in an accuracy benefit as compared to prior art methods.

Automotive joints are the second main part of a BIW to be conceptualized. Currently, the most usual techniques rely on the reduction of a joint in a *superelement* (SE), which is defined by reduced stiffness and mass matrices. In order to guarantee structural continuity between beams and joints in the whole concept structure, an interface between the concept 1D beam model and the detailed 3D joint model is created before applying joint reduction. The latter is then achieved by condensing the joint stiffness and mass properties to the nodes on the beam side of each beam/joint interface, as it will be explained in Section 2. Therefore, in the reduction process, the central nodes of the beam/joint interfaces represent the master degrees of freedom (DOFs) to be preserved, while the DOFs of the nodes belonging to the 3D FE structure of the joint are removed (slave DOFs). Figure 2 shows a typical BIW structure of a commercial vehicle and a typical joint and beam-like member used in automotive bodies. In the same figure, a graph showing the overall scheme of the technique proposed here for 1D modelling of beams and SE representation of joints is also illustrated. The reduction techniques on SE can be categorized into two types: static or dynamic. *Guyan* reduction [7] is the most common method for static condensation. It returns an exact reduced stiffness matrix and an approximated mass matrix, exploiting some static considerations between the master nodes of the joint. On the contrary, all the dynamic methods make use of the vibration normal modes of the structure, but they differ from each other for the applied boundary conditions and for the selection of enrichment vectors in addition to the normal modes. Two well-established examples are the *Craig-Bampton fixed interface* [8] and *MacNeal's* [9] approach. In the former approach, which is used in the research presented

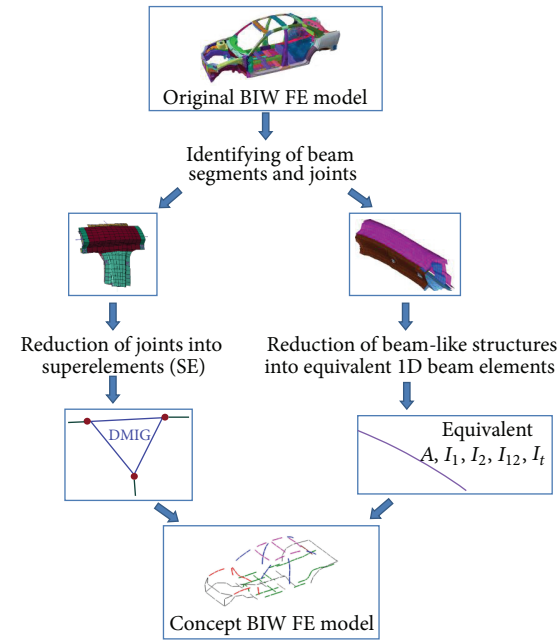

Figure 2: Workflow for the creation of beam and joint FE concept models.

here, the normal modes are computed with the structure clamped at the connection interfaces, while the enrichment vectors are determined as constraint modes. The latter method uses the normal modes of the component in free-free conditions, while the enrichment vectors consist of residual flexibility modes.

These dynamic reduction methods are reliable and easy to implement. However, in the specific application of thin-walled automotive joints, the accuracy of these methods is strongly dependent on the type of connection models that are used at each beam-joint interface. Rigid connection elements, such as Nastran RBE2 elements [10], can make the entire structure excessively stiff, while general-purpose interpolation elements, such as Nastran RBE3 elements [10], can lead to coarse inaccuracies especially with regard to the torsional stiffness.

For this reason, a new multipoint constraint (MPC) connection element is proposed and validated here, in order to overcome the limitations of standard connection elements and achieve more accurate concept models of automotive joints. The proposed MPC allows correlating displacements and rotations of the dependent node (i.e., the central node

of the joint end section) with the displacements of the peripheral section nodes. These relationships are based on static considerations and return a transformation matrix, whose implementation process is explained in detail. To verify the improved accuracy of the proposed model, a comparative analysis has been carried out between a structure where concept joints are reduced by using rigid spiders as connection elements and another where the new MPC connection elements are employed.

The paper is organized as follows. Section 2 describes the mathematical definition of the new connection element. Section 3 describes the detailed 3D and the concept 1D FE models of the spot welded structure that are used for validation purposes. The dynamic validation results are reported in Section 4, demonstrating the improvements that can be obtained using the proposed connection elements. Section 5 concludes the paper, by reviewing the results achieved and providing an outlook on the foreseen next steps.

2. Definition of New MPC Connection Element

In this paper, a new MPC connection element is defined, which enables to create an interface between the concept 1D beam model and the detailed 3D joint model, as shown in Figure 3. For such purpose, the kinematic relationships between the displacements and rotations of the beam node (dependent node of the connection element) and the displacements of the nodes of the detailed 3D FE model of the joint at the interface section (independent nodes of the connection element) are derived in the form of a transformation matrix $[R]$, by using a static approach based on equilibrium conditions [11]. The basic idea is to obtain a second transformation matrix $[S]$ that defines the relationship between the total forces at the central node of the beam/joint interface and the nodal loads over the section, considering theoretical stress fields resulting from the Saint-Venant assumptions with respect to axial, bending, shear, and torsion load-cases for a beam-like structure [12]. In linear elastic field, this loads correlation can be inverted, returning the searched kinematic relationship.

The transformation matrix $[S]$ is obtained by calculating the product of two submatrices:

(i) the *stress recovery matrix* $[S_1]$, which correlates the sectional stresses applied to the nodes of shell elements and resultant loads applied on the central node of equivalent 1D beam element, by using load-stress relationships of Saint-Venant for beam-like structures;

(ii) the *form nodal load matrix* $[S_2]$, which links all the nodal forces and the nodal stresses of the section, by using the shape functions of linear finite elements.

In the next subsections each of these matrices is described and explained in detail.

2.1. The Stress Recovery Matrix $[S_1]$. Starting from the sectional load resultant at the interface, the stress recovery matrix $[S_1]$ is defined by the assumptions of linear elastic, homogeneous, and isotropic material. First, it is assumed that the thickness is sufficiently small with respect to the cross-section dimensions, which allows using the stress distribution properties of thin-walled beams.

Furthermore, for a spot welded structure, which is open in some cross-sections but closed in those regions where spot welds are applied, the global behaviour can be assumed as similar to that of closed section; for this reason, the stress equations for closed thin-walled sections are used. For a 3D beam model, the stress-load relationship for each simple load case can be written at the interface section, with respect to a reference system placed on the centre of gravity, with *z-axis* directed along the longitudinal neutral axis and *x-* and *y-axes* along the principal and secondary bending directions, respectively. The matrix relation can be given as follows:

$$\{\sigma\} = [S_1]\{F\}, \tag{1}$$

where $\{\sigma\}$ is the vector of nodal stresses, $[S_1]$ is the stress recovery matrix, and $\{F\}$ is the vector of total forces applied to the central node. In particular, (1) for a generic rectangular cross-section can be detailed as follows:

$$\begin{Bmatrix} \tau_{xz}^{(1)} \\ \tau_{yz}^{(1)} \\ \sigma_z^{(1)} \\ \tau_{xz}^{(2)} \\ \tau_{yz}^{(2)} \\ \sigma_z^{(2)} \\ \vdots \end{Bmatrix} = \begin{bmatrix} \dfrac{S_y^{*(1)}}{I_y\left(2b^{(1)}\right)} & 0 & 0 & 0 & 0 & p\left(\dfrac{1}{2\Omega b^{(1)}}\right) \\ 0 & \dfrac{S_x^{*(1)}}{I_x\left(2b^{(1)}\right)} & 0 & 0 & 0 & q\left(\dfrac{1}{2\Omega b^{(1)}}\right) \\ 0 & 0 & \dfrac{1}{A_{\text{tot}}} & -\dfrac{y^{(1)}}{I_x} & -\dfrac{x^{(1)}}{I_y} & 0 \\ \dfrac{S_y^{*(2)}}{I_y\left(2b^{(2)}\right)} & 0 & 0 & 0 & 0 & p\left(\dfrac{1}{2\Omega b^{(2)}}\right) \\ 0 & \dfrac{S_x^{*(2)}}{I_x\left(2b^{(2)}\right)} & 0 & 0 & 0 & q\left(\dfrac{1}{2\Omega b^{(2)}}\right) \\ 0 & 0 & \dfrac{1}{A_{\text{tot}}} & -\dfrac{y^{(2)}}{I_x} & -\dfrac{x^{(2)}}{I_y} & 0 \\ \vdots & \vdots & \vdots & \vdots & \vdots & \vdots \end{bmatrix} \begin{Bmatrix} F_x \\ F_y \\ F_z \\ M_x \\ M_y \\ M_z \end{Bmatrix}. \tag{2}$$

The physical meaning of each parameter is given in Table 1.

The superscript (i) indicates the global node number. For the transition region between two different values of thickness, an average value is set at the node between two adjacent shell elements. Note that the effects of individual loads are considered uncoupled; in addition, the contribution of linear shear stresses, perpendicular to the shear direction, are not considered, because their global effect on displacements and rotations of the central node is zero, as well as the global effect of warping in torsion load cases [13]. Figure 4 shows the stress distributions in these two cases.

2.2. The Form Nodal Load Matrix $[S_2]$. The form nodal load matrix $[S_2]$ provides a relationship between nodal forces and nodal stresses of the 3D beam model. First, the nodal loads on one shell element k at the interface are examined. This is a bilinear 4-node shell element, then only two nodes (i and j) must be considered for the interface (Figure 5).

The stress distributions on the interface of k element are found by averaging the nodal stresses of nodes i and j. Then, the average stresses of k element, f_x^k, f_y^k, and f_z^k, in x, y, and z directions, respectively, it can be written as follows:

$$\begin{aligned}\tilde{\tau}_{xz}^{(k)} &= \frac{\tau_{xz}^{(i)} + \tau_{xz}^{(j)}}{2};\\ \tilde{\tau}_{yz}^{(k)} &= \frac{\tau_{yz}^{(i)} + \tau_{yz}^{(j)}}{2};\\ \tilde{\sigma}_{z}^{(k)} &= \frac{\sigma_{z}^{(i)} + \sigma_{z}^{(j)}}{2}.\end{aligned} \tag{3}$$

Since the average stresses at the interface are constant, the nodal loads for i and j can be calculated by using shape functions, yielding

$$\begin{aligned}f_x^{(k,i)} &= \int_{s_i}^{s_j} N_i \tilde{\tau}_{xz}^{(k)} b^{(k)} ds = \frac{A^{(k)}}{4}\left(\tau_{xz}^{(i)} + \tau_{xz}^{(j)}\right);\\ f_x^{(k,j)} &= \int_{s_i}^{s_j} N_j \tilde{\tau}_{xz}^{(k)} b^{(k)} ds = \frac{A^{(k)}}{4}\left(\tau_{xz}^{(i)} + \tau_{xz}^{(j)}\right),\\ f_y^{(k,i)} &= \int_{s_i}^{s_j} N_i \tilde{\tau}_{yz}^{(k)} b^{(k)} ds = \frac{A^{(k)}}{4}\left(\tau_{yz}^{(i)} + \tau_{yz}^{(j)}\right);\\ f_y^{(k,j)} &= \int_{s_i}^{s_j} N_j \tilde{\tau}_{yz}^{(k)} b^{(k)} ds = \frac{A^{(k)}}{4}\left(\tau_{yz}^{(i)} + \tau_{yz}^{(j)}\right),\\ f_z^{(k,i)} &= \int_{s_i}^{s_j} N_i \tilde{\sigma}_{z}^{(k)} b^{(k)} ds = \frac{A^{(k)}}{4}\left(\sigma_{z}^{(i)} + \sigma_{z}^{(j)}\right);\\ f_z^{(k,j)} &= \int_{s_i}^{s_j} N_j \tilde{\sigma}_{z}^{(k)} b^{(k)} ds = \frac{A^{(k)}}{4}\left(\sigma_{z}^{(i)} + \sigma_{z}^{(j)}\right),\end{aligned} \tag{4}$$

where $A^{(k)}$ is the area of the element, N indicates the shape function, and s is the local coordinate, useful to measure the length of element.

The same relations are valid for all the other elements along the interface and, then, an assembled matrix relationship can be obtained between nodal forces and nodal stresses:

$$\{f\} = [S_2]\{\sigma\}, \tag{5}$$

where $\{f\}$ is the vector of total nodal forces, $[S_2]$ is the form nodal load matrix, and $\{\sigma\}$ is the vector of total nodal stresses. In extended notation, (5) can be rewritten as follows:

$$\begin{Bmatrix} f_x^{(1)} \\ f_y^{(1)} \\ f_z^{(1)} \\ f_x^{(2)} \\ f_y^{(2)} \\ f_z^{(2)} \\ \vdots \end{Bmatrix} = \frac{1}{4}\begin{bmatrix} A^{(1)} & 0 & 0 & A^{(1)} & 0 & 0 & \cdots \\ 0 & A^{(1)} & 0 & 0 & A^{(1)} & 0 & \cdots \\ 0 & 0 & A^{(1)} & 0 & 0 & A^{(1)} & \cdots \\ A^{(1)} & 0 & 0 & A^{(1)} + A^{(2)} & 0 & 0 & \cdots \\ 0 & A^{(1)} & 0 & 0 & A^{(1)} + A^{(2)} & 0 & \cdots \\ 0 & 0 & A^{(1)} & 0 & 0 & A^{(1)} + A^{(2)} & \cdots \\ \vdots & \vdots & \vdots & \vdots & \vdots & \vdots & \vdots \end{bmatrix}\begin{Bmatrix} \tau_{xz}^{(1)} \\ \tau_{yz}^{(1)} \\ \sigma_z^{(1)} \\ \tau_{xz}^{(2)} \\ \tau_{yz}^{(2)} \\ \sigma_z^{(2)} \\ \vdots \end{Bmatrix}. \tag{6}$$

Note that, for open sections, the forces applied on internal nodes receive the contribution of average stresses relating to both adjacent elements; instead, external nodes belong to a single element and then their values are considerably lower. Therefore, by combining (1) and (5), it is possible to obtain the relation between the total forces at the central node, $\{F\}$, and the nodal forces on the outer contour of the section $\{f\}$:

$$\{f\}_{3n\times 1} = [S_2]_{3n\times 3n}[S_1]_{3n\times 6}\{F\}_{6\times 1} = [S]_{3n\times 6}\{F\}_{6\times 1}, \tag{7}$$

where n denotes the maximum number of nodes on the interface.

To obtain the $[R]$ matrix that relates 1D beam displacements and rotations and 3D displacement values at the interface, linear relations between forces and displacements are assumed. In this way, it is sufficient to transpose $[S]$:

$$[R] = [S]^T. \tag{8}$$

The searched kinematic relationship can be written as follows:

$$[R]_{6\times 3n}\{q\}_{3n\times 1} = \{Q\}_{6\times 1}, \tag{9}$$

where $\{Q\}_{6\times 1}$ is the nodal displacements and rotations vector of the beam node and $\{q\}_{3n\times 1}$ is the nodal displacements vector of the 3D finite element model.

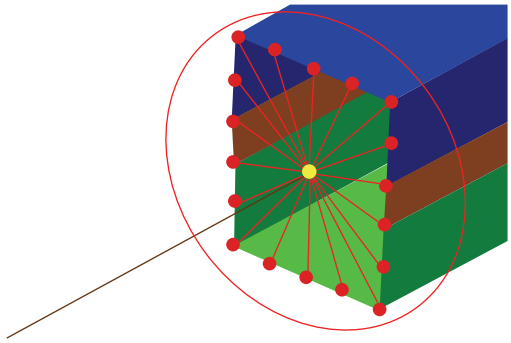

Figure 3: The interface element (circled in red) between equivalent 1D beam model and detailed 3D joint model. The central node is in yellow (dependent node on the beam side) while the peripheral nodes are in red (independent nodes on the joint side).

Table 1: Nomenclature for the $[S_1]$ matrix.

A_{tot} is the total area of the thin-walled cross-section	Ω is the area encompassed by the middle perimeter line
$x^{(i)}$ and $y^{(i)}$ are the position coordinates of the ith node	$b^{(i)}$ is the thickness average value relating to the ith node
$S_x{}^{*(i)}$ and $S_y{}^{*(i)}$ are the cross-section static moments about x- and y-axes for ith node	I_x and I_y are the cross-section moments of inertia about x- and y-axes
p is a factor equal to 1 on the upper horizontal wall, −1 on the lower, 0.5 on the nodes at intersections, and 0 on the vertical walls.	q is a factor equal to 1 on the right vertical wall, −1 on the left, 0.5 on the nodes at intersections, and 0 on the horizontal walls.

3. Application Case

This section describes an application model, on which the proposed new connection element has been validated. The geometry of the reference 3D structure is described in Section 3.1. Thereafter, Section 3.2 describes the 1D concept model of the structure.

3.1. 3D Model Description. The 3D application model consisted of three beams, connected with a joint. Each beam was one meter long and defined by two thin-walled sheets with C-shaped section, whose geometry and dimensions are shown in Figure 6(a). The cross-section had a vertical axis of symmetry and the centre of gravity has been considered coincident with the shear centre. This assumption is very important for two reasons. First, because it allows reducing detailed 3D beams with the dynamic method using uncoupled differential equations for flexural and torsional vibrations. Additionally, it also allows considering the effects due to the various stresses in the joint reduction as uncoupled. Since the sheet thickness was much smaller than the two transversal dimensions, it was possible to mesh each beam member by using 4-node finite shell elements. The three beams intersected in a joint, having the same cross-section and also modelled with shell elements.

Therefore, this structure was composed of two parts, the upper and the lower parts, separated from each other. These parts have been connected by a set of equally spaced welding points along each of the longitudinal walls. The distance between spot welds has been chosen according to the typical layout in automotive beams, that is, equal to 100 mm. Each welding point has been created as a small Hexa solid element, connected to corner nodes of flanges by generic interpolation elements (Figures 6(b) and 6(c)). The *Structures* environment of LMS Virtual. Lab software [14] has been used to create the whole FE model.

The material assigned to the model, assumed homogeneous and isotropic, was typical steel with the following properties:

(i) elasticity modulus: $E = 210000$ MPa;

(ii) Poisson's ratio: $\nu = 0,3$;

(iii) mass density: $\rho = 7,9 \cdot 10^{-9}$ ton/mm^3.

In order to compare the detailed 3D FE model and the concept structure also in terms of modal shapes, a beam centre line has been created in the 3D structure by defining a proper number of central nodes, located at a distance of 100 mm from each other along the longitudinal direction of the beam. Each central node has been connected to the nodes of detailed 3D model in the same cross-section (boundary nodes) by an interpolation RBE3 element, so that the modal displacements of each centre node have been estimated by interpolation of the modal displacements of the boundary nodes. Figure 7 shows the complete detailed 3D model of the structure.

3.2. Concept Model Description. To define the concept structure, simplified concept models of the joint and of the three beams were created. For the beams, a dynamic FE-based method for the estimation of equivalent cross-section properties was used [6].

The main advantage of the method is that it takes into account all possible discontinuities and variations (like spot welds) that may occur along a beam and that affect its stiffness, especially under torsional loads. This method consists of two principal steps:

(1) firstly, the natural frequencies of a given beam-structure have been estimated by means of a modal analysis of the detailed 3D FE model, in free-free conditions;

(2) secondly, the cross-sectional stiffness properties were obtained from the flexural and torsional frequencies, using the differential equations of beam vibrations [15].

In particular, an unconstrained nonlinear minimization algorithm (the Nelder-Mead simplex algorithm [16]) was used to estimate beam section properties. The implemented objective function consisted of minimizing the squared sum of differences between the frequencies reference vector, obtained from the detailed 3D FE model, and a frequencies vector, iteratively computed by applying non-linear equations derived from the beam modal model [6]. For the spot-welded beam model under study, the equivalent stiffness parameters

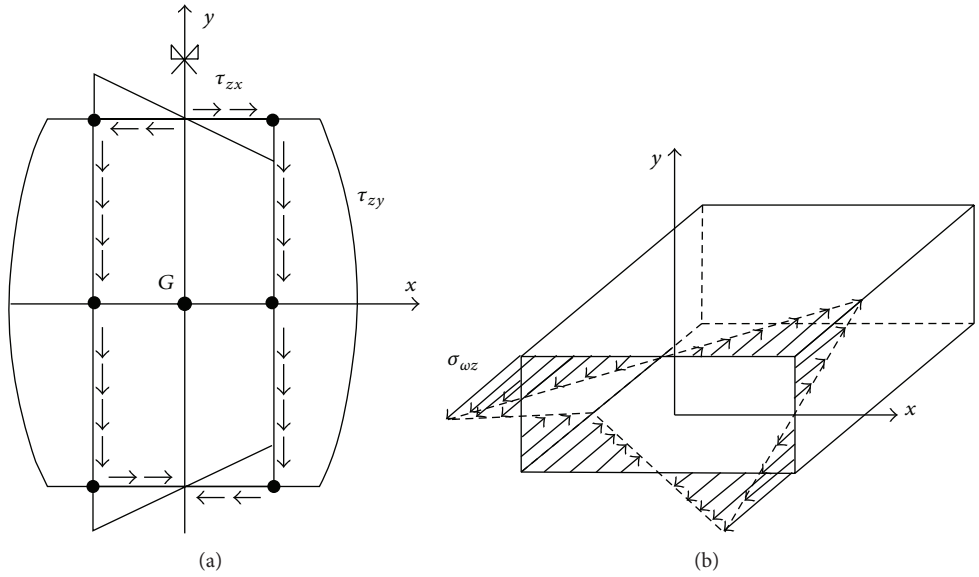

Figure 4: Stress distribution along rectangular cross-sections, due to vertical shear (τ_{zx} and τ_{zy} in (a)) and warping torsion (σ_z in (b)): the global effect of linear parts in the central node is zero.

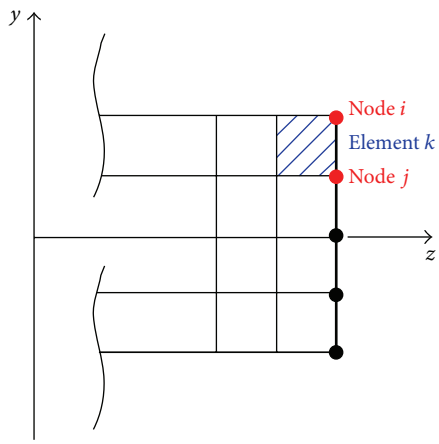

Figure 5: Profile of detailed 3D beam model: a generic shell element k and the two nodes at interface, i and j [11].

Table 2: Equivalent beam properties estimated by the dynamic FE-based method.

Parameters	Values for 1D beam model
A_{eq}	178 mm^2
K_x	0,144
K_y	0,104
I_x	69420 mm^4
I_y	48164 mm^4
I_t	25702,80 mm^4
I_w	3,094e + 08 mm^6

estimated for the 1D concept beams are listed in Table 2. Figure 8(a) shows the concept model, before the joint is reduced.

Instead, for the joint reduction, the Craig-Bampton fixed interface technique was applied as follows; in the final concept model the joint was represented by a SE, consisting of a stiffness and a mass matrix condensed to a set of master nodes, which includes one node on the beam side of each beam/joint interface. Therefore, the Craig-Bampton reduction was implemented with Nastran software [17], by keeping the DOFs of the central nodes at the three beam/joint interfaces as master and the DOFs of the nodes belonging to the detailed 3D FE model of the joint as slave. Figure 8(b) shows the concept structure, where an SE representation of the joint replaces the detailed 3D joint model while guaranteeing the structural continuity of the whole concept model. Two different concept models of the joint have been created: in one model, the Craig-Bampton dynamic reduction was applied to the detailed 3D FE model with rigid RBE2 elements at each beam/joint interface; in the other model, the proposed MPC elements were used to connect the central node to nodes placed on the cross-section at each interface.

Note that the joint region has been defined in such a way that the distance of each interface from the joint centre is sufficiently large (100 mm in this case) to avoid any violation of the Saint-Venant beam assumptions. Note also that the detailed 3D model has over 60000 degrees of freedom (DoFs), while the concept model has 180 DoFs only, which allows a significant reduction of the computational time required by the FE simulations.

4. Dynamic Validation

A dynamic analysis has been carried out, to show the improvements on the predictive accuracy of the concept structure with the proposed MPC connection elements. A FE modal analysis in free-free conditions was performed using Nastran software as FE solver, in order to compare, in

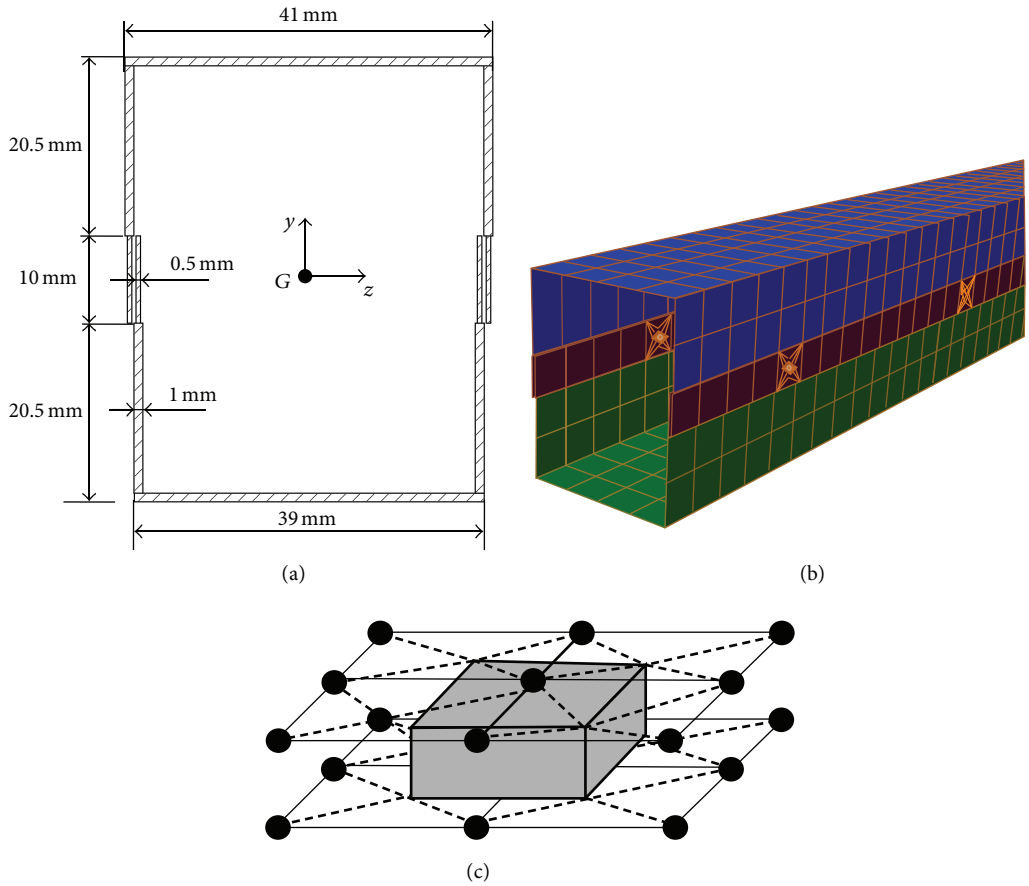

Figure 6: Application model: cross-section geometry of beams (a), mesh of detailed 3D beam model with welding zones (b), and spot weld model, with a central Hexa solid element connected to nodes of flanges by interpolation elements (c).

Table 3: Dynamic comparison between the original and the two-concept FE models, in terms of natural frequencies, % errors, and modal correlation factors.

			Concept model with RBE2			Concept model with new MPC		
	Mode *n*.	Frequency 3D model (Hz)	Frequency 1D model (Hz)	Frequency difference (%) 3D − 1D	MAC values	Freq. 1D model (Hz)	Frequency difference (%) 3D − 1D	MAC values
	1	41,63	41,85	0,53%	0,99	40,40	−2,97%	0,99
	2	55,46	55,55	0,17%	0,99	54,86	−1,09%	0,99
	3	79,23	79,44	0,26%	0,99	78,77	−0,59%	0,99
1st Flex-Tors	4	188,52	229,57	21,77%	0,96	179,99	−4,53%	0,99
2nd Flex-Tors	5	196,49	225,76	14,90%	0,90	190,38	−3,11%	0,96
	6	197,18	197,55	0,19%	0,97	194,60	−1,31%	0,98
	7	256,67	256,90	0,09%	0,97	256,01	−0,26%	0,99
3rd Flex-Tors	8	266,65	396,93	38,73%	0,86	260,47	−2,32%	0,98
4th Flex-Tors	9	285,98	364,37	27,41%	0,62	280,23	−2,01%	0,90
	10	293,74	292,37	−0,47%	0,95	289,72	−1,37%	0,97
	11	382,43	397,78	4,01%	0,93	391,22	2,30%	0,84
	12	410,85	417,10	1,52%	0,99	406,66	−1,02%	0,99
Average				9,09%			1,91%	
Maximum				38,73%			4,53%	

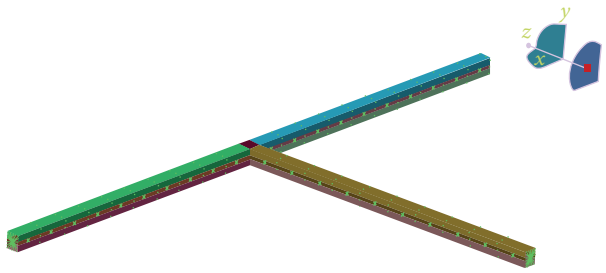

Figure 7: Application case: detailed 3D FE model of the structure.

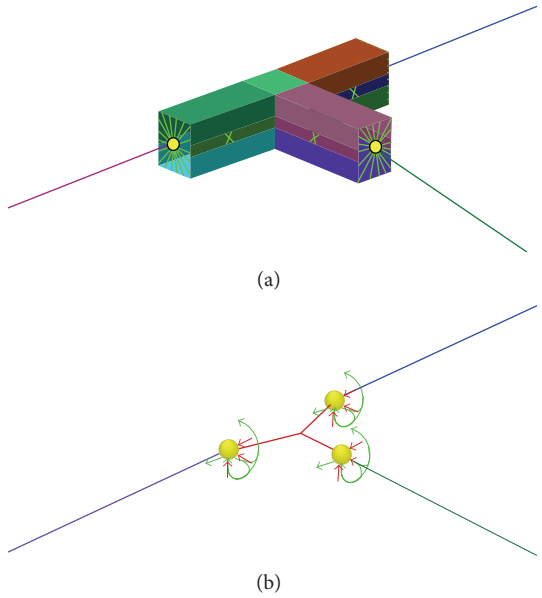

(a)

(b)

Figure 8: Concept model: before (a) and after (b) the reduction of joint in SE. The three master nodes of SE are in yellow.

terms of natural frequencies and mode shapes, the detailed 3D model to two different concept models. In both concept models, the properties of equivalent 1D beam elements have been estimated by using the dynamic FE-based technique described in Section 3.2. In the first concept structure, the joint reduction has been achieved by using Craig-Bampton technique and rigid RBE2 connection elements; in the second one, the proposed MPC connection elements have been used. Table 3 reports the natural frequencies of the first 12 global modes estimated for the detailed and for the two equivalent concept FE models, together with the percentage differences between each concept model and the reference structure. The diagonal values of the modal assurance criterion (MAC) matrix [18], obtained in *Noise and Vibration* environment of LMS Virtual. Lab, are reported as well.

It can be observed that the concept model with rigid connection elements approximates very precisely the first vibration modes, in terms of frequencies and MAC values, concerning in particular axial and flexural vibrations; however, for flexural-torsional modes, significant differences between the concept and the detailed 3D model can be appreciated, with a maximum and an average value of 38.73% and 9.09%, respectively. This means that the stiffness of the joint is overestimated, especially when the interfaces undergo torsional deformation. Instead, the second concept structure, where the proposed MPC connection elements have been used, shows good accuracy for all modes, with a maximum and an average difference value of 4.53% and 1.91%, respectively. In particular, for modes involving torsional deformation at one or more joint/beam interfaces, the second concept model is up to 16 times more accurate than the first concept model.

5. Conclusions and Outlook

In this paper, new concept modelling methodologies, enabling an improved accuracy of beam and joint concept models, have been proposed and validated. For equivalent 1D beam elements, a dynamic FE-based method was applied, able to define equivalent characteristics of concept beam models, starting from the flexural and torsional natural frequencies of complex 3D beam models. Instead, for joint concept modelling, the Craig-Bampton dynamic reduction approach was used. This method is very fast and accurate, but it is strongly affected by the FE connection element between central and peripheral nodes of the joint/beam interface sections. For this reason, a new multipoint constraint connection element has been defined and implemented, in order to interpolate displacements of peripheral nodes and obtain displacements and rotations of the centre node with an increased accuracy, as compared to conventional connection elements, such as rigid spiders.

To assess the accuracy of the proposed method, an application case was analysed, consisting of a 3D structure where three spot welded beams are connected by a joint with the same cross-section geometry. By comparing two different concept models (one using rigid RBE2 and the second using the new MPC connection elements for the reduction of joint in SE) with the detailed 3D model in terms of natural frequencies and MAC values, it was proved that the proposed method has a good predictive accuracy. This confirmed that the proposed MPC connection elements permit to estimate the mass and stiffness characteristics of the reduced joint at each joint end section more accurately than with rigid spiders.

The proposed methodologies have been developed with the aim of enabling early predictions of static and dynamic behaviours in vehicle bodies already in the concept phase of the development cycle. However, it is worthy to notice that such concept modelling techniques can be exploited also in other application fields.

The next steps of this research will aim at extending the applicability of the proposed method to structures with general cross-section shape. If the assumption of double-symmetry is removed, coupled effects of torsion and bending must be taken into account while calculating both the equivalent 1D beam properties and the coefficient of the MPC beam/joint connection elements.

Conflict of Interests

The authors declare that there is no conflict of interests regarding the publication of this paper.

Acknowledgments

The authors gratefully acknowledge the European Commission for their support of the Marie Curie IAPP project "INTERACTIVE" (Innovative Concept Modelling Techniques for Multi-Attribute Optimization of Active Vehicles), with contract number 285808; see http://www.fp7interactive.eu.

References

[1] D. Mundo, R. Hadjit, S. Donders, M. Brughmans, P. Mas, and W. Desmet, "Simplified modelling of joints and beam-like structures for BIW optimization in a concept phase of the vehicle design process," *Finite Elements in Analysis and Design*, vol. 45, no. 6-7, pp. 456–462, 2009.

[2] D. Mundo, G. Stigliano, S. Donders, and H. van der Auweraer, "Concept design of vehicle bodies using reduced models of beams, joints and panels," *International Journal of Vehicle Design*, vol. 57, no. 1, pp. 71–83, 2011.

[3] A. Moroncini, L. Cremers, and M. Croiss, "NVH structural optimization using beams and shells FE concept models in the early car development phase at BMW," in *Proceedings of the International Conference on Noise and Vibration Engineering (ISMA '10)*, Leuven, Belgium, 2010.

[4] S. Corn, J. Piranda, and N. Bouhaddi, "Simplification of finite element models for structures having a beam-like behaviour," *Journal of Sound and Vibration*, vol. 232, no. 2, pp. 331–354, 2000.

[5] J. Piranda, S. J. Huang, S. Corn, C. Stawicki, and X. Bohineust, "Improvement of dynamic models in car industry," in *Proceedings of the 15th International Modal Analysis Conference (IMAC '97)*, pp. 85–91, February 1997.

[6] G. de Gaetano, F. I. Cosco, C. Maletta, D. Mundo, and S. Donders, "Dynamic FE-based method for concept modelling of vehicle beam-like structures," in *Proceedings of the International Conference on Noise and Vibration Engineering (ISMA '12)*, Leuven, Belgium, September 2012.

[7] R. Guyan, "Reduction of stiffness and mass matrices," *AIAA Journal*, vol. 3, no. 2, pp. 380–387, 1965.

[8] R. R. Craig Jr., *Structural Dynamics—An Introduction to Computer Methods*, John Wiley & Sons, New York, NY, USA, 1981.

[9] R. H. MacNeal, "A hybrid method of component mode synthesis," *Computers & Structures*, vol. 1, no. 4, pp. 581–601, 1971.

[10] A. Maressa, D. Mundo, S. Donders, and W. Desmet, "A wave-based substructuring approach for concept modeling of vehicle joints," *Computers and Structures*, vol. 89, no. 23-24, pp. 2369–2376, 2011.

[11] S. Huimin, *Rigorous joining of advanced reduced-dimensional beam models to 3D finite element models [Ph.D. thesis]*, Aerospace Engineering, Institute of Technology, Georgia, Ga, USA, May 2010.

[12] E. Viola, *Scienza delle Costruzioni—Teoria della Trave*, Pitagora Editrice, Bologna, Italy, 1992.

[13] O. A. Bauchau, *Aerospace Structural Analysis*, Georgia Institute of Technology, 2002.

[14] LMS International, LMS Virtual.Lab Rev10-SL2, 2011, http://www.lmsintl.com/virtuallab.

[15] I. Senjanović, I. Ćatipović, and S. Tomašević, "Coupled flexural and torsional vibrations of ship-like girders," *Thin-Walled Structures*, vol. 45, no. 12, pp. 1002–1021, 2007.

[16] J. C. Lagarias, J. A. Reeds, M. H. Wright, and P. E. Wright, "Convergence properties of the Nelder-Mead simplex method in low dimensions," *SIAM Journal on Optimization*, vol. 9, no. 1, pp. 112–147, 1999.

[17] MSC, "MSC.Nastran 2011," 2011.

[18] W. Heylen, S. Lammens, and P. Sas, *Modal Analysis Theory and Testing*, Department of Mechanical Engineering, Katholieke Universiteit Leuven, 2nd edition, 1997.

Hindawi Publishing Corporation
Shock and Vibration
Volume 2014, Article ID 393867, 7 pages
http://dx.doi.org/10.1155/2014/393867

Research Article

Influence of Sleepers Shape and Configuration on Track-Train Dynamics

Roman Bogacz,[1,2] Włodzimierz Czyczuła,[1] and Robert Konowrocki[3]

[1] *Krakow University of Technology, Warszawska 24, 31-155 Kraków, Poland*
[2] *Warsaw University of Technology, SiMR, Ulica Narbutta 84, Warsaw, Poland*
[3] *Institute of Fundamental Technological Research, PAN, Pawińskiego 5B, Warsaw, Poland*

Correspondence should be addressed to Roman Bogacz; rbogacz@ippt.gov.pl

Received 12 July 2013; Accepted 10 March 2014; Published 2 July 2014

Academic Editor: Miguel M. Neves

Copyright © 2014 Roman Bogacz et al. This is an open access article distributed under the Creative Commons Attribution License, which permits unrestricted use, distribution, and reproduction in any medium, provided the original work is properly cited.

The paper is devoted to the study of dynamical behaviour of railway tracks as continuous systems (rails) supported by periodically spaced sleepers and subjected to moving concentrated loads. Several cases of dynamical problems, where elastically supported beams are excited by a moving concentrated force, are considered. In particular, the study is focused on interactions with structure periodic in the space. Results on one-dimensional structures are extended to the case of a two-dimensional system. The problems of stopping bands, passing bands, and mistuning are also mentioned.

1. Introduction

Nowadays, the load carrying capacity of trains, high-speed, and environment protection against the noise force rapid development of railway transportation. The classic and reinforced railway track is composed of two rails separated from the sleepers by viscoelastic pads. There are numerous simplifications in railway track modelling. The sleeper spacing and ballast stiffness are usually treated as uniform and repre- sented by constant parameters in the analyses. The rails are modelled as the infinite Euler-Bernoulli or Timoshenko beam models, sleepers by lumped masses or elastic bodies (beams), and ballast as viscoelastic foundation. The basic qualitative feature of the classic railway track is the periodicity of sleeper spacing. The sleeper spacing influences the periodicity of viscoelastic supports coefficient and additional mass of sleepers with rotational inertia. In the case of classic periodically supporting sleepers, one can observe passing bands in the frequency of moving and oscillating forces. The solution method which allows determining the stopping and passing bands in the case of tracks, proposed in [1], is based on direct application of Floquet's theorem. The motion of rails and sleepers in selected parts of excitation period T is shown in Figure 2. It is visible that, for the boundary value of frequency between passing and stopping bands, a qualitative change of solution describing rails and sleepers' vibrations occurs. The wheel/rail response, due to the parametric excitation by the varying dynamic stiffness of a periodically supported rail, has been studied using a spatially quasistatic method, based on the fact that the speed of wave propagation in the rail is much greater than the train speed, but as we can see in [1] or [2] this assumption is not adequate. From the study of the influence of random sleeper spacing [3] follows the fact that the phenomenon of the pinned-pinned resonance may be suppressed by the random sleeper spacing. Unfortunately, the random ballast stiffness distribution has no influence on the vibration behaviour. It seems to be obvious that some randomness usually occurs, but the deterministic spacing of supporting points can be the aim of engineering design. The difference between the mutual kinetic excitation of two wheelsets of the bogie in the stopping and passing band is significant. The passing band in track with classic sleepers is related to the rotation of rails in the classic fastening system. Some changes are possible using mistuning or replacing the single fastening system on the sleeper into the double-point

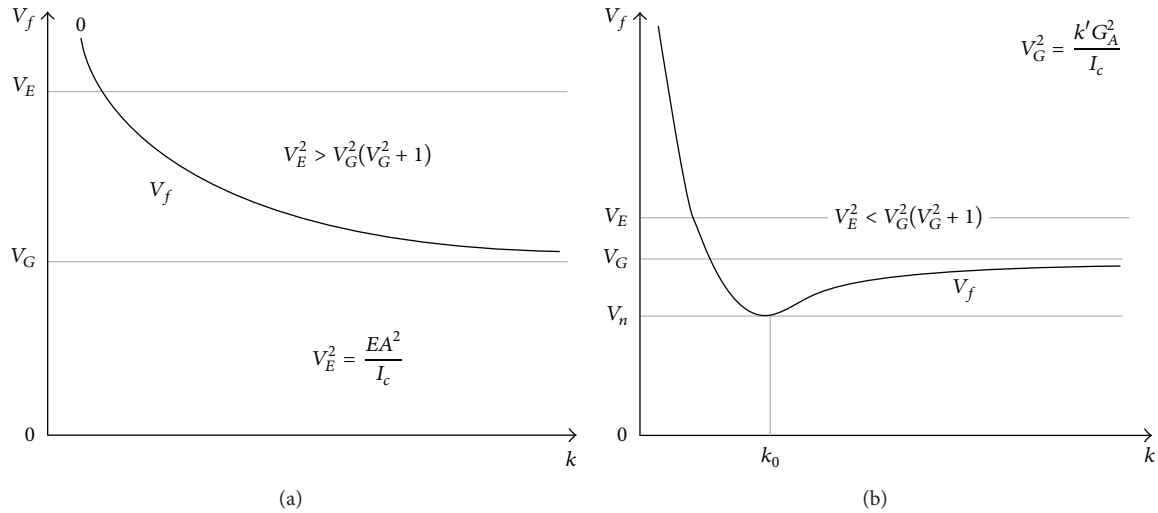

Figure 1: Phase waves velocities V_f versus wave number dependent on the beam parameters (inequality (3)).

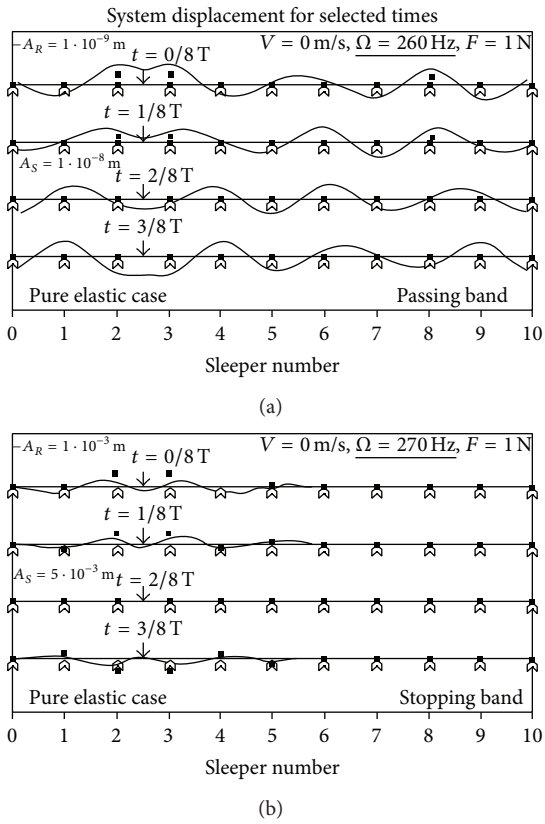

Figure 2: Waves in railway track as periodic structure-passing band and stopping band.

one, which transforms the features of railway tracks. The theory used in the investigation of the track dynamics is limited to linear analysis despite nonlinear characteristics of the pad. It is known that the wheelset dynamics in front of the train is different from the wheelset dynamics in the middle of the train. One of the reasons is connected with the above mentioned nonlinearity of the fastening system characteristics, in particular, the nonlinearity of the pad which changes the reference point of oscillation. This change is connected with a quasistatic preload under the train, which can be substituted by a distributed load [4].

2. Classic Design of Track: Response of Beam to Moving Load

The problem of a flexibly supported beam vibration, when the beam is subjected to the moving distributed load, can be composed of solution for the limiting case of load described by the following Heaviside function $F_0H(x-Vt)$ and moving concentrated oscillating force described by the function $F_1(\cos\omega t)\delta(x-Vt)$:

$$EIw_{,xxxx} + Tw_{,xx,} + mw_{,tt} + hw_{,t} + cw = F_0H(x-Vt) + F_1(\cos\omega t)\,\delta(x-Vt), \quad (1)$$

where w is the beam displacement, EI is the beam stiffness, T is the longitudinal compressive force in the beam, m is the mass density, h is the damping coefficient, c is the elasticity coefficient of the foundation, ω is the frequency of the force oscillation and V is velocity of load motion.

The first case and the case of the beam on a viscoelastic semispace were studied [4, 5]. The superposition of the obtained solution allows studying various kinds of moving loads distributed on a finite-length segment. The second term describing moving and oscillating load was discussed in [2]. The case of the Timoshenko beam on an elastic foundation subjected to uniformly distributed moving loads has been studied by several authors; see, for example, [4, 6]

$$EI\varphi_{,xx} + k'AG(w_{,x} - \varphi) - mI\varphi_{,tt} = 0,$$
$$k'AG(w_{,xx} - \varphi_{,x}) - mw_{,tt} - hw_{,t} - cw = -F_0H(x-Vt) + F_1(\cos\omega t)\,\delta(x-Vt), \quad (2)$$

where φ is the angle of rotation of beam due to pure shear, k' is the shear coefficient, G is the modulus of elasticity in shear, A is the cross-sectional area, and h is the damping coefficient.

The first stationary solution obtained for the case of the Timoshenko beam on an elastic foundation was obtained by Achenbach and Sun [6]. The solution obtained in [6] is valid in full range of velocity but only for the set of parameters fulfilling the following inequality:

$$E > k'G\left(1 + k'GA^2(Ic)^{-1}\right). \tag{3}$$

The dependence of phase velocity versus wave number in this case is shown on left side of Figure 1, where wave velocities V_E and V_G are expressed as in Figure 1.

The generalisation of the results obtained by Achenbach and Sun and the discussion of qualitatively different travelling wave solution depending on the beam parameters are presented in [4]. The results of this study can be used for determination of quasistatic preload under the train.

2.1. Response of Periodic Beam Structure to Moving Concentrated Loads. The guideways for high-speed vehicles are composed of repetitive elements or cells which form a periodic structure. The steady-state system response is determined for a moving disturbances source in the form of constant and periodic force (1).

The equation of motion is completed by interface conditions at the supports which depend on the model assumed, for example, for the railway track condition of continuity (4) and equilibrium of vertical forces (5), which are required:

$$\begin{aligned} w(nl+,t) &= w(nl-,t); \\ w_{,x}(nl+,t) &= w_{,x}(nl-,t); \\ w_{,xx}(nl+,t) &= w_{,xx}(nl-,t); \end{aligned} \tag{4}$$

$$w_{,xxx}(nl-,t) - w_{,xxx}(nl+,t) = R(nl,t), \tag{5}$$

while for the supports of maglev model, one requires continuity of position, vanishing bending moment, and equilibrium of vertical forces.

The solution method proposed in such a case is based on the direct application of Floquet's theorem to the differential equations of motion with periodic parameters [1, 7] describing periodicity in space. Another approach (by the use of perturbation method) for periodic mass and stiffness distribution along the beam was applied by Popp and Mueller [8] in order to approximate the sleepers in the track. In this case, for the realistic system of parameters, the differences were very small. With some extended study of railway track and maglev track, we can state that the application of Floquet's theorem allows solving the problem of free and forced vibration of periodic structures subjected to moving load [1]. The motion of harmonic travelling load generates the set of stopping or passing bands, but from engineering point of view it is sufficient to take into consideration waves corresponding to the first and second passing bands.

As examples of qualitative difference of solution in the passing band and stopping band in Figure 2 are shown, the shapes of rail for two frequencies and time are $0, T/8, T/4$, and $3T/8$.

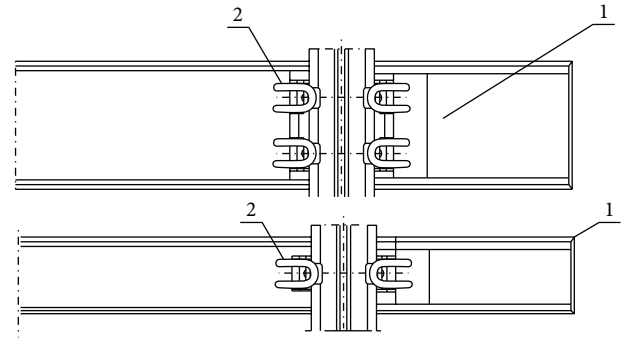

Figure 3: Two kinds of sleepers with different fastening systems.

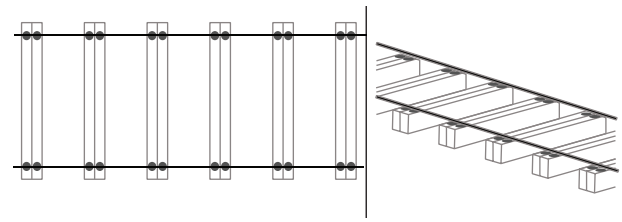

Figure 4: Railway track with stiff type of sleepers with double-point fastening systems.

2.2. Mistuning and Change of the Track Periodicity. The passing bands occurring in the track with classic sleepers in the ballast or in slab track are related to the rotation of rails in the classic fastening system. Some changes are possible using mistuning or change of single fastening system described by the conditions:

$$\begin{aligned} &\left(w_{,x}(nl+,t) = w_{,x}(nl-,t); \right. \\ &\left. w_{,xx}(nl+,t) = w_{,xx}(nl-,t)\right). \end{aligned} \tag{6}$$

This is possible by the change of sleepers with single support to the system of sleepers with double-point fastening. It seems to be successful in the change of railway track features. Such sleepers were shown in Figure 3.

The sleeper with double-point fastening system is much stiffer and heavier compared to the classic concrete sleeper (Figure 4). The double-point fastening system influences the periodicity track which becomes also double-periodic. Additionally, the track with such sleepers is much more convenient for the ballast [9], due to lower pressure. The initial experimental investigation of such sleepers and fasteners confirms advantages in application for the high-speed trains' lines. The results will be described in next papers.

A very important problem in railway engineering is connected with the transition zones, when the foundation stiffness changes more rapidly, that is, before or behind of the bridge abutment, than the dynamical behaviour of sleepers and ballast during exploitation which lead to the plastic

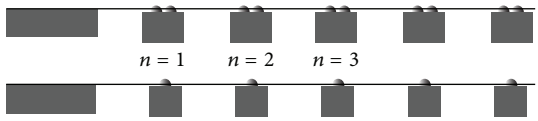

Figure 5: Scheme of track in transition zone with two types of sleepers and fastening systems.

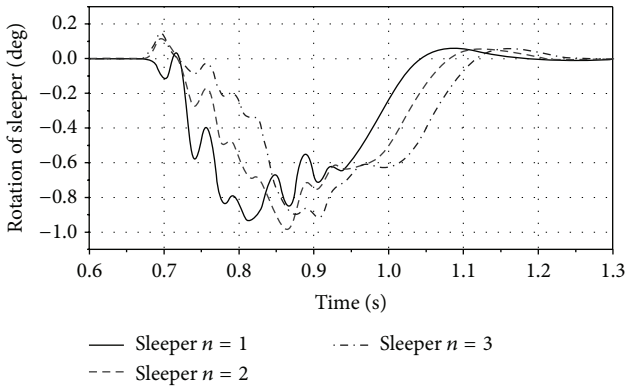

Figure 6: Rotation of three sleepers with double-point fastening during motion in the zone behind the bridge abutment.

deformations of the track. A simple model of such zones is shown in Figure 5.

As an example, the results of numerical study of the sleepers' motion in the transition zone behind the bridge and of the stiff sleepers with double-point fastening system are shown in Figures 6 and 7. The speed of the vehicle is assumed equal to 20 m/s. In Figure 6, are shown some results of three successive sleepers' rotation, which are located in the transition zone, just after the rigid foundation. We can see that the response of consecutive sleepers is dependent on the time and distance of the sleeper from the boundary of rigid foundation. The vertical displacement of sleepers is presented in Figure 7.

The above shown results indicate that use of sleepers with double fastening system induces decreasing vertical displacements and rotation of sleepers in comparison with classic track (Figures 6 and 7). In Figure 8, a comparison of the sleeper rotation of two different sleepers with different types of fastening systems and different weights is presented.

The differences of sleepers' rotation (Figure 8) and differences of the rail rotation around the horizontal axis perpendicular to the direction of vehicle motion (Figure 9) for different fastening systems and different sleepers are essential.

The research of railway track dynamics is carried out intensively in several railway centres. However, in engineering practice the attention and understanding of wave phenomena is very limited. There are also much simpler ways to change the features of the track. One of them is mistuning used by the change of geometry which can be supplemented by the change of stiffness parameters. An example of change of the spacing in order to obtain track with better dynamic behaviour is shown in Figure 10. The optimal difference of

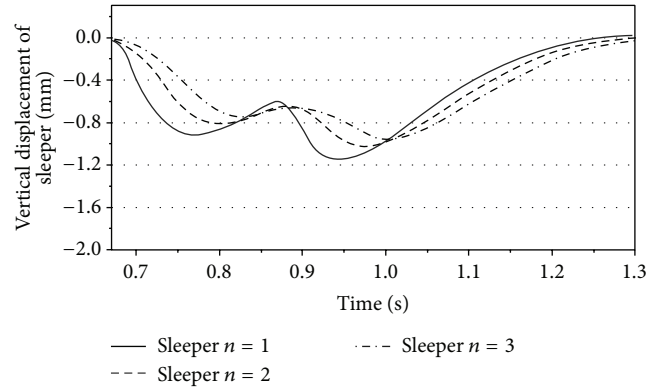

Figure 7: Vertical displacement of the sleepers with double-point fastening during motion in the zone behind the rigid base.

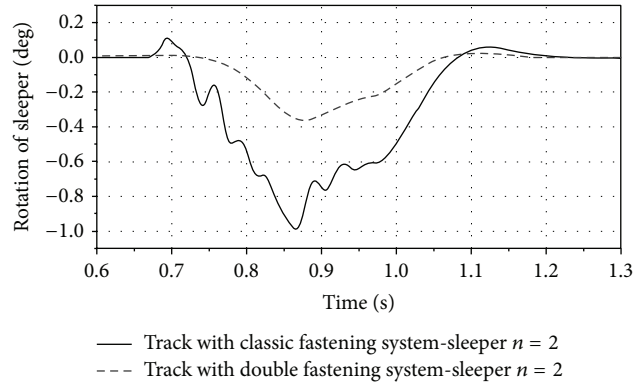

Figure 8: Comparison of rotation of two sleepers with different weight and fastening systems—vehicle speed 20 m/s.

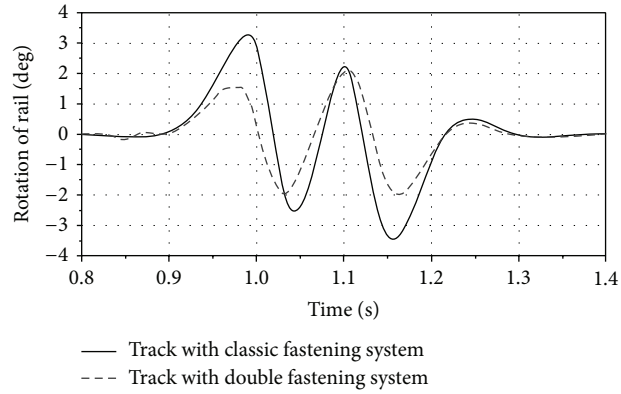

Figure 9: Rail rotation in the tracks with different sleepers and fastening systems at the vehicle speed 20 m/s.

distance between sleepers seems to be stochastic in definite range but in engineering practice the spacing can be taken as follows: $d_i = d_1 + \Delta_i$; $\Delta_1 = 0$, $\Delta_2 = 25$ mm, and $\Delta_3 = 50$ mm (Figure 10).

The change of stiffness parameters without change of geometry can influence only the selected modes of travelling waves. For example, the pin-pin mode is not sensitive to

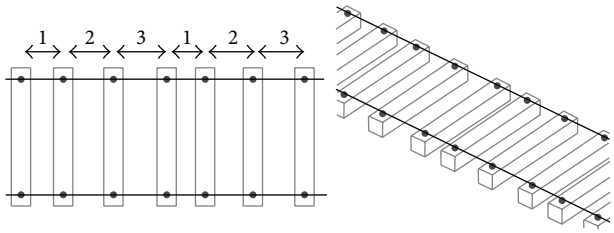

Figure 10: Scheme of rack with the change of sleeper spacing, distances $d_i = d_1 + \Delta_i$.

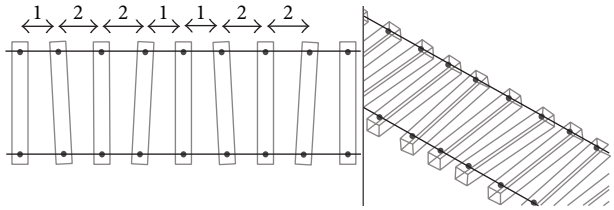

Figure 11: Track mistuning by the change of sleeper spacing (rotation of every second sleeper).

the stiffness of supports. That is why the change of spacing ought to be used. The next possibility of change of periodicity is loss of symmetry as the factor that eliminates the regularity and periodicity of the motion. The change of periodic property of the track due to change of geometry of sleeper spacing can be obtained by rotation of every second or third sleeper in the positive or negative direction; such an example is shown in Figure 11.

It is also important that the length of the wheel circumferences is about 3 m (in classic track, it is equal to distance of five sleepers). Also the dynamic coupling between both axles of the bogie is important issue.

It can be done by application of "Y-shaped" sleepers made of steel. This kind of sleepers is made of steel. Such spacing is, similarly to the case shown in Figure 11, asymmetric to the left and right wheels of the wheelset. The dynamic response in this case is strongly dependent on vehicle speed [10].

The main advantages of the track with "Y-shaped" sleepers are

(i) increased resistance to horizontal forces;

(ii) increased inertia by incorporation of the ballast into the vertical and horizontal vibrations;

(iii) higher stiffness of the track becoming a plate-like structure;

(iv) stabilization of the vehicle motion due to the alternate periodic vertical stiffness of both rails—the vehicle geometrical centre exhibits considerably lower oscillations.

The principal idea of using the "Y-shaped" sleepers is to increase the transversal stiffness and to enlarge the inertia of the track by incorporating the ballast into the C-shaped parts of sleepers. Experimental parts of the track exhibit lower noise level. Numerical simulations show reduced vertical amplitudes. The Y-type track is designed for moderate speed.

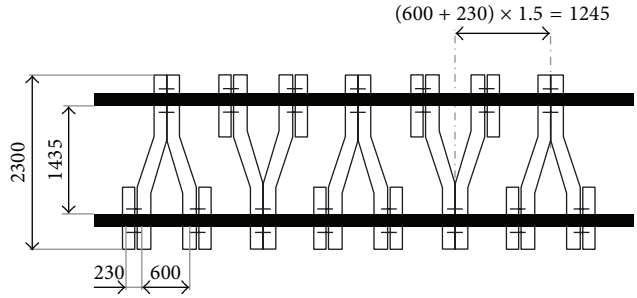

Figure 12: Track "Y-shaped" sleepers spacing as visible above.

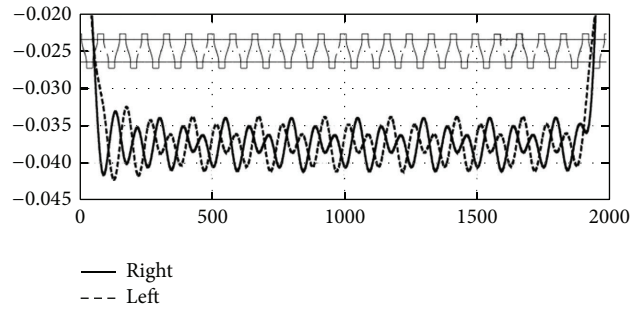

Figure 13: Vertical displacements of the vehicle/track contact points at the speed 30 m/s [11, 12].

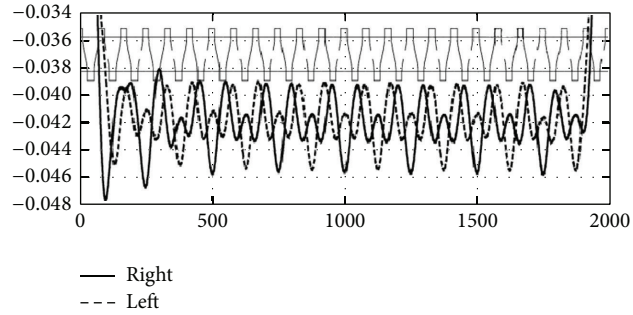

Figure 14: Vertical displacements of the vehicle/track contact points at the speed 50 m/s [11, 12].

Some results of simulations for selected values of speed are shown in Figures 12, 13, and 14. It is visible that, with increasing speed and time of motion, the effect of synchronization occurs. The next important dynamical feature is associated with decreasing of vibration with the distance between excitation points. Simulations show (Figures 15 and 16) that vertical displacements of rails in the front of the contact points of the buggy are much larger in classic track than in the case of track with "Y" shaped sleepers. The great advantage of the "Y-shaped" track is connected with application on curved track because of its higher resistance to horizontal forces.

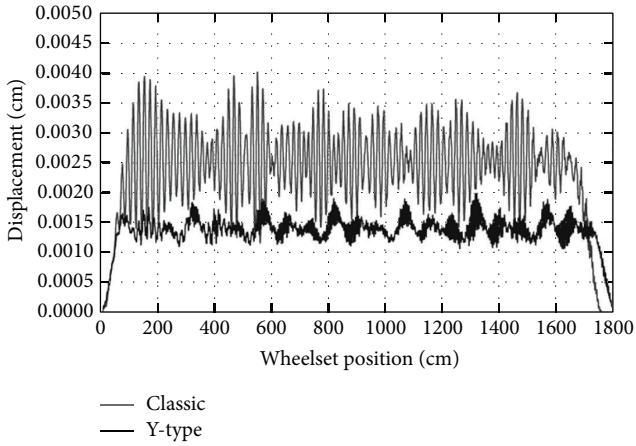

Figure 15: Vertical displacements of rails registered 120 cm in front of the contact points of the buggy for classic and "Y"-type track at the speed 40 m/s [12].

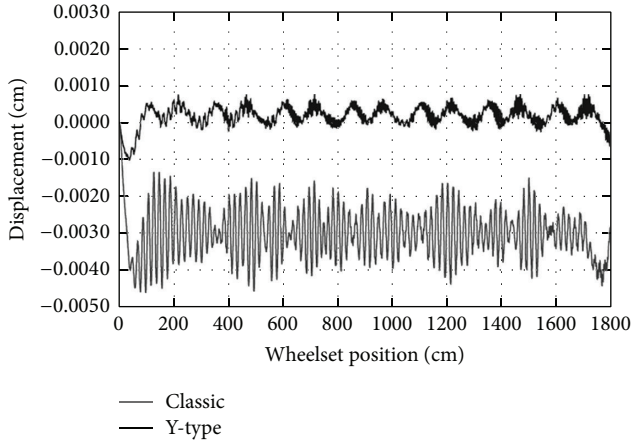

Figure 16: Vertical displacements of rails registered 180 cm in front of the contact points of the buggy for classic and "Y"-type track at the speed 40 m/s [12].

3. Conclusions

The periodicity of sleeper spacing is the basic qualitative feature of the classic railway track [13, 14]. It influences the periodicity of viscoelastic supports, coefficients, and additional mass of sleepers with rotational inertia. In the case of classic periodically supporting sleepers, we can observe the passing bands in the frequency of moving and oscillating forces. The solution method which allows determining the stopping and passing bands in the case of track with periodically spaced sleepers and stationary motion is based on direct application of Floquet's theorem. The difference between the mutual kinetic excitation of two wheelsets of the bogie in the stopping and passing bands is significant. Loss of the periodicity of spacing is connected to a mistuning of wave propagation and irregular contact forces, which can be positive, from the dynamical point of view, process for vehicle-track interaction. In the case of transient motion, as in the case of a transition zone, an advantage of double fasteners is obtained and visibly different sleeper motion dependent on the distance is shown. The vertical displacements of rails registered in front and behind of the contact points of the buggy for classic and "Y"-type track show one of the advantages of the track with "Y"-type sleepers.

Conflict of Interests

The authors declare that there is no conflict of interests regarding the publication of this paper.

Acknowledgment

The paper was supported by the Polish National Science Centre of Ministry of Science and Higher Education Research Project no. N 509 5376 40.

References

[1] R. Bogacz, T. Krzyżynski, and K. Popp, "On vertical and lateral dynamics of periodic guideways for maglev vehicle," in *Dynamical Problems in Mechanical Systems*, R. Bogacz and K. Popp, Eds., pp. 219–233, Polish Academy of Sciences, Warszawa, Poland, 1993.

[2] R. Bogacz and T. Krzyżyński, "On the Bernoulli-Euler beam on a viscoelastic foundation under moving oscillating load," Inst. Fund. Technol. Res. Report 38, 1–40.

[3] T. X. Wu and D. J. Thompson, "The influence of random sleeper spacing and ballast stiffness on the vibration behaviour of railway track," *Acustica*, vol. 86, no. 2, pp. 313–321, 2000.

[4] R. Bogacz, "On dynamics and stability of continuous systems subjected to a distributed moving load," *Ingenieur-Archiv*, vol. 53, no. 4, pp. 243–255, 1983.

[5] P. Koziol and C. Mares, "Wavelet approach for vibration analysis of fast moving load on a viscoelastic medium," *Shock and Vibration*, vol. 17, no. 4-5, pp. 461–472, 2010.

[6] J. D. Achenbach and C. T. Sun, "Moving load on a flexibly supported Timoshenko beam," *International Journal of Solids and Structures*, vol. 1, no. 4, pp. 353–370, 1965.

[7] R. Bogacz, T. Krzyzynski, and K. Popp, "On the dynamics of linearly extended and cyclic periodic structures," in *Dynamics of Continua*, D. Besdo and R. Bogacz, Eds., pp. 55–64, Shaker, Bad Honnef, Germany, 1998.

[8] K. Popp and P. C. Mueller, "Ein Beitrag zur Gleisdynamik," *Zeitschrift für Angewandte Mathematik und Mechanik*, vol. 62, pp. T65–T67, 1982.

[9] R. Bogacz and W. Czyczuła, "Mechanical analysis of track loading for high speed operation—track with PS-08 slipers and other track structures," in *Modern Technologies and Systems Increasing the Efficiency of Managing Railway Transport*, pp. 39–55, Kraków, Poland, 2010.

[10] R. Bogacz and C. Bajer, "On modelling of contact problems in railway engineering," in *Recent Advances in Applied Mechanics*, J. T. Katsikadelis, D. E. Beskos, and E. E. Gdoutos, Eds., pp. 77–86, National Technical University of Athens, Athens, Greece, 2000.

[11] R. Bogacz and C. Bajer, "Vibration of the train/track system with two types of sleepers," in *Proceedings of the 21th International Congress on Theoretical and Applied Mechanics (ICTAM '04)*, IUTAM, Warsaw, Poland, August 2004.

[12] C. Bajer and R. Bogacz, "Dynamics of "Y-Type" Track," in *Proceedings of the 21st Symposium on Vibrations in Physical Systems*, pp. 3–7, Poznań-Kiekrz, Poland, 2004.

[13] R. Bogacz, T. Krzyżyński, and P. Koziol, "An analysis of the dynamic effects of periodic structures subject to a moving load," in *Proceedings of the 1st International Conference on Railway Technology: Research, Development and Maintenance*, J. Pombo, Ed., Paper 116, Civil-Comp Press, Stirlingshire, UK, 2012.

[14] K. L. Knothe and S. L. Grassie, "Modelling of railway track and vehicle/track interaction at high frequencies," *Vehicle System Dynamics*, vol. 22, no. 3-4, pp. 209–262, 1993.

Hindawi Publishing Corporation
Shock and Vibration
Volume 2014, Article ID 937967, 8 pages
http://dx.doi.org/10.1155/2014/937967

Research Article

Regular and Chaotic Dynamics of Flexible Plates

J. Awrejcewicz,[1,2] E. Yu. Krylova,[3] I.V. Papkova,[3] and V. A. Krysko[3]

[1] *Department of Automation, Biomechanics and Mechatronics, Lodz University of Technology, 1/15 Stefanowski Street, 90-924 Lodz, Poland*
[2] *Department of Vehicles, Warsaw University of Technology, 84 Narbutta Street, 02-524 Warszawa, Poland*
[3] *Department of Mathematics and Modeling, Saratov State Technical University, Russian Federation, Politehnicheskaya 77, Saratov 410054, Russia*

Correspondence should be addressed to J. Awrejcewicz; awrejcew@p.lodz.pl

Received 27 June 2013; Accepted 19 December 2013; Published 1 July 2014

Academic Editor: Nuno Maia

Copyright © 2014 J. Awrejcewicz et al. This is an open access article distributed under the Creative Commons Attribution License, which permits unrestricted use, distribution, and reproduction in any medium, provided the original work is properly cited.

Nonlinear dynamics of flexible rectangular plates subjected to the action of longitudinal and time periodic load distributed on the plate perimeter is investigated. Applying both the classical Fourier and wavelet analysis we illustrate three different Feigenbaum type scenarios of transition from a regular to chaotic dynamics. We show that the system vibrations change with respect not only to the change of control parameters, but also to all fixed parameters (system dynamics changes when the independent variable, time, increases). In addition, we show that chaotic dynamics may appear also after the second Hopf bifurcation. Curves of equal deflections (isoclines) lose their previous symmetry while transiting into chaotic vibrations.

1. Introduction

Plates as thin-walled structural members are widely applied in various branches of industry, civil engineering, and factories producing measurement devices. Nowadays modeling procedures and dynamics investigation are very complex and require confirmation of the reliability and validity of results obtained. One of the ways to get more reliable results is to develop more adequate mathematical models for studying of continuous mechanical systems. The developed models are expected to exhibit important nonlinear effects including the influence of geometric nonlinearity as well as external load properties on the system chaotic dynamics. Nonlinear vibrations of real continuous systems can be very complicated. Majority of the signals (time series) obtained through the numerical experiments are nonstationary ones; that is, they strongly change in time. Therefore, in spite of the traditional approaches, including FFT (fast Fourier transform), additional methods are highly required. We illustrate the advantages of application of wavelet transforms for detecting and monitoring local properties of the analyzed time series (signals). The latter approach allows for the detection of local signal properties.

It is clear that modeling of plates/shells dynamics has a long history, and there are numerous papers and monographs dedicated to this research area. We refer only to a few of them more adequately fitting our research aims and the used methods. The existence of heteroclinic loops, Smale horseshoes, chaotic dynamics, and symmetry breaking phenomena of a nearly squared plate are discussed in [1, 2].

Chaotic vibrations of a shallow cylindrical shell subjected to harmonic lateral excitation are studied via the Galerkin approach allowing for a reduction of the initial infinite problem to that of finite dimension (multiple degrees of freedom) by Yamaguchi and Nagai [3]. Luo derived analytical conditions for the chaotic dynamics of axially travelling thin plates using the incremental energy approach. Poincaré mapping sections are used for monitoring of chaotic motions in primary resonant and homoclinic separation zones [4]. Nonlinear dynamics of bimetallic circular plates under time-varying temperature load is studied by Wang [5], where the onset of chaos, transient chaos, period doubling, and reversed period doubling scenario, among other items, are illustrated and discussed. A transition from regular to wave turbulence regime exhibited by thin plates harmonically loaded is illustrated and discussed in references [6, 7].

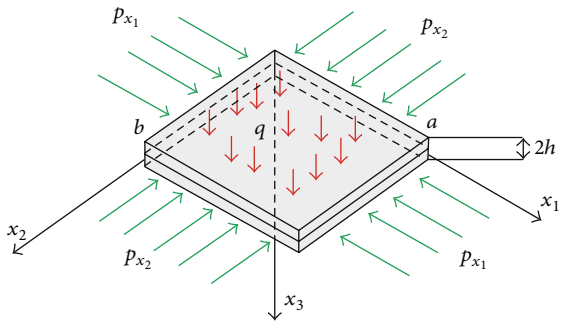

FIGURE 1: Plate computational scheme.

Transitions into the system with finite (many) degrees of freedom chaotic dynamics are reported in a series of references [8–12]. The advantages of wavelet-oriented analysis of nonlinear vibrations of continuous mechanical systems are described in [13]. Although we aim here at numerical investigations, it should be noted that there is a possibility to apply the method of an artificial perturbation parameter to study nonlinear plate vibrations [14].

2. Differential and Difference Governing Equations

The mathematical model of vibrations of a flexible rectangular plate (shown in Figure 1) with constant stiffness subjected to the action of time periodic longitudinal load distributed along the plate perimeter is constructed on the basis of the kinematic Kirchhoff-Love approach taking into account the nonlinear dependence between deformations and displacements. We introduce small initial static load in the initial time interval $t \in [0; 1]$. In rectangular coordinates the system of 3D space is presented in the following form:

$$\Omega = \{x_1, x_2, x_3 \mid (x_1, x_2) \in [0; a] \times [0; b], \quad x_3 \in [-h; h]\}, \quad 0 \le t < \infty. \tag{1}$$

We apply the following nondimensional PDEs governing dynamics of our plate:

$$\begin{aligned} &\frac{1}{12(1-\mu^2)}\left(\nabla_\lambda{}^4 w\right) - L(w, F) + \frac{\partial^2 w}{\partial t^2} \\ &\quad + \varepsilon\frac{\partial w}{\partial t} - q(x_1, x_2, t) = 0, \\ &\nabla_\lambda{}^4 F + \frac{1}{2}L(w, w) = 0, \end{aligned} \tag{2}$$

where

$$\begin{aligned} \nabla_\lambda{}^4 &= \frac{1}{\lambda^2}\frac{\partial^4}{\partial x_1{}^4} + \lambda^2\frac{\partial^4}{\partial x_2{}^4} + 2\frac{\partial^4}{\partial x_1{}^2 \partial x_2{}^2}, \\ L(w, F) &= \frac{\partial^2 w}{\partial x_1{}^2}\frac{\partial^2 F}{\partial x_2{}^2} + \frac{\partial^2 w}{\partial x_2{}^2}\frac{\partial^2 F}{\partial x_1{}^2} - 2\frac{\partial^2 w}{\partial x_1 \partial x_2}\frac{\partial^2 F}{\partial x_1 \partial x_2} \end{aligned} \tag{3}$$

are the nonlinear operators and w and F are the functions describing deflection and stresses, respectively.

Simple boundary conditions are attached to (2):

$$\begin{aligned} &w = 0; \quad \frac{\partial^2 w}{\partial x_1{}^2} = 0; \quad F = 0; \quad \frac{\partial^2 F}{\partial x_1{}^2} = p_{x_2} \\ &\qquad \text{for } x_1 = 0; 1; \\ &w = 0; \quad \frac{\partial^2 w}{\partial x_2{}^2} = 0; \quad F = 0; \quad \frac{\partial^2 F}{\partial x_2{}^2} = p_{x_1} \\ &\qquad \text{for } x_2 = 0; 1, \end{aligned} \tag{4}$$

and the following initial conditions are applied:

$$w(x_1, x_2)\big|_{t=0} = 0, \qquad \left.\frac{\partial w}{\partial t}\right|_{t=0} = 0. \tag{5}$$

Equations (2)–(5) are reduced to the nondimensional form using the following nondimensional parameters: $\lambda = a/b$; $x_1 = a\overline{x}_1$, $x_2 = b\overline{x}_2$ are the nondimensional parameters regarding x_1 and x_2, respectively; $w = 2h\overline{w}$ is the deflection; $F = E(2h)^3\overline{F}$ is the stress function; $t = t_0\overline{t}$ is time; $q = (E(2h)^4/a^2b^2)\overline{q}$ is the external pressure; $\varepsilon = (2h)\overline{\varepsilon}$ is the damping coefficient; and $p = E(2h)^3\overline{p}$ is the external longitudinal load. Bars over the nondimensional quantities are already omitted in the governing equations. Additionally, a and b are the plate dimensions regarding x_1 and x_2, respectively; μ is Poisson's coefficient.

In "Mechanics" the degrees of freedom are understood as the set of independent coordinates, which together with their time derivatives describe the mechanical system state [15]. The choice of the number of degrees of freedom of the studied system depends on a real system behavior. Since in majority of the real world mechanical systems the constraints are not absolutely stiff, the real number of degrees of freedom equals a triple number of the atoms associated with the system material volume. In the case of the continuous system we deal with the infinite number of degrees of freedom. In many cases in the engineering practice, approximations are used which enable a drastic decrease of the degrees of freedom, not exceeding six. It is clear that this drastic approximation may lead either directly to erroneous results, that is decrease of modes number.

Dynamical systems may exhibit four different types of stationary regimes: equilibrium, periodic, quasiperiodic, and chaotic dynamics. The mentioned regimes are associated with attractors in the form of a stable equilibrium point, limit cycle, and quasiperiodic attractor (multiple dimensional torus) as well as strange chaotic attractor, respectively. Recall that the quasiperiodic and chaotic attractors may appear in dynamical systems with the space phase dimension being larger than three.

In order to reduce a continuous system to the system with lumped parameters regarding spatial variables x_1 and x_2, the FDM (finite difference method) with approximation of $O(h^2)$ is applied, allowing us to consider flexible rectangular plates

Table 1: Plate bifurcations.

Points		1st bifurcation	2nd bifurcation	3rd bifurcation	4th bifurcation	Difference between theoretical and computed value in %
12	$S_{0,n}$	13.675	13.735	13.7465	13.74894	
	d_n		5.217391	4.713115		0.22006
14	$S_{0,n}$	13.44	13.49	13.500078125	13.502232	
	d_n		4.96124...	4.67906679...	...	0.21847
16	$S_{0,n}$	13.27	13.323	13.334	13.33635	
	d_n		4.818182	4.673519		0.21821

as the mechanical systems with infinite degrees of freedom. The application of FDM to the continuous system yields the following set of the difference-operator equations:

$$
\begin{aligned}
&-\frac{1}{12\left(1-\mu^2\right)}\left(\lambda^{-2}\Lambda_1^2 w_{ij}+2\Lambda_{12}^2 w_{ij}+\lambda^2\Lambda_2^2 w_{ij}\right)\\
&\quad-\Lambda_1 w_{ij}\cdot\Lambda_2 F_{ij}-\Lambda_2 w_{ij}\cdot\Lambda_1 F_{ij}+\Lambda_{12} w_{ij}\cdot\Lambda_{12} F_{ij}\\
&\quad+q_i=\left(w_{tt}+\varepsilon w_t\right)_{i,j},\\
&\left(\lambda^{-2}\Lambda_1^2 F_{ij}+2\Lambda_{12}^2 F_{ij}+\lambda^2\Lambda_2^2 F_{ij}\right)\\
&\quad=-\Lambda_1 w_{ij}\cdot\Lambda_2 w_{ij}+\left(\Lambda_{12} w_{ij}\right)^2,
\end{aligned}
\tag{6}
$$

where

$$
\begin{aligned}
\Lambda_i y&=\frac{1}{h_i^2}\left[y\left(x_i-h_i\right)-2\cdot y\left(x_i\right)+y\left(x_i+h_i\right)\right],\\
&\qquad\qquad i=1,2,\\
\Lambda_{12} y&=\frac{1}{4h_1h_2}\left[y\left(x_1+h_1,x_2+h_2\right)+y\left(x_1-h_1,x_2-h_2\right)\right.\\
&\qquad\left.-\left(x_1+h_1,x_2-h_2\right)-\left(x_1-h_1,x_2+h_2\right)\right],\\
\Lambda_i^2 y&=\frac{1}{h_i^4}\left[y\left(x_i-2h_i\right)-4y\left(x_i-h_i\right)+6y\left(x_i\right)\right.\\
&\qquad\left.-4y\left(x_i+h_i\right)+y\left(x_i+2h_i\right)\right]\quad i=1,2,\\
\Lambda_{12}^2 y&=\frac{1}{h_1^2h_2^2}\left[y\left(x_1-h_1,x_2-h_2\right)-2y\left(x_1-h_1,x_2\right)\right.\\
&\qquad+y\left(x_1-h_1,x_2-h_2\right)-2\left(x_1,x_2-h_2\right)\\
&\qquad+4y\left(x_1,x_2\right)-2y\left(x_1,x_2+h_2\right)\\
&\qquad+y\left(x_1+h_1,x_2-h_2\right)\\
&\qquad\left.-2\left(x_1+h_1,x_2\right)+y\left(x_1+h_1,x_2+h_2\right)\right].
\end{aligned}
\tag{7}
$$

Equations (7) are supplemented with boundary conditions (4), which have the following difference representation (flexible nonstretched (uncompressed) ribs support):

$$
\begin{aligned}
&w_{n,j}=0,\qquad w_{n,j}=-w_{n-2,j},\qquad F_{n,j}=0,\\
&F_{n,j}=p_{x_2}+F_{n-2,j},\\
&\qquad\qquad j=1,\ldots,m-1,\\
&w_{i,m}=0,\qquad w_{i,m}=-w_{i,m-2},\qquad F_{i,m}=0,\\
&F_{i,m}=p_{x_1}+F_{i,m-2},\\
&\qquad\qquad i=1,\ldots,n-1,
\end{aligned}
\tag{8}
$$

and the following initial conditions:

$$
\begin{aligned}
w_{ij}&=f_1\left(x_{1k},x_{2k}\right),\qquad w_n'=f_2\left(x_{1k},x_{2k}\right),\\
&\qquad\qquad(0\le k\le n).
\end{aligned}
\tag{9}
$$

After reduction to the normal form, (7)–(9) are solved via the fourth-order Runge-Kutta method, where on each time step we need to solve a large system of linear algebraic equations regarding time, and a time step is yielded by the Runge principle.

3. Numerical Results

One of the fundamental problems of nonlinear dynamics concerns the existence of a threshold between chaotic and multimode turbulent dynamics. In this work we address this problem using a 2D continuous system as the plate, where first we illustrate numerically the scenarios of transitions from periodic to chaotic plate dynamics via period doubling bifurcations. The computed Feigenbaum constant is compared with the known value $d = 4.66916224\ldots$ (see [16]) for different choice of the partition of spatial variables while applying FDM. Values of the series $q_{0,n}$ and d_n versus partition numbers (points) used in FDM are given in Table 1. Observe that an increase of the partition numbers implies an increase of DoF (degrees of freedom) of the studied system. The numerical analysis shows that the approximation to 64 DoF (number of partitions 8) is not sufficient to achieve reliable results regarding the dynamics of studied

continuous mechanical systems in the form of rectangular plates. An increase of DoF of the considered mathematical model implies the earlier illustrated occurrence of the first and successive period doubling bifurcations for the fixed amplitude of the periodic load action. The same holds for the case of chaotic dynamics. However, the obtained results are not in good agreement with the theoretically obtained Feigenbaum constant value. Applying partition number 12 we have good coincidence of the theoretical and computed Feigenbaum constant (the difference is 0.22006%), and the obtained result can be even improved through the increase of the partition number. We have used further 14 points in all computations while applying FDM.

As we have mentioned, we study regular and chaotic dynamics of a rectangular plate simply supported subjected to the periodic load action $p_{x_1} = p_{x_2} = p_0 \sin \omega_p t = p$ on the plate perimeter, where ω_p and p_0 are the frequency and amplitude of the external load, respectively.

Vibrations are studied in the time interval $t \in [0, 286]$, for $\lambda = a/b = 1$, dissipation factor $\varepsilon = 1$, and the Poisson coefficient $\mu = 0.3$. Results obtained for the center of the middle plate surface are generalized into the whole plate [13]. In the numerical experiment with the excitation frequency $\omega_p = 2.9$ a new modified Feigenbaum scenario has been obtained (see Table 2).

First of all it should be emphasized that already for small values of the amplitude of the excitation load with the frequency $\omega_p = 2.9$, the plate vibrates at the frequency $\omega_1 = 1.45$; that is, the first subharmonic vibration regime appears. An increase of the amplitude of the longitudinal load forces the plate to vibrate harmonically, but a further increase of this parameter provokes the occurrence of frequencies associated with the second bifurcation ($\omega_3 = 0.725$ and $\omega_2 = 2.175$), and the obtained frequencies have the power that is essentially higher than that corresponding to the frequency $\omega_p = 2.9$. When the excitation amplitude achieves 0.749, new frequency $\omega_1 = 1.45 = \omega_p/2$ appears. The power of frequencies ω_1 and ω_p are commensurable but essentially lesser than the powers corresponding to frequencies ω_3 and ω_2. Therefore, after the third bifurcation, the plate exhibits chaotic dynamics in the whole time interval. The curves of equal deflection lose their symmetry only in the chaotic plate vibration regime.

Since we study the squared plate ($\lambda = 1$) and since the same load is applied to all plate edges, the equal deflection curves are called symmetric only if they have four axes of symmetry.

A numerical experiment, where the excitation frequency coincides with plate natural frequency ($\omega_p = \omega_0 = 5.8$), allowed us to monitor the Feigenbaum scenario to chaos different from the so far illustrated scenarios (Table 3). Here for small load amplitude we have harmonic vibrations, but its increase implies the occurrence of the next bifurcation and also an essential modification of vibration properties, which is well characterized by the 2D wavelet spectrum for $P = 0.8$. In the initial part of the studied time interval the excitation frequency dominates, whereas for $t \approx 50$ a key role plays $\omega_1 = 2.9 = \omega_p/2$. Since in this case the change of the system vibrations is realized via a narrow chaotic window, then a direct application of the classical Fourier analysis to this case is not suitable. Namely, it does not allow us to monitor peculiarities of time evolutions of the frequency characteristics of the studied vibrations.

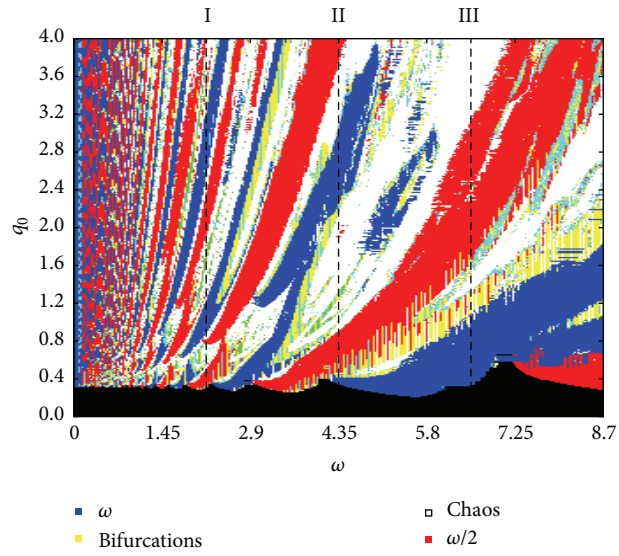

Figure 2: Chart of the character of plate vibrations.

It should be emphasized that in each of the considered time intervals we compare the obtained results with the wavelet spectrum, and the results obtained through different methods, that is, the Fourier and wavelet analyses, coincide with each other. The second bifurcation takes place for $p = 1.1$ and it appears for $t \geq 126$. A further increase of the excitation amplitude implies the occurrence of intermittency windows, which finally pulls the system into chaotic dynamics exhibited in the whole time interval. The so far described process is well illustrated via the 2D frequency wavelet spectra. Symmetry breaking of the curves of equal deflections appears only in chaotic zones.

The scenario detected via a third experiment ($\omega_p = 8.7$) begins, as in the previous case, with superiority of the first bifurcation (Table 4). Then the spectrum is periodic and an increase of the excitation frequency implies the occurrence of the first and second bifurcations. It should be emphasized that after the second bifurcation the intermittency windows occur on the wavelet spectrum, which then play a key role in the road to chaos. Another important observation is that symmetry breaking of the curves having equal deflections (isoclines) occurs already for the quasiperiodic vibrations, and the vibrations associated with the second bifurcation ($p = 2.1$) exhibit only two axes of symmetry. Chaotic plate vibrations violate in full the previous symmetry of isoclines.

We follow here a recipe given by H. Poincaré, who suggested to study instead of only one solution, a set of solutions for the chosen control parameters. Here we take the amplitude and frequency of the excitation acting on the plate perimeter as two control parameters. In order to construct a vibration type chart with the resolution 300×300, we solved and analyzed 90 000 numerical problems (Figure 2). Each of the tasks required a construction and study of time

Table 2: Applied dynamic characteristics ($\omega_p = 2.9$).

p_0 $\omega_p = 2.9$	Poincaré map $w_t(w_{t+T})$	Fourier power spectrum $S(\omega)$	Curves of equal deflections	2D Morlet wavelet
0.4	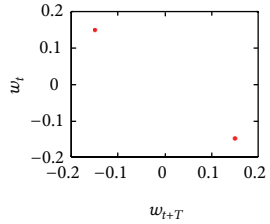	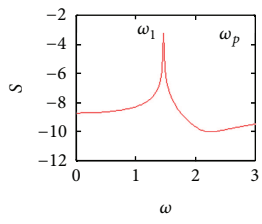	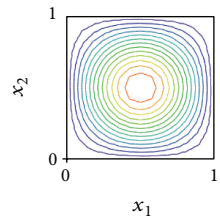	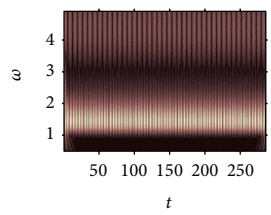
0.5	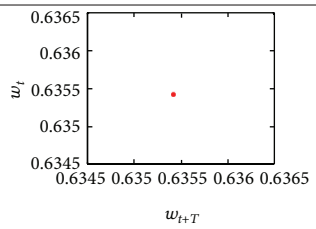	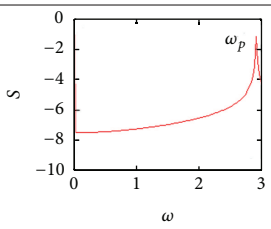	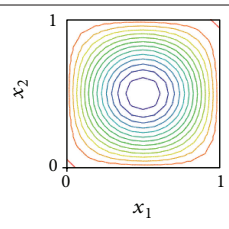	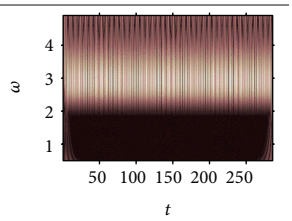
0.745	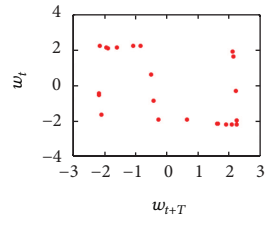	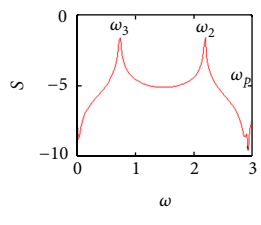	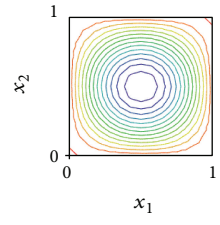	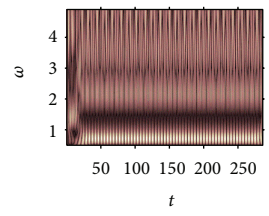
0.749	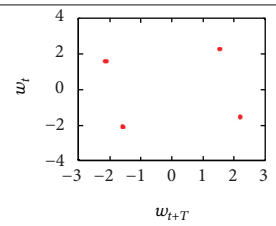	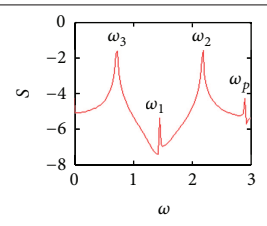	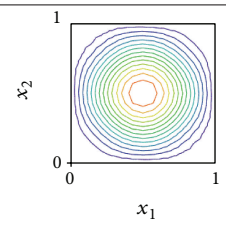	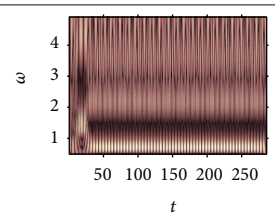
0.75	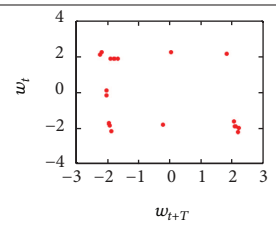	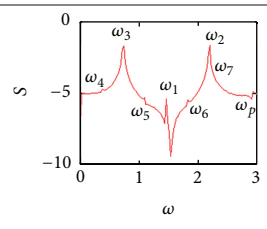	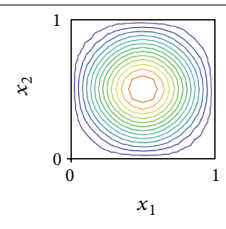	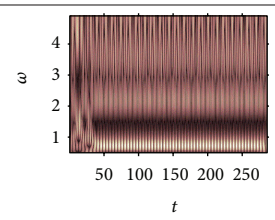
0.95	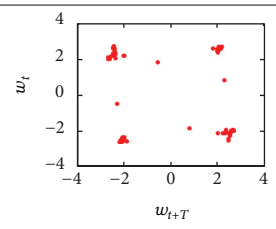	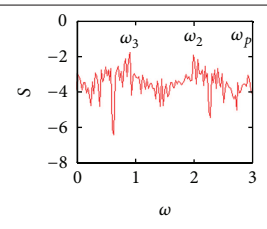	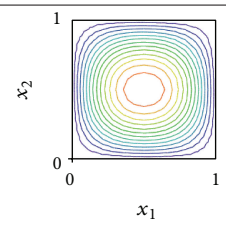	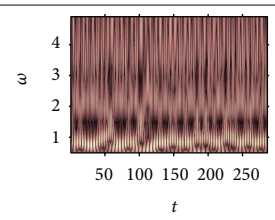

series (signals), phase and modal portraits, Poincaré maps, Fourier and wavelet spectra, autocorrelation functions, and the Lyapunov exponents. Owing to the results reported in the chart, for small load amplitudes, a zone of damped oscillations is observed. For small frequency values $\omega \leq 2$, narrow subharmonic zones are interlaced with narrow zones of periodic vibrations. An increase of the excitation frequency implies an increase of the area of these zones and their mixing with chaotic zones. The occurrence of a large amount of subharmonic vibrations corresponds to the physical aspect of the studied process which can be treated as the reliability and validity confirmation of the obtained numerical results.

Table 3: Applied dynamic characteristics ($\omega_p = \omega_0 = 5.8$).

p_0 $\omega_p = \omega_0 = 5.8$	Poincaré map $w_t(w_{t+T})$	Fourier power spectrum $S(\omega)$	Curves of equal Deflections $w(x_1, x_2)$	2D Morlet wavelet spectrum
0.3	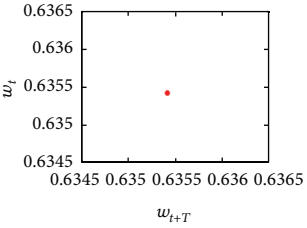	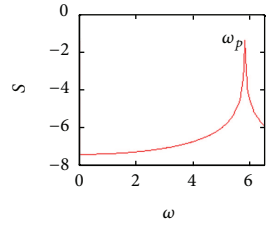	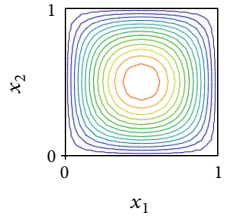	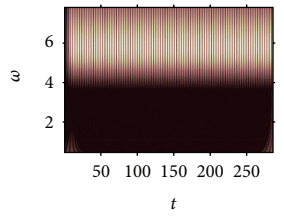
0.9	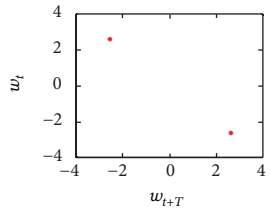	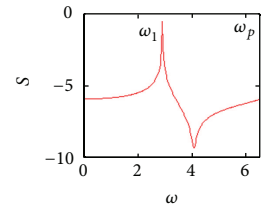	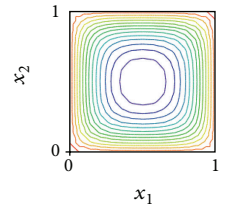	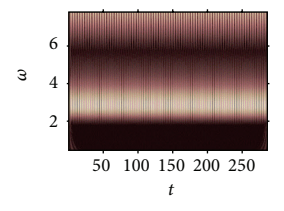
1.1	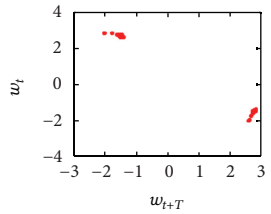	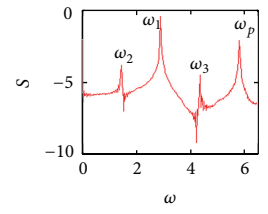	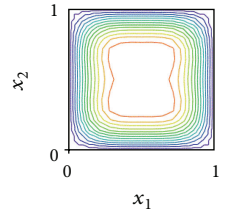	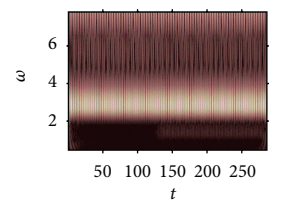
		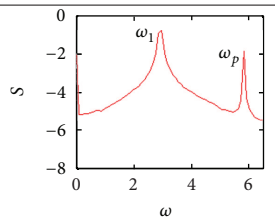 $p = 1.1,\ t \in [0, 125]$	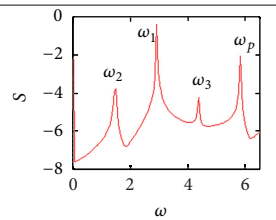 $p = 1.1, t \in [126, 286]$	
1.15	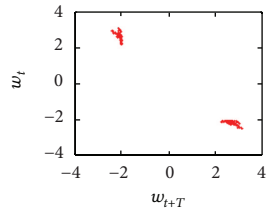	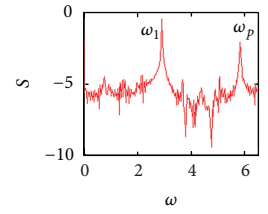	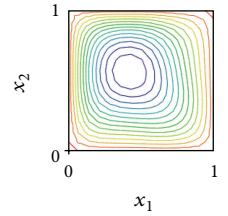	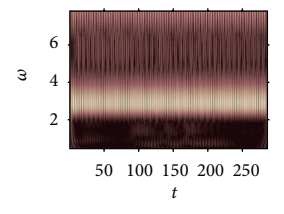
2.05	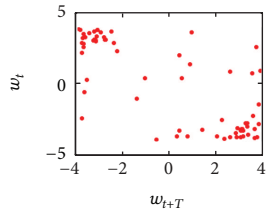	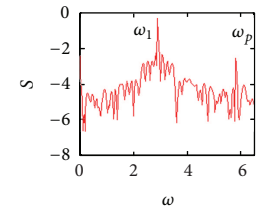	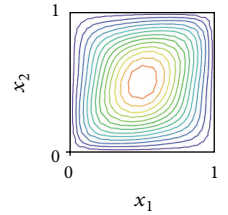	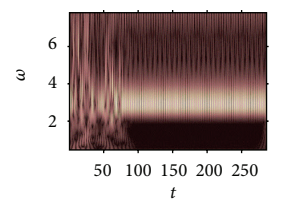
2.1	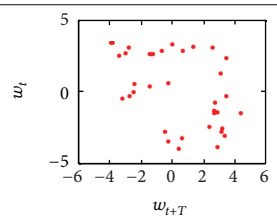	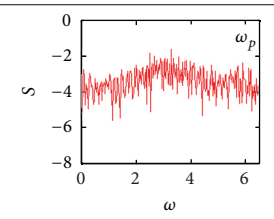	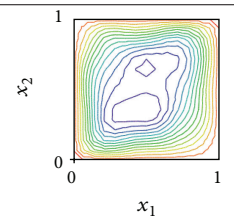	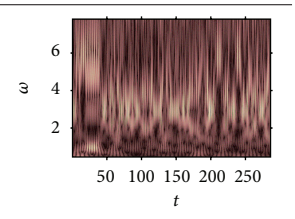

Table 4: Applied dynamic characteristics ($\omega_p = 8.7$).

p_0 $\omega_p = 8.7$	Poincaré map $w_t(w_{t+T})$	Fourier power spectrum $S(\omega)$	Curves of equal Deflections $w(x_1, x_2)$	2D Morlet wavelet spectrum
0.3	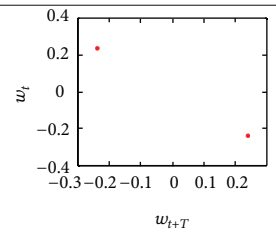	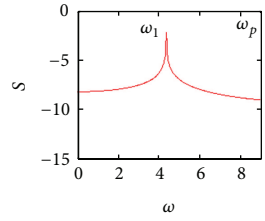	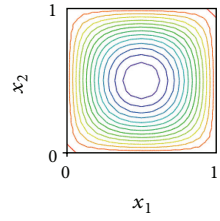	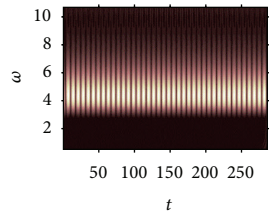
0.65	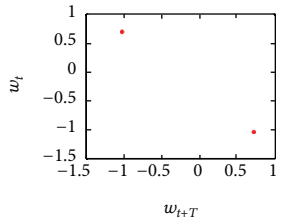	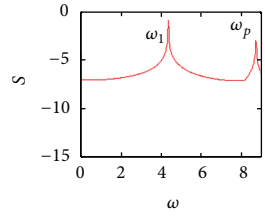	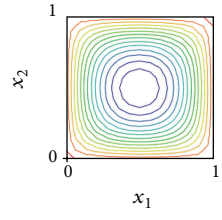	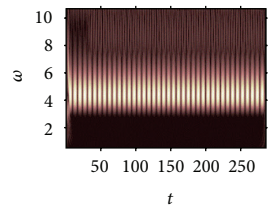
0.75	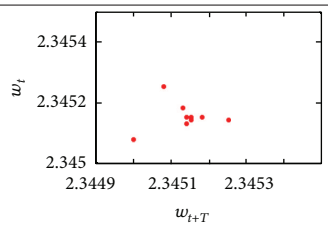	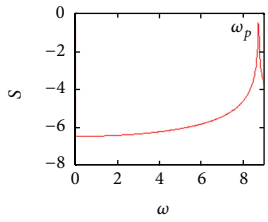	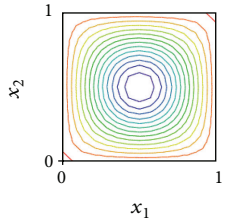	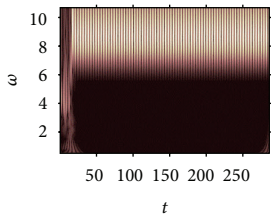
1.1	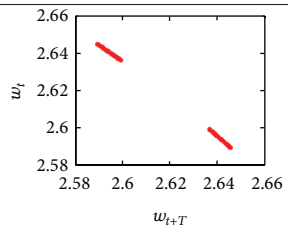	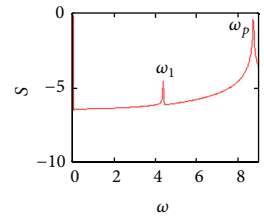	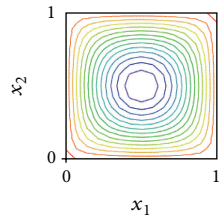	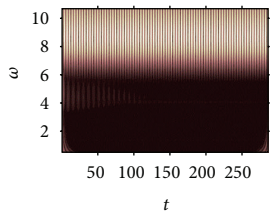
2.1	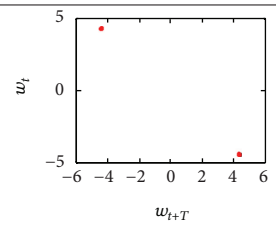	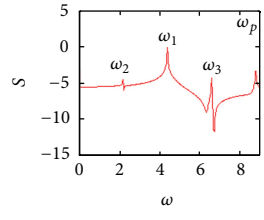	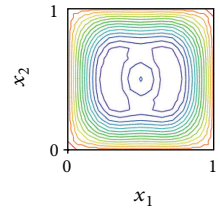	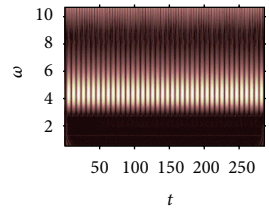
2.7	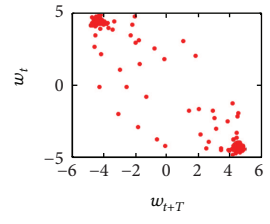	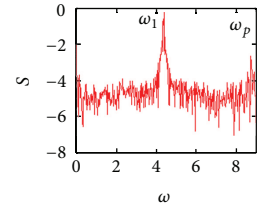	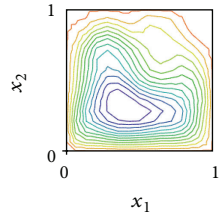	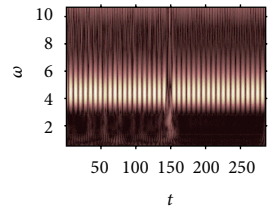

4. Concluding Remarks

In this work a simultaneous application of the Fourier and wavelet analyses allowed us to construct three different modifications of the classical Feigenbaum scenarios. It has been reported and illustrated that the plate vibration type undergoes qualitative changes not only in a standard way through the changes of the values of system parameters but also for the all fixed parameters; that is, vibrations change qualitatively when time is increased. This problem refers to estimation of the computational time unless an attractor is finally achieved. We have shown in Table 3 ($p = 1.1$) that for

simulation interval of the nondimensional time [0, 125] the Fourier spectrum exhibits only two frequencies ω_p and ω_1. However, within time interval (126,286) our investigated system undergoes a second bifurcation associated with occurrence of two additional frequencies, ω_2 and ω_3.

It has also been shown that chaos appears already after the second Hopf bifurcation. It has been illustrated that in all studied cases the symmetry breaking of the curves of equal deflections (isoclines) occurs while transiting into a chaotic regime.

The constructed vibration chart allows us to control the dynamics of a studied continuous mechanical system. Namely, one may choose parameters of the system keeping its dynamics in a safe periodic regime. When the system dynamics is shifted into a chaotic zone, this causes loss of its stability and catastrophe.

Conflict of Interests

The authors declare that there is no conflict of interests regarding the publication of this paper.

Acknowledgments

This work has been supported by the National Center of Science under the Grant MAESTRO 2, no. 2012/04/A/ST8/00738 for the years 2012–2015 (Poland). J. Awrejcewicz acknowledges also a support of the Humboldt Foundation Award.

References

[1] X. L. Yang and P. R. Sethna, "Local and global bifurcations in parametrically excited vibrations of nearly square plates," *International Journal of Non-Linear Mechanics*, vol. 26, no. 2, pp. 199–220, 1991.

[2] X. L. Yang and P. R. Sethna, "Non-linear phenomena in forced vibrations of a nearly square plate: antisymmetric case," *Journal of Sound and Vibration*, vol. 155, no. 3, pp. 413–441, 1992.

[3] T. Yamaguchi and K. Nagai, "Chaotic vibrations of a cylindrical shell-panel with an in-plane elastic-support at boundary," *Nonlinear Dynamics*, vol. 13, no. 3, pp. 259–277, 1997.

[4] A. C. J. Luo, "Chaotic motions in resonant separatrix zones of periodically forced, axially travelling, thin plates," *Proceedings of the Institution of Mechanical Engineers K: Journal of Multi-Body Dynamics*, vol. 219, no. 3, pp. 237–247, 2005.

[5] Y. Wang, "Bifurcations and chaos of bimetallic circular plates subjected to periodic heat load," *Zeitschrift für Angewandte Mathematik und Mechanik*, vol. 88, no. 4, pp. 256–266, 2008.

[6] C. Touzé, O. Thomas, and M. Amabili, "Transition to chaotic vibrations for harmonically forced perfect and imperfect circular plates," *International Journal of Non-Linear Mechanics*, vol. 46, no. 1, pp. 234–246, 2011.

[7] C. Touzé, S. Bilbao, and O. Cadot, "Transition scenario to turbulence in thin vibrating plates," *Journal of Sound and Vibration*, vol. 331, no. 2, pp. 412–433, 2012.

[8] M. Amabili, A. Sarkar, and M. P. Païdoussis, "Chaotic vibrations of circular cylindrical shells: Galerkin versus reduced-order models via the proper orthogonal decomposition method," *Journal of Sound and Vibration*, vol. 290, no. 3–5, pp. 736–762, 2006.

[9] J. Awrejcewicz, V. A. Krysko, and A. V. Krysko, "Spatio-temporal chaos and solitons exhibited by von Kármán model," *International Journal of Bifurcation and Chaos in Applied Sciences and Engineering*, vol. 12, no. 7, pp. 1465–1513, 2002.

[10] J. Awrejcewicz, V. A. Krysko, I. V. Papkova, and A. V. Krysko, "Routes to chaos in continuous mechanical systems. Part 1: mathematical models and solution methods," *Chaos, Solitons and Fractals*, vol. 45, no. 6, pp. 687–708, 2012.

[11] A. V. Krysko, J. Awrejcewicz, I. V. Papkova, and V. A. Krysko, "Routes to chaos in continuous mechanical systems. Part 2: modelling transitions from regular to chaotic dynamics," *Chaos, Solitons and Fractals*, vol. 45, no. 6, pp. 709–720, 2012.

[12] J. Awrejcewicz, A. V. Krysko, I. V. Papkova, and V. A. Krysko, "Routes to chaos in continuous mechanical systems. Part 3: the Lyapunov exponents, hyper, hyper-hyper and spatial-temporal chaos," *Chaos, Solitons and Fractals*, vol. 45, no. 6, pp. 721–736, 2012.

[13] J. Awrejcewicz, I. V. Papkova, E. U. Krylova, and V. A. Krysko, "Wavelet-based analysis of the regular and chaotic dynamics of rectangular flexible plates subjected to shear-harmonic loading," *Shock and Vibration*, vol. 19, no. 5, pp. 979–994, 2012.

[14] I. V. Andrianov, V. V. Danishevs'Kyy, and J. Awrejcewicz, "An artificial small perturbation parameter and nonlinear plate vibrations," *Journal of Sound and Vibration*, vol. 283, no. 3–5, pp. 561–571, 2005.

[15] J. Awrejcewicz, *Classical Mechanics—Dynamics*, Springer, New York, NY, USA, 2012.

[16] M. J. Feigenbaum, "Quantitative universality for a class of nonlinear transformations," *Journal of Statistical Physics*, vol. 19, no. 1, pp. 25–52, 1978.

Hindawi Publishing Corporation
Shock and Vibration
Volume 2014, Article ID 260206, 8 pages
http://dx.doi.org/10.1155/2014/260206

Research Article

Satellite Attitude Control System Design considering the Fuel Slosh Dynamics

Luiz Carlos Gadelha de Souza and Alain G. de Souza

National Institute for Space Research (INPE/DMC), Avenida dos Astronautas 1758, 12227-010 São José dos Campos, SP, Brazil

Correspondence should be addressed to Luiz Carlos Gadelha de Souza; gadelha@dem.inpe.br

Received 26 June 2013; Accepted 8 January 2014; Published 26 June 2014

Academic Editor: Nuno Maia

Copyright © 2014 L. C. G. de Souza and A. G. de Souza. This is an open access article distributed under the Creative Commons Attribution License, which permits unrestricted use, distribution, and reproduction in any medium, provided the original work is properly cited.

The design of the satellite attitude control system (ACS) becomes more complex when the satellite structure has different type of components like, flexible solar panels, antennas, mechanical manipulators, and tanks with fuel. A crucial interaction can occur between the fuel slosh motion and the satellite rigid motion during translational and/or rotational manoeuvre since these interactions can change the satellite centre of mass position damaging the ACS pointing accuracy. Although, a well-designed controller can suppress such disturbances quickly, the controller error pointing may be limited by the minimum time necessary to suppress such disturbances thus affecting the satellite attitude acquisition. As a result, the design of the satellite controller needs to explore the limits between the conflicting requirements of performance and robustness. This paper investigates the effects of the interaction between the liquid motion (slosh) and the satellite dynamics in order to predict what the damage to the controller performance and robustness is. The fuel slosh dynamics is modelled by a pendulum which parameters are identified using the Kalman filter technique. This information is used to design the satellite controller by the linear quadratic regulator (LQR) and linear quadratic Gaussian (LQG) methods to perform a planar manoeuvre assuming thrusters are actuators.

1. Introduction

The problem of interaction between fluid and structure is important when one needs to study the dynamic behavior of offshore and marine structures and road and railroad containers partially filled with a fluid [1, 2]. In space missions the sloshing problem appears when the spacecraft is spinning and there is liquid inside it. An example is the damp device involving fluid as the damping material, whose motion can interact with flexible panels and/or manipulators [3]. An interesting approach to analyze a rigid container mounted on flexible springs interacting with a perfect fluid including sloshing effects has been done by Lui and Lou [4]. The success of a space mission can depend on taking into account the knowledge of the interaction between fluid motion (slosh) and structure dynamics since this interaction can damage the ACS pointing requirements. A space structure, like rockets, geosynchronous satellites, and the space station, usually contains liquid in tanks that can represent more than 40% of the initial mass of the system. As a result, the first step to design its ACS is to obtain a detailed dynamics model of the space structure. When the fuel tanks are only partially filled and suffer a transverse acceleration and/or rotational motion, large quantities of fuel move uncontrollably inside the tanks and generate the sloshing effects. Agrawal [5] has shown that the dynamics interaction between the fuel motion and the rigid and/or flexible body dynamics can result in some kind of control instability. For minimizing these effects the ACS must be designed using a robust control method in order to assure stability and good performance to achieve the attitude control system requirement [6]. When a rigid-flexible satellite with fuel tanks inside is subjected to large angle manoeuvre its dynamics is only captured by complex nonlinear mathematical model. Besides, the remaining flexible and/or liquid vibration can introduce a tracking error resulting in a minimum attitude acquisition time. Souza [7] has done a detailed investigation of the influence of the nonlinearities introduced by the panel's flexibility into the ACS design. It was shown that system parameters variation can degrade the control system performance, indicating the necessity to improve

the ACS robustness. An experimental controller robustness and performance investigation was done by Conti and Souza [8], where the estimation of the platform inertia parameters was introduced as part of the platform ACS design. The problem of designing satellite nonlinear controller for rigid satellite has been done by Souza and Gonzales [9] using the state-dependent Riccati equation (SDRE) method which is able to deal with high nonlinear plants. Due to the complexity of modeling the fluid and/or flexible dynamic of the system it is common to use mechanical systems analogies that describe this dynamic. Besides, if one needs to know some physical parameters related with the slosh or the flexibility dynamics it is common to obtain them by experimental apparatus or some kind of estimating method such as Kalman filter [10].

2. Satellite with Sloshing Model

The phenomenon of sloshing is due to the movement of a free surface of a liquid that partially fills a compartment and this movement is oscillating. It depends on the shape of the tank, the acceleration of the gravity, and on the axial/rotational acceleration of the tank. As a representative of the behavior of the total weight of the system it is accepted that when the mass of the liquid oscillates the mass center of the rigid body also oscillates, thereby disturbing the rigid-flexible part of the vehicle under consideration. As an oscillating movement it is natural to consider the wave generated by the movement of the liquid as a stationary wave in all oscillation modes. Each mode of oscillation has a special feature of this phenomenon under study and one observes, in a quantitative sense, how much mass is displaced. Among all the modes that cause the greatest disruption in the system are the first and the second modes. Despite the fact that oscillation has lower frequency it is capable of resulting in violent shifting of the center of mass of the liquid creating an oscillation in the system as a role. The other oscillation modes act as a less aggressive and it may not even vary the position of its center of mass due to the symmetry of the wave which on average causes no displacement. Due to its complexity, the sloshing dynamics is usually represented by mechanical equivalents that describe and reproduce faithfully the actions and reactions due to forces and torques acting on the system. The main advantage of replacing the fluid model with an equivalent oscillating model [11] is simplifying the analysis of motion in the rigid body dynamics compared to the fluid dynamics equations. Due to the complexity of establishing an analytical model for the fluid moving freely within a closed tank, a simplified system is used, taking into account the following criteria [6]: (a) small displacements, (b) a rigid tank, and (c) no viscous, incompressible, and homogeneous liquid. Under these conditions the dynamics of the sloshing can be approximated by mechanical system consisting of a mass-spring or pendulum. Consider a rigid spacecraft moving in a fixed plane with a spherical fuel tank and including the lowest frequency slosh mode. Based on the Lagrange equation and the Rayleigh dissipation function one can model systems using the mechanical mass-spring and pendulum type system, respectively. Figure 1 shows a satellite model where slosh dynamics is represented by its pendulum analogous mechanical system, where the mass of the satellite and the moment of inertia, regardless of the fuel, are given by m and I, respectively, and the mass equivalent of fuel and its inertia moment are given by M_f and I_f, respectively. The attitude control of the spacecraft is done by the force f and by the pitch moment M. The constant thrust F is responsible for the orbital transfer of the spacecraft with respect to the inertial reference system (x, y, z) and it acts on the center of mass of spacecraft in the longitudinal axis. Also it is given the velocity of the center of the fuel tank v_x, v_z and the attitude angle θ of the spacecraft with respect to a fixed reference (X, Y, Z). Besides, V represents the linear velocity and ω represents the angular velocity of the rigid body. The length of the pendulum is a, the distance from satellite center of mass to the pendulum connected point is b, and the angle of the pendulum with respect to the spacecraft longitudinal axis is ψ, which is assumed in the equilibrium position ($\psi = 0$) about the reference axis X.

3. The Satellite Equations of Motion

The satellite equations of motion can be derived using the Lagrange equations [10] given by

$$\begin{aligned} \frac{\mathrm{d}}{\mathrm{dt}}\left(\frac{\partial L}{\partial V}\right) + \omega^{\times}\frac{\partial L}{\partial V} &= \tau_t, \\ \frac{\mathrm{d}}{\mathrm{dt}}\left(\frac{\partial L}{\partial \omega}\right) + \omega^{\times}\frac{\partial L}{\partial \omega} + V^{\times}\frac{\partial L}{\partial V} &= \tau_r, \\ \frac{\mathrm{d}}{\mathrm{dt}}\left(\frac{\partial L}{\partial \dot{\psi}}\right) - \frac{\partial L}{\partial \psi} + \frac{\partial R}{\partial \dot{\psi}} &= 0. \end{aligned} \tag{1}$$

Details of the equations of motion derivation can be found in [12], where L is the Lagrangian of the system, the generalized coordinates are V and ω, R is the Rayleigh dissipation function, τ_r is the internal torque, and τ_t is the external torque. Assume that $R, \tau_r, \tau_t, \omega, V$ are given by

$$\begin{aligned} R &= \frac{1}{2}\varepsilon\dot{\psi}^2; \qquad V = \begin{bmatrix} v_x \\ 0 \\ v_z \end{bmatrix}; \qquad \omega = \begin{bmatrix} 0 \\ \dot{\theta} \\ 0 \end{bmatrix}; \\ \tau_t &= \begin{bmatrix} F \\ 0 \\ f \end{bmatrix}; \qquad \tau_r = \begin{bmatrix} 0 \\ M + fb \\ 0 \end{bmatrix}. \end{aligned} \tag{2}$$

The position vector of the satellite mass center with respect to the inertial reference system (x, y, z) (see Figure 1) is

$$\vec{r} = (x - b)\, i + z\hat{k}. \tag{3}$$

Assuming the relations $v_x = \dot{x} + z\dot{\theta}$ and $v_z = \dot{z} - x\dot{\theta}$ the satellite velocity is given by

$$\dot{\vec{r}} = v_x\hat{i} + \left(v_z + b\dot{\theta}\right)\hat{k}. \tag{4}$$

The position of the mass of fuel with respect to the inertial reference system (x, y, z) (see Figure 1) is given by

$$\vec{r}_f = \left(x - a\cos(\psi)\right)\hat{i} + \left(z + a\sin(\psi)\right)\hat{k}. \tag{5}$$

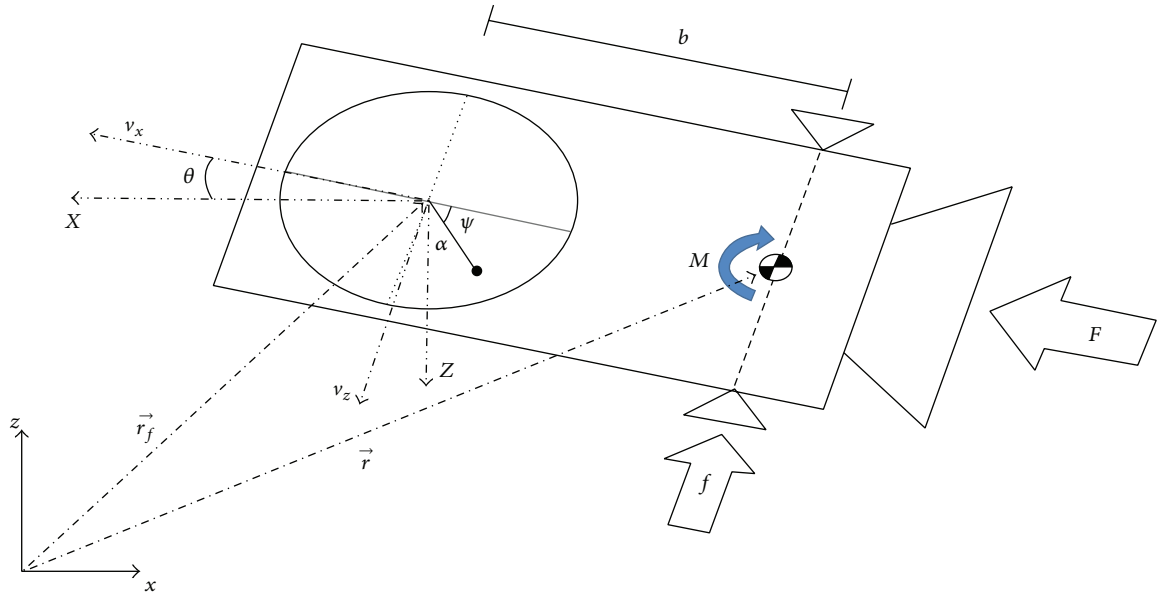

Figure 1: Satellite model with slosh dynamics pendulum analogous mechanical system.

As a result, the mass of the fuel velocity is

$$\dot{\vec{r}}_f = \left(v_x + a\sin(\psi)\left(\dot{\theta}+\dot{\psi}\right)\right)\hat{i} + \left(v_z + a\cos(\psi)\left(\dot{\theta}+\dot{\psi}\right)\right)\hat{k}. \tag{6}$$

The Lagrangian of the entire system is given by

$$L = \frac{1}{2}m\dot{\vec{r}}^2 + \frac{1}{2}m_f\dot{\vec{r}}_f^2 + \frac{1}{2}I_f\left(\dot{\theta}+\dot{\psi}\right)^2 + \frac{1}{2}I\dot{\theta}^2. \tag{7}$$

Substituting (4) and (6) into (7), using the relations given by (2), and performing the derivations of (1), one obtains the satellite equations of motion given by

$$\left(m+m_f\right)\left(\dot{v}_x + v_z\dot{\theta}\right) + mb\dot{\theta} + m_f a\left(\ddot{\psi}+\ddot{\theta}\right)\sin(\psi) + m_f a\left(\dot{\theta}+\dot{\psi}\right)^2\cos(\psi) = F, \tag{8}$$

$$\left(m+m_f\right)\left(\dot{v}_z - v_x\dot{\theta}\right) + m_f a\left(\ddot{\theta}+\ddot{\psi}\right)\cos(\psi) - m_f a\left(\dot{\theta}+\dot{\psi}\right)^2\sin(\psi) mb\ddot{\theta} = f, \tag{9}$$

$$\left(I_f + mb^2\right)\ddot{\theta} + mb\left(\dot{v}_z - v_x\dot{\theta}\right) - \varepsilon\dot{\psi} = M + bf, \tag{10}$$

$$\left(m_f a^2 + I_f\right)\left(\ddot{\theta}+\ddot{\psi}\right) + m_f a\left(\left(\dot{v}_x + v_z\dot{\theta}\right)\sin(\psi) + \left(\dot{v}_z - v_x\dot{\theta}\right)\cos(\psi)\right) + \varepsilon\dot{\psi} = 0. \tag{11}$$

Assuming the relations $a_x = \dot{v}_x + v_z\dot{\theta}$, $a_z = \dot{v}_z - v_x\dot{\theta}$ and substituting them into (8) and (9), one can isolate and obtain the satellite accelerations given by

$$a_x = \frac{F - mb\dot{\theta} - m_f a\left(\ddot{\psi}+\ddot{\theta}\right)\sin(\psi) - m_f a\left(\dot{\theta}+\dot{\psi}\right)^2\cos(\psi)}{m+m_f},$$

$$a_z = \frac{f - m_f a\left(\ddot{\theta}+\ddot{\psi}\right)\cos(\psi) + m_f a\left(\dot{\theta}+\dot{\psi}\right)^2\sin(\psi) - mb\ddot{\theta}}{m+m_f}. \tag{12}$$

All equations derived previously are nonlinear. However, in order to design LQR and LQG controllers and estimate the sloshing parameters using the Kaman filter technique one has to get the linear set of equations of motion, which is obtained assuming that the system makes small movements around the point of equilibrium very close to zero; that is, $(\theta, \dot{\theta}, \psi, \dot{\psi}) = (0, 0, 0, 0)$.

Now, substituting (12) into (10) and (11) and assuming the linearization conditions, one has the satellite equation of motion given by

$$\ddot{\theta}\left(I_f + m^*\left(a^2 - ba\right)\right) + \psi\left(I_f + m^* a^2\right) + am_f^* F\psi + \varepsilon\dot{\psi} = -am_f^* f,$$

$$\ddot{\theta}\left(I + m^*\left(b^2 - ba\right)\right) - m^* ab\psi - \varepsilon\dot{\psi} = M + b^* f, \tag{13}$$

where $b^* = bm_f/(m+m_f)$, $m^* = mm_f/(m+m_f)$, and $m_f^* = m_f/(m+m_f)$.

4. Kalman Filter (KF)

The Kalman filter estimates the instantaneous state of a dynamic system from the reading of measurements. In other words the Kalman filter is the optimal solution of minimum variance, which means that the equations of the Kalman filter can be deduced from this premise [7]. The Kalman filtering can be divided into two steps: time update and measurement update.

4.1. Time Update. This step propagates the states and the covariance of the time t_{k-1} to t_k. For this it just integrates the following equations, with the boundary conditions $\overline{\mathbf{x}}_{k-1} = \widehat{\mathbf{x}}_{k-1}$ and $\overline{\mathbf{P}}_{k-1} = \widehat{\mathbf{P}}_{k-1}$. Herein $\mathbf{P}$ is the covariance matrix and $\mathbf{x}$ is the vector state:

$$\dot{\overline{\mathbf{x}}} = f(\overline{\mathbf{x}}), \tag{14}$$

where f is a nonlinear vector function of the state $\mathbf{x}$ and time f. Consider

$$\dot{\overline{\mathbf{P}}} = \mathbf{F}\overline{\mathbf{P}} + \overline{\mathbf{P}}\mathbf{F}^t + \mathbf{G}\mathbf{Q}\mathbf{G}^t, \tag{15}$$

where $\mathbf{G}$ is a matrix that adds noise to the system dynamic, $\mathbf{Q}$ is the process noise covariance, and $\mathbf{F}$ is the Jacobian matrix of f.

4.2. Measurement Update. This step updates the state and covariance to the time t due to the measurement $\mathbf{y}$. Consider the following:

$$\begin{aligned} \mathbf{K}_k &= \overline{\mathbf{P}}_k\mathbf{H}_k^t\left(\mathbf{H}_k\overline{\mathbf{P}}_k\mathbf{H}_k^t + \mathbf{R}_k\right)^{-1}, \\ \widehat{\mathbf{P}}_k &= \left(\mathbf{I} - \mathbf{K}_k\mathbf{H}_k\right)\overline{\mathbf{P}}_k, \\ \widehat{\mathbf{x}}_k &= \overline{\mathbf{x}}_k + \mathbf{K}_k\left[\mathbf{y}_k - h_k\left(\overline{\mathbf{x}}_k\right)\right], \end{aligned} \tag{16}$$

where K_k is the filter gain, H_k is the Jacobian matrix of h which in turn is a vectorial nonlinear function of the state, and $\mathbf{y}$ is the measurement vector.

5. Linear Quadratic Gaussian (LQG)

This method is, basically, the union with the LQR [13] and the Kalman filter. In the LQR method one assumes that all states are available to be feedback but in reality that is not true. Therefore, when there is any state that is not available one has to use the Kalman filter to estimate it in order to be a feedback. The separation principle ensures that each step of this process can be made independently of each other; one may first solve the LQR problem and then design the optimal estimator (Kalman filter), or vice versa, so that the global solution is always the same.

Assume a plant described by the linear state equations given by

$$\begin{aligned} \dot{\mathbf{x}}(t) &= \mathbf{A}\mathbf{x}(t) + \mathbf{B}\mathbf{u}(t) + \Gamma w, \\ \mathbf{y} &= \mathbf{C}\mathbf{x}(t) + \upsilon, \end{aligned} \tag{17}$$

where $\mathbf{x}$ represents the state vector, the matrix $\mathbf{A}$ is the state matrix, $\mathbf{B}$ is the input matrix, $\mathbf{y}$ is the output vector, $\mathbf{C}$ is the output matrix, υ and w are white noise, and $\mathbf{u}$ is the control law. In the LQG method [14] the control law gain is obtained by the LQR method and it is given by

$$\mathbf{K}_c = \mathbf{R}^{-1}\mathbf{B}^T\mathbf{P}_c, \tag{18}$$

where $\mathbf{R}$ is real symmetric positive definite matrix and $\mathbf{P}_c$ is the symmetrical solution of the LQR Riccati equation given by

$$\mathbf{A}^T\mathbf{P}_c + \mathbf{P}_c\mathbf{A} - \mathbf{P}_c\mathbf{B}\mathbf{R}^{-1}\mathbf{B}^T\mathbf{P}_c + \mathbf{M}^T\mathbf{Q}\mathbf{M} = \mathbf{0}. \tag{19}$$

Similarly the Kalman filter gain now is given by

$$\mathbf{K}_f = \mathbf{P}_f\mathbf{C}^T\mathbf{V}^{-1}, \tag{20}$$

where $\mathbf{V}$ is real symmetric positive definite matrix and $\mathbf{P}_f$ is the symmetrical solution matrix of the KF Riccati equation given by

$$\mathbf{P}_f\mathbf{A}^T + \mathbf{A}\mathbf{P}_f - \mathbf{P}_f\mathbf{C}^T\mathbf{V}^{-1}\mathbf{C}\mathbf{P}_f + \Gamma^T\mathbf{W}\Gamma = 0, \tag{21}$$

where $\mathbf{P}_c = \mathbf{P}_c^T \geq 0$ and $\mathbf{P}_f = \mathbf{P}_f^T \geq 0$ and $\mathbf{Q}, \mathbf{R}, \mathbf{V}$, and $\mathbf{W}$ are weight matrices which can be regarded as setting parameters (tuning) that must be manipulated until they find one acceptable response to the system.

A necessary and sufficient condition to guarantee the existence of the $\mathbf{K}_c$ and $\mathbf{K}_f$ is if the system is completely controllable and observable. The LQG method is more realistic than the LQR method, since the states are not always available to be feedback or need to be measurable with the aid of sensors. The inclusion of the noise in the model which represents imperfections of the system is also one advantage of the LQG method.

6. Simulations and Results

The first simulation is the design of the control law using the LQR and LQG control theories, for the spacecraft with a partially filled tank, to account for the sloshing dynamics by the mechanically analog pendulum type. The pendulum physical parameters used in the simulations are as follows: $m = 600\,\text{kg}$, $m_f = 100\,\text{kg}$, $I = 720\,\text{kg/m}^2$, $I_f = 90\,\text{kg/m}^2$, $a = 0.3\,\text{m}$, $b = 0.3\,\text{m}$, $F = 500\,\text{N}$, and $\varepsilon = 0.19\,\text{kg m}^2/\text{s}$. The equations of motion that describe the dynamics of the system are given by (13) which need to be put in state space form. These equations describe the angular displacement of the spacecraft and the angular displacement of the pendulum and the initial conditions used are $\theta = 2^\circ$, $\dot{\theta} = 0.57^\circ/\text{s}$, $\psi = 1^\circ$, and $\dot{\psi} = 0^\circ$.

Figures 2 and 3 show that the LQR control law performance is better than the LQG and the reason is because the first one considers that the sloshing variables are available to be feedback which is not true.

The performance of the LQG control law is damaged because the sloshing motion is controlled indirectly and

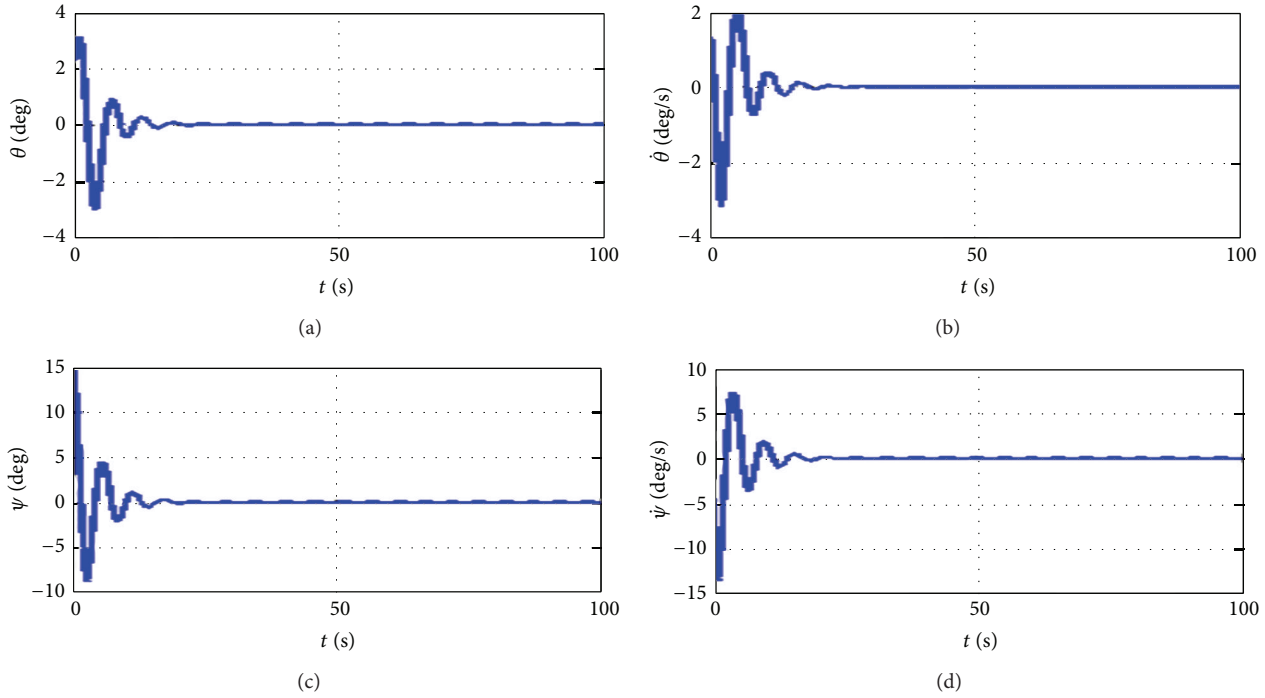

Figure 2: Performance of the LQR control law.

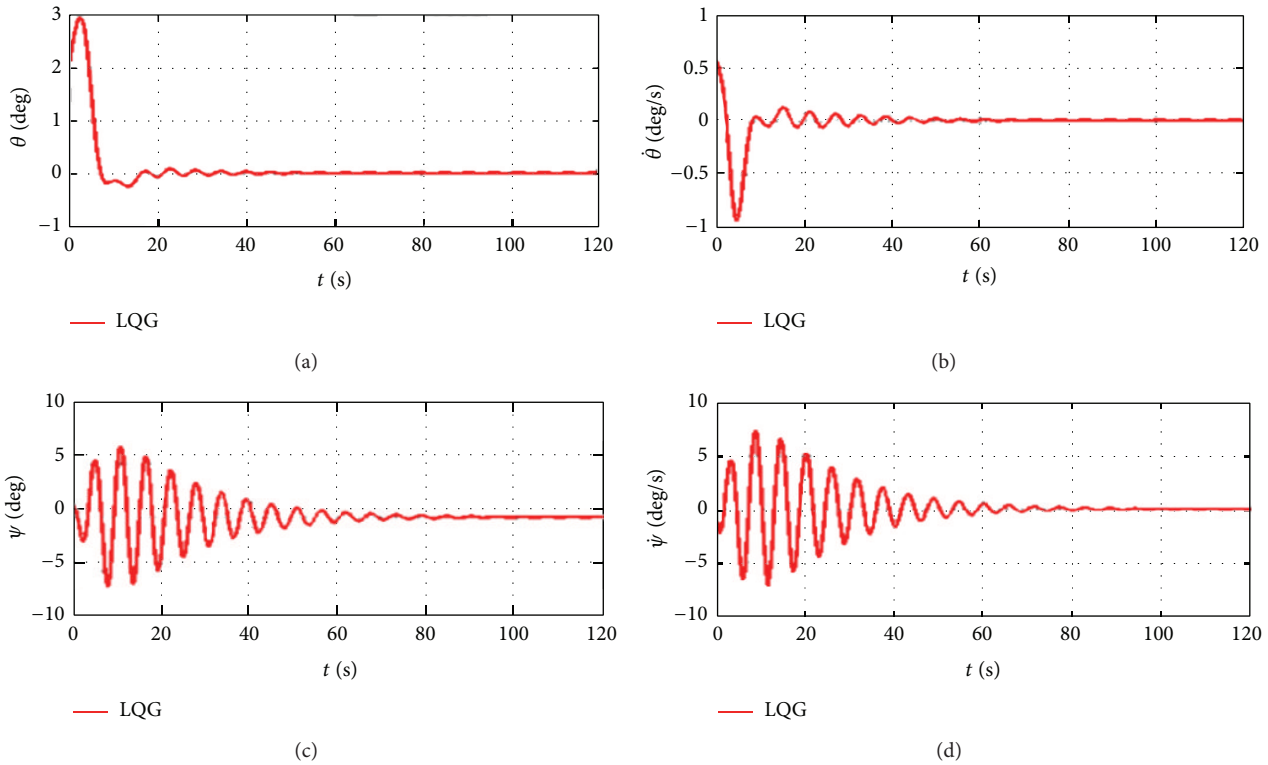

Figure 3: Performance of the LQG control law.

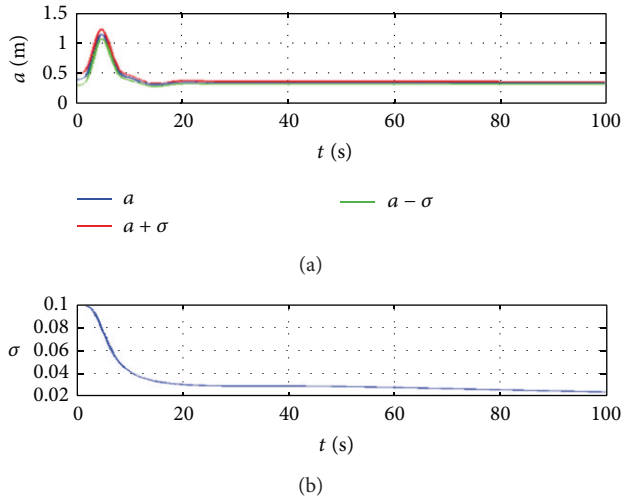

Figure 4: The estimation of the rod length.

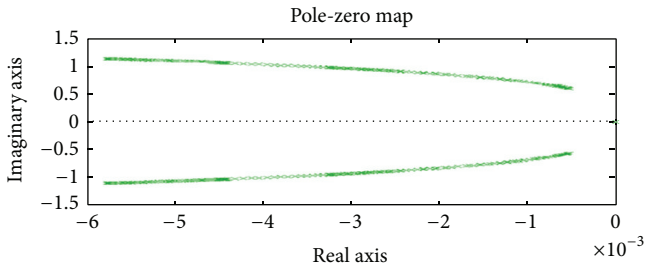

Figure 5: Poles position during the estimation.

the sloshing state variables are not available to be feedback and they need to be estimated by the Kalman filter.

Now one uses the Kalman filter to estimate the rod length of the pendulum using a database containing the time evolution of the variables θ and $\dot{\theta}$. The rod length a is now considered as state variable so one has a system with five state variables which can be estimated. Using the same control LQR law, it is possible to analyze the control system performance during the estimation of the rod length. Besides, one inserts a white noise in the measurements θ and $\dot{\theta}$, given by the noise process $\nu_k = N(0, 0.001)$.

Figure 4 shows that the estimated value of the rod length is $a = 0.33$ m, remembering that the "actual" value of the rod is 0.3 m. Figure 5 shows that plant of the system depends on the estimation of the rod, since at the time that the rod length is varying the position of the poles also moves.

Figures 6 and 7 show the LQR and the LQG controllers during the rod length estimation. One observes that the system is controlled in less than approximately 15 seconds and that the slosh motion is more oscillatory with the LQG controller. This is because the sloshing motion is controlled indirectly and the sloshing state variables are being estimated by the Kalman filter.

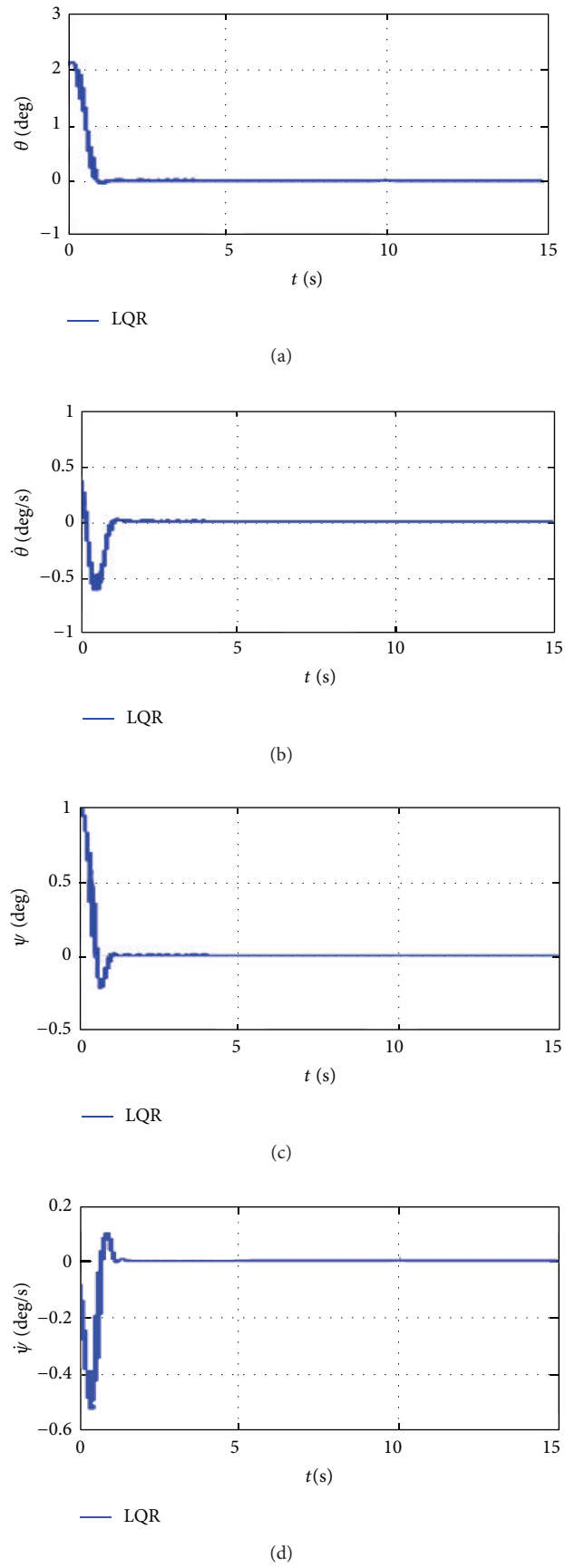

Figure 6: LQR controller during the rod estimation.

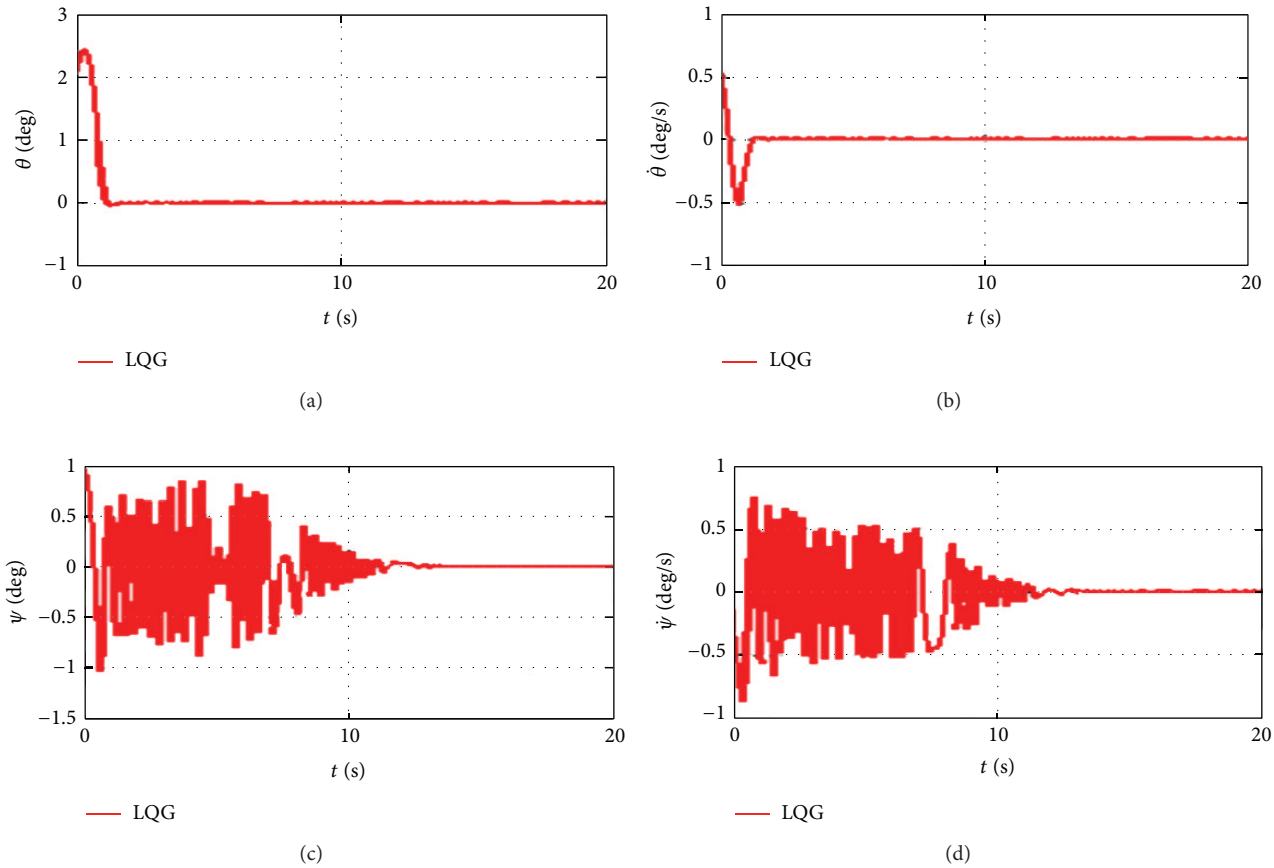

Figure 7: LQG controller during the rod estimation.

7. Conclusions

In this paper one described briefly the concepts of the sloshing phenomenon which is associated with the dynamics of a liquid moving into at partially fills reservoir. Deriving the equation of motion of a spacecraft with liquid inside the sloshing phenomenon is represented by its mechanical analog of a pendulum type. One uses the Kalman filter technique to estimate the pendulum length. One shows that the performance of the LQR control is better than the LQG control during the estimation process. The reason the LQG control degraded is because the sloshing states need to be estimated by the filter. This degradation was expected, because as it has been demonstrated by [15] the introduction of the Kalman filter degrades the stability margin of the LQG. One way to improve the performance of LQG is to make the dynamics of the filter faster than the dynamics of LQR. However, this must be done carefully since this time will depend on the on-board computer capacity. These results show that control of spacecraft with sloshing and flexibility is not an easy task and needs to be investigated better. One has also observed that the estimation of the rod length alters the plant of the system causing the poles to walk to and from the imaginary system, leaving in the end the plant more stable.

Conflict of Interests

The authors declare that there is no conflict of interests regarding the publication of this paper.

References

[1] R. Barron and S. W. R. Chng, "Dynamic analysis and measurement of sloshing of fluid in containers," *Journal of Dynamic Systems, Measurement and Control*, vol. 111, no. 1, pp. 83–90, 1989.

[2] S. K. Chakrabarti, "Internal waves in a large offshore storage tank," *Journal of Energy Resources Technology*, vol. 115, no. 2, pp. 133–141, 1993.

[3] D. E. Hill and J. R. Baumgarten, "Control of spin-stabilized spacecraft with sloshing fluid stores," *Journal of Dynamic Systems, Measurement and Control*, vol. 114, no. 4, pp. 728–731, 1992.

[4] A. P. C. Lui and J. Y. K. Lou, "Dynamic coupling of a liquid-tank system under transient excitations," *Ocean Engineering*, vol. 17, no. 3, pp. 263–277, 1990.

[5] B. N. Agrawal, "Dynamic characteristics of liquid motion in partially filled tanks of a spinning spacecraft," *Journal of Guidance, Control, and Dynamics*, vol. 16, no. 4, pp. 636–640, 1993.

[6] M. J. Sidi, *Spacecraft Dynamics and Control*, Cambridge University Press, New York, NY, USA, 1997.

[7] L. C. G. Souza, "Robust controllers design for flexible space system using a combination of LQG/LTR and PRLQG methods," in *Dynamics and Control of Structure in Space III*, C. L. Kirk and D. J. Inman, Eds., pp. 151–166, Computational Mechanics, 1996.

[8] G. T. Conti and L. C. G. Souza, "Satellite attitude control system simulator," *Shock and Vibration*, vol. 15, no. 3-4, pp. 395–402, 2008.

[9] L. C. G. Souza and R. G. Gonzales, "Satellite simulator control system design using SDRE method," *Journal of Mechanics Engineering and Automation*, vol. 1, pp. 123–132, 2011.

[10] L. C. G. Souza, "Inertia parameters estimation of a satellite simulator," in *Advances in Astronautical Sciences*, vol. 1304, pp. 969–979, 2008.

[11] R. A. Ibrahim, *Liquid Sloshing Dynamics, Theory and Applications*, Cambridge University Press, New York, NY, USA, 2005.

[12] A. G. Souza, *Study of the effects of liquid movement and flexibility in performance and robustness of the attitude control system of an artificial satellite [Master of Space Mechanics and Control]*, National Institute for Space Research (INPE), São José dos Campos, Brazil, 2013, http://urlib.net/8JMKD3MGP7W/3DG55TB.

[13] D. E. Kirk, *Optimal Control Theory: An Introduction*, Dover, Mineola, NY, USA, 1998.

[14] L. C. G. de Souza and X. C. Méndez Cubillos, "Using of H-infinity control method in attitude control system of rigid-flexible satellite," *Mathematical Problems in Engineering*, vol. 2009, Article ID 173145, 9 pages, 2009.

[15] J. C. Doyle, "Guaranteed margins for LQG regulator," *IEEE Transactions on Automatic Control*, vol. 23, no. 4, pp. 756–757, 1978.

Hindawi Publishing Corporation
Shock and Vibration
Volume 2014, Article ID 925437, 22 pages
http://dx.doi.org/10.1155/2014/925437

Research Article

Fundamental Frequencies of Vibration of Footbridges in Portugal: From *In Situ* Measurements to Numerical Modelling

C. S. Oliveira

ICIST/Instituto Superior Técnico, Universidade de Lisboa, Avenida Rovisco Pais, 1049-001 Lisbon, Portugal

Correspondence should be addressed to C. S. Oliveira; csoliv@civil.ist.utl.pt

Received 6 August 2013; Accepted 13 February 2014; Published 18 June 2014

Academic Editor: Nuno Maia

Copyright © 2014 C. S. Oliveira. This is an open access article distributed under the Creative Commons Attribution License, which permits unrestricted use, distribution, and reproduction in any medium, provided the original work is properly cited.

Since 1995, we have been measuring the *in situ* dynamic characteristics of different types of footbridges built in Portugal (essentially steel and precast reinforced concrete decks) with single spans running from 11 to 110 m long, using expedite exciting and measuring techniques. A database has been created, containing not only the fundamental dynamic characteristics of those structures (transversal, longitudinal, and vertical frequencies) but also their most important geometric and mechanical properties. This database, with 79 structures organized into 5 main typologies, allows the setting of correlations of fundamental frequencies as a negative power function of span lengths L ($L^{-0.6}$ to $L^{-1.4}$). For 63 footbridges of more simple geometry, it was possible to obtain these correlations by typology. A few illustrative cases representing the most common typologies show that linear numerical models can reproduce the *in situ* measurements with great accuracy, not only matching the frequencies of vibration but also the amplitudes of motion caused by several pedestrian load patterns.

1. Introduction

The great development of footbridges (also referred to as "pedestrian bridges") in Portugal in the last 2 decades is related to the large amount of freeways or motorways constructed in recent years and the need for pedestrians to cross them. Also, footbridges were built over railways, in railway stations, near shopping centers and schools, and so forth. In a few cases, they were built as part of bicycle routes. Footbridges are in general quite different from viaducts over freeways, not only due to differences in the loading but also because the former can profit more easily from the advances in material developments and architectural creativity. In general, they are lighter, built with high strength materials, spanning quite large distances, and having a wide variety of structural designs. They tend to become slender structures with less mass, but they show more pronounced dynamic effects due to possible resonance in the passage of pedestrians. Large vibration amplitudes are in the range of discomfort, and so this phenomenon deserves much attention to understand the problems that may arise and the way they should be dealt with.

This paper is divided into two parts. In the first part we present and explore a database with *in situ* information on frequencies of vibrations. The second part is dedicated to numerical modelling of a few footbridges that were subjected to *in situ* testing.

For several years, we have been building a database on the main dynamic characteristics of different types of footbridges built in Portugal. In this paper, we report a group of 79 footbridges of different typologies, setting correlations between the fundamental frequencies in the three orthogonal directions and their larger span length, (Table 1 [1–5]). We also look at numerical modelling of a few structures representative of the most common footbridges in Portugal, and compare the results of these models with those of *in situ* testing, both for the fundamental frequencies and for the amplitudes produced by given pedestrian loading. The *in situ* experiments made consisted in single person walking, jogging or running and jumping.

We summarize the work by Silva [6], partially presented in Oliveira and Silva, [7], who has studied a steel and a reinforced concrete (RC) deck footbridge, subjected to

Table 1: Geometric characterization and first *in situ* transverse, longitudinal, and vertical frequencies.

Name	Place	Constr. year	Height (m)	Width (m)	Deck development	Deck cross section	Largest span (m)	Right stair position	Left stair position	Frequencies		
										f-transv. (Hz)	f-long (Hz)	f-Vert. (Hz)
Steel Box-Girders												
Relógio_Gago_Coutinho	Lisbon	1995	6.6	1.7	slight curve	trapezoidal	37	L	L	1.86	3.42	2.29
Entreposto Olivais	Lisbon	2000	8.0	1.8	slight curve	trapezoidal	39	T	T	2.44	3.22	3.25
CP_Gago Coutinho	Lisbon	1998	8.3	2.2		trapezoidal	28	T	T	2.15	2.16	3.42
Relógio_Gomes Costa_West	Lisbon	2000	8.0	2.0	slight curve	trapezoidal	42	T	T	2.70	3.71	3.12
Av. Padre Cruz	Lisbon	2000	7.7	2.0		trapezoidal	37	TL	TL	2.25	5.08	3.42
Acesso 25 Abril Alvito	Lisbon	2000	8.0	2.0	large curve	trapezoidal	37	N	N	3.90	3.90	5.60
Belém (Café)	Lisbon	2001	6.7	1.7	large curve	trapezoidal	43	L	L	3.42	5.20	5.05
2ª Circular East Colegio Alemao*	Lisbon	2000	5.2	2.0	slight curve	trapezoidal	26	T	T	6.70	2.54	3.52
Termas S. Pedro Sul	S. Pedro Sul	1997	2.6	2.0		trapezoidal	53	L	RC	2.90	2.00	2.25
2ª Circular Colegio Alemao	Lisbon	2000	5.0	2.0	slight curve	rectangular	41	T	L	1.95	3.67	2.25
Belém FIL Café-Bar	Lisbon	2001	6.3	2.0		rectangular	14	TL	T	2.93	7.70	9.30
Churrasqueira Campo Grande	Lisbon	2000	5.0	2.0		rectangular	20	L	L	6.93	2.54	3.52
Av. Ceuta South	Lisbon	2002	5.3	2.1		rectangular	32	T	T	1.76	3.80	1.76
Faro_Calouste Gulbenkian	Faro	2003	3.5	2.0		rectangular	29	T	T	3.70	3.40	2.00
Lagos-Nova CML	Lagos	2004	4.6	2.0		rectangular	16	T	T	3.65	3.65	7.10

Table 1: Continued.

Name	Place	Constr. year	Height (m)	Width (m)	Deck development	Deck cross section	Largest span (m)	Right stair position	Left stair position	Frequencies		
										f-transv. (Hz)	f-long (Hz)	f-Vert. (Hz)
Steel Truss I + I												
Teatro Camões Parque Nações	Lisbon	2010	7.0	2.5		I + I	21	L	L	6.80	4.30	4.30
Coimbra 1A	Coimbra	2004	5.5	2.0		I + I	21	L	L	2.00	5.00	5.20
Coimbra 1B	Coimbra	2004	5.5	2.0		I + I	28	L	L	2.00	5.00	4.08
Coimbra 2A	Coimbra	2004	4.5	2.0		I + I	17	L	T	3.36	11.00	9.60
Pupilos Exercito South	Lisbon	1999	10.0	1.7		I + slab	38	T	T	1.17	1.86	3.03
Braga NE	Braga	2002	5.0	2.0		truss 2D	25	T	T	4.79	2.64	4.77
Av Gomes Costa (East)	Lisbon	2002	5.6	2.8		truss 2D	30	T	T	2.73	2.73	3.42
Rego	Lisbon	1999	6.3	2.4		truss 2D	46	Truss	Truss	1.95	1.95	3.81
Conde Almoster over railway	Lisbon	2001	8.0	3.0	n/straight	truss 2D	50	T	T	2.25	2.93	2.93
IP3-Lameira	Coimbra	2000	5.6	2.0		truss 2D	21	L	L	2.26	3.87	2.66
Universidade Covilhã	Covilhã	2010	6.0	1.4		truss 2D	20	T	N	2.07		2.07
IP3-CEPSA_Aguieira	Coimbra	2000	5.8	2.0		truss 2D	22	T	T	5.03	3.22	7.72
A1-Antuã	A1 km 260	1995	4.3	2.5		truss 2D	42	RC	RC	2.73	2.91	4.98
Bela Vista-Feira Nova	Lisbon	2008	12.0	2.5		truss 3D	48	N	N	2.20	3.00	5.60
Massamá	Salg Maia		4.7	2.5		truss 3D	26	L	L	5.40	5.40	6.54
EN-125_Chinicato	Lagos	2001	5.0	2.0		tubular	20	T	T	3.20	3.20	7.40
Pinhão-Douro	Pinhão	2011	6	3.3	light curve	tubular	51	N	N	3.16	4.24	3.16
Exit Camacha	Madeira	2002	4.0	2.0		triangle	28	N	N	2.44		1.86
Aeroporto	Madeira	2002	4.0	2.0		triangle	19	T	T	3.71	4.32	2.50
São Gonçalo	Madeira	2002	4.0	2.0		triangle	28	N	N	3.32	2.64	1.86
Conde Almoster	Lisbon	2001	8.0	2.0		triangle	22	T	T	5.40	4.70	4.20

Table 1: Continued.

Name	Place	Constr. year	Height (m)	Width (m)	Deck development	Deck cross section	Largest span (m)	Right stair position	Left stair position	Frequencies		
										f-transv. (Hz)	f-long (Hz)	f-Vert. (Hz)
Reinforced Concrete												
Alfredo Bensaude (West)	Lisbon	1997	5.0	2.1		I + slab + I	30	T	T	4.32	2.93	2.88
Alfredo Bensaude (East)	Lisbon	1997	5.0	2.1		I + slab + I	30	T	T	3.91	2.05	2.73
Av. EUA_Chelas East	Lisbon	2000	9.0	2.5		I + slab + I	25	TL	T	2.91	1.70	4.00
Vale Formoso (Chelas)	Lisbon	2000	7.2	2.5		I + slab + I	28	T	T	1.76	2.00	3.81
Figueira_Foz_Lidl	Figueira Foz	2002	6.0	2.5		I + slab + I	19	T	T	5.57	3.42	6.45
Lusófona (Campo Grande)*	Lisbon	2001	6.0	2.0		I + slab + I	26	T	T	3.73	2.77	3.79
EN-125_Faro_Mercedes	Faro	2003	6.3	1.5		I + slab + I	29	T	T	1.90	2.90	1.90
Gambelas Rotunda Aeroporto	Faro	2005	5.8	1.8		I + slab + I	38	T	T	2.06	2.51	2.30
EN-125 Faro-Metalo-Farense	Faro	2005	6.0	1.8		I + slab + I	32	T	T	1.80	2.20	3.10
EN-125 Faro-Patacao (center)*	Faro	2005	5.0	2.0		I + slab + I	22	TL	TL	2.60	2.60	3.58
EN-125 Faro-Patacao (N part)	Faro	2005	5.0	2.0		I + slab + I	13	TL	TL	2.60	2.35	10.70
EN-125 Faro-Patacao (S part)	Faro	2005	5.0	2.0		I + slab + I	11	TL	TL	2.60	2.50	13.50
EN-125 Faro-Paga Pouco	Faro	2005	5.0	2.0		I + slab + I	22	T	T	3.55	2.25	5.05
EN-125 Faro-Coord Seguros Eng	Faro	2005	5.0	1.5		I + slab + I	23	T	T	4.10	2.15	3.50
Pupilos Exercito North	Lisbon	1999	10.0	1.7		I + slab	31	T	T	1.37	1.86	4.49
Conde Almoster	Lisbon	2001	7.0	2.0	n/straight	triangle	22	RC	RC	5.40	4.70	4.20

Table 1: Continued.

Name	Place	Constr. year	Height (m)	Width (m)	Deck development	Deck cross section	Largest span (m)	Right stair position	Left stair position	Frequencies		
										f-transv. (Hz)	f-long (Hz)	f-Vert. (Hz)
Reinforced Concrete												
IP25-Aveiro	Aveiro	1999	4.0	2.0	large curve	trapezoidal	36	L	L	1.24	1.44	2.57
EN-125_Exit Aeroporto (Ibis)	Faro	2003	5.0	2.0		U	37	T	T	2.10	1.65	1.90
Circular Praia da Rocha	Portimão	1970	5.0	2.0		U	21	L	L	6.90	5.10	6.90
Entreposto Escola_Herc_Carvalho	Lisbon	2001	5.7	2.3		T + T	20	T	T	1.60	3.12	3.50
Amadora Cacém	Amadora	1995	6.0	4.0		rectangular	22	T	T	6.30	6.20	3.71
IC-19 Queluz	N117	2001	6.0	2.0		U	31	T	T	2.52	2.40	2.76
IC-19 Estaçao Massamá-Barcarena	Exit 7	2001	6.0	2.0		U/V	32	L	T	2.52	4.12	3.13
IC-19 Cacém West Cemitério)	Exit 9	2001	6.0	2.2		U/V	41	T	T	2.52	1.84	2.32
IC-19 Cacém Leste	Exit 9	2001	6.0	2.4		U/V	46	T	T	2.07	1.80	2.12
IC-19 Cacém Leste Gasolina BP	Exit 8	2001	6.0	2.0		U/V	39	T	T	2.76	2.34	2.58
Guimarães	S-Exit A7	2001	6.0	2.0		U/V	25	T	T	3.00	2.12	3.76
Steel variable cross-section												
SMPC_Av Calouste Gulbenkian	Lisbon	2010	8.6	4.0		trapezoidal	38	N	N	7.30	2.80	3.86
Olaias-Bela Vista	Lisbon	2011	15.0	4.0		I + I	56	N	N	2.16	3.04	1.90

Table 1: Continued.

Name	Place	Constr. year	Height (m)	Width (m)	Deck development	Deck cross section	Largest span (m)	Right stair position	Left stair position	Frequencies		
										f-transv. (Hz)	f-long (Hz)	f-Vert. (Hz)
Other Types												
Parque Nações near Vodafone	Lisbon	2010	7.0	2.5		Timber U	25	L	L	5.80		5.80
Green park_Benavente	Benavente	2007	3.0	2.5		Steel ribbon	48	N	N	1.12	1.76	2.36
FEUP Campus* [1]	Oporto	2001	5.0	2.8		RC ribbon	32	N	N	2.15	2.54	0.81
CC Vasco Gama North*	Lisbon	1998	8.0	2.4		Steel arch	75	N	N	1.83		0.94
CC Vasco Gama South	Lisbon	1998	8.0	2.4		Steel arch	75	N	N	1.70		0.88
Guarda near railway station* [2]	Guarda	2007	7.0	2.0		Steel bow-string	90	N	N	0.63		2.33
Microsoft Porto Salvo	Oeiras	2001	6.0	2.0		Steel bow-string	25	T	L	3.22	5.66	3.22
Infante D. Henrique	Lisbon	1978	5.6	2.5		Fiber-glass	30	L	L	2.70	8.00	5.37
Av. Marech Gomes Costa (East)	Lisbon	1978	5.6	2.5		Fiber-glass	32	T	T	4.00	3.90	5.37
Ribeira Carpinteira	Covilhã	2009	39.0	4.4	S-shape	Steel [+] 2D	49	N	N	1.36	2.11	2.47
Pedro e Inês* [3]	Coimbra	2006	10.0	4.0	n/straight	S + RC arch-girder	110	N	N	0.91		1.95
Movable cable-stayed—Open* [4]	Viana Castelo	2007	8.0	2.5		Steel cantilever	36	N	N	0.98		1.03
Movable cable-stayed—Closed*	Viana Castelo	2007	8.0	2.5		Steel cantilever	36	N	N	4.09		3.17
Circular ribbon* [5]	Aveiro	2009	5.0	2.0	ring	Cable-stayed	ext diameter = 13	L	N			3.17

*Analytical studies; N: no stair; L: longitudinal; T: transversal; TL: oblique; Right: pointing W-N-E-; [.]: reference.

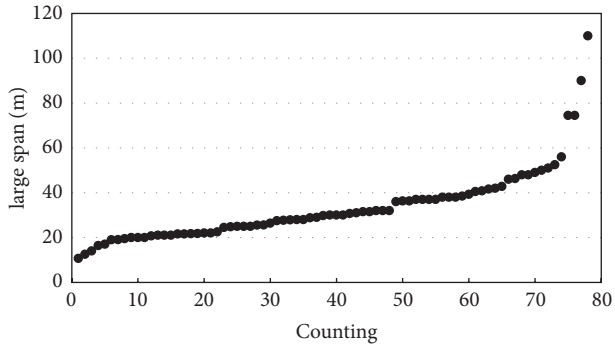

Figure 1: Largest span of analyzed footbridges (circular ribbon footbridge not included).

a pedestrian-load pattern and to the seismic action corresponding to the Portuguese Code [8]. Other analytical studies made in more complex structures [9] or as part of a campaign for evaluating seismic vulnerability of typical footbridges [10] are also synthesized.

This work aims to contribute to the understanding of footbridge behavior under pedestrian loading, verifying the reliability of standard structural analysis programs to obtain a correct representation of these types of structures. This is in line of recent studies merging analytical modelling with *in situ* experiments (see [1]). The correlations obtained between frequencies in the vertical direction and span lengths are quite good for certain typologies and can therefore be used as a first estimation for design or amplitude assessment.

Although in many cases the footbridges do not show structural problems with pedestrian crossings, they may notice excessive vibration problems under specific loading, making the crossing uncomfortable and even scary. The case that called attention to this phenomenon was the Millennium Bridge, in London. In the inauguration's day, when thousands of pedestrians crossed the footbridge, excessive horizontal vibrations were observed caused by a synchronized transverse movement of the crowd. This effect was known as "lock-in effect" [11].

2. Main Footbridge Typologies Existing in Portugal

The present database refers to 79 footbridges of several geometric layouts, structural types, deck cross sections, materials, and largest span length varying from 11 to 110 m, Figure 1. The most common typologies are the steel box-girder deck and the precast RC deck with prestressed beams. Other typologies used different materials such as fibre-glass and timber or combinations of tubular supporting structures. A classification of decks of the most common footbridge typologies in Portugal (Figure 2), whose images are shown in Figure 3, is as follows: (a) steel box-girders (BG) with trapezoidal and rectangular cross sections; (b) steel truss into a 2D or 3D special geometry; (c) RC lateral precast beams with concrete slabs; (d) steel variable cross sections; and (e) other types for larger spans, such as bow strings, suspended, and cable-stay. In this category we also consider footbridges of materials different from steel and RC.

Even though more than 50% of the reported footbridges refer to the region of Lisbon, the author has selected a number of cases in each typology in other regions of the country to gain some statistical significance. Also, there is a set of recently built footbridges, which represent landmarks in the modern Portuguese scenario for their outstanding design, such as the stress-ribbon in the FEUP Campus (Oporto) [1], the "Pedro e Inês" in Coimbra [3], the circular footbridge in Aveiro [5], the movable cable-stayed footbridge in Viana do Castelo [4], the bow-string in Guarda [2], and the S-shape Carpinteira footbridge in Covilhã [12], which were added to the database for completeness. The main properties of some of these structures were taken from data and results published in the literature (see Table 1).

The above most common (a) to (d) typologies built in Portugal are also seen in many other countries and, consequently, the results presented herein may be extrapolated outside Portugal. These footbridges, in a total of 63 cases, are essentially single span long over an entire free-way, supported in lateral columns or pillars, made of cylindrical hollow steel or of RC precast elements, with cylindrical or elongated cross sections. The access to the deck in an elevated level is made in different ways, commonly by RC stairways or ramps, running longitudinal with the axis of the footbridge (L), transversal to it (T), or at an angle (LT). For bicycle routes generally there is no ramp (N) and the deck sits directly in the abutments.

Foundations of columns vary from case to case but, in general, they are made of concrete blocks. Connections at the top of the columns and to the stairways or ramps also differ quite considerably. But as the majority of these structures are precast, these connections are weak points of the structure especially for seismic loadings.

The dynamic characterization of these structures is of most importance for a number of reasons. As they are slender structures, with continuous distribution of mass and stiffness, most of them spanning lengths of 20 to 60 m (Figure 1), the passage of pedestrians may cause large amplitude vibrations. In some cases, resonance effects in the vertical and/or transverse directions, beyond becoming uncomfortable, they may induce damage.

Frequencies and damping characteristics are probably the most important parameters controlling the dynamic behavior, together with the frequency of walking pedestrians (number of people, velocity, synchronization of stepping, etc.). The frequencies of the structure depend on the geometry and mechanical properties. For geometry they vary with the number of spans, the type of connections, the lateral pathway (ramp and stairways in the longitudinal or transversal directions), the height of columns, the width of deck, and the curvature in elevation and its development in plant. For mechanical properties, the main characteristics to be accounted are the weight and the modulus of elasticity.

The main information contained in the database for each one of the 5 above mentioned typologies refers to the following parameters, obtained either from design drawings (a few cases) or from direct measurements of structural elements: (1) identification—name; (2) location—place; (3) construction

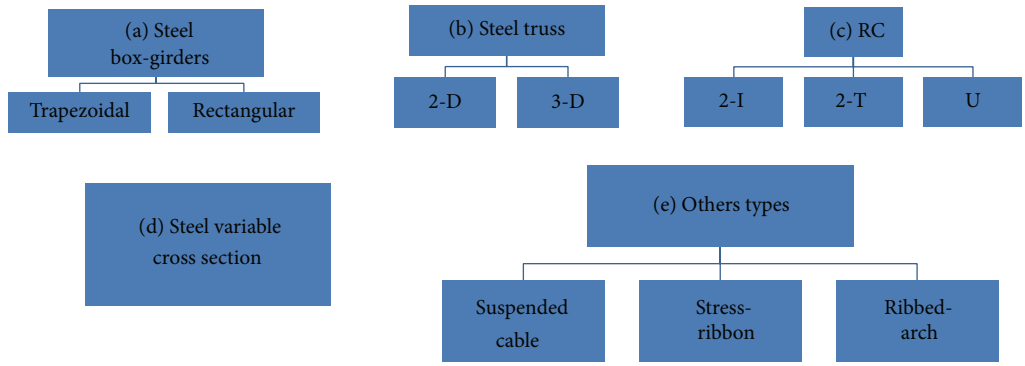

Figure 2: Main structural deck types for footbridges in Portugal.

year; (4) height of deck; (5) width; (6) deck development; (7) deck cross section; (8) largest span; (9) and (10) lateral access; (11) to (13) frequencies of first mode in the transversal, longitudinal, and vertical directions. Table 1 presents this information for the 79 footbridges in the database, the majority of them subjected to *in situ* dynamic testing. The entire database contains more information such as the designer/contractor; state of conservation; total length; number of spans; deck cross section and columns dimensions; date of testing; other identified modal frequencies, especially the ones with more pronounced effect; and amplitudes of vibration for 1 pedestrian walking at "normal" speed. For most cases, GIS information is used to locate the footbridge and a photo or sketch is annexed.

3. *In Situ* Campaign and Analysis of Results

3.1. In Situ Experiments and Data Treatment. *In situ* expedite experiments were performed with a single 3-component accelerometric station equipped with a "force-balance" 3-component sensors with a resolution below 0.5×10^{-2} mg, acquiring data at 200 Hz. Samples of 60 sec duration were averaged out after band-pass filtered with Butterworth with 4-poles between 0.03 and 25 Hz. Samples were visually reviewed to avoid the ones with anomalous spikes.

Data treatment consisted in analyzing peak acceleration values, predominant frequencies of vibrations in the three orthogonal directions through FFT techniques, and damping from amplitude decay in a few cases. A cross examination of results, together with the interpretation of modal shapes for the most simple geometrical layouts, led to the identification of first modal frequencies in the three directions of space (T: transversal; L: longitudinal; V: vertical). For all analyzed structures, damping is quite small with values varying in the interval $1\% > \zeta > 0.5\%$, even for large amplitude motions. All these values were transported to the database. Whenever an analytical model was available, identification of various modal shapes was achieved with this single 3-component instrument.

In several situations we repeat the *in situ* testing not only to check the robustness of the readings, but also to use different resolution instrumentation. In the first measurements we used 12-bit instruments with 100 mg of full scale and more recently we used 18-bit at a 1000 mg full scale, which allows a much better signal/noise ratio. Frequencies were obtained in general with an error of ±0.05 Hz.

The experiments were of two types, with measurements performed with the accelerometric station located at mid-span and at quarter-span as follows:

(1) measurements for noise vibration produced by car traffic passing underneath, for mode identification;

(2) measurements for a set of typified tests with the passage of pedestrians at different velocities: (a) one person at slow walking; (b) one person at normal walking; (c) one person at fast walking; (d) one person jogging (slow running); (e) forced vibration caused by the movement of one person in resonance conditions; and (f) impulsive action derived from "jumping." For details, see [6].

This technique, using a single instrument, can only be used with confidence for footbridges with simple geometric layouts, in which modes are easily separated into the three directions and no interaction is taking place. For more complex geometries, either in plan or in the vertical direction, multiple instrumentation with common time is required for identification of frequencies and modal shapes. The case of the Ribeira da Carpinteira (Covilhã) footbridge, a S-shape plan view with two lateral steel beams ([+] cross section) is the situation where modes are coupled in the 3 directions of space with an important participation of torsion of deck [12]. Only the frequencies were identified, but it was impossible with a single 3-component instrument to assign them to any particular mode shape with the exception of the first ones. Most of the "other types" footbridges (Figure 2) fall into this category.

3.2. Analysis of Results. The main results are presented in Figure 4, where the frequencies of first mode in the T, L, and V directions are plotted against the largest span length. Various representations are made to understand the correlation of measured frequencies with the larger span. Most of the footbridges can be considered as simple supported beams with constant mass and stiffness. A curve fitting of the first frequency of vibration (f) versus the span length (L) was

Figure 3: Main typologies of footbridges in Portugal.

essayed for the frequency in each direction and for each typology class (Figure 2). A power function ($f = a \times L^{-\alpha}$) was used. As expected, the correlation for the vertical frequency of steel box-girders (Figure 4(e)) (especially if the two larger curvature footbridges are eliminated from the plot, $R^2 = 0.667$, not presented in Figure 4) and RC footbridges (Figure 4(g)) is much higher than for the other directions. However, for steel truss structures, the existing variety, with 2D, 3D, and so forth cases, is so large that no correlation can be observed even in the V direction. A more detailed analysis entering with other parameters, namely, the material and the location of stairways, would certainly increase the correlation, especially in the T and L directions. But to do that and keep some statistical insight we need to perform more tests, increasing our database.

Even though the steel structures are much lighter than RC, a comparison of their vertical frequencies shows similar results (Figure 5). As the ratio (pedestrian)/(full dead-load) is much higher for steel structures than for RC structures, this causes higher amplifications in steel structures (see Section 4.2).

Figure 6 shows that the V and L frequencies do not correlate with each other, probably because the frequency in the L direction depends very much on the stiffness of columns

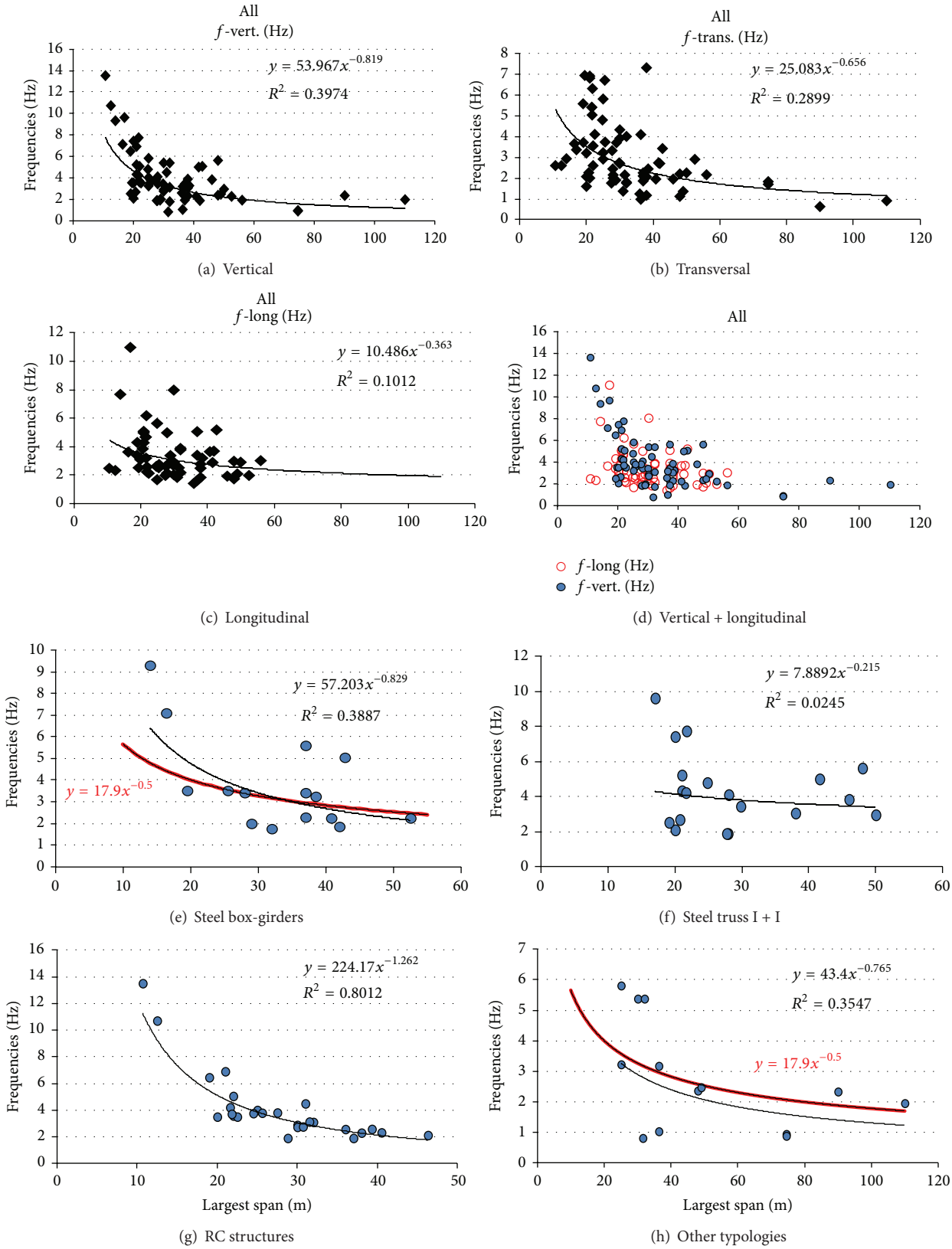

Figure 4: Frequencies of 1st mode in the three directions (T, L, and V) as a function of largest span: (a) to (c) all typologies for V, T, L, and (d) V + L; (e) to (h) vertical for steel box-girders, truss structures, RC structures, and other structures, respectively. Red curves are explained in Section 3.3.

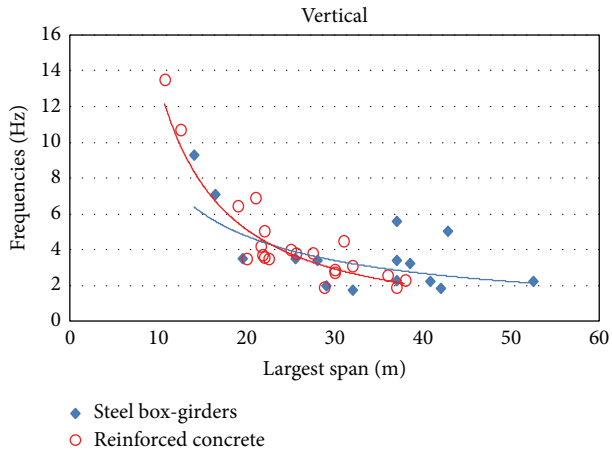

Figure 5: Comparison of frequencies for steel box-girders and RC footbridges.

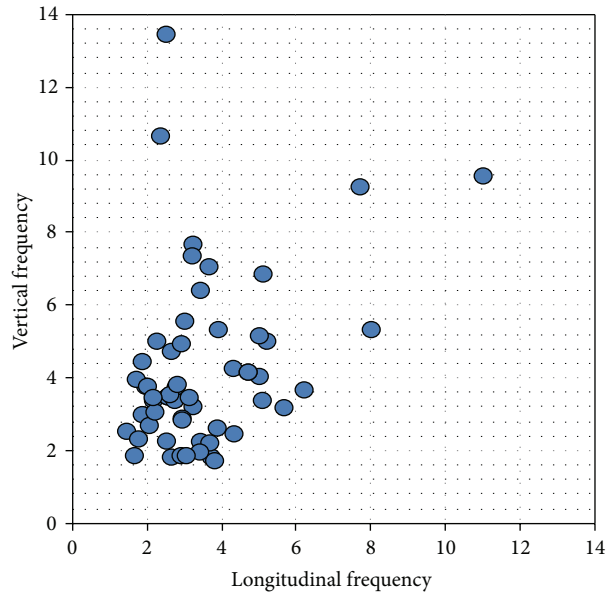

Figure 6: Correlation of V and L frequencies for all footbridges.

and on the position of stairs or ramps. If we took these aspects into consideration, the correlations would probably be much better. Numerical modelling, presented in Section 5 for various typologies and stairways locations, shows that the analytical frequencies are very similar to the *in situ* measurements in all three directions of space, precluding the better above-mentioned correlation.

3.3. Estimating the Natural Vibration Frequency of Footbridges. An empirical formula to compute the fundamental vertical frequency of a footbridge would be very useful for a designer to quickly assess its response to pedestrian crossing.

Let us consider a footbridge as a simple supported beam (length L) with constant mass $\overline{m}$ per unit length and constant inertia I, made of material with modulus of elasticity E.

The frequency (Hz) of the first mode is given by Clough and Penzien [13]:

$$f = \frac{1}{2\pi} \times \pi^2 \sqrt{\frac{EI}{\overline{m}L^4}} \quad (1)$$

which corresponds to a sinusoidal shape. Higher modes have frequencies 4, 9, and so forth times the fundamental frequency. Assuming that the maximum deflection of the beam under dead load should not surpass L/1000; then the frequency is only function of L and given by

$$f = 17.9 \times L^{-0.5} \quad (f \text{ in Hz; } L \text{ in m}). \quad (2)$$

For built-in supports (clamp-clamp), the first frequency is about 2.27 times larger than for simple supported. And the effect of changing the assumption of maximum deflection permitted, or of the stiffening of the supports, would only affect the initial constant, not the exponent of L.

Expression (2) is in the lower bound of decrease of frequency with length ($L^{-0.5}$). Usually the exponent, observed from the fitting ([14], after *in situ* testing of 67 footbridges, arrived to a fitting $f = 33.6 \times L^{-0.73}$, exhibiting large dispersion and not making any distinction among typologies), is higher denoting that frequency attenuates faster with L. Steel box-girders attenuate with $L^{-0.9}$, RC with $L^{-1.4}$, and other types with $L^{-0.8}$. It means that the assumption of maximum deflection which implies (3) given by

$$\frac{I}{\overline{m}} \cong f\left(L^3\right) \quad (3)$$

is not suitable and the ratio $I/\overline{m}$ is more likely proportional to L^2. In many cases the cross section varies along the length, and the maximum deflection is not given by a simple expression as used for the simple supported beam with constant mechanical properties. Also the principle of displacement-controlled design may not apply, prevailing a constant extension (ε) assumption.

We plotted the values produced by (2) in Figures 4(e) and 4(h) to check the differences to the empirical fitting.

4. Characterization of Pedestrian Loading

The dynamic loading in footbridges is essentially due to the passage of persons alone, in groups, randomly walking, jogging, running, or a combination of all previous cases. Also, sudden loads provoked by jumps, fall of objects, or rhythm action may arise. Sometimes the passage of bicycles or motorbikes may be observed. The "lock in effect" is another resonant effect, induced by the bridge itself, which influences the walking pattern. We will concentrate only on the passage of a single person walking, jogging, or running. Also excitation near to resonance by one single person was also performed. However, the response of footbridges for groups of pedestrians walking in rhythm or randomly walking was not analyzed.

4.1. Pedestrian Loading Pattern. There are three levels to be considered in the definition of pedestrian loading. The first

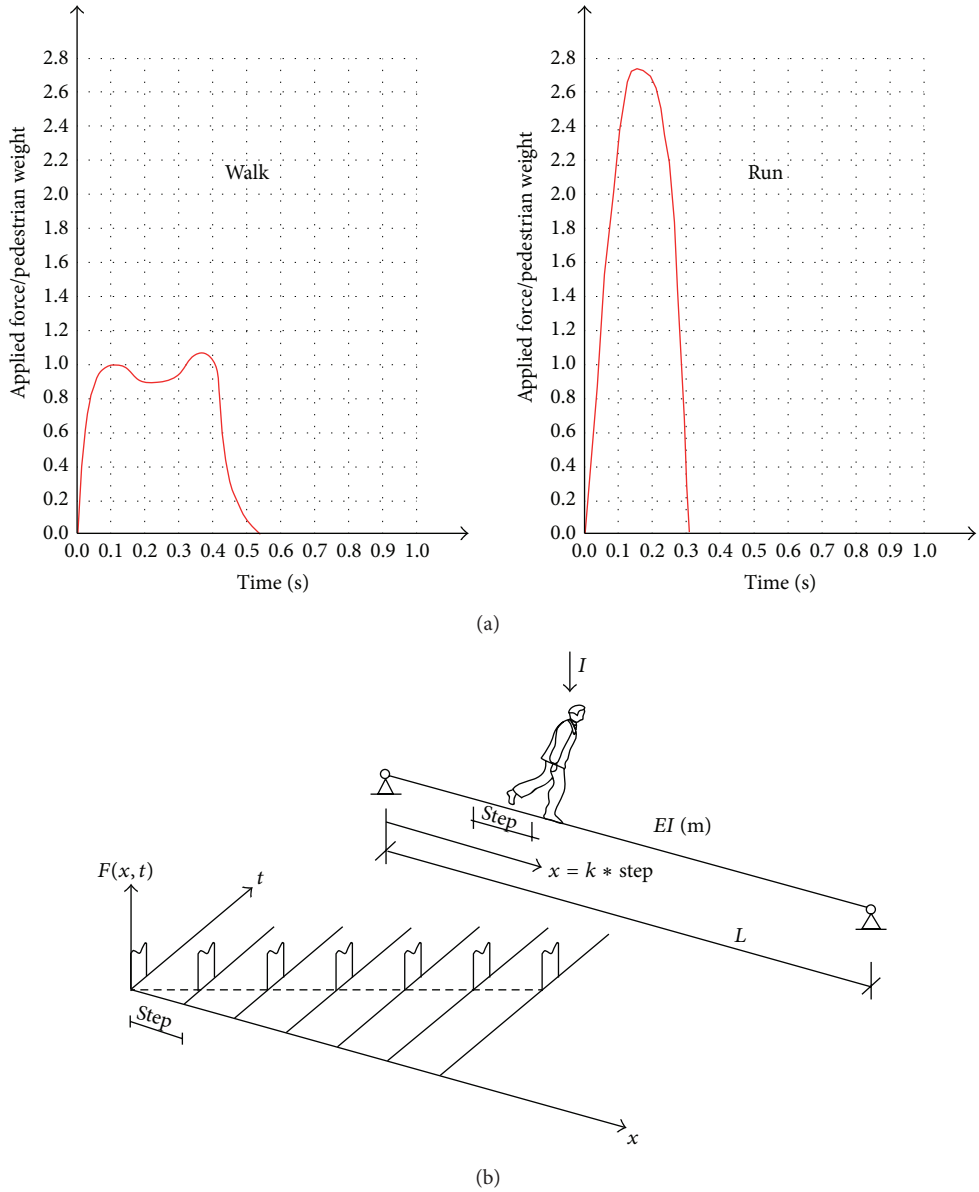

FIGURE 7: (a) *Force-time* typical diagram for different movements: left-step frequency < 2.2 Hz, right-step frequency > 2.2 Hz; (b) variation in *time-space* imposed by the walking movement [15].

TABLE 2: Frequency range (Hz) for different patterns of movement (adapted from [14]).

	Slow	Normal	Fast	Total
Walk	1.4–1.7 Hz	1.7–2.2 Hz	2.2–2.4 Hz	1.4–2.4 Hz
Jogging	1.9–2.2 Hz	—	—	1.9–2.2
Running	—	—	3.0–3.4 Hz	3.0–3.4 Hz

one attends to the frequency of movement, resulting from a speed of 0.5 m/s to 0.8 m/s (for slow walk) to 3.5 m/s (for jogging-slow running) with a step size from 0.65 m for slow walk and not exceeding 1.7 m for fast running (Table 2).

The second and third levels are related to the contact form of the foot with the deck, with one vertical and two horizontal components. This contact form depends on the pattern of movement [2, 15]: the contact time between the foot and the floor; the time interval among two consecutive steps; the relation between the applied force and the pedestrian's weight; and the step length. Figure 7 shows the form of how we applied the foot loading along the *time-space*.

We generated a load curve of the form shown in Figure 7(a) and applied it at successive nodal points, at different time intervals, Figure 7(b).

Whereas the vertical component of the load always applys in each step due to the gravitational force in the same direction, the horizontal action introduces a force alternating to the right and left, according to the stepping foot.

These functions were programmed to be used with standard linear dynamic analysis software using the time history

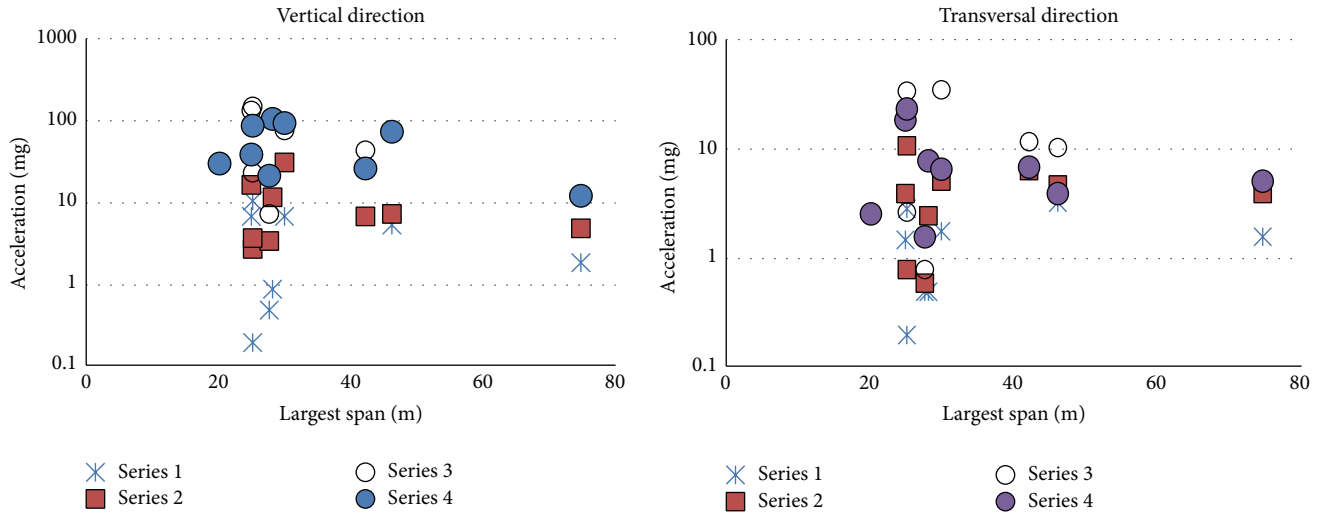

Figure 8: Amplitude values in mg of the measured maximum motion at mid-span. Series 1: noise; Series 2: 1 person walking at "normal" pace (2 Hz); Series 3: 1 person jumping from 30 cm; Series 4: excitation close to resonant conditions.

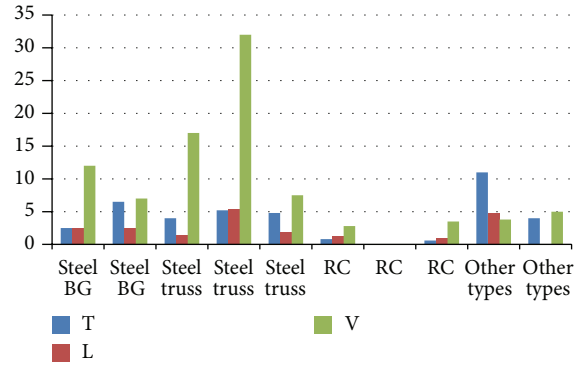

Figure 9: Amplitude values in mg of the measured maximum motion at mid-span (T; L; V): 1 person walking at "normal" pace (2 Hz) in different typologies (Series 2).

integration. For the L direction the intensity of loading is 50% of V, whereas in the T direction it is between 3 and 10% of V. The frequency in L direction is equal to the V direction, whereas in T direction the frequency is half of the V direction [16, 17]. These patterns are also observed in the database of the present work.

4.2. In Situ Amplitude Values. Table 3 and Figure 8 present the values of the measured maximum amplitudes of motion at mid-span for a group of 10 footbridges in the T, L, and V directions, for the following loading conditions: (1) noise; (2) 1 person walking at "normal" pace (2 Hz); (3) 1 person jumping from 30 cm; and (4) excitation close to resonant conditions. It is observed that amplitudes in the vertical direction are almost 10 times the ones in the transversal direction, and walking produces lower amplitudes than jumping or exciting in resonant conditions.

Figure 9 shows the amplitudes by typology for 1 person walking at "normal" pace. It is clear that RC structures have much lower amplitudes than all other typologies. We can look at these differences as a phenomenon of amplification, in which the amplification of response for the same load type of steel box-girders and steel truss is much larger than for RC footbridges.

As far as amplitudes are concerned, if we take the excitation amplitude given by the equivalent single degree of freedom under resonant conditions, the values are also similar to those indicated by measurements, for the low damping observed ($1\% > \xi > 0.5\%$).

5. Code Provisions and Acceptable Comfort Levels

Currently, there are two different design procedures for footbridges under dynamic loading, which are contemplated by the international standards.

They are essentially based on discomfort and resonance: (i) peak acceleration values in the vertical and horizontal directions should not surpass certain limits for given load patterns and (ii) fundamental frequencies should be outside the so-called *interval of critical frequencies*. There are several international recommendations practiced in various countries such as BSI [18], AASHTO [19], EN 1990, 2003 [20], DIN-ENV [21], ISO 10317 [22], OHBDC, 1983 [23], or the Japanese Footbridge Design Code, 1979 [24]. If the criterion is based on the amplitude value, these recommendations fix values quite different from one another [25], such as in the case of a peak acceleration that should be below, say, 70 mg in vertical and 10–20 mg in horizontal, or a function of the footbridge frequency, Figure 10(a) and Table 4. If the criterion is separation of resonant conditions [26], the recommendations are as shown in Figure 10(b). In a different approach, Kazakevitch and Zakora [27] establish a maximum load (k), dependent on natural frequency (f), to reduce the resonance effect, given by $k = 4/(1 + 1.5f^2)$ kN/m^2.

Table 3: Amplitude values in mg of the measured maximum motion at mid-span for a group of 10 footbridges in the transverse (T), longitudinal (L), and vertical (V) directions.

Name	Length (m)	Noise			1 person walk			Jump			Excitation			Typology
		T	L	V	T	L	V	T	L	V	T	L	V	
CP_Gago Coutinho	28	0.5	0.5	0.9	2.5	2.5	12				8	5	109	Steel BG
Relógio_Gomes Costa_W	42				6.5	2.5	7	12	6	45	7	3	27	Steel BG
Braga NE	25	1.5	1	7	4	1.4	17	24	9.6	138	19	18	40	Steel truss
Av Gomes Costa (Leste)	30	1.8	2	7	5.2	5.4	32	36	7.1	79	6.7	7.6	97	Steel truss
Rego	46	3.3	1.1	5.5	4.8	1.9	7.5	10.6	10	77	4	8.1	76	Steel truss
Av. EUA_Chelas Leste	25	0.2	0.2	0.2	0.8	1.3	2.8	2.7	1	24				RC
Entreposto Escola_Herc_Carvalho	20										2.6	4	31	RC
Vale Formoso (Chelas)	28	0.5	0.2	0.5	0.6	1	3.5	0.8	0.9	7.5	1.6	1.4	22	RC
Microsoft Porto Salvo	25	2.9	0.9	10.8	11	4.8	3.8	35	9.6	155	24	7.6	90	Other types
CC Vasco Gama Norte	75	1.6		1.9	4		5				5.2		12.5	Other types

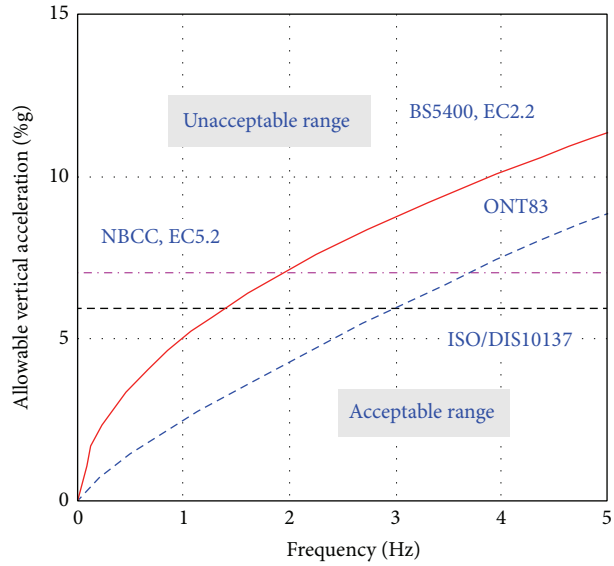

(a)

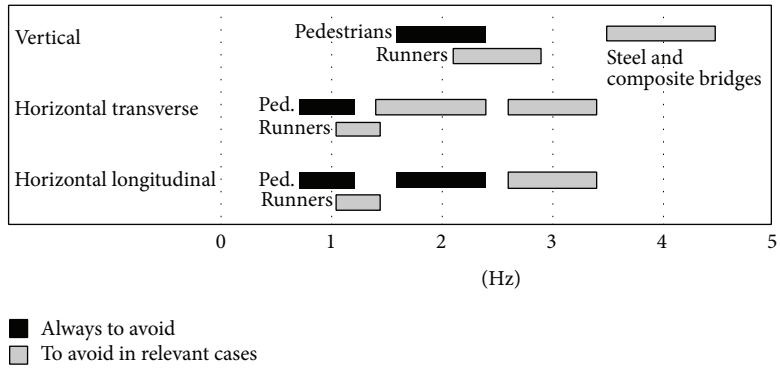

(b)

Figure 10: (a) Allowable vertical accelerations as a function of frequency of vertical mode [26], (b) frequencies to be avoided [14, 17].

Table 4: Acceleration limits recommended in some codes (Figure 10(a)).

Regulation	Vertical acceleration (m/s^2)	Horizontal acceleration (m/s^2)
BS5400 [18]	$a_{\max} \leq 0.5 \cdot \sqrt{f}$	—
OHBDC (1983) [23]	$a_{\max} \leq 0.5 \cdot (f_0)^{0.28}$	—
Eurocode [20]	$a_{\max} \leq 0.7$	$a_{\max} \leq 0.2$
Hong Kong (2002) [28]	$a_{\max} \leq 0.5 \cdot \sqrt{f}$	$a_{\max} \leq 0.15$

Živanović et al. [11], Heinemayer et al.[29], SÉTRA [30], and HIVOSS Project [2] are three important references summarizing topics and restrictions for comfort and safety of footbridges. More recent advancements were produced and are presented in publications such as Footbridge-2008 [31] and Footbridge-2011 [32].

6. Dynamic Modelling

Four types of structures were the object of a detailed analytical study: two of them correspond to the most common types built recently in Portugal, (1) a steel box-girder and (2) a prefabricated RC I + I beam; the third (3) is a steel inclined arch with a large span; and the fourth (4) is a RC I + I beam, similar to (2) but with 3 spans and inclined stairways. Essentially, we were interested in checking how analytical models could be validated by *in situ* measurements of several modal frequencies. Also, for three cases, the response of the footbridge for pedestrian crossing was compared with the measured values.

In model definition several parameter values are uncertain, such as the elastic material properties (E, modulus of elasticity) and the detail of boundary conditions including the foundation stiffness. Another important issue is the level of discretization of the model, represented in its finite element (FE) description, which has to be sufficiently detailed to account, for instance, with torsion. In this study we just adjusted E and checked the boundary conditions. Model calibration was done taking into account the measured frequency for one specific mode shape, usually the fundamental one. Once the analytical frequency of this mode is tuned to the *in situ* measurement (sources of errors were essentially due to the supporting connections), the other analytical frequencies will adjust to the *in situ* identified frequencies, without need for further corrections to the model.

6.1. Steel Box-Girder [6]. This structure, with 2.0 m wide and spanning 25.5 m at a height of 5.2 m, has a steel box-girder deck supported in two cylindrical, partially hollow columns and connected to 2 adjacent stairways, one at each side of the deck (Figure 11). The main geometric characteristics of deck cross section are the trapezoidal shape with 65 cm height and the columns with diameter $\phi = 29.5$ cm and thickness of 1.4 cm, filled up almost to the top with concrete.

The analytical model of this footbridge, including the stairways, was made with SAP2000 [33], using both "beam" and "plate" elements (Figure 11). Table 5 compares analytical and measured frequency values. With the exception of torsion modes (which require the use of more than one instrument), the agreement is very good, also for high frequency modes.

This structure was also subjected to a set of *in situ* experimental testings to determine the peak amplitude of motion ($a_{\max}$) for different situations as defined in Table 2. Table 6 presents the results for the three orthogonal directions and marks the values exceeding the recommended limits according to several codes. It is clear that in many instances the limits of discomfort are widely exceeded, especially for the cases of stepping at a frequency close to resonance.

Tests of the model feasibility were made to reproduce the walking of a person at different speeds, by comparing the peak acceleration amplitudes obtained in the model with the measurement *in situ* [6]. Even though difficulties arise in controlling the experimental testing (correct speed, frequency of walking), the results (Figure 12) show a good agreement with the analytical model for the vertical direction. The results are not so good for the longitudinal and transversal directions, probably due to the difficulty in reproducing the pedestrian loading in those directions. Also, in the *in situ* case, the resonance situation was never attained with walking experiments.

6.2. RC Structure [6]. The analyzed structure spans 25.6 m, has a height of approximately 5-6 m, and is 2.0 m wide, Figure 13. The deck, formed by two precast and prestressed I beams, $h = 1.23$ m, is supported by two RC columns. Between the columns and beams there are neoprene pads. The pavement is made of RC plates, with thickness of 13 cm, supported on the lower flanges (Figure 13(b)). The columns have rectangular cross section with variable dimensions $1.40 \times 0.45\,\text{m}^2$ at the base and $0.7 \times 0.45\,\text{m}^2$ at the top, just below the opening up for the support of the deck (Figure 13(c)).

Concrete is a B45.1 for the beams and B30.1 for the precast elements (plates, columns, and stairways). Stairways run perpendicular to the bridge axis and are supported in square columns at 1/3 height.

Similarly to what was done for the steel structure, we compare in Table 7 results (SAP2000 [33]) of measurements *in situ* for mode frequencies and present in Table 8, with analytical values for peak acceleration amplitudes. Figure 14 shows the comparison for walking situations.

From the analysis of Tables 7 and 8 and Figure 14, we can say that the analytical model reproduces quite well the measurements *in situ* for frequencies, but not so accurately for pedestrian loading. The difficulties in controlling with accuracy the experimental conditions, in what concerns the frequency of the excitation and the intensity of the pedestrian steps, are the main reasons for the deviations observed.

(a) (b)

Figure 11: Steel box-girder structure under study: (a) analytical model; (b) view of column, deck, and stairway.

Table 5: Comparison of frequencies (Hz) between measurements *in situ* and the analytical model.

Mode direction	Measurements *in situ*	Analytical model
Longitudinal	2.54	2.55
Vertical	3.42 to 3.52	3.52
Torsion about x (longitudinal)	?	5.27
Torsion about z (vertical)	?	5.74
Transversal	6.74 to 6.84	6.38

Table 6: Peak acceleration amplitudes for different tests.

Walking load	a_{max} (mg)		
	Vertical	Longitudinal	Transversal
1 Person[*]—walk at $f = 1.8$ Hz	18.9	2.7	3.8
1 Person—walk at $f = 2.2$ Hz	29.1	5.2	6.1
1 Person—jogging at $f = 2.5$ Hz	38.2	20.2[#]	12.1
1 Person—jogging at $f = 3.3$ Hz	251.3[†]	16.5	21.4[#]
1 Person—jogging at $f = 3.7$ Hz	252.6[†]	12.5	24.5[#]
2 Person—walk at $f = 1.7$ Hz	26.3	6.4	5.8
2 Person—walk at $f = 2.1$ Hz	38.3	25.3[#]	7.0
2 Person—jogging at $f = 2.25$ Hz	74.4[‡]	28.9[#]	19.0
3 Person—walk at $f = 2.1$ Hz	71.5[‡]	29.1[#]	14.1
7 or 8 kids (30 to 40 kg)—slow walk	16.3	6.2	10.3
Noise	6.8	0.9	2.6
Jump	198.1[†]	21.1[#]	83.4[#]
Excitation in transversal direction (resonance)	27.9	3.2	15.5
Impulse in transversal direction	39.8	3.8	17.0
Excitation in vertical direction (resonance)	239.2[†]	11.7	16.1

[*]74 kg.

[†]Values of vertical accelerations exceeding the less stringent limit (93.8 mg); [‡]the most stringent limit (66.7 mg); [#]values exceeding the code ones for horizontal vibrations (20 mg, EN 1990 [20]).

Table 7: Comparison of frequencies (Hz) between measurements *in situ* and the analytical model.

Mode direction	Measurements *in situ*	Analytical model
Longitudinal	2.77	2.77
Vertical	3.79	3.34
Transversal	3.73	3.73
Torsion about z (vertical)	?	5.71
Torsion about x (longitudinal)	7.91	8.80

Table 8: Peak acceleration amplitudes for different tests.

Walking load	a_{max} (mg) Vertical	Longitudinal	Transversal
1 Person*—walk at $f = 2.0$ Hz	7.3	1.7	2.9
1 Person*—walk at $f = 2.2$ Hz	10.1	1.8	3.1
1 Person*—walk at $f = 2.5$ Hz	8.3	4.9	8.0
1 Person*—walk at $f = 2.6$ Hz	11.6	12.2	13.5
1 Person*—walk at $f = 3.0$ Hz	15.5	7.8	15.8
1 Person*—walk at $f = 3.7$ Hz	32.7	11.8	25.4†
2 Jumps at mid-span	61.1	34.2†	90.2†
Impulse in transversal direction	8.5	5.2	15.6

*74 kg.
†Values exceeding the code limits for horizontal vibration (20 mg). EN-1990 [20]).

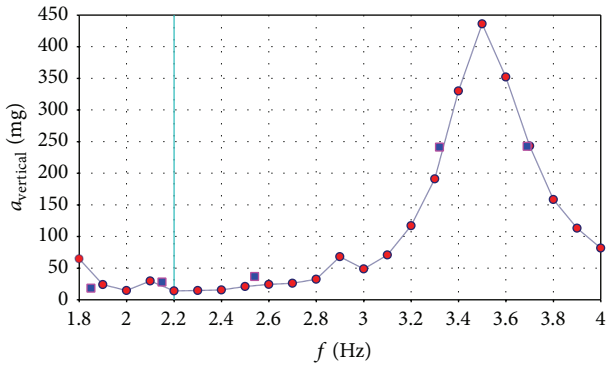

Figure 12: Comparison of amplitudes at mid-span (vertical acceleration) between *in situ* measurements and the analytical model: 1 person walking at various speeds (steel box-girder structure). Red circles: analytical model; blue squares; *in situ* measurements; vertical line at 2.2 Hz separates "walk" from "running."

Comparing the RC structure with the steel structure, we see that the former is much more rigid, with peak values almost 1/2 to 1/3 below the latter, depending on the direction considered. This means that RC footbridges amplify much more the response for the same loading characteristics than the steel box-girders, as already mentioned in Section 4.2.

6.3. Passage between the Orient Station and the Shopping Centre "CC Vasco da Gama". This footbridge is located in Avenue D. João II in Lisbon and makes the connection between the Orient Station and the Shopping Centre Vasco da Gama. There are two identical footbridges, with length of 86.6 m and usable width of 2.4 m. Each one is constituted essentially by three tubular steel sections and thirty-seven pieces with variable "*I*" section that make the connection with the previous ones. Two of the tubular sections are straight and support the bridge deck, while the third one forms an arch that rises through the footbridge making an angle of 31.9° to the ground. The deck and lateral guards are made by thick glasses supported by secondary metallic profiles (Figure 15).

The footbridge is simply supported in the two extremes, still having an intermediate support at 1/4 span, counted from the West side (Orient Station). The material used for the construction is the structural steel S355 (for details, see [9]).

The analytical model of this footbridge was made with SAP2000 [33]. After defining all the structure with 3D "beam" elements, the remaining permanent load of 2.48 kN/m has been applied, corresponding to the weight of the floor glasses, the guards, and the small metallic profiles that support the pavement glass plates. The final analytic model of the footbridge is presented in Figure 15(b).

The frequencies of the first 15 modes obtained by the analytical model and by *in situ* measurements are compared in Table 9.

The first vibration mode corresponds essentially to a vertical oscillation (Figure 16) and there is no significant torsion. In the higher modes the significant displacements are due essentially to lateral oscillations and rotation around the several axes, sometimes occurring the coupling of translational and torsional modes.

It should be noted that, even though the two footbridges connecting the Orient Station to Vasco da Gama Shopping Centre are essentially identical, the *in situ* measured first vibration frequency of the one located to the north is about 6% higher than the other to the south.

To simulate a pedestrian's passage on the structure, the load functions as mentioned in Section 4.1 were used to represent the several movement types. For each analytical run the acceleration envelope was obtained for the three directions. The computed accelerations for the several movement types of a single pedestrian are always below 0.15 m/s^2 in the vertical and lateral directions. The value is much lower than that required by the regulations for the vertical direction. However, for the lateral direction, this value corresponds exactly to the maximum limit indicated by the Hong Kong Structures Design Manual for Highways and Railways, [28].

In general, it is verified that the results from the analytic model are conservative, because the acceleration is, in most cases, larger than the values measured experimentally. Table 10 shows the values obtained for the "normal" walking with two different acceleration transducers (number 133 and number LN874) to check the robustness of the measurements. The measurements were

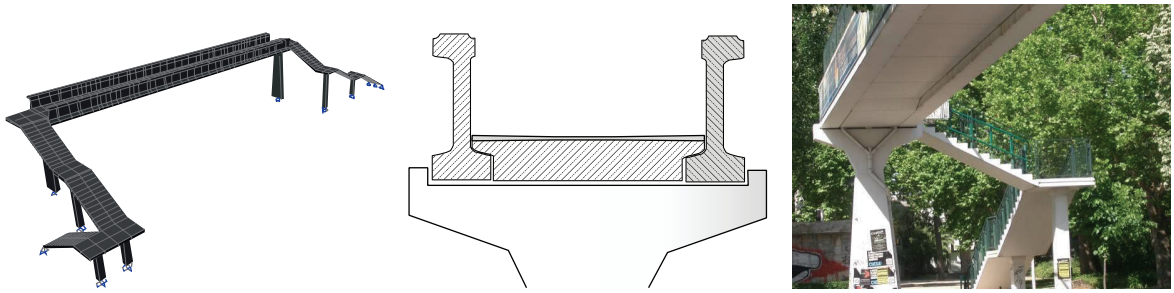

(a) (b) (c)

Figure 13: RC structure under study: (a) analytical model; (b) deck cross section; (c) view of column, deck, and stairway.

Table 9: Comparison of frequencies (Hz) between the analytical model and measurements *in situ*.

MODES	1	2	3	4	5	6	7	8	9	10	11	12	13	14	15
Analytical	0.84	1.23	1.48	2.23	2.59	3.30	3.56	4.22	4.89	5.27	5.49	6.04	6.53	6.98	7.52
In situ	0.88		1.7		3.12	3.55	4.52	5.06	5.66			6.59			

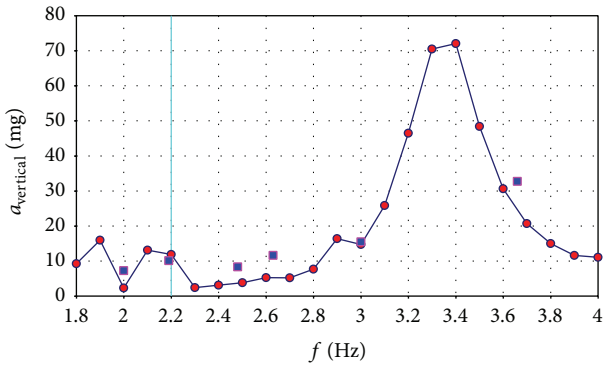

Figure 14: Comparison of amplitudes at mid-span (vertical acceleration) between *in situ* measurements and the analytical model: one person walking at various speeds (RC structure). Red circles: analytical model; blue squares: *in situ* measurements; vertical line at 2.2 Hz separates "walk" from "running."

Table 10: Acceleration measured at 1/2 span for the normal walking.

Direction	Acceleration at 1/2 span [mg]		
	Measuring device		Analytic model
	133	LN874	
Longitudinal	0.25	0.20	0.24
Lateral	2.00	2.00	2.00
Vertical	3.50	3.20	4.50

carried out at the same location but in a different epoch of the year.

These acceleration obtained for one or two pedestrians is below the maximum values indicated by the design guidelines, so for one or two persons the footbridge accomplishes the regulations. However, it is foreseen that for people's groups these limits are no longer respected. According to research related to the Millennium Bridge, there is a critical number N of pedestrians needed to bring about the situation of lateral *lock-in* where feedback of lateral forces cancels out the positive action of damping of the structure, resulting in unbounded growth of response [34]:

$$N = \frac{8\pi \cdot f_i \cdot \xi \cdot m_i}{k}, \tag{4}$$

where f_i, ξ, and m_i are lateral mode i frequencies, damping, and unit-normalized modal masses, and k is an empirical constant estimated as 300 Ns/m.

Considering that the vibration mode which has significant lateral oscillation is mode 4, $f = 2.23$ Hz, with a participation mass about 35% in this direction, the estimated N value for this footbridge is 6 pedestrians. Assuming a structure total span of 87 m (74 m largest span), it is easy to reach that number in normal conditions of use, because the total time needed to cross the bridge, is very large and many pedestrians can be present simultaneously.

The solution to this type of problem can be found by introducing mass-tuning dampers, which will reduce significantly the vibration levels compatible to the estimated pedestrian flux [11, 35]).

6.4. Overpass RC Footbridge with Precast (I + slab + I). The work developed by Oliveira [10] focuses on the vulnerability of a footbridge located near Faro, south of Portugal, serving as an overpass on EN125. This footbridge was chosen based on its location, in a region of high seismic load. In a circle of 8 km there are 9 very identical footbridges, which vary only in the span length and disposition of the lateral access that can be in form of stairs or ramps. These ways of communication are very important for the region in a scenario of catastrophe caused by a seismic event, especially because EN125 is the main route for accessing the hospital and for evacuating the population in case of tsunami.

In here we concentrate only on the comparison of frequency values from *in situ* and from a simplified analytical model through a dynamic linear analysis with SAP2000 [33].

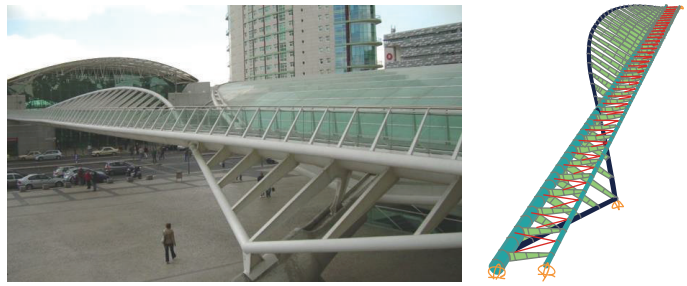

(a) (b)

Figure 15: (a) Vision of the CC Vasco da Gama (Calatrava) structure; and (b) analytical model.

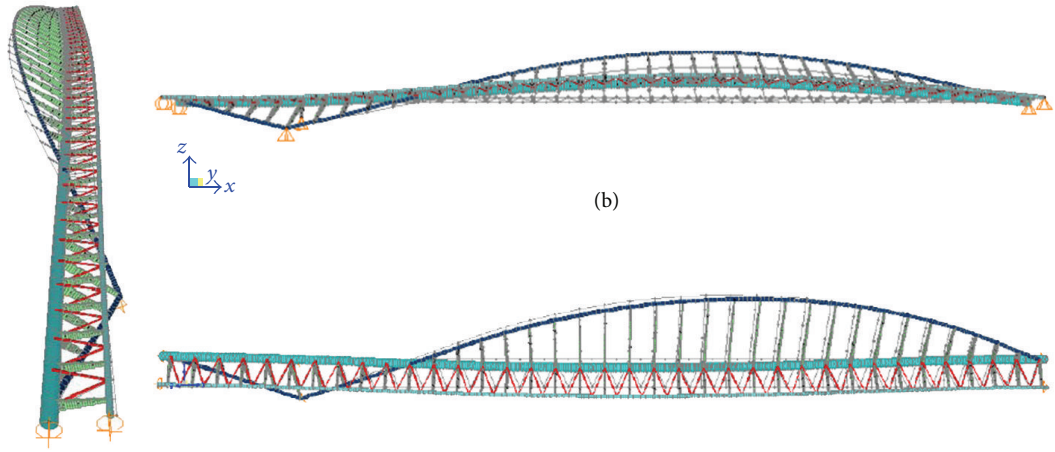

(a) (b) (c)

Figure 16: First vibration mode with $f = 0.84$ Hz with predominant vertical movement: (a) front view; (b) from above; (c) lateral view.

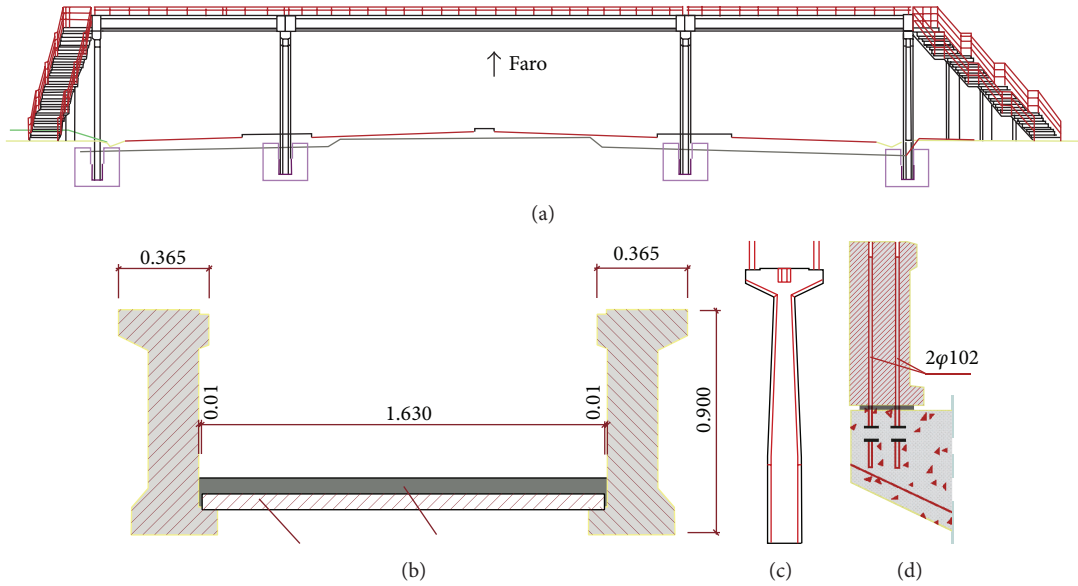

(a) (b) (c) (d)

Figure 17: RC footbridge in Faro: (a) front view; (b) cross-section with precast (I + slab + I); (c) central column (longitudinal view); (d) column-beam connection (units in m).

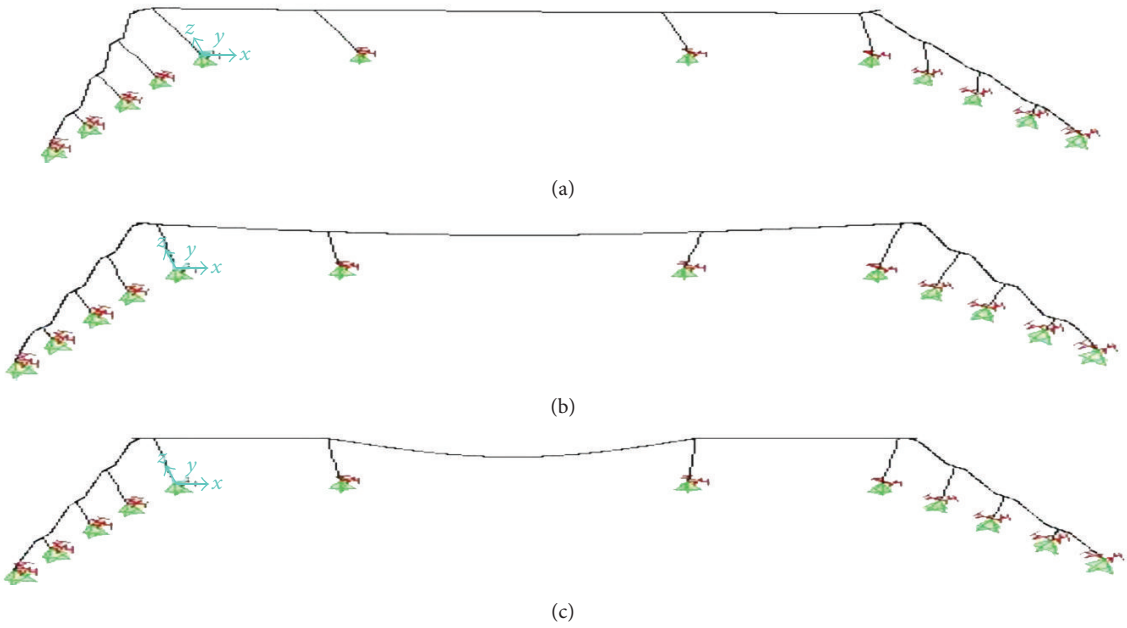

Figure 18: Modes of vibration: (a) 1st longitudinal; (b) 2nd tranversal; (c) 3rd vertical, central span.

The whole structure consists of prefabricated elements of reinforced concrete. The deck is 1.63 m wide and 45.3 m long, developed in a straight line, divided in 3 spans, Figure 17. The cross section of deck is made of precast RC (I + slab + I) and columns have an elongated shape almost constant in height, with $0.82 \times 0.5\ m^2$ at the base, but forming an enlargement when approaching the deck support.

The connection between the beams and columns is provided by two vertical bars of 20 mm on top of these columns, crossing the ends of each beam through holes made during the molding of the pieces. The holes were filled during the assembly phase, by a grout. A neoprene plaque was interposed between the column and the beam to distribute the contact stresses.

The access to the deck is made through four flights of stairs in each side. The stairs are almost perpendicular to the deck. Each set of stairs is formed by an independent prefabricated part, supported only on the ends. The steel used in reinforcing concrete was A500NR. Three types of concrete were used in this footbridge: C20/25 for the foundations, C35/45 in the prestressed beams, and C25/30 in the other parts. The concrete cover is 2.5 cm in the columns and beams and 5 cm in the foundations elements. Each span of the deck is formed by two prestressed reinforced concrete I beams.

The deck was modulated as a single bar with cross section as given in Figure 17(a). This option has been taken to ensure the simplicity of the model, considering that the links are used to guarantee that the deck behaves as only one piece. To simplify the model, the section of the columns was considered constant, with $0.82 \times 0.5\ m^2$. The height of the columns in the model is equal to reality. The stairs were modulated as a beam element with $1.6 \times 0.2\ m^2$ and the stairs columns with a square section of $0.3 \times 0.6\ m^2$ throughout its height.

The connection between the columns and other elements was made through steel bars. To simulate the contribution of these bars in the absorption of flexural moments, without giving excessive rigidity to allow for some flexibility, the modelling was done considering that on top of the columns there is an elastic support given by springs, which absorb some of the existing moments. These springs also help to simulate the effect of the slab, because the beams have no continuity above the columns, but the slab does.

The analysis of the *in situ* records led to the following values (Figure 18 and Table 11): the first mode is longitudinal, with a frequency of 2.2 Hz; the second mode is transversal, with a frequency of 2.6 Hz; the third mode is vertical in the central span (22 m), with a frequency of 3.6 Hz; the right lateral span presents a vertical vibration mode with a frequency of 10.7 Hz; the left lateral span has a vertical vibration mode with a frequency of 13.9 Hz. The damping ratio is 1.0%.

From Table 11 we can see an excellent agreement between the *in situ* and the analytical model for different spans. It is worth noting that the presence of stairways influences the first two mode shapes (L and T directions).

7. Conclusions and Final Remarks

We have been creating a database with geometrical and mechanical properties of many footbridges built in Portugal in the last two decades, representing the most common structural types. These structures, with larger spans varying from 11 to 110 m long, tend to become light and slender structures made of diverse materials and cross sections. They may show a pronounced dynamic amplification with the passage of pedestrians due to possible resonant effects.

Table 11: Comparison of frequencies (Hz) between measurements *in situ* and the analytical model.

Mode direction	Span 22 m		Span 12.5 m		Span 10.7 m	
	In situ	Analytical	*In situ*	Analytical	*In situ*	Analytical
Longitudinal	2.2	2.25	—	—	—	—
Transversal	2.6	2.69	—	—	—	—
Vertical	3.58	3.51	10.7	10.64	13.5	14.5

These large vibration amplitudes may be excited to a point of discomfort or even structural failure, and so the phenomenon deserves special attention [7].

We present a simple method to derive the main dynamic properties of these structures based on experimental *in situ* testing for loading caused by pedestrian crossing, allowing the estimation of most important frequencies and damping and amplification factors. This database, with 79 structures organized in 5 typologies, allow the setting of correlations of fundamental frequencies as a negative power function of span lengths L ($L^{-0.5}$ to $L^{-1.5}$), for different typologies and access situations. An analytical expression for the vertical direction, the sole direction exhibiting a reasonable correlation with span length, (2), based on simplified assumptions, is in the lower bound of attenuation with length ($L^{-0.5}$). Usually, frequency decreases faster with L: steel box-girders attenuate with $L^{-0.8}$, RC with $L^{-1.4}$, and "other types" with $L^{-0.8}$.

The experimental results are essential to calibrate analytical studies (presented for four cases) and detect sources of errors, essentially due to the supporting connections and a few simplifications in the model. The localization and type of stairways influences drastically the frequencies and modal shapes, especially in the transversal and the longitudinal directions of the structures and, consequently, the vibration levels.

Once the analytical model has been calibrated for the first frequency, agreement of other higher frequencies between measured and modelling was very good.

In relation to amplitudes, the results are not always so good, especially for RC structures, due to difficulty in setting proper pedestrian loading, so that the loading model well represents the *in situ* testing. Only with an accurate measurement of the input loading during the pedestrian passage, as Caetano et al. 2011 [1] tried to do, it would be possible to get better matching results between *in situ* and analytical modelling. Due to the difficulty in measuring accurately the input of a single pedestrian loading, modern guidelines are increasingly relying on the use of stochastic models instead of single pedestrian loading [2].

Despite these small details which need improvements in both the experimental techniques (for measuring the dynamic applied forces) and in the analytical modelling, we can say that both the used *in situ* expedite technique and linear modelling are quite robust for footbridges of simple geometry. For complex geometries *in situ* multiple instrumental setup is required for modal identification, together with a force-measurement setup provoked by the pedestrian passage.

We believe that the information contained in this database, involving a number of different structural types, allows the extrapolation of results to similar footbridges in other countries.

As a final result of practical importance, the measured peak acceleration values under pedestrian loading for steel structures are well above the limits defined in the international recommendations, especially for the case of jogging. This aspect confirms the idea, already stated in previous studies [7], that the majority of the steel footbridges in Portugal and in particular in the region of Lisbon suffer of excessive amplitude of vibration.

For the RC structures the situation is reversed. The measured peak acceleration values under pedestrian loading are well contained within the limits of the international recommendations, causing a better sensation of comfort and structural safety.

Several topics should be developed in future work:

(i) develop standard experimental techniques for routine testing of footbridges based on simple methods as the one presented to obtain the transfer function of these types of structures, making use of *in situ* load/deflection input and frequency/damping output estimations;

(ii) use more parameters of the collected data to reduce dispersion on the correlations;

(iii) from the convolution of the results obtained with the passage of a single person, obtain a simple analytical formula to estimate peak amplitude motion as function of number of people and velocity of crossing. Stochastic representation of pedestrian crossing can be analyzed in future work if we use the response of a footbridge produced by a single person at different speeds as a "green function" to obtain the stochastic formulation;

(iv) develop dissipation systems to damp out the large amplitudes of vibration observed in steel and long spanned structures, as suggested by Caetano et al. [35];

(v) estimate seismic vulnerability functions for these structures, as their collapse over main road access lines may be critical in case of earthquake emergency.

Conflict of Interests

The author declares that there is no conflict of interests regarding the publication of this paper.

Acknowledgments

This paper was partially supported by the Programa Pluri-Anual of "Fundação para a Ciência e a Tecnologia" (FCT). A special acknowledgment is due to T. Nunes da Silva, Ana Chagas, and Rui Oliveira for the modelling and computations. An anonymous reviewer made substantial contributions to improve the initial paper. Dr. I. Viseu revised the final text.

References

[1] E. Caetano, A. Cunha, and L. Câncio Martins, "Assessment of running pedestrian induced vibration on a stress-ribbon footbridge," in *International Conference of Footbridges (Footbridge '11)*, pp. 402–403, Wroclaw, Poland, 2011.

[2] HIVOSS Project, "Human Induced Vibrations of Steel Structures, in Design of Footbridges," Background Document, RFS2-CT-2007-00033, Research Fund for Coal and Steel, 2007.

[3] E. Caetano, A. Cunha, F. Magalhães, and C. Moutinho, "Studies for controlling human-induced vibration of the Pedro e Inês footbridge, Portugal. Part 1: assessment of dynamic behaviour," *Engineering Structures*, vol. 32, no. 4, pp. 1069–1081, 2010.

[4] E. Barbosa, F. Magalhães, E. Caetano, and A. Cunha, "The Viana footbridge: construction and dynamic monitoring," *Proceedings, ICE - Bridge Engineering*, vol. 166, no. BE4, pp. 273–290, 2013.

[5] C. Rebelo, E. Júlio, H. Varum, and A. Costa, "Cable tensioning control and modal identification of a circular cable-stayed footbridge: dynamic testing of civil engineering structures series," *Experimental Techniques*, vol. 34, no. 4, pp. 62–68, 2010.

[6] T. N. Silva, *Caracterização dos Principais Passadiços Existentes em Portugal e Análise Dinâmica de duas Passagens Superiores para Peões*, Final Course Monography, IST, Lisbon, Spain, 2005, (Portuguese).

[7] C. S. Oliveira and T. N. Silva, "Dynamic behavior of various types of Pedestrian bridges," in *International Conference Experimental Vibration Analysis for Civil Engineering Structures (EVACES '07)*, University of Porto, Porto, Portugal, 2007, CD Rom.

[8] RSA, *Regulamento de Segurança e Acções para Estruturas de Edifícios e Pontes*, Imprensa Nacional—Casa da Moeda, Lisboa, Portugal, 1983, (Portuguese).

[9] A. Chagas, *Estudos do Comportamento Dinâmico de uma Passagem de Peões: Centro Comercial Vasco da Gama [M.S. thesis]*, IST, Lisbon, Portugal, 2007, (Portuguese).

[10] R. Oliveira, *Estudos do comportamento dinâmico de uma passagem de Peões: no Algarve [M.S. thesis]*, IST, Lisbon, Portugal, 2010, (Portuguese).

[11] S. Živanović, A. Pavic, and P. Reynolds, "Vibration serviceability of footbridges under human-induced excitation: a literature review," *Journal of Sound and Vibration*, vol. 279, no. 1-2, pp. 1–74, 2005.

[12] J. Fonseca, C. Pinto, and C. Azevedo, "About construction and dynamic behavior of Carpinteira footbridge," in *International Conference of Footbridges (Footbridge '11)*, pp. 378–379, Wroclaw, Poland, 2011.

[13] R. W. Clough and J. Penzien, *Dynamic of Structures*, McGraw-Hill, New York, NY, USA, 1975.

[14] H. Bachmann, ""Lively" footbridges—a real challenge," *Bautechnik*, vol. 81, no. 4, pp. 227–236, 2004.

[15] J. C. Vinagre, *Análise Dinâmica de Pontes para Peões [M.S. thesis]*, IST, Lisbon, Portugal, 1989, (Portuguese).

[16] M. Willford, "Dynamic actions and reactions of pedestrians," in *International Conference of Footbridges (Footbridge '02)*, Paris, France, 2002.

[17] B. Briseghella, G. Meneghini, and E. Siviero, "Consideration onthe vibrational problem in recently built footbridges and theadoptable solution to smoothen their effects," in *International Conference of Footbridges (Footbridge '02)*, Paris, France, 2002.

[18] BSI, BS 5400; British Standards Institution, "Steel, Concrete and Composite Bridges: Specification for Loads. BSI, Part 2, Appendix C," 1978.

[19] AASHTO, *Guide Specifications for Design of Pedestrian Bridges*, Pittsburgh, Pa, USA, 1988, (Revised in 1997 and 2008).

[20] EN 1990, *Eurocode 0, Eurocode Basis of Structural Design, EN 1990:2002*, European Committee for Standardization, Brussels, Belgium, 2003.

[21] DIN-ENV 1992-2, *European Committee for Standardization*, Brussels, Belgium, 2003.

[22] ISO 10317, *Bases for Design of Structures—Serviceability of Buildings and Walkways against Vibrations*, 2nd edition, 2007.

[23] OHBDC, *Ontario Highway Bridge Design Code*, Ontario Ministry of Transport, Toronto, Canda, 1983.

[24] Japanese Footbridge Design Code, 1979.

[25] M. Schlaich, "Planning conditions for footbridges," in *International Conference of Footbridges (Footbridge '02)*, Paris, France, 2002.

[26] S. Stoyanoff, M. Hunter, and D. D. Byers, "Human-induced vibrations on footbridges," in *International Conference of Footbridges (Footbridge '02)*, Paris, France, 2002.

[27] M. Kazakevitch and O. Zakora, "Influence of pedestrian load on dynamics of bridges," in *International Conference of Footbridges (Footbridge '02)*, Paris, France, 2002.

[28] Hong Kong, *Structures Design Manual for Highway and Railways*, Highway Department, Government of the Honk Kong Special Administrative Region, 2002.

[29] C. Heinemayer, C. Butz, A. Keil et al., "Design of lightweight footbridges for human Induced vibrations," Joint Report, JRC, 2009.

[30] SÉTRA, *Footbridges—Assessment of Vibration Behavior of Footbridges under Pedestrian Loading*, Association Française de Genie Civil, Paris, France, 2006.

[31] Footbridge 2008. Proceedings, Oporto, Portugal, 2008.

[32] Footbridge 2011. Proceedings, Wroclaw, Poland, 2011.

[33] CSI, *SAP2000*, Computers and Structures, Inc., Berkeley, Calif, USA, 2008.

[34] P. Dallard, A. J. Fitzpatrick, A. Flint et al., "The London millennium footbridge," *Structural Engineer*, vol. 79, no. 22, pp. 17–33, 2001.

[35] E. Caetano, A. Cunha, and C. M. R. Moutinho, "Implementation of passive devices for vibration control at Coimbra footbridge," in *International Conference Experimental Vibration Analysis for Civil Engineering Structures (EVACES '07)*, University of Porto, Porto, Portugal, 2007, CD Rom.

Hindawi Publishing Corporation
Shock and Vibration
Volume 2014, Article ID 162781, 11 pages
http://dx.doi.org/10.1155/2014/162781

Research Article

Study of the Complex Stiffness of a Vibratory Mechanical System with Shape Memory Alloy Coil Spring Actuator

Samuell A. Holanda,[1] Antonio A. Silva,[1] Carlos J. de Araújo,[1] and Alberdan S. de Aquino[2]

[1] *Federal University of Campina Grande (UFCG), 58420-140 Campina Grande, PB, Brazil*
[2] *Federal Institute of Paraíba (IFPB), 58015-430 João Pessoa, PB, Brazil*

Correspondence should be addressed to Antonio A. Silva; almeida@dem.ufcg.edu.br

Received 15 July 2013; Accepted 3 March 2014; Published 18 June 2014

Academic Editor: Miguel M. Neves

Copyright © 2014 Samuell A. Holanda et al. This is an open access article distributed under the Creative Commons Attribution License, which permits unrestricted use, distribution, and reproduction in any medium, provided the original work is properly cited.

The vibration control is an important area in the dynamic of structures that seeks to reduce the amplitude of structural responses in certain critical frequency ranges. Currently, the scientific development leads to the application of some actuators and sensors technologically superior comparing to the same features available on the market. For developing these advanced sensors and actuators, smart materials that can change their mechanical properties when subjected to certain thermomechanical loads can be employed. In this context, Shape memory alloys (SMAs) may be used for developing dynamic vibration dampers which are capable of acting on the system providing proper tuning of the excitation frequency and the natural frequency. This paper aims to analyze the behavior of the stiffness and damping of a SMA helical coil spring actuator coupled to a mechanical system of one degree of freedom (1 DOF) subjected to an unbalanced excitement force and a temperature control system. By analyzing the effect of these parameters on the structural response and considering the concept of complex stiffness, it can be possible to predict the system's behavior within certain acceptable ranges of vibration, already in the design phase.

1. Introduction

In the current stage of scientific and technological development, design of structures becomes increasingly complete and comprehensive to meet the diverse performance requirements. Among these requirements, we highlight the need for increasingly lighter and resilient structures, dynamic behavior to ensure stability and accuracy, and attenuation of vibrations to ensure the structural integrity and better comfort [1].

Structural systems are constantly susceptible to excitations that can lead to mechanical vibrations. These vibrations are in most cases undesirable, because they can endanger the structural integrity of the system itself and, in some cases, the safety of users.

Recently, shape memory alloys (SMA) appear as potentially viable actuators for vibration control. The shape memory effect, superelasticity, and changes of mechanical properties with temperature allow the application of these smart materials in various fields of engineering [2]. However, the behavior of SMA is nonlinear, which makes its modeling and numerical simulation more complex, since the changes of parameters such as temperature and excitation frequency should be considered. This behavior requires further study to determine the intrinsic characteristics of SMA such as complex stiffness, which considers the energy dissipation per cycle and the frequency dependence that lead to variations of the structural damping.

The natural frequency depends on the mass and stiffness of a mechanical system and SMA has the capacity to alter the elastic modulus. Then, employing these smart materials, it is possible to change the stiffness of a mechanical system and consequently change resonance regions. Some studies indicate that this effect can attenuate the amplitude of vibrations in a critical frequency range for making the transition for resonance; it also allows changing the vibration modes of the structure [3].

SMAs are naturally classified as metallic materials with high damping capacity, consequence of a hysteretic behavior related to phase transformations of the material [2, 3].

The damping factor of the system also changes with the change of stress or temperature of the SMA actuator. However, the influence of damping vibration levels and system response, due to a change in the SMA behavior, needs to be further investigated and understood [4]. In many cases, for vibration attenuation, SMAs are used in the form of helical coil springs [3, 5–10].

Very recently, Aguiar et al. [5] realized an experimental investigation of vibration reduction using SMA springs. The vibration analysis revealed that SMA elements introduce complex behaviors to the studied system and that different thermomechanical loadings are of concern showing the main aspects of the SMA dynamical response. The results establish that adaptability due to temperature variations is defined by a competition between stiffness and hysteretic behavior changes. In another recent work, Aguiar et al. [6, 7] studied specifically the modeling, simulation, and experimental analysis of SMA helical springs. Basically, it is assumed that a one-dimensional constitutive model to describe its thermomechanical shear behavior and, afterwards, helical springs are modeled by considering classical approach. Savi et al. [8] investigated the nonlinear dynamics of an adaptive tuned vibration absorber (ATVA) with a SMA element. The influence of the hysteretic behavior due to stress-induced phase transformation of the SMA is considered. The hysteretic behavior introduces complex characteristics to the system dynamics but also changes the absorber response allowing vibration reduction in different frequency ranges.

SMA springs were investigated by Rackza [9] on a structure of controllable-stiffness springs which might be utilized in vibration reduction systems, for example, in driver seats. Mirzaeifar et al. [10] studied analytically and numerically the pseudoelastic response of SMA helical springs under axial force. Analytical and numerical results are compared and it is shown that the solution based on the SMA curved bar torsion gives an accurate stress analysis in the cross section of the helical SMA spring in addition to the global load-deflection response. Toi et al. [11] proposed a finite element formulation for the analysis of superelastic behaviors of SMA helical spring considering the asymmetric tensile and compressive behavior and the torsional deformation. The developed program has applied to the superelastic, large deformation analysis of NiTi helical springs under tensile loading and unloading.

In this paper, the effects of stiffness and damping of a SMA helical spring actuator on the dynamic response of a mechanical system of one degree of freedom (1 DOF) subjected to free vibration and harmonic excitation from an unbalanced motor were studied. The main objective is to introduce the concept of complex stiffness in a mechanical system incorporating SMA, not explored in the aforementioned works.

2. Model of Unbalanced Rotating and Complex Stiffness

The studied mechanical system is excited harmonically through a motor with unbalanced rotating. This condition can be simplified and better understood from the model

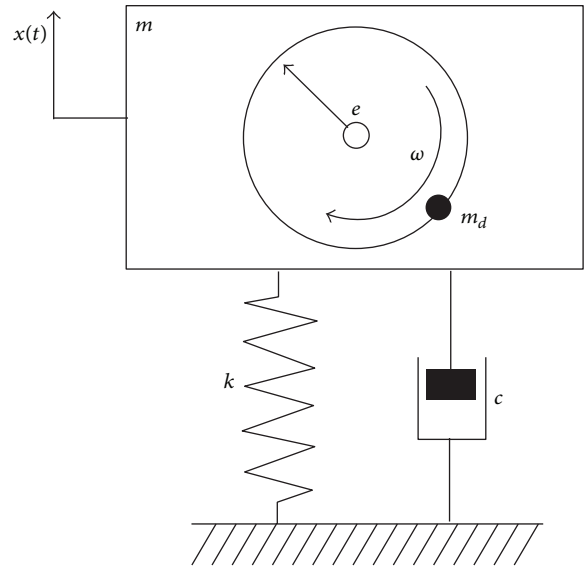

Figure 1: Physical model of unbalanced rotating system with one SMA coil spring (k, c).

of rotating unbalanced machines, illustrated in Figure 1. In this physical model, k and c characteristics are a function of temperature, provided by a SMA helical coil spring.

The equation that governs the system defined in Figure 1 is given by [12]

$$m\ddot{x} + c\dot{x} + kx = m_d e\omega^2 \sin \omega t, \tag{1}$$

where m_d, e, and ω are, respectively, the unbalanced mass, imposed eccentricity, and excitation frequency. Solving (1), the frequency response for this condition is given by

$$\frac{mX}{m_d e} = \frac{r^2}{\sqrt{\left(1 - r^2\right)^2 + \left(2\zeta r\right)^2}}, \tag{2}$$

where $r = \omega/\omega_n$ is the frequency ratio and $\zeta = c/c_c$ is the damping factor of the system [12].

Considering Figure 1 and a harmonic motion of the type $x = Xe^{i\omega t}$, the force is given by the sequence of the following equations:

$$F(t) = kx + c\dot{x}, \tag{3}$$

$$F(t) = kXe^{i\omega t} + ic\omega Xe^{i\omega t}, \tag{4}$$

$$F(t) = (k + i\omega c)\, x. \tag{5}$$

From (4), the concept of complex stiffness can be established as follows:

$$k\left(1 + i\frac{c\omega}{k}\right),$$
$$k^* = k\left(1 + i\eta\right). \tag{6}$$

Here η is called the loss factor and k^* is defined as complex stiffness of the SMA coil spring actuator.

The imaginary part of the complex stiffness, $i\eta$, corresponds to the energy dissipated in the system, since the loss factor can be written as defined in the following equation:

$$\eta = \frac{c\omega}{k}. \tag{7}$$

The material loss factor can be determined by the equivalent viscous damping factor, ζ_{eq}, which can be obtained by the relation of the logarithmic decrement for slightly damped systems:

$$\delta \cong 2\pi\zeta_{eq} \cong \pi\eta, \tag{8}$$

$$\zeta_{eq} \cong \frac{\eta}{2}. \tag{9}$$

From (9), the relation between the damping factor ζ_{eq} and the loss factor η is $\eta \cong 2\zeta_{eq}$.

3. Thermomechanical Properties of the SMA Actuator

3.1. Elastic Modulus and Loss Factor of the SMA Material. For the fabrication of the SMA coil spring, a NiTi wire with 2.02 mm in diameter supplied by Memory-Metalle (Germany) was employed. In order to eliminate some of the strain hardening of the supplied material, the NiTi SMA wire was annealed at 400°C for 30 minutes and cooled at room temperature. This heat treatment at a temperature lower than 650°C ensures a high elastic response of the manufactured NiTi spring, on the order of 40% of its undeformed length, even in the martensitic state. After this heat treatment, two specimens were removed to determine some thermomechanical properties of the SMA material.

The first sample with 1.5 mm in length and 0.0065 g was used to determine the phase transformation temperatures of the NiTi SMA wire by DSC (differential scanning calorimetry). The second sample with 31.2 mm in length and 0.663 g was used for two tests. In the first test, the sample was studied using a dynamic mechanical analyzer (DMA, model Q800, TA Instruments) at three different temperatures (30°C, 50°C, and 70°C) corresponding to regions with different crystalline phases (martensite, mixture, and austenite). These experiments were carried out in a single cantilever beam mode by applying a tip force with variable oscillating frequency (8 to 150 Hz) for a constant amplitude deflection of 5 μm. The second experiment performed with the second sample was realized to verify the influence of the frequency on the stiffness (elastic modulus) and damping (Tan δ) for a range of temperatures starting from 25°C to 100°C, for four different frequencies (1 Hz, 5 Hz, 10 Hz, and 12 Hz).

3.2. Mathematical Model for the Stiffness of the SMA Spring. In this work, the simplified mathematical Ikuta model [13] was adapted to describe the behavior of the theoretical stiffness of the SMA spring as a function of temperature and simulate the experimental results. The following equations represent, respectively, the stiffness behavior of the SMA spring during heating and cooling:

$$k_{SMA-A} = k_{min} + \left((k_{max} - k_{min}) - \frac{(k_{max} - k_{min})}{1 + e^{((6,2/(A_F - A_S)) \cdot (T \cdot ((A_F + A_S)/2)))}} \right), \tag{10}$$

$$k_{SMA-M} = k_{min} + \left((k_{max} - k_{min}) - \frac{(k_{max} - k_{min})}{1 + e^{((6,2/(M_S - M_F)) \cdot (T \cdot ((M_F + M_S)/2)))}} \right), \tag{11}$$

where

k_{SMA-A} is stiffness of SMA spring during heating;
k_{SMA-M} is stiffness of SMA spring during cooling;
k_{min} is minimum stiffness of SMA spring;
k_{max} is maximum stiffness of SMA spring;
M_S is martensite start temperature;
M_F is martensite final temperature;
A_S is austenite starts temperature;
A_F is austenite final temperature;
T is spring temperature.

3.3. Damping Factor of the Mechanical System. The equivalent damping factor ζ_{eq} was calculated from the free vibration response of the mechanical system with the SMA spring subject to an input impulse given by an impact hammer (PCB Piezotronics; model 086C03). From this excitement was possible to obtain the envelope curve of exponential nature that involves the signal and characterizes the decay of displacements with time. For this, the method of logarithmic decrement was employed, calculating the ratio between two chosen signal amplitudes.

Previous studies [14, 15] show that the damping factor for SMA material is generally less than 0.1. In this case, the equation for calculating the damping factor by the method of logarithmic decrement can be simplified and used as defined by the following:

$$\zeta = -\frac{1}{2\pi n} \ln\left(\frac{A_n}{A_1}\right), \tag{12}$$

where n is the number of cycles, A_1 is the amplitude of the first cycle, and A_n is the amplitude of n cycle.

3.4. Forced Vibration Tests. Several tests were performed with the mechanical system subjected to a harmonic excitation in order to compare the response of the system when the SMA spring is in the martensitic phase (25°C) and in the austenitic phase (70°C).

The system was excited in frequency ranges corresponding to the two resonance frequencies (martensite and austenite phases). Analyzing the structural responses in the time

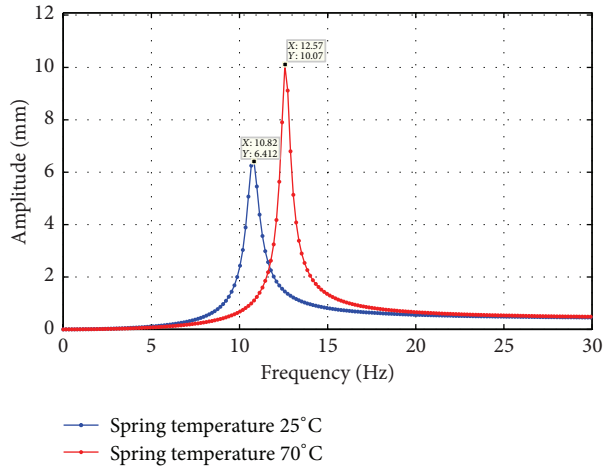

Figure 2: Typical frequency response for the system under unbalanced rotating.

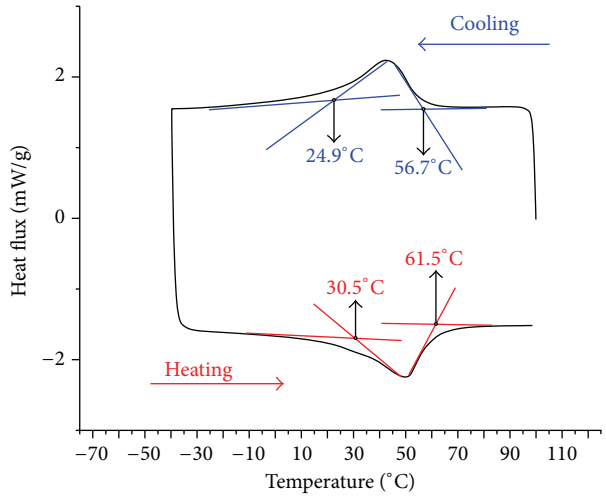

Figure 3: Transformation temperatures of the NiTi SMA wire obtained by DSC.

and frequency domains for these conditions, it was possible to analyze the system behavior and to better understand how variations of parameters of the SMA actuator affect the dynamic response of this typical mechanical model.

Figure 2 illustrates two typical frequency responses of the system with unbalanced rotating using physical parameters of the test bench. The blue curve represents the response with the SMA spring at 25°C (martensite phase), while the red curve represents the response with the SMA spring at 70°C (austenite phase). Two peaks corresponding to the natural frequencies and the influence of the stiffness and damping of the SMA spring on the dynamic behavior of the system can be verified. The heating process increases the stiffness of the NiTi SMA spring, causing an increase in frequency and reducing the damping (resulting in a peak of higher amplitude).

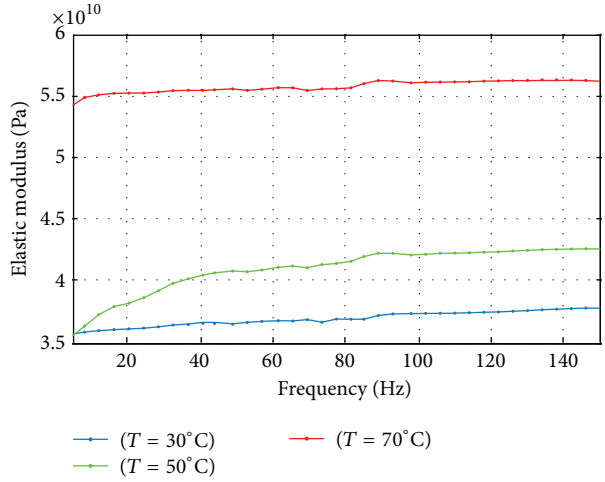

Figure 4: Elastic modulus as a function of frequency for the NiTi SMA wire at three temperatures: 30°C, 50°C, and 70°C.

4. Results and Discussion

4.1. Thermomechanical Characterization of the SMA Wire. The phase transformation temperatures were determined using a DSC calorimeter (TA Instruments; model Q20). The experiment was performed with a heating and cooling rate of 5°C/min and a temperature range between 0°C and 100°C. Figure 3 shows the characteristic DSC peaks for the NiTi SMA wire employed to manufacture the SMA spring actuator.

The phase transformation temperatures obtained were $M_s = 56.7^\circ\text{C}$ (martensite start) and $M_f = 24.9^\circ\text{C}$ (martensite finish) during cooling and $A_s = 30.5^\circ\text{C}$ (austenite start) and $A_f = 61.5^\circ\text{C}$ (austenite finish) during heating. Comparing the two temperatures of the DSC peaks, it can be verified that this NiTi SMA wire presents a low thermal hysteresis, of the order of $\Delta T = 8^\circ\text{C}$.

In parallel, two analyses of the dynamic behavior of the NiTi SMA wire were performed using a commercial DMA analyzer (TA Instruments; model Q800) in order to verify the influence of the excitation frequency and temperature on the elastic modulus and loss factor of the material. The results of these DMA tests with variable frequency are shown in Figures 4 and 5.

The increase of temperature in Figure 4 changes significantly the elastic modulus, which showed values of about 36 GPa (30°C), 41 GPa (50°C), and 55 GPa (70°C), taking as reference the frequency of 80 Hz. The behavior of elastic modulus as a function of frequency showed small variations, mainly for the martensitic (30°C) and austenitic (70°C) stable states, with a tendency to stabilize above 100 Hz.

The behavior of the loss factor was the inverse of the elastic modulus as pointed out in Figure 5. As expected [14], a reduction in the measured values with increasing temperature was verified. The damping in the austenitic phase (70°C) is smaller than the values measured in the martensitic phase (30°C). A variation of the loss factor was observed as

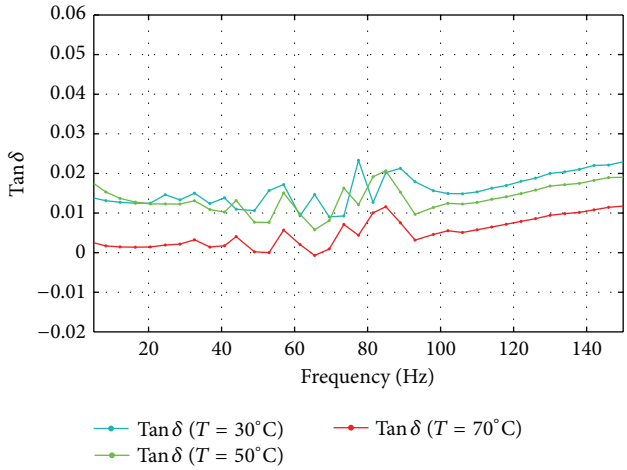

Figure 5: Loss factor as a function of frequency for the NiTi SMA wire at three temperatures: 30°C, 50°C, and 70°C.

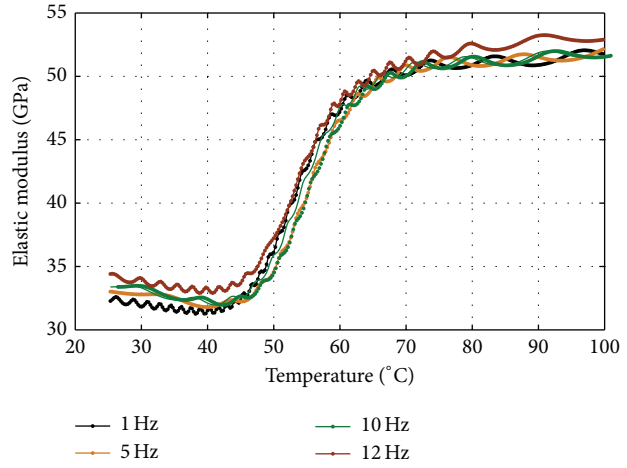

Figure 6: Behavior of the elastic modulus of the NiTi SMA wire with the change of excitation frequency.

a function of frequency with a tendency to increase linearly for frequencies higher than 100 Hz.

Figures 6 and 7 show the characteristic curves for the NiTi SMA wire obtained with the DMA analyzer. The behavior of elastic modulus is not much affected by the frequency, being more dependent on the temperature. For example, in Figure 6 for martensitic state (30°C) the elastic modulus increases of about 3 GPa between 1 Hz and 12 Hz. However, a considerable increase is observed in the elastic modulus for all frequencies along the phase transformation during heating. This increase of elastic modulus with temperature indicates a corresponding increase in the stiffness of the SMA material, resulting in less energy dissipation at high temperatures by the structure.

Figure 7 shows the behavior of the loss factor as a function of temperature and frequency. It is observed that the highest peaks of loss factor appear during the phase transformation

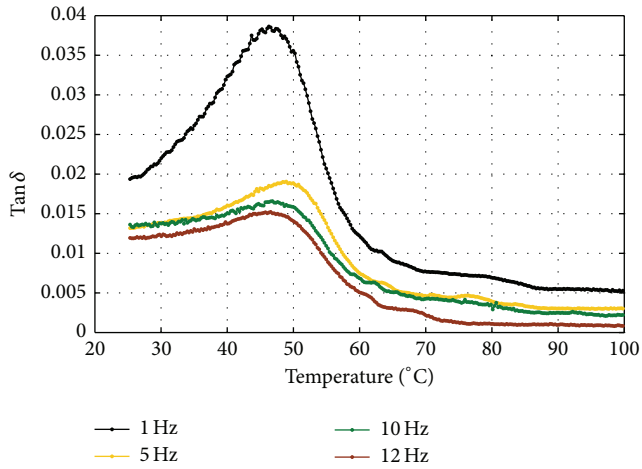

Figure 7: Behavior of the loss factor of the NiTi SMA wire with the change of excitation frequency.

for the lowest frequency (1 Hz). Higher excitation frequencies tend to inhibit the Tan δ peaks, so that for frequencies higher than 5 Hz peak values decrease rapidly.

The variation of stiffness and damping observed in Figures 6 and 7 is related to the internal movements of martensite variants into the SMA material, with lower stiffness and high damping in the martensitic phase compared to austenitic phase [14, 15].

4.2. Characterization of SMA Spring Stiffness. In order to stabilize the phase transformation of the SMA spring manufactured from the NiTi wire, a thermal cycling procedure was performed for training the spring actuator, as shown in Figure 8. In this procedure, 500 cycles of heating and cooling were performed in order to stabilize the behavior of shape memory effect of the SMA spring. In a training cycle, the NiTi SMA spring was heated to 80°C and then immediately cooled to 3°C, under a constant load (dead weight).

For determining the SMA spring stiffness during heating and cooling, a universal testing machine (INSTRON 5582) equipped with a controlled heating chamber was used. For this one, the NiTi SMA spring was subjected to five cycles of compression loading and unloading, with 10 mm of maximum deflection in a temperature range between 25°C and 70°C in steps of 5°C. For this imposed displacement the NiTi SMA spring presents an elastic response in both phases, martensite (25°C) and austenite (70°C), without presenting residual deformation. Table 1 shows the experimental results of stiffness and the theoretical stiffness obtained with the adapted Ikuta models (11) and (12).

Figure 9 shows the stiffness behavior of the NiTi SMA spring as a function of temperature. It can be verified that the stiffness increased 1.37 times at the end of heating when compared with the initial value. For temperatures higher than 60°C the stiffness tends to stabilize, due to the fact that from this point the crystalline structure of the SMA spring is fully austenitic. Similarly, stabilization of stiffness can be

Table 1: Stiffness of the NiTi SMA spring actuator as a function of temperature.

Temperature (°C)	Stiffness (N/m)	
	Heating	Cooling
25	2280.3	2396.3
30	2337.1	2382.5
35	2388.6	2474.8
40	2502.6	2654.1
45	2701.6	2907.4
50	2897.2	3044.7
55	3053.8	3110.3
60	3083.1	3128.4
65	3117.4	3137.6
70	3134.5	3144.4

Table 2: Main parameters of the experimental test bench.

Parameter	Value
Total mass (kg)	0.4998
Unbalanced mass (kg)	0.006
Eccentricity (m)	0.033
Spring material	NiTi SMA
Number of active coils	7
Undeformed spring length (mm)	34
Spring wire diameter (mm)	2.02
Spring effective diameter (mm)	12

obtained at temperatures below 25°C when the SMA gets fully martensitic.

Comparing Figures 6 and 9 a qualitative similar behavior is observed between the pure elastic modulus of the NiTi SMA and stiffness of the smart spring as a function of temperature.

4.3. Test Bench: Specifications and Control System. The experimental set-up and fuzzy control system applied in this study was developed by Aquino [16] and subsequently used by Holanda [17]. This mass-spring system with 1 DOF is excited by an unbalanced motor assembled on an aluminum bar attached to the SMA spring. The mass is driven by two vertical rods assembled into a steel plate through two linear ball bearings. The rotational speed of the electrical motor was controlled with a frequency inverter that allows adjustment of the excitation in a range between 0 and 40 Hz, including the two regions of resonances. Figure 10 shows the test bench developed for the experimental analysis.

Table 2 shows the specifications of the test bench showed in Figure 10. The experimental test bench is composed by (1) SMA spring; (2) unbalanced motor; (3) minicooler; (4) electrical heating system for SMA spring (Joule effect); (5) accelerometer; (6) impact hammer; (7) LabVIEW Interface.

The block diagram for temperature control of the NiTi SMA spring is shown in Figure 11. The controller aims to send information that will allow the activation of SMA actuator by changing its temperature. The heating of the SMA spring is realized in order to change the stiffness and consequently change the natural frequency causing the system to leave the resonance condition, leading to vibration reduction. The temperature control of the NiTi SMA spring is based on a fuzzy controller implemented in the LabVIEW software. The heating was done by Joule effect and the cooling was done by forced convection. The developed controller was not able to carry out a temperature sweep considering, for example, a sinusoidal temperature change. In this case, the user indicated the desired temperature and the controller is in charge of taking the system to that temperature and to keep it constant. Figure 12 shows the system actuation for temperature control of the NiTi SMA spring. A good performance of the temperature control can be observed, both for heating and cooling, with temperature stabilization of the SMA spring according to the reference temperature.

4.4. Free Vibration Response. Figures 13 and 14 show the exponential decay of the system with SMA spring in two selected conditions: 25°C and 70°C, respectively.

The damping transfered to the system by the SMA spring is a function of temperature. For 25°C the damping factor (ζ_{eq}) measured was 0.0303, while for SMA spring at 70°C the obtained value was 0.0194. In the condition of Figure 13 the damping of the SMA spring is higher, and consequently the decay of the displacements is faster than that found in Figure 14. For the stiffness test and using the same temperature range, the results shown in Figure 15 were obtained, with the values of the damping factor of the system of Table 3.

By analyzing Figure 15, it can be observed that the damping peaks appear during the phase transformation, between 40°C and 45°C. At these temperatures, the measured damping factors were 0.0327 and 0.0324, respectively. The minimum damping was verified at the austenitic phase (70°C), with the value of 0.0194. In the martensitic phase, the damping factor measured was 0.0303.

The qualitative behavior of the damping factor shown in Figure 15 is similar to the one of Tan δ for the SMA wire measured in the DMA, as pointed out in Figure 7. The damping peak verified during phase transformation is observed mainly due to the transient character of this region, which is related to accommodation of austenite-martensite variants during thermally induced transformation.

4.5. Vibration Response with Temperature Control in the Resonance Condition. In order to verify the reduction in the amplitude of resonance for the two conditions of SMA spring (martensite and austenite phases), the mechanical system was excited in the natural frequency and then the temperature control was activated, heating or cooling the SMA spring.

In the first test, the system was put in resonance with the SMA spring at 25°C (blue curve) and then heated to 70°C (red curve). Figure 15 shows the time response for that test

(a) (b) (c)

Figure 8: Details of thermomechanical cycling for training the NiTi SMA spring. (a) Cooling (~3°C); (b) delay; (c) heating by electrical current (~80°C).

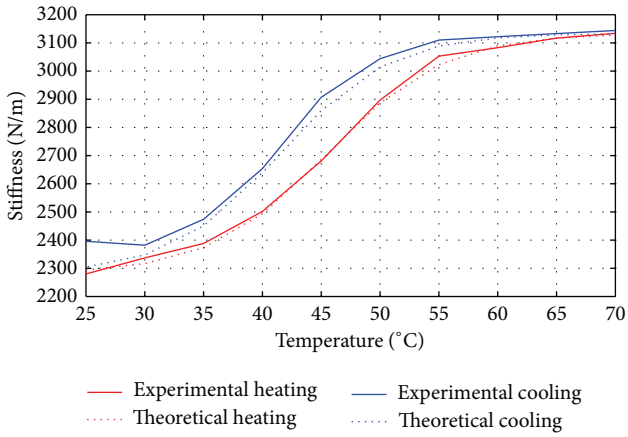

Figure 9: Theoretical and experimental stiffness of the NiTi SMA spring as a function of temperature.

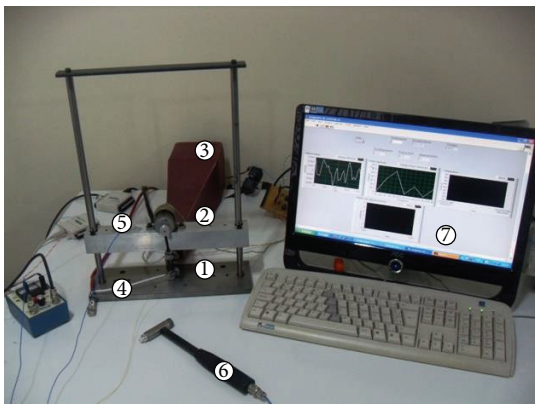

Figure 10: Experimental test bench: (1) SMA spring; (2) unbalanced motor; (3) minicooler; (4) electrical heating system (Joule effect); (5) accelerometer; (6) impact hammer; (7) LabVIEW Interface.

condition. In the blue range of Figure 16 the maximum amplitude was 6 mm. After heating, the system got out of resonance with maximum amplitudes of 2.7 mm, corresponding to 55% of reduction in the displacement levels. These amplitudes are lower than 10 mm, which was the displacement imposed for SMA spring in elastic regime during the thermomechanical characterization of stiffness as a function of temperature (Table 1, Figure 9).

In the second test, the system was put in resonance with the SMA spring at 70°C (red curve) and then cooled to 25°C (red curve). Figure 17 shows the time response for that test condition. In the blue range of Figure 17 the maximum amplitude was 12 mm. After heating, the system got out of resonance with maximum amplitudes of 5.7 mm, corresponding to 60% of reduction in the displacement levels. Typically, the linear region of a superelastic NiTi spring corresponds to about 40% of its undeformed length, as can be seen in the work of Aguiar et al. [7]. Then, as the amplitude of vibration did not exceed 35% of the undeformed spring length, it is estimated that there is no energy dissipation in the system due to a possible stress-induced phase transformation in the SMA spring. To make this hysteretic dissipation occurs it is necessary to achieve much higher strain levels in the SMA spring.

Figure 18 shows the vibration levels measured when the system is put into resonance at three different temperatures. With increasing temperature and variation of damping of the system, the amplitudes change. The damping is higher in the martensitic phase, showing a slight peak in the region of phase transformation, and is minimal in the austenite phase, as pointed out in Figure 7. These characteristics can be noted when considering the amplitude of vibrations at the resonance zones. Lower amplitudes are observed at 45°C, temperature where the maximum damping occurs. At 70°C, the amplitudes are higher than the ones measured previously due to the lower damping of the SMA spring in this temperature range (25°C to 45°C). These amplitude signals were collected separately, placing the system in resonance for each temperature examined.

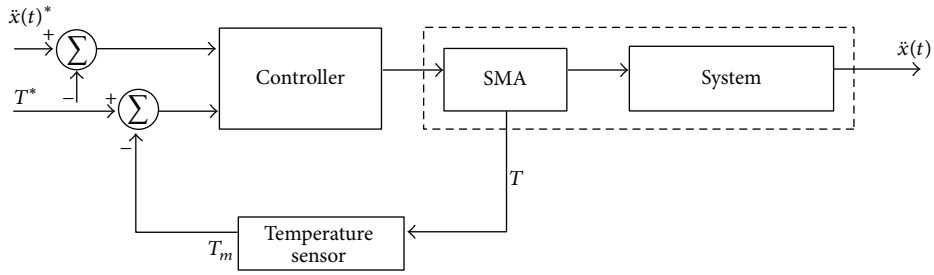

Figure 11: Representation of the temperature control system for the SMA spring actuator.

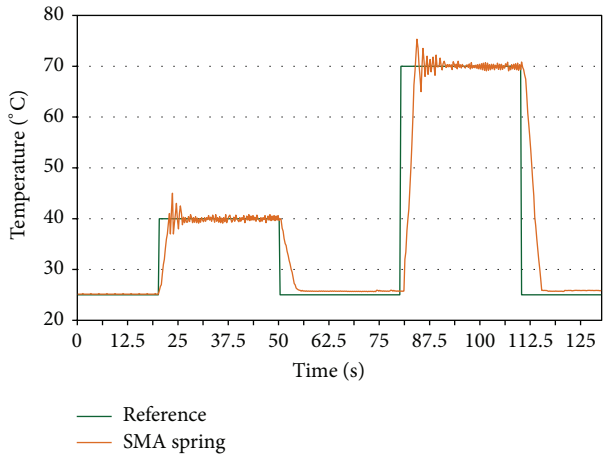

Figure 12: Performance of the temperature control system for the SMA spring.

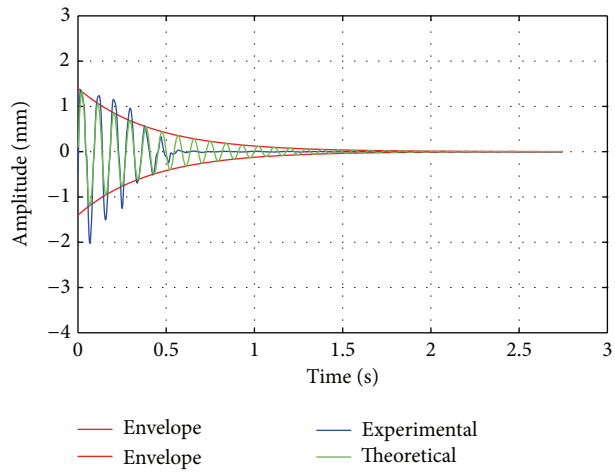

Figure 13: Impulse response of the mechanical system at 25°C.

Table 3: Experimental damping factor of the mechanical system as a function of temperature.

Temperature (°C)	Damping factor ζ_{eq}	
	Heating	Cooling
25	0.03037	0.02976
30	0.03096	0.03091
35	0.03124	0.03158
40	0.03179	0.03277
45	0.03241	0.03054
50	0.02823	0.02669
55	0.02465	0.02293
60	0.02048	0.02069
65	0.02027	0.02047
70	0.01947	0.02013

Table 4: Relationship between damping factor and loss factor for the resonance condition.

Temperature (°C)	$2 * \text{damping factor } (2\zeta_{eq})$	Loss factor η
25	0.06074	0.07204
30	0.06192	0.07265
35	0.06248	0.07529
40	0.06358	0.07643
45	0.06482	0.07635
50	0.05646	0.05988
55	0.0493	0.05043
60	0.04096	0.04268
65	0.04054	0.03810
70	0.03894	0.03385

Table 4 allows verification of the validity of the relationship between the loss factor and the damping factor, $\eta = 2\zeta_{eq}$. As this relationship is valid only when the system is in resonance, the loss factor (14) of the NiTi SMA spring was calculated from the simplification of (13), considering the ratio of frequency equal to 1 (in resonance condition). Consider

$$X = \frac{F_0/k}{\sqrt{\left(1 - r^2\right)^2 + \left(2\zeta r\right)^2}}, \tag{13}$$

$$\eta = \frac{F_0/k}{X}. \tag{14}$$

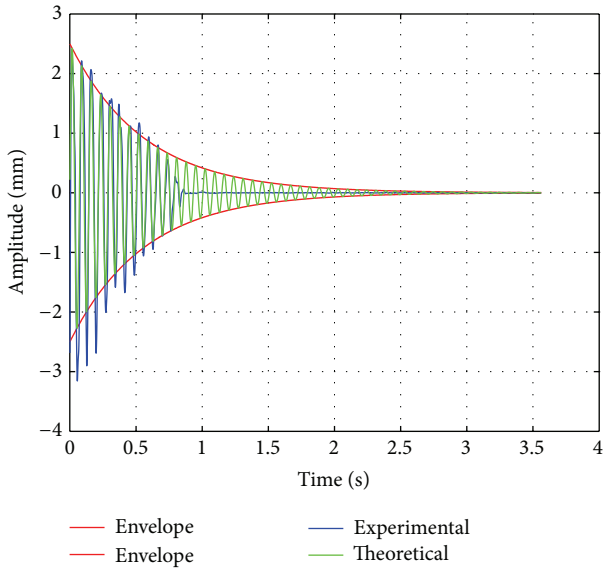

Figure 14: Impulse response of the mechanical system at 70°C.

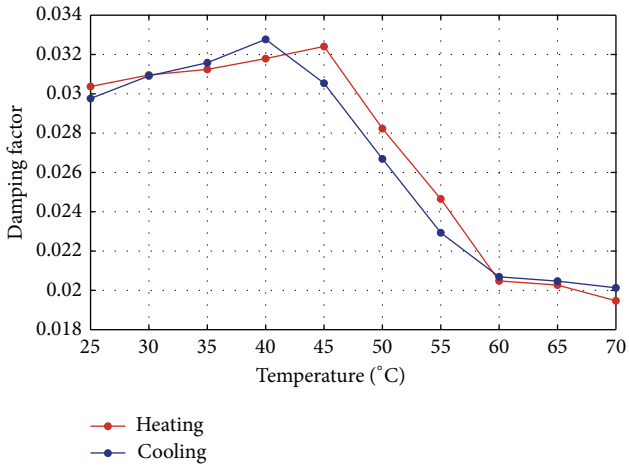

Figure 15: Damping factor of the mechanical system as a function of temperature.

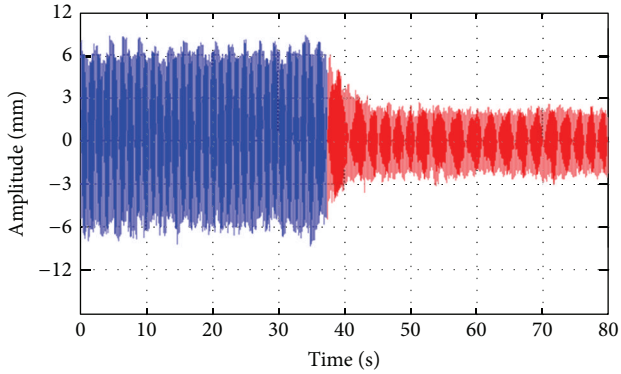

Figure 16: Time response of the mechanical system in the resonance condition with temperature variation and SMA spring initially in the martensitic phase (blue curve; f_n = 10.83 Hz).

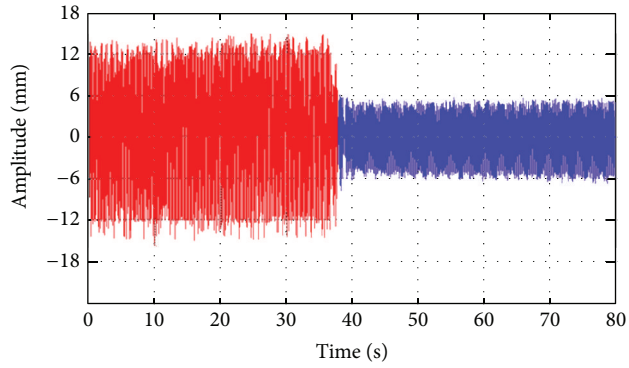

Figure 17: Time response of the mechanical system in the resonance condition with temperature variation and SMA spring initially in the austenitic phase (red curve; f_n = 12.70 Hz).

Figure 19 represents graphically the values of damping factor and loss factor of Table 4. Therefore, it is possible to validate the relationship between the loss factor and the damping factor defined by (10). In this case, errors smaller than 12% were verified.

5. Conclusions

This paper investigated the thermomechanical characterization of a shape memory alloy coil spring actuator, as well as its application as vibration attenuator in a mass-spring system with single degree of freedom. The main conclusions that can be outlined from the obtained results are the following:

(i) The elastic modulus of the NiTi SMA wire increases slightly with frequency. Furthermore, the modulus increases significantly during phase transformation, verifying the influence of a temperature increasing. At about of 60% of the elastic modulus increasing was observed when comparing the values of the martensitic phase with the austenitic phase.

(ii) By the DMA analysis it was observed that increasing the excitation frequency of the NiTi SMA wire leads to a decay of the damping capacity (Tan δ), much due to decreased mobility in the crystalline structure.

(iii) The experimental SMA spring stiffness showed good agreement with the behavior estimated by the theoretical model proposed by Ikuta et al. [13]. The stiffness of the SMA spring at the austenitic phase (hot) became 1.37 times higher than in the martensitic phase (cool).

(iv) The damping factor of the system measured experimentally shows a maximum value at the martensitic region (cool) and a minimum at the austenitic phase (hot). The behavior of the damping is the opposite of the stiffness and each of these parameters interferes differently in the dynamic response of the mechanical system.

(v) The system showed distinct dynamic responses in the different temperatures studied. With the SMA spring at 25°C the natural frequency of the system was

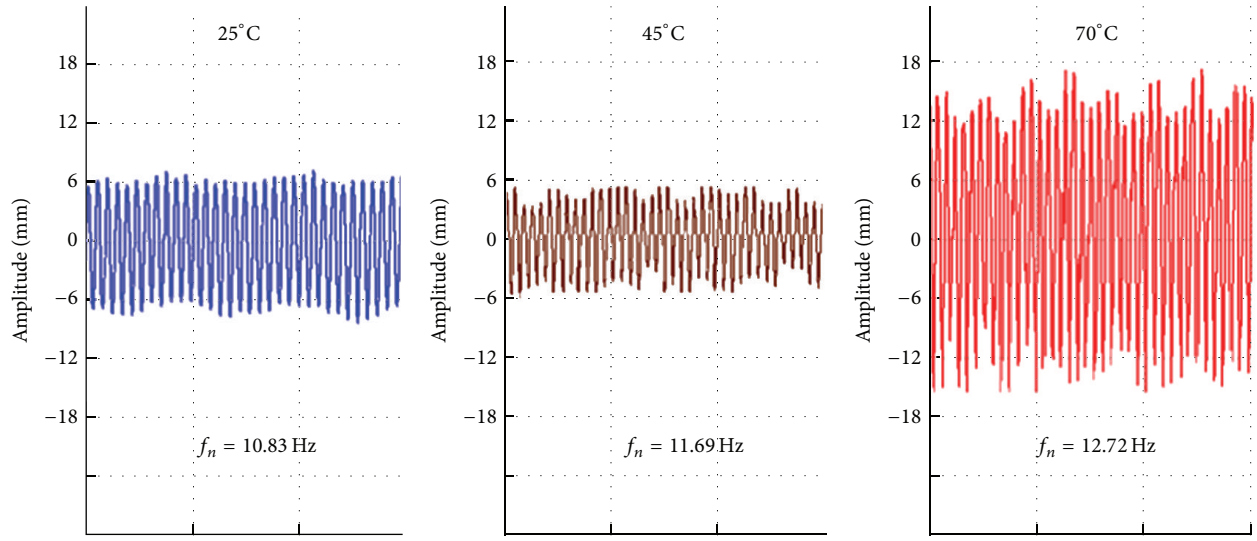

Figure 18: Time response of the mechanical system in resonance for the SMA spring at three temperatures.

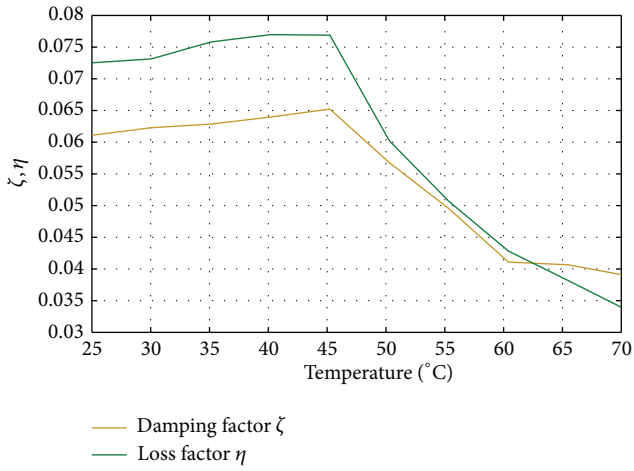

Figure 19: Loss factor and damping factor of the mechanical system as a function of temperature.

10.8 Hz with maximum amplitudes levels of 6 mm. At this temperature the SMA spring presents smaller stiffness and higher damping when compared with the properties of the SMA spring at 70°C. In this last condition the resonance frequency shifted to 12.7 Hz and the maximum amplitude of displacement peaks reached 12 mm.

(vi) Analyzing the system responses in the time and frequency domains was possible to prove the validity of the relationship between the damping factor $2\zeta_{eq}$ and the loss factor η. There is a good agreement between the theoretical formulation and experimental procedure employed.

Conflict of Interests

The authors declare that there is no conflict of interests regarding the publication of this paper.

Acknowledgments

The authors would like to acknowledge the CNPq Brazilian research agency for funding the following projects: National Institute of Science and Technology—Smart Structures in Engineering (Grant 574001/2008-5), Casadinho UFCG-UFRJ-ITA (Grant 552199/2011-7), Universal 14/2012 (Grant 474524/2012-4), and PQ2 (Grant 302320/2011-3).

References

[1] Y. J. Yan and L. H. Yam, "A synthetic analysis on design of optimum control for an optimized intelligent structure," *Journal of Sound and Vibration*, vol. 249, no. 4, pp. 775–784, 2002.

[2] D. C. Lagoudas, *Shape Memory Alloys: Modeling and Engineering Applications*, Springer, New York, NY, USA, 2008.

[3] M. Yuvaraja and M. Senthil Kumar, "Experimental studies on SMA spring based dynamic vibration absorber for active vibration control," *European Journal of Scientific Research*, vol. 77, no. 2, pp. 240–251, 2012.

[4] M. M. Barzegari, M. Dardel, A. Fathi, and M. H. Pashaei, "Effect of shape memory alloys wires on natural frequency of plates," *Journal of Mechanical Engineering and Automation*, vol. 2, no. 1, pp. 23–28, 2012.

[5] R. A. A. Aguiar, M. A. Savi, and P. M. C. L. Pacheco, "Experimental investigation of vibration reduction using shape memory alloys," *Journal of Intelligent Material Systems and Structures*, vol. 24, no. 2, pp. 247–261, 2013.

[6] R. A. A. de Aguiar, W. C. de Castro Leão Neto, M. A. Savi, and P. M. Calas Lopes Pacheco, "Shape memory alloy helical springs performance: modeling and experimental analysis," *Materials Science Forum*, vol. 758, pp. 147–156, 2013.

[7] R. A. A. Aguiar, M. A. Savi, and P. M. C. L. Pacheco, "Experimental and numerical investigations of shape memory alloy helical springs," *Smart Materials and Structures*, vol. 19, no. 2, Article ID 025008, 2010.

[8] M. A. Savi, A. S. De Paula, and D. C. Lagoudas, "Numerical investigation of an adaptive vibration absorber using shape memory alloys," *Journal of Intelligent Material Systems and Structures*, vol. 22, no. 1, pp. 67–80, 2011.

[9] W. Rackza, "Testing of a spring with controllabe stiffness," *Mechanics*, vol. 25, no. 2, pp. 79–86, 2006.

[10] R. Mirzaeifar, R. Desroches, and A. Yavari, "A combined analytical, numerical, and experimental study of shape-memory-alloy helical springs," *International Journal of Solids and Structures*, vol. 48, no. 3-4, pp. 611–624, 2011.

[11] Y. Toi, J.-B. Lee, and M. Taya, "Finite element analysis of superelastic, large deformation behavior of shape memory alloy helical springs," *Computers and Structures*, vol. 82, no. 20-21, pp. 1685–1693, 2004.

[12] D. J. Inman, *Engineering Vibration*, Prentice Hall, 2nd edition, 2000.

[13] K. Ikuta, M. Tsukamoto, and S. Hirose, "Mathematical model and experimental verification of shape memory alloy for designing micro actuator," in *Proceedings of the IEEE Micro Electro Mechanical Systems (MEMS '91)*, pp. 103–108, February 1991.

[14] N. J. Da Silva, E. N. D. Grassi, and C. J. De AraúJo, "Dynamic properties of NiTi shape memory alloy and classic structural materials: a comparative analysis," *Materials Science Forum*, vol. 643, pp. 37–41, 2010.

[15] J. San Juan and M. L. Nó, "Damping behavior during martensitic transformation in shape memory alloys," *Journal of Alloys and Compounds*, vol. 355, no. 1-2, pp. 65–71, 2003.

[16] A. S. Aquino, *Controle de vibração de um sistema sob desbalanceamento rotativo utilizando atuador de liga com memória de forma [Ph.D. thesis]*, Universidade Federal da Paraíba, João Pessoa, Brazil, 2011.

[17] S. A. Holanda, *Estudo da rigidez complexa de um sistema vibratório incorporando atuador com memória de forma [M.S. thesis]*, Universidade Federal de Campina Grande, Campina Grande, Brazil, 2013.

Hindawi Publishing Corporation
Shock and Vibration
Volume 2014, Article ID 872492, 9 pages
http://dx.doi.org/10.1155/2014/872492

Research Article

Use of Time- and Frequency-Domain Approaches for Damage Detection in Civil Engineering Structures

V. H. Nguyen,[1] J. Mahowald,[1] S. Maas,[1] and J.-C. Golinval[2]

[1] *Faculty of Science, Technology and Communication, University of Luxembourg, 6 rue Richard Coudenhove-Kalergi, 1359 Luxembourg, Luxembourg*
[2] *Department of Aerospace and Mechanical Engineering, University of Liege, 1 Chemin des Chevreuils, B52, 4000 Liège, Belgium*

Correspondence should be addressed to V. H. Nguyen; vietha.nguyen@uni.lu

Received 27 July 2013; Accepted 12 December 2013; Published 15 June 2014

Academic Editor: Nuno Maia

Copyright © 2014 V. H. Nguyen et al. This is an open access article distributed under the Creative Commons Attribution License, which permits unrestricted use, distribution, and reproduction in any medium, provided the original work is properly cited.

The aim of this paper is to apply both time- and frequency-domain-based approaches on real-life civil engineering structures and to assess their capability for damage detection. The methodology is based on Principal Component Analysis of the Hankel matrix built from output-only measurements and of Frequency Response Functions. Damage detection is performed using the concept of subspace angles between a current (possibly damaged state) and a reference (undamaged) state. The first structure is the Champangshiehl Bridge located in Luxembourg. Several damage levels were intentionally created by cutting a growing number of prestressed tendons and vibration data were acquired by the University of Luxembourg for each damaged state. The second example consists in reinforced and prestressed concrete panels. Successive damages were introduced in the panels by loading heavy weights and by cutting steel wires. The illustrations show different consequences in damage identification by the considered techniques.

1. Introduction

Modal identification and damage detection methods using output-only measurements are very attractive in the field of structural health monitoring (SHM) when the ambient excitation is unknown (e.g., in civil engineering structures submitted to wind or traffic excitation). A review of vibration-based health monitoring methods can be found in [1, 2].

For the purpose of modal analysis, time-domain methods such as the stochastic subspace identification (SSI) method are currently applied. For damage detection, methods such as Principal Component Analysis (PCA) and Second-Order Blind Identification (SOBI) were also recently developed. The robustness of these methods was improved by making use of the Hankel matrix instead of the observation matrix leading to the following variant approaches: Enhanced PCA, Null Subspace Analysis (NSA), or Enhanced SOBI. Their efficiency has been demonstrated in earlier studies mainly on numerical examples and laboratory experiments [3, 4]. They were also tested successfully on industrial examples to perform machine condition monitoring using a reduced set of sensors [5].

The aim of this paper is to present some applications of a PCA-based damage detection technique to civil engineering structures. The first structure consists in the Champangshiehl Bridge which is a two-span concrete box girder bridge located in Luxembourg. Next, precast reinforced and prestressed concrete slabs are considered. A sensitivity analysis for PCA in the frequency domain is used for the purpose of damage localization.

2. Dynamic Feature Extraction Using Principal Component Analysis

Let us consider a dynamical system characterized by a set of vibration measurements collected in the observation matrix $\mathbf{X}$:

$$\mathbf{X} = \begin{bmatrix} \mathbf{x}_1 & \mathbf{x}_2 & \cdots & \mathbf{x}_k & \cdots & \mathbf{x}_N \end{bmatrix}, \qquad \mathbf{x}_k \in \mathbf{R}^m, \tag{1}$$

where $\mathbf{x}_k$ is the output vector at time step k, m is the number of output sensors, and N is the number of time samples. Principal Component Analysis (PCA) aims to reduce the dimensionality of the observed data while preserving most of

information contained in the data set [6]. This is realized by finding p principal axes, which allow a data projection onto the p-dimensional subspace so that the mean square distance between the original points and corresponding projection is minimal. The dimension p corresponding to the number of principal components defines the rank of matrix $\mathbf{X}$ and is directly related to the order of the system. In practice, PCA is often performed by singular value decomposition (SVD) of matrix; that is,

$$\mathbf{X} = \mathbf{U}\boldsymbol{\Sigma}\mathbf{V}^{\mathrm{T}}, \tag{2}$$

where $\mathbf{U}$ and $\mathbf{V}$ are orthonormal matrices, the columns of $\mathbf{U}$ defining the principal components (PCs). The order p of the system is determined by selecting the first p nonzero singular values in $\boldsymbol{\Sigma}$ which have a significant magnitude ("energy") as described in [7].

The null subspace (NSA) and enhanced-PCA method (EPCA) proposed in [3, 4], respectively, are variant methods of the PCA method obtained by exploiting Hankel matrices of the dynamical system [8]. The data-driven block Hankel matrix is defined in (3), where $2i$ is a user-defined number of row blocks, each block contains m rows (number of measurement sensors), and j is the number of columns (practically $j = N - 2i + 1$). The Hankel matrix $\mathbf{H}_{1,2i}$ consists of $2im$ rows and is split into two equal parts of i block rows, which represent past and future data, respectively. Compared to the observation matrix $\mathbf{X}$, the Hankel matrix is built using time-lagged vibration signals and not instantaneous representations of responses. This enables taking into account time correlations between measurements when current data depend on past data. Therefore, the objective pursued here in using block Hankel matrices rather than observation matrices is to improve the sensitivity of the detection method:

$$\mathbf{H}_{1,2i} = \left[\begin{array}{ccccc} \mathbf{x}_1 & \mathbf{x}_2 & \cdots & \cdots & \mathbf{x}_j \\ \mathbf{x}_2 & \mathbf{x}_3 & \cdots & \cdots & \mathbf{x}_{j+1} \\ \cdots & \cdots & \cdots & \cdots & \cdots \\ \mathbf{x}_i & \mathbf{x}_{i+1} & \cdots & \cdots & \mathbf{x}_{i+j-1} \\ \hline \mathbf{x}_{i+1} & \mathbf{x}_{i+2} & \cdots & \cdots & \mathbf{x}_{i+j} \\ \mathbf{x}_{i+2} & \mathbf{x}_{i+3} & \cdots & \cdots & \mathbf{x}_{i+j+1} \\ \cdots & \cdots & \cdots & \cdots & \cdots \\ \mathbf{x}_{2i} & \mathbf{x}_{2i+1} & \cdots & \cdots & \mathbf{x}_{2i+j-1} \end{array}\right] \equiv \left[\begin{array}{c} \mathbf{H}_p \\ \hline \mathbf{H}_f \end{array}\right] \equiv \begin{array}{c} \text{“past”} \\ \hline \text{“future”} \end{array}, \tag{3}$$

where the subscripts of $\mathbf{H}_{1,2i}$ denote the subscript of the first and last element of the first column in the block Hankel matrix.

3. Damage Detection Based on the Concept of Subspace Angle

The principal components contained in matrix $\mathbf{U}$ span a subspace, which characterizes the dynamic state of the system. Without any damage or variation of environmental conditions, the characteristic subspace $\mathbf{U}$ remains unchanged. Any change in the dynamic behaviour caused by a modification of the system state modifies consequently its characteristic subspace. This change may be estimated using the definition of subspace angles [9]. As illustrated by a two-dimensional case in Figure 1, the concept of subspace angle can be seen as a tool to quantify existing spatial coherence between two data sets resulting from observations of a vibration system. In the figure, an active subspace is built from two principal components (column vectors) of matrix $\mathbf{U}$.

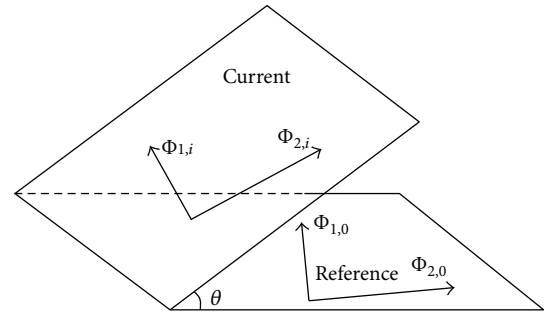

Figure 1: Angle θ formed by active subspaces according to the reference and current states, due to a dynamic change.

4. Damage Detection in the Champangshiehl Bridge

4.1. Description of the Bridge. The Champangshiehl Bridge shown in Figure 2 is a two-span concrete box girder bridge built in 1966 and located in the centre of Luxembourg. The bridge has a total length of 102 m divided into two spans of 37 m and 65 m, respectively. It is prestressed by 112 steel wires as illustrated in Figure 2(b). Before its complete destruction, the bridge was monitored and a series of damages were artificially introduced as summarized in Table 1. The four damage cases considered are illustrated in Figures 3(a)–3(d).

The measurement setup considered in the present work is given in Figure 4. Ten sensors were located on each side A and B of the deck (the distance between each sensor is about 10 m). Vibration monitoring under impact excitation was performed on the healthy structure and at each damage state. More detailed descriptions of the bridge can be found in [10].

4.2. Analysis Results. The bridge may be analyzed through a well established modal identification method proposed in [11] which relies on the use of stochastic subspace identification (SSI). Two first eigenfrequencies obtained for the four damage cases (D1–D4) are compared to the eigenfrequencies of the healthy structure as reported in Table 2.

Table 2 shows that the decrease of the eigenfrequencies is proportional to the damage level for damage cases D1, D3, and D4. Only damage case D2 exhibits a different behaviour as the first eigenfrequency increases by an amount of 1.6% with respect to the healthy case. Moreover, the second eigenfrequency is affected by the larger decrease (5.42%) of all the damage states. This is in good agreement with an earlier analysis reported in [12].

The application of the concept of subspace angle on the Champangshiehl Bridge data allows detecting all the damage

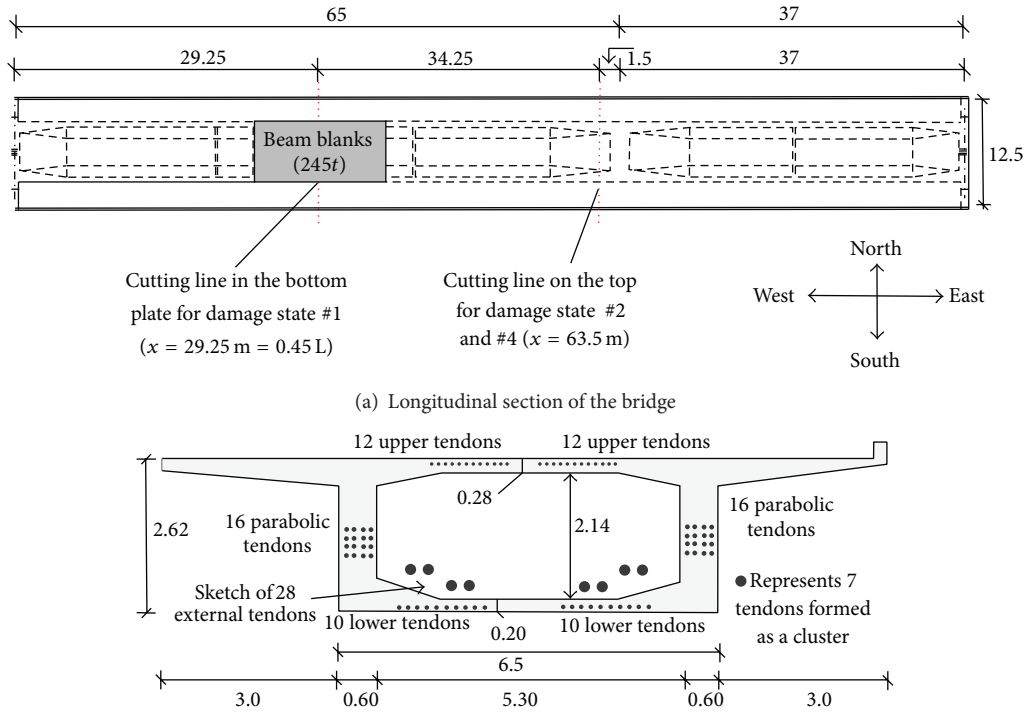

(a) Longitudinal section of the bridge

(b) Schematic cross section of the box girder with location of the tendons

Figure 2: The Champangshiehl Bridge.

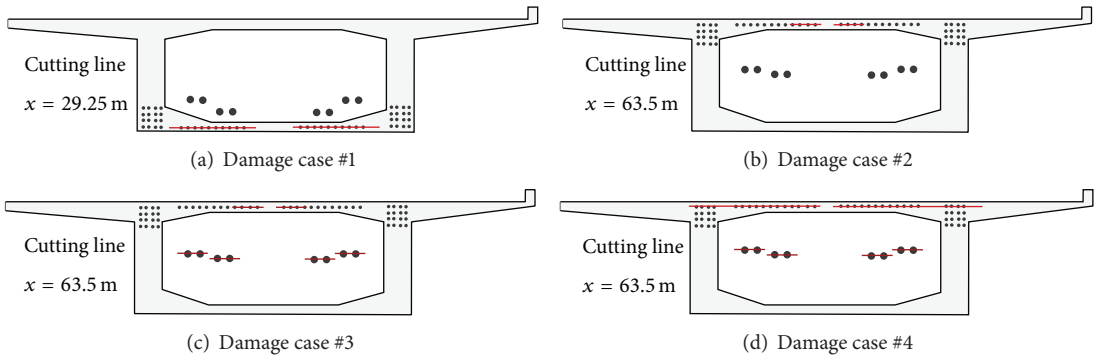

(a) Damage case #1

(b) Damage case #2

(c) Damage case #3

(d) Damage case #4

Figure 3: Damage scenarios.

Table 1: Description of the damage scenarios according to the cutting sections shown in Figure 2.

State	Damage	Percentage cutting (100% equals all tendons in the defined section cut)	
		0.45 L	Over the pylon
#0	Undamaged state		
#1	Cutting straight lined tendons in the lower part, at 0.45 L (20 tendons)	33.7%	0%
#2	#1 + cutting 8 straight lined tendons in the upper part, over the pylon	33.7%	12.6%
#3	#2 + cutting external tendons (56 wires)	46.1%	24.2%
#4	#3 + cutting 16 straight lined tendons in the upper part and 8 parabolic tendons	46.1%	62.12%

Table 2: Change in the eigenfrequencies (identified by SSI).

	f_1		f_2	
	Value (Hz)	Δf_1 (%)	Value (Hz)	Δf_2 (%)
Healthy	**1.92**		**5.54**	
D1	1.87	−2.6	5.45	−1.62
D2	1.95	1.6	5.24	−5.42
D3	1.82	−5.21	5.39	−2.71
D4	1.75	−8.85	5.3	−4.33

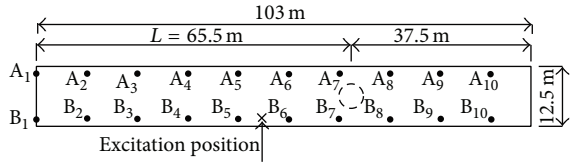

Figure 4: Location of the sensors on the bridge deck.

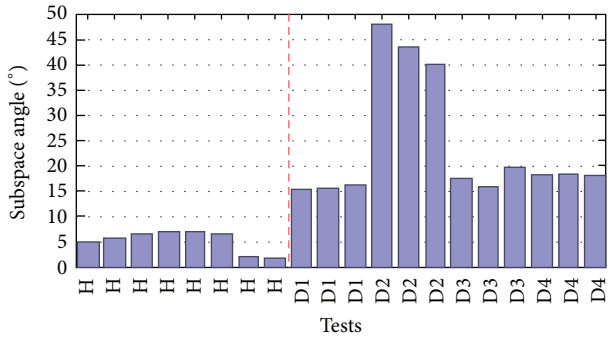

Figure 5: Damage detection results using EPCA.

cases (D1–D4) using the single first principal component (PC) of the Hankel matrix. The detection remains good and even more evident when 2, 3, and 4 PCs are used.

On the other hand, the use of more PCs (higher than 4) deteriorates the quality of the distinction between the damaged and the healthy states. Indeed, the highest PCs (associated with small singular values, that is, low energy) come from noise present in the data and are not dynamic features of the system. As an example, the detection results obtained on the basis of 3 PCs are shown in Figure 5. In this figure, a total of 20 tests were considered: eight tests on the healthy structure (H) and twelve tests corresponding to the four levels of damages D1–D4. It can be observed that all the damage cases are well detected and that damage cases D2 present the largest damage indexes.

5. Damage Detection on Precast Panels

5.1. Description of the Panels. The two investigated panels are manufactured by the Luxembourg company ECHOLUX and both are of the same type (one prestressed concrete (PrC), one special fabricated nonprestressed, reinforced concrete (RC) for testing purposes only). They are made of concrete C50/60 with an elastic modulus of 42700 N/mm^2 and a measured compressive strength of 58.3 N/mm^2 (quality control of manufacturer). The quality of the reinforcement is St 1470/1670 and the corresponding elastic modulus 205000 N/mm^2. In the upper section of the panel, there are 4 wires with a diameter of 5 mm and in the lower Section 12 wires with a diameter of 7 mm. Before testing, the concrete at the bottom side in the middle of the slab along axis C (Figure 6(b)) was removed, as shown in Figure 6(a), to give access to the reinforcement for the later procedures of cutting tendons.

Both static and dynamic tests were performed on the slabs to compare their behavior in each condition [13]. The dynamic responses were measured using impact testing. The sample rate of the data acquisition is set to 200 Hz; signals were recorded during 8 seconds after the introduction of impact. The measurements are set with a quite dense grid (Δ = 14.55 cm, Figure 7) for the sake of studying damage localization later. There are 45 impact points at each side of the slabs and three accelerometers (Ref. 1–Ref. 3 in Figure 7) are used to capture dynamic responses. So, in each condition, we have 3 sets of data containing 90 signals.

Damages were introduced by static mass loading (Figure 6(b)), cutting of steel wires and are resumed in Table 3.

5.2. Analysis of the Results. Relating to frequency, damages show influence principally on the first component. Table 5 presents the first eigenfrequency shift, identified by the peak picking and SSI methods, respectively.

The results obtained in Table 5 for the RC slab show a good agreement between the peak picking and SSI methods. It shows a clear decrease of frequency values following the increasing levels of damage. However, for the PrC slab, the eigenfrequencies vary very slightly between different conditions; only the intact state (#0) and the state before the failure (#3*) are clearly distinct. The values identified by SSI cannot classify levels #0 to #2*. This is consistent with the observations and cracking described in Table 4: no change is noticed between state #0 to #1*. It reveals that, in comparison with the RC slab, apparent damage occurs very late in the PrC slab; the crack formation and hence the deformation are negligible until failure, which makes the detection more difficult.

Before the implementation of the static and dynamic tests, cracking loads were calculated for each structure. For the RC slab, the cracking load is expected for a load of two steel weights (G_1 and G_2 in Figure 6(b)) without cutting of

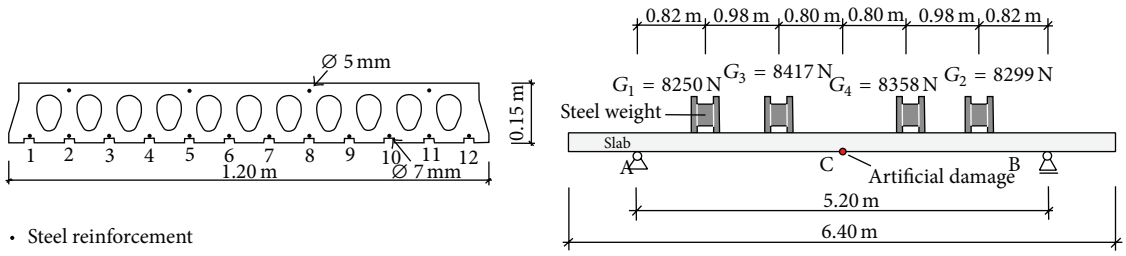

(a) Cross section of the panels

(b) Schema of loading and location of cracks (point C)

Figure 6: Panel structure and experiment schema.

Table 3: Damage scenarios.

Number	Damage scenario	Cutting percentage	Remark
#0	Intact state-no damage	—	Later we consider states #0, #0*, #1*, #2*, #3*. *denotes a state after loading and then removing of 4 heavy weights from the slab (shown in Figure 6(b))
#1	Cutting of 2 tendons (numbers 6 and 7-refer to Figure 6(a))	16.7%	
#2	Cutting of 4 tendons (numbers 6, 7, 2, and 11)	33.3%	
#3	Cutting of 6 tendons (numbers 6, 7, 2, 11, 4, and 9)	50%	
#4	Cutting of 8 tendons (numbers 6, 7, 2, 11, 4, 9, 3, and 10)	66.7%	

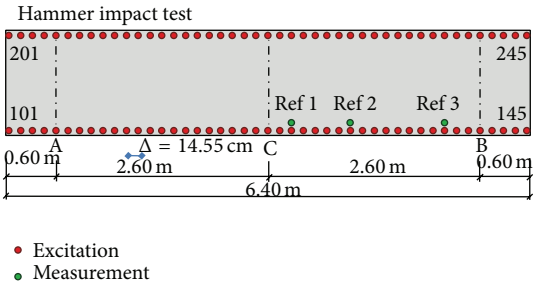

Figure 7: Measurement setup: impact point (101–145 and 201–245) and accelerometer positions (Ref. 1–Ref. 3).

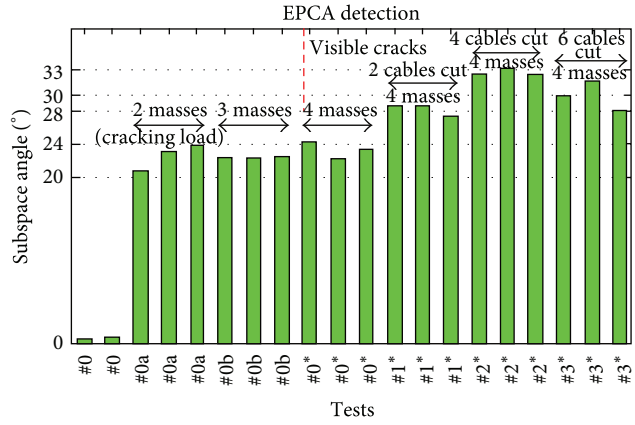

Figure 8: EPCA detection for the RC slab (always unloaded state).

any wires. Contrarily, the cracking load for the PrC slab is expected for an additional load of four steel weights (G_1, G_2, G_3, and G_4) and cutting of 6 to 7 wires.

As presented in Figure 8, EPCA detects dynamic change in the RC slab from the loading of 2 masses, what corresponds already to the cracking load, while visible cracks are noticed only after the loading of 4 masses. Furthermore, the results distinguish clearly the tests before and after cutting tendons: larger subspace angles are obtained for the last cases. All signals processed here were measured after a procedure of charging then removing masses. Each condition is represented by 3 sets of measurement; one set of measurement in the intact state is provided for reference data.

For the PrC slab, it is theoretically proven that the cracking load can be reached much later with respect to the RC slab. Only a hairline crack occurs after the loading of 4 masses in addition to the cutting of 4 tendons (#2*). In this circumstance, for a more precise comparison between different conditions in the PrC slab, we examine only the correlation of states after a procedure of loading then removing the 4 masses. All data refer to the intact state #0* after removing the masses. As presented in Figure 9, the EPCA method is able to detect well the damages caused in the slab. As in the visible observations, subspace angles do not reveal much difference between damages #1* to #3*.

5.3. Localization of Damage. In this paper, damage localization in beam-like structures is based on the use of sensitivity analysis of measurements. A review on modal updating methods including the sensitivity of both frequencies and mode-shapes is given in [14]. Natural frequency sensitivity has been used extensively for the purpose of damage localization. However, most of the methods based

Table 4: Description of damages.

Number	Reinforced concrete (RC) slab	Prestressed concrete (PrC) slab
#0	No damage	No damage
#0*	Appearance of a decisive crack pattern, large creep	No crack observed
#1*	No further cracks, current cracks grow and also creep	No crack observed, no considerable deformation
#2*	As above	Appearance of a hairline crack, minimal deformation
#3*	As above	As above
#4*	Collapse	Collapse

Table 5: The shift of the first eigenfrequency (Hz) from the intact state until before the collapse (always unloaded state).

	RC slab					PrC slab				
State	#0	#0*	#1*	#2*	#3*	#0	#0*	#1*	#2*	#3*
f by peak picking	11	9.18	8.07	7.85	7.69	11.75	11.70	11.65	11.65	11.55
f by SSI	11	9.20	8.00	7.70	7.60	11.73	11.65	11.61	11.56	11.33

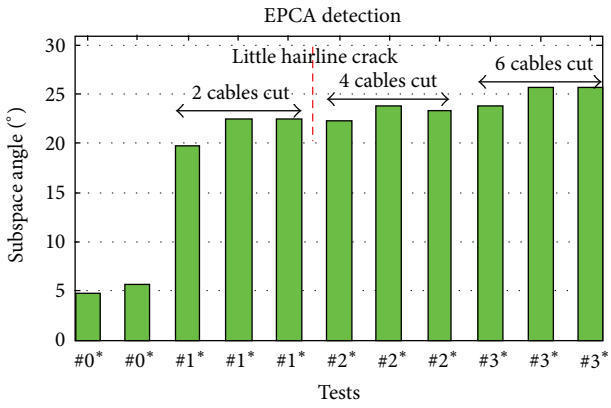

Figure 9: EPCA detection for the PrC slab (always unloaded state).

on frequency sensitivity with respect to damage variables require an accurate analytical model. In [15], an extension of the frequency sensitivity approach is proposed to eliminate this requirement. However, an optimization procedure is still needed to estimate the unknown system matrices through an identified model using input-output measurement data.

Natural frequencies are known to be very efficient in characterizing changes in dynamical systems. Mode-shapes are considered efficient to recognize spatial changes, since they condense most of the deformation database of the structure. In the present work, the sensitivity of mode-shapes is considered. However, the construction of an analytical model is not necessary for the localization procedure.

5.3.1. Index for Localization. In the previous sections, the SSI and EPCA methods were used in the time-domain for modal identification and damage detection. Damage may be located based on the estimation of flexibility from the identified mode-shapes as presented in [10]. In this section, Principal Component Analysis (PCA) is used for damage localization based on a sensitivity analysis in the frequency-domain. The technique is described in earlier works [4, 16, 17] and is summarized here briefly.

Let us consider the Frequency Response Functions (FRFs) $\mathbf{H}^s(\omega)$ for a single input at location s:

$$\mathbf{H}^s(\omega) = \left[\mathbf{h}(\omega_1) \;\; \mathbf{h}(\omega_2) \;\; \cdots \;\; \mathbf{h}(\omega_N)\right], \tag{4}$$

where vector $\mathbf{h}(\omega_k)$ is of dimension m (the number of measured coordinates) and N is the number of frequency lines. The rows of $\mathbf{H}^s$ represent the responses at the measured degrees of freedom (DOFs), while the columns are "snapshots" of the FRFs at different frequencies. We will assume that the dynamical system matrices depend on a vector of parameters $\mathbf{p}$. This vector of parameters may consist of system parameters or state variables. We can assess its principal components through Singular Value Decomposition (SVD) as represented in (2). As $\mathbf{H}^s$ belongs to the frequency-domain, the left singular vectors in $\mathbf{U}$ give spatial information, the right singular vectors in $\mathbf{V}$ represent modulation functions depending on frequency, and the diagonal matrix of singular values $\mathbf{\Sigma}$ contains scaling parameters of descending order $\sigma_1 > \sigma_2 > \cdots > \sigma_m$. In other words, the SVD of $\mathbf{H}^s$ separates information depending on space and frequency.

From (2), a sensitivity analysis can be performed by taking the derivative of the observation matrix $\mathbf{H}^s$ with respect to $\mathbf{p}$:

$$\frac{\partial \mathbf{H}^s}{\partial \mathbf{p}} = \frac{\partial \mathbf{U}}{\partial \mathbf{p}}\mathbf{\Sigma}\mathbf{V}^{\mathrm{T}} + \mathbf{U}\frac{\partial \mathbf{\Sigma}}{\partial \mathbf{p}}\mathbf{V}^{\mathrm{T}} + \mathbf{U}\mathbf{\Sigma}\frac{\partial \mathbf{V}^{\mathrm{T}}}{\partial \mathbf{p}}. \tag{5}$$

Through this equation, the sensitivity of the system dynamic response shows its dependence on the sensitivity of each SVD term. Junkins and Kim [18] developed a method to compute the partial derivatives of SVD factors. Here, for the sake of localization, we are more particularly interested in spatial information contained in the left singular vector $\mathbf{U}$; its sensitivity with respect to a parameter p_k is simply given by the following equation:

$$\frac{\partial \mathbf{U}_i}{\partial p_k} = \sum_{j=1}^{m} \alpha_{ji}^k \mathbf{U}_j \text{ with}$$
$$\alpha_{ji}^k = \frac{1}{\sigma_i^2 - \sigma_j^2}\left[\sigma_i\left(\mathbf{U}_j^{\mathrm{T}}\frac{\partial \mathbf{H}^s}{\partial p_k}\mathbf{V}_i\right) + \sigma_j\left(\mathbf{U}_i^{\mathrm{T}}\frac{\partial \mathbf{H}^s}{\partial p_k}\mathbf{V}_j\right)^{\mathrm{T}}\right]. \tag{6}$$

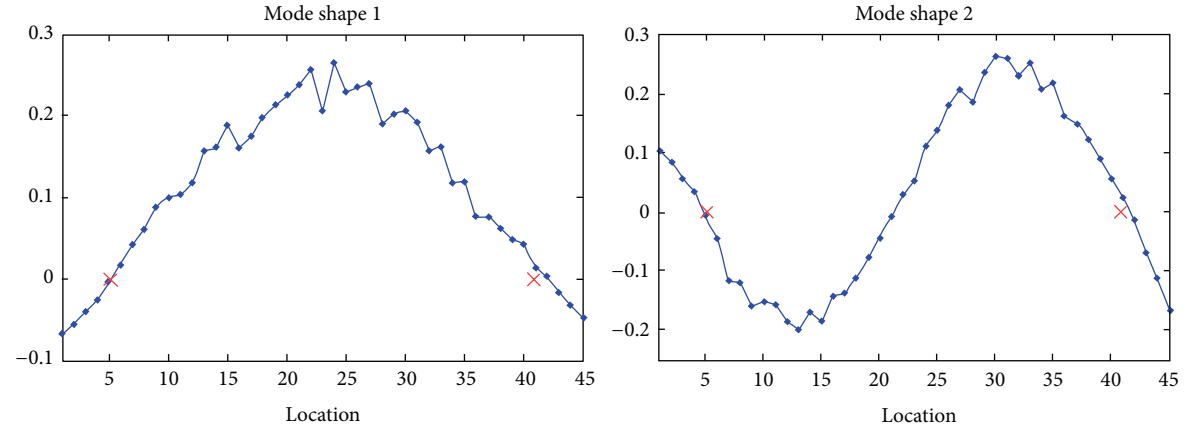

(a) Mode-shapes obtained by SSI

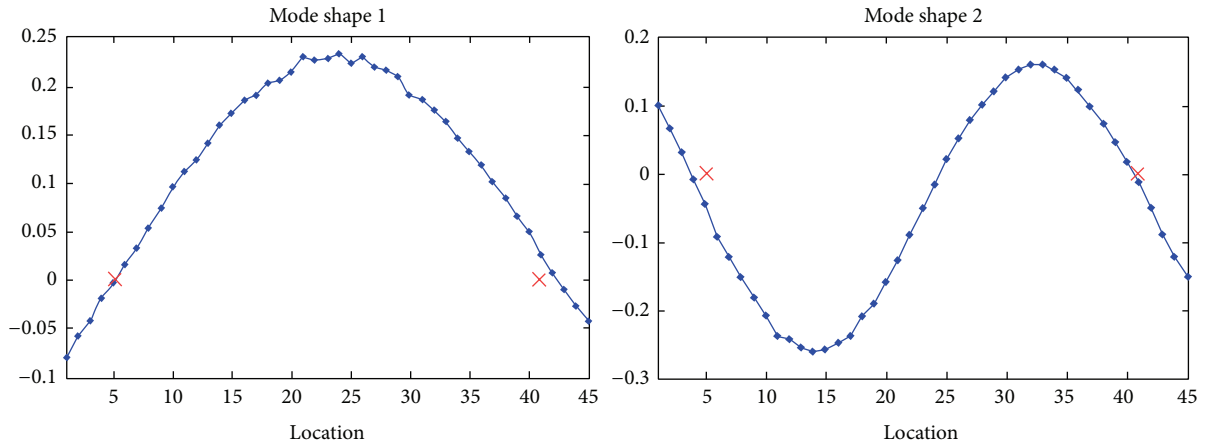

(b) Mode-shapes obtained by the sensitivity analysis

FIGURE 10: Comparison of mode-shapes obtained by SSI and the sensitivity analysis (×: position of support).

It is shown in [18] that the diagonal coefficients α_{ii}^{k} keep only their imaginary part (their real parts are empty).

So, the sensitivity of the ith principal component can be computed through coefficients α_{ji}^{k} which depend on an unknown $\partial \mathbf{H}^{s}/\partial p_k$. It is proven in [16] that when the system matrices are symmetric, if parameter of interest is some coefficient k_e of the stiffness matrix, the sensitivity of the FRF matrix may be simply determined by the following formula:

$$\frac{\partial \mathbf{H}^{s}}{\partial p_k} = -\mathbf{H}_{k_e} \cdot \mathbf{H}_{k_e,s}, \tag{7}$$

where $\mathbf{H}_{k_e}$ is just the row vector corresponding to coefficient k_e in the FRF matrix in (4) and $H_{k_e,s}$ is the s element of this vector.

Once $\partial \mathbf{H}^{s}/\partial p_k$ has been computed, the sensitivity of the left singular vectors is a good candidate for resolving localization problems of linear-form structures, for example, chain-like or beam-like structures. In each working condition of the system, we can compute the sensitivity $\partial \mathbf{U}_i/\partial p_k$. The reference state is denoted by $\partial \mathbf{U}_i{}^{R}/\partial p_k$, and the deviation of the current condition may be assessed as follows:

$$\Delta \frac{\partial \mathbf{U}_i}{\partial p_k} = \frac{\partial \mathbf{U}_i}{\partial p_k} - \frac{\partial \mathbf{U}_i{}^{R}}{\partial p_k}. \tag{8}$$

The last vector allows the maximization of useful information for damage localization.

5.3.2. Application on the Precast Panels. First, let us note that the sensitivity analysis of the FRF data allows extracting structural mode-shapes thanks to the principal component vectors contained in matrix $\mathbf{U}$. For the sake of conciseness, only the signals coming from one slab side are used here (from points 101 to 145 in Figure 7). Figure 10 compares the mode-shapes identified through SSI and the sensitivity analysis, respectively. It clearly shows that the mode-shapes obtained by the sensitivity analysis are smoother than by SSI. The SSI modes show larger variations at points of high amplitude.

As stated before, damage produces a crack pattern in the middle of the slab. So it is expected that the damage

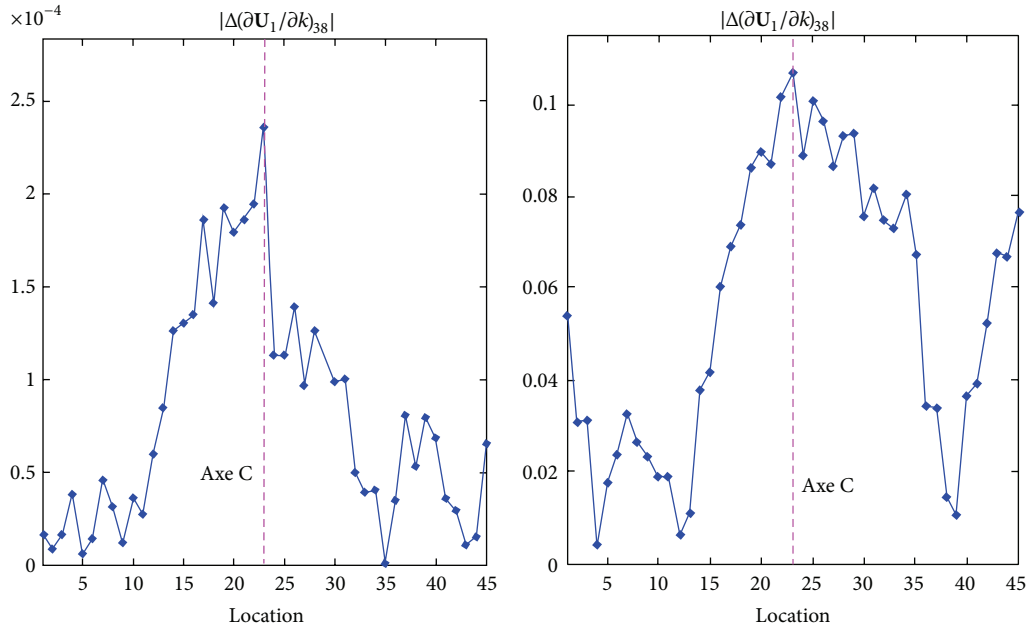

(a) Based on mode 1 (b) Based on mode 2

Figure 11: Damage localization in the RC slab for damage #2*.

localization procedure will point out damage around this zone, that is, along axis C passing through point 23 (see Figure 7) which marks the middle of the slab.

Let us remind you that in PCA, a large number of data are one of the requirements so that a principal component in $\mathbf{U}$ converges to a modal vector; so a frequency range should be chosen large enough for a sufficient observation of data in $\mathbf{H}^s(\omega)$. For the RC slab, the frequency range of [4 Hz–26 Hz] corresponding to mode 1 is first selected to eliminate low-frequency noise and higher frequency modes.

The results for $|\Delta(\partial \mathbf{U}_1/\partial p_k)|$ shown in Figure 11 are obtained from the set of measurement number 3. As the sensor was located at point 38 for this set of measurement, parameter p_k is chosen to correspond to k_{38} according to the 38th element of the "experimental" stiffness matrix. The "undamaged" vector of $\partial \mathbf{U}_1/\partial p_k$ is extracted from state #0 which is considered as reference. The diagrams of $|\Delta(\partial \mathbf{U}_1/\partial p_k)|$ in Figure 11 show for both modes 1 and 2 that the highest peaks are located close to point 23 (axe C) where the cracks gather. To take into account higher frequency component (mode 2), the frequency range of [4 Hz–50 Hz] is considered and the results are given in Figure 11(b). It should be noticed that the first principal component represents mode 2 of the structure, as shown in Figure 10(b). Mode 2 which is more dominant than mode 1 is also more sensitive to damage. If only mode 1 is used, damages are only detected in cases #2* and #3* but they are detected in all cases #0*–#3* when mode 2 is used. For the sake of conciseness, only the results for damage #2* are presented here as an example.

In the case of PrC slab, damages are detected much later and less apparent than in the RC slab, just before its collapse.

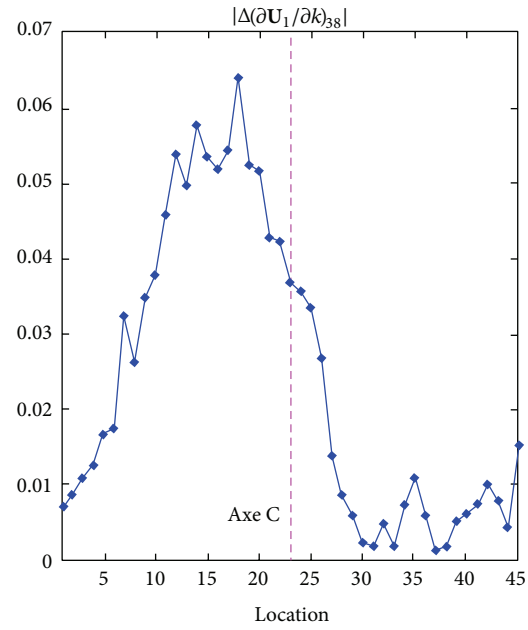

Figure 12: Damage localization in the PrC slab for damage #2*, based on mode 2.

It is confirmed by very small changes in frequencies under different conditions.

The localization procedure does not give any interesting outcome for the PrC slab when only mode 1 is considered. However, as in the RC slab, the use of mode 2 also allows a better localization. Damages #3* and #2* can be similarly localized as shown in Figure 12. The peak does not arise exactly at point 23 (along axis C) but in the neighboring area.

6. Conclusion

Several variants of Principal Component Analysis have been used in this study for detection and localization of damage. The advantage of PCA over classical modal identification methods relies on its easiness of use. The first results obtained on the Champangshiehl bridge are very encouraging. Furthermore, damage localization and the influence of environmental conditions on the diagnosis will be considered. The examples of the precast panels showed that the damages were better distinguished on the basis of the first eigenfrequency (especially for the RC slab) while they were localized in a more effective manner using the second mode-shape.

Conflict of Interests

The authors declare that there is no conflict of interests regarding the publication of this paper.

Acknowledgment

The author V. H. Nguyen is supported by the National Research Fund, Luxembourg.

References

[1] D. Montalvão, N. M. M. Maia, and A. M. R. Ribeiro, "A review of vibration-based structural health monitoring with special emphasis on composite materials," *Shock and Vibration Digest*, vol. 38, no. 4, pp. 295–324, 2006.

[2] W. Fan and P. Qiao, "Vibration-based damage identification methods: a review and comparative study," *Structural Health Monitoring*, vol. 10, no. 1, pp. 83–111, 2011.

[3] A.-M. Yan and J.-C. Golinval, "Null subspace-based damage detection of structures using vibration measurements," *Mechanical Systems and Signal Processing*, vol. 20, no. 3, pp. 611–626, 2006.

[4] V. H. Nguyen, *Damage detection and fault diagnosis in mechanical systems using vibration signals [Ph.D. dissertation]*, University of Liège, 2010.

[5] V. H. Nguyen, C. Rutten, and J.-C. Golinval, "Fault diagnosis in industrial systems based on blind source separation techniques using one single vibration sensor," *Shock and Vibration*, vol. 19, no. 5, pp. 795–801, 2012.

[6] G. Kerschen and J.-C. Golinval, "Non-linear generalization of principal component analysis: from a global to a local approach," *Journal of Sound and Vibration*, vol. 254, no. 5, pp. 867–876, 2002.

[7] P. de Boe and J.-C. Golinval, "Principal component analysis of a piezosensor array for damage localization," *Structural Health Monitoring*, vol. 2, no. 2, pp. 137–144, 2003.

[8] P. V. Overschee and B. de Moor, *Subspace Identification for Linear Systems: Theory, Implementation, Applications*, Kluwer Academic Publishers, Dordrecht, The Netherlands, 1997.

[9] G. H. Golub and C. F. van Loan, *Matrix Computations*, The Johns Hopkins University Press, Baltimore, Md, USA, 1996.

[10] J. Mahowald, S. Maas, D. Waldmann, A. Zürbes, and F. Scherbaum, "Damage identification and localisation using changes in modal parameters for civil engineering structures," in *Proceedings of the International Conference on Noise and Vibration Engineering*, pp. 1103–1117, Leuven, Belgium, 2012.

[11] B. Peeters and G. de Roeck, "Stochastic system identification for operational modal analysis: a review," *Journal of Dynamic Systems, Measurement and Control*, vol. 123, no. 4, pp. 659–667, 2001.

[12] J. Mahowald, S. Maas, F. Scherbaum, D. Waldmann, and A. Zürbes, "Dynamic damage identification using linear and nonlinear testing methods on a two-span prestressed concrete bridge," in *Proceedings of the 3rd International Symposium on Life-Cycle Civil Engineering (IALCCE '12)*, pp. 157–164, CRC Press, Vienna, Austria, October 2012.

[13] J. Mahowald, V. Bungard, D. Waldmann, S. Maas, A. Zürbes, and G. de Roeck, "Comparison of linear and nonlinear static and dynamic behaviour of prestressed and non-prestressed concrete slab elements," in *Proceedings of the International Conference on Noise and Vibration Engineering*, pp. 717–728, Leuven, Belgium, 2010.

[14] J. V. Araújo dos Santos, N. M. M. Maia, C. M. Mota Soares, and C. A. Mota Soares, "Structural damage identification: a survey," in *Trends in Computational Structures Technology*, B. H. V. Topping and M. Papadrakakis, Eds., chapter 1, pp. 1–24, Saxe-Coburg Publications, Stirlingshire, UK, 2008.

[15] L. J. Jiang and K. W. Wang, "An experiment-based frequency sensitivity enhancing control approach for structural damage detection," *Smart Materials and Structures*, vol. 18, no. 6, Article ID 065005, 2009.

[16] V. H. Nguyen and J.-C. Golinval, "Damage localization in linear-form structures based on sensitivity investigation for principal component analysis," *Journal of Sound and Vibration*, vol. 329, no. 21, pp. 4550–4566, 2010.

[17] D. Todd Griffith, "Analytical sensitivities for principal components analysis of dynamical systems," in *Proceedings of the 27th IMAC Conference & Exposition on Structural Dynamics*, Orlando, Fla, USA, February 2009.

[18] J. L. Junkins and Y. Kim, *Introduction to Dynamics and Control of Flexible Structures*, AIAA Education Series, American Institute of Aeronautics and Astronautics, Reston, Va, USA, 1993.

Hindawi Publishing Corporation
Shock and Vibration
Volume 2014, Article ID 102157, 8 pages
http://dx.doi.org/10.1155/2014/102157

Research Article

Analysis of Vibroacoustic Modulations for Crack Detection: A Time-Frequency Approach Based on Zhao-Atlas-Marks Distribution

A. Trochidis,[1] L. Hadjileontiadis,[2] and K. Zacharias[1]

[1] *Department of Mathematical, Physical and Computational Sciences, Aristotle University of Thessaloniki, 54124 Thessaloniki, Greece*
[2] *Department of Electrical & Computer Engineering, Aristotle University of Thessaloniki, University Campus, 54124 Thessaloniki, Greece*

Correspondence should be addressed to L. Hadjileontiadis; leontios@auth.gr

Received 11 July 2013; Accepted 7 January 2014; Published 12 June 2014

Academic Editor: Nuno Maia

Copyright © 2014 A. Trochidis et al. This is an open access article distributed under the Creative Commons Attribution License, which permits unrestricted use, distribution, and reproduction in any medium, provided the original work is properly cited.

The vibro-acoustic modulation (VAM) technique is probably the most widely used nonlinear method for crack detection. The VAM method is based on the effect of modulation of high-frequency acoustic waves by a low-frequency vibration. The intensity of the modulation is related to the severity of the damage and has been used so far as a damage index. The damage index simply based on the amplitude of the first side bands in the spectral domain often leads to controversial results about the severity of the damage. In this work, the nonlinear characteristics of the vibro-modulation were systematically investigated by employing time-frequency analysis based on the Zhao-Atlas-Marks (ZAM) distribution. The results of the analysis show that the amplitude of the sideband components is modulated by the low frequency vibration and the modulation amplitude depends on the size of the crack. Based on the obtained results, a new damage index was defined in relation to the strength of the modulation. The new damage index is more sensitive and robust and correlates better with crack size compared to the index based on the amplitude of the sidebands.

1. Introduction

Structures with inhomogeneities or defects exhibit strong nonlinear vibrational and acoustical effects. In particular, strong nonlinear effects were observed in structures with cracks. These effects include the generation of higher harmonics and intermodulation of a high-frequency acoustic wave by a low-frequency vibration [1] and provide the foundation for developing different techniques for nondestructive testing.

The vibroacoustic modulation (VAM) method is based on the fact that a high-frequency ultrasound probing wave propagating in a structure is modulated by a low-frequency vibration. The modulation is generated by the nonlinear interaction of waves caused by the presence of the crack. The mechanisms, however, behind these effects are still poorly understood [2–4]. The phenomenon of VAM is usually measured in the frequency domain and it is manifested as sidebands around the carrier peak of the ultrasound wave at frequencies equal to the sum and difference of the excitation frequencies and their integer multiples. Modulation effects have been observed in several applications. Ekimov et al. [5] employed VAM of high-frequency torsional waves for crack detection in a rod. Zaitsev et al. [6] presented applications of nonlinear modulation for crack detection in structures and discussed possible sources of nonlinearity in damaged structures. Donskoy and Sutin [7] used VAM to investigate the existence of cracks, delaminations, or poor quality bonding. Further application of VAM techniques can be found in Zagrai et al. [8] who studied crack detection in aluminum plates. Duffour et al. [9] investigated the sensitivity of VAM technique and compared the conventional damping test with an impact-based vibroacoustic modulation. The majority of the existing studies are related to the detection of damage in metallic structures. More recently, studies of the application of VAM techniques to composite structures [10, 11] and chiral sandwich panels [12] have been reported.

When VAM is applied for damage detection, damage indices are defined relating the size of the damage to

the intensity of modulation. These indices rely on the amplitude of the carrier frequency at the sidebands. Despite the successful application of VAM in various damage problems, it appears that the damage indices in the frequency domain used so far are not accurate and in many cases provide unreliable results [13].

The primary aim of the present work is to investigate vibroacoustic modulation in the time-frequency domain by employing time-frequency analysis based on the Zhao-Atlas-Marks (ZAM) distribution, which has the advantage of significantly reducing cross-terms between signal components, through its cone-shaped kernel function. We hypothesized that the characteristics of modulation responses in time domain might be proved more sensitive compared to those in the frequency domain and the combination of both could lead to damage indices that are more sensitive and robust. Furthermore, it is believed that the time-frequency analysis of the modulation responses can highlight the underlying nonlinear mechanisms and enable more efficient applications of the method for damage detection.

2. Methodology

2.1. Vibroacoustic Modulation (VAM) Technique. In structures with damage (e.g., cracks), strong nonlinear vibrational and acoustical effects occur. Exploitation of these phenomena has led to the formation of the vibroacoustic modulation (VAM) technique, which is probably the most widely used nonlinear, nondestructive testing (NDT) method for crack detection. In particular, the VAM technique involves monitoring of the amplitude modulation of a high-frequency (f_H) vibration field transmitted through a cracked specimen undergoing an additional low-frequency (f_L) structural vibration (typically one of the first structural modes). If the specimen is undamaged and appropriately supported, the two vibration fields do not interact. However if a crack is present, then the low-frequency structural vibration slowly opens and closes the crack. This periodically modifies the dynamic characteristics of the system, hence, modulating the amplitude of the ultrasound transmitted through a cracked specimen. This modulation expresses itself as sidebands ($f_{S_k}^{\pm}$) around the high-frequency component f_H at frequencies equal to the sum and difference of the excitation frequencies and their integer multiples, that is,

$$f_{S_k}^{\pm} = f_H \pm k f_L, \quad k = 1, 2, 3, \ldots. \tag{1}$$

The intensity of the modulation is related to the severity of the damage and has been used so far as a spectral FFT-based damage index ($\mathrm{DI}_{\mathrm{FFT}}$) in the form

$$\mathrm{DI}_{\mathrm{FFT}} = \frac{\left(\left|\mathrm{FFT}\left(f_{S_1}^{-}\right)\right| + \left|\mathrm{FFT}\left(f_{S_1}^{+}\right)\right|\right)}{2\left|\mathrm{FFT}\left(f_H\right)\right|}, \tag{2}$$

where $|\mathrm{FFT}(f_{S_1,H}^{\pm})|$ denote the FFT magnitude at the first left and right sidebands and f_H, respectively.

2.2. Zhao-Atlas-Marks (ZAM) Distribution. Time-frequency (TF) analysis provides the means for exploiting the energy-related characteristics of the crack response signals that may vary in both time and frequency. Many of the TF approaches suffer from the effect of the appearance of cross-terms, which deteriorate the discrimination power at the TF domain. To avoid this distortion, the Zhao-Atlas-Marks (ZAM) distribution [7] was adopted as a methodological tool to express the information in a clearer way at the TF domain. In particular, ZAM distribution belongs to the category of quadratic time-frequency representations and, especially, to the group of reduced interference distributions (RIDs). RIDs are members of Cohen's class and thus, for a time series $X(t)$, they can be described by the following general expression:

$$\mathrm{RID}_X(t, f; \Phi) = \iint_{-\infty}^{+\infty} \Phi(\xi, \tau)\, A_X(\xi, \tau) \times e^{-j2\pi(f\tau + \xi t)}\, d\xi\, d\tau, \tag{3}$$

where t and f denote time and frequency, respectively, while τ and ξ denote the delay and the doppler, respectively, in the ambiguity plane. $A_X(\xi, \tau)$ represents the ambiguity function, which is associated with the Wigner-Ville distribution via a two-dimensional Fourier transform [8]. $\Phi(\xi, \tau)$ is the, so-called, parameterization or kernel function. The ZAM distribution is derived by choosing the kernel function as follows:

$$\Phi(\xi, \tau) = h(\tau)\,|\tau|\,\frac{\sin(\pi\xi\tau)}{\pi\xi\tau}, \tag{4}$$

where $h(\tau)$ is a window function that leads to smoothing along the frequency axis. Thus, the following expression can be obtained that defines the ZAM distribution:

$$\mathrm{ZAM}_X(t, f) = \int_{-\infty}^{+\infty} \left[h(\tau) \int_{t-|\tau|/2}^{t+|\tau|/2} X\left(s + \frac{t}{2}\right) \times X^*\left(s - \frac{t}{2}\right) ds \right] \times e^{-j2\pi f\tau}\, d\tau. \tag{5}$$

ZAM distribution was selected among RIDs due to its advantage of significantly reducing cross-terms between signal components, through its cone-shaped kernel function (4) [7]. In the present study, the ZAM-based TF representation was computed under a $N \times N$ TF resolution; N denotes the number of samples of the signal. Smoothing was performed using Hamming windows of $N/7$-samples and $N/6$-samples for time and frequency, respectively.

2.3. ZAM-Based Modulation Effects Analysis. Taking the ZAM distribution of the time series $X(t)$ of beam responses to the VAM stimulation, that is, $\mathrm{ZAM}_X(t, f)$, a more detailed exploitation of the modulation effects can be achieved by analyzing the mean amplitude and fluctuation of $\mathrm{ZAM}_X(t, f)$ at the main sidebands ($f_{S_k}^{\pm}$) around the high-frequency component, that is, mean/fluct($|\mathrm{ZAM}_X(t, f_{S_1}^{\pm})|$), along with the mean amplitude and fluctuation of $\mathrm{ZAM}_X(t, f)$ at the f_H excitation frequency, that is, mean/fluct($|\mathrm{ZAM}_X(t, f_H)|$). From this perspective, changes in the mean value and

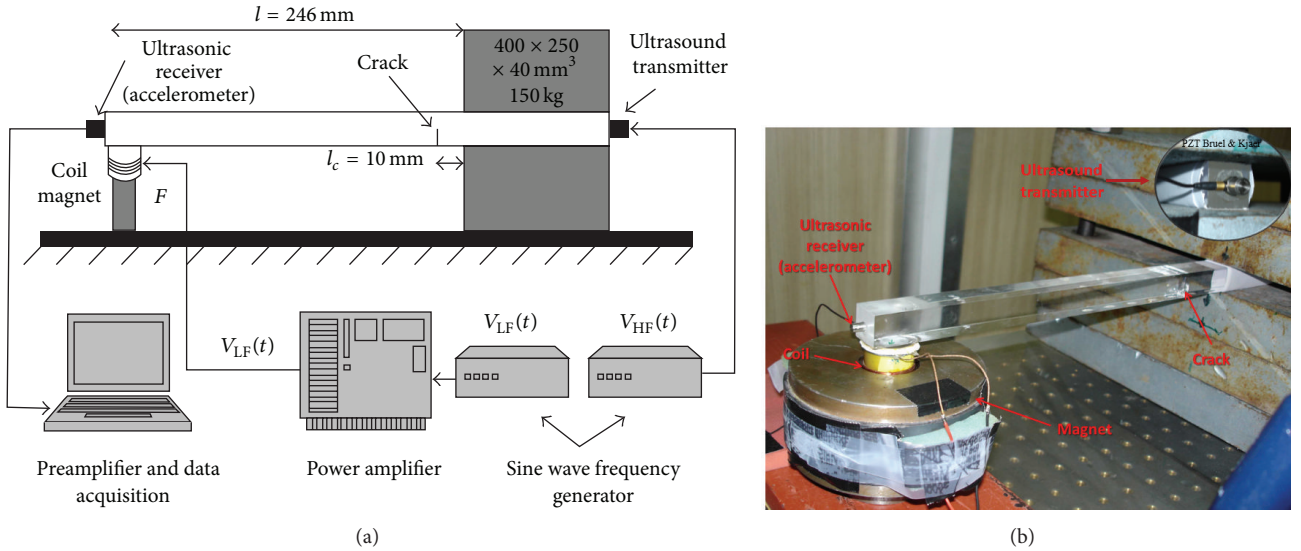

FIGURE 1: A schematic representation (a) and the actual realization (b) of the experimental setup.

the dynamic range of amplitude fluctuation, combined with the inspection of the spectral characteristics of this fluctuation, could correlate with the crack depth and provide insight into the way the presence of the crack affects the beam response during VAM stimulation.

3. Experiments

Tests were performed on Plexiglas beams to obtain nonlinear modulation responses for further signal processing. The beams used in the experiments had dimensions of 2 × 2 × 40 cm and they were clamped between two heavy steel jaws. To avoid additional damping and distortion due to couplings, the beam was excited with a force F by using a small voice coil weighting 2 gr attached to the beam. The coil was placed in the field of a permanent magnet and was excited by two waveform generators using sinus signals. A miniature transducer was used to pick up the vibration response, which was transferred to an acquisition system and stored for further analysis. A very narrow cut was initially introduced to the beam. Next, the beam was subjected to controlled dynamical loading which caused crack propagation. Due to the structure of Plexiglas, the propagation of the crack could not be accurately controlled resulting in arbitrary crack depths. A Bruel and Kjaer 4393 piezoelectric charge transducer was used for the high-frequency excitation. A schematic representation and a photo from the actual implementation set-up are depicted in Figures 1(a) and 1(b), respectively. Initially, a fatigue crack of 7% depth was introduced at $l_c = 10$ mm from the clamped end. Then, its depth was increased to 20% and finally to 45%. During the experiments two continuous sine waves were simultaneously introduced to the beam. The first ($V_{HF}(t)$) was the high-frequency ultrasound probe wave at $f_H = 31.3$ kHz. The second wave ($V_{LF}(t)$) was the low-frequency vibration at a frequency of $f_L = 92$ Hz, equal to the resonance frequency of the intact beam. The sampling frequency used was 192 kHz. Figure 2 depicts an excerpt from the measured response

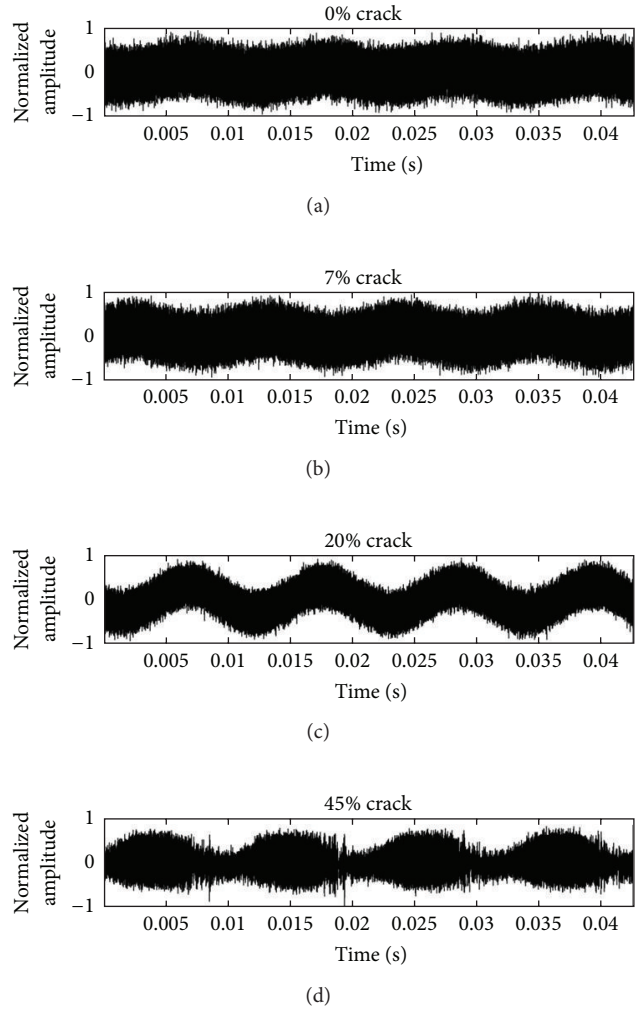

FIGURE 2: The experimental data excerpt (8192 samples, sampling frequency 192 kHz) used in the ZAM analysis for the uncracked, 7%, 20%, and 45% of the crack depth cases ((a) to (d)).

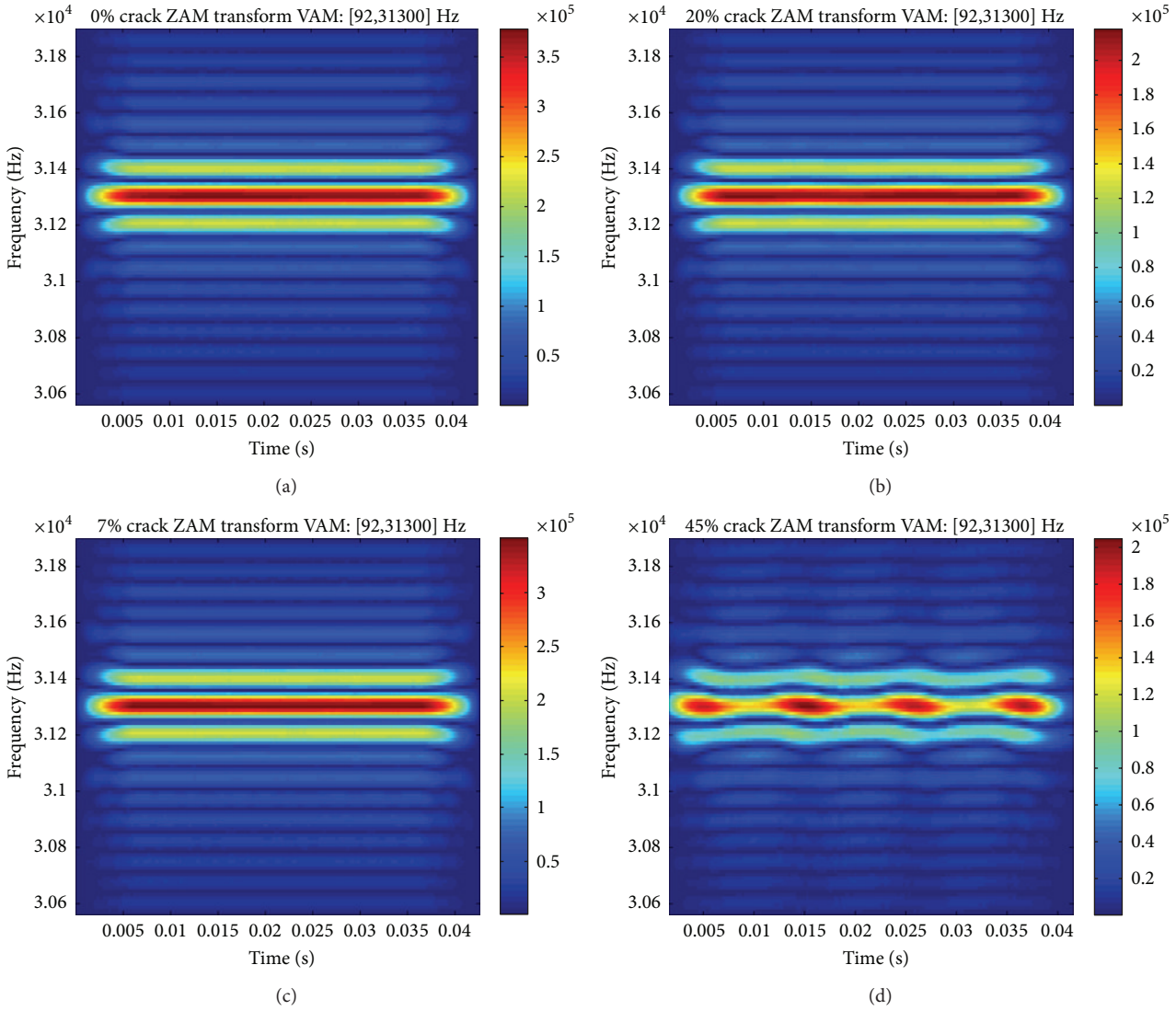

Figure 3: Results from the ZAM analysis of the experimental data of Figure 2 for 0% (a), 7% (c), 20% (b), and 45% (d) crack size, respectively.

for the uncracked and the three different crack depth cases ((a) to (d)), respectively. As it can be seen from Figure 1, strong modulation components are present and increase with increasing crack depth.

4. Results and Discussion

Figure 3 shows the estimated $\mathrm{ZAM}_X(t, f)$ of the data depicted in Figure 2 for the four examined crack depths, that is, 0%, 7%, 20%, and 45%, zoomed in the area of the $f_H = 31.3$ kHz.

Apparently, from these plots it is clear that a series of $f_{S_k}^{\pm}$ sidebands is evident, with the $f_{S_1}^{\pm}$ at $f_{S_1}^{-} = 31208$ Hz and $f_{S_1}^{+} = 31392$ Hz being the most noticeable, compared to the rest. It is noteworthy that as the crack depth is increased towards 45% (Figure 3(d)), a fluctuation at the $f_{S_1}^{\pm}$ frequencies is noticed, whereas there is a more concentrated activity at f_H across the time axis (in the form of peaks rather than frequency line ridges), indicating, possibly, the existence of a "breathing-crack" mechanism. It should be noted that the latter behavior is also noticed in the time domain (see Figure 2), as we move from the 0% to the 45% crack depth. More specifically, the periodic behavior of the breathing mechanism is clearly noticed in the modulated amplitude of the time series, with a more profound example being the case of 20% crack depth (Figure 2(c)), where the 92 Hz imposed frequency is driving the breathing effect. Nevertheless, when focusing at the high-frequency area, as the subfigures of Figure 3 do, only the case of 45% crack depth reflects the consequences of the breathing effect at the central and side lobe-frequencies, as previously described (see Figure 3(d)).

The amplitude of the estimated $\mathrm{ZAM}_X(t, f)$ of Figure 3 at the corresponding VAM frequencies, that is, 31392 Hz (a), 31300 Hz (b), and 31208 Hz (c) for each crack size (0%, 7%, 20%, and 45%), respectively, is depicted in Figure 4. From the latter, it is clear that the $\mathrm{ZAM}_X(t, f)$ amplitude is inversely

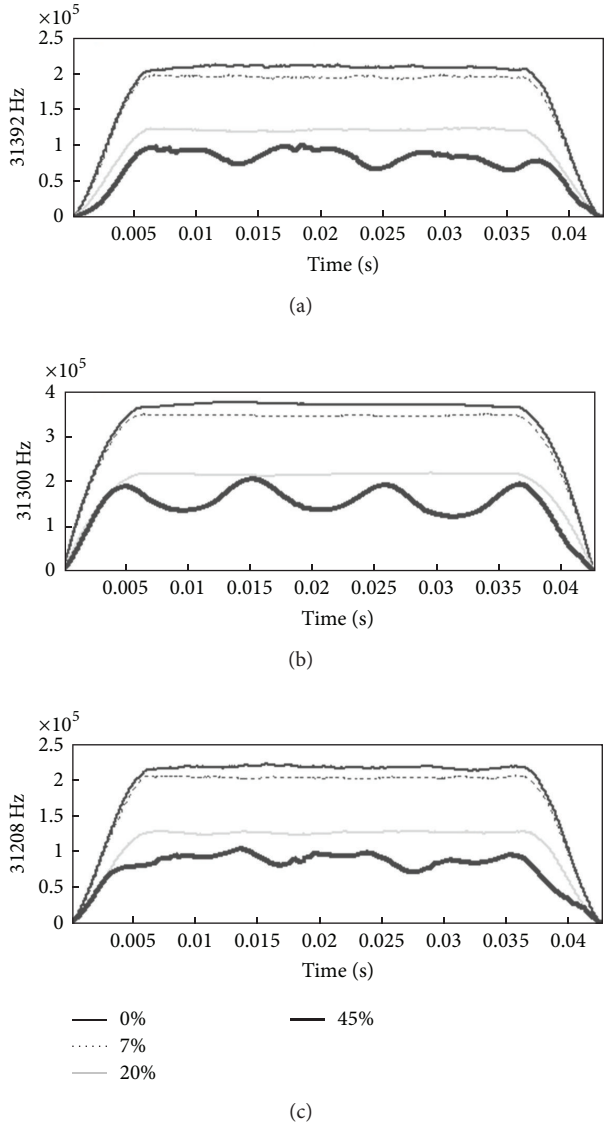

Figure 4: The amplitude fluctuation of the ZAM transform at the corresponding VAM frequencies, that is, 31392 Hz (a), 31300 Hz (b), and 31208 Hz (c) for each crack size (0%, 7%, 20%, and 45%), respectively.

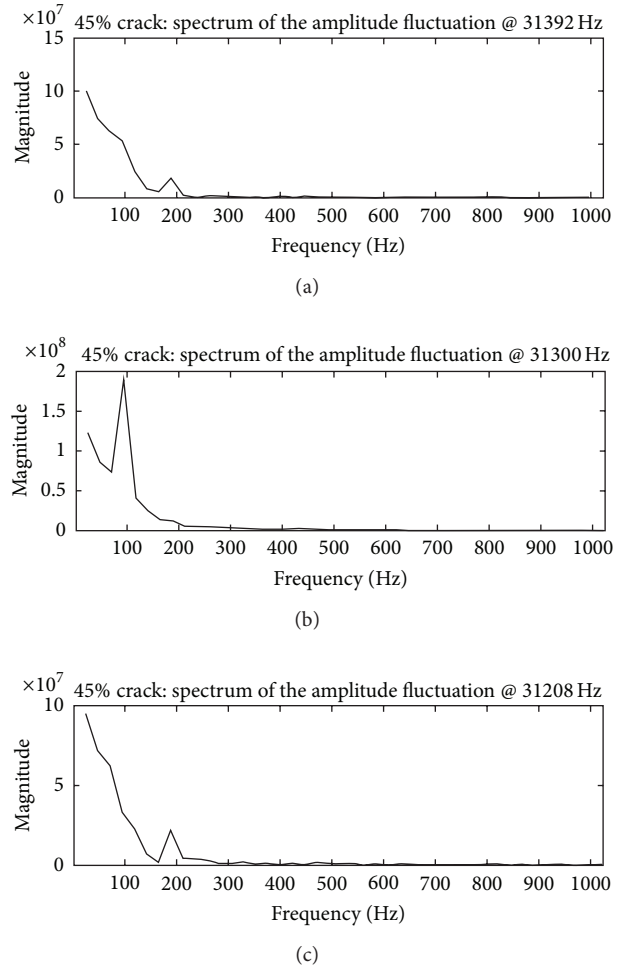

Figure 5: The spectrum of the amplitude fluctuation of the ZAM transform at the corresponding VAM frequencies, that is, 31392 Hz (a), 31300 Hz (b), and 31208 Hz (c), for the crack size of 45%, respectively.

proportional to the crack depth, whereas the amplitude fluctuation fluct($|\mathrm{ZAM}_X(t, f^{\pm}_{S_{1,H}})|$) is highly increased as the crack depth also increases. This might be justified when taking into account the occurrence of nonlinear dissipation effects due to "crack breathing" that are more pronounced as the crack depth increases. Moreover, there is a clear periodicity in the amplitude modulation for the case of f_H (Figure 4(b)); a noticeable, yet not so intense, one is evident in the amplitude modulation of $f^{\pm}_{S_1}$. This is further examined in Figure 5, where the spectrum of the amplitude fluctuation of the ZAM transform at the corresponding VAM frequencies, that is, 31392 Hz (a), 31300 Hz (b), and 31208 Hz (c), for the crack size of 45%, respectively, is illustrated.

As it is clear from Figure 5, the low excitation frequency $f_L = 92$ Hz modulates the amplitude of $\mathrm{ZAM}_X(t, f_H)$ (Figure 5(b)), whereas mainly the first harmonic of f_L, that is, $2f_L = 184$ Hz, causes the amplitude fluctuation $|\mathrm{ZAM}_X(t, f^{\pm}_{S_1})|$ (Figures 5(a) and 5(c), resp.).

Focusing at the 45% crack depth case, the frequency modulation (fluctuation of ridges) seen in Figure 3(d) is further examined. In particular, Figure 6 reveals the corresponding spectral characteristics of this modulation at the corresponding VAM frequencies, that is, 31392 Hz (a), 31300 Hz (b), and 31208 Hz (c).

Similarly to the spectral characteristics of the amplitude modulation of ZAM transform seen in Figure 5, here the low excitation frequency $f_L = 92$ Hz modulates the frequency fluctuation $|\mathrm{ZAM}_X(t, f^{\pm}_{S_1})|$ (Figures 6(a) and 6(c), resp.), whereas a coexistence of $f_L = 92$ and $2f_L = 184$ Hz modulates the frequency fluctuation of $\mathrm{ZAM}_X(t, f_H)$ (Figure 6(b)). The separate damage indices (sDI) (all normalized to the corresponding value of 45% crack depth case after

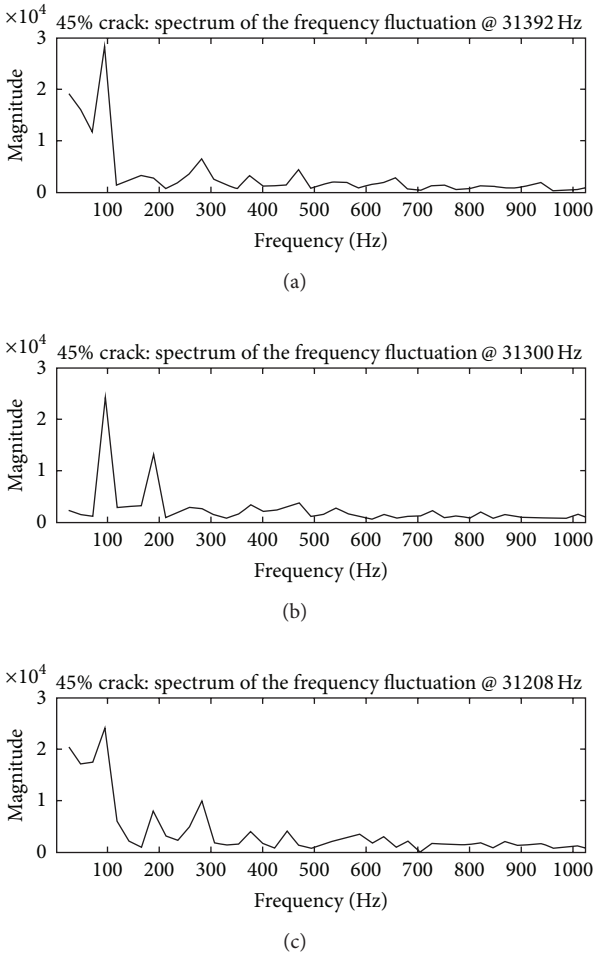

Figure 6: The spectrum of the frequency modulation of the ZAM transform at the corresponding VAM frequencies, that is, 31392 Hz (a), 31300 Hz (b), and 31208 Hz (c), for the crack size of 45%, respectively.

bias elimination for the 0% crack depth case) based on the $1/|\mathrm{ZAM}_X(t, f)|$ (first row), the MAX-MIN range (second row), the corresponding standard deviation (third row) of the ZAM transform, and the normalized FFT magnitude (fourth row), at the corresponding VAM frequencies, that is, 31208 Hz (left column), 31300 Hz (middle column), and 31392 Hz (right column), respectively, are shown in Figure 7. From the latter it is deduced that the sensitivity of $1/|\mathrm{ZAM}_X(t, f)|$ according to the crack depth change is significantly higher than all other sDI, which mainly capture the transition from 20% to 45% crack depth, exhibiting less efficient performance in tracking smaller cracks.

Consequently, the mean value of the sDI for the case of the $1/|\mathrm{ZAM}_X(t, f)|$ (Figure 7, first row) could be defined as the most efficient ZAM-based DI, namely, $\mathrm{DI}_{\mathrm{ZAM}}$. Figure 8 depicts the $\mathrm{DI}_{\mathrm{ZAM}}$ along with the $\mathrm{DI}_{\mathrm{FFT}}$ defined in (2). Apparently, the $\mathrm{DI}_{\mathrm{ZAM}}$ surpasses $\mathrm{DI}_{\mathrm{FFT}}$ in terms of higher sensitivity in the crack depth change, as it better captures crack changes, even in small crack depths.

When comparing the presented work with the one of Zaitsev et al. [6], a similar behavior in the crack detection could be identified. Both works conclude that the damage index based on the amplitude modulation is better than the one based on the frequency modulation. Nevertheless, the latter damage index of [6] unexpectedly increases non-monotonically as the severity of crack increases; here, as it is derived from Figure 7 (second and third rows), the damage indices based on the frequency fluctuation (range and std) of the ZAM distribution increase monotonically with the crack depth, exhibiting, though, reduced sensitivity in the small cracks identification. This, in turn, is compensated by the damage index based on the inverse of the ZAM amplitude. Moreover, the analysis in [6] is prone to the mode-mixing effect; that is, a single intrinsic mode function (IMF) derived from the Empirical Mode Decomposition employed in [6] consists either of signals of widely disparate scales or a signal of a similar scale residing in different IMF components. Mode-mixing is often a consequence of signal intermittency, which could not only cause serious aliasing in the time-frequency distribution, but also make the physical meaning of individual IMF unclear [9]. Perhaps the mode-mixing effect could be the reason for this unexpected behavior of Zaitsev's et al. [6] damage index based on the frequency modulation. The proposed analysis here does not produce any mode-mixing effect, as it is clearly shown in the time-frequency distributions of Figure 3, making the relevant damage indices more robust to any signal intermittencies.

5. Conclusion

In this work, the investigation of the vibroacoustic modulation of cracked beam is approached in the time-frequency domain, using time-frequency analysis based on the Zhao-Atlas-Marks (ZAM) distribution. ZAMs efficient time-frequency representation of the vibrational information, with reduced cross-terms between signal components through its cone-shaped kernel function, allowed for detailed monitoring of the VAM effects on beam behavior due to the existence of a crack. The hypothesis adopted here, that is, the characteristics of modulation responses in time domain might be proved more sensitive compared to those in the frequency domain and the combination of both could lead to damage indices that are more sensitive and robust, was proved valid. This was justified by the experimental results derived when applying VAM on Plexiglas beams with a varying crack depth of 0%, 7%, 20%, and 45%. Considering the responses at the ZAM domain and, especially, the reduction of mean ZAM amplitude at the sidebands and excitation high frequency with the increase of the crack depth a new damage index was formed, that is, $\mathrm{DI}_{\mathrm{ZAM}}$. The latter led to a more sensitive response compared to the one based on the spectral characteristics of the beam response, that is, $\mathrm{DI}_{\mathrm{FFT}}$, better capturing crack changes, even in small crack depths. The promising results presented here enable more efficient applications of the proposed method in nondestructive damage detection applications.

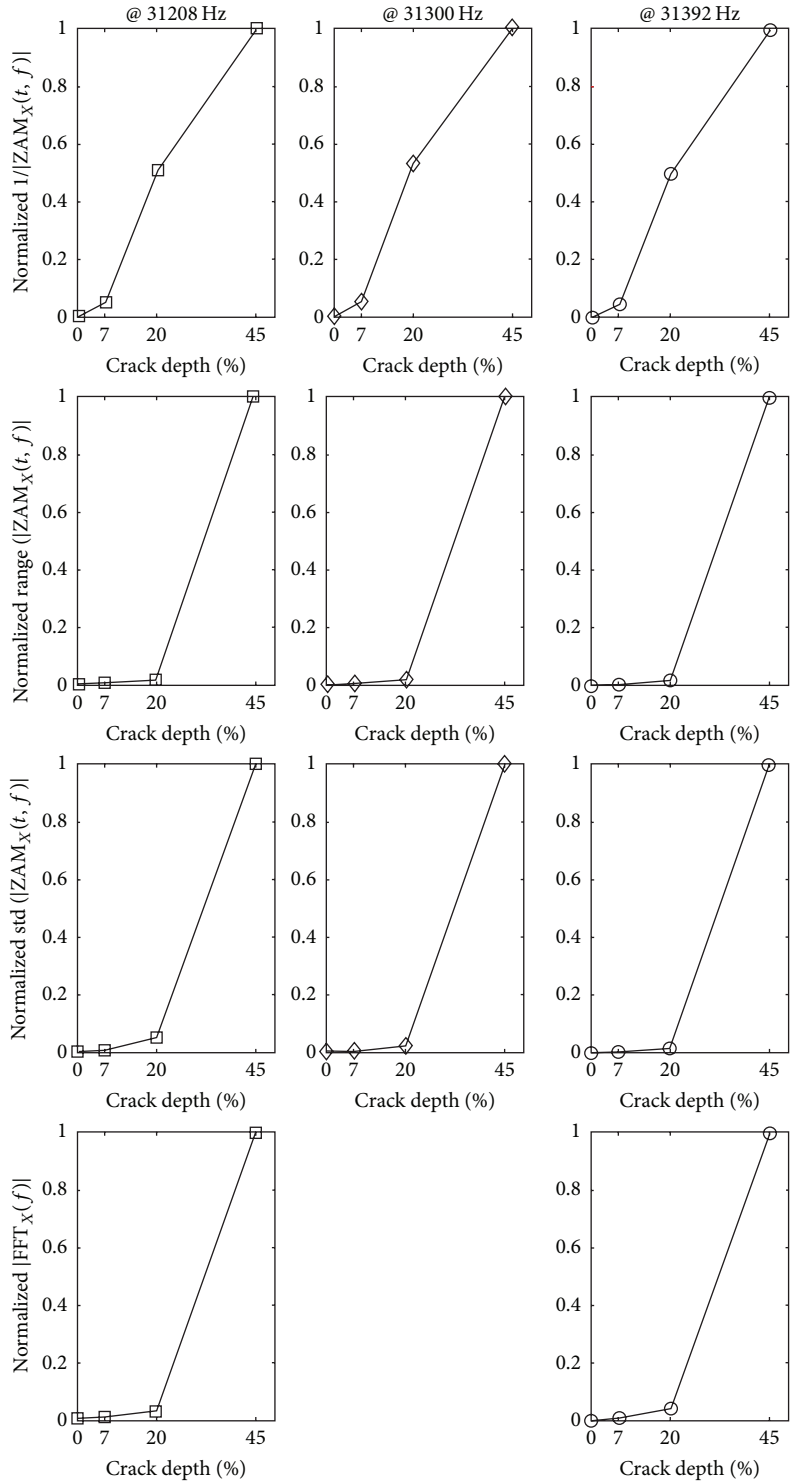

FIGURE 7: The separate damage indices (sDI) based on the $1/|\mathrm{ZAM}_X(t, f)|$ (first row), the MAX-MIN range (second row), the corresponding standard deviation (third row) of the ZAM transform, and the normalized FFT magnitude (fourth row) at the corresponding VAM frequencies, that is, 31208 Hz (left column), 31300 Hz (middle column), and 31392 Hz (right column), respectively. Note that, for the FFT-based analysis, only the 31208 Hz (left column) and 31392 Hz (right column) were considered, since the FFT amplitude at the central high-frequency (31300 Hz) was used as a normalization factor. Moreover, in the ZAM-based analysis, all values were estimated for the time span of 0.006–0.036 sec to avoid edge effects, while all data samples acquired (92001) were used in the FFT-based analysis to increase its frequency resolution.

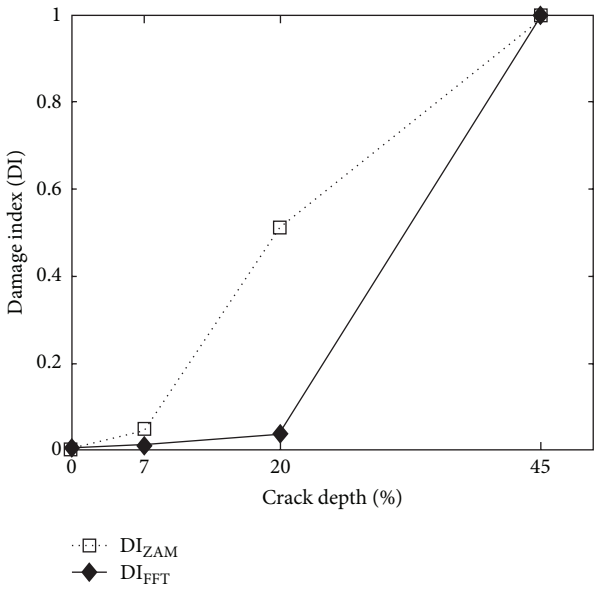

FIGURE 8: The damage index (DI) derived as the mean value of the sDI for the case of the $1/|\mathrm{ZAM}_X(t, f)|$ (Figure 7, first row)-$\mathrm{DI}_{\mathrm{ZAM}}$ and the $|\mathrm{FFT}(f)|$ (Figure 7, fourth row)-$\mathrm{DI}_{\mathrm{FFT}}$. The increase in the sensitivity of the $\mathrm{DI}_{\mathrm{ZAM}}$ over the $\mathrm{DI}_{\mathrm{FFT}}$ is evident.

Conflict of Interests

The authors declare that there is no conflict of interests regarding the publication of this paper.

References

[1] L. A. Ostrovsky and P. Johnson, "Dynamic nonlinear elasticity in geomaterials," *Rivista del Nuovo Cimento*, vol. 24, no. 7, pp. 1–46, 2001.

[2] A. Moussatov, V. Gusev, and B. Castagnede, "Self-induced hysteresis for nonlinear acoustic waves in cracked material," *Physical Review Letters*, vol. 90, no. 12, article 124301, 2003.

[3] A. Klepka, W. J. Staszewski, R. B. Jenal, M. Szwedo, J. Iwaniec, and T. Uhl, "Nonlinear acoustics for fatigue crack detection-experimental investigations of vibro-acoustic wave modulations," *Structural Health Monitoring*, vol. 11, no. 2, pp. 197–211, 2012.

[4] V. Zaitsev, V. Gusev, and B. Castagnede, "Thermoelastic mechanism for logarithmic slow dynamics and memory in elastic wave interactions with individual cracks," *Physical Review Letters*, vol. 90, no. 7, Article ID 075501, 2003.

[5] A. E. Ekimov, I. N. Didenkulov, and V. V. Kazakov, "Modulation of torsional waves in a rod with a crack," *Journal of the Acoustical Society of America*, vol. 106, no. 3, pp. 1289–1292, 1999.

[6] V. Zaitsev, V. Nazarov, V. Gusev, and B. Castagnede, "Novel nonlinear-modulation acoustic technique for crack detection," *NDT & E International*, vol. 39, no. 3, pp. 184–194, 2006.

[7] D. M. Donskoy and A. M. Sutin, "Vibro-acoustic modulation nondestructive evaluation technique," *Journal of Intelligent Material Systems and Structures*, vol. 9, no. 9, pp. 765–771, 1999.

[8] A. Zagrai, D. Donskoy, A. Chudnovsky, and E. Golovin, "Micro- and macroscale damage detection using the nonlinear acoustic vibro-modulation technique," *Research in Nondestructive Evaluation*, vol. 19, no. 2, pp. 104–128, 2008.

[9] P. Duffour, M. Morbidini, and P. Cawley, "Comparison between a type of vibro-acoustic modulation and damping measurement as NDT techniques," *NDT & E International*, vol. 39, no. 2, pp. 123–131, 2006.

[10] A. Klepka, L. Pieczonka, W. J. Staszewski, and F. Aymerich, "Impact damage detection in laminated composites by nonlinear vibro-acoustic wave modulation," *Composites B: Engineering*, 2013.

[11] F. Aymerich and W. J. Staszewski, "Experimental study of impact-damage detection in composite laminates using a cross-modulation vibro-acoustic technique," *Structural Health Monitoring*, vol. 9, no. 6, pp. 541–553, 2010.

[12] A. Klepka, W. J. Staszewski, D. di Maio, and F. Scarpa, "Impact damage detection in composite chiral sandwich panels using nonlinear vibro-acoustic modulations," *Smart Materials and Structures*, vol. 22, no. 8, Article ID 084011, 2013.

[13] H. F. Hu, W. J. Staszewski, N. Q. Hu, R. B. Jenal, and G. J. Qin, "Crack detection using nonlinear acoustics and piezoceramic transducers—instantaneous amplitude and frequency analysis," *Smart Materials and Structures*, vol. 19, no. 6, Article ID 065017, 10 pages, 2010.

Hindawi Publishing Corporation
Shock and Vibration
Volume 2014, Article ID 845106, 9 pages
http://dx.doi.org/10.1155/2014/845106

Research Article

Perspectives of Second-Order Blind Identification for Operational Modal Analysis of Civil Structures

C. Rainieri

Structural & Geotechnical Dynamics Lab "StreGa", DiBT Department, University of Molise, Via Duca degli Abruzzi, 86039 Termoli, Italy

Correspondence should be addressed to C. Rainieri; carlo.rainieri@unimol.it

Received 19 July 2013; Accepted 24 February 2014; Published 11 June 2014

Academic Editor: Nuno Maia

Copyright © 2014 C. Rainieri. This is an open access article distributed under the Creative Commons Attribution License, which permits unrestricted use, distribution, and reproduction in any medium, provided the original work is properly cited.

Innovative methods for output-only estimation of the modal properties of civil structures are based on blind source separation techniques. In the present paper attention is focused on the second-order blind identification (SOBI) algorithm and the influence of its analysis parameters on computational time and accuracy of modal parameter estimates. These represent key issues in view of the automation of the algorithm and its integration within vibration-based monitoring systems. The herein reported analyses and results provide useful hints for reduction of computational time and control of accuracy of estimates. The latter topic is of interest in the case of single modal identification tests, too. A criterion for extraction of accurate modal parameter estimates is identified and applied to selected experimental case studies. They are representative of the different levels of complexity that can be encountered during real modal tests. The obtained results point out that SOBI can provide accurate estimates and it can also be automated, confirming that it represents a profitable alternative for output-only modal analysis and vibration-based monitoring of civil structures.

1. Introduction

Time domain methods have been proved to be very effective for operational modal analysis (OMA) purposes. They fit a mathematical model to the (correlation functions of the) observed data in order to extract the modal properties [1]. Thus, one of the main problems is related to the optimal setting of the parameters of the model in order to obtain reliable and accurate estimates of the dynamic properties. In practical applications a conservative approach is usually adopted. It is based on the overspecification of the order of the model. This is set large enough to ensure the identification of all physical modes. The amount of overspecification depends on the characteristics of the analyzed dataset. Overmodeling introduces spurious poles besides the physical poles. This makes the modal parameter estimation more complicated. The discrimination between physical and spurious poles is usually based on the construction of the stabilization diagram.

The automatic interpretation of the stabilization diagram is still a challenge. Even if several research efforts have been made to improve its quality (see, for instance, [2–5]) and to automatically identify the physical poles (see, for instance, [6, 7]), the proposed methods are often computationally intensive and require the computation of a number of parameters and hard and soft validation criteria (see, for instance, [6]); moreover, the reliability of results and the generality of the methods are limited by the need of calibrating thresholds and other analysis parameters for each monitored structure [7]. On the other hand, nonparametric methods do not require the interpretation of stabilization diagrams and, as such, can more easily be automated [8–10].

The use of blind source separation (BSS) techniques in the context of OMA and structural health monitoring (SHM) has been recently proposed [11–15]. BSS techniques extract a set of signals, the so-called sources, from observations of their mixtures [16] based on fairly general assumptions about the sources and the mixing process. BSS techniques can be classified as linear [17] or nonlinear [18], depending on the type of combination of the sources. Moreover, static mixing [17] and convolutive mixing [19] can be considered.

An increasing number of applications in the field of structural dynamics have recently appeared in the literature [15, 20–22]. Even if the time response of structures is related to the excitation through a convolutive mixture, the dynamic response of a structure can also be interpreted as a static mixture of sources (the modal coordinates) in the field of modal identification [15]. The physical interpretation of sources as modal coordinates becomes clear by comparing the modal expansion of the dynamic response (1) with the linear and static mixture of sources (2):

$$\{y(t)\} = [\Phi]\{q(t)\}, \quad (1)$$

$$\{y(t)\} = [A]\{s(t)\}. \quad (2)$$

In fact, the source signals $\{s(t)\}$ play the role of the modal coordinates $\{q(t)\}$ and, on the analogy, there is a one-to-one relationship between the modal matrix $[\Phi]$ and the mixing matrix $[A]$. Thus, in the context of modal identification, BSS techniques aim at recovering the mixing matrix $[A]$, holding the information about the mode shapes, and the modal responses, here represented by the sources $\{s(t)\}$, from their observed mixtures $\{y(t)\}$.

No mathematical model is assumed to describe the process that produced the measured data. The mixing model is the only assumption. Thus, BSS techniques can be referred to as time domain, nonparametric methods for OMA. The absence of stabilization charts to be interpreted or model parameters to be set simplifies the automation and makes BSS techniques an interesting alternative to the classical time domain modal identification methods. Nevertheless, the use of BSS techniques in structural dynamics is still a challenge [14], and a performance assessment of BSS techniques in the context of output-only modal identification of civil structures is certainly of interest.

Some limits in the use of BSS for OMA can be traced back to the basic assumptions of the different techniques, which show different degree of compatibility with the dynamic systems of interest. The applicability of principal component analysis (PCA) to real case studies has been limited by the need for information about the mass matrix [15]. Independent component analysis (ICA) has been recognized to be much more suitable than PCA to vibration data processing for modal identification purposes [15]. The main drawbacks are related to the use of high-order statistics, whose computation is time consuming and difficult in the presence of a scarcity of data, and to the poor modal identification performance of the method for systems characterized by damping ratios larger than 1% [15]. Methods based on second-order statistics of the observed signals assume that the sources are uncorrelated for all delays and have different spectra. Among these, the second-order blind identification (SOBI) algorithm [17] has been recognized as a promising alternative for modal parameter identification in a number of studies [20–22]. When SOBI is applied to vibration data, the real valued mixing matrix implies real valued mode shape estimates. This can be a drawback of the method in the presence of complex modes. However, taking into account that the basic assumptions of SOBI fit the needs of the output-only identification of dynamics systems and that civil engineering structures often show real modes, in the following sections attention is focused on SOBI and its performance for OMA of civil structures.

After a discussion about how SOBI can be adapted to the analysis of random responses in the context of OMA, the present study investigates the influence of the analysis parameters on accuracy of modal parameter estimates and computational time. The identification performance of SOBI is also assessed against a number of experimental case studies related to civil structures and characterized by increasing degree of complexity. The final objective is the definition of rules of thumbs for the application and automation of SOBI in the context of OMA and vibration-based SHM of civil structures.

2. SOBI and Modal Identification

The basics of SOBI are briefly reported in this section to highlight, at the end, how the method has been herein adapted to the analysis of random responses for OMA purposes. This discussion puts in evidence the analysis parameters of the algorithm. Their influence on the quality of modal parameter estimates is investigated in the next section.

When some (additive) noise $\{n(t)\}$ is present in the measured response, (2) can be rewritten as

$$\{y(t)\} = [A]\{s(t)\} + \{n(t)\}. \quad (3)$$

The l recorded time histories are, therefore, modelled as a linear combination of N_m modal responses (the sources) plus noise. As a consequence, if there are N_m modes in the frequency range under investigation, they can be identified only if $\text{rank}([A]) = N_m$. Since the mixing matrix has dimension $l \times N_m$, this implies that the number of measurement channels has to be larger than or equal to the number of active modes: $l \geq N_m$. Thus, SOBI can be classified as a low-order method for OMA. Moreover, since the columns of the mixing matrix represent estimates of the mode shapes of the structure under test, a judicious choice of sensor locations is needed so that the observed mode shape vectors are linearly independent and the rank of $[A]$ is preserved.

The issues related to the identifiability of a limited number of modes can be mitigated through the repeated application of band-pass filtering until the entire frequency range of interest is investigated. However, this procedure leads to a major increase in the time of analysis.

A fundamental assumption in SOBI is that the sources are stationary, uncorrelated, and scaled to have unit variance, so their covariance matrix is the identity matrix:

$$[R_{ss}(0)] = E\left\{\{s(t)\}\{s(t)\}^T\right\} = [I], \quad (4)$$

where the superscript T denotes transpose. The additive noise is assumed to be a temporally and spatially white stationary random process, with

$$E[\{n(t)\}] = \{0\}, \quad (5)$$

$$[R_{nn}(0)] = E\left[\{n(t)\}\{n(t)\}^T\right] = \sigma^2[I]. \quad (6)$$

If the added noise is also independent of the source signals, this implies

$$E\left[\{n(t)\}\{s(t)\}^T\right] = [0]. \tag{7}$$

The first step of the algorithm consists of whitening the signal part of the observed data $\{x(t)\} = [A]\{s(t)\}$. This is achieved by applying a linear transformation to $\{x(t)\}$ such that the whitened data $\{z(t)\}$ are uncorrelated and have unit variance:

$$\begin{aligned}\{z(t)\} = [W]\{x(t)\} &\Longrightarrow \left[R_{zz}(0)\right] \\ &= E\left[\{z(t)\}\{z(t)\}^T\right] = [I].\end{aligned} \tag{8}$$

The matrix $[W]$ defining this transformation is referred to as the *whitening matrix*. From (8) and (4) it is easy to check that

$$\begin{aligned}\left[R_{zz}(0)\right] &= [W][A]\,E\left[\{s(t)\}\{s(t)\}^T\right][A]^T[W]^T \\ &= [W][A][A]^T[W]^T = [I].\end{aligned} \tag{9}$$

Thus, if $[W]$ is a whitening matrix, $[A'] = [W][A]$ is an $N_m \times N_m$ unitary matrix. As a consequence, the mixing matrix can be factored as the product of the inverse of the whitening matrix and a unitary matrix (to be determined).

Whitening of the measured response $\{y(t)\}$ also obeys a linear model:

$$\begin{aligned}[W]\{y(t)\} &= [W]([A]\{s(t)\} + \{n(t)\}) \\ &= \left[A'\right]\{s(t)\} + [W]\{n(t)\}.\end{aligned} \tag{10}$$

From the covariance matrix of the observed mixture

$$\left[R_{yy}(0)\right] = E\left[\{y(t)\}\{y(t)\}^T\right] = [A][A]^T + \sigma^2[I], \tag{11}$$

the following equation is obtained:

$$[A][A]^T = \left[R_{yy}(0)\right] - \sigma^2[I]. \tag{12}$$

Combining (10) with (12) and taking into account (4), (6), and (7), it is possible to show that the whitening matrix $[W]$ can be derived from the covariance matrix $[R_{yy}(0)]$, provided that the noise covariance matrix is known or can be estimated.

From a practical point of view, once the measured data have been centralized by removal of the mean value from each component of $\{y(t)\}$, whitening is obtained as follows. First of all, the eigenvalue decomposition of $[R_{yy}(0)]$ is computed:

$$\left[R_{yy}(0)\right] = E\left[\{y(t)\}\{y(t)\}^T\right] = [V][D][V]^T, \tag{13}$$

where $[V]$ is the matrix of eigenvectors and $[D]$ is the diagonal matrix of eigenvalues. If only the N_m largest eigenvalues $d_1, \ldots, d_{N_m}$ and the corresponding eigenvectors $\{v_1\}, \ldots, \{v_{N_m}\}$ of $[R_{yy}(0)]$ are retained, the average of the remaining $l - N_m$ eigenvalues yields an estimate σ^2 of the noise variance, under the assumption of white noise [17]. The whitened signals are then computed from the largest eigenvalues and the corresponding eigenvectors as

$$\begin{aligned}\{z(t)\} &= \left(\left[D_{N_m}\right] - \sigma^2\left[I_{N_m}\right]\right)^{-1/2}\left[V_{N_m}\right]^T\{y(t)\} \\ &= [W]\{y(t)\},\end{aligned} \tag{14}$$

where $[D_{N_m}]$ is the submatrix of $[D]$ holding only the N_m largest eigenvalues, $[V_{N_m}]$ is the submatrix of $[V]$ collecting the eigenvectors corresponding to the N_m largest eigenvalues of $[R_{yy}(0)]$, and the whitening matrix is given by

$$[W] = \left(\left[D_{N_m}\right] - \sigma^2[I]\right)^{-1/2}\left[V_{N_m}\right]^T. \tag{15}$$

In (6) the noise variance is assumed to be the same for all channels in agreement with the original formulation of the method [17]. However, in practical applications the noise distribution can vary from sensor to sensor, even if it is typically assumed that two sensors show uncorrelated noise (see, for instance, [23]). Moreover, sensor noise is often $1/f$-type noise rather than temporally white noise. The white noise assumption is needed to get an estimate σ^2 of the noise variance as the average of the smallest $l - N_m$ eigenvalues of $[R_{yy}(0)]$; see (14), (15), and (16). However, as clarified at the end of this section, the estimation of the noise variance before the extraction of the sources can be avoided for OMA purposes. In fact, SOBI is applied to estimate the correlation functions of both the sources and the noise. The discrimination between modal responses and noise is carried out in a second stage. Thus, the different noise distributions do not affect the modal identification performance of the method in practical applications. The assumption of spatially white noise is not a limiting factor in the context of OMA. However, from a general point of view, the blind identification problem when $[R_{nn}(0)]$ is a full matrix can be solved by carrying out a robust whitening, based on the decomposition of a linear combination of a set of covariance matrices taken at nonzero time lags [24], instead of the classical whitening given by (13) and (15).

Once the whitened signals have been obtained, the following p time-shifted covariance matrices have to be computed:

$$\left[R_{zz}(\tau_k)\right], \quad k = 1, \ldots, p. \tag{16}$$

In order to estimate the sources and the mixing matrix, SOBI carries out an approximate joint diagonalization of those p time-shifted covariance matrices according to the joint approximate diagonalization (JAD) technique [17]. The objective of the JAD is to find the unitary matrix $[\Psi]$ that approximately diagonalizes the time-shifted covariance matrices. An optimization problem is defined with respect to the matrix $[\Psi]$ that minimizes the sum of all off-diagonal terms of $[\Psi]^T[R_{zz}(\tau_k)][\Psi]$ $(k = 1, \ldots, p)$ for the p time-shifted covariance matrices:

$$\min_{[\Psi]} \sum_{k=1}^{p} \operatorname{off}\left([\Psi]^T\left[R_{zz}(\tau_k)\right][\Psi]\right). \tag{17}$$

The solution to the minimization problem is found by means of a numerical algorithm based on the Jacobi rotation technique [17]. Two parameters have to be set: the number p of time-shifted covariance matrices to be jointly diagonalized and the threshold t used to stop JAD. Concerning the threshold t, the problem of its setting has been analyzed in [25], showing that very small values for t have no sense

because the diagonality criterion is approximate itself. Thus, it is usually unnecessary to push the accuracy of the rotation matrix to the machine precision. Setting the value of t to the square root of the machine precision is sufficient. Concerning the number p of time-shifted covariance matrices, the diagonalization performance improves when p increases and it rapidly converges in most cases [17]. Once the matrix $[\Psi]$ has been obtained, the demixing matrix $[U]$ and the mixing matrix $[A]$ can be computed:

$$[U] = [\Psi]^T [W], \tag{18}$$

$$[A] = [W]^+ [\Psi], \tag{19}$$

where the superscript + denotes pseudoinverse. The resulting sources are shift-uncorrelated because the matrices $[R_{ss}(\tau_k)]$ are nearly diagonal. The sources are obtained as follows:

$$\{s(t)\} = [U]\{y(t)\}. \tag{20}$$

The mode shapes of the structure are obtained from the columns of the mixing matrix. The technique for the estimation of natural frequencies and damping ratios depends on the type of data used for modal identification. In the literature SOBI has been applied to free responses, impulse responses, and responses to random excitation [20–22]. In the first two cases, the estimation of natural frequencies and damping ratios from the obtained sources is straightforward. In fact, taking into account that the free vibration response can be expressed as a sum of exponentially decaying sinusoids, fitting this expression to the data allows the estimation of the modal parameters (refer to [22] for more details). In the case of response to random excitation, while the estimation of natural frequencies from the identified sources is again straightforward, this is not the case of damping ratios, whose estimation requires the knowledge of the applied random excitation [20]. However, the extension of SOBI to the analysis of random responses for the estimation of modal parameters including damping is immediate by recognizing that also the correlation function can be expressed as a sum of decaying sinusoids. This is the same basic assumption adopted by the NExT-type procedures [1]. In this case, there is no need to recover the sources, because natural frequencies and damping ratios can be directly estimated from their correlations $R_{ss}(\tau_k)$ as obtained from the JAD.

A simplified approach to the estimation of the modal properties by SOBI in the case of random response can be outlined as follows.

(i) Compute the whitening matrix $[W]$ from the centralized dataset according to (13) and (15); since the number of modes is not known a priori and the criterion for appropriate selection of the number N_m of eigenvalues to be retained is still debated, it is possible to set $N_m = l$; thus, l sources are extracted from the data even if the number of modes is likely lower than l; as a result, the sources associated with the actual structural modes have to be selected in a second stage based, for instance, on the error in fitting the correlations $R_{ss}(\tau_k)$ with exponentially damped harmonic functions; this approach was originally proposed in [20] for the analysis of impulse responses.

(ii) Compute the whitened dataset $\{z(t)\}$.

(iii) Compute the time-shifted covariance matrices $[R_{zz}(\tau_k)]$ and select p of them to apply the JAD.

(iv) The JAD of the p time-shifted covariance matrices $[R_{zz}(\tau_k)]$ with $k = 1, \ldots, p$ provides the unitary matrix $[\Psi]$, which allows the computation of the mixing matrix $[A]$ according to (19) and the autocorrelations $R_{ss}(\tau_k)$;

(v) Natural frequencies and damping ratios are finally estimated; different approaches can be adopted, such as regression on zero-crossing times and logarithmic decrement, or single-degree-of-freedom (SDOF) curve fitting estimators; the use of SDOF curve fitting estimators allows the computation of the fitting error; this makes a quantitative selection of the correlations associated with actual structural modes in the absence of noise rejection in the computation of the whitening matrix possible; the selection of the number of time lags p now plays a primary role in the process, since it not only is responsible for the matrix $[\Psi]$ but also defines the length of the correlation functions $R_{ss}(\tau_k)$; thus, taking into account the physics of the problem, p has to be set as a function of the period of the fundamental mode so that a sufficient number of cycles are present in the correlation of the source associated with the fundamental mode; a criterion for setting of p is given in Section 3.

(vi) The mode shapes are obtained from the columns of the mixing matrix corresponding to the source correlations selected in the previous step of analysis.

It is interesting to note that, unlike the other two-stage modal identification methods, SOBI provides the mixing matrix and, therefore, the mode shape estimates, first; natural frequencies and damping ratios are obtained in a second stage through postprocessing of the obtained sources. Finally, it is worth pointing out that SOBI can identify distinct, eventually closely spaced modes but it shows serious limitations in the presence of repeated modes [26].

3. Performance Assessment of SOBI for OMA of Civil Structures

In this section the effect of the parameters p and t on accuracy of modal parameter estimates and computational time of SOBI is investigated. SOBI is applied to OMA of selected case studies. Both simulated and real datasets have been considered. The final objective is the definition of rules of thumbs for the application and automation of SOBI for output-only modal analysis and vibration-based SHM of civil structures. The problem of the definition of criteria and approaches to reject the noise and, therefore, define in advance the expected number of modes is out of the scope of the present paper. SOBI is herein applied in order to extract

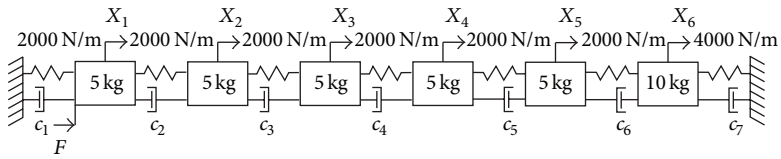

Figure 1: The benchmark 6-DOF system.

a number of modes equal to the number of measurement channels, as mentioned in the previous section. The obtained source correlations can represent both modal responses and noise sources. However, noise sources are distinguishable from modal responses [20] (this makes the definition of noise rejection mechanisms less critical in SOBI with respect to parametric time domain modal identification methods, which try to fit a model to the measured system response) and they can be eliminated in the second stage of the analysis aimed at estimating the natural frequencies and damping ratios. After the selection of the sources associated with modal responses, in this study the natural frequency of the ith mode is estimated by a linear regression on the zero-crossing times of the associated correlation function $R_{ss}(\tau_k)$, while damping ratio is calculated through the logarithmic decrement technique on the analogy with another well-established OMA technique, the enhanced frequency domain decomposition (EFDD) [27].

Sensitivity analyses have been carried out in order to assess the effect of the parameters governing the JAD (the number p of time-shifted covariance matrices to be jointly diagonalized and the threshold t used to stop the numerical procedure) on accuracy and computational time of SOBI when it is applied to output-only modal analysis. The first analyzed record is represented by the simulated response to a Gaussian white noise applied to degree-of-freedom (DOF) number 1 of the 6-DOF system shown in Figure 1. Rayleigh damping is adopted. Assuming 1% damping for the first and the last mode, the following proportionality constants have been obtained: $a_0 = 0.1523$ for the mass matrix and $a_1 = 4.15E-4$ for the stiffness matrix. The modal properties of the system are reported in Table 1. The response of the system has been simulated at all the six DOFs and it has been sampled at 100 Hz and decimated at 10 Hz before processing. White noise has also been added to the time series in order to simulate measurement noise. A signal-to-noise ratio of 5 dB has been considered. The adopted sampling frequency after decimation results in the extraction of four modal responses and two noise sources.

The results obtained from the application of SOBI to the simulated data have then been validated against operational response measurements of a number of real civil structures. Good quality data from a reinforced concrete structure characterized by well-separated modes (the Tower of the Nations in Naples [28]) and a reinforced concrete structure characterized by two closely spaced modes (the School of Engineering Main Building in Naples [29]) and noisy data from a masonry bell tower characterized by two closely spaced modes (S. Maria del Carmine Bell Tower in Naples [30]) are the considered benchmark record. They have been used also to validate an innovative automated OMA procedure in [9]. The selected real test cases are representative of modal identification problems typically encountered in civil engineering and characterized by different degree of difficulty. Reference modal parameters have been extracted from these records by well-established techniques, such as frequency domain decomposition (FDD) [31] and stochastic subspace identification (SSI) [1, 32], which have provided very consistent estimates.

Table 1: Modal properties of the simulated 6-DOF system.

Mode number	Natural frequency [Hz]	Damping ratio [%]
I	1.509	1.00
II	2.823	0.80
III	3.810	0.81
IV	4.737	0.87
V	5.593	0.95
VI	6.167	1.00

The results of the sensitivity analyses on the simulated dataset are presented first. According to these results, some rules of thumbs for the application of SOBI to modal identification are defined and applied to the real case studies. Validation of the effectiveness of the proposed criterion for the selection of p is based on comparisons with the modal estimates provided by FDD and SSI. Even if SOBI and its variants have already been applied to the modal identification of real civil structures [33], this study represents an interesting example of systematic application of SOBI to modal identification problems typically encountered in civil engineering and characterized by different degree of difficulty.

Concerning parameter settings, a careful literature review has provided a recommended value for t, as discussed in the previous section. However, this value has been determined according to a theoretical framework and not in view of the application of SOBI to output-only modal analysis and vibration-based SHM. Even if the computational time might not be a problem for single modal identification tests, its control can be of interest for continuous, automated monitoring. The computational time can range from fractions of seconds to several minutes or hours depending on the settings of t and p and the number of measurement channels. Figure 2 shows the dependence of the computational time from p and t for a real dataset consisting of 12 measurement channels. As expected, the larger the number of measurement channels, the higher the computational time of the algorithm, and it increases when p becomes larger and t decreases.

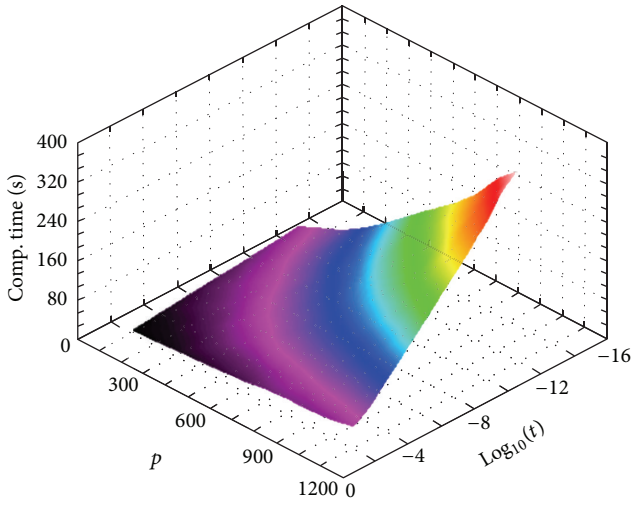

FIGURE 2: Sensitivity of computational time (sample plot).

The assessment of the influence of t and p on the modal identification results can provide effective hints to ensure accurate modal estimates or to reduce the computational time with little or no accuracy losses. To this aim, the simulated dataset has been processed by SOBI, and the identified modes in the range 0–5 Hz have been compared with the theoretical values for different settings of t and p. The cumulative frequency scatter J_f and the cumulative discrepancy between corresponding mode shapes J_s

$$J_f = \sum_{i=1}^{N_m} \left| \frac{f_i^{\text{SOBI}} - f_i^{\text{ref}}}{f_i^{\text{ref}}} \right| \cdot 100, \qquad (21)$$

$$J_s = \sum_{i=1}^{N_m} \left[1 - \text{MAC}\left(\left\{ \phi_i^{\text{SOBI}} \right\}, \left\{ \phi_i^{\text{ref}} \right\} \right) \right] \cdot 100$$

quantify the accuracy of the modal identification results. In (21) N_m is the number of identified structural modes, while the MAC between theoretical and estimated mode shapes is computed as per its definition [34]. The plot of $J_f + J_s$ versus p and t for the simulated dataset is shown in Figure 3(a). It is possible to recognize that accuracy is mainly influenced by p, while a weak variation with t can be observed. In particular, for t not larger than $1E-8$, results do not change anymore. This limit value for t is expected to be data dependent. However, similar sensitivity analyses carried out on real datasets provided the same results. Even if it is impossible to extrapolate a general rule, the obtained results seem to confirm that this value can be assumed as reference to obtain very stable results. Moreover, the little effect of t on the accuracy of estimates allows setting a threshold larger than $1E-8$ in order to reduce the computational time. The obtained results suggest that t can be increased up to $1E-4$ with negligible effects on the obtained modal parameter estimates and relevant reduction of computational time, in particular when the number of measurement channels is large. Above that value the approximations start inducing major effects on the estimates. Concerning the effect of p on accuracy, Figure 3(a) shows that the overall accuracy first improves and then gets worse for increasing values of p. This is an effect of the trend of J_f versus p, since J_s monotonically and slowly decreases with increasing values of p (even if for a single mode the J_s versus p plot could not be monotonic), as shown in Figure 3(b). This is consistent with the higher robustness of SOBI to noise with respect to other BSS methods based on second-order statistics, such as AMUSE [35]. This robustness is the result of the joint diagonalization of several time-shifted covariance matrices instead of the eigenvalue decomposition of a single covariance matrix evaluated at a certain time lag. On the other hand, the trend of J_f is probably due to the fact that the larger the value of p, the larger the effect of the disturbance beyond a certain decay level. As a final result, an optimal setting of p able to maximize the overall accuracy of modal estimates can be obtained from the minimum of the $J_f + J_s$ function.

Repeating the sensitivity analysis for different values of the sampling frequency, in order to reduce or increase the number of modes in the frequency range of interest, the trend of the $J_f + J_s$ function is kept, but the value of p corresponding to its minimum changes, as expected. However, when the sampling frequency changes by a factor of x, the optimal setting for p changes by the same factor. Attention has been therefore focused on the source associated with the fundamental mode, which is obviously present in all the analyses, and on the decay level associated with the optimal value of p. The decay level was found to be the same for different values of the sampling frequency. In particular, it was in the order of 10% of the maximum amplitude of the first cycle occurring at $\tau_k > 0$ (for $\tau_k = 0$ R_{ss} is always equal to one). Thus, the time to observe a given amplitude decay rather than the number of samples is responsible for the accuracy of estimates. This is consistent with the change of the optimal setting of p with the adopted sampling frequency and with the increasing effect of noise when p becomes too large.

The analysis of the decay level associated with the optimal setting of p seems to suggest the following rule for its evaluation. The optimal value of p can be determined in a couple of iterations by applying SOBI for a generic value of p and changing it in a way able to achieve a ratio of about 10% between the amplitudes of the last (depending on the value of p) and the first cycle (at $\tau_k > 0$) of the source correlation associated with the fundamental mode (Figure 4).

This rule has been validated through its application to real datasets. Taking into account the influence of t on the accuracy of modal parameter estimates, a value of 1E-8 has been adopted in the analyses. The obtained modal identification results are reported in Table 2 in comparison with reference estimates. A very good agreement can be observed, confirming that the proposed rule makes an effective setting of the analysis parameters able to provide accurate output-only modal identification results possible.

In order to validate further the proposed rule for the setting of p, the real datasets have been analyzed also for different values of p. The function $J_f + J_s$ versus p (Figure 5) has been evaluated around the estimated optimal value of p. The reference values of the natural frequencies and mode shapes are those provided by the SSI method (however,

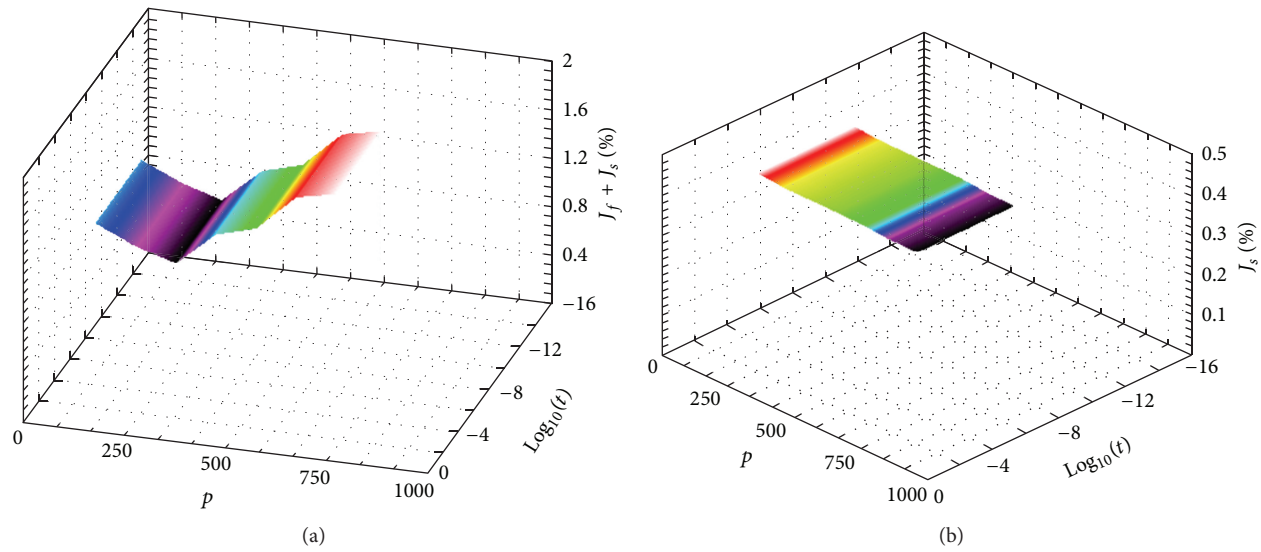

FIGURE 3: Sensitivity of overall accuracy (a) and mode shape accuracy (b) to p and t.

TABLE 2: Test cases, modal identification results, and comparisons.

Case study	Characteristics	l	(f_s [Hz], p)	Mode number	f_{SOBI} [Hz]	f_{ref} [Hz]	ξ_{SOBI} [%]	ξ_{ref} [%]	MAC
6-DOF system	Simulated data	6	(10, 400)	I	1.51	1.51	0.97	1.00	0.998
				II	2.82	2.82	0.73	0.80	0.999
				III	3.81	3.81	0.88	0.81	0.999
				IV	4.73	4.74	0.81	0.87	0.998
Tower of the Nations (Naples)	Well-separated modes	8	(5, 360)	I	0.81	0.81	0.36	0.40	≈1
				II	1.38	1.38	0.97	1.17	≈1
				III	1.66	1.66	0.69	0.63	≈1
School of Engineering (Naples)	Closely spaced modes	12	(10, 400)	I	0.92	0.92	1.23	1.32	≈1
				II	0.99	0.99	1.17	1.02	0.999
				III	1.30	1.30	0.58	0.64	≈1
S. Maria del Carmine Bell Tower (Naples)	Closely spaced modes, noisy data	12	(5, 300)	I	0.70	0.70	0.96	0.92	≈1
				II	0.76	0.76	0.92	0.83	≈1

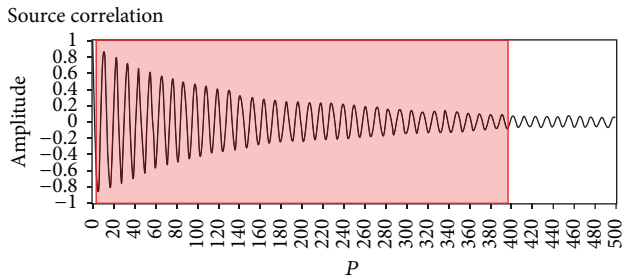

FIGURE 4: Illustration of the rule of thumbs for setting of p.

similar results have been obtained considering as reference estimates those provided by the FDD method). Figure 5 shows that the proposed rule is able to properly evaluate the optimal setting of p even in the case of real datasets.

The proposed approach for the optimal setting of p can easily be automated and used for the development of SOBI-based automated OMA procedures for vibration-based SHM. It is worth pointing out that the possibility of automatically setting the analysis parameters without any preliminary calibration is a fundamental requirement for the development of automated OMA procedures. An effective control of computational efforts is possible by appropriate setting of t, taking into account that it negatively affects the accuracy of modal parameter estimates beyond the limit value of $1E-4$. Thus, the present paper provides a contribution towards the development of innovative automated OMA procedures able to satisfy widely accepted target criteria reported in the literature [6, 7, 9]. However, automated OMA based on SOBI is out of the scope of the paper.

4. Conclusions

In the present paper the applicative perspectives of SOBI for OMA of civil structures have been discussed. Attention has been focused on SOBI because of its interesting performance,

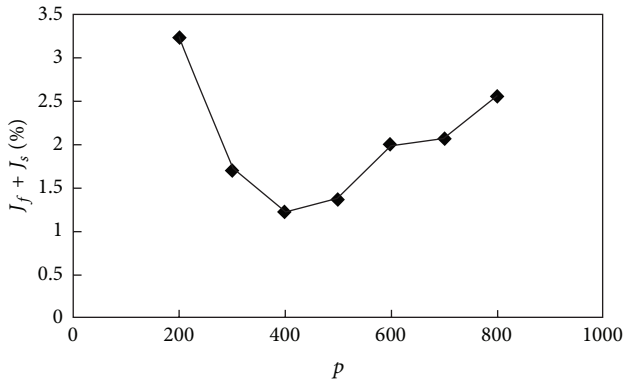

FIGURE 5: Validation of the proposed rule for setting of p ($t = 10^{-8}$, *real dataset*: "*School of Engineering in Naples*").

among the BSS methods, in the field of output-only modal identification and vibration-based SHM. In fact, the moderate complexity and computational demand of the algorithm and the separation of modal contributions make it suitable for automation and integration into SHM systems. In this perspective the influence of the JAD parameters on accuracy of modal estimates and computational time has been analyzed. The performed sensitivity analyses have made the definition of rules of thumbs for their optimal setting possible. These rules have also been validated against real datasets. The selected real case studies were representative of the different degree of complexity of modal identification test cases usually encountered in civil engineering. The good agreement between the modal property estimates provided by SOBI and those obtained by well-established OMA techniques, such as FDD and SSI, confirms SOBI as a valid alternative for output-only modal identification of civil structures. The results of the analyses reported in this paper have also provided the basis for the rational development of SOBI-based automated OMA procedures able to provide accurate estimates and effective control of computational efforts. However, the development of automated OMA procedures based on SOBI is out of the scope of the paper. It will be the object of future studies.

Conflict of Interests

The author declares that there is no conflict of interests regarding the publication of this paper.

References

[1] C. Rainieri and G. Fabbrocino, *Operational Modal Analysis of Civil Engineering Structures—An Introduction and Guide for Applications*, Springer, New York, NY, USA, 2014.

[2] C. Rainieri, G. Fabbrocino, and E. Cosenza, "Some remarks on experimental estimation of damping for seismic design of civil constructions," *Shock and Vibration*, vol. 17, no. 4-5, pp. 383–395, 2010.

[3] E. Reynders, R. Pintelon, and G. de Roeck, "Uncertainty bounds on modal parameters obtained from stochastic subspace identification," *Mechanical Systems and Signal Processing*, vol. 22, no. 4, pp. 948–969, 2008.

[4] B. Cauberghe, P. Guillaume, P. Verboven, S. Vanlanduit, and E. Parloo, "On the influence of the parameter constraint on the stability of the poles and the discrimination capabilities of the stabilisation diagrams," *Mechanical Systems and Signal Processing*, vol. 19, no. 5, pp. 989–1014, 2005.

[5] C. Rainieri, G. Fabbrocino, and E. Cosenza, "On damping experimental estimation," in *Proceedings of the 10th International Conference on Computational Structures Technology*, Valencia, Spain, 2010.

[6] E. Reynders, J. Houbrechts, and G. de Roeck, "Fully automated (operational) modal analysis," *Mechanical Systems and Signal Processing*, vol. 29, pp. 228–250, 2012.

[7] F. Magalhães, A. Cunha, and E. Caetano, "Online automatic identification of the modal parameters of a long span arch bridge," *Mechanical Systems and Signal Processing*, vol. 23, no. 2, pp. 316–329, 2009.

[8] R. Brincker, P. Andersen, and N. J. Jacobsen, "Automated frequency domain decomposition for operational modal analysis," in *Proceedings of the 25th SEM International Modal Analysis Conference*, Orlando, Fla, USA, 2007.

[9] C. Rainieri and G. Fabbrocino, "Automated output-only dynamic identification of civil engineering structures," *Mechanical Systems and Signal Processing*, vol. 24, no. 3, pp. 678–695, 2010.

[10] C. Rainieri, G. Fabbrocino, and E. Cosenza, "Near real-time tracking of dynamic properties for standalone structural health monitoring systems," *Mechanical Systems and Signal Processing*, vol. 25, no. 8, pp. 3010–3026, 2011.

[11] C. Zang, M. I. Friswell, and M. Imregun, "Structural damage detection using independent component analysis," *Structural Health Monitoring*, vol. 3, no. 1, pp. 69–83, 2004.

[12] M. J. Roan, J. G. Erling, and L. H. Sibul, "A new, nonlinear, adaptive, blind source separation approach to gear tooth failure detection and analysis," *Mechanical Systems and Signal Processing*, vol. 16, no. 5, pp. 719–740, 2002.

[13] J. Antoni, L. Garibaldi, S. Marchesiello, and M. Sidhamed, "New separation techniques for output-only modal analysis," *Shock and Vibration*, vol. 11, no. 3-4, pp. 227–242, 2004.

[14] J. Antoni, "Blind separation of vibration components: principles and demonstrations," *Mechanical Systems and Signal Processing*, vol. 19, no. 6, pp. 1166–1180, 2005.

[15] G. Kerschen, F. Poncelet, and J. C. Golinval, "Physical interpretation of independent component analysis in structural dynamics," *Mechanical Systems and Signal Processing*, vol. 21, no. 4, pp. 1561–1575, 2007.

[16] B. Ans, J. Hérault, and C. Jutten, "Adaptive neural architectures: detection of primitives," in *Proceedings of the COGNITIVA '85*, pp. 593–597, Paris, France, June 1985.

[17] A. Belouchrani, K. Abed-Meraim, J. Cardoso, and E. Moulines, "A blind source separation technique using second-order statistics," *IEEE Transactions on Signal Processing*, vol. 45, no. 2, pp. 434–444, 1997.

[18] J. Storck and G. Deco, "Nonlinear independent component analysis and multivariate time series analysis," *Physica D: Nonlinear Phenomena*, vol. 108, no. 4, pp. 335–349, 1997.

[19] H. N. Thi and C. Jutten, "Blind source separation for convolutive mixtures," *Signal Processing*, vol. 45, no. 2, pp. 209–229, 1995.

[20] F. Poncelet, G. Kerschen, J. Golinval, and D. Verhelst, "Output-only modal analysis using blind source separation techniques," *Mechanical Systems and Signal Processing*, vol. 21, no. 6, pp. 2335–2358, 2007.

[21] W. Zhou and D. Chelidze, "Blind source separation based vibration mode identification," *Mechanical Systems and Signal Processing*, vol. 21, no. 8, pp. 3072–3087, 2007.

[22] S. I. McNeill and D. C. Zimmerman, "A framework for blind modal identification using joint approximate diagonalization," *Mechanical Systems and Signal Processing*, vol. 22, no. 7, pp. 1526–1548, 2008.

[23] R. Brincker and J. A. Larsen, "Obtaining and estimating low noise floors in vibration sensors," in *Proceedings of the 25th SEM International Modal Analysis Conference*, Orlando, Fla, USA, 2007.

[24] A. Belouchrani and A. Cichocki, "Robust whitening procedure in blind source separation context," *Electronics Letters*, vol. 36, no. 24, pp. 2050–2051, 2000.

[25] J. F. Cardoso and A. Souloumiac, "Jacobi angles for simultaneous diagonalization," *SIAM Journal on Matrix Analysis and Applications*, vol. 17, no. 1, pp. 161–164, 1996.

[26] C. Rainieri and G. Fabbrocino, "Performance assessment of selected oma techniques for dynamic identification of geotechnical systems and closely spaced structural modes," *Journal of Theoretical and Applied Mechanics*, vol. 49, no. 3, pp. 825–839, 2011.

[27] S. Gade, N. B. Møller, H. Herlufsen, and H. Konstantin-Hansen, "Frequency domain techniques for operational modal analysis," in *Proceedings of the 1st International Operational Modal Analysis Conference*, pp. 261–271, Copenhagen, Denmark, 2005.

[28] C. Rainieri, G. Fabbrocino, and G. M. Verderame, "Non-destructive characterization and dynamic identification of a modern heritage building for serviceability seismic analyses," *NDT and E International*, vol. 60, pp. 17–31, 2013.

[29] C. Rainieri, G. Fabbrocino, and E. Cosenza, "Integrated seismic early warning and structural health monitoring of critical civil infrastructures in seismically prone areas," *Structural Health Monitoring*, vol. 10, no. 3, pp. 291–308, 2011.

[30] C. Rainieri and G. Fabbrocino, "Operational modal analysis for the characterization of heritage structures," *Geofizika*, vol. 28, no. 1, pp. 109–126, 2011.

[31] R. Brincker, L. M. Zhang, and P. Andersen, "Modal identification of output-only systems using frequency domain decomposition," *Smart Materials and Structures*, vol. 10, no. 3, pp. 441–445, 2001.

[32] P. van Overschee and B. de Moor, *Subspace Identification for Linear Systems: Theory—Implementation—Applications*, Kluwer Academic, Dordrecht, The Netherlands, 1996.

[33] B. Hazra, *Hybrid time and time-frequency blind source separation towards ambient system identification of structures [Ph.D. thesis]*, University of Waterloo, Waterloo, Canada, 2010.

[34] R. J. Allemang and D. L. Brown, "A correlation coefficient for modal vector analysis," in *Proceedings of the 1st SEM International Modal Analysis Conference*, Orlando, Fla, USA, 1982.

[35] L. Tong, R. W. Liu, V. C. Soon, and Y. F. Huang, "Indeterminacy and identifiability of blind identification," *IEEE Transactions on Circuits and Systems*, vol. 38, no. 5, pp. 499–509, 1991.

Hindawi Publishing Corporation
Shock and Vibration
Volume 2014, Article ID 597827, 12 pages
http://dx.doi.org/10.1155/2014/597827

Research Article

Control of Limit Cycle Oscillation in a Three Degrees of Freedom Airfoil Section Using Fuzzy Takagi-Sugeno Modeling

Douglas Domingues Bueno,[1] Luiz Carlos Sandoval Góes,[1] and Paulo José Paupitz Gonçalves[2]

[1] *Aeronautical Institute of Technology (ITA), 12 228-900 São José dos Campos, SP, Brazil*
[2] *Universidade Estadual Paulista (UNESP), 17 033-360 Bauru, SP, Brazil*

Correspondence should be addressed to Douglas Domingues Bueno; ddbueno@ita.br

Received 14 July 2013; Accepted 10 March 2014; Published 10 June 2014

Academic Editor: Miguel M. Neves

Copyright © 2014 Douglas Domingues Bueno et al. This is an open access article distributed under the Creative Commons Attribution License, which permits unrestricted use, distribution, and reproduction in any medium, provided the original work is properly cited.

This work presents a strategy to control nonlinear responses of aeroelastic systems with control surface freeplay. The proposed methodology is developed for the three degrees of freedom typical section airfoil considering aerodynamic forces from Theodorsen's theory. The mathematical model is written in the state space representation using rational function approximation to write the aerodynamic forces in time domain. The control system is designed using the fuzzy Takagi-Sugeno modeling to compute a feedback control gain. It useds Lyapunov's stability function and linear matrix inequalities (LMIs) to solve a convex optimization problem. Time simulations with different initial conditions are performed using a modified Runge-Kutta algorithm to compare the system with and without control forces. It is shown that this approach can compute linear control gain able to stabilize aeroelastic systems with discontinuous nonlinearities.

1. Introduction

The requirement for more accurate tools for predictions of nonlinear effects has motivated many research groups to investigate aeroelastic systems considering nonlinearities. In particular, the problem involving freeplay in control surfaces has called attention of various researchers because it can be a cause of limit cycle oscillation (LCO) leading to serious consequences such as fatigue, pilot handling/ride quality, confined manoeuvrings envelope, weapon aiming of military aircraft, and induced flutter.

Another motivation to consider control surface freeplay is that the requirements for aircraft design according to military specification can be quite difficult to achieve in practice, increasing the manufacturing and maintenance costs. Considerable experimental and analytical efforts have been devoted to obtain representative aeroelastic models and develop methodologies to study the freeplay problem.

In this context, many works in literature have presented studies to understand and characterize nonlinear aeroelastic behaviour. Conner et al. [1, 2] presented results for a typical airfoil section based on time domain simulations. The authors showed accuracy between numerical and experimental data. Tang and colleagues published theoretical and experimental results considering an aeroelastic apparatus and the high order Harmonic Balance methods [3]. This method was introduced by Kryloff and Bogoliuboff in 1947 and it has been studied by different researchers as shown in [4–8].

Kholodar and Dickinson studied the effects of aileron freeplay in different configurations of a real aircraft [9]. Time domain simulations were used to confirm the limit cycles previously predicted using the Harmonic Balance method. Also considering similar approaches, Anderson and Mortara presented results for the F-22 aircraft including control surface freeplay [10]. The authors discussed the limits of freeplay to keep the system stable. Recently, Abdelkefi and

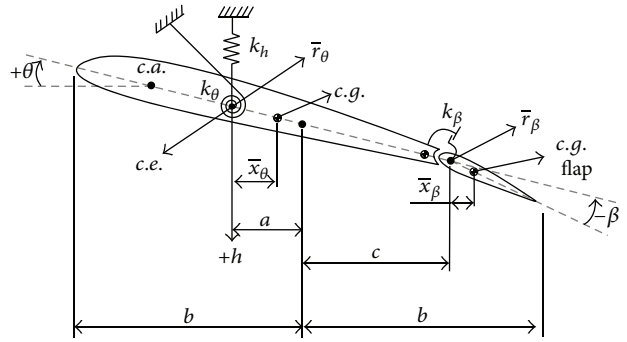

Figure 1: Typical section airfoil.

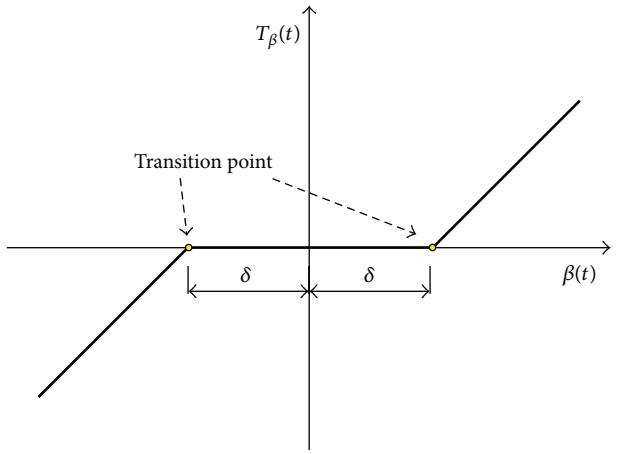

Figure 2: Freeplay nonlinearity.

colleagues performed numerical and experimental investigations using a pitch and plunge rigid airfoil supported by a torsional spring. The authors studied different mathematical representations of freeplay nonlinearity, such as polynomial expansion and hyperbolic tangent [11, 12]. Also considering a two degrees of freedom airfoil, Guo and Chen employed multivariable and Floquet theories to detect the fold bifurcation and amplitude jump phenomenon in supersonic flow [13].

Several control strategies with focus on LCO suppression on aeroelastic systems have been developed in these last years. Kurdila et al. [14] presented an extensive review of nonlinear control methods for high energy LCO. Experimental works on controlling aeroelastic apparatus are presented in [15, 16]. In [17] Li et al. designed a suboptimal controller using the state-dependent Riccati equation considering cubic nonlinearity. Adaptive filters cut-off frequency with feedback gain has also been used to suppress limit cycles and chaotic motions [18]. The authors investigated an augmented controller with time delay parameter to determine regions of instabilities in closed-loop configurations.

This paper proposes a control strategy based on fuzzy Takagi-Sugeno (FTS) solved using linear matrix inequalities (LMIs) to control the LCO of a nonlinear aeroelastic system. Techniques based on LMIs have been used to solve linear aeroelastic problems, mainly considering structural uncertainties [19, 20]. However, their application for solving nonlinear aeroelastic problems is rarely found in the literature. The advantage of using LMIs to design a control strategy is based on the robust interior point algorithms that provides a guarantee for finding optimal solutions, if that exists.

The aeroelastic system is formulated in state space form and is integrated in time domain using the forth order Runge-Kutta method and Hénon's technique [21]. Hénon's technique is used to locate the switching points in the procedure of numerical integration, as discussed herein. Theodorsen aerodynamic forces are transformed to time domain using rational function approximation. However, the proposed approach is valid for other aerodynamic theories. Finally, numerical simulations are performed on the benchmark airfoil problem to demonstrate that LMIs combined with FTS modeling can be used to design controllers for nonlinear aeroelastic problems.

2. Aeroelastic System with Freeplay

The typical section airfoil shown in Figure 1 with a trailing edge control surface is normally used to represent an aeroelastic system with three degrees of freedom that includes pitch $\alpha(t)$, plunge $h(t)$, and control surface rotation $\beta(t)$. This modeling was previously proposed in [22]. The structural properties of this system are represented by the springs k_α, k_h, and k_β, structural damping, and inertial properties. Theodorsen theory is used to compute the aerodynamic forces; however, the same control strategy could be adopted for other aerodynamic theories [22, 23].

The nonlinear discontinuity (freeplay) is considered to occur in the control surface spring k_β. So that the equation of motion for this system can be represented by

$$\mathbf{M}\ddot{\mathbf{u}}(t) + \mathbf{D}\dot{\mathbf{u}}(t) + \mathbf{F}(\mathbf{K}, \mathbf{u}, t) = q\mathbf{Q}\mathbf{u}(t) + \mathbf{B}_{oc}\mathbf{u}_c(t), \quad (1)$$

where $\mathbf{M}$ and $\mathbf{D}$ are, respectively, the structural mass and damping matrices, $\mathbf{Q}$ is a matrix of aerodynamic coefficients that depend on the airfoil geometry, $q = (1/2)\rho V^2$ is the dynamic pressure, and ρ is the air density and V is the airspeed. $\mathbf{B}_{oc}$ is a matrix of input (forces or moments). The vector $\mathbf{u}(t) = \{h(t) \;\; \alpha(t) \;\; \beta(t)\}^T$ represents the physical displacements and $\mathbf{u}_c(t)$ is the control force. The vector $\mathbf{F}$ represents the elastic restoring moment which depends on the control surface restoring moment $T_\beta(t)$ shown in Figure 2.

By considering a freeplay amplitude of 2δ, the elastic restoring moment can be written as

$$\begin{aligned}
&\mathbf{F}(\mathbf{K}, \mathbf{u}, t) = \{F_h(t) \;\; T_\alpha(t) \;\; T_\beta(t)\}^T \text{ such that} \\
&F_h(t) = k_h h(t), \\
&T_\alpha(t) = k_\alpha \alpha(t), \\
&T_\beta(t) = 0 \quad \text{if } |\beta(t)| \le \delta, \\
&T_\beta(t) = k_\beta [\beta(t) - \delta] \quad \text{if } |\beta(t)| > \delta.
\end{aligned} \quad (2)$$

The expressions in (2) are rearranged in a matrix form and the nonlinear function f_{nl} is introduced such that the stiffness is defined as a nonlinear structural stiffness matrix $\mathbf{K}_{\text{nl}}$ given by

$$\mathbf{K}_{\text{nl}} = \begin{bmatrix} k_h & 0 & 0 \\ 0 & k_\alpha & 0 \\ 0 & 0 & k_\beta f_{nl} \end{bmatrix} \Longrightarrow \mathbf{F}(\mathbf{K}, \mathbf{u}, t) = \mathbf{K}_{\text{nl}}\mathbf{u}(t), \quad (3)$$

where

$$\begin{aligned} f_{\text{nl}} &= 0 \quad \text{if } |\beta(t)| \le \delta, \\ f_{\text{nl}} &= 1 - \frac{\delta}{\beta(t)} \quad \text{if } |\beta(t)| > \delta. \end{aligned} \quad (4)$$

2.1. Representation in State Space Form. In order to obtain a nonlinear state space model, a rational function is used to write the aerodynamic forces in time domain. Jones in 1940 solved this problem using a rational function approximation to approximate unsteady aerodynamic loads for the typical section [24].

After Jones' work, different formulations have been used to approximate generalized aerodynamic forces for arbitrary motion, as, for instance, the approach based on Chebyshev's polynomials introduced by Dinu and colleagues with focus on aeroservoelasticity [25]. Karpel proposes the Minimum-State method with accuracy per model order superior to previous works, but it is more complicated and computing-time consuming because it involves nonlinear problems [26]. Vepa proposes a numerical technique based on Padè approximation and according to the author the main advantage of this method is that it can be generalized to three-dimensional lifting surfaces [27]. Recently, Biskri and colleagues present a very interesting method based on a combination of the Least Squares (or Roger's approach) and Minimum-State methods, of which the main idea is to minimize the number of lag terms without passing through a long iterative algorithm [28].

In this paper Roger's approach is used. This approximation involves identifying every matrix $\mathbf{Q}_j$ shown in (5) using a Least Square algorithm as proposed by Roger [29] and summarized in [30]. The approximation contains a polynomial part representing the forces on the typical section acting directly connected to the displacements $\mathbf{u}(t)$ and their first and second derivatives. Also, this equation has a rational part representing the influence of the wake acting on the section with a time delay. Consider

$$\mathbf{Q}(s) \approx \left[\sum_{j=0}^{2} \mathbf{Q}_j s^j \left(\frac{b}{V} \right)^j + \sum_{j=1}^{n_{\text{lag}}} \mathbf{Q}_{(j+2)} \left(\frac{s}{s + (b/V)\beta_j} \right) \right] \mathbf{u}(s), \quad (5)$$

where s is the Laplace variable, n_{lag} is the number of lag terms, β_j is the jth lag parameter ($j = 1, \ldots, n_{\text{lag}}$), and b is the aerodynamic semichord.

Substituting (5) into (1) and considering (3) it is possible to write the equation of motion for the aeroelastic system in state space format:

$$\dot{\mathbf{x}}(t) = \mathbf{A}_{\text{nl}}\mathbf{x}(t) + \mathbf{B}\mathbf{u}_c(t), \qquad \mathbf{y}(t) = \mathbf{C}\mathbf{x}(t), \quad (6)$$

where $\mathbf{x}(t) = \{\dot{\mathbf{u}}(t) \;\; \mathbf{u}(t) \;\; \mathbf{u}_a(t)\}^T$ is the state vector and $\mathbf{u}_a(t)$ are states of lags required for the approximation of matrix $\mathbf{Q}$. The matrix of outputs $\mathbf{C} = [\mathbf{C}_v \;\; \mathbf{C}_d \;\; \mathbf{C}_z]$ has dimension $2m \times m(2 + n_{\text{lag}})$, where $\mathbf{C}_v$ and $\mathbf{C}_d$ are, respectively, the velocity and displacement output matrices and the submatrix $\mathbf{C}_z$ has only zeros to complete the matrix dimension, and m is the number of degrees of freedom. Matrix $\mathbf{A}_{\text{nl}}$ is presented in the following form:

$$\mathbf{A}_{\text{nl}} = \begin{bmatrix} -\mathbf{M}_a^{-1}\mathbf{D}_a & -\mathbf{M}_a^{-1}\mathbf{K}_{a(\text{nl})} & q\mathbf{M}_a^{-1}\mathbf{Q}_3 & \cdots & q\mathbf{M}_a^{-1}\mathbf{Q}_{(2+n_{\text{lag}})} \\ \mathbf{I} & \mathbf{0} & \mathbf{0} & \cdots & \mathbf{0} \\ \mathbf{I} & \mathbf{0} & \left(-\frac{V}{b}\right)\beta_1\mathbf{I} & \mathbf{0} & \cdots \\ \vdots & \vdots & \mathbf{0} & \ddots & \cdots \\ \mathbf{I} & \mathbf{0} & \vdots & \cdots & \left(-\frac{V}{b}\right)\beta_{n_{\text{lag}}}\mathbf{I} \end{bmatrix}, \quad (7)$$

where

$$\begin{aligned} \mathbf{M}_a &= \mathbf{M} - q\left(\frac{b}{V}\right)^2\mathbf{Q}_2, \qquad \mathbf{D}_a = \mathbf{D} - q\left(\frac{b}{V}\right)\mathbf{Q}_1, \\ \mathbf{K}_{a(\text{nl})} &= \mathbf{K}_{\text{nl}} - q\mathbf{Q}_0, \qquad \mathbf{B} = \left[\mathbf{M}_a^{-1} \;\; \mathbf{B}_{oc} \;\; \mathbf{0}\right]^T, \end{aligned} \quad (8)$$

where $\mathbf{M}_a$ and $\mathbf{D}_a$ are, respectively, the aeroelastic mass and damping matrices, $\mathbf{K}_{a(\text{nl})}$ is the nonlinear aeroelastic stiffness matrix, $\mathbf{B}$ is the input matrix, $\mathbf{I}$ is an identity matrix, and $\mathbf{0}$ is a matrix of zeros with appropriated dimension.

2.2. Time Integration. To calculate the time response of the system with freeplay a modified 4th order Runge-Kutta algorithm using Hénon method is used. Hénon method is necessary in order to identify changes in the stiffness due to the freeplay. This approach is used to minimize integration errors mainly with respect to the phase shifts.

The main idea considered in Hénon's method is to change the independent variable (time) to the degree of freedom with freeplay (a spacial variable) always that the stiffness changes with the freeplay region. In these cases, the time becomes the dependent variable and the integration step is done in the degree of freedom related to the freeplay. The size of the step is the amount necessary for this degree of freedom to coincide with the transition points shown in Figure 2. Once the control surface position is the transition point, the system of equations is rewritten considering the time as the independent variable. See complementary information in [2, 21, 31].

3. Development of Fuzzy Takagi-Sugeno Controller

A fuzzy model uses rules, which are linguistic IF-THEN statements involving fuzzy sets, fuzzy logic, and fuzzy inference. These rules play a key role in representing expert control/modeling knowledge and experience and in linking the input variables of fuzzy controllers/models to output variable (or variables). To explain the procedure, consider the open loop nonlinear aeroelastic system described in following form:

$$\dot{x}_i(t) = \sum_{j=1}^{N} f_{ij}(\mathbf{x}(t))\, x_j(t), \tag{9}$$

where $\mathbf{u}_c = 0$, $N = n(2 + n_{\text{lag}})$, $i = 1, \ldots, N$, and $f_{ij}(\mathbf{x}(t)) = f_k$ represents the kth nonlinear function, where $k = 1, \ldots, N_{\text{nl}} \leq N^2$.

The nonlinear system described by (9) can be represented by the Takagi-Sugeno model using the following rule:

Rule i:

$$\begin{aligned} &\text{if } z_1(t) \text{ is } M_{i1} \text{ and} \ldots \text{and } z_p(t) \text{ is } M_{ip} \\ &\text{Then } \dot{\mathbf{x}}(t) = \mathbf{A}_i \mathbf{x}(t), \quad \mathbf{y}(t) = \mathbf{C}\mathbf{x}(t), \quad i = 1, \ldots, r, \end{aligned} \tag{10}$$

where M_{ij} is the fuzzy set and r is the number of model rules; $z_1(t), \ldots, z_p(t)$ are known premise variables that in general may be functions of the state variables, external disturbances, and/or times. Each linear model represented by $\mathbf{A}_i$ is called a subsystem [32].

Taniguchi et al. [33] present a simple method to identify the subsystems. The basic idea is to write each nonlinear function f_k as a linear combination of its maximum $f_k^{\max}$ and minimum $f_k^{\min}$ values both given, respectively, by

$$\begin{aligned} f_k^{\max} &= \max\left[f_k(\mathbf{x}(t))\right], \\ f_k^{\min} &= \min\left[f_k(\mathbf{x}(t))\right]. \end{aligned} \tag{11}$$

From these maximum and minimum values, each nonlinear function can be represented by

$$f_k(\mathbf{x}(t)) = \left[g_k^{\min}(\mathbf{x}(t))\right] f_k^{\min} + \left[g_k^{\max}(\mathbf{x}(t))\right] f_k^{\max}, \tag{12}$$

where

$$\begin{aligned} &0 \leq g_k^{\min}(\mathbf{x}(t)), \qquad g_k^{\max}(\mathbf{x}(t)) \leq 1, \\ &g_k^{\min}(\mathbf{x}(t)) + g_k^{\max}(\mathbf{x}(t)) = 1, \\ &g_k^{\min}(\mathbf{x}(t)) = \frac{\left[f_k(\mathbf{x}(t)) - f_k^{\max}\right]}{\left[f_k^{\min} - f_k^{\max}\right]} \text{ then,} \\ &g_k^{\max}(\mathbf{x}(t)) = 1 - g_k^{\min}(\mathbf{x}(t)). \end{aligned} \tag{13}$$

If $[g_k^{\min}(\mathbf{x}(t)) + g_k^{\max}(\mathbf{x}(t)) = 1]$, $\forall k = 1, \ldots, N_{\text{nl}}$, then each nonlinear function can be conveniently written as

$$\begin{aligned} &f_k(\mathbf{x}(t)) \\ &= \prod_{j=1, j\neq k}^{N_{\text{nl}}} \left\{g_j^{\min}(\mathbf{x}(t)) + g_j^{\max}(\mathbf{x}(t))\right\} \\ &\quad \times \left\{\left[g_k^{\min}(\mathbf{x}(t))\right] f_k^{\min} + \left[g_k^{\max}(\mathbf{x}(t))\right] f_k^{\max}\right\}, \end{aligned} \tag{14}$$

or

$$f_k(\mathbf{x}(t)) = \sum_{j=1}^{r_1} N_j(\mathbf{x}(t))\, f_k^{\min} + \sum_{j=r_1+1}^{(2^{N_{\text{nl}}})} N_j(\mathbf{x}(t))\, f_k^{\max}, \tag{15}$$

where $r_1 = 2^{(N_{\text{nl}}-1)}$ and $N_j(\mathbf{x}(t))$ is given by

$$N_j(\mathbf{x}(t)) = \prod_{k=1}^{N_{\text{nl}}} g_k^{(\cdot)}(\mathbf{x}(t)), \qquad \sum_{j=1}^{2^{N_{\text{nl}}}} N_j(\mathbf{x}(t)) = 1, \tag{16}$$

and the superscript $(\cdot)$ indicates the combination between maximum and minimum values for each kth function $g_k^{(\cdot)}(\mathbf{x}(t))$.

Considering that $\mathbf{A}_{\text{nl}} = \mathbf{A}_{\text{nl}}(f_1, f_2, \ldots, f_{N_{\text{nl}}})$ and substituting each f_k according to (15), the nonlinear equation of motion (17) is rewritten after some rearrangement as

$$\dot{\mathbf{x}}(t) = \left(\sum_{j=1}^{2^{N_{\text{nl}}}} N_j(\mathbf{x}(t))\, \mathbf{A}_j\right) \mathbf{x}(t) + \left(\sum_{j=1}^{2^{N_{\text{nl}}}} N_j(\mathbf{x}(t))\, \mathbf{B}_j\right) \mathbf{u}_c(t), \tag{17}$$

where each linear matrix $\mathbf{A}_j$ is the original nonlinear matrix at which the N_{nl} functions f_k are substituted by the combination of maximum and minimum values $f_k^{\max}$ and $f_k^{\min}$. In this case $\mathbf{B}_j = \mathbf{B}$ $\forall j$.

Particularly for the typical section including freeplay nonlinearity, there are three nonlinear functions ($N_{\text{nl}} = 3$) into the matrix $\mathbf{A}_{\text{nl}}$ and they are given by

$$\begin{aligned} f_1 &= a_{\text{nl}(1,6)} = -\mathbf{M}_{a(1,3)}^{-1}\left[k_\beta f_{\text{nl}} - \rho 0.5 V^2 \mathbf{Q}_{0(1,3)}\right], \\ f_2 &= a_{\text{nl}(2,6)} = -\mathbf{M}_{a(2,3)}^{-1}\left[k_\beta f_{\text{nl}} - \rho 0.5 V^2 \mathbf{Q}_{0(2,3)}\right], \\ f_3 &= a_{\text{nl}(3,6)} = -\mathbf{M}_{a(3,3)}^{-1}\left[k_\beta f_{\text{nl}} - \rho 0.5 V^2 \mathbf{Q}_{0(3,3)}\right], \end{aligned} \tag{18}$$

where $a_{\text{nl}(i,j)}$ indicates an element into matrix $\mathbf{A}_{\text{nl}}$ and the subscripts (i, j) indicate the ith row and jth column in each respective matrix. These functions f_k depend on f_{nl} which is illustrated in Figure 3.

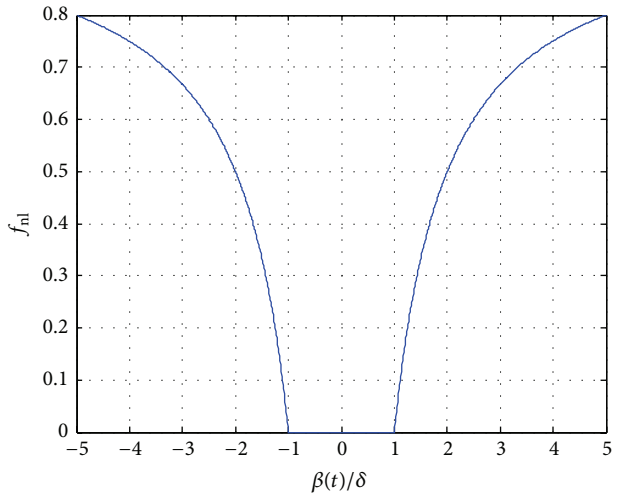

FIGURE 3: The nonlinear function f_{nl} represented in a particular range of $\beta(t)$.

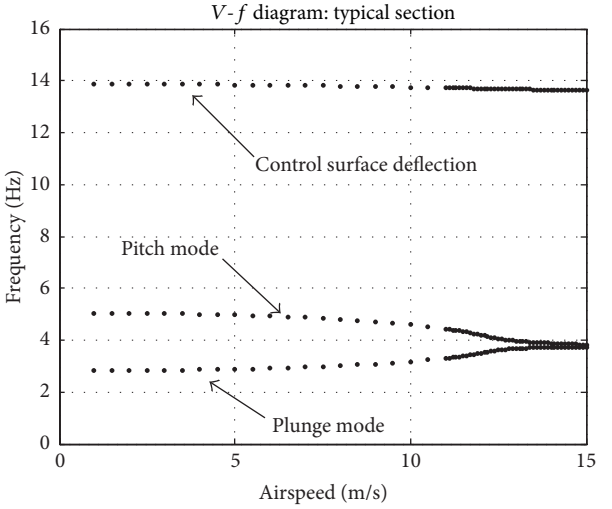

FIGURE 4: Linear flutter analysis: V-f diagram.

3.1. Closed-Loop Takagi-Sugeno Controller. In this section a feedback control strategy is used to control the amplitude of oscillation in the control surface. The feedback force is obtained by applying a feedback gain to the state systems states, such that the control inputs are given by $\mathbf{u}_c(t) = -\mathbf{G}\mathbf{x}(t)$, where $\mathbf{G}$ is the feedback gain matrix. The feedback gain is calculated using linear matrix inequality to solve Lyapunov's function for stability, in this case

$$\dot{\mathbf{x}}(t) = \left[\sum_{j=1}^{2^{N_{nl}}} N_j(\mathbf{x}(t))\left(\mathbf{A}_j - \mathbf{B}_j\mathbf{G}\right)\right]\mathbf{x}(t), \tag{19}$$

$$\dot{V}_L = \left(\sum_{j=1}^{2^{N_{nl}}} N_j(\mathbf{x}(t))\left[\mathbf{A}_j - \mathbf{B}_j\mathbf{G}\right]\mathbf{x}(t)\right)^T \mathbf{P}\mathbf{x}(t) + \mathbf{x}(t)^T\mathbf{P}\left(\sum_{j=1}^{2^{N_{nl}}} N_j(\mathbf{x}(t))\left[\mathbf{A}_j - \mathbf{B}_j\mathbf{G}\right]\mathbf{x}(t)\right) < 0, \tag{20}$$

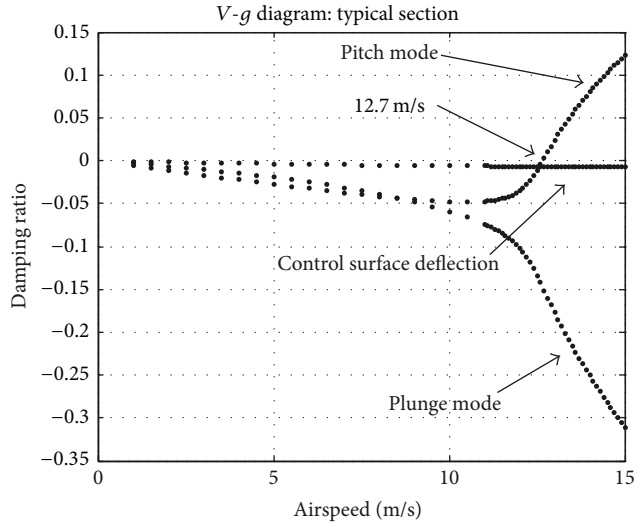

FIGURE 5: Linear flutter analysis: V-g diagram.

TABLE 1: Physical and geometric properties of the 2D airfoil.

Parameter	Value
Semichord—b	0.15 m
Airfoil mass—M	5.0 kg
Air density—ρ	1.225 kg/m^3
c	0.6%
a	−0.4%
$\overline{x}_\theta$	0.2 m/m
$\overline{r}_\beta$	$(6.25 \times 10^{-3})^{-1/2}$ m/m
$\overline{x}_\beta$	0.0125 m/m
$\overline{r}_\theta$	$(0.25)^{-1/2}$ m/m
Plunge frequency—f_h	3.0 Hz
Pitch frequency—f_θ	4.5 Hz
Control surface deflection—f_β	12.0 Hz
Parameters of lag—β_j $(j = 1, \ldots, 4)$	0.2, 1.2, 1.6, 1.8
Reduced frequency—k	[0.1, 2.0], $\Delta k = 0.1$

where $V_L = \mathbf{x}^T\mathbf{P}\mathbf{x}$ is the Lyapunov function. The stability of this system is assured if there is a positive-definite matrix $\mathbf{P}$ such that the inequality of (20) is true. After some rearrangement this equation can be rewritten such as [32]

$$\mathbf{x}^T(t)\sum_{j=1}^{2^{N_{nl}}} N_j(\mathbf{x}(t)) \times \left[\left(\mathbf{A}_j - \mathbf{B}_j\mathbf{G}\right)^T\mathbf{P} + \mathbf{P}\left(\mathbf{A}_j - \mathbf{B}_j\mathbf{G}\right)\right]\mathbf{x}(t) < 0, \tag{21}$$

and finally, the solution of this inequality is equivalent to the solution of all the following inequalities satisfied simultaneously [34]:

$$\left(\mathbf{A}_j - \mathbf{B}_j\mathbf{G}\right)^T\mathbf{P} + \mathbf{P}\left(\mathbf{A}_j - \mathbf{B}_j\mathbf{G}\right) < 0 \quad j = 1, \ldots, 2^{N_{nl}}. \tag{22}$$

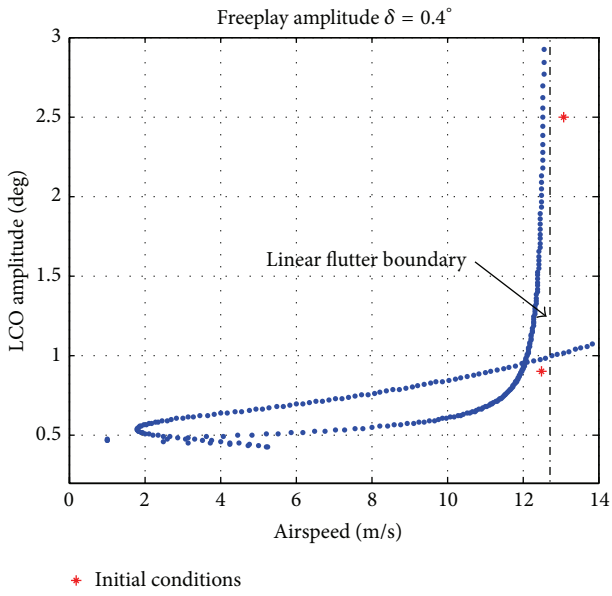

Figure 6: LCO prediction for $|\delta| = 0.4^\circ$.

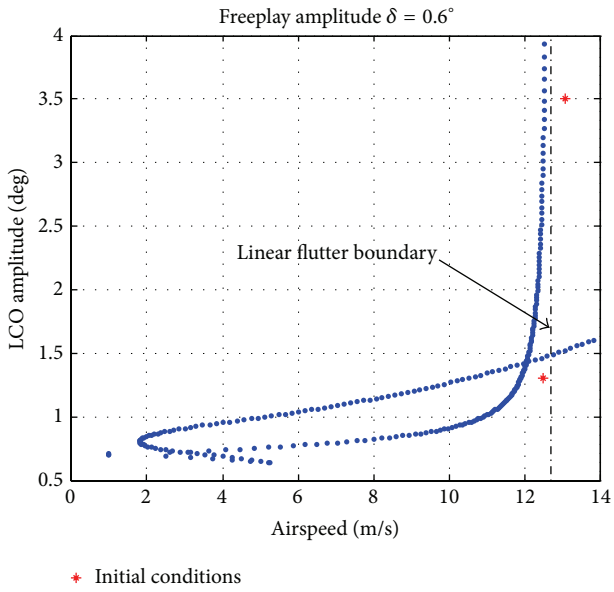

Figure 7: LCO prediction for $|\delta| = 0.6^\circ$.

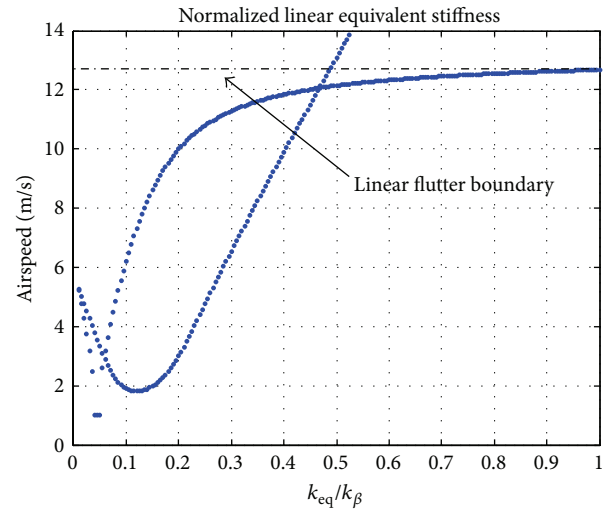

Figure 8: Linear equivalent stiffness from the HBM.

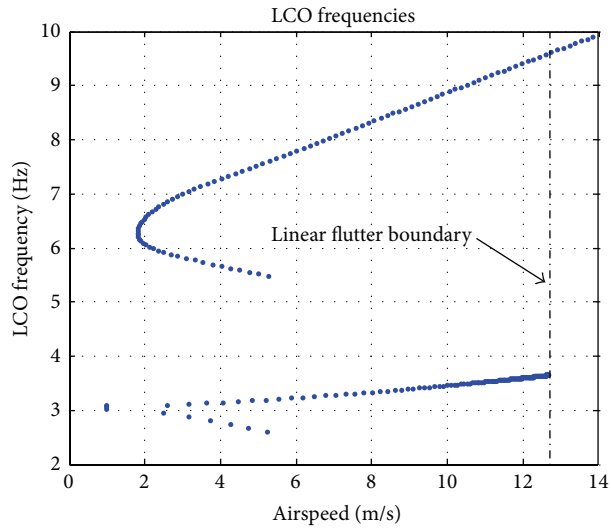

Figure 9: LCO frequencies obtained from the HBM.

Inequality (22) is not linear: then considering $\mathbf{X} = \mathbf{P}^{-1}$, $\mathbf{G}_x = \mathbf{G}\mathbf{X}$, it is possible to write the following linear matrix inequality:

$$\mathbf{X}\mathbf{A}_j^T - \mathbf{G}_x^T\mathbf{B}_j^T + \mathbf{A}_j\mathbf{X} - \mathbf{B}_j\mathbf{G}_x < 0 \quad j = 1, \ldots, 2^{N_{nl}} \tag{23}$$

such that $\mathbf{G} = \mathbf{G}_x\mathbf{X}^{-1}$.

Although the control gain $\mathbf{G}$ has been computed using inequality (23), the required control force $\mathbf{u}_c(t)$ can exceed desired limits. In this case, the control gain is multiplied by a constant g between the interval [0 1], conveniently adjusted during the control design. The control force is rewritten as

$$\bar{\mathbf{u}}_c(t) = g\mathbf{u}_c(t) \quad \text{or} \quad \bar{\mathbf{u}}_c(t) = -g\mathbf{G}\mathbf{x}(t). \tag{24}$$

4. Numerical Application

To illustrate the method, numerical simulations were performed using the three degrees of freedom airfoil section for which the equations of motion are presented by Theodorsen et al. in [23]. The structural mass, stiffness, and aerodynamic forces matrices can be found in [17, 22, 35].

Initially, the linear flutter boundary was found extracting the eigenvalues from the state space dynamic matrix without freeplay. After that preliminary verification, the first order harmonic balance method (HBM) was used to predict the

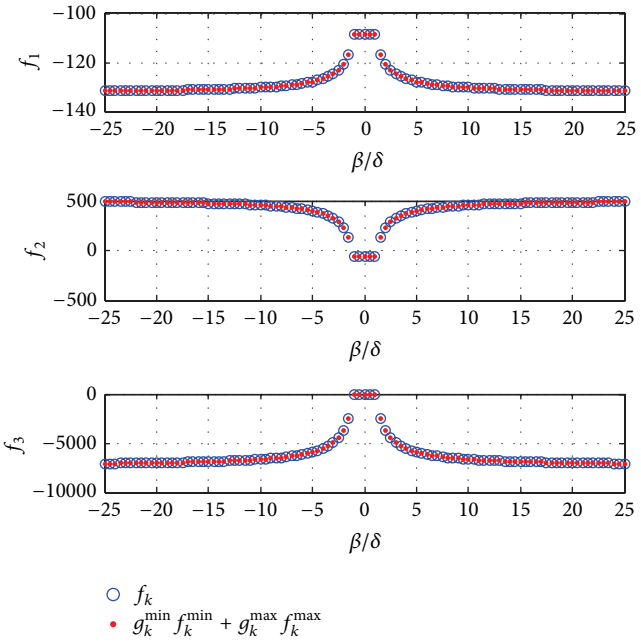

FIGURE 10: Values of f_k: actual versus computed using TS approach.

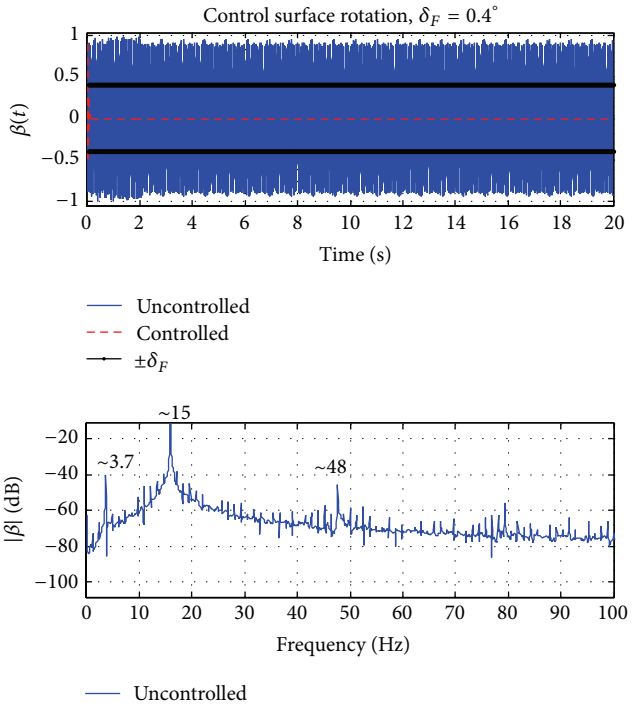

FIGURE 11: Case 1: control surface rotation ($|\delta| = 0.4^\circ$ and $V = 12.5$ m/s).

LCO amplitudes. Different researchers have used HBM methods to study limit cycles oscillations in aeroelastic systems, as shown in [3, 6, 36, 37].

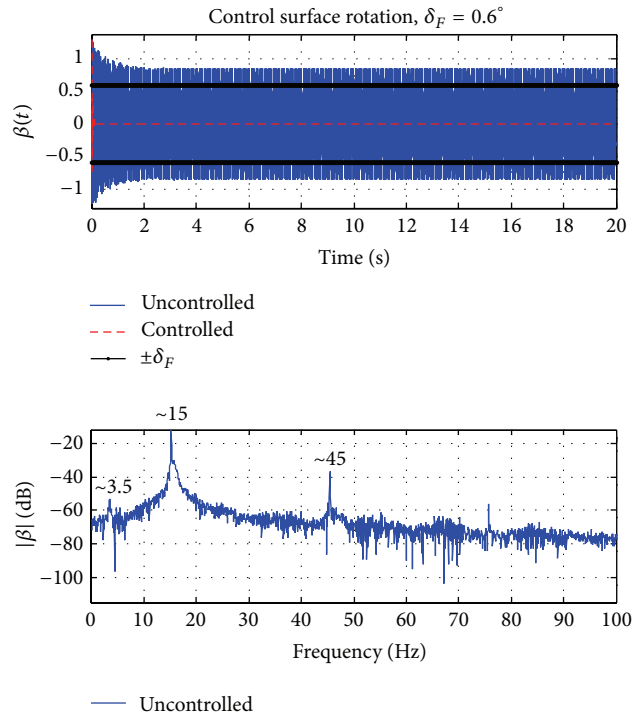

FIGURE 12: Case 1: control surface rotation ($|\delta| = 0.6^\circ$ and $V = 12.5$ m/s).

4.1. Linear Flutter Boundary. Figure 1 illustrates the model and its physical and geometric properties are presented in Table 1. Figures 4 and 5 show, respectively, the classical V-f and V-g diagrams for the linear flutter solution. According to these results flutter speed is equal to 12.7 m/s.

4.2. LCO Preliminary Predictions. After the preliminary linear analysis to identify the flutter boundary, the first order HBM was used to predict the LCO amplitudes. The results shown in Figures 6 and 7 were obtained by extracting the eigenvalues from the matrix $\mathbf{A}_{\text{nl}}$ defined for different values of equivalent stiffness k_{eq}, that is, the control surface stiffness assuming values from zero to k_β. The values of k_{eq}/k_β are shown in Figure 8, where the nonlinear function f_{nl} assumed a unitary value and the control force $\mathbf{u}_c(t) = 0$. The HBM also provided an estimate for the first harmonic of the system response according to Figure 9.

4.3. Controller Design. Using the methodology described in Section 4, three nonlinear functions were used to describe the aeroelastic system with freeplay (f_k, $k = 1, 2, 3$). These functions were computed assuming the maximum oscillation amplitude equal to five degrees; that is, $-5^\circ \leq \beta(t) \leq 5^\circ$. Figure 10 shows a comparison between their actual values and computed values by (12).

This leads to eight (2^3) dynamic matrices that are written combining the maximum and minimum values of these

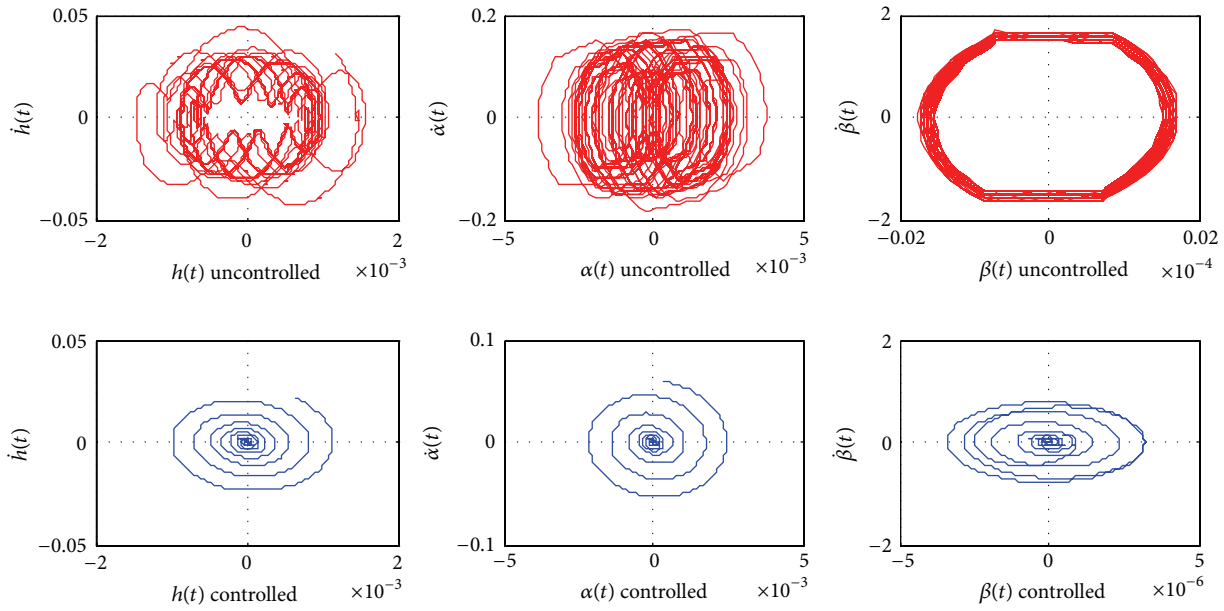

Figure 13: Case 1: phase plan ($|\delta| = 0.4^{\circ}$ and $V = 12.5$ m/s).

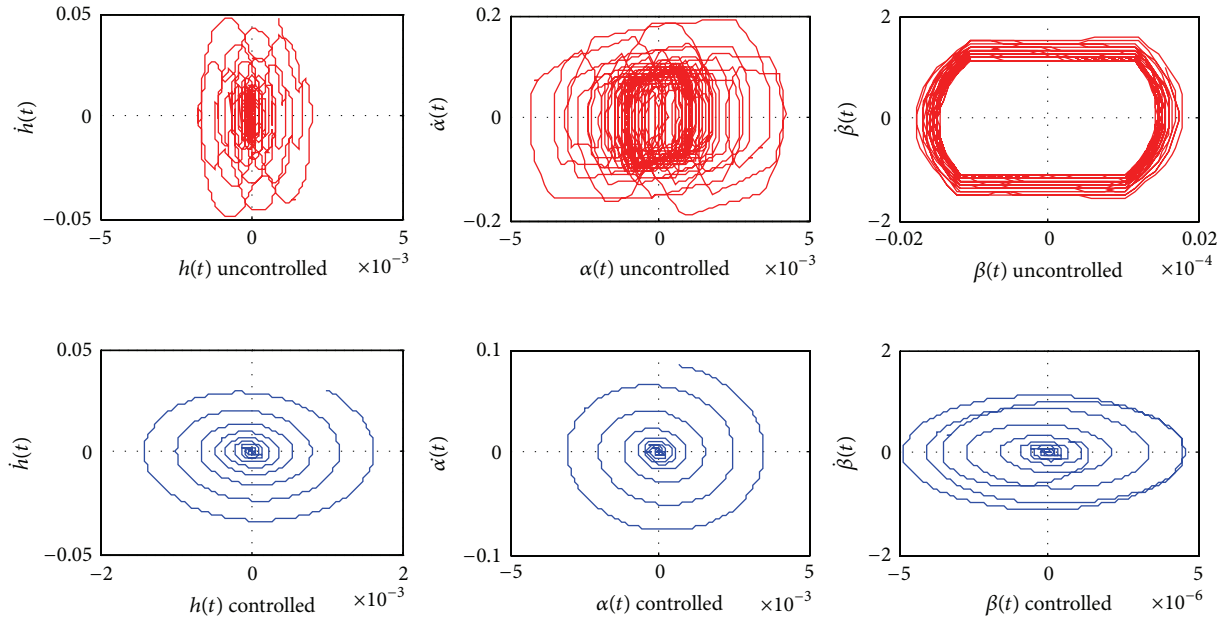

Figure 14: Case: phase plan ($|\delta| = 0.6^{\circ}$ and $V = 12.5$ m/s).

functions, such that

$$\mathbf{A}_1 = \mathbf{A}\left(f_1^{\max}, f_2^{\min}, f_3^{\min}\right), \quad \mathbf{A}_2 = \mathbf{A}\left(f_1^{\max}, f_2^{\max}, f_3^{\min}\right),$$
$$\mathbf{A}_3 = \mathbf{A}\left(f_1^{\min}, f_2^{\max}, f_3^{\min}\right), \quad \mathbf{A}_4 = \mathbf{A}\left(f_1^{\min}, f_2^{\min}, f_3^{\min}\right),$$
$$\mathbf{A}_5 = \mathbf{A}\left(f_1^{\max}, f_2^{\min}, f_3^{\max}\right), \quad \mathbf{A}_6 = \mathbf{A}\left(f_1^{\max}, f_2^{\max}, f_3^{\max}\right),$$
$$\mathbf{A}_7 = \mathbf{A}\left(f_1^{\min}, f_2^{\max}, f_3^{\max}\right), \quad \mathbf{A}_8 = \mathbf{A}\left(f_1^{\min}, f_2^{\min}, f_3^{\max}\right). \tag{25}$$

The results shown in this section were obtained considering two different freeplay amplitudes and a time step equal to 0.001 seconds. To compute the control gain, a column input matrix was used to represent an actuator applying force on the control surface ($\mathbf{B}_{oc} = \{0\ 0\ 1\}^T$). Also, it was considered that the parameter g is equal to 1.0 for all cases. However, in particular for experimental applications where limitations exist on the actuator force, the parameter g can be conveniently chosen between $]0, 1[$.

For the cases in which the freeplay amplitude was $|\delta| = 0.4^{\circ}$, the initial conditions were $\beta(0) = 0.9^{\circ}$ and 2.5°. Similarly, for the cases in which $|\delta| = 0.6^{\circ}$, the initial conditions were

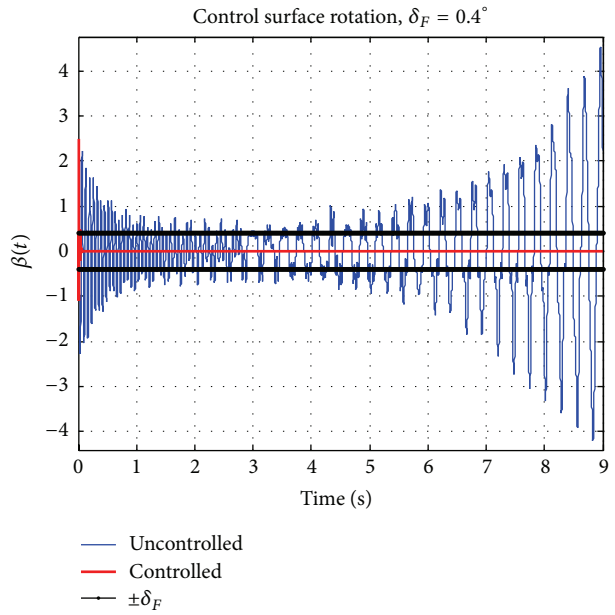

FIGURE 15: Case 2: control surface rotation ($|\delta| = 0.4^\circ$ and $V = 13.1$ m/s).

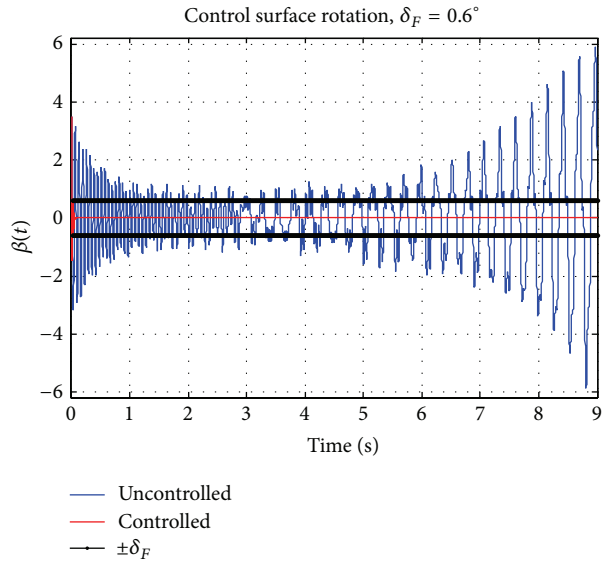

FIGURE 16: Case 2: control surface rotation ($|\delta| = 0.6^\circ$ and $V = 13.1$ m/s).

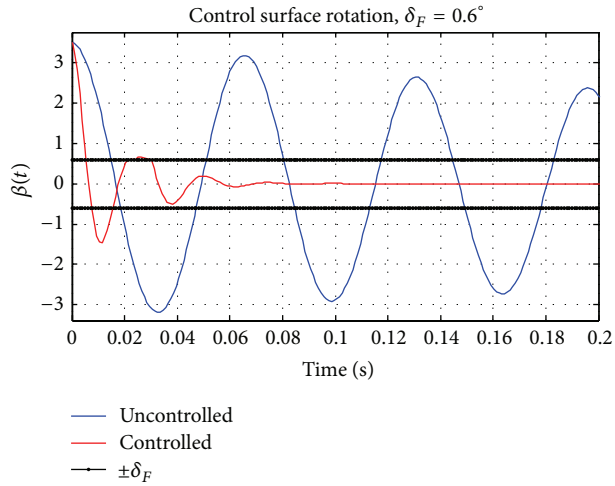

FIGURE 17: Case 2: zoom selection area for the control surface rotation ($|\delta| = 0.6^\circ$ and $V = 13.1$ m/s).

$\beta(0) = 1.3^\circ$ and 3.5°. These values were defined based on the results obtained from the HBM, as discussed in Section 4.2.

Two different conditions of airspeed were considered to demonstrate the method. Different controllers were designed for each case. In first case was chosen a condition of stable limit cycle for each freeplay amplitude. In the second one, unstable limit cycles were chosen in order to evaluate the effectiveness of the approach. Consider if all neighboring trajectories approach the LCO, it is stable; otherwise, the LCO is unstable. Definitions and a detailed discussion about stable and unstable limit cycles can be found in [38].

Case 1 (stable LCO). In the first case $V = 12.5$ m/s was considered for both freeplay amplitudes. Figures 11 and 12 show that the uncontrolled system response exhibits a limit cycle oscillation with first harmonic around 3.7 Hertz and amplitude approximately equal to 1 degree. It is possible to note in those figures that although the first order HBM cannot predict, the system response exhibits a dominant component around 15 Hertz. In addition, the plunge and pitch degrees of freedom behavior can be observed in the phase plan shown in Figures 13 and 14. In these cases of stable LCOs the designed controllers were able to suppress the limit cycles. The appendix presents details involved to compute the Fourier transform when Hénon's technique is used for the time integration process.

Case 2 (unstable LCO). In this case was considered $V = 13.1$ m/s for both freeplay amplitudes. Figures 15 and 16 show that the uncontrolled system response exhibits an unstable limit cycle. However, the controller gains computed using the proposed approach are able to suppress those nonlinear responses. To improve the comprehension, Figure 17 shows a zoom selection area for the control surface rotation considering the second freeplay amplitude.

For this second case the plunge and pitch degrees of freedom behavior can be observed in the phase plan shown in Figures 18 and 19. Finally, Figure 20 shows the control force for $\delta_F = 0.6^\circ$ and similar results were obtained for the other cases. Note that the parameter $g < 1.0$ can be chosen in order to decrease the required control force mainly for the first time steps.

5. Conclusions

This paper presents a methodology to control limit cycle oscillations in a typical section airfoil with control surface

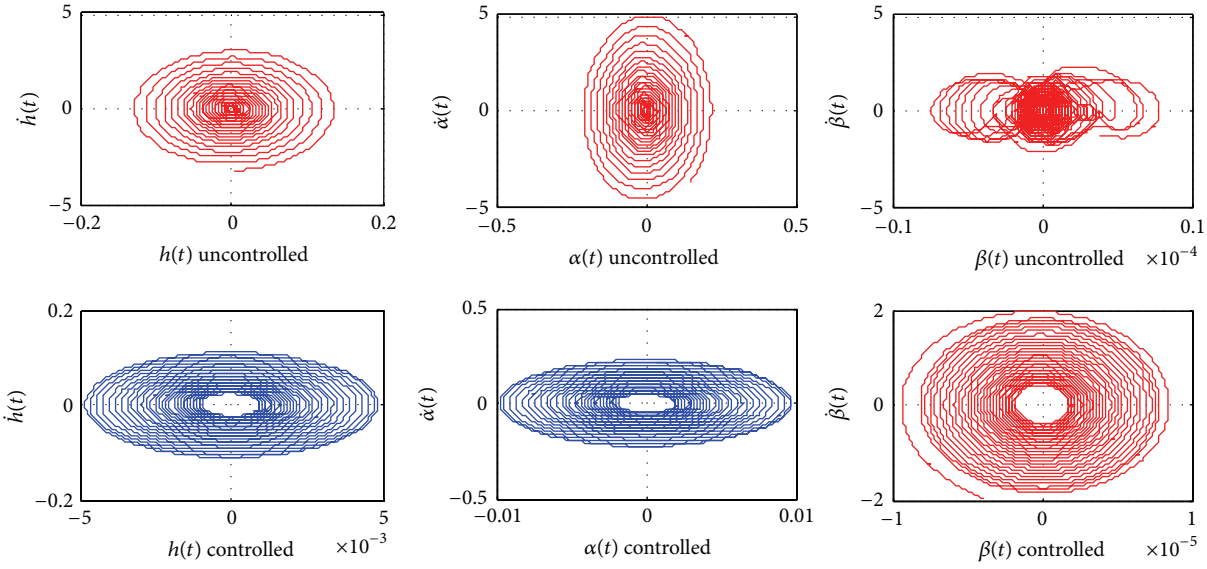

Figure 18: Case 2: phase plan ($|\delta| = 0.4^{\circ}$ and $V = 13.1$ m/s).

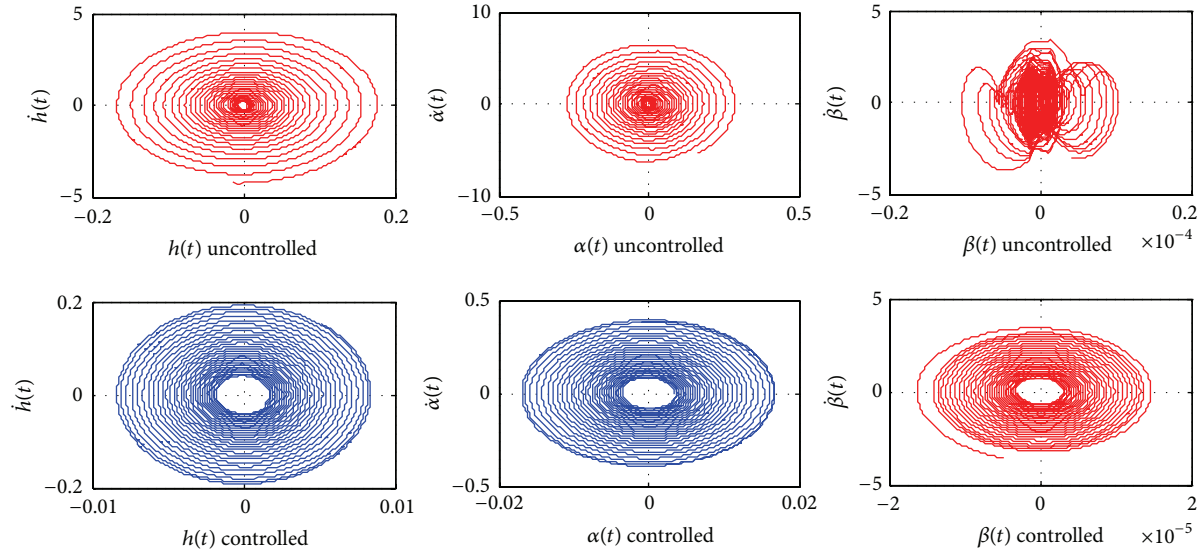

Figure 19: Case 2: phase plan ($|\delta| = 0.6^{\circ}$ and $V = 13.1$ m/s).

freeplay. The idea was to use the fuzzy Takagi-Sugeno modeling to describe the nonlinear aeroelastic system through linear matrix inequalities. The closed-loop problem was written using a convex space and a linear control force was computed using convex optimization. A linear flutter analysis was performed to identify the flutter boundary. Also, the first order harmonic balance method was solved to predict the limit cycle oscillation envelope. After these first predictions two freeplay amplitudes were defined and two airspeeds were chosen to demonstrate stable and unstable limit cycles. Finally, numerical simulations presented different nonlinear aeroelastic responses comparing the controlled and uncontrolled system. The results show that fuzzy TS modeling is an efficient tool for solving this kind of problem.

Appendix

The integration process involving Hénon's technique can result in different time steps, as discussed in Section 2.2 and shown in Figure 21. However, in order to apply the Fourier transform to compute the system responses in frequency domain, it is necessary to keep a constant time step. In this case, after using the amount dt' to identify the transition point shown in Figure 2, another time integration can be performed considering the time step $(dt - dt')$. Then, the system response for the constant time step cannot include that preliminary point obtained using dt'. This procedure was employed to compute the responses plotted in Figures 11 and 12.

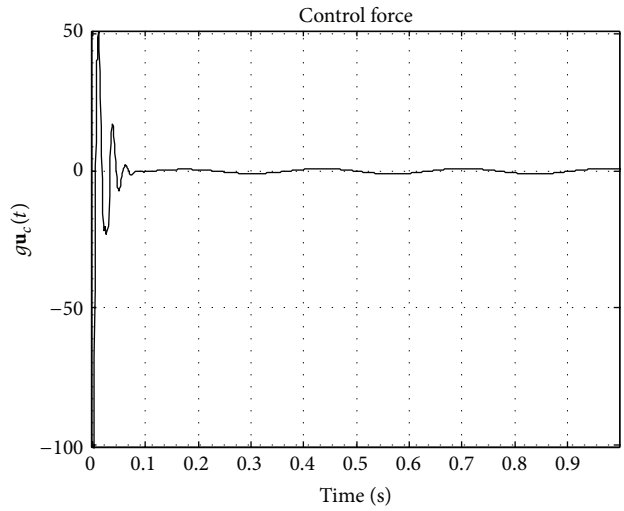

Figure 20: Case 2: control force ($|\delta| = 0.6^\circ$ and $V = 13.1$ m/s).

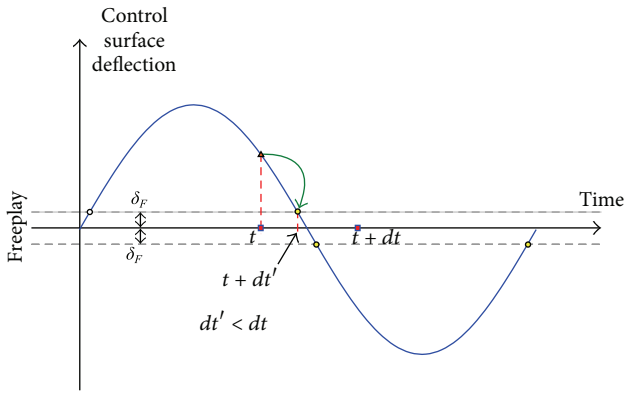

Figure 21: Illustrative scheme of integration process using Hénon's technique.

Conflict of Interests

The authors declare that the research was conducted in the absence of any commercial or financial relationships that could be construed as a potential conflict of interests.

References

[1] M. D. Conner, D. M. Tang, E. H. Dowell, and L. N. Virgin, "Nonlinear behavior of a typical airfoil section with control surface freeplay: a numerical and experimental study," *Journal of Fluids and Structures*, vol. 11, no. 1, pp. 89–109, 1997.

[2] M. D. Conner, L. N. Virgin, and E. H. Dowell, "Accurate numerical integration of state-space models for aeroelastic systems with free play," *AIAA Journal*, vol. 34, no. 10, pp. 2202–2205, 1996.

[3] D. Tang, E. H. Dowell, and L. N. Virgin, "Limit cycle behavior of an airfoil with a control surface," *Journal of Fluids and Structures*, vol. 12, no. 7, pp. 839–858, 1998.

[4] N. Kryloff and N. Bogoliuboff, *Introduction to Nonlinear Mechanics*, Princeton University Press Books, 1947.

[5] H. Y. Hu, E. H. Dowell, and L. N. Virgin, "Stability estimation of high dimensional vibrating systems under state delay feedback control," *Journal of Sound and Vibration*, vol. 214, no. 3, pp. 497–511, 1998.

[6] G. Dimitriadis, *Investigation of nonlinear aeroelastic system [Ph.D. thesis]*, University of Manchester, 1999.

[7] S. T. Trickley, L. N. Virgin, and E. H. Dowell, "The stability of limit-cycle oscillations in a nonlinear aeroelastic system," *Proceedings of the Royal Society A: Mathematical, Physical and Engineering Sciences*, vol. 458, no. 2025, pp. 2203–2226, 2002.

[8] L. Liu and E. H. Dowell, "Harmonic balance approach for an airfoil with a freeplay control surface," *AIAA Journal*, vol. 43, no. 4, pp. 802–815, 2005.

[9] D. Kholodar and M. Dickinson, "Aileron freepaly," in *Proceedings of the International Forum of Aeroelasticity and Structural Dynamics (IFASD '10)*, 2010.

[10] W. D. Anderson and S. Mortara, "Maximum control surface freeplay, design and flight testing approach on the F-22," in *Proceedings of the 48th AIAA/ASME/ASCE/AHS/ASC Structures, Structural Dynamics, and Materials Conference*, AIAA Paper 07-1767, pp. 767–778, April 2007.

[11] A. Abdelkefi, R. Vasconcellos, F. D. Marques, and M. R. Hajj, "Modeling and identification of freeplay nonlinearity," *Journal of Sound and Vibration*, vol. 331, no. 8, pp. 1898–1907, 2012.

[12] R. Vasconcellos, A. Abdelkefi, F. D. Marques, and M. R. Hajj, "Representation and analysis of control surface freeplay nonlinearity," *Journal of Fluids and Structures*, vol. 31, pp. 79–91, 2012.

[13] H. Guo and Y. Chen, "Dynamic analysis of two-degree-of-freedom airfoil with freeplay and cubic nonlinearities in supersonic flow," *Applied Mathematics and Mechanics*, vol. 33, no. 1, pp. 1–14, 2012.

[14] A. J. Kurdila, T. W. Strganac, J. L. Junkins, J. Ko, and M. R. Akella, "Nonlinear control methods for high-energy limit-cycle oscillations," *Journal of Guidance, Control, and Dynamics*, vol. 24, no. 1, pp. 185–192, 2001.

[15] T. W. Strganac, J. Ko, D. E. Thompson, and A. J. Kurdila, "Identification and control of limit cycle oscillations in aeroelastic systems," *Journal of Guidance, Control, and Dynamics*, vol. 23, no. 6, pp. 1127–1133, 2000.

[16] G. Platanitis and T. W. Strganac, "Control of a nonlinear wing section using leading-and trailing-edge surfaces," *Journal of Guidance, Control, and Dynamics*, vol. 27, no. 1, pp. 52–58, 2004.

[17] D. Li, S. Guo, and J. Xiang, "Aeroelastic dynamic response and control of an airfoil section with control surface nonlinearities," *Journal of Sound and Vibration*, vol. 329, no. 22, pp. 4756–4771, 2010.

[18] R. B. Alstrom, P. Marzocca, E. Bollt, and G. Ahmadi, "Controlling chaotic motions of a nonlinear aeroelastic system using adaptive control augmented with time delay," in *Proceedings of the AIAA Guidance, Navigation, and Control Conference*, Number 8146, August 2010.

[19] S. da Silva and V. L. Júnior, "Active flutter suppression in a 2-D airfoil using linear matrix inequalities techniques," *Journal of the Brazilian Society of Mechanical Sciences and Engineering*, vol. 28, no. 1, pp. 84–93, 2006.

[20] C. Gao, G. Duan, and C. Jiang, "Robust controller design for active flutter suppression of a two-dimensional airfoil," *Nonlinear Dynamics and Systems Theory*, vol. 9, no. 3, pp. 287–299, 2009.

[21] M. Henon, "On the numerical computation of Poincaré maps," *Physica D: Nonlinear Phenomena*, vol. 5, no. 2-3, pp. 412–414, 1982.

[22] T. Theodorsen, "General theory of aerodynamic instability and the mechanism of flutter," NACA Report 496, National Advisory Committee for Aeronautics—NACA, 1935.

[23] T. Theodorsen, I. E. Garrick, and NACA Langley Research Center, *Mechanism of Flutter a Theoretical and Experimental Investigation of the Flutter Problem*, National Advisory Committee for Aeronautics, 1940.

[24] R. T. Jones, "The unsteady lift of a wing of finite aspect ratio," Tech. Rep. 681, National Advisory Committee for Aeronautics—NACA, 1940.

[25] A. D. Dinu, R. M. Botez, and I. Cotoi, "Aerodynamic forces approximations using the chebyshev method for closed-loop aeroservoelasticity studies," *Canadian Aeronautics and Space Journal*, vol. 51, no. 4, pp. 167–175, 2005.

[26] M. Karpel, "Design for active and passive flutter suppression and gust alleviation," TR 3482, National Aeronautics and Space Administration—NASA, 1981.

[27] R. Vepa, "Finite state modeling of aeroelastic systems," Contractor Report CR 2779, NASA—National Aeronautics and Space Administration, 1977.

[28] D. Biskri, R. M. Botez, N. Stathopoulos, S. Thérien, A. Rathe, and M. Dickinson, "New mixed method for unsteady aerodynamic force approximations for aeroservoelasticity studies," *Journal of Aircraft*, vol. 43, no. 5, pp. 1538–1542, 2006.

[29] K. L. Roger, "Airplane math modelling methods for active control design," *AGARD Conference Proceeding*, vol. 9, pp. 4. 1–4. 11, 1977.

[30] I. Arbel, "An analytical technique for predicting the characteristics of a flexible wing equipped with an active flutter-suppression system and comparison with wind-tunnel data," TP 1367, National Aeronautical and Space Administration—NASA, 1979.

[31] J. Awrejcewicz and P. Olejnik, "Numerical analysis of self-excited by friction chaotic oscillations in two-degrees-of-freedom system using exact henon method," *Machine Dynamics Problems*, vol. 26, no. 4, pp. 9–20, 2002.

[32] K. Tanaka and H. O. Wang, *Fuzzy Control Systems Design and Analysis: A Linear Matrix Inequality Approach*, Wiley-Interscience, 2001.

[33] T. Taniguchi, K. Tanaka, H. Ohtake, and H. O. Wang, "Model construction, rule reduction, and robust compensation for generalized form of Takagi-Sugeno fuzzy systems," *IEEE Transactions on Fuzzy Systems*, vol. 9, no. 4, pp. 525–537, 2001.

[34] B. R. Barmish, "Necessary and sufficient conditions for quadratic stabilizability of an uncertain system," *Journal of Optimization Theory and Applications*, vol. 46, no. 4, pp. 399–408, 1985.

[35] D. Dessi and F. Mastroddi, "Limit-cycle stability reversal via singular perturbation and wing-flap flutter," *Journal of Fluids and Structures*, vol. 19, no. 6, pp. 765–783, 2004.

[36] S. F. Shen, "An approximate analysis of nonlinear flutter problem," *Journal of the Aerospace Sciences*, vol. 26, no. 1, pp. 25–32, 1959.

[37] G. A. Vio and J. E. Cooper, "Limit cycle oscillation prediction for aeroelastic systems with discrete bilinear stiffness," *International Journal of Applied Mathematics and Mechanics*, vol. 3, pp. 100–119, 2005.

[38] S. H. Strogatz, *Nonlinear Dynamic and Chaos*, Perseus Books Publishing, 1994.

Hindawi Publishing Corporation
Shock and Vibration
Volume 2014, Article ID 106531, 16 pages
http://dx.doi.org/10.1155/2014/106531

Research Article

Feedback Linearisation for Nonlinear Vibration Problems

S. Jiffri,[1] P. Paoletti,[1] J. E. Cooper,[2] and J. E. Mottershead[1]

[1] *Centre for Engineering Dynamics, School of Engineering, The University of Liverpool, Brownlow Hill, Liverpool L69 3GH, UK*
[2] *Department of Aerospace Engineering, University of Bristol, Queens Building, University Walk, Bristol BS8 1TR, UK*

Correspondence should be addressed to S. Jiffri; s.jiffri@liv.ac.uk

Received 4 July 2013; Accepted 7 January 2014; Published 5 June 2014

Academic Editor: Nuno Maia

Copyright © 2014 S. Jiffri et al. This is an open access article distributed under the Creative Commons Attribution License, which permits unrestricted use, distribution, and reproduction in any medium, provided the original work is properly cited.

Feedback linearisation is a well-known technique in the controls community but has not been widely taken up in the vibrations community. It has the advantage of linearising nonlinear system models, thereby enabling the avoidance of the complicated mathematics associated with nonlinear problems. A particular and common class of problems is considered, where the nonlinearity is present in a system parameter and a formulation in terms of the usual second-order matrix differential equation is presented. The classical texts all cast the feedback linearisation problem in first-order form, requiring repeated differentiation of the output, usually presented in the Lie algebra notation. This becomes unnecessary when using second-order matrix equations of the problem class considered herein. Analysis is presented for the general multidegree of freedom system for those cases when a full set of sensors and actuators is available at every degree of freedom and when the number of sensors and actuators is fewer than the number of degrees of freedom. Adaptive feedback linearisation is used to address the problem of nonlinearity that is not known precisely. The theory is illustrated by means of a three-degree-of-freedom nonlinear aeroelastic model, with results demonstrating the effectiveness of the method in suppressing flutter.

1. Introduction

The effects of nonlinearity are everywhere to be seen in nature and it is true to say that many problems in structural dynamics are nonlinear, but in the past it has been convenient and easier to assume linearity. This linear analysis approach has necessarily led to conservative design of engineering structures that operate dynamically. In the last few decades the need to assume linearity has been increasingly challenged, mainly because of the high cost of fuel and materials and the need to preserve the earth's valuable natural resources. This is particularly true of the aerospace industries where the need to produce lightweight, fuel efficient aircraft is an unremitting pressure on design engineers. One problem is, of course, that nonlinear dynamic analysis is complicated and the useful linear-analysis methods, such as modal decomposition, are not applicable.

Inevitably active control will increasingly be seen as a solution for problems of nonlinearity in elastomechanics and aeroelasticity. One option is to design lightweight, fuel efficient aircraft and use active control to nullify the effects of the nonlinearity. By this approach, well-understood linear analysis methods can still be used. Feedback linearisation, described, for example, by Isidori [1], is a technique now well established in the active control community. Depending upon the implementation it is able to completely or partially linearise the nonlinear system. In the latter case there remains a (generally nonlinear) subsystem with dynamics that must be investigated to ensure stability. Of course, the linear part can be used for the attainment of a chosen control objective using conventional linear time invariant (LTI) techniques. *An important aspect of feedback linearisation is that for the desired control objectives to be met precisely, the nonlinearity must be known in terms of its physical location, its type (e.g. cubic, quartic, free-play, etc.), and the numerical values of its parameters.* This seems initially to pose a serious restriction on its application, but fortunately there exist techniques, such as adaptive feedback linearisation, that are able to account for incorrectly estimated nonlinear terms.

It is apparent from the literature that the feedback linearisation method, which holds much promise, has found only very limited application in active vibration suppression.

Examples include Fossen and Paulsen [2] who applied adaptive feedback linearisation to the automatic steering of ships. In aeroelasticity, Ko and his colleagues [3–5] used feedback linearisation methods (including adaptation) and carried out a series of wind-tunnel tests on a two degree of freedom aerofoil with either one or two control surfaces. They found that with an erroneous nonlinear parameter, but without adaptation, their system reached a nonzero equilibrium, rather than the zero equilibrium that is usually sought. Monahemi and Krstic [6] employed adaptive feedback linearisation to update the aerodynamic parameters in their nonlinear model and thereby suppress wing-rock motion, a phenomenon triggered primarily by aerodynamic nonlinearities. Poursamad [7] implemented a hybrid neural-network controller for antilock braking with adaptive feedback linearisation to handle nonlinear and time-varying brake parameters. Bechlioulis and Rovithakis [8] developed a multiple-input, multiple-output tracking controller with adaptive feedback linearisation and Shojaei et al. [9] demonstrated the ability of adaptive feedback linearisation in aiding effective trajectory tracking in the presence of both parametric and nonparametric uncertainties in wheeled robots. Tuan et al. [10] designed a controller based on partial feedback linearisation of the nonlinear dynamics of a 3D overhead crane.

In this paper the problem of active control of nonlinear systems of the form

$$\mathbf{A}_1\ddot{\mathbf{x}} + \mathbf{A}_2\dot{\mathbf{x}} + \mathbf{A}_3\mathbf{x} + \mathbf{f}_{\text{nl}}(\mathbf{x}, \dot{\mathbf{x}}) = \mathbf{B}\mathbf{u}, \tag{1}$$

representative of nonlinear vibration problems in elastomechanics and aeroelasticity, is considered. The vectors $\mathbf{x}$, $\dot{\mathbf{x}}$, and $\mathbf{u}$ typically contain the state variables and inputs, respectively. The nonlinearity $\mathbf{f}_{\text{nl}}$ is given as a function of $\mathbf{x}$ and $\dot{\mathbf{x}}$ and the matrices $\mathbf{A}_1, \mathbf{A}_2, \mathbf{A}_3, \mathbf{B}$ represent the usual system parameters. This class of problem, characterised by the second-order matrix differential equation with additional nonlinearity confined to the left-hand side of (1), prevails to a very large extent in engineering mechanics and is therefore worthy of the special attention devoted to it in this paper. The classical output feedback linearisation [1] may be greatly simplified in the case of elastomechanical or aeroelastic systems described by (1). In particular,

(i) the essential theory is carried out entirely using the second-order matrix differential equation familiar to structural and aero-structural dynamicists, with the result that the need for repeated differentiation, usually described using the Lie-algebra notation, is rendered unnecessary,

(ii) a linear transformation applies between the state variable in (1) and the coordinates of the linearised system,

(iii) cancellation of the whole of the open-loop system dynamics (not just the nonlinear terms) results in a set of independent linear single degree of freedom systems for the application of conventional LTI control methods,

(iv) complete linearisation may be achieved with an equal number of actuators and sensors. If the number of actuators and sensors is less than the dimension of the system, then there will remain a nonlinear subsystem of dimension equal to the difference between the dimension of the full system and the number of sensors (and actuators). This subsystem can be made independent of the linearised part and methods are described to check its stability.

(v) Adaptive feedback linearisation is described for the treatment of an incorrect estimate of the nonlinearity. This makes use of Lyapunov stability criteria and results in a parameter update rule that evolves with time to ensure stability of the system.

The method is illustrated by means of a three degree of freedom aeroelastic system consisting of a flexible wing described in terms of two assumed modes in bending and torsion and a third degree of freedom that describes the angular motion of an underslung pylon-engine assembly. The parameters and dimensions of the system are carefully chosen to have realistic values.

2. Active Feedback Linearisation

Feedback linearisation [1] is a process whereby a nonlinear system is rendered linear by virtue of active control. Unlike Jacobian linearisation, it is exact, and does not entail an approximation at any stage. The method is implemented by transforming a nonlinear system into a linear one. For the class of second-order systems given by (1) considered in this paper,

$$\ddot{\mathbf{x}} = \mathbf{f}(\mathbf{x}, \dot{\mathbf{x}}) + \mathbf{G}\mathbf{u}, \qquad \mathbf{f}(\mathbf{x}, \dot{\mathbf{x}}) = \boldsymbol{\Psi}\mathbf{x} + \boldsymbol{\Phi}\dot{\mathbf{x}} + \boldsymbol{\Omega}\mathbf{f}_{\text{nl}},$$
$$\boldsymbol{\Psi} = -\mathbf{A}_1^{-1}\mathbf{A}_3, \quad \boldsymbol{\Phi} = -\mathbf{A}_1^{-1}\mathbf{A}_2, \quad \boldsymbol{\Omega} = -\mathbf{A}_1^{-1}, \quad \mathbf{G} = \mathbf{A}_1^{-1}\mathbf{B}, \tag{2}$$

becomes

$$\ddot{\mathbf{z}} = \overline{\boldsymbol{\Psi}}\mathbf{z} + \overline{\boldsymbol{\Phi}}\dot{\mathbf{z}} + \overline{\mathbf{G}}\overline{\mathbf{u}}. \tag{3}$$

In these equations $\mathbf{u}$ and $\overline{\mathbf{u}}$ are, respectively, the actual (or physical) input applied to the nonlinear system and the so-called "artificial" input to the linear system. The matrices $\overline{\boldsymbol{\Psi}}$, $\overline{\boldsymbol{\Phi}}$, $\overline{\mathbf{G}}$ are dependent on the chosen inputs $\mathbf{u}$. The mapping from the nonlinear domain to the linearised domain is achieved through a nonsingular, linear, coordinate transformation. The actual input is designed to neutralise the effect of the nonlinearity, a procedure which can sometimes be achieved in full, and sometimes partially, as will be explained theoretically and by means of illustrative examples.

The process is quite straightforward for elastomechanical and aeroelastic systems described by second-order matrix differential equations with nonlinearity in the system parameters. The method described by Isidori [1] allows for greater generality, including nonlinearity in the input and output as well as in the system parameters, which is not required here and its omission leads to simplifications which aid the understanding of an otherwise fairly complicated procedure.

The feedback linearisation procedure classically, using the Lie algebra, entails repeated differentiation of each of the

outputs with respect to time, until the input terms appear. The classical procedure is greatly simplified in the case of second-order matrix systems such as those in elastomechanics or aeroelasticity, as explained in the sequel. The present work addresses two cases. The first case is that of complete input-output linearisation, meaning a full complement of outputs and inputs at every degree of freedom of the system. In this case, since the number of outputs is equal to the dimension of the system, it is possible to linearise the entire nonlinear system. The complete dynamics of the original system are preserved during the transformation. In the second case, an incomplete system of equal numbers of inputs and outputs is assumed. In this case, as the number of inputs and outputs is less than the dimension of the overall model only a partial linearisation of the system can be achieved. The portion that remains untransformed will contribute to what is known as the *internal dynamics*, whose stability must be ensured for stability of the overall closed-loop system. This is achieved by examining the stability of the zero dynamics [1], which is obtained by setting all coordinates of the linearised subsystem to zero in the expressions for the internal dynamics. Expressions for the latter are obtained such that their time-derivatives are orthogonal to the inputs, rendering the zero dynamics uncontrollable. The zero dynamics may be either linear or nonlinear.

2.1. Complete Input-Output Linearisation (n-Inputs, n-Outputs). In the present case the number of inputs and outputs is equal to the dimension of the system. The matrices and vectors of the original nonlinear system, given in (2), have the dimensions $\boldsymbol{\Psi}, \boldsymbol{\Phi}, \boldsymbol{\Omega}, \mathbf{G} \in \mathbb{R}^{n\times n}$; $\mathbf{x}, \mathbf{u}, \mathbf{f} \in \mathbb{R}^{n\times 1}$ and those given by the desired linearised equation (3) by $\overline{\boldsymbol{\Psi}}, \overline{\boldsymbol{\Phi}}, \overline{\mathbf{G}} \in \mathbb{R}^{n\times n}$; $\overline{\mathbf{z}}, \overline{\mathbf{u}} \in \mathbb{R}^{n\times 1}$. The first step is to choose the vector of actual inputs that cancels the nonlinearity,

$$\mathbf{u} = \mathbf{G}^{-1}\left(\overline{\mathbf{u}} - \mathbf{f}\left(\mathbf{x}, \dot{\mathbf{x}}\right)\right). \tag{4}$$

It can be seen that the nonlinearity is indeed cancelled by substituting (4) into (2). In fact, this is a special case where not only the nonlinearity, but also the complete open loop dynamics is cancelled by the choice of actual input. The result is the linearised system of independent, second-order, single degree of freedom equations

$$\begin{pmatrix} \ddot{x}_1 \\ \ddot{x}_2 \\ \vdots \\ \ddot{x}_n \end{pmatrix} = \begin{pmatrix} \overline{u}_1 \\ \overline{u}_2 \\ \vdots \\ \overline{u}_n \end{pmatrix}. \tag{5}$$

In fact, these equations are a special case of single degree of freedom equations, where each equation is simply a double integrator. Equation (5) is a particular form of (3), where also it is seen particularly that $\mathbf{x} = \mathbf{z}$. The simplicity of (5) is an advantage of the complete cancellation of the open-loop dynamics in (4). The choice of the artificial input $\overline{\mathbf{u}}$ necessarily depends upon the control objective, for example, the assignment of a pair of complex conjugate poles in each of the systems in (5) to avoid resonances. Whatever the control objective is, it will result in the determination of gains defined here in terms of negative feedback as

$$\begin{aligned} \overline{u}_1 &= -\begin{bmatrix} \varsigma_1 & \nu_1 \end{bmatrix} \begin{Bmatrix} x_1 \\ \dot{x}_1 \end{Bmatrix} \\ \overline{u}_2 &= -\begin{bmatrix} \varsigma_2 & \nu_2 \end{bmatrix} \begin{Bmatrix} x_2 \\ \dot{x}_2 \end{Bmatrix} \\ &\vdots \\ \overline{u}_n &= -\begin{bmatrix} \varsigma_n & \nu_n \end{bmatrix} \begin{Bmatrix} x_n \\ \dot{x}_n \end{Bmatrix}. \end{aligned} \tag{6}$$

In this special case where the entire open loop dynamics are cancelled, the control results in a closed-loop system that is comprised of n decoupled, single degree of freedom subsystems. Then, having defined the artificial inputs, the actual inputs that provide the desired linearisation are determined from (4). It is seen that the nonlinearity in (2) is neutralised and the closed-loop system is indeed linear with the required dynamics.

If the actual input were chosen to cancel the nonlinearity alone (not the complete open-loop dynamics), then (4) would be replaced by

$$\mathbf{u} = \mathbf{G}^{-1}\left(\overline{\mathbf{u}} - \boldsymbol{\Omega}\mathbf{f}_{\mathrm{nl}}\right), \tag{7}$$

and the linearised equations would remain coupled (unlike (5)) and consequently the gains in (6) would take a different form, as

$$\begin{Bmatrix} \overline{u}_1 \\ \overline{u}_2 \\ \vdots \\ \overline{u}_n \end{Bmatrix} = -\begin{bmatrix} \varsigma_{11} & \nu_{11} & \varsigma_{12} & \nu_{12} & \cdots & \varsigma_{1n} & \nu_{1n} \\ \varsigma_{21} & \nu_{21} & \varsigma_{22} & \nu_{22} & \cdots & \varsigma_{2n} & \nu_{2n} \\ \vdots & \vdots & \vdots & \vdots & \ddots & \vdots & \vdots \\ \varsigma_{n1} & \nu_{n1} & \varsigma_{n2} & \nu_{n2} & \cdots & \varsigma_{nn} & \nu_{nn} \end{bmatrix} \times \begin{Bmatrix} x_1 \\ \dot{x}_1 \\ \hline x_2 \\ \dot{x}_2 \\ \hline \vdots \\ \hline x_n \\ \dot{x}_n \end{Bmatrix}. \tag{8}$$

Clearly, there are a greater number of control gains in (8) than in (6), which means that there is more control flexibility, which might be used, for example, to assign the eigenvectors as well as the eigenvalues. This may be readily achieved using methods such as that presented in [11] and is illustrated through a numerical example later on.

2.2. Partial Input-Output Linearisation (m-Inputs, m-Outputs, $m < n$). The inputs and outputs (actuators and sensors), $\mathbf{u}, \mathbf{x}_{(1:m)} \in \mathbb{R}^{m\times 1}$, in equal numbers are now fewer than the dimension of the system. Linearisation results in similar

expressions to those obtained for the complete input-output case presented above. Equation (2) is now rewritten as

$$\begin{Bmatrix} \ddot{x}_1 \\ \vdots \\ \ddot{x}_m \\ \hline \ddot{x}_{m+1} \\ \vdots \\ \ddot{x}_n \end{Bmatrix} = \begin{Bmatrix} f_1(\mathbf{x}, \dot{\mathbf{x}}) \\ \vdots \\ f_m(\mathbf{x}, \dot{\mathbf{x}}) \\ \hline f_{m+1}(\mathbf{x}, \dot{\mathbf{x}}) \\ \vdots \\ f_n(\mathbf{x}, \dot{\mathbf{x}}) \end{Bmatrix} + \begin{bmatrix} g_{1,1} & \cdots & g_{1,m} \\ \vdots & \ddots & \vdots \\ g_{m,1} & \cdots & g_{m,m} \\ \hline g_{m+1,1} & \cdots & g_{m+1,m} \\ \vdots & \ddots & \vdots \\ g_{n,1} & \cdots & g_{n,m} \end{bmatrix} \begin{Bmatrix} u_1 \\ \vdots \\ u_m \end{Bmatrix}, \tag{9}$$

and the coordinate system which maps the original nonlinear system to the partially linearised system may be expressed as

$$\begin{pmatrix} z_1 & z_2 & \cdots & z_m \end{pmatrix}^T = \begin{pmatrix} x_1 & x_2 & \cdots & x_m \end{pmatrix}^T, \tag{10}$$

which is identical to the full output feedback case, except of course that there are now only m outputs. Further $(n\text{-}m)$ coordinates are needed and are chosen as coefficients of the orthonormal basis of the null space of $\mathbf{G}^T_{(1:n,1:m)}$ so that

$$\begin{gathered} \begin{pmatrix} x_1 \\ \vdots \\ x_n \end{pmatrix} = \mathbf{V} \begin{pmatrix} z_{m+1} \\ \vdots \\ z_n \end{pmatrix}, \\ \mathbf{V}^T\mathbf{V} = \mathbf{I}_{(n-m)\times(n-m)}, \quad \mathbf{V}^T\mathbf{G}_{(1:n,1:m)} = \mathbf{0}, \\ \mathbf{V} \in \mathbb{R}^{n\times(n-m)}. \end{gathered} \tag{11}$$

As with the full output feedback case, it is now necessary to choose actual inputs so that the nonlinearity is eliminated. This is achieved by

$$\begin{gathered} \mathbf{u} = \left[\mathbf{G}_{1:m,1:m}\right]^{-1} \left(\overline{\mathbf{u}} - \mathbf{f}(\mathbf{x}, \dot{\mathbf{x}})_{(1:m,1)}\right), \\ \mathbf{f}(\mathbf{x}, \dot{\mathbf{x}})_{(1:m,1)} = \mathbf{\Psi}_{(1:m,:)}\mathbf{x} + \mathbf{\Phi}_{(1:m,:)}\dot{\mathbf{x}} + \mathbf{\Omega}_{(1:m,:)}\mathbf{f}_{\text{nl}}, \end{gathered} \tag{12}$$

and substitution of (12) into the upper partition of (9) leads to m independent linear second-order systems with artificial inputs $\overline{\mathbf{u}} = \{\overline{u}_1 \quad \cdots \quad \overline{u}_m\}^T$, expressed as

$$\begin{pmatrix} \ddot{z}_1 \\ \ddot{z}_2 \\ \vdots \\ \ddot{z}_m \end{pmatrix} = \begin{pmatrix} \ddot{x}_1 \\ \ddot{x}_2 \\ \vdots \\ \ddot{x}_m \end{pmatrix} = \begin{pmatrix} \overline{u}_1 \\ \overline{u}_2 \\ \vdots \\ \overline{u}_m \end{pmatrix}. \tag{13}$$

Then by combining (9), (10), and (11) it is found that

$$\begin{Bmatrix} \ddot{z}_{m+1} \\ \vdots \\ \ddot{z}_n \end{Bmatrix} = \mathbf{V}^T \begin{Bmatrix} f_1(\mathbf{z}, \dot{\mathbf{z}}) \\ \vdots \\ f_n(\mathbf{z}, \dot{\mathbf{z}}) \end{Bmatrix} + \mathbf{V}^T\mathbf{G}_{(1:n,1:m)} \begin{Bmatrix} u_1 \\ \vdots \\ u_m \end{Bmatrix}, \tag{14}$$

so that from (11),

$$\begin{Bmatrix} \ddot{z}_{m+1} \\ \vdots \\ \ddot{z}_n \end{Bmatrix} = \mathbf{V}^T \begin{Bmatrix} f_1(\mathbf{z}, \dot{\mathbf{z}}) \\ \vdots \\ f_n(\mathbf{z}, \dot{\mathbf{z}}) \end{Bmatrix}, \tag{15}$$

which ensures uncontrollability of the nonlinear internal dynamics (15).

The stability of the complete system is then determined by the *zero dynamics*, which are generally nonlinear, obtained by setting to zero in (15) the external coordinates $(z_1, \ldots, z_m)$ of the partially linearised system in (13). The equations of the zero dynamics and their stability will be addressed for a specific aeroelastic example in the sequel.

As before, the artificial inputs in (13) may be chosen as a linear combination of the instantaneous displacement and velocity to fulfil a control objective. When the zero dynamics are found to be globally stable, then the desired control behaviour is unaffected by the nonlinearity confined to the internal dynamics.

3. Aeroservoelastic Model

The governing equation of aeroservoelastic systems takes the usual form [12] given by

$$\mathbf{A}\ddot{\mathbf{q}} + \left(\rho V\mathbf{B} + \mathbf{D}\right)\dot{\mathbf{q}} + \left(\rho V^2\mathbf{C} + \mathbf{E}\right)\mathbf{q} + \mathbf{f}_{\text{nl}}(\mathbf{q}) = \mathbf{f}_{\text{ext}}, \tag{16}$$

where $\mathbf{A}$, $\mathbf{D}$, $\mathbf{E}$ are the inertia, structural damping, and structural stiffness matrices, respectively, $\mathbf{B}$, $\mathbf{C}$ are the aerodynamic damping and aerodynamic stiffness matrices, respectively, and ρ, V are air density and velocity, respectively, (the present $\mathbf{B}$ is different from the input distribution matrix, also denoted by $\mathbf{B}$, in Section 1). The vector $\mathbf{q}$ contains generalised coordinates describing the motion of the system, whereas the vector $\mathbf{f}_{\text{ext}}$ contains externally applied generalised forcing terms, including control forces and gusts. The nonlinearity is confined to $\mathbf{f}_{\text{nl}}(\mathbf{q})$. Modified aerodynamic strip theory is used to compute the lift and pitch moment and an additional unsteady aerodynamic derivative term is included to account for significant unsteady effects [12], which appears in the matrix $\mathbf{B}$. In practice, the aerodynamic matrices are frequency dependent [12] and the time domain model would need to include aerodynamic states to account for this. The approach used is perfectly adequate for low speed, high aspect ratio wings. The system consists of a wing with an underslung engine attached by a pylon. Aerodynamic forces/moments acting on the pylon-engine arrangement are assumed to be negligible compared to those acting on the wing.

In the analysis presented here the wing deflection is described in terms of two assumed modes and a further generalised coordinate representing the angular displacement of the engine about the axis of the wing. The assumed modes are depicted in Figure 1, which also shows the coordinate system with its origin at the root, leading edge of the wing.

The vertical deflection of the wing $\zeta(x, y)$ is then given by

$$\zeta = y^2\, q_1 + y\left(x - x_f\right) q_2, \tag{17}$$

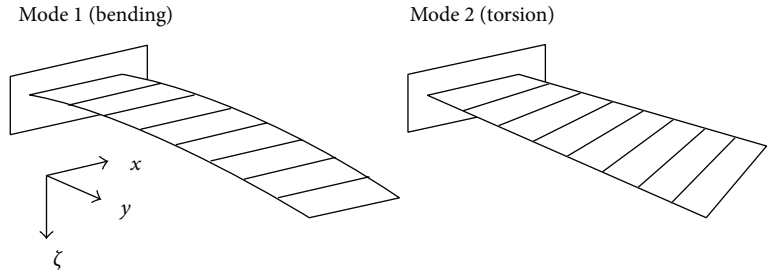

Figure 1: The two deflection patterns assumed for the flexible wing.

where q_1, q_2 are generalised coordinates that quantify the amount of bending and torsion modes present in the overall deflection, and x_f is the x-coordinate of the wing flexural axis. The pylon-engine is modelled as a rigid body, connected to the wing by a nonlinear stiffness. A sketch of the pylon-engine and also the complete wing-pylon-engine system may be found in [13].

The pylon-engine rotational degree of freedom ϑ_{pe} is the deflection of the pylon-engine *relative* to the wing. The absolute rotation θ_{pe} may be obtained by adding the wing twist angle at the engine attachment location, χ_2, to ϑ_{pe}. The absolute pylon-engine rotation becomes a coordinate in the assumed-modes domain, $q_{\text{pe}} = \theta_{\text{pe}}$. The coordinate transformation matrix **T** is defined by

$$\begin{Bmatrix} \zeta_1 \\ \chi_2 \\ \vartheta_{\text{pe}} \end{Bmatrix} = \begin{bmatrix} y_1^2 & 0 & 0 \\ 0 & y_2 & 0 \\ 0 & -y_2 & 1 \end{bmatrix} \begin{Bmatrix} q_1 \\ q_2 \\ q_{\text{pe}} \end{Bmatrix}, \tag{18}$$

where ζ_1 and χ_2 denote the vertical displacement at point "1" (the intersection of the wing flexural axis with the local x-axis at the point of attachment of the pylon to the wing) and the angular wing twist at point "2" (the intersection of the quarter-semi-span with the quarter-chord). The y-coordinates of points 1 and 2 are identical ($y_1 = y_2$). The system matrices, **A**, **B**, **C,** and **E** are given in terms of the parameters of the wing and pylon-engine system in [13], whereas vectors $\mathbf{f}_c$ and $\mathbf{f}_{\text{nl}}$ may be found in Appendix A in this paper. Note that in the present text, k_T, K_T are used to describe the coefficients of the linear and cubic components of coupling stiffness, respectively, which is different to the notation used in [13].

4. Numerical Simulation

The dimensions and parameters chosen for the model are given in [13], with $K_T = 300 \times k_T$. For the flexible wing, the values chosen are based on those used in a numerical example given in [12]. The dimensions and mass of the pylon-engine arrangement are chosen to be representative of a real aircraft (e.g. [14]).

The three degree of freedom aeroservoelastic model is used initially to determine the flutter speed of the linear system. Then, the cubic hardening term, K_T, is included in the torsional spring connecting the wing to the pylon-engine, and the nonlinear time-domain response to initial conditions is produced at an air speed just above the flutter speed.

The aeroservoelastic matrices are given in general terms in [13] and expressed here in terms of specific parameter values in consistent units (to three significant figures) as

$$\begin{aligned}
\mathbf{A}_w &= 10^5 \begin{bmatrix} 9.49 & 0.0633 & 0 \\ 0.0633 & 0.0942 & 0 \\ 0 & 0 & 0 \end{bmatrix}, \\
\mathbf{E}_w &= 10^8 \begin{bmatrix} 1.10 & 0 & 0 \\ 0 & 0.142 & 0 \\ 0 & 0 & 0 \end{bmatrix}, \\
\mathbf{A}_{\text{pe}} &= 10^3 \begin{bmatrix} 4.76 & 0 & 1.51 \\ 0 & 0 & 0 \\ 1.51 & 0 & 0.647 \end{bmatrix}, \\
\mathbf{E}_{\text{pe}} &= 10^6 \begin{bmatrix} 0 & 0 & 0 \\ 0 & 1.90 & -0.958 \\ 0 & -0.958 & 0.511 \end{bmatrix}, \\
\mathbf{B} &= 10^4 \begin{bmatrix} 2.98 & 0 & 0 \\ -0.229 & 0.0169 & 0 \\ 0 & 0 & 0 \end{bmatrix}, \\
\mathbf{C} &= 10^3 \begin{bmatrix} 0 & 4.97 & 0 \\ 0 & -0.406 & 0 \\ 0 & 0 & 0 \end{bmatrix}.
\end{aligned} \tag{19}$$

A simplification in the matrix subscripts previously defined in [13] has been made here. The control force distribution matrix is given (as a function of air speed) by

$$\begin{aligned}
\mathbf{f}_c = 10^2 &\begin{bmatrix} -3.19V^2 & -2.89V^2 & 0 \\ -0.302V^2 & -0.120V^2 & -0.0188 \\ 0 & 0 & 0.01 \end{bmatrix} \\
&\times \begin{Bmatrix} \beta_1 \\ \beta_2 \\ T_{\text{pe}} \end{Bmatrix},
\end{aligned} \tag{20}$$

where β_1 and β_2 are control surface (flap) angles and T_{pe} is a control torque applied directly to the pylon-engine assembly. The nonlinear internal force is given by

$$\mathbf{f}_{\text{nl}} = 10^8 \begin{Bmatrix} 0 \\ -2.87 \\ 1.53 \end{Bmatrix} \vartheta^3, \quad y_2 = y_1 = 1.875. \tag{21}$$

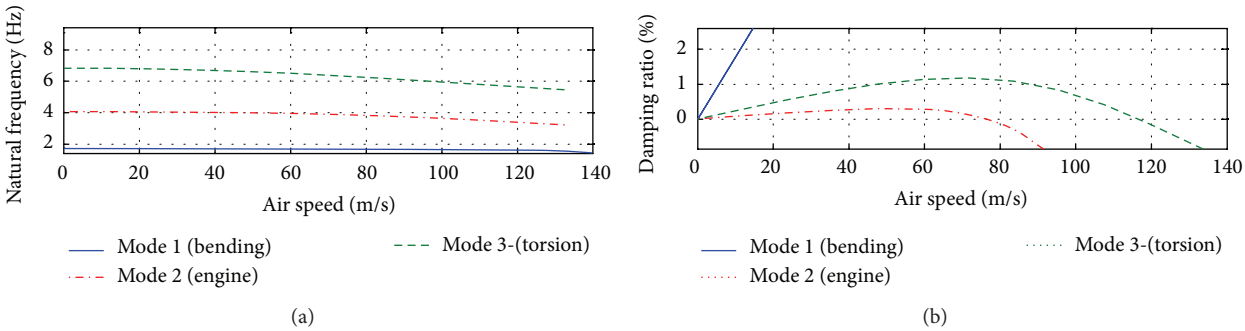

Figure 2: V-ω and V-ζ plots for the wing-pylon-engine model.

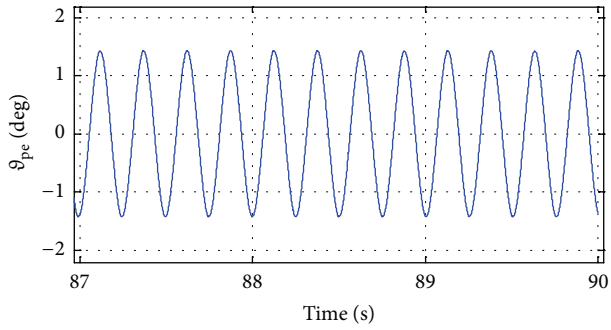

Figure 3: Steady-state LCO in ϑ_{pe} response.

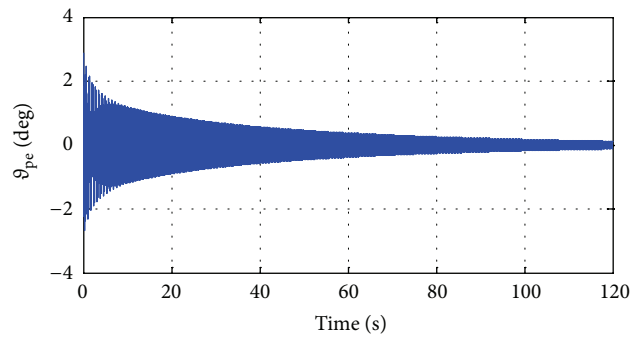

Figure 4: Decaying response, just below linear flutter speed.

Further information on the general form of the control and nonlinear spring forces can be found in Appendix A.

4.1. Uncontrolled Linear System: Natural Frequencies, Damping and Flutter Speed. The structural modes in the linear model (nonlinearity neglected) occur at 1.71 Hz (bending), 4.06 Hz (pylon-engine mode), and 6.83 Hz (torsional). It is evident from Figure 2 that flutter occurs at an airspeed of 77.6 ms^{-1}, involving coupling of the pylon-engine mode and wing bending modes.

4.2. Nonlinear Time-Domain Response. The nonlinear system is simulated at an airspeed of 80 ms^{-1}, just above the flutter point, under the application of the initial conditions $\zeta_1 = 0.333$ mm, $\chi_2 = 0.00333$ rad, and $\vartheta_{pe} = 0.05$ rad. These values have been chosen as they are representative of typical physical displacements one might expect in practice, for the wing-pylon-engine system specified in [13]. The resulting response of the system clearly exhibits limit cycle oscillation (LCO). A sample of the response for the ϑ_{pe} coordinate is shown in Figure 3.

For comparison, the simulated response for the ϑ_{pe} coordinate just below the linear flutter speed, at an airspeed of 75 ms^{-1}, is shown in Figure 4. As expected the response continues to decay and converges to the origin.

In the following section, linearising feedback control is applied to the nonlinear model in the assumed-modes domain. In the examples considered, the control objective is the assignment of the poles of the system. Judicious placement of the poles can be used to increase the flutter speed of the system, thereby increasing the flight envelope. Of course, other control objectives could be used instead. The resulting linearised system consists of the uncoupled single degree of freedom subsystems referred to previously in (5). Two cases are considered: those of 3 inputs and 3 outputs (denoted 3I3O) and of 2 inputs and 2 outputs (denoted 2I2O) which are representative of the analysis in Section 2.

4.3. Feedback Linearisation: 3I3O Case. The poles of the system are assigned for the uncoupled linearised system in (5) (by cancellation of the entire open-loop dynamics) and with feedback law (6), so that the natural frequencies and damping values are given by

$$\begin{aligned} \omega_1 &= 0.93\ \text{Hz}, \qquad \xi_1 = 0.01, \\ \omega_2 &= 2.9\ \text{Hz}, \qquad \xi_2 = 0.01, \\ \omega_3 &= 4.95\ \text{Hz}, \qquad \xi_3 = 0.01, \end{aligned} \tag{22}$$

at an air speed of 80 ms^{-1}. The first mode is predominantly wing bending, the second is pylon-engine deformation and the third is mainly the twisting motion of the wing. With initial conditions the same as the uncontrolled case (Section 4.2), namely $\zeta_1 = 0.333$ mm, $\chi_2 = 0.00333$ rad, and $\vartheta_{pe} = 0.05$ rad and in the absence of any nonlinear parameter error the poles of the linearised system are assigned exactly. The system response now decays to zero as shown in Figure 5, whereas the

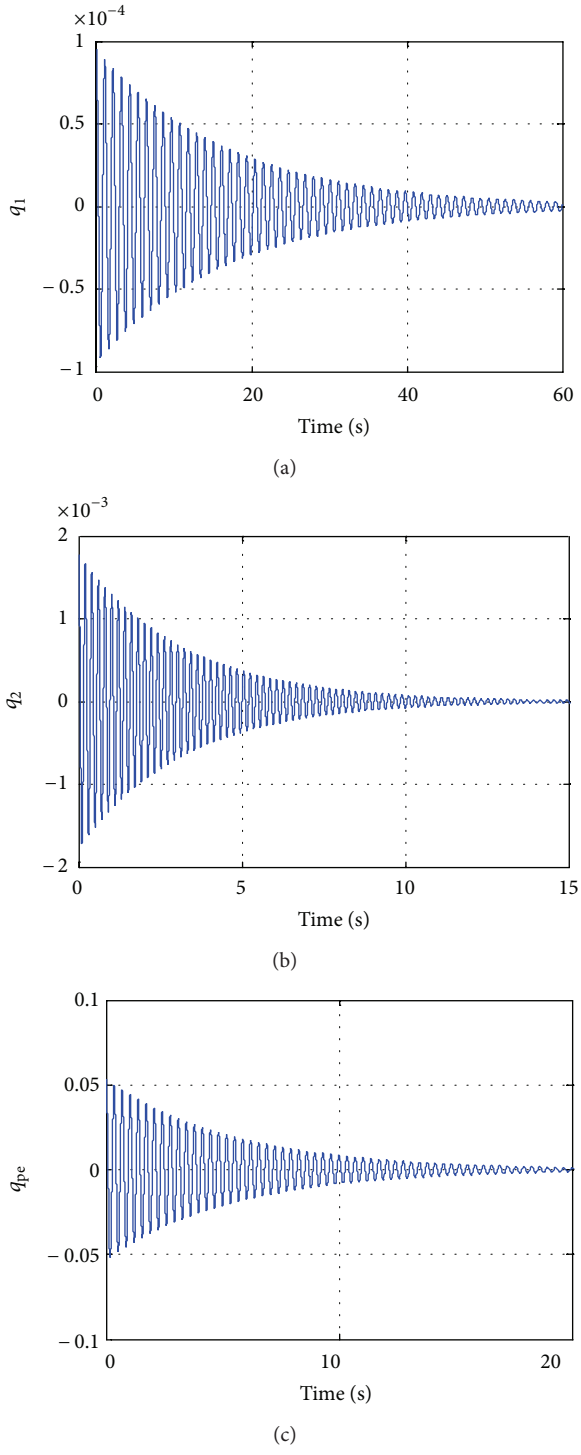

FIGURE 5: Feedback linearisation: response at 80 ms^{-1} (assumed-modes coordinates).

uncontrolled nonlinear system exhibited a limit cycle. The required control surface and actuator inputs are shown in Figure 6, where it can be seen that the input magnitudes are feasible in practice.

Now, suppose the linearising control is chosen to cancel the nonlinearity alone, in which case the linearised equations

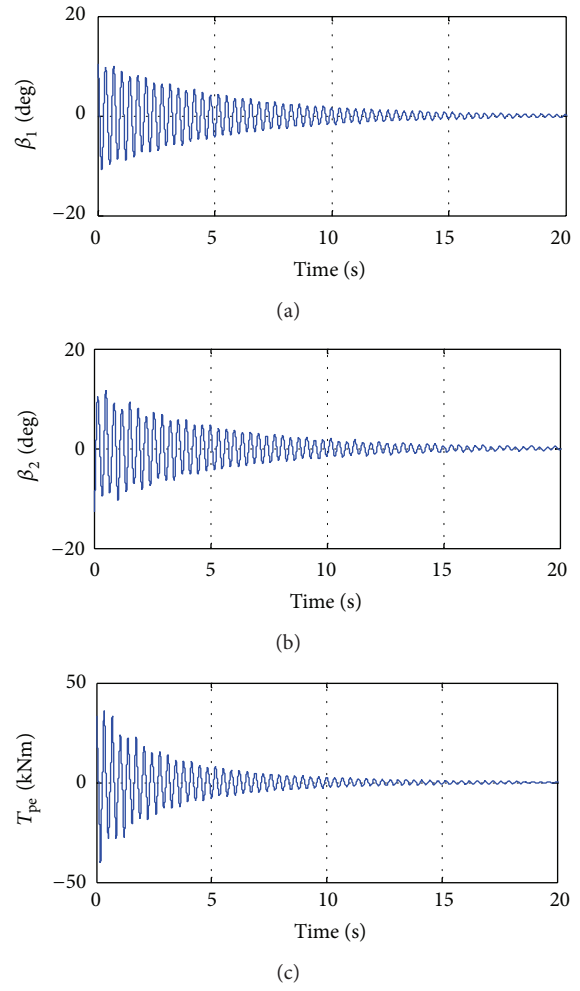

FIGURE 6: Control surface deflection angles and actuator torques for exact feedback linearization.

generally remain coupled, resulting in a greater number of control gains in (8) and greater control flexibility as explained in Section 2.1. One is then able to assign eigenvectors corresponding to the assigned poles. The same pole-placement above is now implemented, with the following respective eigenvectors assigned:

$$\mathbf{v}_1 = \{1 \quad 1 \quad 0\}^T, \qquad \mathbf{v}_2 = \{1 \quad -1 \quad 0\}^T, \qquad \mathbf{v}_3 = \{0 \quad 0 \quad 1\}^T. \tag{23}$$

Thus, it is desired to deliberately couple the bending and torsion in the first two modes, whilst leaving the pylon-engine mode decoupled. The resulting closed-loop responses and control inputs are shown in Figures 7 and 8, respectively.

It is evident from the first two plots in Figure 7 that a mixing of modes has occurred, as these two responses now contain multiple harmonics. The third coordinate, however, remains unchanged. This is expected, as the eigenvector assignment commanded that the pylon-engine mode should remain uncoupled. It can also be seen from the first two plots in Figure 8 that the required control surface deflections have increased; it is easier to control the uncoupled modes than the deliberately coupled ones. Thus, in the case of

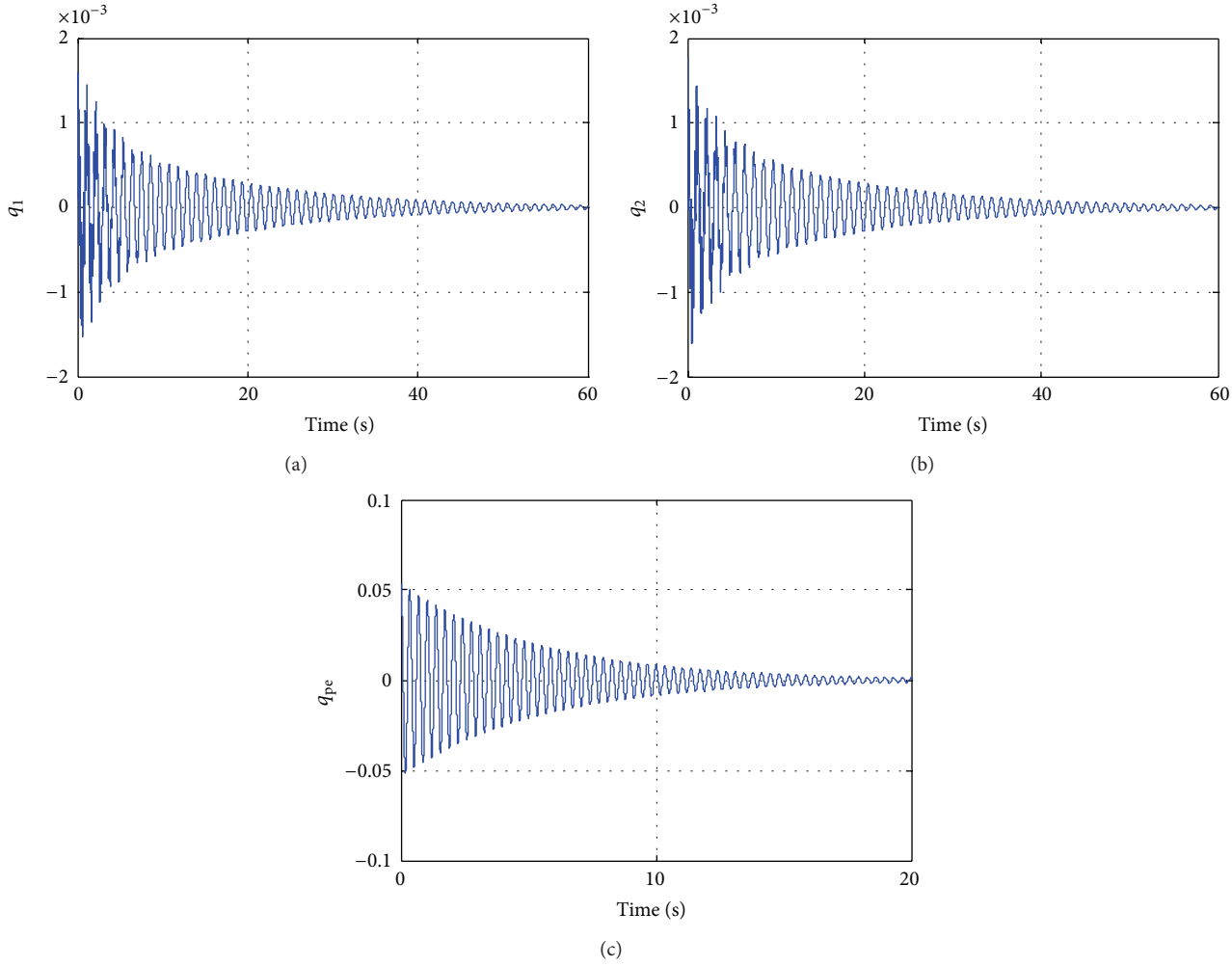

FIGURE 7: Feedback linearisation with cancellation of nonlinearity only and with eigenvector assignment: response at 80 ms^{-1} (assumed-modes coordinates).

the three degree of freedom wing-pylon-engine system there is some merit in using feedback linearisation to cancel the entire open loop dynamics despite the loss of control flexibility. For the remainder of this simulation and those appearing later on, only the case where the entire open loop dynamics are cancelled will be considered.

When a +40% error in K_{nl} is incorporated, and the closed-loop response is simulated based on the above feedback parameters and with the same initial conditions, an unstable response sets in from the very beginning, as seen in Figure 9. The nonlinear spring, connected between wing twist and rotation of the pylon-engine assembly, is not capable of suppressing the response (in the assumed-modes coordinates) into a limit cycle. The problem of error in the nonlinear parameter is of practical importance, since it is seldom possible to be precise in estimating the magnitude of nonlinear terms. This problem is addressed in the sequel.

4.4. Feedback Linearisation: 2I2O Case. The three degree of freedom system is now considered to be instrumented with only two inputs, trailing edge control-surface (flap) angles β_1 and β_2, and two outputs, discrete wing displacement ζ_1 and twist χ_2. In this case there is no control torque T_{pe}. The measurement of ϑ_{pe} is necessary, but only for determination of $\mathbf{f}(\mathbf{z}, \dot{\mathbf{z}})$. The zero dynamics of the 2I2O aeroservoelastic problem are given in Appendix B and stabilised by the introduction of structural damping

$$\mathbf{D}_{\text{mod}} = 10^5 \begin{bmatrix} 2.05 & 0.0103 & 0.00220 \\ 0.0103 & 0.0767 & -0.00282 \\ 0.00220 & -0.00282 & 0.00356 \end{bmatrix}, \tag{24}$$

which corresponds to 1% of modal damping. The introduction of structural damping increases the flutter speed of the system from 77.6 ms^{-1} to 95.05 ms^{-1}, and thus the simulation is carried out above the new speed, at 97.5 ms^{-1}. Pole-placement is specified such that

$$\begin{aligned} \omega_1 &= 0.93\ \text{Hz}, \qquad \xi_1 = 0.01, \\ \omega_2 &= 4.95\ \text{Hz}, \qquad \xi_2 = 0.01. \end{aligned} \tag{25}$$

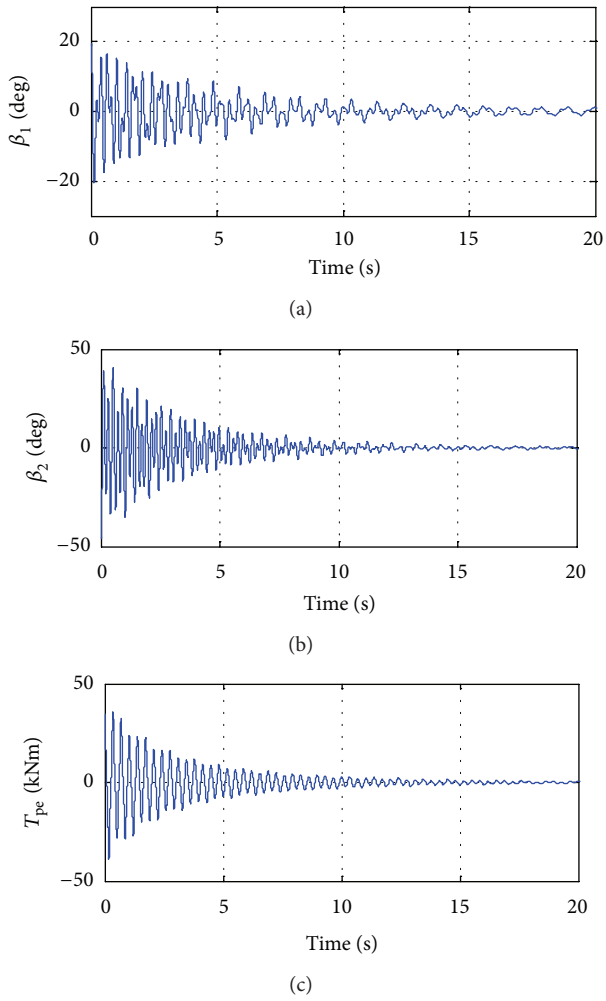

FIGURE 8: Control surface deflection angles and actuator torques for exact feedback linearisation: cancellation of nonlinearity only, with assignment of eigenvectors.

As before, feedback linearisation successfully places the poles to the desired values and the transient response shown in Figure 10 is obtained.

It is evident from the third subplot in Figure 10 that the coordinate q_{pe} eventually stabilises because the zero dynamics of the system are stable. When a +40% error in K_{nl} is incorporated and the closed-loop response is simulated based on the same feedback parameters instability does not occur (as in the 3I3O case) but a degradation in performance is observed in Figure 11 where it is seen that the control fails to eliminate an LCO.

5. Treatment of Nonlinear Parameter Error: Adaptive Feedback Linearisation

The treatment of error in the numerical value of a nonlinear parameter is carried out using adaptive feedback linearisation, which makes use of Lyapunov stability theory. It results in an updating rule for the erroneous parameter, which evolves with time. This approach ensures that the system remains stable; the original control objectives might be compromised because of evolution of the nonlinear parameter estimate. This might be acceptable in many cases depending upon engineering judgment.

An erroneous estimate, $\mathbf{f}'_{nl}$, is now assumed in place of the true nonlinear force vector, $\mathbf{f}_{nl}$. The corresponding erroneous input is then determined, by comparison with (2) and (4), as

$$\mathbf{u}' = \mathbf{G}^{-1}\left(\overline{\mathbf{u}} - \mathbf{f}'(\mathbf{x})\right), \quad \mathbf{f}'(\mathbf{x}) = \boldsymbol{\Psi}\mathbf{x} + \boldsymbol{\Phi}\dot{\mathbf{x}} + \boldsymbol{\Omega}\mathbf{f}'_{nl}, \tag{26}$$

and substituting (26) into (2) leads to

$$\ddot{\mathbf{x}} = \overline{\mathbf{u}} + \boldsymbol{\Omega}\boldsymbol{\varepsilon}, \quad \boldsymbol{\varepsilon} = \mathbf{f}_{nl} - \mathbf{f}'_{nl}. \tag{27}$$

Recall (6) from Section 2.1 earlier. This may be combined into a single equation

$$\overline{\mathbf{u}} = \boldsymbol{\Gamma}\begin{Bmatrix}\mathbf{x}\\ \dot{\mathbf{x}}\end{Bmatrix}, \quad \boldsymbol{\Gamma} \in \mathbb{R}^{n\times 2n}. \tag{28}$$

The artificial inputs may be expressed in terms of the state variables, $\mathbf{x}$, by using the above equation together with the coordinate transformation

$$\mathbf{z} = \mathbf{T}_{zx}\mathbf{x} \tag{29}$$

defined in (10) and (11).

Thus,

$$\overline{\mathbf{u}} = \boldsymbol{\Gamma}'\begin{Bmatrix}\mathbf{x}\\ \dot{\mathbf{x}}\end{Bmatrix} = \begin{bmatrix}\boldsymbol{\Gamma}'_1 & \boldsymbol{\Gamma}'_2\end{bmatrix}\begin{Bmatrix}\mathbf{x}\\ \dot{\mathbf{x}}\end{Bmatrix}, \quad \boldsymbol{\Gamma}' = \boldsymbol{\Gamma}_z\begin{bmatrix}\mathbf{T}_{zx} & \mathbf{0}\\ \mathbf{0} & \mathbf{T}_{zx}\end{bmatrix}, \tag{30}$$

and the second-order equation of the closed-loop system is then cast as

$$\ddot{\mathbf{x}} = \boldsymbol{\Gamma}'_1\mathbf{x} + \boldsymbol{\Gamma}'_2\dot{\mathbf{x}} + \boldsymbol{\Omega}\boldsymbol{\varepsilon}. \tag{31}$$

Equation (31) shows that the nonlinear parameter error results in an input to the closed-loop system. It may be readily shown, for the 3I3O system, that

$$\boldsymbol{\Gamma}'_{1,z} = -\begin{bmatrix}\varsigma_1 & & \\ & \varsigma_2 & \\ & & \varsigma_2\end{bmatrix}, \quad \boldsymbol{\Gamma}'_{2,z} = -\begin{bmatrix}\nu_1 & & \\ & \nu_2 & \\ & & \nu_2\end{bmatrix}. \tag{32}$$

The system is then represented in state-space as

$$\dot{\overline{\mathbf{z}}} = \overline{\mathbf{A}}\overline{\mathbf{z}} + \Delta K_T \vartheta_{pe}^3 \overline{\mathbf{B}}\boldsymbol{\Omega}\left(\mathbf{T}_{(3,:)}\right)^T,$$

$$\overline{\mathbf{A}} = \begin{bmatrix}\mathbf{0} & \mathbf{I}\\ \boldsymbol{\Gamma}'_{1,z} & \boldsymbol{\Gamma}'_{2,z}\end{bmatrix}, \tag{33}$$

$$\overline{\mathbf{B}} = \begin{bmatrix}\mathbf{0}\\ \mathbf{I}\end{bmatrix}, \quad \overline{\mathbf{z}} = \begin{Bmatrix}\mathbf{z}\\ \dot{\mathbf{z}}\end{Bmatrix},$$

where $\mathbf{T}$ is defined in (18) and where the erroneous nonlinear parameter is given by

$$K'_T = K_T + \Delta K_T, \tag{34}$$

$$\boldsymbol{\varepsilon} = \Delta K_T \vartheta_{pe}^3 \boldsymbol{\Omega}\left(\mathbf{T}_{(3,:)}\right)^T. \tag{35}$$

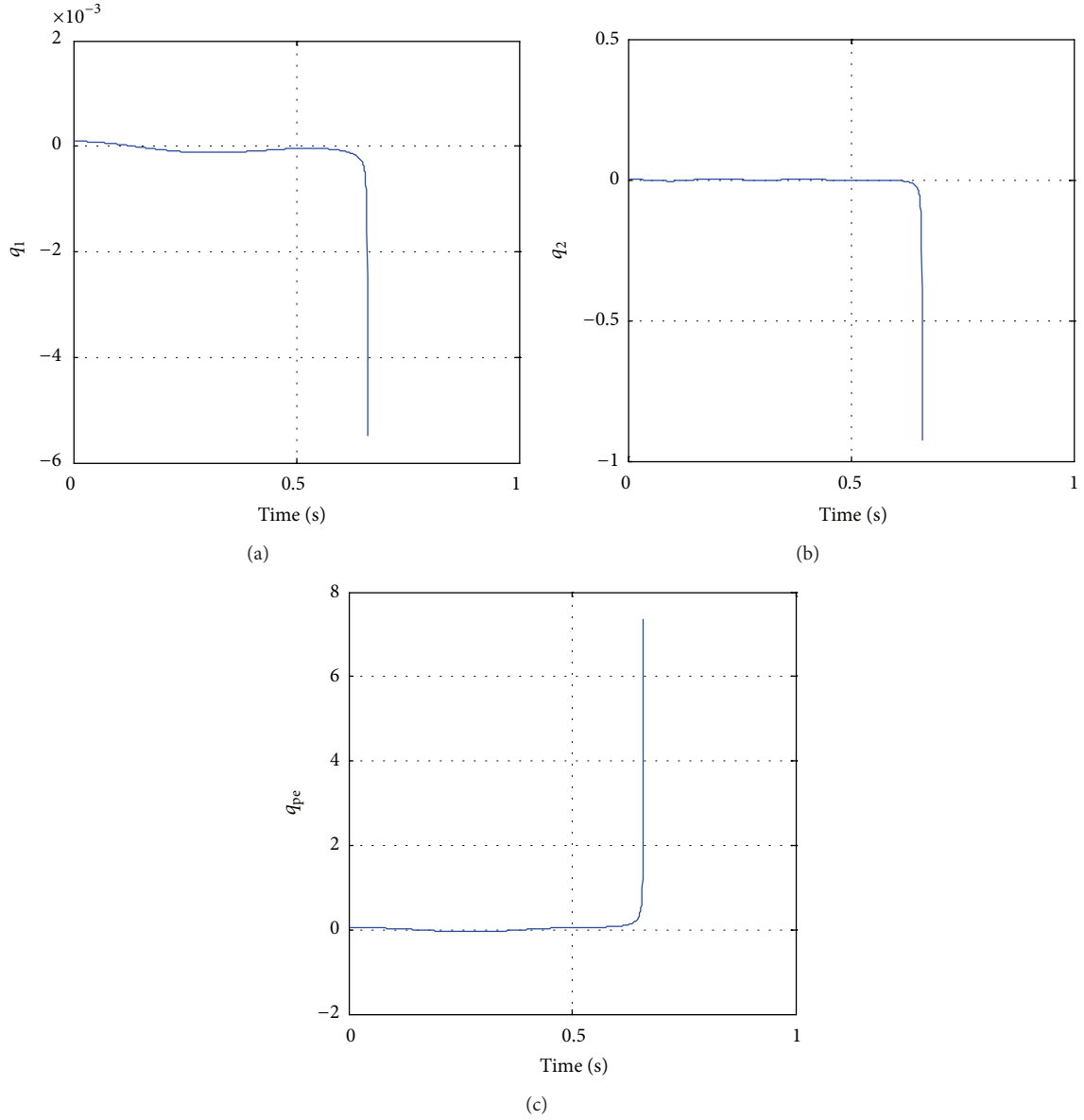

FIGURE 9: Feedback-linearisation with nonlinear parameter error: response at 80 ms^{-1}.

It is conceivable that this additional (unknown) input may potentially destabilise the system, or at least degrade the control performance. This possibility may be eliminated by accounting for the nonlinearity errors using an adaptive algorithm. Such an algorithm seeks to guarantee asymptotic stability of the closed-loop response.

A scalar Lyapunov function V in $\overline{\mathbf{z}}, \Delta K_T$ may be defined, such that asymptotic stability of the closed-loop system is guaranteed by ensuring that $V > 0$ and its time-derivative $\dot{V} < 0$ [15]. Such a function may be used as a basis for computing a parameter update law. The Lyapunov function,

$$V\left(\overline{\mathbf{z}}, \Delta K_T\right) = \overline{\mathbf{z}}^T \mathbf{P} \overline{\mathbf{z}} + \Delta K_T^2 > 0 \tag{36}$$

is considered, where $\mathbf{P} = \mathbf{P}^T \succ 0$. Differentiating the above equation with respect to time, one obtains

$$\dot{V}\left(\overline{\mathbf{z}}, \Delta K_T\right) = \dot{\overline{\mathbf{z}}}^T \left(\mathbf{P} + \mathbf{P}^T\right) \overline{\mathbf{z}} + 2\Delta K_T \frac{\mathrm{d}\left(\Delta K_T\right)}{\mathrm{d}t}. \tag{37}$$

Now, by combining (33) and (37) and expanding and rearranging

$$\dot{V}\left(\overline{\mathbf{z}}, \Delta K_T\right) = \overline{\mathbf{z}}^T \left(\overline{\mathbf{A}}^T \mathbf{P} + \mathbf{P}\overline{\mathbf{A}}\right) \overline{\mathbf{z}} + 2\Delta K_T \left(\frac{\mathrm{d}\left(\Delta K_T\right)}{\mathrm{d}t} + \vartheta_{\text{pe}}^3 \mathbf{T}_{(3,:)} \boldsymbol{\Omega}^T \overline{\mathbf{B}}^T \mathbf{P} \overline{\mathbf{z}}\right), \tag{38}$$

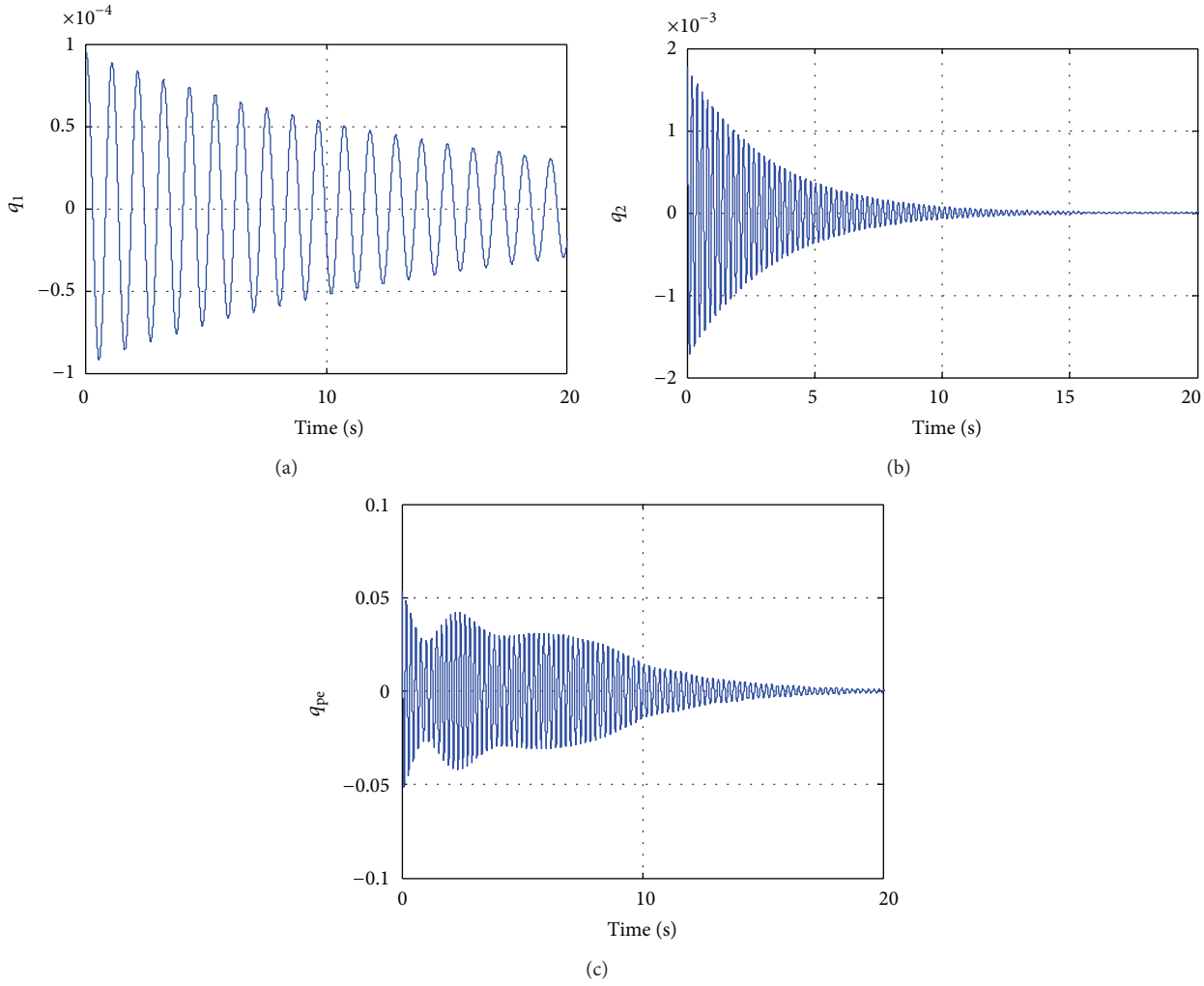

FIGURE 10: Feedback-linearisation: response at 97.5 ms^{-1} (assumed-modes coordinates).

it becomes evident that

$$\frac{\mathrm{d}\left(\Delta K_T\right)}{\mathrm{d}t} = -\vartheta_{\mathrm{pe}}^3 \mathbf{T}_{(3,:)} \boldsymbol{\Omega}^T \overline{\mathbf{B}}^T \mathbf{P} \overline{\mathbf{z}} \tag{39}$$

eliminates the second term on the right-hand-side of (38), resulting in

$$\dot{V}\left(\overline{\mathbf{z}}, \Delta K_T\right) = \overline{\mathbf{z}}^T \left(\overline{\mathbf{A}}^T \mathbf{P} + \mathbf{P}\overline{\mathbf{A}}\right) \overline{\mathbf{z}}. \tag{40}$$

Now, from the definition of ΔK_T in (34) and knowing that the actual nonlinear parameter K_T is constant, it is seen that

$$\frac{\mathrm{d}\left(\Delta K_T\right)}{\mathrm{d}t} = \frac{\mathrm{d}\left(K_T\right)}{\mathrm{d}t} - \frac{\mathrm{d}\left(K_T'\right)}{\mathrm{d}t} = -\frac{\mathrm{d}\left(K_T'\right)}{\mathrm{d}t}. \tag{41}$$

Combining (41) and (39), an update law for K_T' corresponding to the latter equation is obtained as

$$\frac{\mathrm{d}\left(K_T'\right)}{\mathrm{d}t} = \vartheta_{\mathrm{pe}}^3 \mathbf{T}_{(3,:)} \boldsymbol{\Omega}^T \overline{\mathbf{B}}^T \mathbf{P} \overline{\mathbf{z}}. \tag{42}$$

Thus, the initially assumed value K_T' of the nonlinear parameter is continually updated at each time step. Effectively, this increases the dimension of the state vector by 1, as K_T' becomes part of the system state. Now, choosing $\mathbf{P}$ such that for arbitrary $\mathbf{Q} \succ 0$,

$$\mathbf{Q} = -\left(\overline{\mathbf{A}}^T \mathbf{P} + \mathbf{P}\overline{\mathbf{A}}\right), \tag{43}$$

it becomes clear that by substituting the above equation into (40), $\dot{V}$ is rendered negative-definite, as required.

For the 2I2O case, an identical approach may be followed to obtain similar expressions. The definition of $\overline{\mathbf{z}}$ changes to $\overline{\mathbf{z}} = \{\mathbf{z}_{(1:2)} \quad \dot{\mathbf{z}}_{(1:2)}\}^T$, and the parameter update rate becomes

$$\frac{\mathrm{d}\left(K_T'\right)}{\mathrm{d}t} = \vartheta_{\mathrm{pe}}^3 \mathbf{T}_{(3,:)} \boldsymbol{\Omega}_{(1:2,:)}^T \overline{\mathbf{B}}^T \mathbf{P} \overline{\mathbf{z}}. \tag{44}$$

The matrices $\overline{\mathbf{A}}$ and $\overline{\mathbf{B}}$ become

$$\overline{\mathbf{A}} = \begin{bmatrix} \mathbf{0} & \mathbf{I}_{2\times 2} \\ \boldsymbol{\Gamma}'_{1,z\ (1:2,1:2)} & \boldsymbol{\Gamma}'_{2,z\ (1:2,1:2)} \end{bmatrix}, \qquad \overline{\mathbf{B}} = \begin{bmatrix} \mathbf{0} \\ \mathbf{I}_{2\times 2} \end{bmatrix}. \tag{45}$$

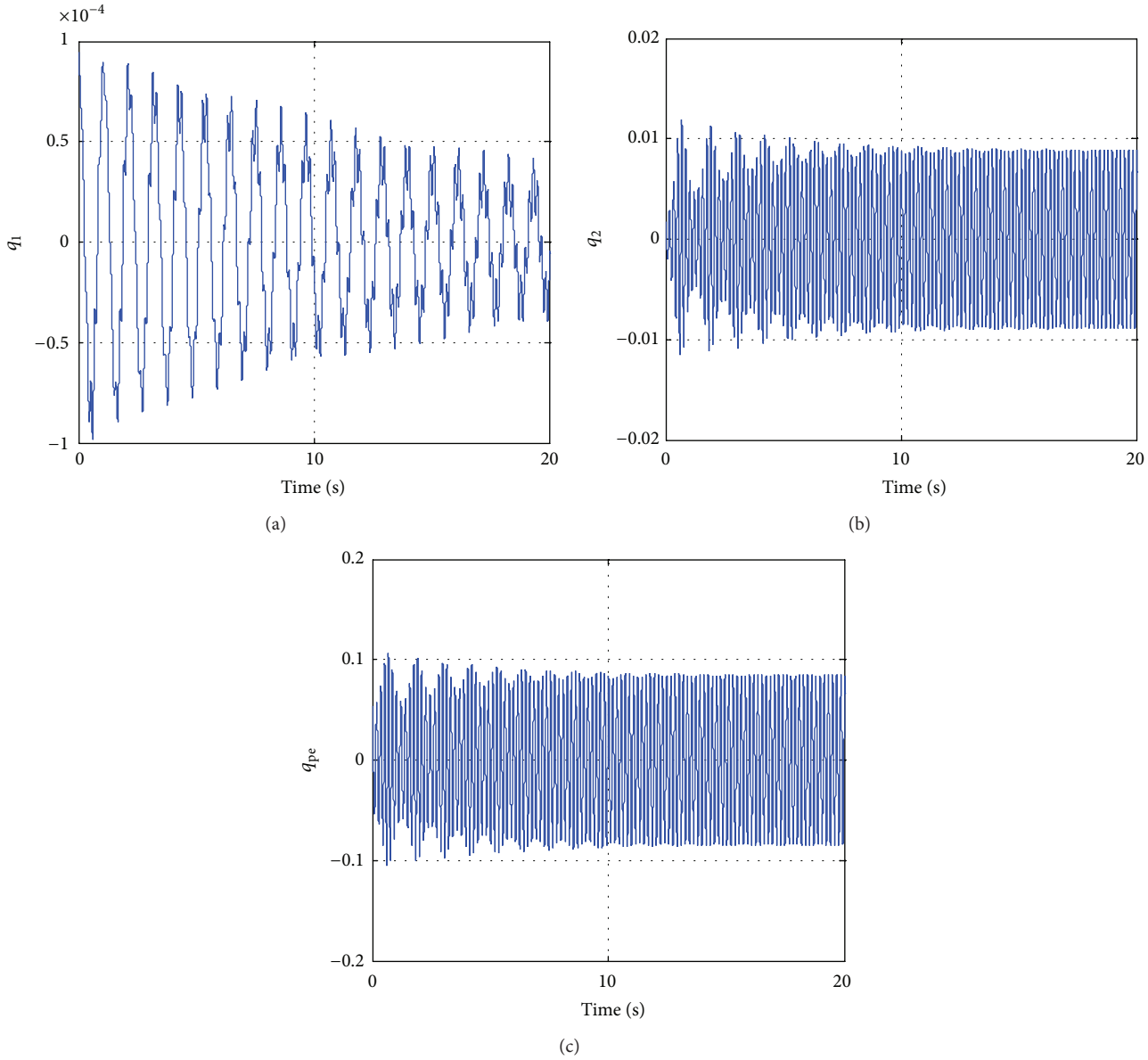

Figure 11: Feedback-linearisation with nonlinear parameter error: response at 97.5 ms^{-1}.

An important consideration in the 2I2O case is the asymptotic stability of the zero dynamics, considered in Appendix B, which is required for the adaptive scheme to work. For the particular 2I2O configuration considered, the presence of structural damping ensures stability of the zero dynamics, thus enabling application of the adaptive method.

Example: Stabilisation of the Aeroelastic System Using Adaptive Feedback Linearisation. The instability shown in Figure 9 may be avoided altogether by implementing the adaptive controller described in Section 5 above. In the 3I3O case, the resulting controlled response, for the same initial conditions, is shown in Figure 12.

A comparison of Figure 12 with Figure 5 shows that the controlled responses are similar, but not identical. Although adaptive feedback linearisation destroys the original pole-placement, it can be seen that the controlled response is stable. In fact, the adaptive controller successfully drives the responses to zero for values of $|\vartheta_{pe}|_{max}$ (set as an initial condition) up to around 0.0735 rad. The required control in this case is accomplished through achievable control surface deflection angles (≈11°) and actuator torque magnitude (55 kNm).

In the case of the 2I2O system, the system response with adaptation shown in Figure 13 should be compared to that in Figure 11, for feedback linearisation without adaptation and the same error in the cubic stiffness parameter. The degradation of the system to LCO is completely removed in Figure 13.

It can also be seen that the controlled responses, as well as the response of the uncontrolled coordinate converge to zero when the adaptive controller is implemented. In fact,

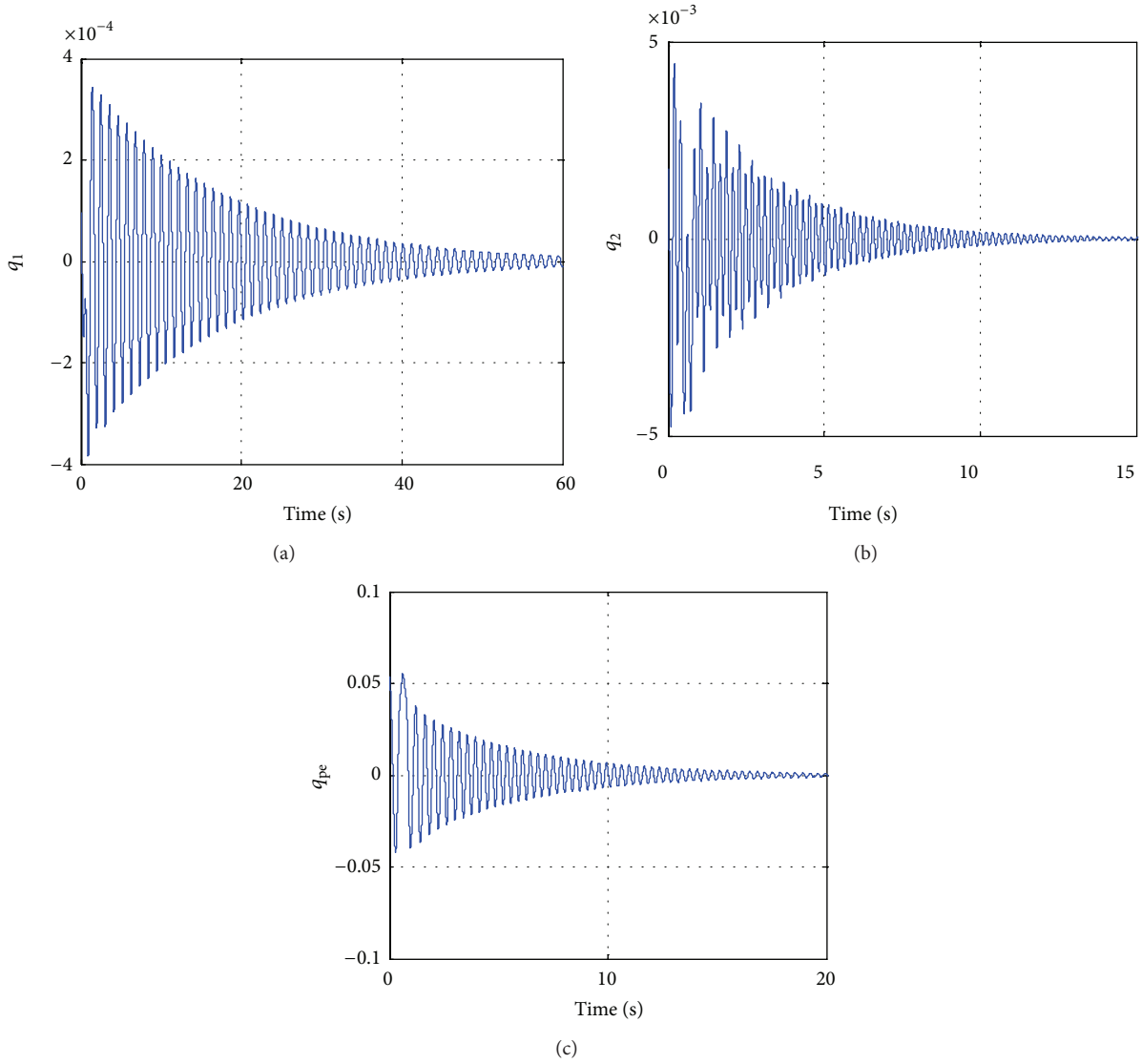

FIGURE 12: 3I3O system with adaptive feedback linearisation: response at 80 ms^{-1}.

this convergence takes place rapidly. When converted to the physical domain, the resulting magnitudes of the coordinates occur within acceptable limits (maximum values of 0.33 mm, 0.24°, 2.92° for ζ_1, χ_2, ϑ_{pe}, resp.). As before, it is found that the control surface deflections required to achieve the responses shown in Figure 13 are feasible (β_1, $\beta_2 \approx 30°$).

6. Conclusions

Nonlinear systems are ubiquitous in vibrations engineering and aeroelasticity, but the analysis is mathematically intricate and complicated. The paper presents the feedback linearisation methodology, whereby a nonlinear system is rendered linear by means of active control. Having neutralised the nonlinearity, the system may be treated using well-understood linear analysis methods such as modal decomposition, which generally cannot be applied to nonlinear systems directly. The technique is formulated using the second-order representation of elastomechanical and aeroelastic systems with stiffness nonlinearity, familiar to the vibrations community. This has certain advantages over the conventional state-space formulation in that repeated output differentiation, usually described using the Lie algebra notation, is unnecessary. The purpose of the linearising controller is to cancel the nonlinearity completely and therefore it results in a truly linear system, rather than linearisation about an operating point limited to small perturbations, or quasi-linearisation as with describing functions. The controller may be designed to cancel the nonlinearity only or to cancel the complete open-loop dynamics. In the former case there is shown to be greater control flexibility, but the latter case is found to have some merit in the particular example considered of a flexible wing-pylon-engine system with decoupled bending, torsional, and pylon-engine modes.

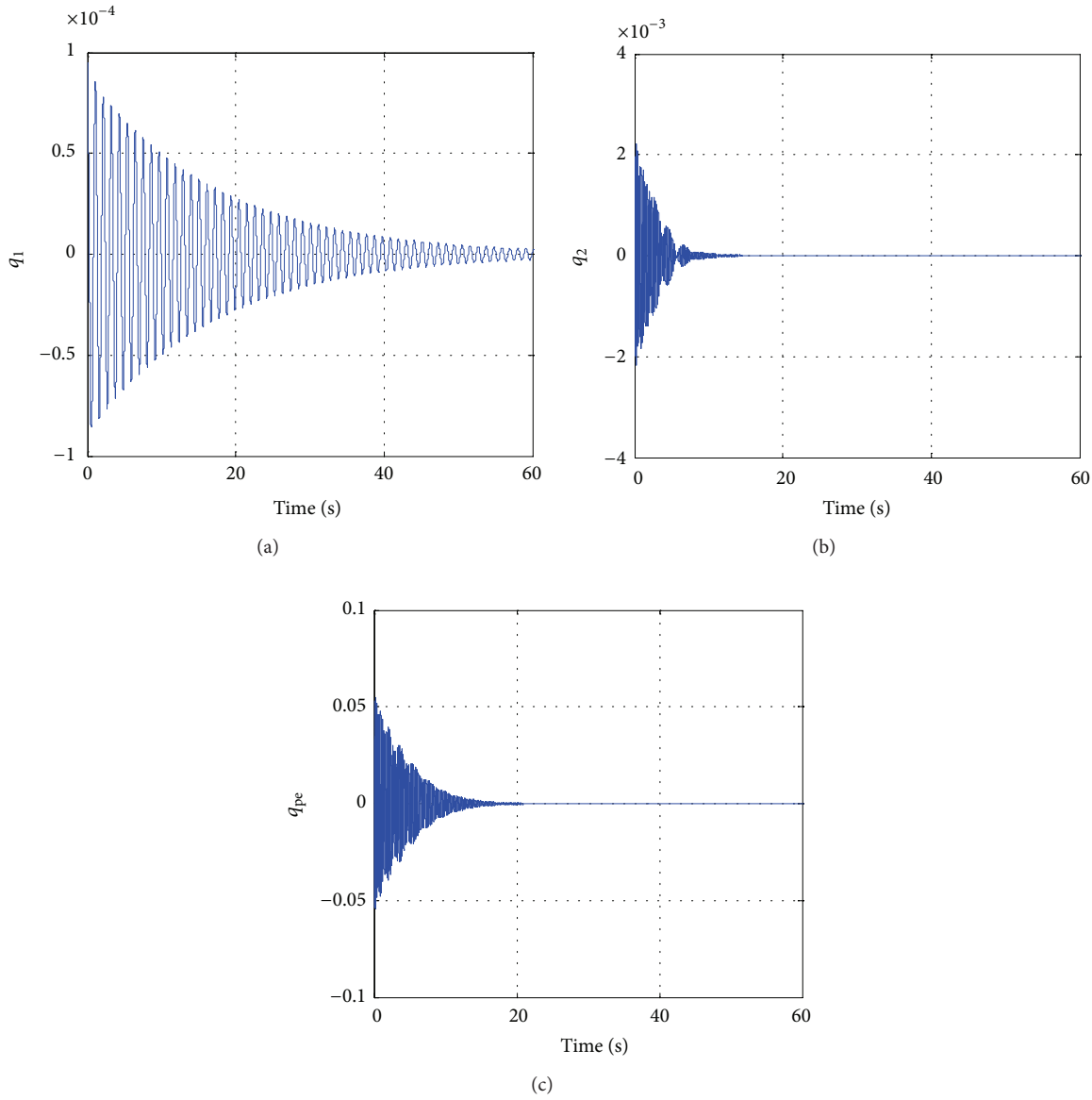

FIGURE 13: 2I2O system with feedback linearisation: response at 97.5 ms^{-1}.

Exact feedback linearisation requires knowledge of the nonlinearity and when every degree of freedom of the system is available for measurement (and actuation) and then linearisation may be achieved completely. When fewer than the full set of degrees of freedom is available for measurement and actuation, then the system can generally be partitioned into independent linear and nonlinear subsystems, with the dimension of the latter being the difference between the number of degrees of freedom and the number of sensors and actuators. If the nonlinear subsystem is stable, then the dynamics of the linear subsystem may be controlled as required. The problem of an imprecisely known nonlinear term was addressed using adaptive feedback linearisation, resulting in a parameter update rule that evolves in time to ensure stability. It requires an additional state variable to do this and is likely to be more expensive than using feedback linearisation without adaptivity.

Feedback linearisation techniques were illustrated using a three degree of freedom aeroelastic model consisting of a flexible wing and a rigid pylon-engine system attached to the wing via a nonlinear torsional spring with pole placement of the fully linearised and partially linearised system corresponding to the measurement (and actuation) at three degrees of freedom (3I3O) and two degrees of freedom (2I2O) respectively. The parameters of the system were chosen carefully to represent a real aircraft. Adaptive linearisation was applied successfully to compensate for a nonlinear parameter error in the case of 3I3O, and in the 2I2O case the nonlinear subsystem was found to be stable. The magnitudes of the aileron deflection angles were physically realisable.

Appendices

A. Control Forces and Nonlinear Spring Forces

Control forces are applied to the wing-pylon-engine system by means of control surfaces. It is assumed in this work that two control surfaces (different from [14]) are available, the first (closest to the wing root) spanning 85% of the length of the wing and the second spanning the remaining length (the contribution of the control surfaces to the dynamics of the overall system is neglected). The widths of the first and second control surfaces are assumed to be 20% and 33.33% of the chord length, respectively. These particular dimensions have been chosen so as to optimise the distribution of work performed by each control surface. In addition to the ailerons, it is assumed that a separate actuator is available to apply a torque T_{pe} directly on the engine rotational degree of freedom. The forcing vector is found to be

$$\mathbf{f}_c = \begin{bmatrix} -\frac{1}{6}\tilde{r}\alpha^3 a_{C,1} s_w & -\frac{1}{6}\tilde{r}\left(1-\alpha^3\right) a_{C,2} s_w & 0 \\ \frac{1}{4}\tilde{r}\alpha^2 b_{C,1} c_w & \frac{1}{4}\tilde{r}\left(1-\alpha^2\right) b_{C,2} c_w & -y_2 \\ 0 & 0 & 1 \end{bmatrix} \times \begin{Bmatrix} \beta_1 \\ \beta_2 \\ T_{\mathrm{pe}} \end{Bmatrix} = \mathbf{B}\mathbf{u}, \tag{A.1}$$

where $\tilde{r} = \rho V^2 c_w s_w^2$, $\alpha = 0.85$ and each surface will have its own deflection angle β_1, β_2 and set of aerodynamic parameters a_C, b_C, which are the rates of change of lift coefficient and moment coefficient, respectively, with respect to control surface deflection angle.

A cubic hardening nonlinearity is assumed in the torsional spring connecting the pylon-engine to the wing. The nonlinear force developed in the spring may be expressed as

$$f_{\mathrm{nl}} = K_T \vartheta_{\mathrm{pe}}^3, \tag{A.2}$$

where K_T is the stiffness coefficient of the cubic nonlinearity. The overall nonlinear force vector then takes the form

$$\mathbf{f}_{\mathrm{nl}} = \mathbf{T}^T \begin{pmatrix} 0 \\ 0 \\ f_{\mathrm{nl}} \end{pmatrix} = \begin{pmatrix} 0 \\ -y_2 f_{\mathrm{nl}} \\ f_{\mathrm{nl}} \end{pmatrix}, \tag{A.3}$$

with $\mathbf{T}$ defined in (18).

B. Zero Dynamics Expressions (2I2O Case)

In the 2I2O configuration and using (11),

$$\begin{Bmatrix} z_1 \\ z_2 \\ z_3 \end{Bmatrix} = \begin{bmatrix} 1 & 0 & 0 \\ 0 & 1 & 0 \\ \sigma_1 & \sigma_2 & \sigma_3 \end{bmatrix} \begin{Bmatrix} x_1 \\ x_2 \\ x_3 \end{Bmatrix}, \tag{B.1}$$

where

$$\sigma_1 = \left(g_{21}g_{32} - g_{31}g_{22}\right), \quad \sigma_2 = \left(g_{31}g_{12} - g_{11}g_{32}\right), \quad \sigma_3 = \left(g_{11}g_{22} - g_{21}g_{12}\right), \tag{B.2}$$

and g_{ij} denotes the ijth term of the matrix $\mathbf{G}$. Then, by inverting the transformation matrix $\mathbf{T}_{zx}$, the following expressions are obtained:

$$x_1 = z_1, \quad x_2 = z_2, \quad x_3 = -\frac{\sigma_1}{\sigma_3} z_1 - \frac{\sigma_2}{\sigma_3} z_2 + \frac{1}{\sigma_3} z_3. \tag{B.3}$$

Then, from (15) and differentiating the bottom row of (B.1) it is found that

$$\ddot{z}_3 = \boldsymbol{\sigma}^T \mathbf{f}\left(\mathbf{z}, \dot{\mathbf{z}}\right), \quad \boldsymbol{\sigma}^T = \left\{\sigma_1 \;\; \sigma_2 \;\; \sigma_3\right\}, \tag{B.4}$$

where

$$\begin{aligned} \mathbf{f}\left(\mathbf{z}, \dot{\mathbf{z}}\right) = {} & \boldsymbol{\Phi}\left\{\dot{z}_1 \;\; \dot{z}_2 \;\; \left(-\frac{\sigma_1}{\sigma_3}\dot{z}_1 - \frac{\sigma_2}{\sigma_3}\dot{z}_2 + \frac{1}{\sigma_3}\dot{z}_3\right)\right\}^T \\ & + \boldsymbol{\Psi}\left\{z_1 \;\; z_2 \;\; \left(-\frac{\sigma_1}{\sigma_3} z_1 - \frac{\sigma_2}{\sigma_3} z_2 + \frac{1}{\sigma_3} z_3\right)\right\}^T \\ & + \boldsymbol{\Omega}\, \mathbf{f}_{\mathrm{nl}}\left(\mathbf{z}\right), \end{aligned} \tag{B.5}$$

$$\mathbf{f}_{\mathrm{nl}}\left(\mathbf{z}\right) = K_T\left(-y_2 z_2 + \left(-\frac{\sigma_1}{\sigma_3} z_1 - \frac{\sigma_2}{\sigma_3} z_2 + \frac{1}{\sigma_3} z_3\right)\right)^3 \times \left(\mathbf{T}_{(3,:)}\right)^T.$$

Evidently, the internal dynamics expressions in (B.4) are nonlinear. Now, the zero dynamics may be obtained by setting to zero the coordinates corresponding to the external dynamics (i.e. the partially linearised system). In this case, the external coordinates are z_1, z_2, $\dot{z}_1$, $\dot{z}_2$ so that the zero dynamics are given by

$$\begin{aligned} \ddot{z}_{3,zd} = {} & \frac{1}{\sigma_3}\boldsymbol{\sigma}^T \boldsymbol{\Psi}_{(:,3)} z_{3,zd} + \frac{1}{\sigma_3}\boldsymbol{\sigma}^T \boldsymbol{\Phi}_{(:,3)} \dot{z}_{3,zd} \\ & + \frac{1}{\sigma_3^3} K_T \boldsymbol{\sigma}^T \boldsymbol{\Omega}\left(\mathbf{T}_{(3,:)}\right)^T z_{3,zd}^3, \end{aligned} \tag{B.6}$$

where the subscript "zd" signifies that the coordinates are specified under zero dynamics conditions.

Zero Dynamics Equilibrium Point Analysis. To obtain the equilibrium points of the zero dynamics, it is necessary to set $\ddot{z}_{3,zd} = \dot{z}_{3,zd} = 0$. Equation (B.6) then produces

$$\left(\boldsymbol{\sigma}^T \boldsymbol{\Psi}_{(:,3)} + K_T \boldsymbol{\sigma}^T \boldsymbol{\Omega}\left(\mathbf{T}_{(3,:)}\right)^T z_{3,zd}^2\right) z_{3,zd} = 0, \tag{B.7}$$

which provides the two solutions

$$z_{3,zd} = 0, \quad z_{3,zd} = \pm\sqrt{-\frac{\boldsymbol{\sigma}^T \boldsymbol{\Psi}_{(:,3)}}{K_T \boldsymbol{\sigma}^T \boldsymbol{\Omega}\left(\mathbf{T}_{(3,:)}\right)^T}}. \tag{B.8}$$

It is found that the term inside the square root is always negative, and therefore the second solution for $z_{3,zd}$ is inadmissible. Thus, the only possible equilibrium point of the zero dynamics is the trivial solution

$$\begin{Bmatrix} z_3 \\ \dot{z}_3 \end{Bmatrix}_{zd} = \begin{Bmatrix} 0 \\ 0 \end{Bmatrix}. \tag{B.9}$$

The nature of the above equilibrium point may be determined by examining the eigenvalues of (B.6), evaluated at the equilibrium point,

$$s^2 - \frac{1}{\sigma_3}\boldsymbol{\sigma}^T\boldsymbol{\Phi}_{(:,3)}s - \frac{1}{\sigma_3}\boldsymbol{\sigma}^T\boldsymbol{\Psi}_{(:,3)} - \frac{1}{\sigma_3^3}K_T\boldsymbol{\sigma}^T\boldsymbol{\Omega}\left(\mathbf{T}_{(3,:)}\right)^T z_{3,zd}^2 \Big|_{\substack{z_{3,zd}=0 \\ \dot{z}_{3,zd}=0}} = 0, \tag{B.10}$$

or

$$s^2 - \frac{1}{\sigma_3}\boldsymbol{\sigma}^T\boldsymbol{\Phi}_{(:,3)}s - \frac{1}{\sigma_3}\boldsymbol{\sigma}^T\boldsymbol{\Psi}_{(:,3)} = 0. \tag{B.11}$$

The roots are found to be complex with negative real parts, thus revealing the type of equilibrium point to be a stable focus.

Conflict of Interests

The authors declare that there is no conflict of interests regarding the publication of this paper.

Acknowledgment

The authors wish to acknowledge the support of EPSRC Grant no. EP/J004987/1 on Nonlinear Active Vibration Suppression in Aeroelasticity.

References

[1] A. Isidori, *Nonlinear Control Systems*, Springer, New York, NY, USA, 1995.

[2] T. I. Fossen and M. J. Paulsen, "Adaptive feedback linearization applied to steering of ships," *Modeling, Identification and Control*, vol. 14, no. 4, pp. 229–237, 1993.

[3] J. Ko, A. J. Kurdila, and T. W. Strganac, "Nonlinear control of a prototypical wing section with torsional nonlinearity," *Journal of Guidance, Control, and Dynamics*, vol. 20, no. 6, pp. 1181–1189, 1997.

[4] J. Ko, A. J. Kurdila, and T. Strganac, "Stability and control of a structurally nonlinear aeroelastic system," *Journal of Guidance, Control, and Dynamics*, vol. 21, no. 5, pp. 718–725, 1998.

[5] J. Ko, T. W. Strganac, and A. J. Kurdila, "Adaptive feedback linearization for the control of a typical wing section with structural nonlinearity," *Nonlinear Dynamics*, vol. 18, no. 3, pp. 289–301, 1999.

[6] M. M. Monahemi and M. Krstic, "Control of wing rock motion using adaptive feedback linearization," *Journal of Guidance, Control, and Dynamics*, vol. 19, no. 4, pp. 905–912, 1996.

[7] A. Poursamad, "Adaptive feedback linearization control of antilock braking systems using neural networks," *Mechatronics*, vol. 19, no. 5, pp. 767–773, 2009.

[8] C. P. Bechlioulis and G. A. Rovithakis, "Robust adaptive control of feedback linearizable MIMO nonlinear systems with prescribed performance," *IEEE Transactions on Automatic Control*, vol. 53, no. 9, pp. 2090–2099, 2008.

[9] K. Shojaei, A. Mohammad Shahri, and A. Tarakameh, "Adaptive feedback linearizing control of nonholonomic wheeled mobile robots in presence of parametric and nonparametric uncertainties," *Robotics and Computer-Integrated Manufacturing*, vol. 27, no. 1, pp. 194–204, 2011.

[10] L. Tuan, S.-G. Lee, V.-H. Dang, S. Moon, and B. Kim, "Partial feedback linearization control of a three-dimensional overhead crane," *International Journal of Control, Automation and Systems*, vol. 11, no. 4, pp. 718–727, 2013.

[11] Y. M. Ram and J. E. Mottershead, "Multiple-input active vibration control by partial pole placement using the method of receptances," *Mechanical Systems and Signal Processing*, vol. 40, no. 2, pp. 727–735, 2013.

[12] J. R. Wright and J. E. Cooper, *Introduction to Aircraft Aeroelasticity and Loads*, Wiley, Chichester, UK, 2007.

[13] S. Jiffri, J. E. Mottershead, and J. E. Cooper, "Adaptive feedback linearisation and control of a flexible aircraft wing," in *Topics in Modal Analysis, Volume 7*, Conference Proceedings of the Society for Experimental Mechanics Series, Springer, 2013.

[14] http://www.airbus.com/aircraftfamilies/passengeraircraft/a330family/a330-200/specifications/.

[15] D. P. Atherton, *Stability of Nonlinear Systems*, John Wiley & Sons, New York, NY, USA, 1981.

Hindawi Publishing Corporation
Shock and Vibration
Volume 2014, Article ID 173786, 8 pages
http://dx.doi.org/10.1155/2014/173786

Research Article

Structural Synthesis for Prescribed Target Natural Frequencies and Mode Shapes

J. A. Hernandes[1] and A. Suleman[2]

[1] *Instituto Tecnológico de Aeronáutica, 12228-900 São José dos Campos, SP, Brazil*
[2] *Department of Mechanical Engineering, University of Victoria, Victoria, BC, Canada*

Correspondence should be addressed to J. A. Hernandes; hernandes@ita.br

Received 8 August 2013; Accepted 7 February 2014; Published 4 June 2014

Academic Editor: Miguel M. Neves

Copyright © 2014 J. A. Hernandes and A. Suleman. This is an open access article distributed under the Creative Commons Attribution License, which permits unrestricted use, distribution, and reproduction in any medium, provided the original work is properly cited.

A new method for the synthesis of structures with prescribed target natural frequencies and mode shapes is presented. The introduction of a modal Rayleigh quotient approximation based on the target mode shapes is the means to propose a structural synthesis problem whose solution is free from eigenvector sensitivity analysis. The frequencies and mode shapes can be adjusted as close as possible to the desired target values, while minimizing the total mass. Several examples corroborate the efficacy of the proposed method.

1. Introduction

Optimization of dynamic systems is an inverse eigenvalue problem with the goal of tailoring the response of a system by estimating the needed change in the design variables to achieve a desired change in the natural frequencies of the structure. The structural synthesis with the inclusion of inequality frequency constraints has been extensively explored in the past in many different works reported in the literature [1]; however the need remains to create an effective method to include not only prescribed frequencies but also prescribed mode shapes in the optimization process. There are important instances where the adjusting of frequencies and mode shapes to given prescribed values is desirable, such as the synthesis of aircraft under aeroelastic constraints or model updating, where an analytical or numerical model is improved based on modal test data [2, 3].

Structural design tailoring applied to simple mass and spring systems has been extensively reported in the literature. For instance, Yee and Tsuei [4, 5] have proposed methods of shifting the desired eigenfrequencies using the forced response of the system and modal analysis. Mass matrix modification has been proposed to achieve desired natural frequencies [6] while the use of concentrated mass elements to shift eigenfrequencies of a rectangular plate has been proposed in [7]. Sivan and Ram [8] have used orthogonality principles to obtain modified stiffness and mass matrices. Gladwell [9] introduced an inverse approach for both the discrete and continuous structures. Mottershead [10] has investigated the concept of resonance and adding mass or springs to the dynamic system.

In other related researches, studies have been reported on the simultaneous assignment of mode frequency and shape, by developing approaches based on both modal data [11] and system physical models [12]. Examples include the assignment of natural frequencies to a multi-degree-of-freedom undamped system using an added mass connected by springs [13], the assignment of natural frequencies and antiresonances by beam modification [14], and the structural modification of a helicopter tail cone [15]. Gladwell and Movahhedy [16] obtained the set of necessary and sufficient conditions to ensure positive mass and stiffness parameters for a three-degree-of-freedom case study.

In Richiedei et al. [17], a convex optimization approach is proposed. A linear matrix difference equation is set based on satisfying the Rayleigh quotient using linearizations of the system stiffness and mass matrices in terms of the design variables. The residual of the resulting system of linear equations

in the design variables is then used to form a convex objective function. The method can deal with general finite element models and has no need of eigenvector sensitivities but is limited in the context of structural synthesis, since it is indifferent to the structural and nonstructural mass mobilized in the solution, thus presenting a difficulty of integration with a general structural synthesis tool; besides it can only deal with linear constraints.

Although it may be immediate to write the statement of an optimization problem where the mode shapes are prescribed, the solution of such a problem may not be an easy task, since directional optimization demands eigenvector sensitivity analysis, which is expensive. Also, and perhaps mainly, numerical difficulties may arise due to complex modal structural behavior of the system, a common feature of many real life finite element discretizations.

A theoretically consistent method for the structural synthesis with prescribed target frequencies and mode shapes seems to be inexistent in literature. If such a method could avoid the use of expensive eigenvector sensitivity analysis, it might be used with great advantage. The objective of the present work is to create an effective method with strong convergence capability for the structural synthesis of general systems with prescribed target free vibration natural frequencies ($\overline{\omega}_j$, $j = 1, \ldots, p$) and mode shapes ($\overline{\boldsymbol{\varphi}}_j$, $j = 1, \ldots, p$), without the use of eigenvector sensitivities. While it is not mandatory, it is also desirable for the structure to have minimum mass.

2. Synthesis Based on Modal Rayleigh Quotient Approximation

The natural free vibration eigenproblem for a discrete system can be written as follows:

$$\left(\mathbf{K} - \lambda_j \mathbf{M}\right) \boldsymbol{\varphi}_j = \mathbf{0} \quad j = 1, \ldots, n, \tag{1}$$

where $\lambda_j = \omega_j^2$ is the eigenvalue corresponding to the natural frequency ω_j. The natural frequencies are related to corresponding mode shapes by means of the Rayleigh quotient, such that

$$\lambda_j = \omega_j^2 = \frac{\boldsymbol{\varphi}_j^T \mathbf{K} \boldsymbol{\varphi}_j}{\boldsymbol{\varphi}_j^T \mathbf{M} \boldsymbol{\varphi}_j} \quad j = 1, \ldots, n. \tag{2}$$

The Rayleigh quotient is classically used to approximate the fundamental frequency of a system and also in algorithms for solution of eigenproblems.

In this work there are s prescribed pairs of target natural frequencies and mode shapes, $(\overline{\omega}_j, \overline{\boldsymbol{\varphi}}_j)$, that are to be imposed on the structure. Therefore, we seek an optimal solution $\mathbf{x}^*$ that will satisfy

$$\left(\mathbf{K}^* - \overline{\lambda}_j \mathbf{M}^*\right) \overline{\boldsymbol{\varphi}}_j = \mathbf{0} \quad j = 1, \ldots, s, \tag{3}$$

where the eigenvalue $\overline{\lambda}_j = \overline{\omega}_j^2$. The target eigenvalues are related to the target mode shapes by the Rayleigh quotient:

$$\overline{\lambda}_j = \frac{\overline{\boldsymbol{\varphi}}_j^T \mathbf{K}^* \overline{\boldsymbol{\varphi}}_j}{\overline{\boldsymbol{\varphi}}_j^T \mathbf{M}^* \overline{\boldsymbol{\varphi}}_j} \quad j = 1, \ldots, s. \tag{4}$$

The symbol * indicates that the stiffness and mass matrices are computed at the optimal solution. It may be possible to satisfy (3) and (4) if we have the appropriate parameters or design variables to adjust in the system we are dealing with.

We define a modal Rayleigh quotient approximation (MRQA), based on the target mode shapes and the current structural stiffness and mass as follows:

$$\mu_j = \frac{\overline{\boldsymbol{\varphi}}_j^T \mathbf{K} \overline{\boldsymbol{\varphi}}_j}{\overline{\boldsymbol{\varphi}}_j^T \mathbf{M} \overline{\boldsymbol{\varphi}}_j} \quad j = 1, \ldots, s. \tag{5}$$

The MRQA quantifies the approximation to the target mode shape $\overline{\boldsymbol{\varphi}}_j$ at the current design, where $\mathbf{K}$ and $\mathbf{M}$ are supposedly calculated. This quantity has in it a great deal of the dynamical structural behavior of the system and can be very helpful.

The MRQA can be used to define the following first statement of our synthesis problem, where we want to generate a structure that will have its eigenvalues and mode shapes the closest possible to the prescribed target pairs $(\overline{\lambda}_j, \overline{\boldsymbol{\varphi}}_j)$, $j = 1, \ldots, s$ as follows:

$$\min \quad \sum_{j=1}^{p} \left\{ a_j \left(\mu_j - \overline{\lambda}_j\right)^2 + b_j \left(\lambda_j - \overline{\lambda}_j\right)^2 \right\}. \tag{6}$$

$$\text{s.t.} \quad \mu_j = \frac{\overline{\boldsymbol{\varphi}}_j^T \mathbf{K} \overline{\boldsymbol{\varphi}}_j}{\overline{\boldsymbol{\varphi}}_j^T \mathbf{M} \overline{\boldsymbol{\varphi}}_j} \quad j = 1, \ldots, s, \tag{7}$$

$$\left(\mathbf{K} - \lambda_j \mathbf{M}\right) \boldsymbol{\varphi}_j = \mathbf{0} \quad j = 1, \ldots, s. \tag{8}$$

The objective function contains the residuals between the target frequency eigenvalues $(\overline{\lambda}_j)$ with both the eigenvalues associated to the system natural frequencies (λ_j) and the MRQA (μ_j). The a_j and b_j are adequate weighting factors. In the synthesis defined by (6)–(8) we will adjust the design variables and thus the stiffness and mass matrices, such that μ_j and λ_j will both converge to the natural prescribed target frequency eigenvalues, $\overline{\lambda}_j$. For instance, admitting that during the optimization iterations the MRQA will converge to the target frequency eigenvalue ($\mu_j \to \overline{\lambda}_j$) implies that the mode shape will also converge to $\overline{\boldsymbol{\varphi}}_j$; that is, we will have $\boldsymbol{\varphi}_j \to \overline{\boldsymbol{\varphi}}_j$.

The problem above is well posed in the sense that it will have a high probability of producing a solution which is the best possible in fulfilling the specified frequencies and mode shapes, but it has no mention of limiting the structural or nonstructural mass mobilized during the solution, and so a probability exists such that a nonoptimal structure in terms of mass and structural weight can be created. Limiting the masses could be an alternative to be exploited, but for now this will be left as an open issue.

The problem statement can be modified with the inclusion of a term containing the structural and nonstructural masses in the objective function so that we can synthesize a system that best fits the prescribed target frequencies and mode shapes but does it with minimum expending of mass. The following new augmented statement of the problem is then proposed with the inclusion of the mass (M) in the

Table 1: Target frequencies (Case 1).

Mode	$\overline{\lambda}_j = \overline{\omega}_j^2$	$\overline{f}_j$ (Hz)
1	425.2	3.28
2	8396.6	14.58
3	47992.1	34.87

Table 2: Target mode shapes (Case 1).

Mode 1	0.000	0.330	0.622	0.842	0.971	1.000	0.930	0.776	0.555	0.289	0.000
Mode 2	0.000	0.437	0.625	0.408	−0.070	−0.576	−0.918	−1.000	−0.833	−0.469	0.000
Mode 3	0.000	0.228	0.197	−0.182	−0.454	−0.189	0.411	0.897	1.000	0.644	0.000

objective function and also range constraints for the frequencies eigenvalues and the MRQAs:

$$\min \quad M + \sum_{j=1}^{p} \left\{ a_j \left(\mu_j - \overline{\omega}_j^2 \right)^2 + b_j \left(\lambda_j - \overline{\omega}_j^2 \right)^2 \right\}, \tag{9}$$

$$\text{s.t.} \quad p\overline{\omega}_j^2 \le \lambda_j \le q\overline{\omega}_j^2 \quad j = 1, \ldots, s, \tag{10}$$

$$p\overline{\omega}_j^2 \le \mu_j \le q\overline{\omega}_j^2 \quad j = 1, \ldots, s, \tag{11}$$

$$\mu_j = \frac{\overline{\boldsymbol{\varphi}}_j^T \mathbf{K} \overline{\boldsymbol{\varphi}}_j}{\overline{\boldsymbol{\varphi}}_j^T \mathbf{M} \overline{\boldsymbol{\varphi}}_j} \quad j = 1, \ldots, s, \tag{12}$$

$$\left(\mathbf{K} - \lambda_j \mathbf{M} \right) \boldsymbol{\varphi}_j = \mathbf{0} \quad j = 1, \ldots, s. \tag{13}$$

The use of the mass augmented objective function of (9) instead of (6) may lead to a compromise solution in which the system mass is minimized but the adjustment between the frequencies and mode shapes to their prescribed values may not be the best. Thus, the range constraints are added ((10)-(11)) so that the problem statement is now given by (9)–(13). Range constraints are used instead of strict equality constraints for two reasons. Firstly, satisfaction of equality of frequencies and mode shapes to their prescribed target values may not be possible depending on the design variables used for the synthesis [3]. Also, because the numerical optimization solution tends to be harder for strict equality constraints, even for the case where they are realizable. Here the multipliers $p \le 1$ and $q \ge 1$ are parameters defining the ranges; for example, $p = 1 - \delta$ and $q = 1 + \delta$, where δ is adjusted during the optimization, departing from say $\delta = 0.1$, and closing the range with say $\delta = 0.0001$. Experience with simple cases now shows that good solutions can be obtained adjusting the ranges smoothly, by means of solving a sequential optimization with decreasing ranges such that in the ith optimization problem $\delta^{(i)} = r\,\delta^{(i-1)}$, where $r < 1$; for example, $0.1 \le r \le 0.5$. Because of the new constraints we can choose the weights a_j and b_j to be null, so defining a cleaner mass-only objective function.

3. Simply Supported Beam

A simply supported beam of length L, with rectangular cross section (b, h), is shown in Figure 1. It has five concentrated masses which are design variables, positioned along its centroidal axis. Also the beam depth, h, is a design variable. The beam behavior includes just in-plane bending which obeys the Euler-Bernoulli theory, without rotary inertia effects. The beam natural free vibration analysis is done by the Rayleigh-Ritz method, using a sine series for the deflections with ten terms. The length of the beam is $L = 5$ m, the modulus of elasticity is $E = 70$ Pa, and the material density is $\rho = 2500\ \text{kg/m}^3$.

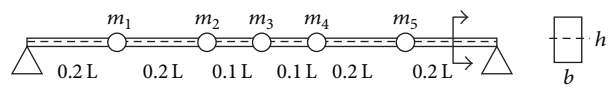

Figure 1: Beam with concentrated masses.

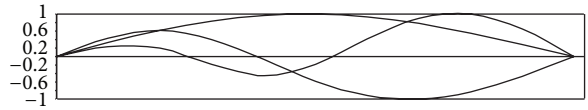

Figure 2: Target mode shapes (Case 1).

To optimize the beam for minimum total mass, we have six design variables (h, m_1, m_2, m_3, m_4, m_5). Three study cases are defined which differ from each other mainly due to the prescribed target values of frequencies and mode shapes.

3.1. Case 1. In this case the beam section width is $b = 50$ mm. The target values of frequencies are those in Table 1, while Table 2 has the target mode shapes.

The frequencies and mode shapes of Tables 1 and 2 were chosen to be the same that can be obtained when the beam has the following properties: $h = 0.2$ m, $m_1 = 200$ kg, $m_2 = 90$ kg, $m_3 = 50$ kg, $m_4 = 30$ kg, and $m_5 = 10$ kg; this will be called the reference design.

The target mode shapes are illustrated in Figure 2, where a tendency to symmetry of mode 1 exists while modes 2 and 3 are a mix of symmetric and antisymmetric parts, making the structural synthesis problem harder when compared to a case with only purely symmetric or antisymmetric modes.

The optimization problem is defined by (9)–(13); however we use the simpler objective function corresponding to mass minimization only, that is, with $a_j = b_j = 0$, $j = 1, \ldots, 3$. A sequential optimization solution was implemented with

Table 3: Optimal design variables (Case 1).

h (m)	Mass	1	2	3	4	5
0.075	(kg)	77.61	34.07	20.11	9.89	0.00

Table 4: Optimal frequencies and MRQA (Case 1).

Mode	$\overline{\omega}_j^2$	λ_j	% Error	μ_j	% Error
1	425.2	425.2	0.01	425.2	0.01
2	8396.6	8397.5	0.01	8395.8	0.01
3	47992.1	47987.3	0.01	47996.9	0.01

Table 5: Optimal mode shapes (Case 1).

1st mode	0.000	0.329	0.620	0.840	0.970	1.000	0.931	0.776	0.555	0.289	0.000
2nd mode	0.000	0.442	0.635	0.424	−0.053	−0.564	−0.912	−1.000	−0.834	−0.471	0.000
3rd mode	0.000	0.243	0.210	−0.182	−0.467	−0.205	0.406	0.902	1.000	0.647	0.000

Table 6: Sequential optimization iteration history (Case 1).

(a)

Iter.	p	q	M (kg)	Max g_λ	Max g_μ
0	0.5	2	1125.	$5.4E-01$	$4.3E-01$
1	0.5	2	23.59	$-3.9E-01$	$1.3E-06$
2	0.95	1.1	77.70	$5.9E-08$	$2.3E-08$
3	0.99	1.01	130.31	$4.2E-08$	$5.4E-10$
4	0.999	1.001	167.60	$2.5E-09$	$4.9E-09$
5	0.9999	1.0001	188.46	$8.7E-10$	$9.0E-10$

(b)

Iter.	h (m)	m_1 (kg)	m_2 (kg)	m_3 (kg)	m_4 (kg)	m_5 (kg)	$\sum m_j$ (kg)
0	0.2000	200	200	200	200	200	1000
1	0.038	0.00	0.00	0.00	0.00	0.00	0.00
2	0.058	18.31	1.01	17.78	4.49	0.00	41.59
3	0.067	46.32	14.34	24.54	3.46	0.00	88.67
4	0.072	66.70	27.11	21.76	7.01	0.00	122.58
5	0.075	77.61	34.07	20.11	9.89	0.00	141.68

varying p and q, having the iteration history presented in Table 6, which will be discussed later.

The optimal values of the six design variables used to minimize the mass and satisfy the target frequencies and mode shapes are presented in Table 3 and correspond to the total mass of 188.46 kg, from which 141.68 kg is made of concentrated masses. The optimal beam has a depth of 0.075 m. The optimal solution is remarkable from the point of view of reduction of the structural and nonstructural masses, when compared to the reference design where the beam depth is 0.020 m and the nonstructural mass is 380 kg.

Table 4 has the eigenvalues (λ_j) and the values of the MRQA (μ_j) obtained for the optimal design, where an almost perfect matching is seen with the target values $\overline{\omega}_j^2$, with deviations around only 0.01%.

Table 5 presents the optimal mode shapes obtained, having a very close agreement with the target modes of Table 2.

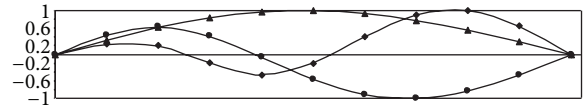

Figure 3: Optimal and target mode shapes (Case 1).

This could be anticipated from the closeness between the MRQA (μ_j) and $\overline{\omega}_j^2$ of Table 4. As a matter of fact, the possibility of achieving this matching is the basis of the solution proposed in this work.

The excellent agreement between optimal and target mode shapes can be seen from Figure 3. The optimal mode shape curves which are marked and the target unmarked can barely be distinguished one from the other.

Table 7: Target frequencies (Case 2).

Mode	$\overline{\lambda}_j = \overline{\omega}_j^2$	$\overline{f}_j$ (Hz)
1	121.97	1.76
2	2569.53	8.08
3	10350.41	16.19

Table 8: Target mode shapes (Case 2).

Mode 1	0.000	0.319	0.605	0.827	0.963	1.000	0.937	0.786	0.565	0.295	0.000
Mode 2	0.000	0.461	0.707	0.594	0.191	−0.339	−0.790	−1.000	−0.910	−0.536	0.000
Mode 3	0.000	0.522	0.611	0.082	−0.492	−0.488	0.050	0.697	1.000	0.697	0.000

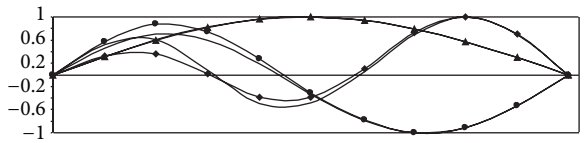

Figure 4: Optimal and target mode shapes (Case 2A).

It is instructive to look at Table 6 with the nice optimization iteration history. Each one of the five iterations corresponds to given values of the constraints range parameters p and q, which were quickly found by trial and error. The second row has the initial design and from the third row on the optimal results after the optimization for the corresponding p and q parameters. The total mass presented in the fourth column of Table 6 decays in the first iteration and then grows rapidly with the tightening of p and q. The optimization behavior was excellent, allowing the use of rapidly decreasing constraint ranges. Furthermore, the optimization would fail if the tightening of p and q was very sharp or the starting values of p and q were too tight. In the fifth column the maximum constraint violation for the constraints in normalized form of (10) is presented as follows:

$$\max\ g_\lambda = \max\left(1 - \frac{\lambda_j}{p\overline{\omega}_j^2}, -1 + \frac{\lambda_j}{q\overline{\omega}_j^2}\right). \tag{14}$$

Similarly results of the 6th column correspond to (11). The constraints are always satisfied at the optimum of every iteration. The second row of Table 6 has the initial design (iter = 0), with a constraint violation of 54% associated with $p = 0.5$ and $q = 2.0$, the values used to solve the first iteration, at the end of which the constraints became satisfied (iter = 1). The solution was obtained with the Solver in Excel.

In the solution presented, the adjustable range constraints were very effective, leading to results as if equality constraints had been imposed, corresponding to $\delta = 0.0001$.

3.2. Case 2. Here $b = 0.03$ m and the target frequencies are smaller, given in Table 7, with the target mode shapes of Table 8.

The values from Tables 7 and 8 can be obtained from the ref-erence design: $h = 0.05$ m, $m_1 = m_2 = 30$ kg, and $m_3 = m_4 = m_5 = 10$ kg.

Table 9: Optimal design variables results (Case 2A).

h (m)	Masses	1	2	3	4	5	$\sum m_j$
0.030	(kg)	5.50	1.32	5.80	0.02	0.67	13.31

Table 10: Optimal frequencies and MRQA (Case 2A).

Mode	$\overline{\omega}_j^2$	λ_j	% Error	μ_j	% Error
1	121.97	124.1	1.8	124.2	1.9
2	2569.5	2572.4	0.1	2564.6	−0.2
3	10350.4	10345.2	−0.1	10363.2	0.1

The problem of (9)–(13) has the same six design variables of Case 1. The beam depth is constrained, with $h \geq 0.03$ m. This time both solutions are going to be examined: without (Case 2A) and with (Case 2B) the range constraints.

For the case without range constraints, we use the weights $a_j = b_j = 1/(\overline{\omega}_j^2)$. The optimum design, obtained using the same initial design of Case 1, is given in Table 9.

The optimal frequencies and MRQA obtained in this run are given in Table 10, showing a very satisfactory agreement between the target $\overline{\omega}_j^2$ and the optimal values of λ_j and μ_j, with errors smaller than 2%.

The optimal mode shapes for the case without range constraints are given in Table 11.

In Figure 4 the optimal mode shapes are depicted in the curves with marks against the unmarked curves of target modes shapes. We can see that the matching is reasonable but not perfect.

The optimal solution for Case 2B with range constraints is given in Table 12. It was obtained using as initial design the solution of Case 2A and the range constraints with $\delta = 0.0001$. As can be observed the solution is very distinct from the one in Table 9 in terms of the design variables values. Besides, the total optimal nonstructural mass is considerably bigger now.

The optimal frequencies and MRQA are given in Table 13, showing an almost perfect matching between the target $\overline{\omega}_j^2$ and the optimal values of λ_j and μ_j. The comparison between Tables 10 and 13 shows that in Case 2B the solution is considerably more precise.

The optimal mode shapes given in Table 14 and depicted in Figure 5 have a close agreement with the target values of

Table 11: Optimal mode shapes (Case 2A).

1st mode	0.000	0.315	0.598	0.819	0.958	1.000	0.940	0.791	0.569	0.297	0.000
2nd mode	0.000	0.576	0.880	0.745	0.273	−0.314	−0.784	−1.000	−0.910	−0.537	0.000
3rd mode	0.000	0.329	0.368	0.016	−0.382	−0.392	0.108	0.729	1.000	0.700	0.000

Table 12: Optimal design variables results (Case 2B).

h (m)	Masses	1	2	3	4	5	$\sum m_j$
0.0333	(kg)	7.83	5.24	5.34	1.09	1.50	21.00

Table 13: Optimal frequencies and MRQA (Case 2B).

Mode	$\overline{\omega}_j^2$	λ_j	% Error	μ_j	% Error
1	121.97	121.96	0.01	121.98	0.01
2	2569.5	2569.3	0.01	2569.8	0.01
3	10350.4	10349.4	0.01	10350.4	0.01

Table 14: Optimal mode shapes (Case 2B).

1st mode	0.000	0.317	0.602	0.823	0.961	1.000	0.938	0.788	0.567	0.296	0.000
2nd mode	0.000	0.510	0.780	0.656	0.222	−0.333	−0.790	−1.000	−0.908	−0.535	0.000
3rd mode	0.000	0.419	0.479	0.046	−0.432	−0.433	0.088	0.719	1.000	0.699	0.000

Table 15: Target frequencies (Case 3).

Mode	$\overline{\lambda}_j = \overline{\omega}_j^2$	$\overline{f}_j$ (Hz)
1	157.91	2
2	1934.44	7
3	8300.34	14.5

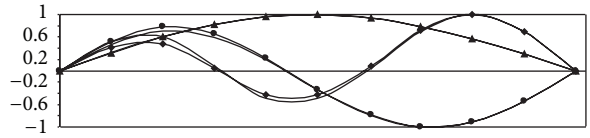

Figure 5: Optimal and target mode shapes (Case 2B).

Table 8. It is worth comparing Figure 5, from the case with range constraints, with Figure 4, from the case without them. It is clear that the solution with range constraints results in better adjusted mode shapes.

3.3. Case 3. Now the beam has the same target mode shapes of Case 2 (see Table 8) but different target frequencies according to Table 15.

The target frequencies were set trying to make Case 3 harder than Case 2. This was done by keeping the same target mode shapes of Case 2 but imposing target frequencies which are not scalable from Case 2. With this in mind, Table 15 was created looking at Table 7 and doing the following: increasing the first target frequency from 1.76 Hz to 2 Hz, decreasing the second target frequency from 8.08 Hz to 7 Hz, and decreasing the third from 16.19 Hz to 14.5 Hz.

The optimization now was done by adjusting the parameters p and q, resulting in the iterations shown in Table 16. The parameters could be decreased up to a corresponding $\delta = 0.03$; values below this would not produce a feasible solution. The values of $p = 1 - \delta$ and $q = 1 + \delta$ used to solve the sequential optimization are given, with the remark that for iter $= 0$ the values have only the purpose of computing the maximum constraint violations in the initial design.

Table 17 shows that the eigenvalues and the MRQAs for the optimal design could be reasonably adjusted to the target values, with a maximum error of 3%.

The mode shapes also were satisfactorily adjusted as Table 18 shows, when compared to the target values of Table 8.

In Figure 6 continuous lines are the prescribed target mode shapes and the lines with marks are the optimal mode shapes. The first mode is practically the same of the target mode; the second mode seems to be a better fitting to the prescribed target mode than is the third mode. This is the case where to obtain a better adjusting for the second and third modes more design variables would be necessary, such as additional point masses or eventually a beam with variable

Table 16: Sequential optimization iteration history (Case 3).

(a)

Iter	p	q	M (kg)	Max g_λ	Max g_μ
0	0.9	1.1	108.75	$2.08E-01$	$2.08E-01$
1	0.9	1.1	23.03	$4.95E-08$	$-4.44E-02$
2	0.95	1.05	24.03	$1.59E-08$	$-2.70E-12$
3	0.97	1.03	186.09	$1.94E-08$	$-7.50E-10$

(b)

Iter	h (m)	m_1 (kg)	m_2 (kg)	m_3 (kg)	m_4 (kg)	m_5 (kg)	$\sum m_j$ (kg)
0	0.0500	30.0	30.0	10.0	10.0	10.0	90.0
1	0.0300	4.46	0.00	2.87	0.000	4.45	11.78
2	0.0300	5.58	0.00	3.12	0.000	4.08	12.78
3	0.0606	74.21	0.00	37.31	11.64	40.23	163.38

Table 17: Optimal frequencies and MRQA (Case 3).

Mode	$\overline{\omega}_j^2$	λ_j	% Error	μ_j	% Error
1	157.9	153.2	3.0	153.9	2.5
2	1934.4	1992.5	3.0	1969.0	1.8
3	8300.3	8549.4	3.0	8051.3	3.0

Table 18: Optimal mode shapes (Case 3).

Mode 1	0.000	0.318	0.601	0.818	0.955	1.000	0.947	0.803	0.583	0.306	0.000
Mode 2	0.000	0.587	0.909	0.792	0.346	−0.224	−0.722	−1.000	−0.961	−0.580	0.000
Mode 3	0.000	0.397	0.430	−0.080	−0.737	−0.970	−0.455	0.435	1.000	0.763	0.000

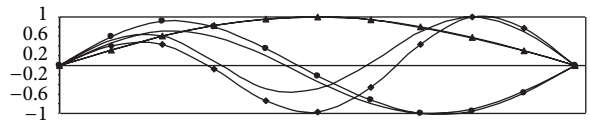

Figure 6: Optimal and target mode shapes (Case 3)

depth. However, the important emphasis here is that this result is expected to be very close to the best possible approximate solution for the problem using the same six design variables used for the solution presented.

4. Concluding Remarks

A new method that is theoretically consistent was presented for the synthesis of structures with prescribed target frequencies and mode shapes. It avoids the use of eigenvector sensitivity and seems to have excellent convergence potential. Its application to a simple beamled to very encouraging results. It must be tested in more complex synthesis problems for mode and frequency adjusting, where we anticipate that it will provide significant advantages compared to many methods presented in the literature.

Conflict of Interests

The authors declare that there is no conflict of interests regarding the publication of this paper.

Acknowledgment

The authors express their gratitude to the Coordenação de Aperfeiçoamento de Pessoal de Nível Superior.

References

[1] R. A. Canfield, "High-quality approximation of eigenvalues in structural optimization," *AIAA Journal*, vol. 28, no. 6, pp. 1116–1122, 1990.

[2] V. L. Bond, R. A. Canfield, A. Suleman, and M. Blair, "Aeroelastic scaling of a joined wing for nonlinear geometric stiffness," *AIAA Journal*, vol. 50, no. 3, pp. 513–522, 2012.

[3] G. M. L. Gladwell, *Inverse Problems in Vibration*, Martinus Noordhoff, 1986.

[4] E. K. L. Yee and Y. G. Tsuei, "Method for shifting natural frequencies of damped mechanical systems," *AIAA journal*, vol. 29, no. 11, pp. 1973–1977, 1991.

[5] E. K. L. Yee and Y. G. Tsuei, "Modification of stiffness for shifting natural frequencies of damped mechanical systems," in *Proceedings of the ASME Design Technical Conference presented at the 13th Biennial Conference on Mechanical Vibration and Noise*, vol. 38, pp. 101–106, September 1991.

[6] A. J. McMillan and A. J. Keane, "Shifting resonances from a frequency band by applying concentrated masses to a thin rectangular plate," *Journal of Sound and Vibration*, vol. 192, no. 2, pp. 549–562, 1996.

[7] K.-O. Kim, "A review of mass matrices for eigenproblems," *Journal of Computers and Structures*, vol. 46, no. 6, pp. 1041–1048, 1993.

[8] D. D. Sivan and Y. M. Ram, "Optimal construction of a mass-spring system with prescribed modal and spectral data," *Journal of Sound and Vibration*, vol. 201, no. 3, pp. 323–334, 1997.

[9] G. M. L. Gladwell, "Inverse vibration problems for finite-element models," *Inverse Problems*, vol. 13, no. 2, pp. 311–322, 1997.

[10] J. E. Mottershead, "On the zeros of structural frequency response functions and their sensitivities," *Mechanical Systems and Signal Processing*, vol. 12, no. 5, pp. 591–597, 1998.

[11] S. G. Braun and Y. M. Ram, "Modal modification of vibrating systems: some problems and their solutions," *Mechanical Systems and Signal Processing*, vol. 15, no. 1, pp. 101–119, 2001.

[12] W. Liangsheng, "Direct method of inverse eigenvalue problems for structure redesign," *Journal of Mechanical Design, Transactions of the ASME*, vol. 125, no. 4, pp. 845–847, 2003.

[13] Y. M. Ram and J. Caldwell, "Physical parameters reconstruction of a free-free mass-spring system from its spectra," *SIAM Journal on Applied Mathematics*, vol. 52, no. 1, pp. 140–152, 1992.

[14] A. Kyprianou, J. E. Mottershead, and H. Ouyang, "Structural modification. Part 2: assignment of natural frequencies and antiresonances by an added beam," *Journal of Sound and Vibration*, vol. 284, no. 1-2, pp. 267–281, 2005.

[15] J. E. Mottershead, M. Ghandchi Tehrani, D. Stancioiu, S. James, and H. Shahverdi, "Structural modification of a helicopter tailcone," *Journal of Sound and Vibration*, vol. 298, no. 1-2, pp. 366–384, 2006.

[16] G. M. L. Gladwell and M. Movahhedy, "Reconstruction of a mass-spring system from spectral data i: theory," *Inverse Problems in Engineering*, vol. 1, no. 2, pp. 179–189, 1995.

[17] D. Richiedei, A. Trevisani, and G. Zanardo, "A constrained convex approach to modal design optimization of vibrating systems," *Journal of Mechanical Design, Transactions of the ASME*, vol. 133, no. 6, Article ID 061011, 2011.

Hindawi Publishing Corporation
Shock and Vibration
Volume 2014, Article ID 502762, 11 pages
http://dx.doi.org/10.1155/2014/502762

Research Article

Wavelet-Based Frequency Response Function: Comparative Study of Input Excitation

K. Dziedziech, W. J. Staszewski, and T. Uhl

Department of Robotics and Mechatronics, Faculty of Mechanical Engineering and Robotics, AGH University of Science and Technology, Al. Mickiewicza 30, 30-059 Kraków, Poland

Correspondence should be addressed to W. J. Staszewski; w.j.staszewski@agh.edu.pl

Received 12 July 2013; Accepted 5 February 2014; Published 4 June 2014

Academic Editor: Nuno Maia

Copyright © 2014 K. Dziedziech et al. This is an open access article distributed under the Creative Commons Attribution License, which permits unrestricted use, distribution, and reproduction in any medium, provided the original work is properly cited.

Time-variant systems can be found in many areas of engineering. It is widely accepted that the classical Fourier-based methods are not suitable for the analysis and identification of such systems. The time-variant frequency response function—based on the continuous wavelet transform—is used in this paper for the analysis of time-variant systems. The focus is on the comparative study of various broadband input excitations. The performance of the method is tested using simulated data from a simple MDOF system and experimental data from a frame-like structure.

1. Introduction

Vibration analysis and dynamic testing traditionally rely either on time-domain or frequency-domain approaches. However, many engineering systems exhibit time-variant behaviour. Examples include aircraft with different configurations of control surfaces during take-off and landing, deployable space structures and manipulator, tooth gear systems in mesh, or robot manipulator arms with modulator/demodulator cascade controllers. It is well known that the classical parametric and nonparametric methods are not suitable for the analysis and identification of such systems. Therefore various approaches have been developed for the analysis time-variant systems, as overviewed in [1, 2]. Wavelets are particularly attractive for the analysis and identification of time-variant systems thanks to their time-frequency (or rather time-scale) nature. Previous work in this area includes various applications in structural dynamics such as damping estimation [3–6] or nonlinear system analysis [7]. The method presented in [8] is an evolutionary approach and is also used for modal identification. Time-scale approaches have been used also for online identification procedures based on adaptive wavelets [9–13]. An overview of different wavelet-based approaches can be found in [13–15]. Some research work has been done to extend the classical input-output modal analysis to time-variant systems. However, the majority of the proposed methods are adaptive approaches, developed mainly in control engineering, signal processing, and mathematics, as discussed in [1]. More recently, the time-dependent frequency response function (FRF) has been proposed [16–18] for the analysis and identification of time-variant systems. The method utilises wavelets [16, 18] and time-frequency transformations/distributions [17] for the calculations of time-dependent FRFs.

Since the classical, that is, Fourier-based FRF is by definition the Fourier transform of the output divided by the Fourier transform of the input, the only condition in this analysis for the input signal is that it should be Fourier-transformable. Virtually the majority of physically realisable signals satisfy this restriction. Therefore the choice of excitation signals is nearly endless. From a linear system theory point of view the estimated FRF should be independent of the nature of excitation. Also, it is important that all vibration modes are excited. Therefore a broadband excitation—such as Gaussian white nose, chirps, or impacts—are used in practice. More information on various classical excitation signals used in modal analysis can be found in [19, 20]. There is no doubt that broadband excitation should be used also for the analysis of time-variant systems since time-variation is unknown. However, in this case the choice of excitation is no longer arbitrary as some important features could go undetected.

This paper aims to compare various forms of broadband excitation in the time-dependent FRF used for analysis of time-variant systems. The structure of the paper is as follows. Section 2 briefly describes the continuous wavelet transform for the sake of completeness. The time-dependent, wavelet-based FRF is presented in Section 3. Various broadband excitation signals used in the paper are described in Section 4. The FRF-based analysis for a simulated time-variant system is presented in Section 5. Similar analysis for an experimental system is given in Section 6. Finally the paper is concluded in Section 7.

2. Continuous Wavelet Transform

For the sake of completeness this section briefly describes the continuous wavelet transform. The material given in this section provides only very basic mathematical definitions with some important comments relevant to the analysis in the current investigations. More information about the method can be found in [21–23].

The continuous wavelet transform is used to divide a continuous time function into set of elementary functions called wavelets. Unlike the Fourier transform, this transform has the ability to construct a time-scale representation of a signal. This representation can be transformed into the time-frequency domain in engineering applications. One of the most desirable parameters of all time-frequency representations is a good localisation of events simultaneously in time and frequency. Other desirable properties are related to time and frequency resolutions. All these parameters are limited by the Heisenberg uncertainty principle. This principle states that the combined time-frequency resolution product has a lower bound. In other words both resolution parameters, time and frequency, cannot be arbitrarily small simultaneously. The continuous wavelet transform offers very good time-frequency localisation with variable time and frequency resolutions that depended on the so-called scale parameter. Mathematically, the CWT can be defined as

$$X_{\omega}(a,b) = \frac{1}{\sqrt{|a|}} \int_{-\infty}^{\infty} x(t)\, \psi^{*}\left(\frac{t-b}{a}\right) dt, \tag{1}$$

where b is translation indicating locality, a is a scale parameter providing frequency resolution, and $\psi(t)$ is a continuous function called the mother wavelet. The normalisation $\sqrt{|a|}$ in the above equation ensures that the integral energy given by each translated and dilated wavelet is independent of the scale parameter a. It is important that the mother wavelet satisfies the so-called admissibility condition given by

$$\int_{-\infty}^{\infty} \frac{|\Psi(f)|^{2}}{|f|} df < \infty, \tag{2}$$

where $\Psi(f)$ is the Fourier transform of $\psi(t)$. This is required to obtain the inverse wavelet transform given by

$$x(t) = \frac{1}{C_{\psi}} \iint_{-\infty}^{\infty} W_{\psi}(a,b)\, \frac{1}{\sqrt{|a|}} \psi^{*}\left(\frac{t-b}{a}\right)\left(\frac{da\, db}{a^{2}}\right). \tag{3}$$

When time-frequency localization is required from the wavelet transform, the mother wavelets must be also a window function. This additionally means that

$$\int_{-\infty}^{\infty} |\psi(t)|\, dt < \infty. \tag{4}$$

Many different wavelet functions can be employed in the time-scale analysis. In this paper the complex Morlet wavelet function defined as

$$\psi(t) = e^{-|t|^{2}/2} e^{j\omega_{0}t} \tag{5}$$

was used as the mother wavelet. Graphical representation of the complex Morlet wavelet in the time and frequency domain is given in Figure 1. This clearly shows limitations when the Morlet wavelet is used for time-frequency analysis. The frequency domain localisation is defined by the bandwidth of the Morlet wavelet function. As it may seem harmless in this particular example, one has to remember that, with scaling of the analysing wavelets, the ratio of frequency bandwidth to the central frequency will remain constant. Thus, when, for example, the central frequency of the analysed signal equals 50 Hz, the wavelet transform will "see" the signal in the 40–60 Hz frequency range. Therefore one has to be very careful when closed vibration modes are analysed with the CWT. In practice shift and scale parameters can be selected adequately to provide correct analysis. This problem is discussed in more details in [3, 5, 16].

3. Wavelet-Based Frequency Response Function

This section briefly describes the wavelet-based FRF introduced in [16–18]. The formal definition is followed by a short description of numerical implementation together with some practical comments related to averaging.

3.1. Definition. The classical FRF can be extended intuitively for time-variant systems to provide time-frequency localisation capability. When the analysis is limited to small periods of time that exhibit time-invariant behaviour, time-variations are negligibly small and the time-dependent FRF can be defined as [16–18]

$$H(t,\omega) = \frac{Y(t,\omega)}{X(t,\omega)} = \frac{\mathrm{TF}[y(t)]}{\mathrm{TF}[x(t)]}, \tag{6}$$

where TF denotes the time-frequency transformation (or distribution if, for example, the Wigner-Ville transform is applied) in the above equation. The work presented in this paper utilises the continuous wavelet transform—defined in Section 2—to obtain input and output time-frequency spectra needed to calculate the time-dependent FRF. Despite the fact that (6) has a relatively simple form, the entire calculation procedure is not straightforward. It is clear that, for values of TF$[x(t)]$ that are close to zero, the $H(t,\omega)$ tends to infinity. This is why additional postprocessing is required

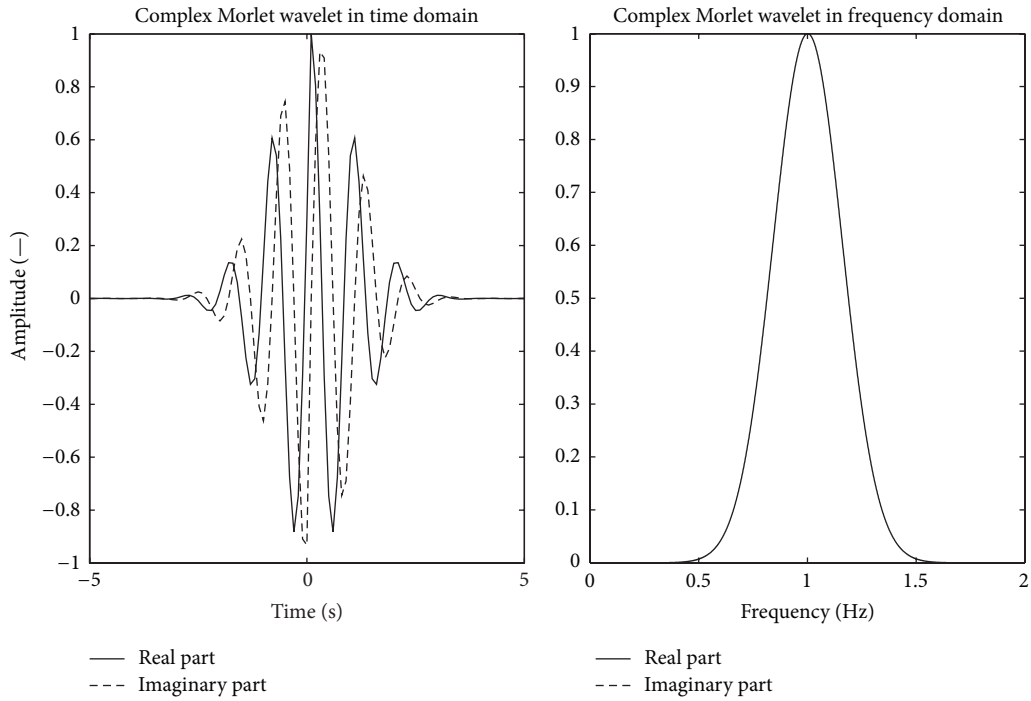

Figure 1: Complex Morlet wavelet function.

to avoid the above problem. In practice, the random Gaussian white noise N is added to the input and output time signals to form biased (noisy) inputs $x_i(t)$ and outputs $y_i(t)$ as

$$\begin{aligned} x_i(t) &= x(t) + N_{\mu,\sigma^2}(t), \\ y_i(t) &= y(t) + N_{\mu,\sigma^2}(t), \end{aligned} \tag{7}$$

where μ and σ^2 are the mean and variance of the Gaussian distribution, respectively. Then, the relevant time-frequency spectra are calculated using the selected transformation to receive

$$\begin{aligned} X_i(t,\omega) &= \mathrm{TF}\left[x_i(t)\right], \\ Y_i(t,\omega) &= \mathrm{TF}\left[y_i(t)\right]. \end{aligned} \tag{8}$$

Finally, the results are averaged to obtain the expected values, that is,

$$\begin{aligned} E\left[X(t,\omega)\right] &= \frac{1}{N}\sum_{i=1}^{N} X_i(t,\omega), \\ E\left[Y(t,\omega)\right] &= \frac{1}{N}\sum_{i=1}^{N} Y_i(t,\omega) \end{aligned} \tag{9}$$

and assembled to receive the time-dependent FRF as

$$H(t,\omega) = \frac{E\left[Y(t,\omega)\right]}{E\left[X(t,\omega)\right]}. \tag{10}$$

3.2. Numerical Implementation. In practice numerical implementation is composed of several steps. Firstly, the autopower functions of input and output signals have to be defined as

$$\begin{aligned} G_{XX}(t,\omega) &= X(t,\omega)\, X^*(t,\omega), \\ G_{YY}(t,\omega) &= Y(t,\omega)\, Y^*(t,\omega), \end{aligned} \tag{11}$$

where the superscript "$*$" in the above equations indicated a complex conjugate. These wavelet-based autopower spectra show how the power in a signal is distributed over the entire time-frequency plane. Both functions could be also used to judge the quality of acquired input and output signals. By analogy, the so-called wavelet-based cross-power spectrum can be defined as

$$G_{XY}(t,\omega) = G_{YX}(t,\omega) = X(t,\omega)\, Y^*(t,\omega). \tag{12}$$

At this point it is possible to compute the wavelet-based FRF. This can be done using different well-known estimators such as H_1, H_2, or H_v. In this paper the H_1 estimator based on wavelet auto- and cross-power and spectra is used as

$$H_1(t,\omega) = \frac{Y(t,\omega)\, X^*(t,\omega)}{X(t,\omega)\, X^*(t,\omega)} = \frac{G_{YX}(t,\omega)}{G_{XX}(t,\omega)}. \tag{13}$$

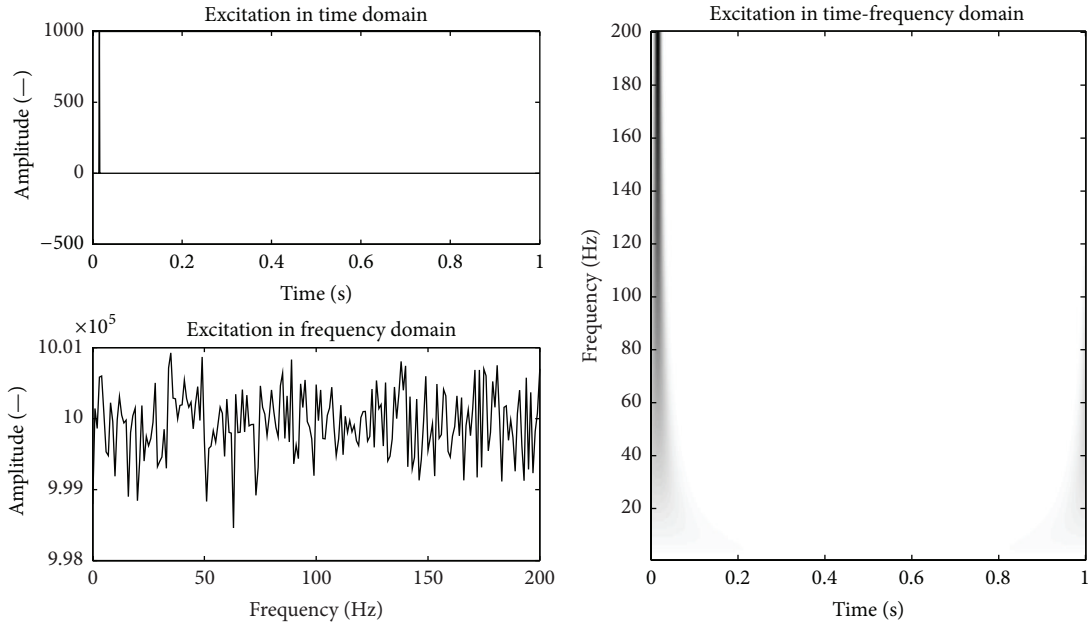

Figure 2: Impact excitation given in the time, frequency, and combined time-frequency domains.

In practice it is advisable to perform averaging of cross- and autopower spectra, as this improves signal-to-noise ratios leading to more reliability. Thus the relevant expected values are calculated, that is,

$$E\left[G_{YX}(t,\omega)\right] = \frac{1}{N}\sum_{i=1}^{N} G_{YX_i}(t,\omega),$$
$$E\left[G_{XX}(t,\omega)\right] = \frac{1}{N}\sum_{i=1}^{N} G_{XX_i}(t,\omega), \tag{14}$$

and finally assembled to receive the wavelet-based FRF as

$$H_1(t,\omega) = \frac{E\left[G_{YX}(t,\omega)\right]}{E\left[G_{XX}(t,\omega)\right]}. \tag{15}$$

Since the H_1 estimator is a complex function additional postprocessing is needed to obtain the amplitude of the wavelet-based FRF. This is simply done by calculating the absolute value of FRF; that is,

$$H_{1_{\text{magnitude}}}(t,\omega) = \text{abs}\left(H_1(t,\omega)\right). \tag{16}$$

This function is used to analyse time-variant systems in the following sections. The process of averaging is quite important in the entire procedure, as explained in [16]. It is also important to note that the phase can be also estimated from the wavelet-based FRF, as shown in [17]. However this characteristic is not used in the current investigations.

4. Input Excitation for Analysis of Time-Variant Systems

This section presents various excitation signals used in the analysis of time-variant systems. Three commonly known broadband signals and one newly proposed signal are compared in the time, frequency, and combined time-frequency domains.

Impact excitation is one of the most widely used forms of excitation in modal analysis. Figure 2 shows that the analysis of impact excitation signal in the time domain gives perfect localization in time, and the analysis in the frequency domain indicates that this excitation exhibits a truly broadband nature. These two important properties are also visible in the combined time-frequency plane. The major drawback associated with this excitation is related to the fact that the system is excited only once for a short period of time. The response is quickly damped and when (15) and (16) are used the relevant input-output wavelet-based FRF analysis will be limited only to such a short period of time.

Another commonly used excitation—which is considered to be broadband—is a chirp excitation. Figure 3 shows that the analysis of this excitation in the frequency domain indicates its broadband nature for a predefined range of frequencies. The time-domain representation of the chirp signal does not reveal immediate interesting features. However, in practice, frequency localisation could be more or less found by analysing zero-crossings and calculating relevant periods of oscillations. This indicates that a chirp is not truly broadband when only small parts of signal are considered. This behaviour is more visible in the time-frequency domain, where the analysis shows which frequency components are present at a given time.

White noise is considered to be a broadband excitation. However, this is only true when the excitation signal is long enough to be ergodic. Figure 4 shows the stationary behaviour of the Gaussian white noise excitation in the time domain. However, if one considers only a small part of this signal, the stationary and broadband behaviour is not so

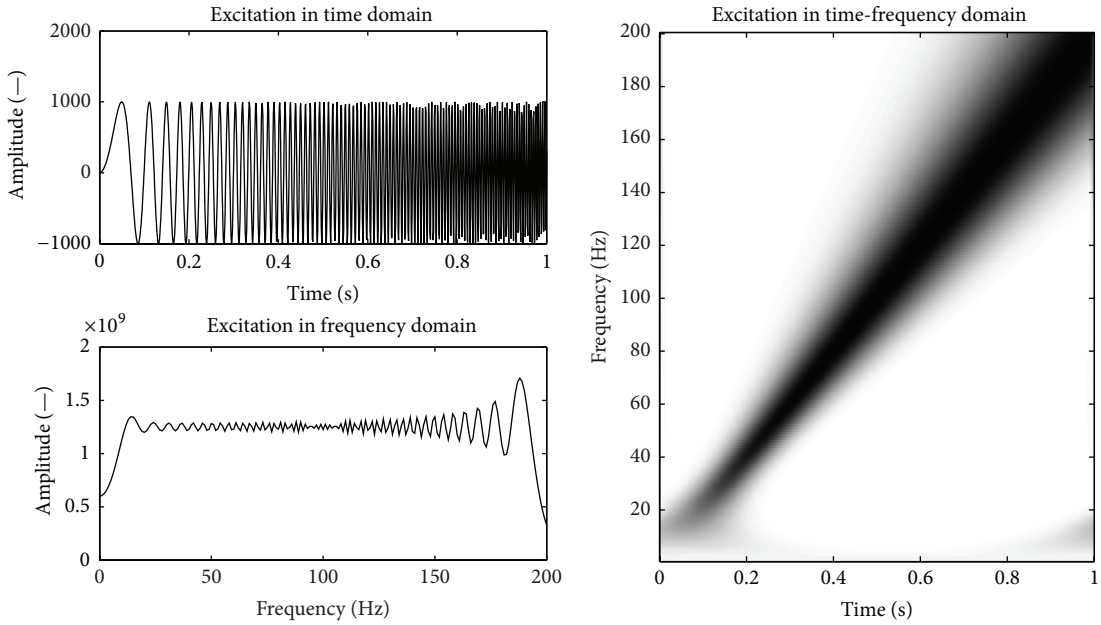

Figure 3: Chirp excitation given in the time, frequency, and combined time-frequency domains.

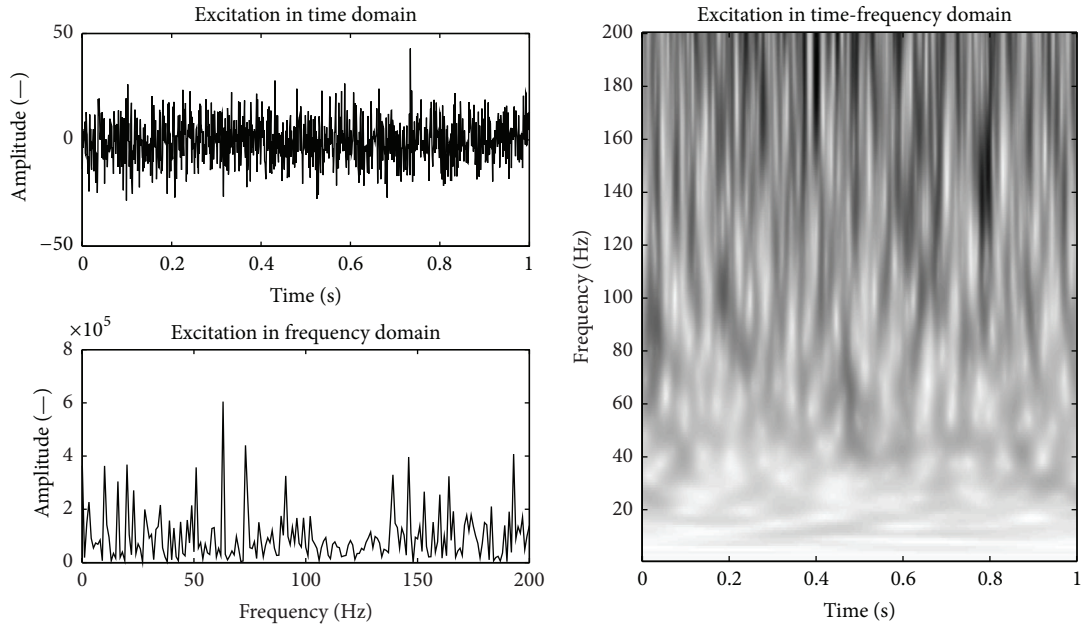

Figure 4: White noise excitation given in the time, frequency, and combined time-frequency domains.

obvious. This is particularly visible in the combined time-frequency domain where the energy distribution of the white noise signal varies with time and frequency from high to near zero amplitudes.

A new type of broadband excitation is proposed in this section. The proposed excitation is composed of randomly distributed series of impacts. Such excitation is broadband at given time instances and provides continuous inflow of energy to the analysed system, as illustrated in Figure 5. This is advantageous when the excitation is compared with the classical impact excitation illustrated in Figure 2. The continuous inflow of energy enables one to observe system dynamic properties and their variations with time.

5. Numerical Simulations and Results

5.1. Simulated MDOF System. A simple two-degree-of-freedom (2-DOF) system was used to compare the performance of input excitation signals in the analysis of time-variant systems. The system consisted of heavily damped mass-spring

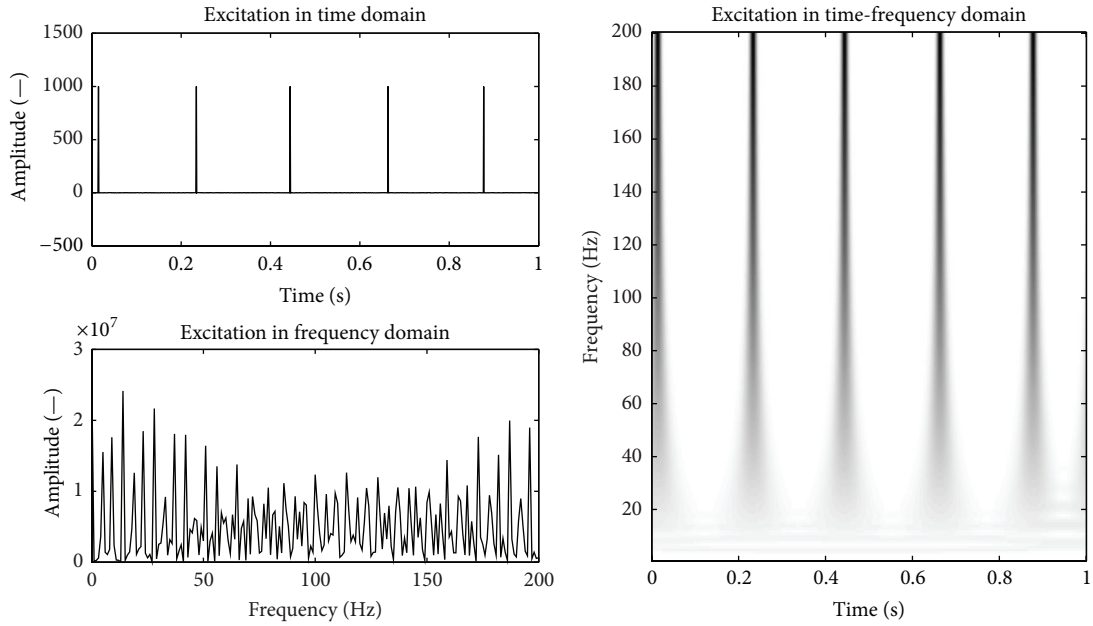

Figure 5: Random impact excitation in the time, frequency, and combined time-frequency domains.

elements. One of the masses involved was varying in time; the mass was decreasing linearly with time. All other relevant physical parameters were constant. The values of physical parameters used were $m = 10\,\text{kg}$, $K_1 = 3000000\,\text{N/m}$, $K_2 = 800000\,\text{N/m}$, $C_1 = 150\,\text{N/(m/s)}$, and $C_2 = 350\,\text{N/(m/s)}$. The M_1 mass element was decreasing linearly in time following the function $M_1(t) = 16–12t\,\text{kg}$. Clearly, this resulted in the increment of the relevant natural frequencies. Theoretical natural frequencies are equal to 40 Hz and 80 Hz (for 0 s) increasing to 160 Hz (for 1 s) with cubic dependence on time. Figure 6 gives a schematic diagram of the simulated system. Numerical simulations were performed using the MATLAB/Simulink platform. The sampling frequency was equal to 1 kHz in all simulations.

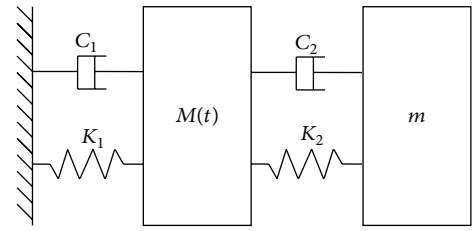

Figure 6: Schematic diagram of the 2-DOF system used in numerical simulations.

5.2. System Identification Results. This section describes system identification results for the simulated time-variant system described in Section 5.1. The focus is on the analysis of varying natural frequencies. Numerical calculations were performed within the MATLAB platform, following the procedure described in Section 3. Signal averaging was used in order to smooth out different disturbances that had impact on the amplitude of the wavelet-based FRF. Four different excitations—described in Section 4—were tested. The classical FRF was also computed for comparison.

Figure 7 shows the results for the impact excitation. The response of the system in the time domain reveals heavy damping in the simulated system; the envelope amplitude decays relatively quickly. The classical FRF clearly exhibits two vibration modes. The first natural frequency was found to be around 39 Hz whereas the second natural frequency could be estimated around 83 Hz. There is very little indication about possible time-variant behaviour, as expected. The second FRF component is more wideband and slightly skewed (or asymmetrical). This could indicate some nonlinearity and/or time-variance. Also, it is very difficult to observe any time-variant behaviour in the amplitude contour plot of the wavelet-based FRF. Harmonic oscillations are dampened too quickly. Some indication on the varying nature is visible in the second vibration mode.

The second considered input signal was a chirp excitation. The results for this excitation are presented in Figure 8. This excitation is renowned for its frequency evolution over time. Therefore both vibration modes are excited not earlier than the chirp sweeps through the relevant natural frequencies. The first natural frequency was found to be around 39 Hz, whereas the second natural frequency was estimated around 104 Hz. The amplitude of the wavelet-based FRF does not indicate any time-varying nature of the system.

White noise excitation differs qualitatively from impact and chirp excitation as it provides energy continuously through the entire excitation time. However, amplitude excitation levels vary for given frequencies. Thanks to this property it is possible to observe time-varying nature of the analysed mechanical system in Figure 9. Although the classical FRF is not clear, two vibration modes can be observed in

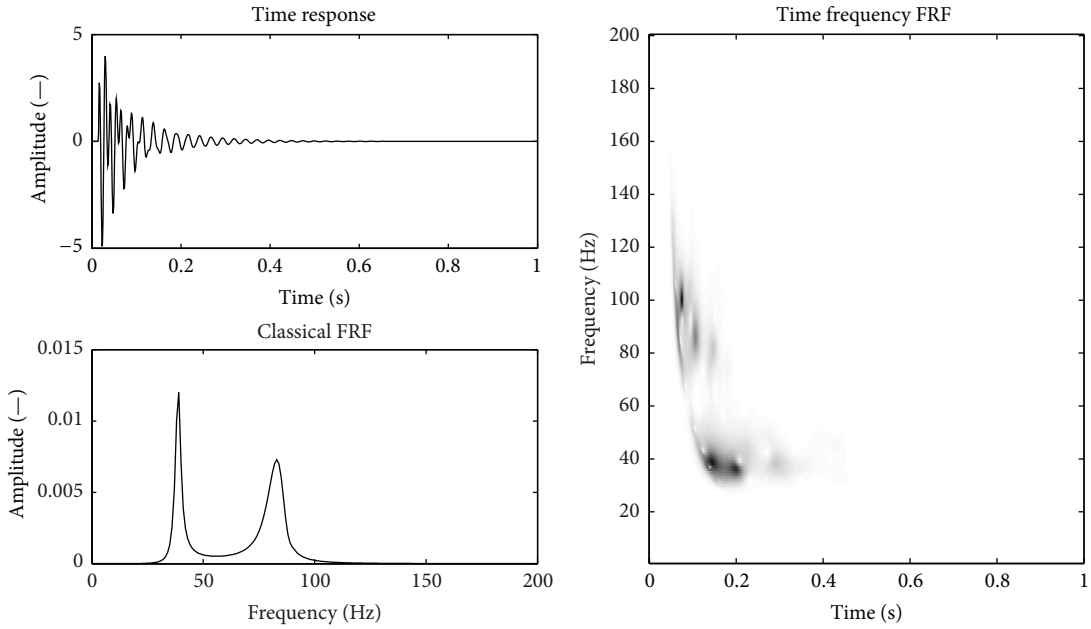

Figure 7: Simulated results obtained for the impact excitation in the time, frequency, and combined time-frequency domains.

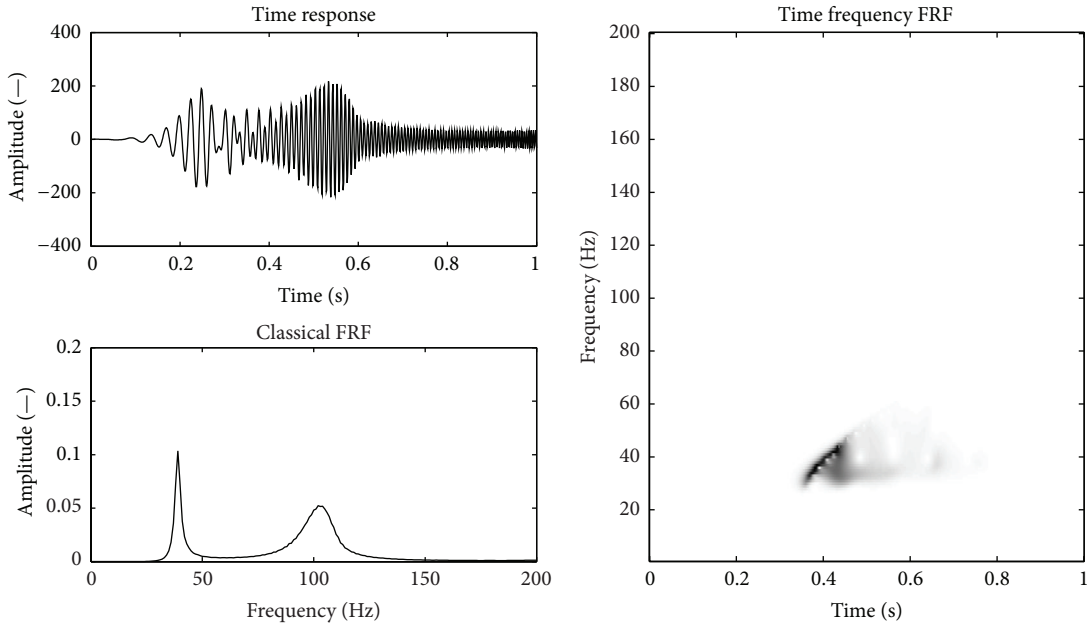

Figure 8: Simulated results obtained for the chirp excitation in the time, frequency, and combined time-frequency domains.

the amplitude of the wavelet-based FRF. The latter can be used to estimate the natural frequencies. The first natural frequency was found to be around 39 Hz whereas the second natural frequency was found to vary between 80 and 150 Hz. The only problem is that the curves displaying vibration modes in the amplitude of the wavelet-based FRF are broken and do not show uniform energy distribution.

The random impact excitation consists of repeated impacts in order to introduce more energy into the system. The amplitude of impacts was constant whereas the repletion time was random in this type of excitation. The results are presented in Figure 10. The time-domain response of the system exhibits five repeated impact responses. However, periods of these impacts are different; that is, the frequency involved increases. The classical FRF displays correctly only the first vibration mode. The time-variant nature can be clearly observed in the amplitude contour plot of the wavelet-based FRF. The first natural frequency was found to be around 39 Hz whereas the second natural frequency was estimated to vary between 80 and 150 Hz. Similarly to the white noise

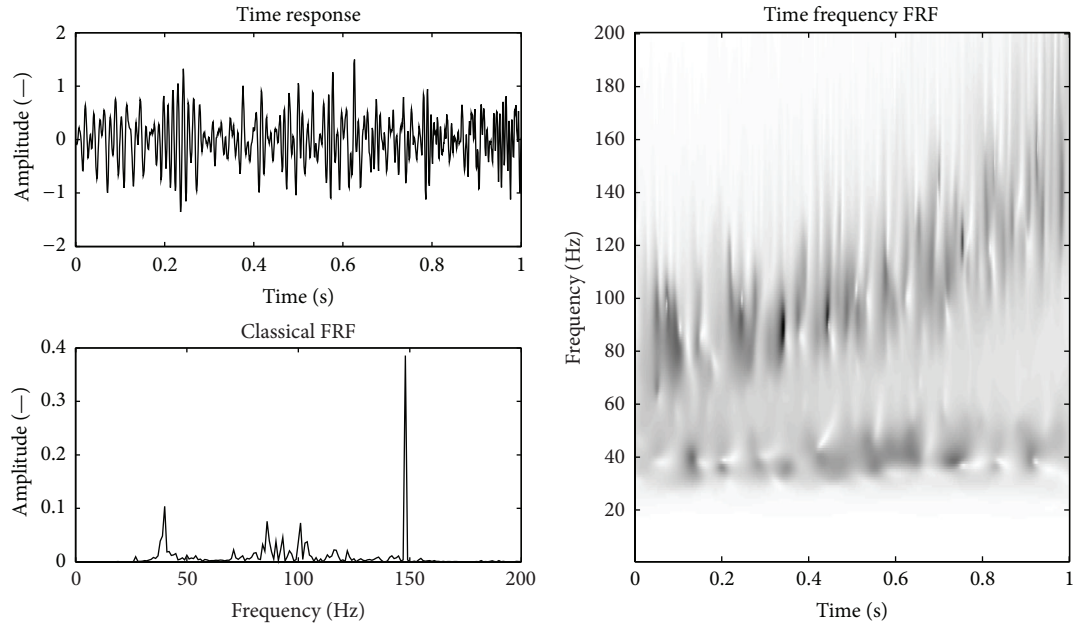

Figure 9: Simulated results obtained for the white noise excitation in the time, frequency, and combined time-frequency domains.

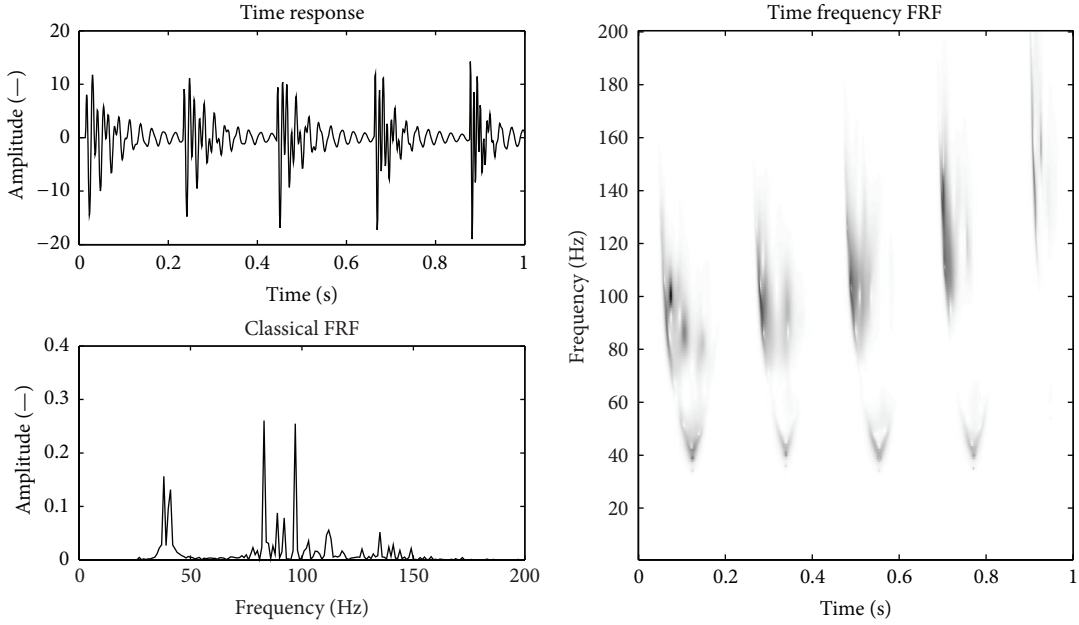

Figure 10: Simulated results obtained for the repeated impact excitation in the time, frequency, and combined time-frequency domains.

excitation, the curves displaying vibration modes in the amplitude of the wavelet-based FRF are broken. However this time the energy distribution for all impacts is more uniform.

In summary, the noise and repeated impact input signals were the only out of the four excitations tested that were able to reveal time-variant nature of the analysed system in the amplitude of the wavelet-based FRF. Therefore these two excitations were further tested using the experimental data, as described in the next section.

6. Experimental Application and Results

A simple experiment was conducted to obtain time-variant vibration data. A frame-like structure—shown in Figure 11—with a tank attached to the free end was used in this experimental work. The vertical arm was 80 cm long, whereas the horizontal arm was 60 cm long. The tank was filled with 3 kg of sand. The tank was draining when vibration measurements were taken using one accelerometer mounted

Figure 11: Experimental time-variant test rig.

in the middle of the vertical arm of frame. Accelerometer was measuring vibrations in horizontal direction. Varying mass of the tank contributed to time-varying behaviour of the entire system. The system was excited with a modal hammer and electrodynamic shaker. The middle of metal block joining horizontal and vertical arms was used as excitation point. Excitation was executed in horizontal direction. Due to the time-varying nature of analysed phenomena, identical multiple measurements—required for averaging—were not possible. Therefore Gaussian white noise was used to corrupt the data. The relevant responses were then calculated using (7). In order to improve the visibility of the results, the entire analysis was limited only to the frequency range from 230 to 300 Hz. The amplitudes of wavelet-based FRFs were calculated. Contour plots together with ridges were used for the analysis of the system. The latter exhibits amplitude where the largest energies are concentrated. These areas correspond to vibration modes. These ridges were calculated following the procedure described in [24].

The results for the noise excitation are shown in Figure 12. Two vibration modes can be observed in the analysed frequency range. The first mode can be seen for the entire period of time, that is, between 0 and 80 s. Its frequency varies from the initial value of 276 Hz (for 0 s) to the final value of 256 Hz (for 80 s). After 5 s the second mode appears. The frequency of this mode remains relatively unchanged and can be estimated as approximately equal to 290 Hz. The results for the repeated impact excitation are given in Figure 13. These results reveal almost the same time-variant behaviour. Only one mode can be observed initially. Its frequency varies from 275 to 259 Hz. Then this mode splits into two modes. The frequency of the new (i.e., second) mode again remains relatively unchanged and can be estimated as 290 Hz; this mode was not visible until 25 s probably due to high damping of the structure. The response amplitude decayed very fast when the impact excitation was used. That was not the case when the white noise excitation was applied. In summary, both types of excitation used, that is, the Gaussian white noise and random repeated impacts, have revealed correctly the varying nature of the analysed system. One important

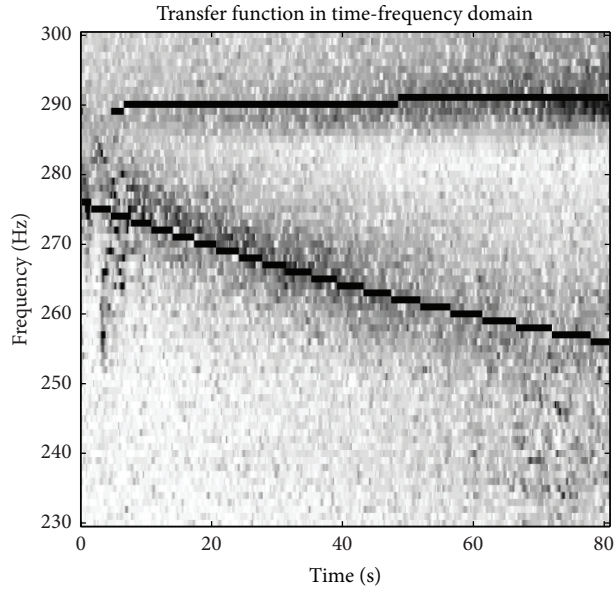

Figure 12: Experimental results obtained for the white noise excitation in the combined time-frequency domain.

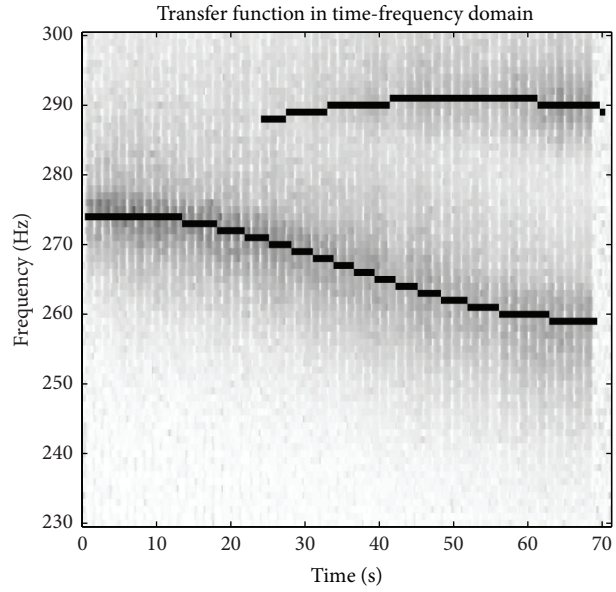

Figure 13: Experimental results obtained for the repeated impact excitation in combined time-frequency domain.

feature can be observed when Figures 12 and 13 are compared. The natural frequency of the first analysed mode shifts downwards more rapidly, that is, from 276 to 256 Hz, when the noise excitation was used in Figure 12.

An additional comment is needed here regarding the change of frequency when mass of structure decreased. It is well known that, for a simple 1-DOF system, the decrease of mass results in the increase of natural frequency. However, this basic theoretical relation does not need to hold for complex MDOF systems, especially for systems where the major mass is concentrated in one part of the structure. Although

this is a common problem found in experimental modal analysis, the observed effect needs further investigations.

7. Conclusions

The wavelet-based FRF was used for the analysis of time-variant systems. The performance of the method was compared for four different types of broadband excitation. Numerical simulations and experimental test data were used in these investigations. A simple heavily dampened 2-DOF system with a time-varying mass was simulated. A frame-like structure with an attached tank was used for experimental tests.

The results show that—for the case investigated—it is impossible to identify time-varying nature of system with the use of impact and chirp excitation. These two excitations do not excite the system continuously in a proper broadband manner. Identification of time-varying systems was possible with the use of two other excitations applied, that is, the white noise and random impact excitations. Both excitations correctly identified time-varying nature of the systems investigated.

It is important to note that the effect of excitation signals was investigated only for the amplitude of the wavelet-based FRF. Future work should involve the analysis of FRF's phase and other modal parameters (than natural frequency). Furthermore, more complex experimental systems should be investigated.

Conflict of Interests

The authors declare that there is no conflict of interests regarding the publication of this paper.

Acknowledgment

The work presented in this paper was supported by funding from the Research Project WELCOME (Foundation for Polish Science, Project no. 2010-3/2).

References

[1] A. G. Poulimenos and S. D. Fassois, "Parametric time-domain methods for non-stationary random vibration modelling and analysis—a critical survey and comparison," *Mechanical Systems and Signal Processing*, vol. 20, no. 4, pp. 763–816, 2006.

[2] M. D. Spiridonakos and S. D. Fassois, "Parametric identification of a time-varying structure based on vector vibration response measurements," *Mechanical Systems and Signal Processing*, vol. 23, no. 6, pp. 2029–2048, 2009.

[3] W. J. Staszewski, "Identification of damping in MDOF systems using time-scale decomposition," *Journal of Sound and Vibration*, vol. 203, no. 2, pp. 283–305, 1997.

[4] W. J. Staszewski and J. E. Cooper, "Wavelet approach to flutter data analysis," *Journal of Aircraft*, vol. 39, no. 1, pp. 125–132, 2002.

[5] T. P. Le and P. Argoul, "Continuous wavelet transform for modal identification using free decay response," *Journal of Sound and Vibration*, vol. 277, no. 1-2, pp. 73–100, 2004.

[6] S. L. Chen, J. J. Liu, and H. C. Lai, "Wavelet analysis for identification of damping ratios and natural frequencies," *Journal of Sound and Vibration*, vol. 323, no. 1-2, pp. 130–147, 2009.

[7] W. J. Staszewski, "Identification of non-linear systems using multi-scale ridges and skeletons of the wavelet transform," *Journal of Sound and Vibration*, vol. 214, no. 4, pp. 639–658, 1998.

[8] P. Tratskas and P. D. Spanos, "Linear multi-degree-of-freedom system stochastic response by using the harmonic wavelet transform," *Journal of Applied Mechanics, Transactions ASME*, vol. 70, no. 5, pp. 724–731, 2003.

[9] T. Uhl, M. Petko, G. Karpiel, and A. Klepka, "Real time estimation of modal parameters and their quality assessment," *Shock and Vibration*, vol. 15, no. 3-4, pp. 299–306, 2008.

[10] A. Klepka and T. Uhl, "Hardware and software tools for in-flight flutter testing," in *Proceedings of the ISMA International Conference on Noise and Vibration Engineering*, vol. 1–8, pp. 1207–1221, 2008.

[11] R. Zouari, L. Mevel, A. Klepka, and M. Basseville, "Adaptive flutter monitoring using wavelet filtering and recursive subspace-based detection," in *Proceedings of the 4th European Workshop on Structural Health Monitoring*, pp. 1137–1144, Krakow, Poland, July 2008.

[12] B. Basu, S. Nagarajaiah, and A. Chakraborty, "Online identification of linear time-varying stiffness of structural systems by wavelet analysis," *Structural Health Monitoring*, vol. 7, no. 1, pp. 21–36, 2008.

[13] S. Nagarajaiah and B. Basu, "Output only modal identification and structural damage detection using time frequency & wavelet techniques," *Earthquake Engineering and Engineering Vibration*, vol. 8, no. 4, pp. 583–605, 2009.

[14] W. J. Staszewski and A. N. Robertson, "Time-frequency and time-scale analyses for structural health monitoring," *Philosophical Transactions of the Royal Society A*, vol. 365, no. 1851, pp. 449–477, 2007.

[15] A. N. Roberston and B. Basu, "Wavelet analysis," in *Encyclopedia on Structural Health Monitoring*, C. Boller, F. K. Chang, and Y. Fujino, Eds., John Wiley & Sons, 2009.

[16] W. J. Staszewski and D. M. Wallace, "Wavelet-based frequency response function for time-variant systems—an exploratory study," *Mechanical Systems and Signal Processing*, vol. 47, no. 1-2, 2014.

[17] K. Dziedziech, W. J. Staszewski, and T. Uhl, "Input-output time-frequency analysis of time-variant systems," in *Proceedings of the International conference on Uncertainty in Structural Dynamics*, pp. 2765–2774, Leuven, Belgium, September 2012.

[18] W. J. Staszewski and J. Giacomin, "Application of the wavelet based FRFs to the analysis of nonstationary vehicle data," in *15th International Modal Analysis Conference*, vol. 3089 of *Proceedings of SPIE*, pp. 425–431, The International Society for Optical Engineering, 1997.

[19] D. Brown, K. Ramsey, and G. Carbon, *Survey of Excitation Techniques Applicable to the Testing of Automotive Structures*, SAE Technical Paper 770029, 1977.

[20] J. Schoukens, R. Pintelon, E. van der Ouderaa, and J. Renneboog, "Survey of excitation signals for FFT based signal analyzers," *IEEE Transactions on Instrumentation and Measurement*, vol. 37, no. 3, pp. 342–352, 1988.

[21] L. Cohen, *Time Frequency Analysis: Theory and Applications*, Prentice Hall, New York, NY, USA, 1st edition, 1994.

[22] R. Carmona, W. L. Hwang, and B. Torrésani, *Practical Time-Frequency Analysis: Gabor and Wavelet Transforms with an Implementation in S*, Academic Press, New York, NY, USA, 1998.

[23] S. Mallat, *A Wavelet Tour of Signal Processing: The Sparse Way*, Academic Press, New York, NY, USA, 3rd edition, 2008.

[24] K. Dziedziech, W. J. Staszewski, and T. Uhl, "Wavelet-based modal analysis for time-variant systems," *Mechanical Systems and Signal Processing*. In press.

Hindawi Publishing Corporation
Shock and Vibration
Volume 2014, Article ID 146802, 7 pages
http://dx.doi.org/10.1155/2014/146802

Research Article

Damage Detection of a Continuous Bridge from Response of a Moving Vehicle

Z. H. Li and F. T. K. Au

Department of Civil Engineering, The University of Hong Kong, Pokfulam Road, Hong Kong

Correspondence should be addressed to Z. H. Li; lizhenhu@hku.hk

Received 17 July 2013; Accepted 19 December 2013; Published 2 June 2014

Academic Editor: Nuno Maia

Copyright © 2014 Z. H. Li and F. T. K. Au. This is an open access article distributed under the Creative Commons Attribution License, which permits unrestricted use, distribution, and reproduction in any medium, provided the original work is properly cited.

This paper presents a multistage multipass method to identify the damage location of a continuous bridge from the response of a vehicle moving on the rough road surface of the bridge. The vehicle runs over the bridge several times at different velocities and the corresponding responses of the vehicle can be obtained. The vertical accelerations of the vehicle running on the intact and damaged bridges are used for identification. The multistage damage detection method is implemented by the modal strain energy based method and genetic algorithm. The modal strain energy based method estimates the damage location by calculating a damage indicator from the frequencies extracted from the vehicle responses of both the intact and damaged states of the bridge. At the second stage, the identification problem is transformed into a global optimization problem and is solved by genetic algorithm techniques. For each pass of the vehicle, the method can identify the location of the damage until it is determined with acceptable accuracy. A two-span continuous bridge is used to verify the method. The numerical results show that this method can identify the location of damage reasonably well.

1. Introduction

The safety of bridge structures is very important to economic development of all countries, so it is very important to make sure that the bridges are in good condition. Various damage detection techniques have been developed to meet this need [1, 2]. The aerospace and offshore oil industries conducted early damage detection since the late 1970s and 1980s, respectively, while, in the civil engineering community, structural health monitoring is a relatively vibrant area of current research [3]. Recording the vibration of the structures, extracting modal properties, and then identifying the damage from changes of the structural properties are the most popular methods among them [4]. This is based on the assumption that commonly measured modal parameters (notably frequencies, mode shapes, and modal damping) are functions of the physical properties of the structure (mass, damping, and stiffness). Therefore, changes in the physical properties, such as reductions in stiffness resulting from the onset of cracks or loosening of a connection, will cause detectable changes in these modal properties. Changes in modal properties or properties derived from these quantities are being used as indicators of damage [1]. One issue of primary importance is the dependence on prior analytical models and/or prior test data for the detection and location of damage [1]. Damage detection methods in time domain can overcome this problem to certain extent. The time-domain approach has become more popular in recent years to examine nonstationary signals [5]. In the short-time Fourier transform method, the total time interval is divided into shorter time intervals for the fast Fourier transform to be applied to each interval. This time windowing method narrows down the time to that of the interval where the damage is located [6]. However, the constraints of the uncertainty principle limit the obtainable resolutions considerably, prompting the emergence of an alternative approach in multiresolution analysis termed wavelet transform [7]. Wavelet transform allows variable-size windows and this is why it is also called a mathematical microscope. This property makes it a suitable method for detection of damage from a response [8]. There are several other methods used for damage detection. One of them, the genetic algorithm, is modified for use in this

study. Genetic algorithms (GAs), originally developed by Holland, are search algorithms based on the mechanics of natural selection and natural genetics [9]. GAs are different from traditional optimization procedures in four ways: (a) GAs work with a coding of the parameter set, but not the parameters themselves; (b) GAs search from a population of points instead of a single point; (c) GAs use objective function information instead of derivatives or other auxiliary knowledge; and (d) GAs use probabilistic transition rules instead of deterministic rules [10]. Since structural damage detection can be transformed into optimization problems, GAs can be used to do the damage detection.

The above-mentioned methods identify the conditions of a bridge through acquiring the bridge response by putting sensors on the bridge. It is also possible to detect the conditions of the bridge by putting sensors on the passing vehicle. Identifying the damage using the vehicle response has certain advantages over putting sensors on the bridge. Firstly, the vehicle is both a sensor and an exciter. It is much more convenient as it makes the closure of bridge much shorter or even unnecessary. Secondly, it is not much influenced by the locations of damage and distributions of sensors because the vehicle runs over and detects the whole bridge. Yang et al. extracted bridge frequencies from a moving vehicle [11–13]. Inspired by this work, Bu et al. proposed a damaged detection method based on the dynamic response sensitivity analysis and regularization technique [5]. Nguyen and Tran [14] applied wavelet transform to the displacement history of a moving vehicle. Zhang et al. [15] extracted the mode shapes square from the response and conducted damage detection. The above work did not consider the roughness of the bridge, which would be a very important factor affecting the vibration of the vehicle. The authors previously applied a modal strain energy based damaged detection method to analyze the response of the vehicle [16] and came up with two possible locations of the damage. This is due to the limitation of the frequency-based damage detection methods [17]. The authors also conducted damage detection using wavelet transform from the response of the vehicle [18]. This paper will consider the influence of the roughness in the vehicle-bridge interaction system on the damage identification. The strategy is a combination of modal strain energy based method and GA techniques. Modal strain energy based method can narrow down the search space for GA algorithms to save computational time and improve the chance of getting the correct solution.

2. Vehicle-Bridge Interaction System

Figure 1 shows the sketch of a typical vehicle-bridge interaction system. It contains a continuous bridge and a vehicle running over it at a constant speed. The bridge is modeled using the finite element method and the vehicle is modeled as a mass-spring-damper system. The vehicle model contains five parameters. The body is simulated by a concentrated mass m_2, the spring stiffness k_2, and the damper c_2. The wheels are simulated using a concentrated mass m_1 and the stiffness k_1 of the spring connecting the wheel and the road surface.

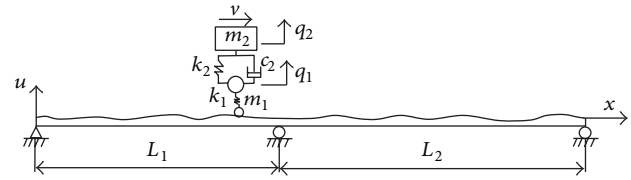

Figure 1: A typical vehicle-bridge interaction system.

2.1. Equation of Motion. When the vehicle moves from one end of the bridge to the other end at a constant speed, both the bridge and the vehicle will vibrate vertically. A vector $u_b(t)$ is used to denote the vertical displacements of a series of nodes in the finite element model of the bridge. Its first and second derivatives with respect to time t, that is, $\dot{u}_b(t)$ and $\ddot{u}_b(t)$, are, respectively, the vertical velocity and acceleration of the corresponding nodes. The symbols $q_1(t)$ and $q_2(t)$ denote the vertical displacement of the wheel and the car body, respectively. As they interact with each other by the contact force, the vibration of the vehicle is influenced by the vibration of the bridge and vice versa. So this is a coupled vibration system. It is assumed that the mass of vehicle is insignificant compared to that of the bridge. The governing equation of motion derived using the fully computerized method is expressed as

$$\begin{bmatrix} M_b & 0 \\ 0 & M_v \end{bmatrix} \begin{Bmatrix} \ddot{u}_b \\ \ddot{q}_v \end{Bmatrix} + \begin{bmatrix} C_b & C_{bv} \\ C_{vb} & C_v \end{bmatrix} \begin{Bmatrix} \dot{u}_b \\ \dot{q}_v \end{Bmatrix} + \begin{bmatrix} K_b & K_{bv} \\ K_{vb} & K_v \end{bmatrix} \begin{Bmatrix} u_b \\ q_v \end{Bmatrix} = \begin{Bmatrix} P_b \\ P_v \end{Bmatrix}, \tag{1}$$

where $q_v = \begin{bmatrix} q_1 & q_2 \end{bmatrix}^T$ is the vertical displacement of the vehicle; $\dot{q}_v$ and $\ddot{q}_v$ are the corresponding velocity and acceleration; M_b and K_b are the mass and stiffness matrices of the bridge obtained by the finite element method, respectively; the damping matrix of the bridge is modeled using Rayleigh damping as $C_b = \alpha_c M_b + \beta_c K_b$, where α_c and β_c are the damping factors;

$$M_v = \begin{bmatrix} m_1 & 0 \\ 0 & m_2 \end{bmatrix},$$

$$C_v = \begin{bmatrix} c_2 & -c_2 \\ -c_2 & c_2 \end{bmatrix}, \tag{2}$$

$$K_v = \begin{bmatrix} k_1 + k_2 & -k_2 \\ -k_2 & k_2 \end{bmatrix}$$

are, respectively, the mass, damping, and stiffness matrices of the vehicle model; C_{bv}, C_{vb}, K_{bv}, and K_{vb} are the coupling damping and stiffness matrices; $K_{vb} = \begin{bmatrix} -k_1 & 0 \end{bmatrix}^T$ and P_b and P_v are the external loads added to the bridge and vehicle, respectively, due to gravity forces, surface roughness, and so forth. Equation (1) can be solved using Newmark-β method, Wilson-θ method, or similar to calculate the responses of the vehicle and the bridge.

2.2. Modeling of Roughness. The random road surface roughness of the bridge can be described by a kind of zero-mean, real-valued, and stationary Gaussian process as [19]

$$r(x) = \sum_{h=1}^{N_T} \alpha_h \cos\left(2\pi\omega_h x + \phi_h\right), \tag{3}$$

where

$$\alpha_h^2 = 4S_r(\omega_h)\Delta\omega,$$
$$\omega_h = \omega_l + \left(h - \frac{1}{2}\right)\Delta\omega, \quad h = 1, 2, \ldots, N_T, \tag{4}$$
$$\Delta\omega = \frac{\omega_u - \omega_l}{N_T},$$

in which ω_l and ω_u are the lower and upper cut-off spatial frequencies, respectively. The power spectral density function $S_r(\omega_h)$ can be expressed in terms of the spatial frequency ω_h of the road surface roughness as

$$S_r(\omega_h) = \begin{cases} \overline{\alpha}\omega_h^{-\beta} & \text{for } \omega_l < \omega_h < \omega_u \\ 0 & \text{elsewhere,} \end{cases} \tag{5}$$

where $\overline{\alpha}$ is a spectral roughness coefficient and the value of β is determined based on the classification of road surface condition according to ISO specification [20].

The contact force f_c between the vehicle and the bridge can be written as

$$f_c = -(m_1 + m_2)g + k_2\left(r(x(t)) + u_b\big|_{x=vt} - q_1\right). \tag{6}$$

The above equation implies that the roughness and the vertical displacement of the corresponding point influence the contact force in a similar manner. If the height of roughness is obviously larger than the value of the displacement of the bridge, the roughness dominates the contact force. So, to identify the information of the bridge, the response of the bridge should be at least comparable to that of roughness.

2.3. Measurement Noise. Measurement noise should also be considered to make the simulation closer to reality. Damage detection is carried out assuming that the signal is contaminated by 5% white noise as shown in

$$\ddot{q}_v^m = \ddot{q}_v\left(1 + 5\%\eta\right), \tag{7}$$

where $\ddot{q}_v^m$ is the simulated measured response of vehicle and η is a normally distributed random array with zero mean and unit variance. The measurement noise does influence the response and identification, but its influence is much smaller than that of roughness.

3. Multistage Multipass Damage Detection Method

This method contains two stages which are modal strain energy based method and modified genetic algorithm method. At the first stage, the modal strain energy based method is simple and fast in roughly estimating the location of damage so as to narrow down the search domain for the second stage. The vehicle can run over the bridge several times and get a series of vehicle responses. Multiple passes are used because different properties of the vehicle and speeds will excite the bridge slightly differently, which will help guarantee the correctness of the identification.

3.1. Modal Strain Energy Based Method. Several modal properties based methods are developed for damage detection. Modal strain energy based method is selected because it is very effective and can estimate the location of the damage if only the frequencies of the damaged structure are available [21–23]. For the intact bridge, the first few mode shapes can be simulated by finite element method or obtained by field tests. If changes in mass are neglected, the fractional change in the ith eigenvalue due to damage is given by

$$Z_i = \frac{\omega_i^{*2} - \omega_i^2}{\omega_i^2} = \frac{f_i^{*2} - f_i^2}{f_i^2}, \tag{8}$$

where ω_i is the ith circular frequency, $f_i = \omega_i/(2\pi)$ is the corresponding frequency, and the asterisk denotes those of the damaged state.

For an MDOF structural system of NE elements and N nodes, the damage may be predicted by the sensitivity equation

$$\sum_{j=1}^{NE} F_{ij}\alpha_j = Z_i \tag{9}$$

in which $\alpha_j \in [-1, 0]$ is the fractional reduction in stiffness of jth element and the fraction of modal energy or sensitivity for the ith mode concentrated at the jth element, F_{ij}, is given by

$$F_{ij} = \frac{\int_{x_j}^{x_{j+1}} EI\left\{\varphi_i''(x)\right\}^2 dx}{\int_0^L EI\left\{\varphi_i''(x)\right\}^2 dx}, \tag{10}$$

where $\varphi_i''(x)$ is the second derivative of the ith mode shape of the bridge; E and I are the elastic modulus and moment of inertia of the bridge, respectively; and x_j and x_{j+1} are the coordinates of the jth and $(j+1)$th nodes that are the left and right nodes of the jth element, respectively. In practice, only the modal amplitudes at limited nodal points are available. By interpolation using spline functions and the element modal amplitude values from the mode shapes of the finite element model, one can generate the function $\varphi_i(x)$ as necessary.

For any two modes m and n, one may obtain the ratio of sensitivities calculated from (9) as

$$\frac{Z_m}{Z_n} = \frac{\sum_{j=1}^{NE} F_{mj}\alpha_j}{\sum_{j=1}^{NE} F_{nj}\alpha_j} = \frac{F_{m1}\alpha_1 + F_{m1}\alpha_1 + \cdots + F_{mq}\alpha_q + \cdots + F_{mNE}\alpha_{NE}}{F_{n1}\alpha_1 + F_{n1}\alpha_1 + \cdots + F_{nq}\alpha_q + \cdots + F_{nNE}\alpha_{NE}}. \tag{11}$$

Assuming that damage occurs only at element q, then $\alpha_j = 0$ when $j \neq q$, but $\alpha_j \neq 0$ when $j = q$. The relationship associated with the mth and nth eigenvalues can be established as

$$\frac{Z_m}{Z_n} = \frac{F_{mq}}{F_n q}. \tag{12}$$

If NM modes are measured, (12) can be extended to

$$\frac{Z_m}{\sum_{k=1}^{NM} Z_k} = \frac{F_{mq}}{\sum_{k=1}^{NM} F_{kq}}. \tag{13}$$

Based on the above equation, an error index e_{mj} can be developed as

$$e_{mj} = \frac{Z_m}{\sum_{k=1}^{NM} Z_k} - \frac{F_{mj}}{\sum_{k=1}^{NM} F_{kj}}, \tag{14}$$

where $e_{mj} = 0$ indicates in particular that the damage is located at the jth element using the mth modal information. To account for all available modes, one can form a single damage indicator for the jth member as

$$DI_j = \left[\sum_{i=1}^{NM} e_{ij}^2 \right]^{-1/2}. \tag{15}$$

The damage is located at element j if DI_j approaches the local maximum point. It has been validated that the damage can be detected if the surface of the road is assumed to be smooth [16].

3.2. Empirical Mode Decomposition. For this frequency-based method, it is important to extract frequencies from the vehicle response. To help identify the frequencies accurately, several signal processing techniques are used, including common filtering techniques and empirical mode decomposition (EMD) proposed by Huang et al. [24]. EMD is used to decompose a signal into a series of intrinsic mode functions (IMFs). Given a set of measured data $X(t)$, the algorithm of the EMD, characterized by the sifting process, is briefly described below.

(a) Identify all the local maxima and minima of the data X(t) and then compute the corresponding interpolating signals by cubic spline curves. These signals are the upper and lower envelopes of the signal. All the extrema should be covered in these two envelopes. Let m_1 denote the mean of the upper and lower envelopes. The difference between the data and the mean m_1 is

$$h_1 = X(t) - m_1. \tag{16}$$

(b) Ideally, h_1 should be the first IMF component. If h_1 does not satisfy the IMF requirements [24], treat it as the original data and repeat the first step until the requirements are satisfied. The first IMF component obtained is designated as c_1.

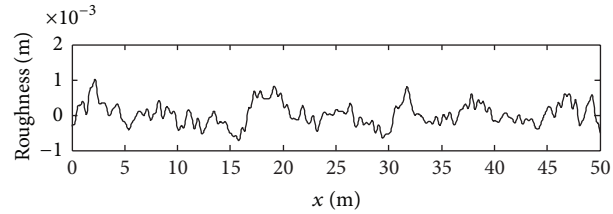

Figure 2: A typical profile of roughness.

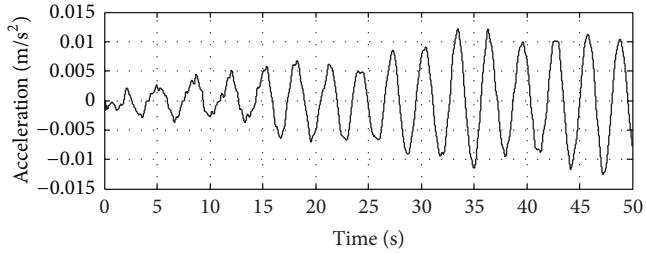

Figure 3: Vertical acceleration of the vehicle running on intact and damaged bridges.

(c) By subtracting c_1 from the original data, one obtains the residue r_1 as

$$r_1 = X(t) - c_1. \tag{17}$$

(d) Repeat the above sifting processes to obtain the next IMFs. Once an IMF is obtained, remove it from the signal until the predetermined criteria are met: either when the component c_n or the residue r_n becomes too small to be physically meaningful or when the residue r_n becomes a monotonic function from which no more IMF can be extracted. Consequently, the data $X(t)$ is decomposed as

$$X(t) = \sum_{i=1}^{n} c_i + r_n. \tag{18}$$

Thus, a decomposition of the data into n-empirical modes is achieved. The process is indeed like sifting: to separate the finest local mode from the data first based only on the characteristic time scale. The sifting process, however, has two effects: (a) to eliminate riding waves and (b) to smooth uneven amplitudes. Applying fast Fourier transform to these IMFs, it is easy to extract higher frequencies.

3.3. Modified Genetic Algorithm. Damage detection can be transformed into an optimization problem. The element stiffness and parameters of roughness can be treated as unknowns. It is assumed that the properties of the bridge without damage are known. The objective function can be set as the difference between the responses of the vehicle running on the bridge at the current and the intact state as

$$e = \left\| \ddot{q}_2^{mu} - \ddot{q}_2^{s} \right\|_2. \tag{19}$$

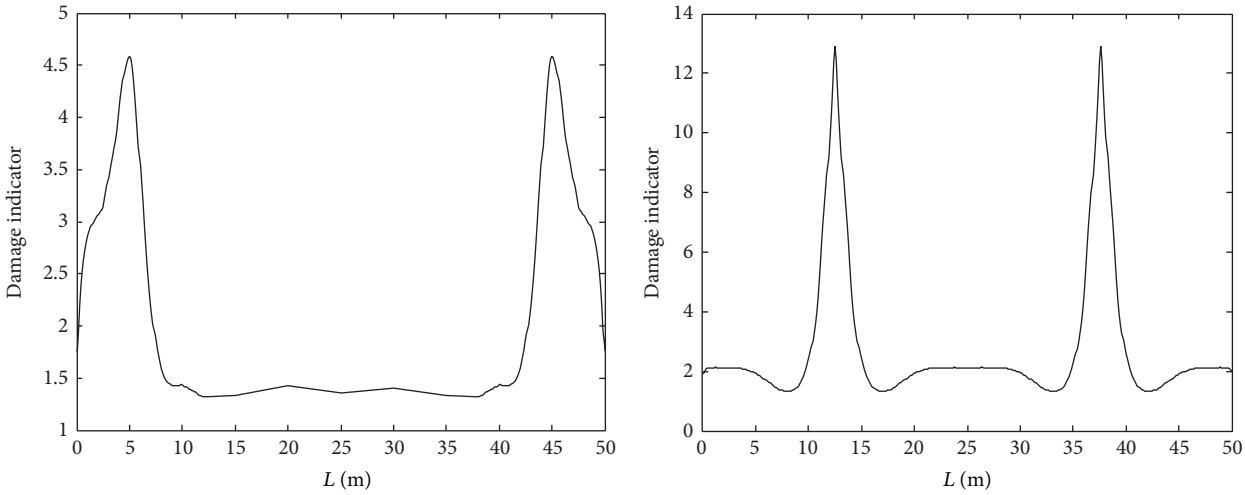

(a) 4th element (b) 10th element

Figure 4: Damage indicator when damage is inflicted at (a) fourth element and (b) tenth element.

The nature of randomness of GA makes it possible for a false alarm to occur sometimes, but multiple passes will prevent this. The responses can be divided into two parts. The first stage makes use of the results from the first part and identifies the location of damage. Usually, this part should at least contain responses from three passes. The GA will roughly identify the location of damage based on these responses. If the identified locations from these passes are the same, no further action is needed. If the result shows that the identified locations from the responses are different, these potential locations will be provided to the second stage. Such a way will greatly reduce the possibility of false alarm and may reduce the search domain. The population size and generation used in the GA will thus be reduced, which will save the computational time.

4. Numerical Study

A two-span continuous bridge is used to demonstrate the damage detection strategy. The properties of the bridge are spans $L_1 = L_2 = 25$ m, Young's modulus of the material $E = 2.75 \times 10^{10}$ N/m^2, density $\rho = 3333$ kg/m^3, and the moment of inertia $I = 0.12$ m^4. The damping is not considered for the moment and the length of elements for finite element analysis is 1.25 m. For the 5-parameter vehicle, the relevant values are chosen as follows: $m_2 = 19840$ kg, $k_2 = 1{\times}10^5$ N/m, $c_2 = 2 \times 10^3$ Ns/m, $m_1 = 160$ kg, and $k_1 = 1 \times 10^5$ N/m. The simulated roughness is shown in Figure 2 as described in the next subsection. The speeds of the vehicle to obtain the vehicle responses are 0.6 m/s, 0.8 m/s, 1 m/s, 1.2 m/s, and 1.4 m/s. The time step for integration is 0.001 second. The damage is modeled as a stiffness reduction at one element of the beam. In this paper, the position of the damage is selected around the first quarter point and middle of the first span of beam which correspond to the fourth and tenth elements of the beam, respectively. The stiffness reduction is set to be 30%. For convenience, the stiffness reduction is reflected in the equivalent Young modulus instead of the presentation of results of damage detection.

4.1. Profile of Roughness. When the values of $\overline{\alpha}$, β, ω_l, ω_u, and N_T are set to be 1×10^{-8} m^2/(m/cycle), 0, 0.05 cycle/m, 2 cycle/m, and 1024, respectively, and two sets of ϕ_k are randomly generated, two profiles of roughness are constructed. One of them is shown in Figure 2.

4.2. Damage Detection at the First Stage. The vertical acceleration of the vehicle can be calculated from (1). When the speed is 1 m/s, the vehicle response is shown in Figure 3. Fast Fourier transform is applied to extract frequencies from these responses. The first five frequencies of both the intact bridge and the damaged bridge can be obtained. Modal strain energy based method is applied to do the damage detection at the first stage. Figure 4 with two peaks each implies that there might be two damaged locations even though the damage is inflicted at one single element. The two nearest elements to each peak are regarded as potential locations of damage. Thus, there are totally four possible solutions for each case.

4.3. Damage Detection at the Second Stage. The first stage can limit the locations of damage to certain elements though it cannot confine the damage to a single element. This will help narrow down the search domain for the subsequent work. For example, Figure 4 shows that the damage may be at the 4th element or the 37th element, which indicates that the second stage only needs to determine which of the two the elements is damaged.

The responses are divided into two parts according to the speeds of the vehicle. The first part contains responses when the vehicle runs at speeds of 0.6 m/s, 1 m/s, and 1.4 m/s, while the remaining responses belong to the second part. Applying GA to the first part, the identified values of Young's modulus of elements are shown in Figure 5. The location

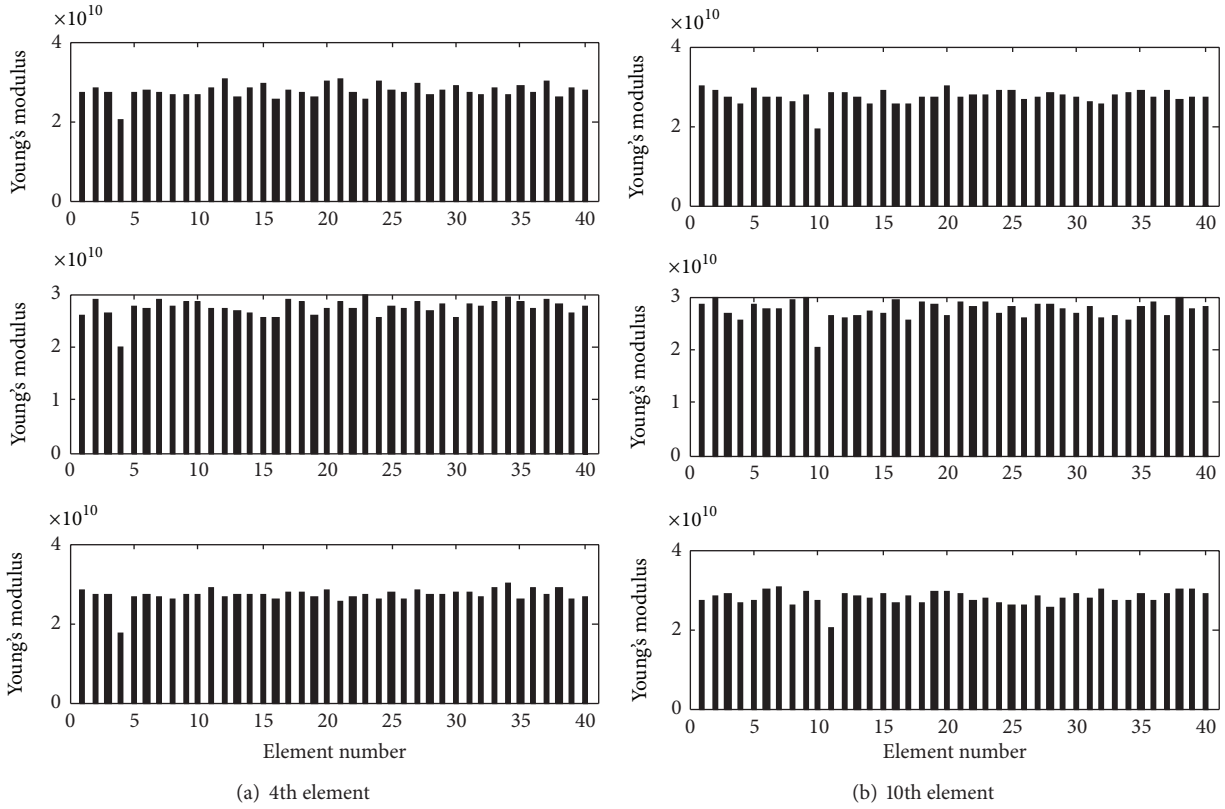

Figure 5: Identified equivalent Young's modulus from first part for damage at (a) fourth element and (b) tenth element.

of damage is determined from the three passes when the damage is inflicted at the 4th element. However, the location for the second case of damage is not yet well determined. Even though this stage does not limit the damage to one element, it not only eliminates half of the possibilities but also provides more information on the profile of roughness. Analyzing the second part of the response using GA, the location of the damage can be determined as shown in Figure 6.

5. Conclusions

A multistage multipass strategy is proposed to identify the location of damage from the response of a vehicle moving over a bridge considering the road surface roughness. The frequencies of the bridge are extracted with the help of empirical mode decomposition first. Modal strain energy based damage detection method is then applied to explore the possible damage locations. The potential locations obtained are then given to GAs for further investigation. The algorithm simultaneously identifies the stiffness of each element and the profile of roughness. The numerical study shows that this combined method can successfully determine the location of damage of a two-span continuous bridge when one element is assumed to be damaged. The measurement noise influences the damage detection much less significantly than roughness. For multiple locations of damage, further work is needed.

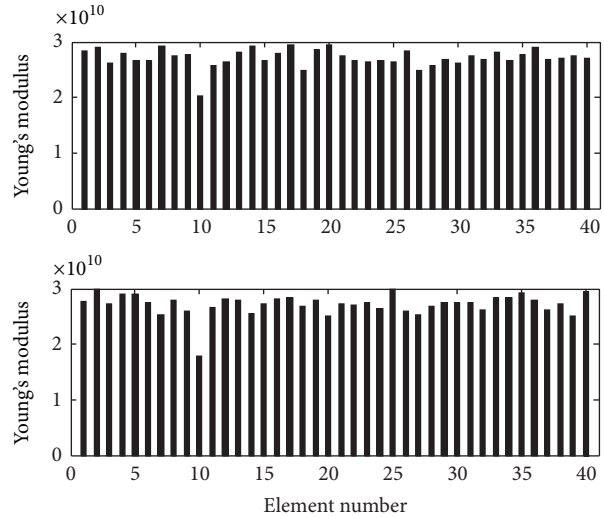

Figure 6: Identified equivalent Young's modulus from second part for damage at tenth element.

Conflict of Interests

The authors declare that there is no conflict of interests regarding the publication of this paper.

Acknowledgments

The work described in this paper has been supported by the Research Grants Council (RGC) of the Hong Kong Special Administrative Region, China (RGC Project no. HKU 7102/08E). The authors would also like to thank Dr. X. T. Si for providing the vehicle-bridge interaction code for computing the responses of vehicle.

References

[1] S. W. Doebling, C. R. Farrar, and M. B. Prime, "A summary review of vibration-based damage identification methods," *Shock and Vibration Digest*, vol. 30, no. 2, pp. 91–105, 1998.

[2] C. R. Farrar, S. W. Doebling, and D. A. Nix, "Vibration-based structural damage identification," *Philosophical Transactions of the Royal Society A: Mathematical, Physical and Engineering Sciences*, vol. 359, no. 1778, pp. 131–149, 2001.

[3] E. P. Carden and P. Fanning, "Vibration based condition monitoring: a review," *Structural Health Monitoring*, vol. 3, no. 4, pp. 355–377, 2004.

[4] K. Worden and J. M. Dulieu-Barton, "An overview of intelligent fault detection in systems and structures," *Structural Health Monitoring*, vol. 3, no. 1, pp. 85–98, 2004.

[5] J. Q. Bu, S. S. Law, and X. Q. Zhu, "Innovative bridge condition assessment from dynamic response of a passing vehicle," *Journal of Engineering Mechanics*, vol. 132, no. 12, pp. 1372–1379, 2006.

[6] D. L. Fugal, *Conceptual Wavelets in Digital Signal Processing : An in-Depth, Practical Approach for the Non-mathematiciAn*, Space & Signals Technical Pub, San Diego, Calif, USA, 2009.

[7] T. Kijewski and A. Kareem, "Wavelet transforms for system identification in civil engineering," *Computer-Aided Civil and Infrastructure Engineering*, vol. 18, no. 5, pp. 339–355, 2003.

[8] H. Kim and H. Melhem, "Damage detection of structures by wavelet analysis," *Engineering Structures*, vol. 26, no. 3, pp. 347–362, 2004.

[9] J. H. Holland, *Adaptation in Natural and Artificial Systems*, vol. 2, Ann Arbor, Mich, USA, University of Michigan Press, 1975.

[10] D. E. Goldberg, *Genetic Algorithms in Search, Optimization, and Machine Learning*, Addison-Wesley, New York, NY, USA, 1989.

[11] Y. B. Yang, C. W. Lin, and J. D. Yau, "Extracting bridge frequencies from the dynamic response of a passing vehicle," *Journal of Sound and Vibration*, vol. 272, no. 3–5, pp. 471–493, 2004.

[12] Y. B. Yang and K. C. Chang, "Extraction of bridge frequencies from the dynamic response of a passing vehicle enhanced by the EMD technique," *Journal of Sound and Vibration*, vol. 322, no. 4-5, pp. 718–739, 2009.

[13] C. W. Lin and Y. B. Yang, "Use of a passing vehicle to scan the fundamental bridge frequencies: an experimental verification," *Engineering Structures*, vol. 27, no. 13, pp. 1865–1878, 2005.

[14] K. V. Nguyen and H. T. Tran, "Multi-cracks detection of a beam-like structure based on the on-vehicle vibration signal and wavelet analysis," *Journal of Sound and Vibration*, vol. 329, no. 21, pp. 4455–4465, 2010.

[15] Y. Zhang, L. Wang, and Z. Xiang, "Damage detection by mode shape squares extracted from a passing vehicle," *Journal of Sound and Vibration*, vol. 331, no. 2, pp. 291–307, 2012.

[16] Z. H. Li and F. T. K. Au, "Damage detection of girder bridges from dynamic response of a moving vehicle," in *Proceedings of the 3rd International Postgraduate Conference on Infrastructure and Environment*, Z. Liu, A. A. Javed, D. Ni, and W. Shen, Eds., pp. 88–95, Hong Kong, 2011.

[17] O. S. Salawu, "Detection of structural damage through changes in frequency: a review," *Engineering Structures*, vol. 19, no. 9, pp. 718–723, 1997.

[18] Z. H. Li and F. T. K. Au, "Feasibility of output-only damage detection method using response of a vehicle moving on a bridge," in *Proceedings of the 14th Asia Pacific Vibration Conference*, pp. 1215–1224, Hong Kong, 2011.

[19] R. Jiang, *Identification of Dynamic Load and Vehicle Parameters Based on Bridge Dynamic Responses*, The University of Hong Kong, Hong Kong.

[20] ISO8608:1995, Mechanical vibration. Road surface profiles. Reporting of measured data. 1996, International Organization for Standardization (ISO).

[21] J. T. Kim and N. Stubbs, "Improved damage identification method based on modal information," *Journal of Sound and Vibration*, vol. 252, no. 2, pp. 223–238, 2002.

[22] J. T. Kim and N. Stubbs, "Crack detection in beam-type structures using frequency data," *Journal of Sound and Vibration*, vol. 259, no. 1, pp. 145–160, 2003.

[23] J. T. Kim, Y.-S. Ryu, H.-M. Cho, and N. Stubbs, "Damage identification in beam-type structures: frequency-based method vs mode-shape-based method," *Engineering Structures*, vol. 25, no. 1, pp. 57–67, 2003.

[24] N. E. Huang, Z. Shen, S. R. Long et al., "The empirical mode decomposition and the Hubert spectrum for nonlinear and non-stationary time series analysis," *Proceedings of the Royal Society A: Mathematical, Physical and Engineering Sciences*, vol. 454, no. 1971, pp. 903–995, 1998.

Hindawi Publishing Corporation
Shock and Vibration
Volume 2014, Article ID 529892, 7 pages
http://dx.doi.org/10.1155/2014/529892

Research Article

Structural Response to Blast Loading: The Effects of Corrosion on Reinforced Concrete Structures

Hakan Yalciner

Civil Engineering Department, Erzincan University, Turkey

Correspondence should be addressed to Hakan Yalciner; hakan.yalciner@emu.edu.tr

Received 1 July 2013; Accepted 1 January 2014; Published 2 June 2014

Academic Editor: Nuno Maia

Copyright © 2014 Hakan Yalciner. This is an open access article distributed under the Creative Commons Attribution License, which permits unrestricted use, distribution, and reproduction in any medium, provided the original work is properly cited.

Structural blast design has become a necessary part of the design with increasing terrorist attacks. Terrorist attacks are not the one to make the structures important against blast loading where other explosions such as high gas explosions also take an important place in structural safety. The main objective of this study was to verify the structural performance levels under the impact of different blast loading scenarios. The blast loads were represented by using triangular pulse for single degree of freedom system. The effect of blast load on both corroded and uncorroded reinforced concrete buildings was examined for different explosion distances. Modified plastic hinge properties were used to ensure the effects of corrosion. The results indicated that explosion distance and concrete strength were key parameters to define the performance of the structures against blast loading.

1. Introduction

Most of the design codes consider essentially the seismic, wind, rain, and snow loads. Blast loads have different place in engineering when they are compared with other loads. Even the fundamentals of blast and seismic design depend on dynamic behaviour and energy dissipation approaches; the design of blast and the response of the structures against blast loads are extremely different than other well-known loads. Unlike seismic and wind loads, blast loads have a short duration, generally in milliseconds (ms). With increasing terrorist attacks on military buildings, blast design has kept its popularity to develop new design codes. From military buildings, blast design has started to be adopted for residential buildings to resist the gas explosions in huge and closed areas. Thus, the first blast design code has been developed by FEMA 427 [1]. On March 20, 2003, the United States attacked Iraq. Over 4,000 US soldiers died in that war. Most of those deaths occurred with suicide truck bomb that exploded in front of military buildings. Figure 1 shows a typical effect of blast load on Canal Hotel in Baghdad, Iraq, in 2003. The building was heavily damaged by using trinitrotoluene (TNT) which exploded at a nearby distance.

If an explosion distance is pretty close and the building walls are not designed by shear walls, the blast also affects the interior side of the buildings. Such an explosion was done by couple car bomb attacks in central Baghdad in 2007. Fifty-nine people died as a result of explosions. Twenty people out of fifty-nine were located inside of the building. For an explosion outside a building, the exterior envelope (i.e., wall, reinforced concrete members, and glass) is the critical line of defence that separates the people, operations, and contents inside the building from the air-blast effects outside the building [2]. Unfortunately, most of the buildings in Iraq were ill-suited to resist the blast loads which could have saved the people that were located inside of the buildings. Not only the reinforced concrete buildings but also bridges, railways, and roads are under the blast risk. Exploded blast load on major bridges in Baghdad caused collapse to the whole truss steel frames and concrete asphalt. Within a short period of explosion, connections of the steel bars were melded with crushed concrete. The released potential energy with blast load is much more effective on steel structures when it is compared with reinforced concrete buildings since steel structures provide little resistance to thermal energy. While the blast load causes the steel structures to melt, it turns the concrete into sand and dust by exceeding yield strength of concrete. At this point not only the amount of the blast load but also the pressure of the wave to the surface of concrete and explosion distance take an important place for

Figure 1: Destroyed reinforced concrete building by blast load [15].

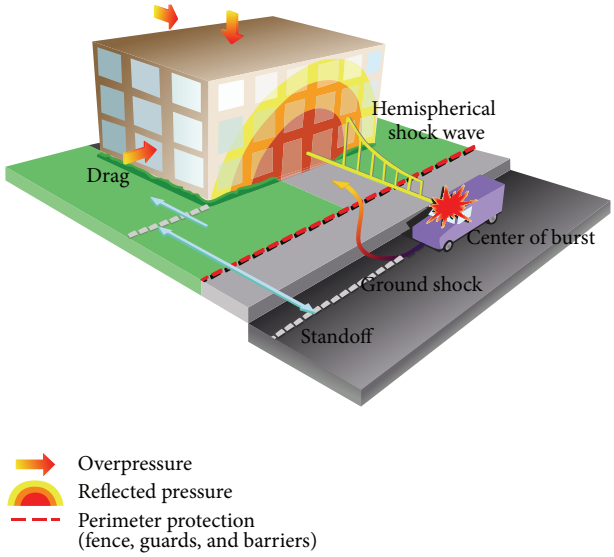

Figure 2: Schematic of a blast load [4].

structures. When a response of a building from blast load is considered, natural period of vibration of the structure is the vital parameter for a given explosion. Ductile elements made of steel and reinforced concrete absorb a lot of strain energy [3]. The effects of blast on reinforced concrete and steel structures have been widely studied by many researchers. To the knowledge of the author, the effects of corrosion with blast loads on reinforced concrete buildings have not been studied. Therefore, in this study, different blast load scenarios were performed for uncorroded and corroded reinforced concrete buildings to investigate the effect of blast loads with corrosion. Performance levels of the reinforced concrete buildings were obtained under the effect of blast loads. The impacts of the blast waves on the surface of the structural members were simulated.

2. Blast and Loadings

Blast can be defined as a rapid phase of a created pressure by a sudden release of energy. This energy provides a blast wave in different shapes. The general generated blast wave has been formed in a hemispherical form away from the blast site as shown in Figure 2.

In this study, the peak static overpressure was calculated based on the model developed by Smith and Hetherington [4]:

$$\begin{aligned} &\text{for} \quad P_s > 10 \text{ bar} \quad P_s = \frac{6.7}{Z^3} + 1 \\ &\text{for} \quad 0.1 < P_s < 10 \text{ bar} \quad P_s = \frac{0.975}{Z} + \frac{1.455}{Z^2} + \frac{5.85}{Z^3}, \end{aligned} \tag{1}$$

where Z is the scaled distance (ft/lb$^{1/3}$) and it can be calculated by the following equation. In (2) R and W denote the explosion distance (ft) and the explosives weight (lb) in TNT, respectively:

$$Z = \frac{R}{W^{1/3}}. \tag{2}$$

Idealized pressure-time history of a blast load and comparison between free-field, or side-on, and reflected pressure-time histories are shown in Figure 3. In Figure 3(a), P_o is the ambient pressure, P_{so} is the peak positive side-on overpressure, P_{so}^- is the peak negative side-on overpressure, $P_s(t)$ is the time varying positive overpressure, $P_s^-(t)$ is the time varying negative overpressure, P_r is the peak reflected overpressure, I_s is the positive-phase-specific impulse (the integration of the positive phase pressure-time history), and i_s^- is the negative-phase-specific impulse (the integration of the negative phase pressure-time history).

The velocity of a wave (U_s) and the maximum pressure were calculated based on the model proposed by Smith and Hetherington [4]. Consider

$$\begin{aligned} U_s &= \sqrt{\frac{6P_s + 7P_o}{7P_o}} \cdot a_o, \\ q_s &= \frac{5P_s^2}{2\left(P_s + 7P_o\right)}, \end{aligned} \tag{3}$$

where a_o is the ambient air pressure ahead of wave, γ is the specific heat ratio, and ρ is the density of air. The reflected pressure, P_r, was then calculated by following equations:

$$\begin{aligned} P_r &= 2P_s + (\gamma + 1)\, q_s, \\ q_s &= \frac{1}{2}\rho_s u_s^2, \\ u_s &= \frac{a_o \cdot P_s}{\gamma P_o}\left[1 + \left[\frac{\gamma + 1}{2\gamma}\right].\frac{P_s}{P_o}\right]^{-1/2}, \\ P_r &= 2P_s\left[\frac{7P_o + 4P_s}{7P_o + P_s}\right]. \end{aligned} \tag{4}$$

In this study, four different explosion distances (i.e., 6 m, 12 m, 18 m, and 24 m) were defined with having the same amount of 150 kg TNT. The mass specific energy for TNT was equal to 4520 kJ/kg.

3. Material Modelling

In order to perform the blast load with combined corrosion effects, stress and strain relationships of concrete and reinforcement bars were defined by user. In this study we used the

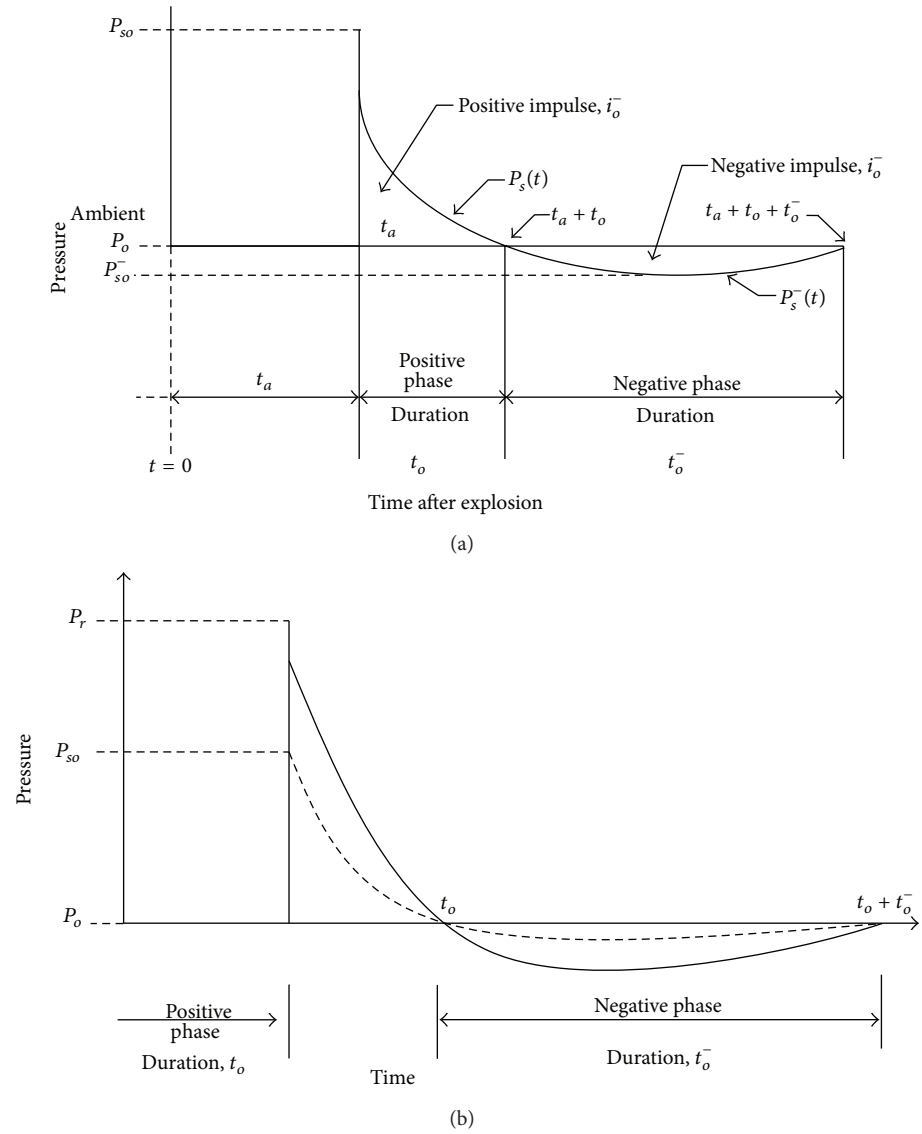

FIGURE 3: (a) Blast wave pressure-time graph. (b) Blast load and comparison [4].

model with more than 30 years developed by Kent and Park [5] to model the stress and strain relationships of concrete. Basically, this model by Kent and Park [5] has two segments. For the first segment (A-B), the curve reaches maximum stress level which is equal to 0.002. After reaching maximum stress, two different other segments occur (B-C, B-D) where two straight lines indicate different behaviour of concrete for confined and unconfined concrete. Figure 4(a) shows Kent and Park [5] model for the stress-strain relationship of reinforced concrete sections. In this study Mander's [6] model was used for the modelling of stress-strain relationship of reinforcement bars. Mander [6] proposed a model which can be used for both softer and harder steel. The model includes linear elastic region up to yield, elastic-perfect-plastic region, and strain hardening region. Mander's model [6] controls both strength and ductility where descending branch of the curve that first branch increase linearly until yield point and then the curve continues as constant. Figure 4(b) shows the model proposed by Mander [6] for stress and strain relationships of reinforcement bars.

The steel and concrete classes were selected as S420 (420 MPa) and C40 (40 MPa), respectively. Elastic modulus of concrete ($E_c = 3250\sqrt{f_c'} + 14000$ MPa) was calculated according to Turkish standards 500 [7], and the elastic modulus of steel (E_s) was taken as 200,000 MPa. A corrosion rate of 0.40 μA/cm^2 was assumed to be used in analyses. A corrosion rate in mm/year was converted to μA/cm^2 by considering that 1 μA/cm^2 is equal to 0.0116 mm/year. Three major effects (i.e., loss in cross-sectional area of reinforcement bars, reduction in concrete strength, and bond-slip relationships) of corrosion were taken into account. Reduction in concrete strength was calculated based on the model developed by Yalciner et al. [8]. The model developed by Yalciner et al.

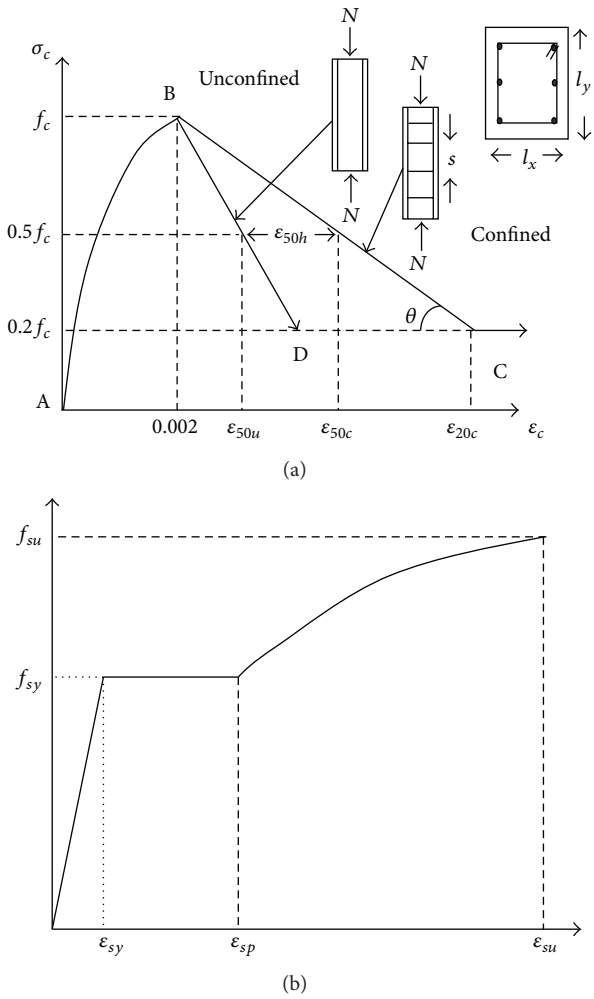

FIGURE 4: (a) Stress-strain relation of reinforced concrete [5]. (b) Stress-strain relation of steel bars [6].

[8] provides calculation of the reduction in concrete strength as a function of corrosion rate or mass loss. The volume of corrosion rust is generally 2 to 4 times larger than the volume of original reinforcement [9]. The porous zone around the reinforcing bars is filled with this corrosion product which results in internal pressure on the surrounding concrete. As a consequence of volumetric expansion inside of concrete, the concrete strengths reduce as a function of corrosion rate which occurs due to increased width. The model developed by Yalciner et al. [8] to calculate the increased width of the structural members due to corrosion is given in

$$b_f - b_0 = n_{\text{bars}} \left(\frac{4\pi d_s(t)}{(1-\nu_c)/(a/b)^{\sqrt{\alpha}} + (1+\nu_c)(b/a)^{\sqrt{\alpha}}} - \frac{2\pi b f_t}{E_{\text{ef}}} \right). \quad (5)$$

In (5), b_f is the width increased by corrosion cracking, b_0 is the section width in the virgin state, n_{bars} is the number of the bars in the top layer (compressed bars), $d_s(t)$ is the thickness of corrosion product form, ν_c is the Poisson's ratio of concrete, f_t is the tensile strength of concrete, E_{ef} is the effective elastic modulus of concrete ($a = (d_b + 2d_0)/2$), d_b is the diameter of reinforcement bars, d_0 is the thickness of the annular layer of concrete pores, b is the outer radii of the of the thick-wall cylinder ($b = S/2$), S is the rebar spacing, and c_5 and c_6 are boundary conditions as proposed by Li et al. [10]. Once the corrosion rate is known, the reduction in concrete strength can be predicted by using the model developed by Yalciner et al. [8]. Yalciner et al. [11] in another study also developed a corrosion model to predict the ultimate bond strength of uncorroded and corroded reinforcement bars as a function of three different concrete cover depths and two different concrete strength levels for different given corrosion levels by using accelerated corrosion method and performed pull-out tests. In this study to calculate the ultimate bond strength of uncorroded structural members, the developed model by Yalciner et al. [11] was used by given (6). In (6), f_c' is the concrete compressive strength, c is the concrete cover depth, and D is the diameter of a steel bar:

$$\tau_{bu} = -2.7143 + 0.3621 f_c' + 2.3296 \left(\frac{c}{D} \right) \text{(MPa)}. \quad (6)$$

In order to calculate and predict the ultimate bond strength of corroded structural members, the following model developed by Yalciner et al. [11] was used. In (7) developed bond strength model by Yalciner et al. [11] considers the limits of corrosion levels for the ascending branch when cover to diameter ratios are equal and greater than two. Consider

$$\text{if } \frac{c}{D} \geq 2, \quad \begin{cases} 0 \leq C_L \leq 1.4 & \text{for } f_c' = 23\,\text{MPa} \\ 0 \leq C_L \leq 0.68 & \text{for } f_c' = 51\,\text{MPa} \end{cases}$$
$$\tau_{bu} = e^{(0.01572 f_c' + 0.22957(c/D) + 0.13946 C_L + 1.75913)} \text{(MPa)}. \quad (7)$$

Calculated bond strengths of structural member were used to predict the slippage of reinforcement bars. For doing this a well-known slip model developed by Alsiwat and Saatcioglu [12] was used. In the model developed by Alsiwat and Saatcioglu [12], the development length was divided into four regions, based on the state of the steel stress-strain relationship (i.e., an elastic region, a yield plateau, a strain hardening region, and a pull-out cone region). Alsiwat and Saatcioglu [12] suggested thatonce extension of a reinforcement bar is calculated, slip rotation can be calculated by using moment-curvature relationships given by

$$\theta_s = \frac{\delta_{\text{ext}}}{d - c}, \quad (8)$$

where d is the section depth, c is the neutral axis of assessed section, and δ_{ext} is the extension of a bar. Calculated reduction in concrete strength (see (5)), loss in cross-sectional area, predicted bond strength (see (6) and (7)), and slip rotations (see (8)) were used to modify the moment-curvature relationships of defined structural member.

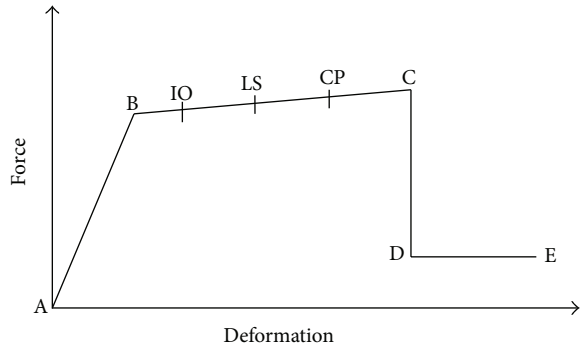

Figure 5: Force-deformation relationship of a plastic hinge.

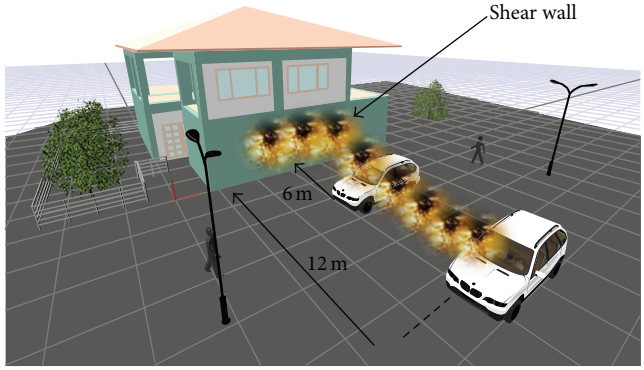

Figure 6: Modelled reinforced concrete building.

4. Blast Analyses and Results

Calculated moment-curvature relationships were used to define the force-deformation relationships. Force-deformation behaviour was defined by using a described standard by FEMA-356 [13]. Figure 5 shows force-deformation relationships to define the behaviour of a plastic hinge by FEMA-356 [13]. On Figure 5 labelled A, B, C, D define force-deformation behaviour which is detail explained by FEMA-356 [13].

The lengths of the plastic hinges (L_p) were calculated according to Park and Paulay [14] by

$$L_p = 0.5H, \tag{9}$$

where H is the related section depth of element. As mentioned earlier, four different explosion distances (i.e., 6 m, 12 m, 18 m, and 24 m) were defined. For this purpose a reinforced concrete building was modelled. The results of the blast effect with combined corrosion damage on building were discussed for designed shear wall as shown in Figure 6.

The first explosion was done with an explosion distance of 6 m and continued with other distances. The results clearly indicated that effect of blast regarding the damage of reinforced concrete building and the resistance of concrete is much more important than the reinforcement bars. At this point, the role of the reinforcement bars on concrete was corrosion. If the reinforcement bars were corroded, with increased cracks within the concrete as a function

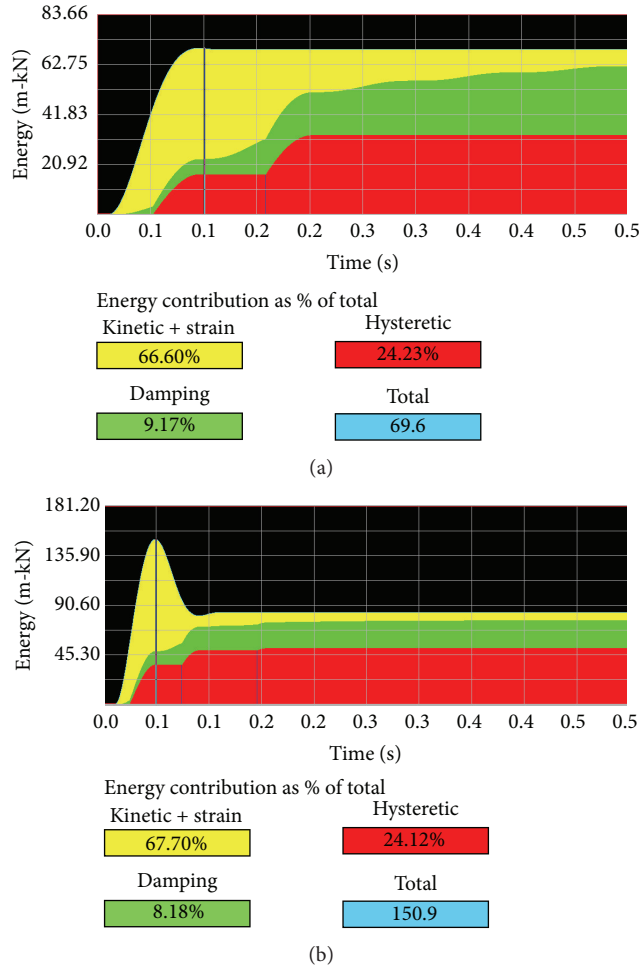

Figure 7: Blast load with a 6 m explosion: (a) uncorroded shear wall and (b) corroded shear wall.

of corrosion rate caused to increase the effect of the blast load. After the first explosion, the results of the energy contributions of the kinetic + strain, damping, and hysteretic energies as well as the total energy are shown in Figure 7. In Figure 7 the hysteretic energy was an indication of structural damage resulting from the application of the blast load.

As shown in Figure 7(a), structural damage resulting from the application of the blast load was less when it was compared with corroded shear wall due to crack width of concrete caused by corrosion. The results of exploded TNT for 18 m and 24 m for both uncorroded and corroded cases were given in Figures 8 and 9, respectively.

In Figure 8, as it was expected, with increased explosion distance, damage to structure was reduced. Moreover, percentage contribution of the hysteretic energy to the total energy was higher for corroded shear wall. The recorded relative percentages of hysteretic energy of uncorroded and corroded concrete members were 3.42% and 7.00%, respectively. These percentages were reduced to zero percentages with an increased explosion distance by 24 m at the same period of 0.15 ms (see Figure 9). Structural damage resulting from the application of the blast load having 0.2 ms was 1.5%

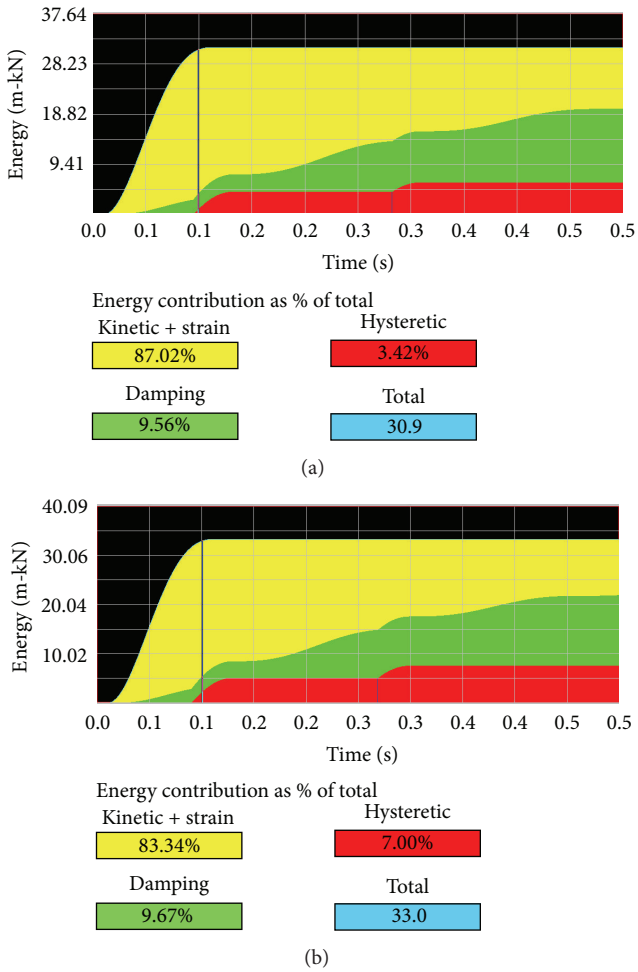

Figure 8: Blast load with 18 m explosion distance: (a) uncorroded shear wall and (b) corroded shear wall.

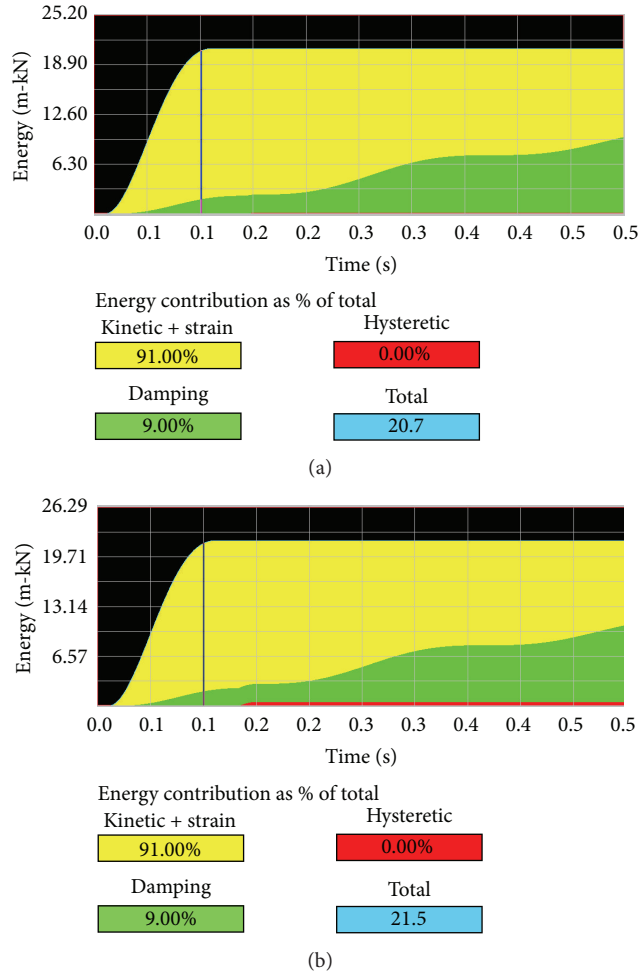

Figure 9: Blast load with a 24 m of explosion distance: (a) uncorroded shear wall and (b) corroded shear wall.

and 2.38% for uncorroded and corroded concrete members, respectively. When two different explosion distances were compared, the recorded 24.23% of relative percentage of hysteretic energy was reduced to zero percentage with increased explosion distance from 6 m to 24 m within 0.10 ms.

5. Conclusion

The effects of blast load on corroded and uncorroded reinforced concrete buildings were studied for different explosion distances. The results clearly indicated that structural damage was reduced with increased explosion distances by depending on amount of TNT that was used in current study. Performed blast loads and obtained results showed that effect of corrosion did not play a major role in the percentage contribution of the hysteretic energy to the total energy by reduction in cross-sectional area of reinforcement bars. Increased crack width of concrete due to corrosion played a major role in the case of corroded structural member. Reduction in cross-sectional area of reinforcement bars directly caused premature yielding of reinforcement bars. Thus, a few amount of energy absorption has been lost during blast load. Since the yield and compressive strength of concrete were vital parameters, slippage of reinforcement bars due to corrosion against blast load with a very close explosion distance measured in milliseconds did not influence the performance of the structure. It is believed that the methodology described here will be a guideline for further studies and novel investigations. Therefore, buckling problems and particularly irregularities of buildings under the effect of blast loads do require further studies. The lessons learned from terrorist events in the recent past could guide us in the design and in the risk assessment of buildings considering their vulnerability to blast loading.

Conflict of Interests

The author declares that there is no conflict of interests regarding the publication of this paper.

References

[1] Federal Emergency Management Agency (FEMA), *Risk Management Series Primer for Design of Commercial Buildings to Mitigate Terrorist Attacks*, FEMA 427, 2003.

[2] D. O. Dusenberry, Ed., *Handbook of Blast Resistant Design of Buildings*, John Wiley & Sons, 2010.

[3] "Design of buildings to optimize resistance to blast loading," in *Blast Effects on Buildings*, G. C. Mays and P. D. Smith, Eds., 1995.

[4] P. D. Smith and J. G. Hetherington, *Blast and Ballistic Loading of Structures*, 2nd edition, 1994.

[5] D. C. Kent and R. Park, "Flexural members with confined concrete," *Journal of Structural Division*, vol. 97, no. 7, pp. 1969–1990, 1997.

[6] J. B. Mander, *Seismic design of bridge piers [Ph.D. thesis]*, University of Canterbury, Canterbury, New Zealand, 1984.

[7] Turkish Standards Institute, "Requirements for design and construction of reinforced concrete structures," Tech. Rep. TS500, Turkish Standards Institute, Ankara, Turkey, 2000.

[8] H. Yalciner, S. Sensoy, and O. Eren, "Time-dependent seismic performance assessment of a single-degree-of-freedom frame subject to corrosion," *Engineering Failure Analysis*, vol. 19, no. 1, pp. 109–122, 2012.

[9] Z. P. Bazant, "Physical model for steel corrosion in concrete sea structures—application," *ASCE Journal of the Structure Division*, vol. 105, no. 6, pp. 1155–1166, 1979.

[10] C. Q. Li, J. J. Zheng, W. Lawanwisut, and R. E. Melchers, "Concrete delamination caused by steel reinforcement corrosion," *Journal of Materials in Civil Engineering*, vol. 19, no. 7, pp. 591–600, 2007.

[11] H. Yalciner, O. Eren, and S. Sensoy, "An experimental study on the bond strength between reinforcement bars and concrete as a function of concrete cover, strength and corrosion level," *Cement and Concrete Research*, vol. 42, no. 5, pp. 643–655, 2012.

[12] J. M. Alsiwat and M. Saatcioglu, "Reinforcement anchorage slip under monotonic loading," *ASCE Journal of Structural Engineering*, vol. 118, no. 9, pp. 2421–2438, 1992.

[13] Federal Emergency Management Agency, *Pre-Standard and Commentary for the Seismic Rehabilitation of Buildings*, The American Society of Civil Engineers for the Federal Emergency Management Agency (FEMA), Washington, DC, USA, 2000, Publications no. 356.

[14] R. Park and T. Paulay, *Reinforced Concrete Structures*, John Wiley & Sons, New York, NY, USA, 1975.

[15] BBC news, 2012, http://www.bbc.co.uk/news/world-middle-east-18422636.

Hindawi Publishing Corporation
Shock and Vibration
Volume 2014, Article ID 607125, 10 pages
http://dx.doi.org/10.1155/2014/607125

Research Article

Localization of Transversal Cracks in Sandwich Beams and Evaluation of Their Severity

G. R. Gillich,[1] Z. I. Praisach,[1] M. Abdel Wahab,[2] and O. Vasile[3]

[1] *Department of Mechanics, "Eftimie Murgu" University of Resita, P-ta Traian Vuia 1-4, 320085 Resita, Romania*
[2] *Department of Mechanical Construction and Production, Ghent University, Technologiepark Zwijnaarde 903, 9052 Zwijnaarde, Belgium*
[3] *Department of Mechanics, University Politehnica of Bucharest, 313 Splaiul Independentei, 060042 Bucharest, Romania*

Correspondence should be addressed to G. R. Gillich; gr.gillich@uem.ro

Received 12 July 2013; Accepted 10 March 2014; Published 1 June 2014

Academic Editor: Nuno Maia

Copyright © 2014 G. R. Gillich et al. This is an open access article distributed under the Creative Commons Attribution License, which permits unrestricted use, distribution, and reproduction in any medium, provided the original work is properly cited.

An algorithm to assess transversal cracks in composite structures based on natural frequency changes due to damage is proposed. The damage assessment is performed in two steps; first the crack location is found, and afterwards an evaluation of its severity is performed. The technique is based on a mathematical relation that provides the exact solution for the frequency changes of bending vibration modes, considering two terms. The first term is related to the strain energy stored in the beam, while the second term considers the increase of flexibility due to damage. Thus, it is possible to separate the problems of localization and severity assessment, which makes the localization process independent of the beams cross-section shape and boundary conditions. In fact, the process consists of comparing vectors representing the measured frequency shifts with patterns constructed using the mode shape curvatures of the undamaged beam. Once the damage is localized, the evaluation of its severity is made taking into account the global rigidity reduction. The damage identification algorithm was validated by experiments performed on numerous sandwich panel specimens.

1. Introduction

Composites consist of two or more constituents with quite different physical and/or chemical properties, separately and distinctively identifiable within the structure. Unlike natural materials, which have predefined properties, composites are elaborated to fulfill predefined needs, permitting a new approach in structural design. Among composites, sandwich structures are a special class; they are manufactured by sheets with different mechanical and physical properties, disposed in a spatial distribution that provides the sandwich composite with high shear stiffness and high bending stiffness to weight ratio. Under static and dynamic loads in various environments, sandwich structures related problems are studied from the mid of the last century. The main attempts are focused on bending and buckling [1–3], optimal design [4–6], shock resistance [7, 8], and vibrational behavior [9–12] with identification of natural frequencies and/or elastic parameters of the sandwich structures. Recent works are devoted to detection of damage in sandwich beams or plates, with different core types and damage configurations [13–16]. Most actual damage detection methods, even for isotropic structures, are difficult to be applied due to the fact that no analytical solution to quantify frequency changes due to damage is available. Furthermore, the damage assessment algorithm has to be an adapted function of boundary conditions and mechanical and geometrical structure characteristics.

Our previous research work [17–20] permitted contriving a mathematical relation that permitting predicting the values of the natural frequencies for damaged beams with any crack type and configuration. This technique is applicable for beams having any support type and slenderness. Based on this technique, we developed a damage detection algorithm that uses the frequency shifts of the weak-axis transversal vibration modes. Because the frequency shift is expressed by two terms, where the first term depends on the damage location and the second on its depth, it is possible to separate the problem of localizing the damage and evaluating its

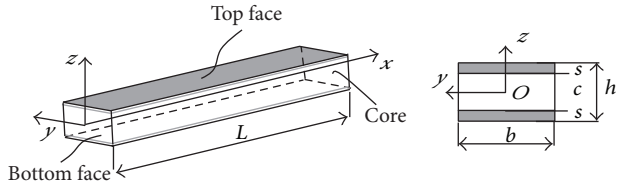

Figure 1: Sandwich beam with three layers.

severity. Consequently, we proposed a damage detection method, which is performed in two steps, that is, first identifying the damage location and afterwards estimating its severity. This paper presents an extension of the method for multilayered beams.

2. Vibration of Sandwich Beams

Since the aim of the research was to establish a proper damage detection method for composite beams, we analyzed first the dynamic behavior of these types of structures. For the analysis, we consider a sandwich beam, having length L, width b, and height h, composed of top and upper steel faces with thickness s and foam core with thickness c as shown in Figure 1. The material parameters of the steel faces are mass density ρ_s; Young's modulus E_s; and Poisson's ratio μ_s. The foam core has mass density ρ_c, Young's modulus E_c, and Poisson's ratio μ_c.

For a symmetrical cross-section like that presented in Figure 1, the core flexural rigidity measured around the neutral axis Oy is given by [4]

$$(EI)_{\text{core}} = \frac{E_c b c^3}{12}. \tag{1}$$

For the two faces, each of cross-sections $A_s = bs$, with the weight center placed at distance $d = (c+s)/2$ from the neutral axis Oy, the flexural rigidity measured around this axis is as follows:

$$(EI)_{\text{faces}} = 2E_s\left(\frac{bs^3}{12} + A_s d^2\right). \tag{2}$$

The equivalent flexural rigidity $(EI)_{\text{eq}}$ of the sandwich beam is the sum of the rigidities of the faces and the core around the neutral axis Oy. It can be expressed as follows:

$$\begin{aligned}(EI)_{\text{eq}} &= \frac{E_s b s^3}{6} + \frac{E_s b s (c+s)^2}{2} + \frac{E_c b c^3}{12} \\ &= \frac{b}{12}\left[2E_s s^3 + 6E_s s(c+s)^2 + E_c c^3\right].\end{aligned} \tag{3}$$

The linear mass for one face is $\widehat{m}_s = \rho_s A_s = \rho_s bs$, while the linear mass for the core is $\widehat{m}_c = \rho_c A_c = \rho_c bc$; thus, the linear mass for the sandwich beam is as follows:

$$\widehat{m}_{\text{eq}} = 2\rho_s bs + \rho_c bc. \tag{4}$$

Consequently, using relations (3) and (4), the equation of motion for an Euler-Bernoulli beam, neglecting the effect of damping, is given by

$$\begin{aligned}&\frac{\partial^4 w}{\partial x^4} + \frac{\widehat{m}_{\text{eq}}}{(EI)_{\text{eq}}} \cdot \frac{\partial^2 w}{\partial t^2} = 0 \text{ or} \\ &\frac{\partial^4 w}{\partial x^4} + \frac{12\left(2\rho_s s + \rho_c c\right)}{2E_s s^3 + 6E_s s(c+s)^2 + E_c c^3} \cdot \frac{\partial^2 w}{\partial t^2} = 0.\end{aligned} \tag{5}$$

Considering that the vertical displacement w depends on distance x and time t, and the evolution in time is harmonic, w can be written as follows:

$$w = X(x) \cdot T(t) = X \cdot \sin \omega t. \tag{6}$$

After derivation and substitution in relation (5), one obtains the following:

$$X^{IV} - \frac{\widehat{m}_{\text{eq}}\omega^2}{(EI)_{\text{eq}}} X = 0. \tag{7}$$

Denoting $\widehat{m}_{\text{eq}}\omega^2/(EI)_{\text{eq}} = \alpha^4$, we find the solution as follows:

$$X = C_1 \sin \alpha x + C_2 \cos \alpha x + C_3 \sinh \alpha x + C_4 \cosh \alpha x. \tag{8}$$

After three derivations, one obtains the system of equations as follows:

$$\begin{aligned}X &= C_1 \sin \alpha x + C_2 \cos \alpha x + C_3 \sinh \alpha x + C_4 \cosh \alpha x \\ X' &= \alpha\left(C_1 \cos \alpha x - C_2 \sin \alpha x + C_3 \cosh \alpha x + C_4 \sinh \alpha x\right) \\ X'' &= \alpha^2\left(-C_1 \sin \alpha x - C_2 \cos \alpha x + C_3 \sinh \alpha x + C_4 \cosh \alpha x\right) \\ X''' &= \alpha^3\left(-C_1 \cos \alpha x + C_2 \sin \alpha x + C_3 \cosh \alpha x + C_4 \sinh \alpha x\right).\end{aligned} \tag{9}$$

If we consider the beam as a cantilever, the boundary conditions are $X(0) = X'(0) = 0$ and $X''(L) = X'''(L) = 0$; thus we obtain the characteristic equation as follows:

$$1 + \cos \lambda \cdot \cosh \lambda = 0, \tag{10}$$

with $\lambda = \alpha L$, which permits calculating the λ_i values for i vibrations modes. Multiplying the expression of α^4 with L^4 and substituting the values of λ_i and the angular frequencies ω_i, consequently the natural frequencies of the undamaged cantilever beam are obtained as follows:

$$\begin{aligned}&f_i = \frac{\lambda_i^2}{2\pi}\sqrt{\frac{(EI)_{\text{eq}}}{\widehat{m}_{\text{eq}} L^4}} \text{ or} \\ &f_i = \frac{\lambda_i^2}{2\pi L^2}\sqrt{\frac{2E_s s^3 + 6E_s s(c+s)^2 + E_c c^3}{12 \cdot \left(2\rho_s s + \rho_c c\right)}}.\end{aligned} \tag{11}$$

Equation (8) shows that the dynamic behavior of a sandwich beam is similar to that of a homogeneous beam in terms of mode shapes, while the natural frequencies are different. This feature was used for the design of a damage detection method applicable to sandwich beams.

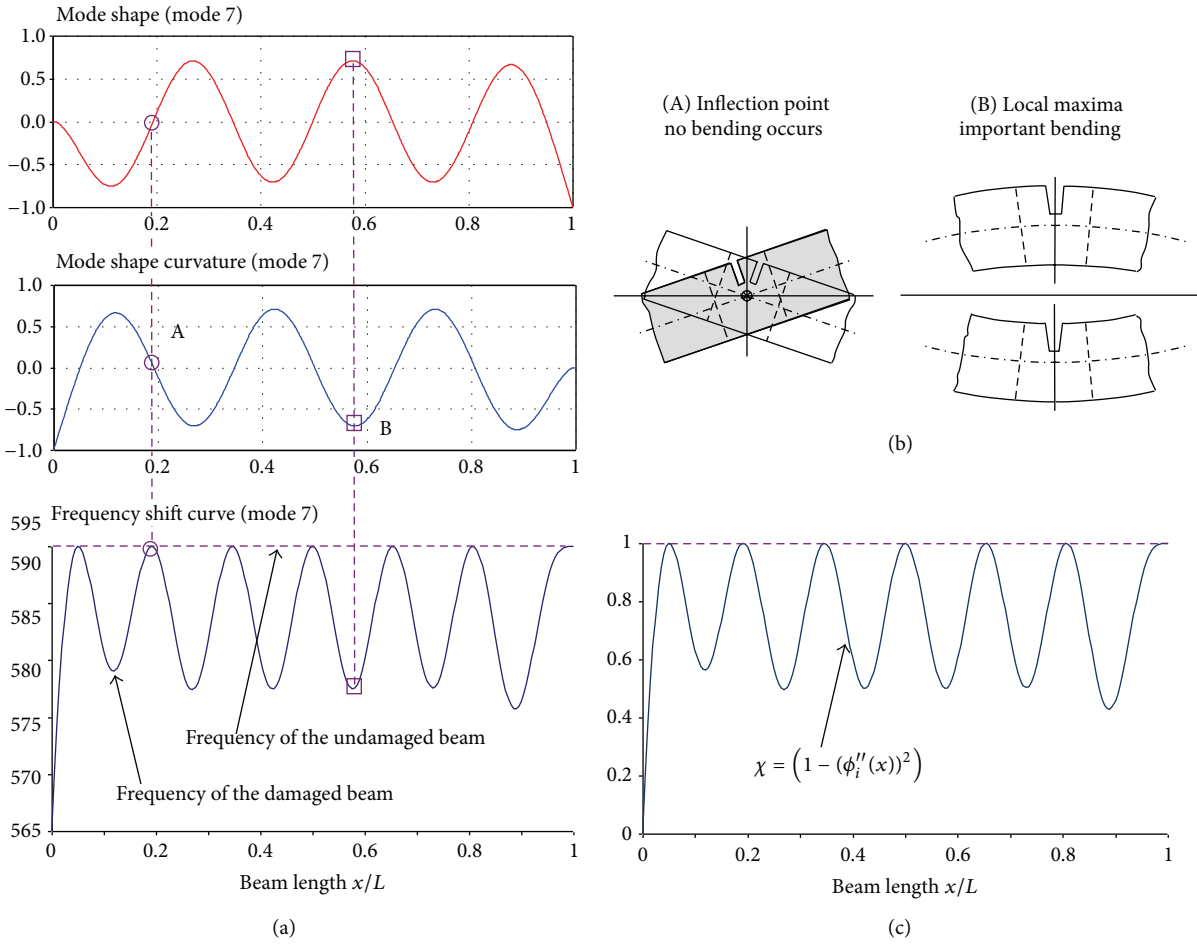

FIGURE 2: (a) Mode shapes, curvature, and natural frequency shift curves for bending mode 7, (b) the behavior of slices placed on characteristic point on the beam, and (c) the representation of function χ for the same bending vibration mode.

3. Exact Solution for the Frequency Changes due to Damage

The effect of a crack on the natural frequency of a certain transversal vibration mode depends on its position on the beam and its geometry, namely, orientation, depth, and width. For transversal cracks with a given location on the beam, the depth increase produces a frequency decrease. On the other hand, a transversal crack with given depth and width produces different frequency shifts for a certain vibration mode when it has different locations along the beam. Similarly, a crack placed in a certain location will produce different frequency shifts for different vibration modes; for example, there are several locations in which the damage will not produce a frequency change at all. This phenomenon happens due to the fact that beam slices are placed in locations where a mode shape curvature has inflection points that undergo no bending and consequently do not contribute to the strain energy stored in the beam for that mode. Thus, when a crack does not lead to loss of energy, the natural frequency of that mode is not affected. On the contrary, a slice placed in a location where the mode shape curvature of a certain vibration mode exhibits local extrema is able to accumulate important amount of strain energy.

Therefore, a crack placed on that location essentially modifies the natural frequencies of that vibration mode. In this paper an example of a cantilever beam, fixed on the left end ($x = 0$), is presented.

Figure 2(a) shows the beam mode shape and its curvature for bending mode 7, with stress on two characteristic points, namely, one of the curvature's inflection points A and one of its local maxima B. Herein, it is also presented as a curve reflecting the damaged beam's frequencies for all possible crack locations along the beam. From Figure 2(a), one observes the good correlation between the characteristic points (i.e., inflexion and local extrema) and the frequency shifts tendency.

Figure 2(b) depicts the behavior of the slices placed on the above mentioned characteristic points. Obviously, the slice placed on an inflection point (e.g., point A) just rotates, being not subjected to bending. This means that no energy is stored in that slice so that a crack located in this location does not affect the global behavior of the beam in mode 7. This means that no energy decrease takes place; thus no frequency change

occurs. On the other hand, it can easily be observed that a crack placed on slice that undergoes severe bending (i.e., high values of the curvature), like that placed on point B, produces an important frequency decrease. This fact is justified by the expression of the strain energy stored in a slice:

$$dU_i(x) = \frac{1}{2} EI\left(\phi_i''(x)\right)^2 dx, \tag{12}$$

where $U_i(x)$ is the strain energy stored in the slice, dx is located at distance x from the fixed end for the vibration mode i, and $\phi_i''(x)$ is the mode shape curvature for mode i at that location. Consequently, the frequency change of a vibration mode i due to a certain crack depends on the energy stored in the affected slice, that is, the square of the mode shape curvature. This means that knowing the effect of a crack placed in the location where the local stored energy (or the curvature square) attends the global maxima, it is possible to find the crack influence on any other position by considering the normalized stored energy in that location. For the cantilever fixed point at $x = 0$, the normalized stored energy in any location is calculated by using the following relation:

$$d\overline{U}_i(x) = \frac{dU_i(x)}{dU_i(0)} = \frac{\left(\phi_i''(x)\right)^2}{\left(\phi_i''(0)\right)^2} = \left(\overline{\phi}_i''(x)\right)^2. \tag{13}$$

Since this paper focuses on Euler-Bernoulli beams, we can use the "normalized curvature square" instead of the "normalized stored energy."

The similarity between the frequency shift curves due to damage and the expression $\chi = (1 - (\phi_i''(x))^2)$ is obvious as can be seen in Figures 2(a) and 2(c). This fact demonstrates that the frequency shift due to a crack placed on the beam is controlled by the normalized curvature square. Evidently, the deeper the crack, the higher the frequency decrease. Based on these observations, we determined a relationship that indicates the frequency shift for any bending vibration mode i, damage depth a, and location x and any beam support type [21]. The relation is presented as follows:

$$f_{i-D}(x,a) = f_{i-U} \cdot \left[1 - \gamma(0,a) \cdot \left(\overline{\phi}_i''(x)\right)^2\right]. \tag{14}$$

The notations used are f_{i-U} for the frequency of the undamaged beam, $f_{i-D}(x,a)$ for the frequency of the damaged beam with a crack of depth a at the position x on the beam, $\gamma(a)$ for a function representing the maximum stiffness reduction (for cantilever beams, it is at the fixed end), and $\overline{\phi}_i''(x)$ for the normalized mode shape curvature having values between −1 and 1. From previous researches, we found the relation for the damage severity as [14]

$$\gamma(a) = 1 - \sqrt{\frac{v_{U\max}(a)}{v_{D\max}(a)}}, \tag{15}$$

where $v_{U\max}(a)$ is the deflection of the undamaged beam and $v_{D\max}(a)$ is the deflection of the damaged beam, under own weight, respectively.

The function $\gamma(a)$ has the same meaning as the massless torsional spring of stiffness $\kappa(a)$ used in many papers to model the damage. In these papers, see, for instance, [21–27], the spring constant is expressed using the empirical expressions of local compliance $P(\overline{a})$ from fracture mechanics as follows:

$$\kappa = \frac{1}{c} \quad \text{for } c = \frac{h}{EI} P(\overline{a}), \tag{16}$$

where $\overline{a} = a/h$ is the dimensionless damage depth and c is the damage severity. In the works of Liebowitz and Claus [21], Liebowitz et al. [22], Rizos et al. [23], or Caddemi and Caliò [24], the local compliance has the following form:

$$\begin{aligned} P(\overline{a}) = 5.346 \cdot \big[&1.862 \cdot (\overline{a})^2 - 3.95 \cdot (\overline{a})^3 + 16.375 \cdot (\overline{a})^4 \\ &- 37.226 \cdot (\overline{a})^5 + 76.81 \cdot (\overline{a})^6 \\ &- 126 \cdot (\overline{a})^7 + 172 \cdot (\overline{a})^8 \\ &- 143.97 \cdot (\overline{a})^9 + 66.56 \cdot (\overline{a})^{10}\big]. \end{aligned} \tag{17}$$

Ostachowicz and Krawczuk [25] instead proposed the following expression:

$$\begin{aligned} P(\overline{a}) = 6\pi(\overline{a})^2 \big[&0.6384 - 1.035(\overline{a}) + 3.7201(\overline{a})^2 \\ &- 5.1773(\overline{a})^3 + 7.553(\overline{a})^4 \\ &-7.332(\overline{a})^5 + 2.4909(\overline{a})^6\big]. \end{aligned} \tag{18}$$

Other expressions of the local compliance are given by Bilello [26]

$$P(\overline{a}) = \frac{\overline{a}(2 - \overline{a})}{0.9(\overline{a} - 1)^2} \tag{19}$$

and by Chondros et al. [27], who have created a lumped cracked flexibility model equivalent to their continuous model as follows:

$$\begin{aligned} P(\overline{a}) = 6\pi\left(1 - \nu^2\right)\big[&0.6272(\overline{a})^2 - 1.04533(\overline{a})^3 + 4.5948(\overline{a})^4 \\ &- 9.9736(\overline{a})^5 + 20.2948(\overline{a})^6 \\ &- 33.0341(\overline{a})^7 + 47.163(\overline{a})^8 \\ &- 40.7556(\overline{a})^9 + 19.6(\overline{a})^{10}\big]. \end{aligned} \tag{20}$$

Figure 3 presents the comparison between the curves plotted using (15), expressed in respect to the dimensionless damage depth $\overline{a}$ and the functions $P(\overline{a})$ determined from fracture mechanics. From Figure 3, we observe a good concordance, which validate our approach.

Opposite to the equations presented in the literature, valid just for rectangular cross-sections, (14) contrived by the authors permits correlating damage depth and severity for any cross-section shape. Furthermore, it is applicable for

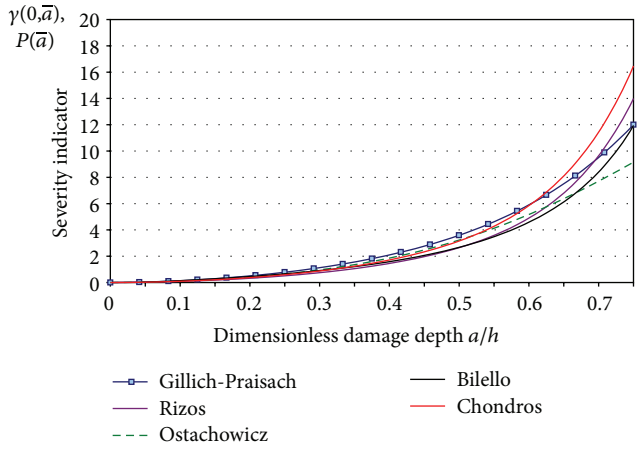

FIGURE 3: Comparison of relations used to express the rigidity loss due to damage versus the dimensionless damage depth.

composites with constant rigidity EI in the healthy state, like sandwich panels or some continuous fiber reinforced composites.

To prove the validity of (14) for some types of composites, simulations were carried out for a cantilever steel beam and a similar sandwich beam (Figure 4), respectively. The damage having the width $\delta = 0.5$ mm is placed in the vicinity of the fixed end and the dimensionless depth a/h varying from 0.1 to 0.9. The results obtained for the two types of structures are presented in Figure 5.

It should be mentioned that, for the steel beam, the damage severity indicator increases constantly until it reaches the value 1 for the theoretical value of damage $a = h$ as presented in Figure 5(a). For the sandwich beam, until the damage does not rift the steel face, the damage severity indicator takes low values. Once the face is completely separated, the damage severity indicator increases dramatically. At this point, the crack extension produces slow increase of the severity indicator, until the bottom steel sheet is reached. If the crack is extending in the bottom steel sheet, the damage severity indicator increases faster with the dimensionless damage depth a/h until it reaches a unit value for the theoretical case $a = h$. These aspects are depicted in Figure 5(b).

4. A Two-Step Damage Assessment Method Based on Pattern Recognition

From (14), we can deduce the frequency shift Δf_i for any bending vibration mode i, damage depth a, and location x as follows:

$$\Delta f_i = f_{i-U} - f_{i-D}(x,a) = f_{i-U} \cdot \gamma(0,a) \cdot \left(\overline{\phi}_i''(x)\right)^2 \quad (21)$$

and the relative frequency shift Δf_i^* of a bending vibration mode as the ratio between the frequency shift and the frequency of the undamaged beam in that mode as

$$\Delta f_i^*(x,a) = \frac{f_{i-U} - f_{i-D}(x,a)}{f_{i-U}} = \gamma(0,a) \cdot \left(\overline{\phi}_i''(x)\right)^2. \quad (22)$$

A novel two-step method to localize and evaluate damage severities was developed based on the contrived relation (22). Considering this relation, at one location on the beam and for n vibration modes, we obtain a series of n terms, in the form of $\Delta f_i^*(x,a) = \gamma(0,a) \cdot (\overline{\phi}_i''(x))^2$, with $i = 1 \cdots n$. Dividing n terms to the highest value of the series, the severity coefficient $\gamma(a)$ is eliminated and the normalized relative frequency shifts $\Phi_i(x) = \Delta f_i^*(x,a)/\max((\Delta f_i^*(x,a))^2)$ for that location are obtained as follows:

$$\Phi_1(x) = \frac{\left(\overline{\phi}_1''(x)\right)^2}{\max\left(\overline{\phi}_i''(x)\right)^2},$$

$$\Phi_2(x) = \frac{\left(\overline{\phi}_2''(x)\right)^2}{\max\left(\overline{\phi}_i''(x)\right)^2}, \quad (23)$$

$$\vdots$$

$$\Phi_n(x) = \frac{\left(\overline{\phi}_n''(x)\right)^2}{\max\left(\overline{\phi}_i''(x)\right)^2}.$$

The series in (23), for which we nominate Spectral Damage Location Index (SDLI), is now independent of depth a. Consequently, it characterizes only the crack location x. Thus, patterns for any damage location can be analytically calculated using the normalized curvature squares as shown in Figure 6, that is, the energy distribution along the beam. It has to be mentioned that only the mode shapes of the healthy beam and the corresponding curvatures are considered, because the mode shapes change insignificantly due to damage. This was proved by vision-based damage detection methods [28], where a subpixel approach is necessary to highlight the mode shape changes. The values extracted from the normalized curvature squares have to be normalized again, thus becoming the highest value, that is, the unit. These patterns can be represented as histograms, as depicted in Figure 7.

On the other hand, the frequency shifts can be determined by measurements. Suppose that, by starting monitoring a beam, the measured frequencies for undamaged beam are $F_U^m : \{f_{1-U}^m, \ldots f_{i-U}^m, \ldots f_{n-U}^m\}$ and for damaged beam are $F_D^m : \{f_{1-D}^m, \ldots f_{i-D}^m, \ldots f_{n-D}^m\}$, with $i = 1 \cdots n$. Applying (14) for the two series F_U^m and F_D^m, we obtain the relative frequency shift for n modes, that is, n dimensionless values: $F^{*m} : \{\Delta f_1^{*m}, \ldots \Delta f_i^{*m}, \ldots \Delta f_n^{*m}\}$. These values can be normalized

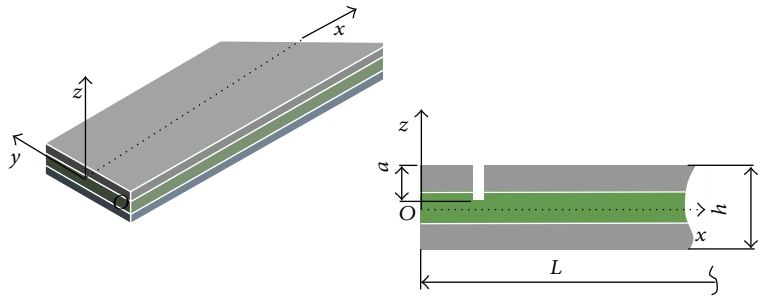

Figure 4: Sandwich beam with damage.

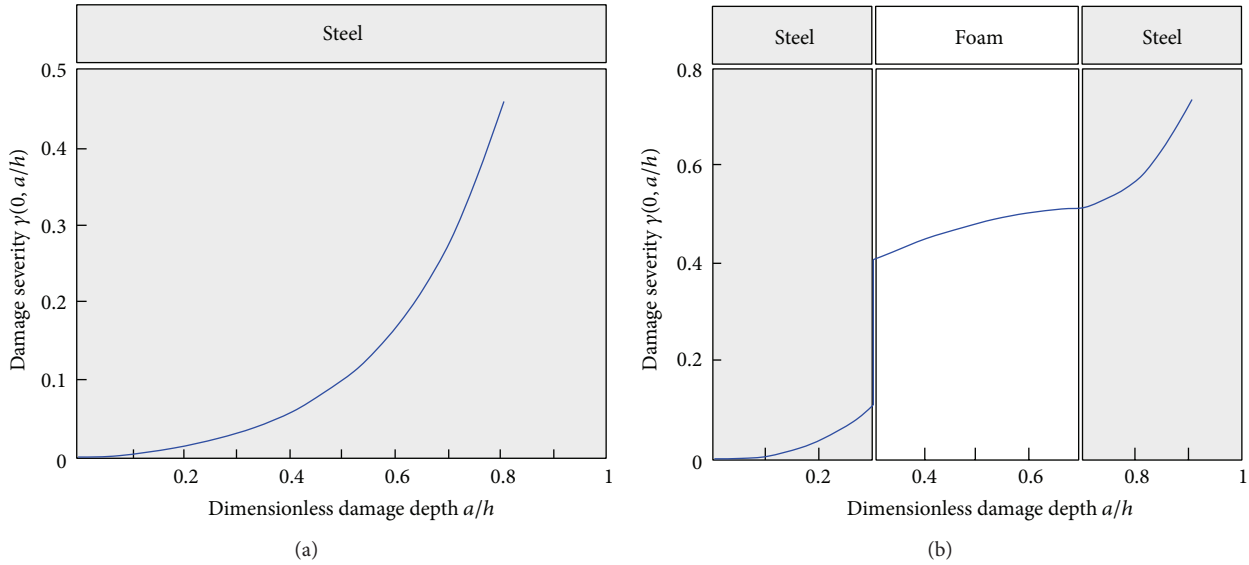

Figure 5: Damage severities versus dimensionless damage depth for (a) the steel beam and (b) the sandwich beam.

by dividing them by the highest value of the series. The mathematical formulation is presented as follows:

$$\Psi_1 = \frac{\Delta f_1^{*m}}{\max\left(\Delta f_i^{*m}\right)},$$
$$\Psi_2 = \frac{\Delta f_2^{*m}}{\max\left(\Delta f_i^{*m}\right)},$$
$$\vdots$$
$$\Psi_n = \frac{\Delta f_n^{*m}}{\max\left(\Delta f_i^{*m}\right)}. \quad (24)$$

Comparing the series Ψ obtained using relation (24) with numerous series Φ obtained from relation (23) by considering a large number of locations x along the beam, one can find the location x_C where the terms of the two series match together. Thus, the crack location is found using only information about the frequency shifts in several vibration modes (determined by measurements), compared with patterns derived from the squares of the healthy beam mode shape curvatures of that vibration modes.

The algorithm can be used for all beams with any support type, simply choosing the adequate mode shape curvatures. Our researches revealed that the number of elements Φ_i involved in the analysis should be from six to ten; more elements are especially necessary when there are modes for which the measured results are not reliable.

Once the damage location x is identified, it is possible to evaluate its severity indicator $\gamma(0, a)$ by rewriting (22) as follows:

$$\gamma(0, a) = \frac{\Delta f_1^*(x, a)}{\left(\overline{\phi}_i''(x)\right)^2}. \quad (25)$$

The relative frequency shift for mode one $\Delta f_1^*(x, a)$ is known from measurements, while the term defining the damage position $\left(\overline{\phi}_i''(x)\right)^2$ is determined as the first member of the SDLI. As soon as the severity indicator $\gamma(0, a)$ is known, the dimensionless damage depth can be determined from diagrams like that presented in Figure 5(a) or 5(b). It has to be mentioned that (25) can be applied for any bending vibration mode, since $\gamma(0, a)$ is mode independent.

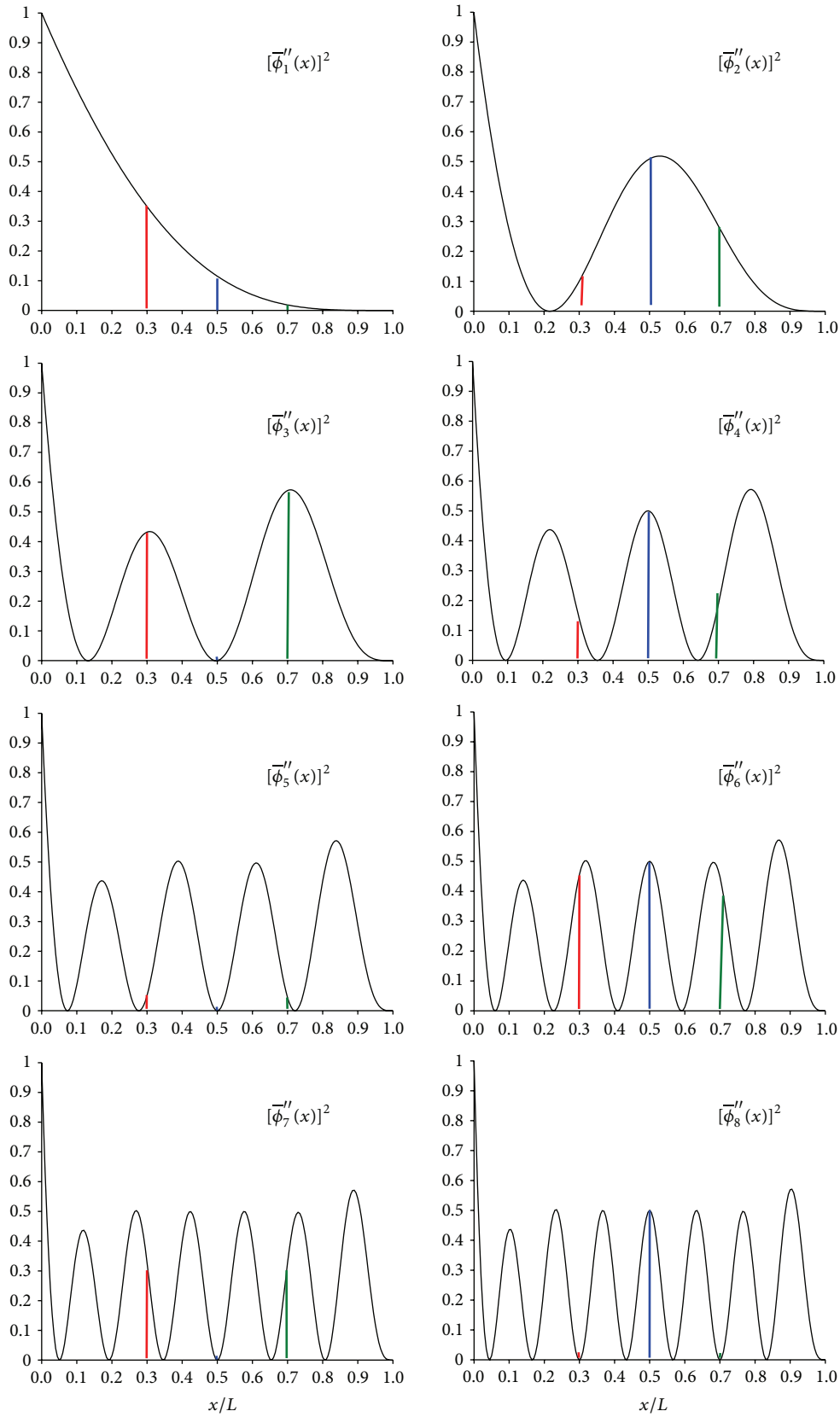

FIGURE 6: Squares of the first eight normalized mode shape curvatures $[\phi_i''(x)]^2$ for the damage placed at $x/L = 0.3$ (red line), $x/L = 0.5$ (blue line), and $x/L = 0.7$ (green line), respectively.

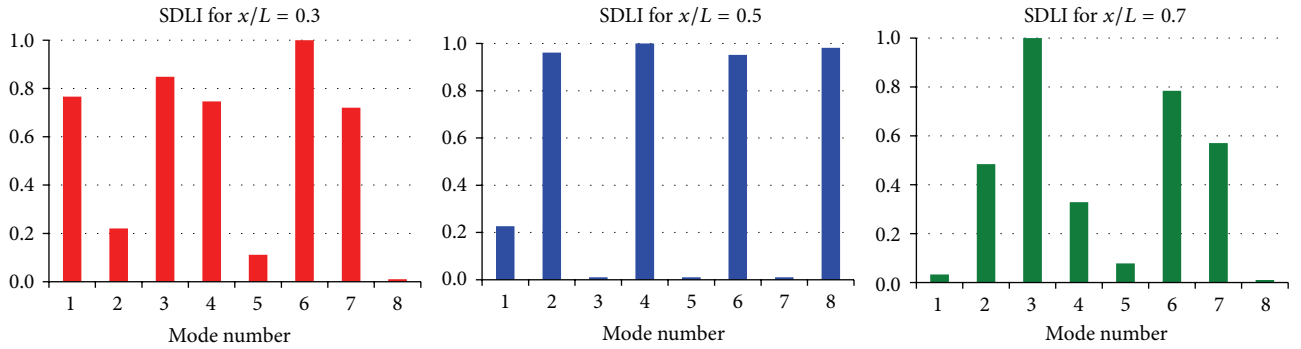

Figure 7: Damage location index for damage placed at $x/L = 0.3$, $x/L = 0.5$, and $x/L = 0.7$, respectively.

Figure 8: Experimental stand.

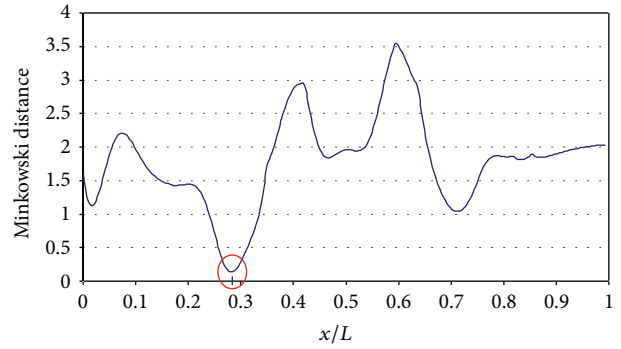

Figure 9: Identification of the crack location using the Minkowski Distance.

5. Experimental Results and Validation of the Method

To prove the method's validity for composite structures, a series of experimental tests were performed on sandwich beams. The experiments presented in this paper are performed on a cantilever beam. The boundary conditions were realized by mounting one of its ends in a rigid support (see Figure 8). The measurement system used for the vibration signal acquisition involved was programming environment LabVIEW, in which a virtual instrument was developed, in order to acquire the time history of acceleration and realize the spectral analysis [29, 30]. This virtual instrument is designed to find the natural frequencies with high accuracy, though early damage detection implies observation of small frequency changes.

The sandwich beam has the following dimensions: length $L = 1000$ mm, width $b = 110$ mm, and height $h = 30$ mm and composed of top and upper steel faces with thickness $s = 1$ mm and foam core with thickness $c = 28$ mm. Our researches include tests on beams with different thicknesses in order to confirm the theory. The material parameters of the steel faces are mass density $\rho_s = 7850\,\text{kg/m}^3$, Young's modulus $E_s = 2.0 \cdot 10^{11}\,\text{N/m}^2$, and Poisson's ratio $\mu_s = 0.3$. For the foam core the similar values are mass density $\rho_c = 30\,\text{kg/m}^3$, Young's modulus $E_c = 1100\,\text{N/m}^2$, and Poisson's ratio $\mu_c = 0.42$.

To find out the natural frequencies for the first six weak-axis bending vibration modes, we measured the accelerations on transversal direction. The accelerometer was placed near the free end of the beam, as shown in Figure 8, in a location assuring reasonable displacement. A transversal force was applied on the beam to bring the mechanical system out of its equilibrium position. By suppressing that force, the beam started to vibrate. We recorded the acceleration values for the undamaged beam and determined the natural frequencies for the first six bending vibration modes. The process was repeated until trustful frequency values were obtained. The results can be improved by replacing the accelerometer on certain points, where the maximum displacement for the corresponding mode is obtained. Afterwards damage with different depths was produced and new series of measurements were realized. The obtained results for a damage depth of 6 mm placed close to the fixed end are presented in Table 1, together with that obtained for the undamaged beam. One observes that for the damaged beam some frequencies show higher changes comparing to the undamaged case, while for other frequencies the changes are not so important. This makes it possible to precisely identify damage location and afterwards its severity by using an algorithm developed by the authors [31].

Using the measured natural frequency values of the weak-axes bending vibrations for the undamaged and damaged case, one can calculate the relative frequency shift $\Delta f_i^*(x)$

Table 1: Measured natural frequencies and corresponding shifts for the analyzed beam.

Mode i	Natural frequency f_i		Relative frequency shift Δf_i^*		Damage location index Φi	
	Undamaged [Hz]	Damaged [Hz]	Percentage [%]	Normalized [—]	$\bar{\phi}_i''$ (0.285) [—]	Normalized [—]
1	15.42	13.782	10.62257	0.827801	0.3815	0.765766
2	94.65	93.048	1.692552	0.131898	0.0721	0.220433
3	261.39	231.114	11.58269	0.902622	0.4107	0.947873
4	498.45	478.91	3.92015	0.305492	0.3913	0.346499
5	803.61	793.584	1.24762	0.097225	0.0531	0.111715
6	1163.13	1013.874	12.83227	1	0.4552	1

in percentage and normalized values with the highest value of the series; the results are also presented in Table 1. It is evident that whereas the relative frequency shift expressed in percentage provides information about the location and depth of damage, the results expressed in dimensionless provide information about the damage location exclusively. For a precise location, it is recommendable to compare first the normalized values obtained from measurements with that obtained analytically and also normalized, for numerous damage locations. To find the location of damage, a program realized by the authors was involved; it uses the Minkowski distance of second order to compare histograms [32]. The damage location was found at distance $x = 0.285$ mm (or $x/L = 0.285$) from the fixed end, as is shown in Figure 9.

Table 1 presents in the last column the damage location index values for the first six vibration modes calculated for damage placed at $x = 285$ mm from the fixed end. One can observe the good concordance between the normalized relative frequency shifts and the normalized SDLI values. Therefore, damage location is reduced to a pattern recognition problem.

Once the damage location is identified at $x = 285$ mm, we can calculate the term defining the damage position $(\bar{\phi}_i''(x))^2$ for mode one and afterwards the damage severity indicator $\gamma(0, a)$. The evaluation of damage depth is made by finding the value of the dimensionless damage depth a/h on a curve similar to that presented in Figure 5(b), for which the damage severity indicator $\gamma(0, a)$ takes the value 0.1283. Thus we estimate the damage penetrated the foam core and a cross-section reduction due to damage above 45%. Dimensional measurements confirmed a damage depth around 14 mm, representing a cross-section reduction of almost 50%.

Tests were performed successfully on sandwich beams, for a large series of damage scenarios.

6. Conclusion

Research performed by the authors, presented in this paper, reveals that damage localization in sandwich panels can be successfully done using the relation contrived by the authors for isotropic materials. Difference appears by the evaluation of damage severity, where the curves representing the severity indicator versus dimensionless damage depth have another allure, given by the mechanical and geometrical characteristics of the constitutive layers.

On the other hand, the relative frequency shifts for sandwich structures with foam core attend higher values as that of steel beams. This makes damage detection and location in composite beams more facile compared to steel beams, but estimation of damage severity more difficult.

Conflict of Interests

The authors declare that there is no conflict of interests regarding the publication of this paper.

Acknowledgments

The work has been cofunded by the Sectoral Operational Programme Human Resources Development 2007–2013 of the Romanian Ministry of Labor, Family, and Social Protection through the Financial Agreement no. POSDRU/89/1.5/S/62557.

References

[1] F. J. Plantema, *Sandwich Construction: The Bending and Buckling of Sandwich Beams, Plates and Shells*, John Wiley & Sons, New York, NY, USA, 1966.

[2] C. M. Wang, J. N. Reddy, and K. H. Lee, *Shear Deformable Beams and Plates*, Elsevier, New York, NY, USA, 2000.

[3] J. M. Gere and B. J. Goodno, *Mechanics of Materials*, Cengage Learning, Boston, Mass, USA, 2009.

[4] V. S. Deshpande, "The design of sandwich panels with foam core," Lecture Notes, Cambridge University, Cambridge, UK, 2002.

[5] L. Valdevit, J. W. Hutchinson, and A. G. Evans, "Structurally optimized sandwich panels with prismatic cores," *International Journal of Solids and Structures*, vol. 41, no. 18-19, pp. 5105–5124, 2004.

[6] E. Magnucka-Blandzi and K. Magnucki, "Effective design of a sandwich beam with a metal foam core," *Journal of Sound and Vibration*, vol. 301, pp. 253–277, 2007.

[7] A. Shahdin, J. Morlier, L. Mezeix, C. Bouvet, and Y. Gourinat, "Evaluation of the impact resistance of various composite sandwich beams by vibration tests," *Shock and Vibration*, vol. 18, no. 6, pp. 789–805, 2011.

[8] K. Malekzadeh, M. R. Khalili, and R. K. Mittal, "Response of composite sandwich panels with transversely flexible core to low-velocity transverse impact: a new dynamic model," *International Journal of Impact Engineering*, vol. 34, no. 3, pp. 522–543, 2007.

[9] E. Carrera, "Assessment of theories for free vibration analysis of homogeneous and multilayered plates," *Shock and Vibration*, vol. 11, no. 3-4, pp. 261–270, 2004.

[10] G. S. Gipson, "Determinantal Rayleigh-Ritz expressions for natural frequencies of sandwich panels with orthotropic face plates," *Mathematical and Computer Modelling*, vol. 12, no. 2, pp. 169–180, 1989.

[11] S. F. Bastos, L. Borges, and F. A. Rochinha, "Numerical and experimental approach for identifying elastic parameters in sandwich plates," *Shock and Vibration*, vol. 9, no. 4-5, pp. 193–201, 2002.

[12] T. Hause and L. Librescu, "Flexural free vibration of sandwich flat panels with laminated anisotropic face sheets," *Journal of Sound and Vibration*, vol. 297, no. 3–5, pp. 823–841, 2006.

[13] R. A. S. Moreira and J. D. Rodrigues, "Static and dynamic analysis of soft core sandwich panels with through-thickness deformation," *Composite Structures*, vol. 92, no. 2, pp. 201–215, 2010.

[14] H. Schwarts-Givli, O. Rabinovitch, and Y. Frostig, "Free vibrations of delaminated unidirectional sandwich panels with a transversely flexible core—a modified Galerkin approach," *Journal of Sound and Vibration*, vol. 301, no. 1-2, pp. 253–277, 2007.

[15] V. S. Deshpande and N. A. Fleck, "Collapse of truss core sandwich beams in 3-point bending," *International Journal of Solids and Structures*, vol. 38, no. 36-37, pp. 6275–6305, 2001.

[16] A. Leopa, S. Nastac, and C. Debeleac, "Researches on damage identification in passive vibro-isolation devices," *Shock and Vibration*, vol. 19, no. 5, pp. 803–809, 2012.

[17] G. R. Gillich, Z. I. Praisach, and D. M. Onchis, "About the effectiveness of damage detection methods based on vibration measurements," in *Proceedings of the 3rd WSEAS International Conference on Engineering Mechanics, Structures, Engineering Geology (EMESEG '10)*, pp. 204–209, Corfu Island, Greece, July 2010.

[18] G. R. Gillich and Z. I. Praisach, "Robust method to identify damages in beams based on frequency shift analysis," in *Health Monitoring of Structural and Biological Systems 2012*, vol. 8348 of *Proceedings of SPIE Smart Structures/NDE, 8348-47*, San Diego, Calif, USA, March 2012.

[19] G.-R. Gillich, Z.-I. Praisach, and I. Negru, "Damages influence on dynamic behaviour of composite structures reinforced with continuous fibers," *Materiale Plastice*, vol. 49, no. 3, pp. 186–191, 2012.

[20] G. R. Gillich and Z. I. Praisach, "Damage-patterns based method to locate discontinuities in beams," in *Health Monitoring of Structural and Biological Systems 2013*, vol. 8695 of *Proceedings of SPIE Smart Structures/NDE, 8695-110*, San Diego, Calif, USA, March 2013.

[21] H. Liebowitz and W. D. Claus Jr., "Failure of notched columns," *Engineering Fracture Mechanics*, vol. 1, no. 2, pp. 379–383, 1968.

[22] H. Liebowitz, H. Vanderveldt, and D. W. Harris, "Carrying capacity of notched columns," *International Journal of Solids and Structures*, vol. 3, no. 4, pp. 489–500, 1967.

[23] P. F. Rizos, N. Aspragathos, and A. D. Dimarogonas, "Identification of crack location and magnitude in a cantilever beam from the vibration modes," *Journal of Sound and Vibration*, vol. 138, no. 3, pp. 381–388, 1990.

[24] S. Caddemi and I. Caliò, "Exact closed-form solution for the vibration modes of the Euler-Bernoulli beam with multiple open cracks," *Journal of Sound and Vibration*, vol. 327, no. 3–5, pp. 473–489, 2009.

[25] W. M. Ostachowicz and M. Krawczuk, "Analysis of the effect of cracks on the natural frequencies of a cantilever beam," *Journal of Sound and Vibration*, vol. 150, no. 2, pp. 191–201, 1991.

[26] C. Bilello, *Theoretical and experimental investigation on damaged beams under moving systems [Ph.D. thesis]*, Università degli Studi di Palermo, Palermo, Italy, 2001.

[27] T. G. Chondros, A. D. Dimarogonas, and J. Yao, "A continuous cracked beam vibration theory," *Journal of Sound and Vibration*, vol. 215, no. 1, pp. 17–34, 1998.

[28] S. Yi-Zhe, C. Bowen, A. Kim et al., "Non-invasive damage detection in beams using marker extraction and wavelets," *Mechanical Systems and Signal Processing*, 2014.

[29] G. R. Gillich and Z. I. Praisach, "Modal identification and damage detection in beam-like structures using the power spectrum and time-frequency analysis," *Signal Processing*, vol. 96, pp. 29–44, 2014.

[30] D. M. Onchis and P. Rajmic, "Generalized Goertzel algorithm for computing the natural frequencies of cantilever beams," *Signal Processing*, vol. 96, pp. 45–50, 2014.

[31] G. R. Gillich, P. F. Minda, Z. I. Praisach, and A. A. Minda, "Natural frequencies of damaged beams—a new approach," *Romanian Journal of Acoustics and Vibration*, vol. 9, no. 2, pp. 101–108, 2012.

[32] P. F. Minda, Z. I. Praisach, N. Gillich, A. A. Minda, and G. R. Gillich, "On the efficiency of different dissimilarity estimators used in damage detection," *Romanian Journal of Acoustics and Vibration*, vol. 10, no. 1, pp. 15–18, 2013.

Hindawi Publishing Corporation
Shock and Vibration
Volume 2014, Article ID 314527, 9 pages
http://dx.doi.org/10.1155/2014/314527

Research Article

Damping Effects Induced by a Mass Moving along a Pendulum

E. Gandino, S. Marchesiello, A. Bellino, A. Fasana, and L. Garibaldi

Department of Mechanical and Aerospace Engineering, Politecnico di Torino, C.so Duca degli Abruzzi 24, 10129 Torino, Italy

Correspondence should be addressed to S. Marchesiello; stefano.marchesiello@polito.it

Received 9 July 2013; Accepted 19 December 2013; Published 1 June 2014

Academic Editor: Nuno Maia

Copyright © 2014 E. Gandino et al. This is an open access article distributed under the Creative Commons Attribution License, which permits unrestricted use, distribution, and reproduction in any medium, provided the original work is properly cited.

The experimental study of damping in a time-varying inertia pendulum is presented. The system consists of a disk travelling along an oscillating pendulum: large swinging angles are reached, so that its equation of motion is not only time-varying but also nonlinear. Signals are acquired from a rotary sensor, but some remarks are also proposed as regards signals measured by piezoelectric or capacitive accelerometers. Time-varying inertia due to the relative motion of the mass is associated with the Coriolis-type effects appearing in the system, which can reduce and also amplify the oscillations. The analytical model of the pendulum is introduced and an equivalent damping ratio is estimated by applying energy considerations. An accurate model is obtained by updating the viscous damping coefficient in accordance with the experimental data. The system is analysed through the application of a subspace-based technique devoted to the identification of linear time-varying systems: the so-called short-time stochastic subspace identification (ST-SSI). This is a very simple method recently adopted for estimating the instantaneous frequencies of a system. In this paper, the ST-SSI method is demonstrated to be capable of accurately estimating damping ratios, even in the challenging cases when damping may turn to negative due to the Coriolis-type effects, thus causing amplifications of the system response.

1. Introduction

The analysis and simulation [1] of mechanical systems with imposed relative motion of components are challenging: time-varying inertia, created by a mass sliding along a rotating member, is associated with Coriolis-type effects. The relative movement can excite or reduce the structure vibration, providing new means or techniques for active amplification or attenuation of vibrations. A variable length mathematical pendulum was used in [2] to examine the concept of controlling the motion of a system through mass reconfiguration, that is, by sliding a mass towards and away from the pivot. A variable length pendulum has also been considered in [3], where a rigorous qualitative investigation of its equation is carried out without any assumption on small swinging amplitudes. In [4] a physical pendulum was considered to present a technique in which a radially moving mass is treated as a controller to attenuate the pendulum swings. A moving mass is a proper characteristic of a time-varying system, which is in general one of the sources of nonstationary signals. Another source can be, in case of a pendulum, nonlinearity due to its large swinging amplitudes. The oscillations are also associated with the effective damping ratio, which is explicitly determined in [4] from energy considerations in terms of the mass motion pattern and the pendulum parameters. This is only one of the several techniques that can be adopted to estimate the damping ratios of a system and in fact it can be seen as part of the larger problem of dynamic identification, as it is actually proposed in this paper.

During the last years, many efforts have been spent in studying nonstationary signals. Among the first works on the identification of time-varying systems, [5, 6] introduced the concept of pseudonatural frequencies that are obtained by the time-varying state transition matrix. The work in [7] proposed a recursive algorithm, based on subspace methods, to identify the state matrices and consequently to determine the modal parameters. Other important approaches are those based on the Kalman Filter [8], or the parametric methods as, for example, the FS-TARMA [9], which is an extension of the classical ARMA techniques. In [10], a Short-Time Stochastic Subspace Identification (ST-SSI) approach has been defined, based on the "frozen" technique, where the classical subspace identification [11] is applied to a sequence of windowed parts of the signal.

The ST-SSI method can be applied to different kinds of nonstationary systems in order to estimate the instantaneous frequencies and, for example, it has been used to estimate the frequency in practical systems showing nonlinear effects [12]. However, instead of extracting a series of time-varying linear models, the identification of a whole parametric nonlinear model is an important instrument for many purposes. Among the past and recent developments [13], the nonlinear subspace identification (NSI) method has been developed in [14] and improved in [15] for identifying large systems with lumped nonlinearities. Both the ST-SSI and the NSI methods have been applied in [16] for estimating the swinging frequency of an experimental time-varying inertia pendulum, whose dynamics is governed by a nonlinear equation of motion due to large swinging amplitudes.

The same pendulum is considered in this paper for investigating a suitable model of damping. The paper starts with the description of the experimental set-up. Signals are acquired from a rotary sensor, but some remarks are also proposed for signals measured by piezoelectric or capacitive accelerometers. After the introduction of the analytical equation of motion, the energy approach of [4] and the ST-SSI method are briefly described and applied for estimating the equivalent damping ratio. When the mass is fixed, the energy approach is employed for updating the preliminary model in order to fit the experimental data. Three moving-mass cases are finally analysed to demonstrate that the estimates of the damping factors obtained by means of ST-SSI are very accurate, when compared with those obtained by an analytical model and by the energy approach.

2. Experimental Set-Up

The structure under test is a pendulum with time-varying inertia: a disk on a cart can slide along a runner, while the pendulum is swinging. This structure cannot be considered simply as a linear time-variant system, the equation of motion of the pendulum being nonlinear for large swinging amplitudes.

2.1. Description. An overview of the design of the structure is presented in this section, together with a description of the instrumentation used for data acquisition. Further details about the experimental set up and the measured characteristics of the considered elements can be found in [16]. The pendulum is formed by a thin aluminium runner allowing the sliding of a cart which can host an added mass: the motion of the mass varies the pendulum inertia. Moreover, in order to avoid a nonoptimal clamp between the runner and the shaft due to the large deformability of aluminium, a small metallic plate has also been added at the root of the aluminium beam, near the hinge, to limit its transverse vibrations.

The travelling mass is a steel disk of mass $m_m = 0.5025\,\text{kg}$, whose motion is regulated by a hand-driven counterbalancing mass. The latter is connected to the moving mass through a system of pulleys and a cable that can be considered as nonextendible. The complete structure is shown in Figure 1(a): the main supports, plates, pulleys, bearings, and precision shaft are visible.

The sensors can also be seen in Figure 1(a). A triaxial and four monoaxial accelerometers have been mounted along the beam. The triaxial accelerometer, a PCB 356B18 piezoelectric sensor (ICP), is used to express some practical considerations in Section 2.2. To show typical measurement errors, some data sets have been acquired by adding a capacitive accelerometer to the system (not shown in the figure), in the same position of the ICP sensor. Each monoaxial accelerometer is a Brüel & Kjær 4507 B 004 piezoelectric sensor, used to measure the transversal vibrations (along the z axis in Figure 1(b)) of the pendulum [16]. Their signals have not been analysed in this paper.

A direct measure of the angular position of the pendulum is given by a Penny+Giles SRS280 sealed rotary sensor, with an accuracy of ±1% over 100°, connected to the precision shaft. A Celesco PT1A linear potentiometer, with a maximum extension of 1.2 m, has been connected to the counterweight (see Figure 1(a)). The position of the travelling mass along the runner can be simply obtained from this measure.

All signals have been acquired and recorded with a sampling frequency of 256 Hz by using an OROS acquisition system, with 32 channels and antialiasing filter.

2.2. Remarks about the Accelerometers. In this section some remarks about the signals measured by the accelerometers are proposed, together with a comparison with the rotary sensor recordings. In the following, $\theta(t)$ is the output of the rotary potentiometer, which is very accurate at these low frequencies; thus the use of supplementary sensors is not needed to describe the dynamics of the SDOF system. However, accelerometers are mounted to give some useful guidelines in case a potentiometer is not available. A piezoelectric sensor (ICP) is not suited to measure the radial acceleration of the pendulum under exam, because it removes the DC component of the output, which is nonnull. This is why a capacitive accelerometer was chosen for comparison.

To show the difference, the two accelerometers have been mounted on the beam in the same position $s_a = 0.93\,\text{m}$, with radial direction (the x axis in Figure 1(b)). The signal $\theta(t)$ of the rotary sensor has been numerically differentiated in order to obtain $\dot{\theta}(t)$, which is used for computing the "actual" value of the radial acceleration $a_r(t) = s_a\dot{\theta}(t)^2$, shown in Figure 2(a). The signals acquired by the accelerometers are represented in Figure 2(b): the ICP measurement $\widetilde{a}_{r,\text{ICP}}(t)$ has zero mean and its value is zero for $\theta = 0$ and $\dot{\theta} = 0$ (at the end of time history), while the capacitive sensor output $\widetilde{a}_{r,\text{cap}}(t)$ is asymmetric and its value tends to g for $\theta = 0$ and $\dot{\theta} = 0$. Clearly, none of the two behaviours can be associated with the actual value of radial acceleration.

Another remark arises from Figure 2(b): the effect of the gravitational acceleration g on the measured signals must be taken into account and removed in order to get the correct value of the radial acceleration. This is due to the fact that the measurement axes of the accelerometer on the pendulum have an orientation that largely changes over time, while most of dynamics applications do not show such a

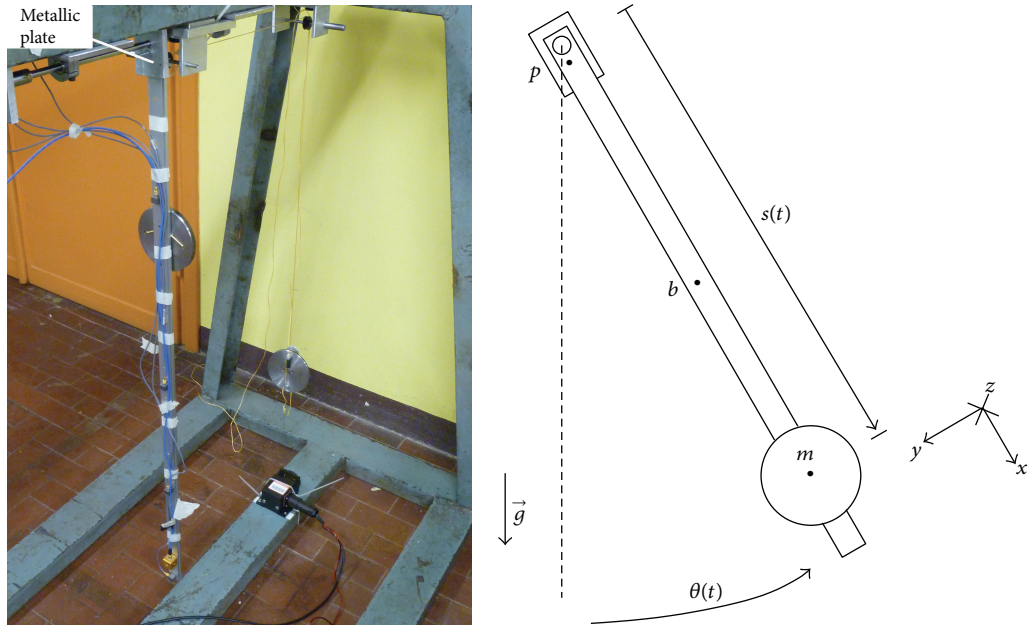

Figure 1: (a) Complete structure. At the top, the reinforcement plate is highlighted. The travelling mass and the counterweight are visible on the left and on the right, respectively. (b) Pendulum with the travelling mass.

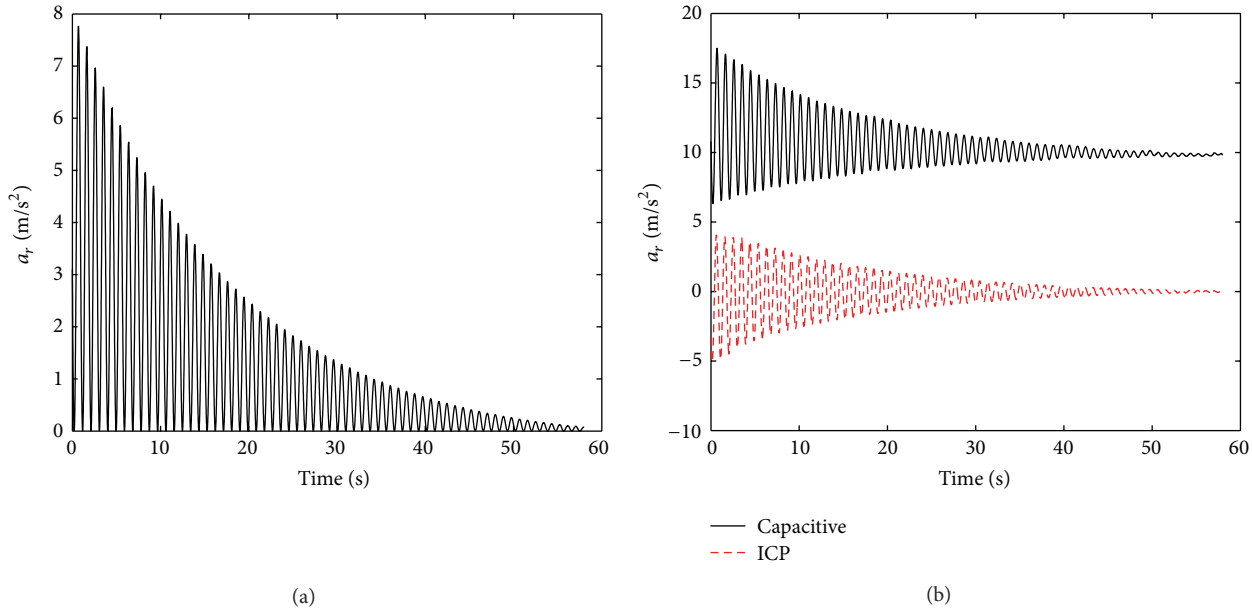

Figure 2: (a) Actual value of the radial acceleration. (b) Measured radial accelerations, by the capacitive and the ICP sensor.

behaviour. A "cleaning" operation can be thought of as being trivial, but it cannot be performed on signals from classical ICP accelerometers, because of the continuous component removal described above. When the capacitive sensor signal is considered as "corrupted" by the presence of g, an estimate (indicated by $\wedge$) of the actual radial acceleration is obtained after cleaning:

$$\widetilde{a}_{r,\mathrm{cap}}(t) = a_r(t) + g\cos\theta(t) \tag{1a}$$

$$\xrightarrow{\text{CLEANING}} \widehat{a}_{r,\mathrm{cap}}(t) = \widetilde{a}_{r,\mathrm{cap}}(t) - g\cos\theta(t). \tag{1b}$$

Figure 3(a) shows a comparison between the actual radial acceleration $a_r(t)$ and the estimate (1b): an almost perfect correspondence is now obtained. A similar approach can be adopted if the tangential direction (the y axis in Figure 1(b)) is considered. By differentiating again the signal $\dot{\theta}(t)$ in order to obtain $\ddot{\theta}(t)$, the "actual" value of the tangential acceleration

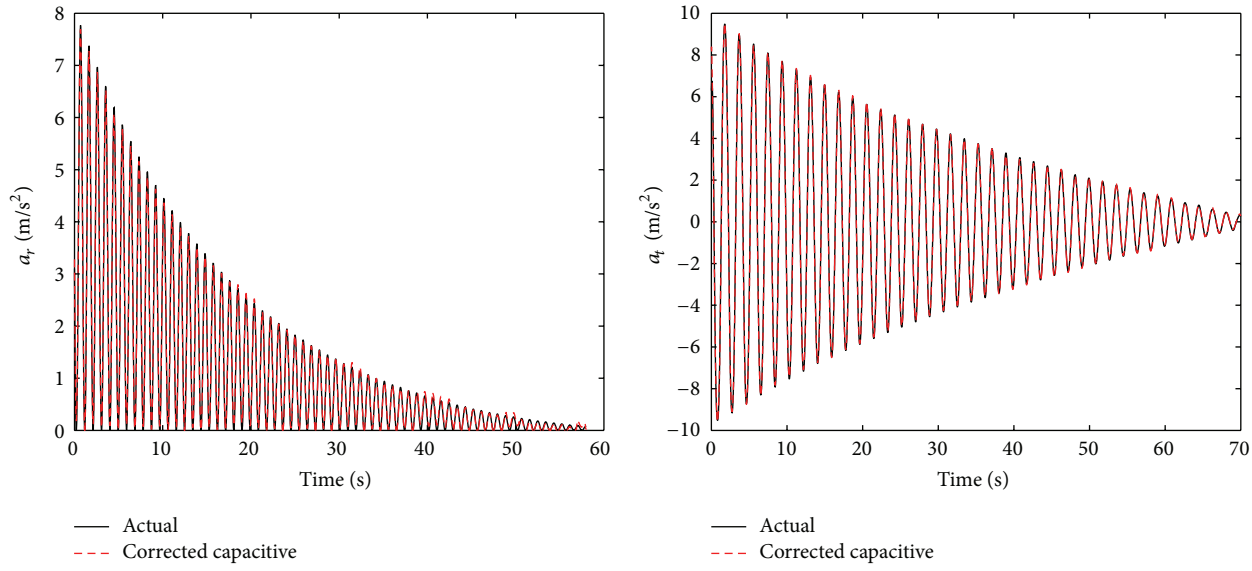

(a) Radial direction

(b) Tangential direction

Figure 3: Comparisons between actual accelerations and corrected capacitive estimates.

$a_t(t) = s_a\ddot{\theta}(t)$ has been computed. The capacitive estimate $\widehat{a}_{t,\mathrm{cap}}(t)$ can be obtained from the measured signal $\widetilde{a}_{t,\mathrm{cap}}(t)$ as $\widehat{a}_{t,\mathrm{cap}}(t) = \widetilde{a}_{t,\mathrm{cap}}(t) - g\sin\theta(t)$. The comparison between the actual tangential acceleration and the capacitive estimate is shown in Figure 3(b): again, a perfect agreement can be observed. In conclusion, an angle measurement is necessary in this kind of problems.

2.3. Equation of Motion. The system shown in Figure 1(b) consists of a rigid bar with no flexural effects; the pendulum is simply a nonlinear SDOF system.

From the rotational equilibrium of the system, the equation of the swinging motion is

$$\begin{aligned}&\left(I_{\mathrm{up}} + m_m s(t)^2\right)\ddot{\theta}(t)\\&\quad + \left(c_v + 2m_m s(t)\,\dot{s}(t)\right)\dot{\theta}(t) + \left(P_{\mathrm{up}} + g m_m s(t)\right)\sin\theta(t)\\&= I_{\mathrm{tot}}(t)\,\ddot{\theta}(t) + C_{\mathrm{tot}}(t)\,\dot{\theta}(t) + P_{\mathrm{tot}}(t)\sin\theta(t) = 0,\end{aligned} \tag{2}$$

in which the subscript "up" refers to the quantities not depending on the mass position $s(t)$. These have been estimated by means of the Nonlinear Subspace Identification (NSI) method in [16], in which an updating procedure was performed to build an accurate model tuned on the measured results. The angle swept by the pendulum is indicated by $\theta(t)$ whilst $s(t)$ is the distance of the disk from the hinge. Other terms appearing in (2) are the gravitational acceleration $g = 9.81\,\mathrm{m/s^2}$ and a viscous damping coefficient c_v. Given the value $m_m = 0.5025\,\mathrm{kg}$ of the travelling mass, model (2) can be completely defined by exploiting the results obtained in [16]: $I_{\mathrm{up}} = 0.1292\,\mathrm{kg\,m^2}$; $P_{\mathrm{up}} = 1.8380\,\mathrm{kg\,m^2\,s^{-2}}$; moreover, an overall estimate of $c_v = 0.035\,\mathrm{kg\,m^2\,s^{-1}}$ is used for preliminary comparisons.

The analytical form of the time-variant viscous damping ratio is then defined as

$$\zeta(t) = \frac{C_{\mathrm{tot}}(t)}{2\sqrt{I_{\mathrm{tot}}(t)\,P_{\mathrm{tot}}(t)}}. \tag{3}$$

3. Methodologies

Two methodologies are adopted in this paper for obtaining estimates of the equivalent viscous damping ratio. The first, based on energy considerations, is evaluated as a baseline for updating the model and is used for comparisons with the second technique, based on subspace identification.

3.1. Energy Considerations. A method for deriving an estimate of the damping ratio, which is briefly described in this section and used for successive comparisons, can be found in [4]. The normalised total energy of the pendulum with moving mass can be written as

$$E(t) = \frac{1}{2}\dot{\theta}(t)^2 + \omega_s(t)^2\left(1 - \cos\theta(t)\right), \tag{4}$$

where $\omega_s(t)^2 = (P_{\mathrm{up}} + g m_m s(t))/(I_{\mathrm{up}} + m_m s(t)^2)$ is related to the "instantaneous" frequency (when mass m_m is at location $s(t)$). The two terms of $E(t)$ can be interpreted as the normalised kinetic and potential energies of the pendulum, respectively. In [4] a mathematically equivalent form of (2) is rewritten, involving $E(t)$ and its rate of change; then, an integral form is considered over one swinging period T and the following approximation of the damping ratio for the pendulum with moving mass is defined:

$$\zeta \cong \frac{1}{4\pi}\frac{E(0) - E(T)}{E(0)}. \tag{5}$$

Thus, the damping ratio is defined in (5) by the normalised energies that can always be calculated for a given set of conditions at the beginning (represented by $E(0)$) and at the end ($E(T)$) of each cycle. In this way, a single value for ζ can be obtained at each cycle, in order to get an approximation of the "instantaneous" damping ratio expressed by (3). This method has two main limitations: (i) every estimate of ζ from (5) can be obtained only if exactly a cycle is considered; (ii) equation (5) involves the application of (4), which implies full knowledge of the pendulum parameters and the mass motion pattern, contained in the definition of $\omega_s(t)$.

3.2. Subspace Identification. The procedure for the identification of linear time-varying systems is called Short-Time Stochastic Subspace Identification (ST-SSI) [10, 17]. The basic idea of the method consists of windowing the signal into many parts and considering the system as time-invariant in each time window: the process is called frozen technique.

If the output data are measured at discrete times with a sampling interval Δt and the input is a discrete signal characterised by a zero-order hold between consecutive sample points, the discrete-time state-space model of a general linear time-varying system at a time instant $t = r\Delta t$ can be obtained. The frozen technique considers constant state matrices during each time step, so that the following representation can be adopted:

$$\begin{cases} x(r+1) = A(r)\,x(r) + B(r)\,u(r) + w(r) \\ y(r) = C(r)\,x(r) + D(r)\,u(r) + v(r) \end{cases} \tag{6a}$$

$$\xrightarrow{\text{FROZEN TECHNIQUE}} \begin{cases} x(r+1) = Ax(r) + Bu(r) + w(r) \\ y(r) = Cx(r) + Du(r) + v(r), \end{cases} \tag{6b}$$

where $A(r)$ and $B(r)$ are not constant and in general their closed forms are unknown [6]; $x(r)$ is the state vector, $u(r)$ the input vector, and $y(r)$ the output vector; $w(r)$ and $v(r)$ are process and measurement error, respectively. The complete time record is split into time windows (frozen system), whose length corresponds to a period T (about 400 samples) for comparing the ST-SSI results with those obtained through the energy approach of previous Section 3.1: such a restriction to a cycle, however, is not a limitation of the present ST-SSI method. Usually, the windows are almost completely overlapped except for a sampling period Δt (or a multiple) and their length can be arbitrarily chosen. If window lengths are short, the data-driven subspace method [11] is preferred with respect to the covariance-driven version [18], which needs more samples to obtain accurate results. Subspace methods do not need any *a priori* knowledge of the system parameters, as they identify the state-space matrices of (6b) starting from the measured system responses. Natural frequencies and damping ratios are then extracted by computing the eigenvalues of the identified matrix A in every window. An extensive study about the time-varying swinging frequency of the pendulum has been performed in [16], in which the contribution of nonlinearity was analysed by means of the Nonlinear Subspace Identification (NSI) method [14]. This paper is focused on the more challenging topic of damping.

4. Results

In this section the results are presented. At first, the mass is fixed and preliminary considerations about the model are drawn: the overall estimate of the viscous damping coefficient is updated to fit the experimental results and an accurate model is thus obtained. Then, three moving-mass cases are considered and the results obtained by the ST-SSI method are validated by comparisons with the method in [4] and the updated analytical model.

4.1. Fixed Mass. By considering the mass fixed in $s(t) = \bar{s} = 49\,\text{cm}$ (and obviously $\dot{s}(t) \equiv 0$), (5) can be applied and the obtained damping factors can be used to compute estimates for the viscous damping coefficient, at each cycle. These values can be then compared with the overall estimate $c_v = 0.035\,\text{kg}\,\text{m}^2\,\text{s}^{-1}$, defined by a preliminary nonlinear identification [16]. The comparison is shown in Figure 4(a): it is clear that a constant c_v value is not proper for representing the experimental evidence. An updating procedure is then carried out for obtaining a new model in which the viscous damping coefficient is no more constant: indeed it is a function of the root mean square (RMS) of angular velocity in each cycle, named $\tilde{\dot{\theta}}$. The updating simply consists of a polynomial fitting of the viscous coefficients obtained through the energy considerations of Section 3.1. In particular, the variable C_{tot} is updated to $\widetilde{C}_{\text{tot}} = c_v(\tilde{\dot{\theta}}) + 2m_m s(t)\dot{s}(t)$ and, consequently, the analytical form (3) of the viscous damping ratio changes into the following "updated" version:

$$\zeta_{\text{up}}(t) = \frac{\widetilde{C}_{\text{tot}}(t)}{2\sqrt{I_{\text{tot}}(t)\,P_{\text{tot}}(t)}}. \tag{7}$$

Figure 4(a) shows the behaviour of $\tilde{c}_v$ during a swinging decay: as expected, it accurately fits the energy approach estimates. In Section 4.2, the new damping model (7) will be the baseline for comparisons in more complicated situations involving the mass moving along the beam.

In order to have a better visualisation of the experimental damping characteristic, the damping force $F_v = c_v(\tilde{\dot{\theta}})\tilde{\dot{\theta}}$ is represented in Figure 4(b) as a function of $\tilde{\dot{\theta}}$. Two zones can be distinguished: for small angular velocities ($\tilde{\dot{\theta}} < 0.05\,\text{rad}\,\text{s}^{-1}$) a Coulomb friction is prevalent, while for larger angular velocities the contribution of the viscous damping is more evident.

4.2. Moving Mass. In this section three moving-mass cases are considered, in order to show the results obtained by means of the ST-SSI method. In Figure 5 the measured mass positions along the beam and the swinging amplitudes over time are shown, for each case.

4.2.1. Case 1. The mass is moving downwards, from the top to the middle of the beam (Figure 5(a)). No evidence of increasing swinging amplitudes due to the Coriolis-type effect can be observed in Figure 5(b), since the velocity $\dot{s}$ is positive.

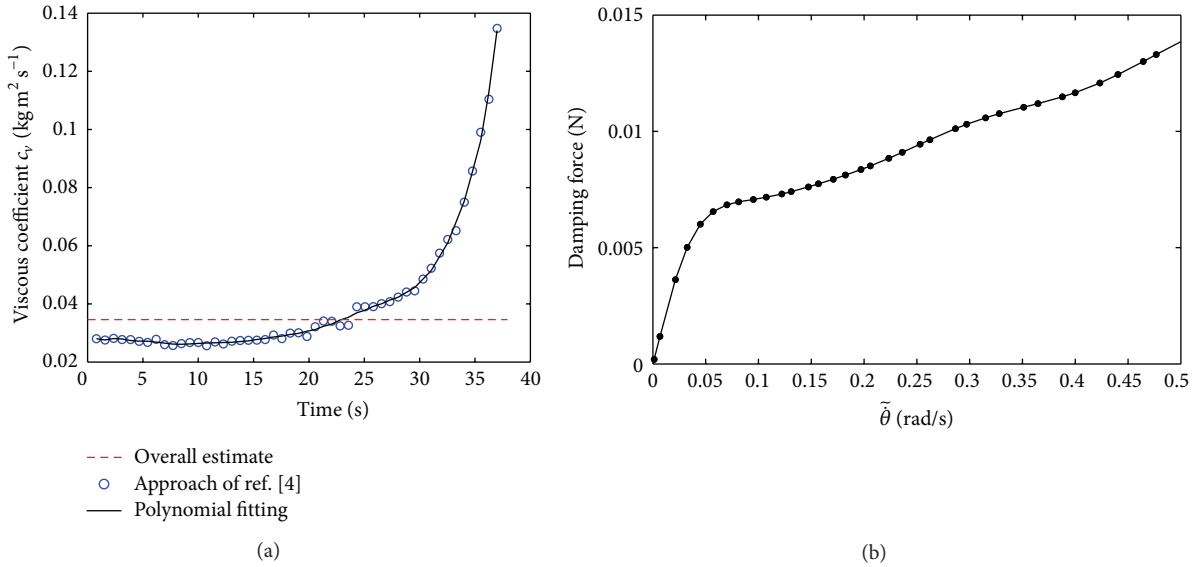

FIGURE 4: Fixed-mass case. (a) Viscous coefficient as a function of time, during a swinging decay. (b) Damping force as a function of $\tilde{\theta}$ at each cycle.

Case 1 is useful for demonstrating once again the need for the updating procedure performed in Section 4.1. Estimates of the damping factors, obtained through the energy approach of Section 3.1 and the ST-SSI method of Section 3.2, are compared with the overall estimate of (3) in Figure 6(a): the energy-approach and the ST-SSI estimates are similar, but there is no correspondence with the overall estimate. The same estimates can be compared with the updated value of (7) in Figure 6(b): a good level of agreement can be observed, confirming the reliability of the damping model obtained in Section 4.1 for a fixed mass. As a general remark emerging from Figure 6, the ST-SSI method gives slightly overestimated values of damping, with respect to those obtained by the energy approach. The reason is the model order n selected for representing the state-space model (6b): in this paper it has been fixed to 2 for simplicity, but more accurate estimates of damping can be obtained by increasing n and by investigating the results by means of stabilisation diagrams.

4.2.2. Case 2. The mass is moving downwards and upwards, in an almost regular way (Figure 5(c)). An excitation of the swinging amplitudes due to the Coriolis-type effect can be observed in Figure 5(d) at about 10 seconds, since the velocity $\dot{s}$ is negative and large enough to change the sign of ζ_{up} in (7). A less clear excitation can also be observed after 20 seconds. These qualitative considerations are confirmed by the damping factors represented in Figure 7(a). The energy-approach and the ST-SSI estimates are compared with the updated value of (7): an excellent agreement can be observed for the ST-SSI estimates.

4.2.3. Case 3. This is the more challenging case: the mass is moving along the beam, in a more irregular way especially from 5 to 12 seconds (Figure 5(e)). From a detailed inspection of Figure 5(f), four zones are recognised, in which an amplification of the swinging amplitudes due to the Coriolis-type effect can be observed: they are marked by letters A, B, C, and D. In particular, zones A and B are short and could be difficult to distinguish, but the representation of the damping factors in Figure 7(b) can be useful in this sense. In fact, Figure 7(b) reveals the four zones in which the equivalent damping factor is negative and these are found to correspond to those of Figure 5(f). Moreover, in Figure 7(b) the energy-approach and the ST-SSI estimates are compared with the updated value of (7): the ST-SSI estimates are very accurate.

As a final consideration, observe that Figures 7(a) and 7(b) are represented on the same scale: Case 3 appears to be more challenging also because larger and fast-varying values of damping factors are involved. However, results are satisfactory even in such a complicated case, in which high mass velocities cause substantial changes in the system dynamics.

5. Conclusions

The experimental study of damping in a time-varying inertia pendulum is presented. The system consists of a disk travelling along a pendulum: this relative motion, which is associated with Coriolis-type effects, can be exploited for attenuation or amplification of the pendulum oscillations. At first, signals measured by piezoelectric or capacitive accelerometers are compared with the output of a rotary sensor: for swinging systems like the pendulum under exam, the piezoelectric sensor is not suited because it removes the DC component of the output. The effect of gravitational acceleration can be taken into account and correctly removed from the measured signal of a capacitive acceleration, but angle measurement is needed.

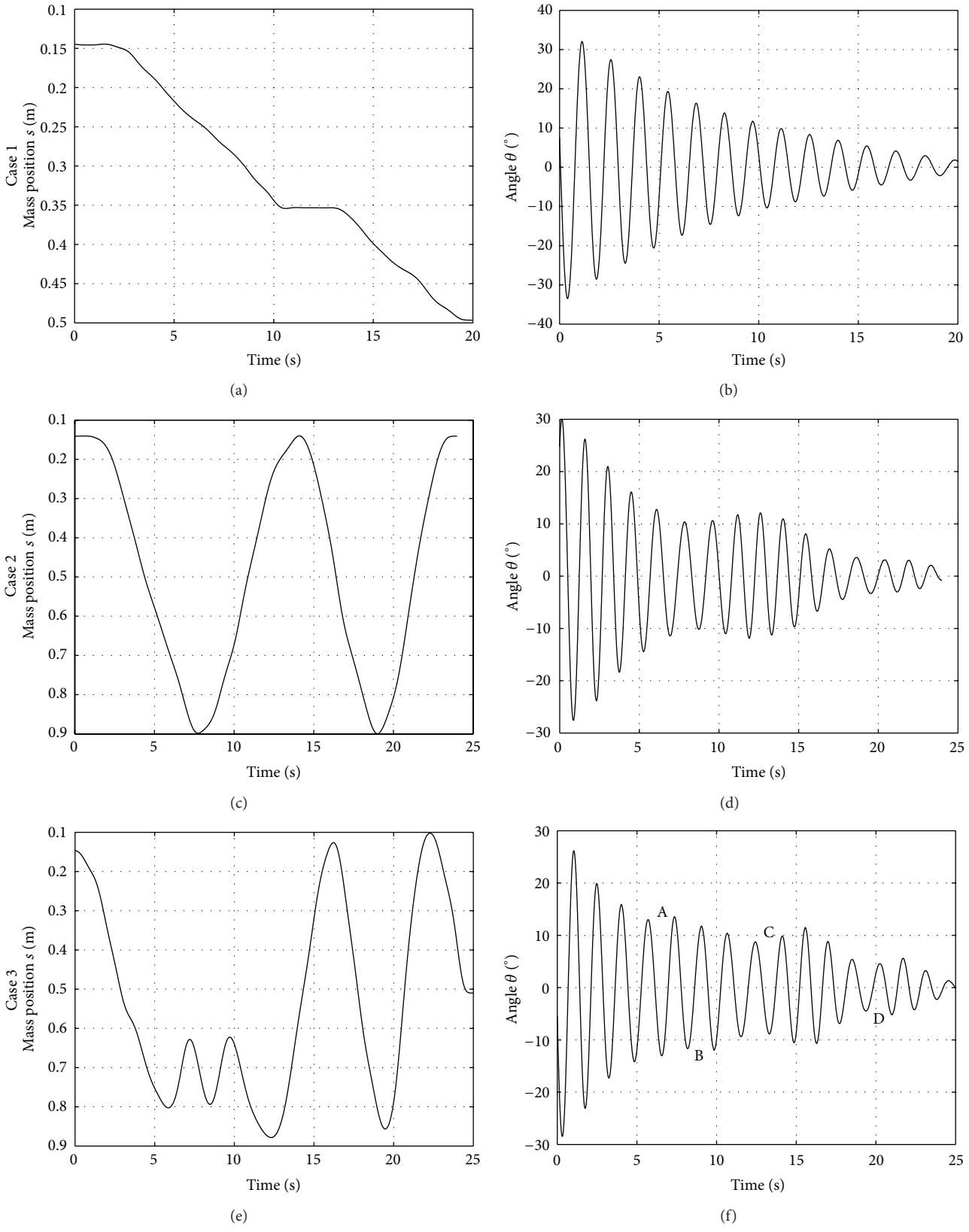

FIGURE 5: Moving mass. (a, b) Case 1. (c, d) Case 2. (e, f) Case 3. (a, c, e) Mass position along the beam. (b, d, f) Swinging amplitude over time.

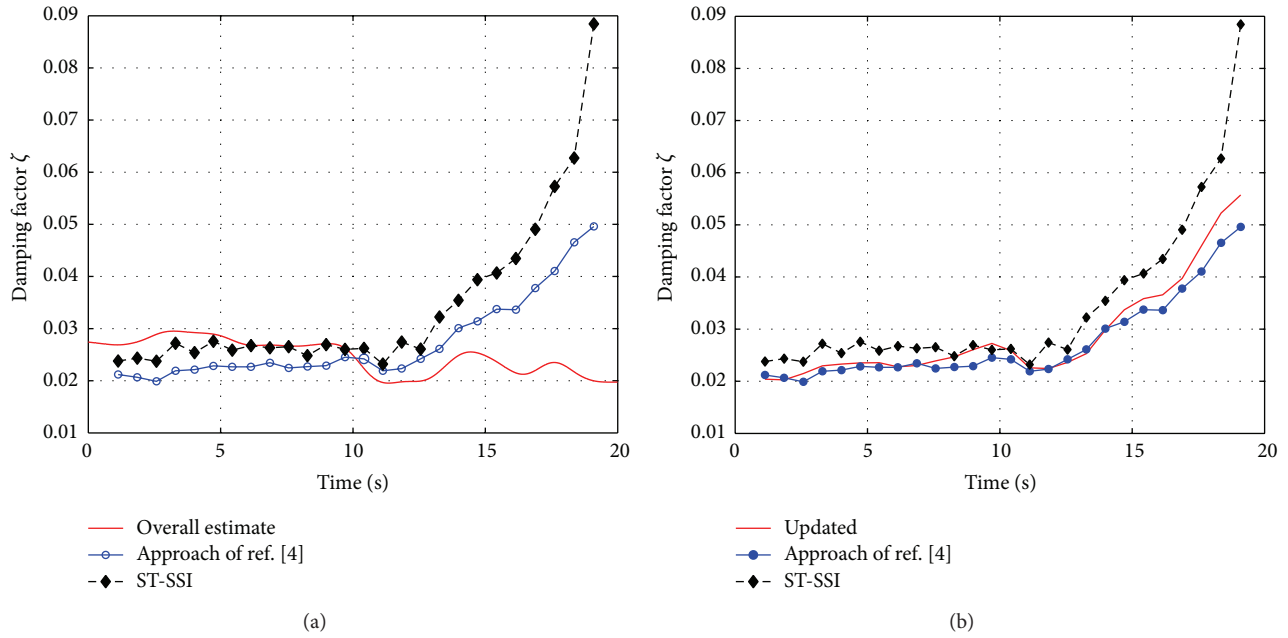

FIGURE 6: Moving-mass Case 1. Estimates of the damping factors, compared with the overall estimate of (3) (a) and with the updated value of (7) (b).

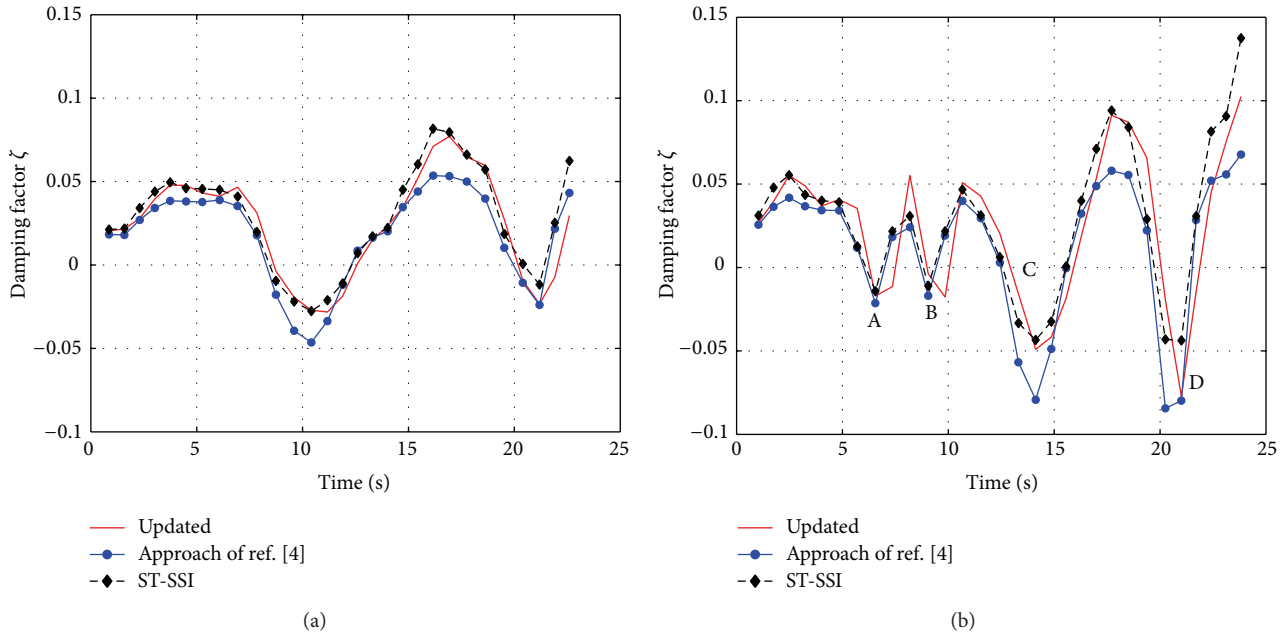

FIGURE 7: Estimates of the damping factors, compared with the updated value of (7). Moving-mass Case 2 (a) and Case 3 (b).

The analytical equation of motion is then introduced and the theoretical viscous damping coefficient is updated in order to obtain an accurate damping model. The updating procedure investigates the approach of a published work in which the damping ratios are derived from energy considerations, provided that the system parameters and the mass motion pattern are known. The system is analysed through the application of the Short-Time Stochastic Subspace Identification (ST-SSI), which is very simple and does not require any *a priori* knowledge about the system. The ST-SSI estimates of the damping factors are compared with those obtained by an analytical model and by the energy approach. Three moving-mass cases are presented, to demonstrate that the ST-SSI estimates are very accurate even in the challenging

cases in which damping may turn to negative due to the Coriolis-type effects.

Conflict of Interests

The authors declare that there is no conflict of interests regarding the publication of this paper.

References

[1] W. Szyszkowski and E. Sharbati, "On the FEM modeling of mechanical systems controlled by relative motion of a member: a pendulum-mass interaction test case," *Finite Elements in Analysis and Design*, vol. 45, no. 10, pp. 730–742, 2009.

[2] W. Szyszkowski and D. S. D. Stilling, "Controlling angular oscillations through mass reconfiguration: a variable length pendulum case," *International Journal of Non-Linear Mechanics*, vol. 37, no. 1, pp. 89–99, 2002.

[3] A. A. Zevin and L. A. Filonenko, "A qualitative investigation of the oscillations of a pendulum with a periodically varying length and a mathematical model of a swing," *Journal of Applied Mathematics and Mechanics*, vol. 71, no. 6, pp. 892–904, 2007.

[4] W. Szyszkowski and D. S. D. Stilling, "On damping properties of a frictionless physical pendulum with a moving mass," *International Journal of Non-Linear Mechanics*, vol. 40, no. 5, pp. 669–681, 2005.

[5] K. Liu, "Identification of linear time-varying systems," *Journal of Sound and Vibration*, vol. 206, no. 4, pp. 487–505, 1997.

[6] K. Liu, "Extension of modal analysis to linear time-varying systems," *Journal of Sound and Vibration*, vol. 226, no. 1, pp. 149–167, 1999.

[7] F. Tasker, A. Bosse, and S. Fisher, "Real-time modal parameter estimation using subspace methods: applications," *Mechanical Systems and Signal Processing*, vol. 12, no. 6, pp. 809–823, 1998.

[8] S.-W. Lee, J.-S. Lim, S. J. Baek, and K.-M. Sung, "Time-varying signal frequency estimation by VFF Kalman filtering," *Signal Processing*, vol. 77, no. 3, pp. 343–347, 1999.

[9] A. G. Poulimenos and S. D. Fassois, "Output-only stochastic identification of a time-varying structure via functional series TARMA models," *Mechanical Systems and Signal Processing*, vol. 23, no. 4, pp. 1180–1204, 2009.

[10] A. Bellino, L. Garibaldi, and S. Marchesiello, "Time-varying output-only identification of a cracked beam," *Key Engineering Materials*, vol. 413-414, pp. 643–650, 2009.

[11] P. van Overschee and B. de Moor, *Subspace Identification for Linear Systems: Theory, Implementation, Applications*, Kluwer Academic Publishers, Boston, Mass, USA, 1996.

[12] A. Bellino, L. Garibaldi, and S. Marchesiello, "Determination of moving load characteristics by output-only identification over the Pescara beams," *Journal of Physics: Conference Series*, vol. 305, no. 1, Article ID 012079, 2011.

[13] G. Kerschen, K. Worden, A. F. Vakakis, and J.-C. Golinval, "Past, present and future of nonlinear system identification in structural dynamics," *Mechanical Systems and Signal Processing*, vol. 20, no. 3, pp. 505–592, 2006.

[14] S. Marchesiello and L. Garibaldi, "A time domain approach for identifying nonlinear vibrating structures by subspace methods," *Mechanical Systems and Signal Processing*, vol. 22, no. 1, pp. 81–101, 2008.

[15] E. Gandino and S. Marchesiello, "Identification of a duffing oscillator under different types of excitation," *Mathematical Problems in Engineering*, vol. 2010, Article ID 695025, 15 pages, 2010.

[16] A. Bellino, A. Fasana, E. Gandino, L. Garibaldi, and S. Marchesiello, "A time-varying inertia pendulum: analytical modelling and experimental identification," *Mechanical Systems and Signal Processing*, vol. 47, no. 1-2, pp. 120–138, 2014.

[17] S. Marchesiello, S. Bedaoui, L. Garibaldi, and P. Argoul, "Time-dependent identification of a bridge-like structure with crossing loads," *Mechanical Systems and Signal Processing*, vol. 23, no. 6, pp. 2019–2028, 2009.

[18] E. Gandino, L. Garibaldi, and S. Marchesiello, "Covariance-driven subspace identification: a complete input-output approach," *Journal of Sound and Vibration*, vol. 332, no. 26, pp. 7000–7017, 2013.

Hindawi Publishing Corporation
Shock and Vibration
Volume 2014, Article ID 863494, 9 pages
http://dx.doi.org/10.1155/2014/863494

Research Article

Structural Health Monitoring under Nonlinear Environmental or Operational Influences

Jyrki Kullaa[1,2]

[1] *Department of Applied Mechanics, Aalto University, P.O. Box 14300, 00076 Espoo, Finland*
[2] *Helsinki Metropolia University of Applied Sciences, P.O. Box 4021, 00079 Helsinki, Finland*

Correspondence should be addressed to Jyrki Kullaa; jyrki.kullaa@metropolia.fi

Received 22 July 2013; Accepted 6 March 2014; Published 29 May 2014

Academic Editor: Nuno Maia

Copyright © 2014 Jyrki Kullaa. This is an open access article distributed under the Creative Commons Attribution License, which permits unrestricted use, distribution, and reproduction in any medium, provided the original work is properly cited.

Vibration-based structural health monitoring is based on detecting changes in the dynamic characteristics of the structure. It is well known that environmental or operational variations can also have an influence on the vibration properties. If these effects are not taken into account, they can result in false indications of damage. If the environmental or operational variations cause nonlinear effects, they can be compensated using a Gaussian mixture model (GMM) without the measurement of the underlying variables. The number of Gaussian components can also be estimated. For the local linear components, minimum mean square error (MMSE) estimation is applied to eliminate the environmental or operational influences. Damage is detected from the residuals after applying principal component analysis (PCA). Control charts are used for novelty detection. The proposed approach is validated using simulated data and the identified lowest natural frequencies of the Z24 Bridge under temperature variation. Nonlinear models are most effective if the data dimensionality is low. On the other hand, linear models often outperform nonlinear models for high-dimensional data.

1. Introduction

In structural health monitoring (SHM), changes in damage-sensitive features are an indication of damage. Also other sources of deviation are often present, for example, environmental or operational variability. If these effects are not taken into account, they can result in false identifications of damage or a loss of sensitivity to detect minor damage. It is important to distinguish between the two sources of changes in the dynamic characteristics. One option is to make a physical model of different environmental or operational phenomena, but it can be too expensive and inaccurate. An alternative is to include the normal variability in the training data and build a model solely based on the data. Using multivariate statistics, the environmental or operational effects can be eliminated even without measuring the underlying variables (see [1] and the references therein). Also a third source of change in the monitoring data is sensor fault. Kullaa [1] proposed a unified model to distinguish between the three sources of changes in a monitoring system.

Most of the models assume linear correlation between the measured variables or features. However, the environmental or operational variations often cause nonlinear effects. For example, as the temperature falls below zero, its influence on the natural frequencies can change abruptly. This often results also in nonlinear correlation between the features, especially if the data dimensionality is low. On the other hand, a linear model may be sufficient with a large data dimensionality, because the correlation structure may become linear [1]. There are only few studies of nonlinear models. Kullaa [2] used the mixture of factor analyzers [3] model to compensate the nonlinear effects. A similar approach was used by Yan et al. [4] having local PCA models for local regions in the data space. Sohn et al. [5] used an autoassociative neural network that can be thought as a nonlinear PCA [6]. Figueiredo et al. [7] applied the Bayesian approach to a mixture model and the Mahalanobis squared distance for the mixture components.

A nonlinear model is studied in this paper. A Gaussian mixture model (GMM) is proposed in Section 2 to compensate for the nonlinear effects. It is based on the mixture of linear models, each modelling a region in the input space. The approach needs a clustering algorithm to assign each new measurement to the corresponding class. Clustering can be performed independently of the local linear models.

Therefore, clustering is first performed identifying a Gaussian mixture model followed by local linear models to eliminate the underlying effects within each class. The number of classes is often unknown but can also be estimated. Minimum mean square error (MMSE) estimation is applied to the local linear models, which is described in Section 3. Damage can be detected from the residuals between the data and the model. Damage detection is discussed in Section 4.

The first applications in Section 5 are numerical studies, in which the objective is to validate the proposed approach. Section 5.3 shows the experimental results of the Z24 Bridge, in which the natural frequencies varied due to the temperature. Finally, concluding remarks are given in Section 6.

2. Gaussian Mixture Model (GMM)

Let $\mathbf{x}$ be the multivariate measurement data (also subsequently called variables), which can be time series (e.g., acceleration or strains) from a simultaneously sampled sensor network, or a feature vector comprising identified dynamic properties of the structure (e.g., natural frequencies or mode shapes). Nonlinear data are not normally distributed and cannot be modelled as a single Gaussian distribution. One may try a mixture of Gaussian components, in which the distribution can be written as a linear superposition of K Gaussian densities in the form [8]

$$p(\mathbf{x}) = \sum_{k=1}^{K} \pi_k N(\mathbf{x} \mid \boldsymbol{\mu}_k, \boldsymbol{\Sigma}_k), \tag{1}$$

which is called a mixture of Gaussians. Each Gaussian density $N(\mathbf{x} \mid \boldsymbol{\mu}_k, \boldsymbol{\Sigma}_k)$ is called a component of the mixture and has its own mean $\boldsymbol{\mu}_k$ and covariance $\boldsymbol{\Sigma}_k$. The parameters π_k are called mixing coefficients, which are positive and are summed to one.

The first step is to identify the model parameters. The difficulty lies in the fact that the data points are unlabeled; that is, it is typically not known which component was responsible for generating each data point. The data labels can be considered as latent variables and the expectation-maximization (EM) algorithm can be used to identify the mixture model. It is momentarily assumed that the number of components is known.

The EM algorithm is iterative and consists of two steps: the E step and the M step. In the expectation step, or E step, the model parameters are held fixed and the posterior probability of the component k (latent variable) given the data point $\mathbf{x}$ is evaluated. In the maximization step, or M step, the latent variables are assumed to be known, and the model parameters are obtained by maximizing the log-likelihood function.

A K-dimensional binary random variable $\mathbf{z}$ is introduced having a 1-of-K representation in which a particular element z_k is equal to 1 and all other elements are zero. For an observation $\mathbf{x}_n$, z_{nk} denotes the kth component of $\mathbf{z}_n$.

The algorithm is outlined as follows. In the E step, the expected value of the indicator variable z_{nk} under the posterior distribution is

$$E[z_{nk}] = \frac{\pi_k N(\mathbf{x}_n \mid \boldsymbol{\mu}_k, \boldsymbol{\Sigma}_k)}{\sum_{j=1}^{K} \pi_j N(\mathbf{x}_n \mid \boldsymbol{\mu}_j, \boldsymbol{\Sigma}_j)}. \tag{2}$$

In the M step, the model parameters are updated to maximize the log-likelihood function, resulting in [8]

$$\begin{aligned} \boldsymbol{\mu}_k^{\text{new}} &= \frac{1}{N_k} \sum_{n=1}^{N} E[z_{nk}]\, \mathbf{x}_n, \\ \boldsymbol{\Sigma}_k^{\text{new}} &= \frac{1}{N_k} \sum_{n=1}^{N} E[z_{nk}] (\mathbf{x}_n - \boldsymbol{\mu}_k^{\text{new}}) (\mathbf{x}_n - \boldsymbol{\mu}_k^{\text{new}})^T, \\ \pi_k^{\text{new}} &= \frac{N_k}{N}, \end{aligned} \tag{3}$$

where N is the number of observations and

$$N_k = \sum_{n=1}^{N} E[z_{nk}]. \tag{4}$$

The log-likelihood is then evaluated:

$$\ln p(\mathbf{X} \mid \boldsymbol{\mu}, \boldsymbol{\Sigma}, \pi) = \sum_{n=1}^{N} \ln \left\{ \sum_{k=1}^{K} \pi_k N(\mathbf{x}_n \mid \boldsymbol{\mu}_k, \boldsymbol{\Sigma}_k) \right\}. \tag{5}$$

The steps are repeated until the log-likelihood converges. It is not guaranteed that the algorithm converges to the global maximum. Therefore, it is often advised to run the algorithm a couple of times with different initial guesses of $\boldsymbol{\mu}_k$ and $\boldsymbol{\Sigma}_k$ to find a satisfactory maximum. An example of convergence to a local maximum is given in Section 5.1. Another problem is that the number of components is often unknown. To that end, different models can be identified by varying K, and the model resulting in the highest log-likelihood is chosen. In order to avoid overfitting, a penalty term $-(1/2)M \ln N$ is added to the log-likelihood [8], where N is the number of training samples and M is the number of model parameters:

$$M = K \left[1 + p + \frac{p(p+1)}{2} \right], \tag{6}$$

where p is the data dimensionality.

Once the model parameters are identified and fixed, the objective is to decide if the new data are generated by the model (undamaged) or by another model (damage). To this end a residual is estimated, which is the difference of the true data point and that estimated by the model:

$$\mathbf{r}_n = \mathbf{x}_n - E[\widehat{\mathbf{x}}_n \mid \mathbf{x}_n], \tag{7}$$

where

$$E[\widehat{\mathbf{x}}_n \mid \mathbf{x}_n] = \sum_{k=1}^{K} \widehat{\mathbf{x}}_{nk}\, p(z_{nk} = 1 \mid \mathbf{x}_n). \tag{8}$$

The last term in the RHS of (8) is obtained using Bayes' theorem:

$$p(z_{nk}=1 \mid \mathbf{x}_n) = \frac{p(z_{nk}=1)\, p(\mathbf{x}_n \mid z_{nk}=1)}{\sum_{j=1}^{K} p(z_{nj}=1)\, p(\mathbf{x}_n \mid z_{nj}=1)} = \frac{\pi_k N(\mathbf{x}_n \mid \boldsymbol{\mu}_k, \boldsymbol{\Sigma}_k)}{\sum_{j=1}^{K} \pi_j N(\mathbf{x}_n \mid \boldsymbol{\mu}_j, \boldsymbol{\Sigma}_j)}, \tag{9}$$

which is the same as (2). The first term in the RHS of (8) is given by the local linear model, which in this paper is the minimum mean square error (MMSE) estimate for each component [9]:

$$\hat{\mathbf{x}}_{nk} = \boldsymbol{\mu}_k + \mathbf{A}_k (\mathbf{x}_n - \boldsymbol{\mu}_k), \tag{10}$$

where the coefficient matrix $\mathbf{A}_k$ is composed of rows estimating the variable corresponding to that row using the remaining variables. Therefore, the diagonal components of $\mathbf{A}_k$ are zero. The MMSE estimation is discussed in the next section.

3. Local Linear Models Using MMSE Estimation

With enough redundancy, a subset of observation $\mathbf{x}$ can be estimated using the remaining variables. Each observation is divided into observed variables $\mathbf{v}$ and missing variables $\mathbf{u}$. It is assumed here that $\mathbf{u}$ is the ith variable x_i and the remaining variables are collected in vector $\mathbf{v}$:

$$\mathbf{x} = \begin{Bmatrix} \mathbf{v}_a \\ \mathbf{u} \\ \mathbf{v}_b \end{Bmatrix}, \qquad \mathbf{v} = \begin{Bmatrix} \mathbf{v}_a \\ \mathbf{v}_b \end{Bmatrix}. \tag{11}$$

The partitioned covariance matrix $\boldsymbol{\Sigma}$ of the training data is

$$\boldsymbol{\Sigma} = \begin{bmatrix} \boldsymbol{\Sigma}_{uu} & \boldsymbol{\Sigma}_{uv} \\ \boldsymbol{\Sigma}_{vu} & \boldsymbol{\Sigma}_{vv} \end{bmatrix} = \begin{bmatrix} \boldsymbol{\Gamma}_{uu} & \boldsymbol{\Gamma}_{uv} \\ \boldsymbol{\Gamma}_{vu} & \boldsymbol{\Gamma}_{vv} \end{bmatrix}^{-1}, \tag{12}$$

where the precision matrix $\boldsymbol{\Gamma}$ is defined as the inverse of the covariance matrix $\boldsymbol{\Sigma}$ and is also written in the partitioned form. A linear minimum mean square error (MMSE) estimate for $\mathbf{u} \mid \mathbf{v}$ ($\mathbf{u}$ given $\mathbf{v}$) is obtained by minimizing the mean square error (MSE)

$$\mathrm{MSE} = E\left[(\mathbf{u} - \hat{\mathbf{u}})^T (\mathbf{u} - \hat{\mathbf{u}})\right] \tag{13}$$

resulting in [9]

$$\hat{\mathbf{u}} = E(\mathbf{u} \mid \mathbf{v}) = \boldsymbol{\mu}_u - \boldsymbol{\Gamma}_{uu}^{-1} \boldsymbol{\Gamma}_{uv} (\mathbf{v} - \boldsymbol{\mu}_v) = \boldsymbol{\mu}_u + \mathbf{H}(\mathbf{v} - \boldsymbol{\mu}_v), \tag{14}$$

where $\boldsymbol{\mu}_u$ and $\boldsymbol{\mu}_v$ are the mean of $\mathbf{u}$ and $\mathbf{v}$, respectively, and $\mathbf{H} = -\boldsymbol{\Gamma}_{uu}^{-1} \boldsymbol{\Gamma}_{uv}$. The error covariance is

$$\mathrm{cov}(\mathbf{uv}) = \boldsymbol{\Gamma}_{uu}^{-1}. \tag{15}$$

An MMSE model is estimated for each mixture component. For component k, the estimate of variable x_i is given by (14). Then, the ith row of matrix $\mathbf{A}_k$ in (10) is composed of the partitioned row matrix $\mathbf{H}$ and a zero:

$$[\mathbf{A}_k]_{i,\bullet} = [\mathbf{H}_a \;\; 0 \;\; \mathbf{H}_b]. \tag{16}$$

The partitioning should be clear from (11). The zero element hits the diagonal in $\mathbf{A}_k$, originating from the fact that x_i is not used to estimate itself, but all the remaining variables are only used. Therefore, the diagonal elements of matrix $\mathbf{A}_k$ are all zeros. The other rows of $\mathbf{A}_k$ are obtained similarly by estimating all variables in turn using the remaining variables. Matrix $\mathbf{A}_k$ is estimated for each mixture component k.

To show the relation between (10) and (14), compute the estimate of the ith variable x_i for a fixed mixture component k using (10). For clarity, the component index k is omitted. Consider

$$\begin{aligned} \hat{\mathbf{x}}_i &= \boldsymbol{\mu}_i + [\mathbf{H}_a \;\; 0 \;\; \mathbf{H}_b](\mathbf{x} - \boldsymbol{\mu}) \\ &= \boldsymbol{\mu}_i + [\mathbf{H}_a \;\; 0 \;\; \mathbf{H}_b] \begin{Bmatrix} \mathbf{v}_a - \boldsymbol{\mu}_a \\ \mathbf{u} - \boldsymbol{\mu}_u \\ \mathbf{v}_b - \boldsymbol{\mu}_b \end{Bmatrix} \\ &= \boldsymbol{\mu}_i + [\mathbf{H}_a \;\; \mathbf{H}_b] \begin{Bmatrix} \mathbf{v}_a - \boldsymbol{\mu}_a \\ \mathbf{v}_b - \boldsymbol{\mu}_b \end{Bmatrix} \\ &= \boldsymbol{\mu}_i + \mathbf{H}(\mathbf{v} - \boldsymbol{\mu}_v), \end{aligned} \tag{17}$$

which is equal to $\hat{\mathbf{u}}$ in (14).

4. Damage Detection

Using the mixture model for damage detection introduces an issue of residual scaling, because each class may have a different error variance (15). Therefore, the residual of each variable within each class is divided with the corresponding standard deviation, which is the square root of (15). Also the data dimensionality may be too high for statistical reliability (curse of dimensionality). Therefore, the first principal component scores [10] of residual (7) are used for damage detection. Control charts [11] are used for damage detection. The control chart used in this study is the Shewhart chart [11], and the plotted variable is the subgroup mean of successive observations. It is believed that the robustness of damage detection increases, because (1) additional variability due to environmental or operational influences can be removed, in this paper using a nonlinear model; (2) PCA is applied to the residuals avoiding the curse of dimensionality; and (3) control charts utilize averaging for better statistical reliability.

5. Experimental Results

The proposed nonlinear model and the subsequent SHM functions are applied to two numerical studies and the experimental data of the Z24 Bridge.

5.1. Five Gaussian Components. The first numerical example is a mixture of five Gaussian components in a two-dimensional space. Each component has 10,000 data points. This

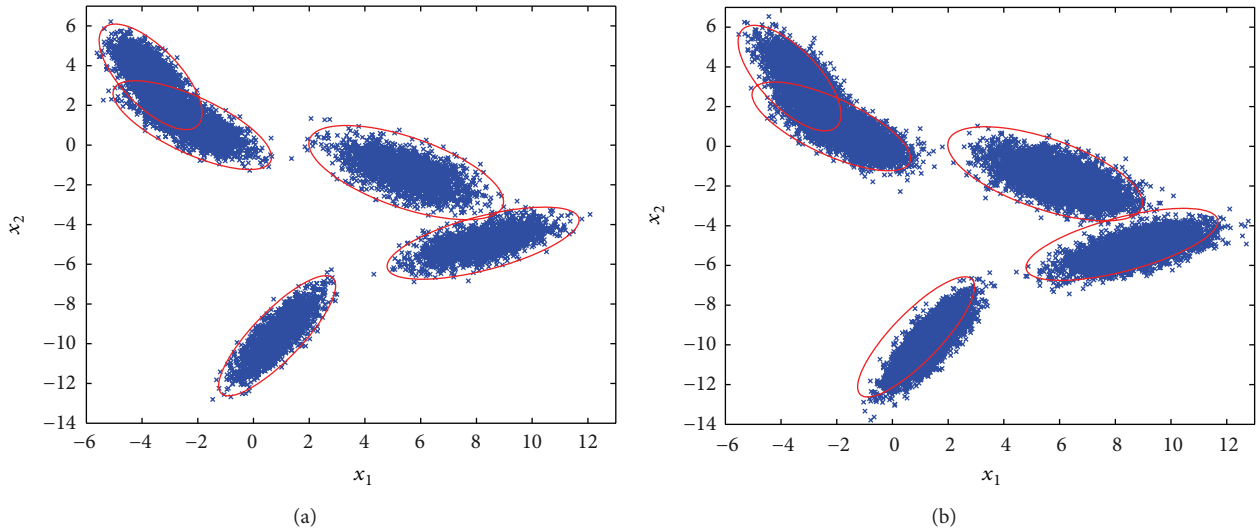

Figure 1: Training data (a) and test data (b) with a change in mean. The identified GMM model is shown in red.

example was chosen because the model assumptions are satisfied. In addition to damage detection, the objective is to test the model identification performance and the number of components selected by the algorithm.

The data were created as follows. The data dimensionality was two and the number of components was five. For each component k, the components of the mean vector $\boldsymbol{\mu}_k$ were sampled from a uniform random distribution between −10 and 10. The covariance matrix was generated by first generating the variances of the principal directions, resulting in a diagonal covariance matrix:

$$\mathbf{D} = \begin{bmatrix} \lambda_1 & 0 \\ 0 & \lambda_2 \end{bmatrix}, \tag{18}$$

where λ_1 and λ_2 were uniform random variables, λ_1 varying between 1 and 2 and λ_2 varying between 0.01 and 0.5. This diagonal covariance matrix was then rotated in a random orientation φ, resulting in covariance matrix $\boldsymbol{\Sigma}_k$:

$$\boldsymbol{\Sigma}_k = \mathbf{U}\mathbf{D}\mathbf{U}^T, \tag{19}$$

where

$$\mathbf{U} = \begin{bmatrix} \cos\varphi & \sin\varphi \\ -\sin\varphi & \cos\varphi \end{bmatrix}. \tag{20}$$

The data were then generated by sampling from a multivariate Gaussian distribution

$$N\left(\mathbf{x} \mid \boldsymbol{\mu}_k, \boldsymbol{\Sigma}_k\right). \tag{21}$$

Once data from each component were generated, all data were concatenated and random permutation was applied to randomize the data labels.

The data are plotted in Figure 1. The training data are the first 10,000 data points shown in Figure 1(a) which were used to identify the model. Because the number of components is often unknown, different models were identified varying the number of components between 1 and 10. The log-likelihoods with the penalty term are plotted in Figure 2(a) for different number of components. The maximum was correctly found with a five-component model. It should be noted that sometimes the components were not correctly identified, but the solution converged to a local maximum (Figure 2(b)). Therefore, it is suggested that the identification is repeated until a satisfying model is obtained, and the model with the highest log-likelihood is selected.

Damage was an equal shift in mean for all components. A bias vector $\mathbf{x}_d = \begin{bmatrix} 0.5 & -0.25 \end{bmatrix}^T$ was added to each data point. The damaged data were the last 25,000 data points plotted in Figure 1(b) together with the identified model for the training data. The shift of mean can be visually observed. The residuals were estimated for all data points and the first principal component scores were used for the control chart. The Shewhart chart was designed with a subgroup size 100 and the in-control samples 1–10,000. The shift in mean was clearly detected (Figure 3).

5.2. Three Piecewise Linear Components. The second example is a more realistic one in which the data are continuous with piecewise linear correlation between the two monitored variables. The piecewise linear regions are not necessarily Gaussian. Also, the variances are different in each region.

The data were created as follows. The data dimensionality was two and the number of piecewise linear components was three. Variable x_1 was uniformly distributed between 0 and 1. Variable x_2 was a piecewise linear function of x_1:

$$x_2 = a_k + b_k x_1, \tag{22}$$

where the parameters and their validity regions are given in Table 1. Gaussian noise was added to the variables, with the standard deviations within each component shown in Table 1.

The test data came from a limited region of component 2. The first half of the test data was healthy and the second half

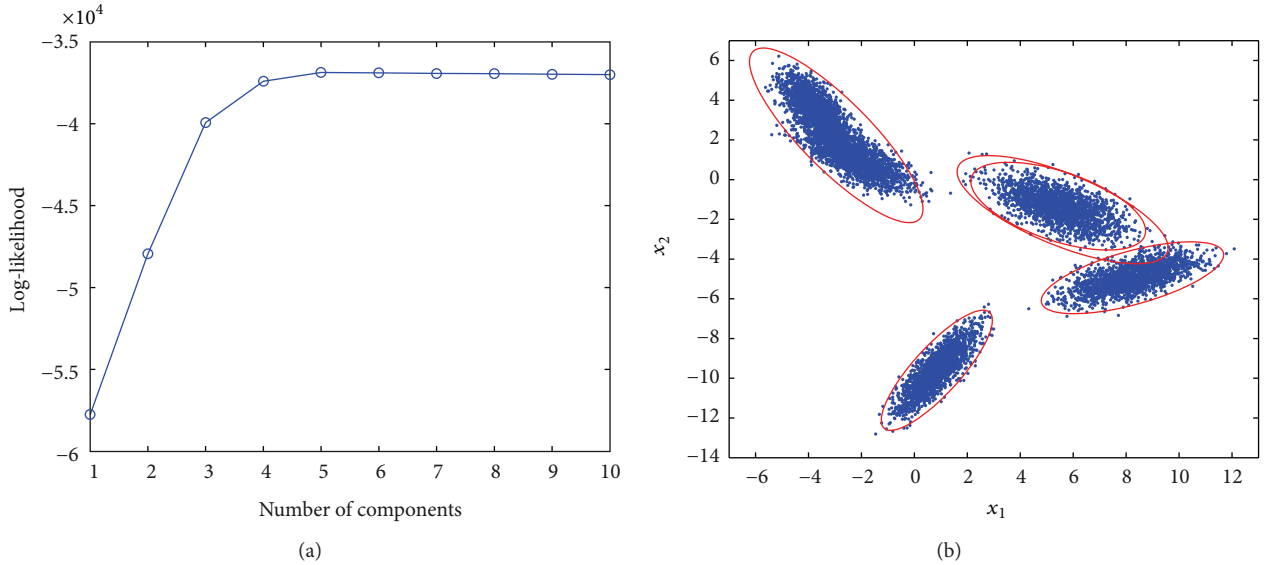

FIGURE 2: Log-likelihood with the penalty term (a) and an identified GMM model (in red) converged to a local maximum (b).

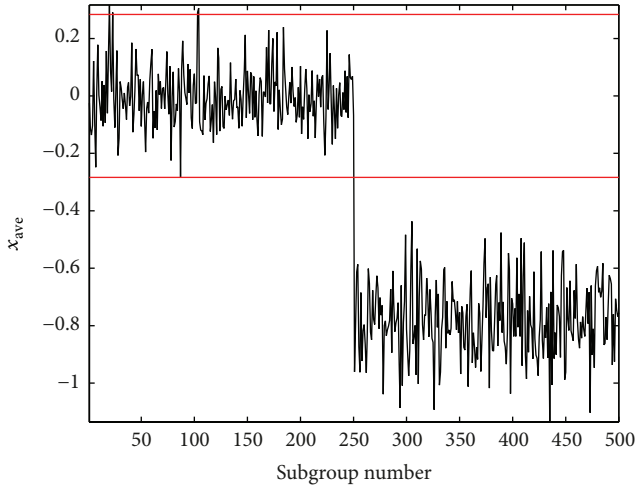

FIGURE 3: Shewhart control chart for damage detection.

TABLE 1: Parameters of the three linear components (22).

Class k	$x_{1,\min}$	$x_{1,\max}$	a_k	b_k	σ_1	σ_2
1	0	0.4	7	−0.2	0.01	0.02
2	0.4	0.6	6.4	1.3	0.02	0.01
3	0.6	1.0	7.84	−1.1	0.04	0.03

included damage, which was a shift in mean. A bias vector $\mathbf{x}_d = [0.1 \quad -0.05]^T$ was added to those data points.

The data are plotted in Figure 4. They consist of 20,000 data points in a two-dimensional space. The first half is randomly distributed in all three regions (Figure 4(a)), but the last 10,000 data points are confined to the middle region (Figure 4(b)).

The training data include a larger variability than the test data. This is also more realistic as the training typically consists of monitoring under a full range of environmental or operational conditions, while the test data often come from a limited number of measurements at more or less constant conditions.

The training data were the first 5,000 data points. The model identification suggested 7 Gaussian components (Figure 5(a)), which are plotted in Figure 4.

Data points 10,001–15,000 are from the undamaged case, and data points 15,001–20,000 are from the damaged case with a shift in mean shown in Figure 4(b) together with the identified model for the training data.

The residuals were estimated for all data points and the first principal component scores were used for damage detection. The Shewhart chart was designed with a subgroup size 100 and the in-control samples 1–5,000. Damage was clearly detected with no false alarms (Figure 5(b)).

5.3. The Z24 Bridge. The data in the last case are the four lowest identified natural frequencies of the Z24 Bridge (see [12] for details) shown in Figure 6. Their pairwise correlation is plotted in Figure 7. It was reported that the frequencies varied considerably due to environmental effects and can be seen to be nonlinearly correlated. The physical reason was the different behaviour of the bridge below and above the freezing point.

Progressive damage test scenarios were introduced: settlement of pier, spalling of concrete, landslide at abutment, failure of a concrete hinge, failure of anchor heads, and rupture of tendons [12]. The first damage was introduced around measurement number 3517, shown with a vertical dashed line in Figure 6.

The training data were the first 3,000 samples shown in blue in Figure 7 and with another vertical dashed line in Figure 6. The training algorithm suggested 6 Gaussian components (Figure 8). After identifying the Gaussian mixture model, the residuals were estimated for all data points and

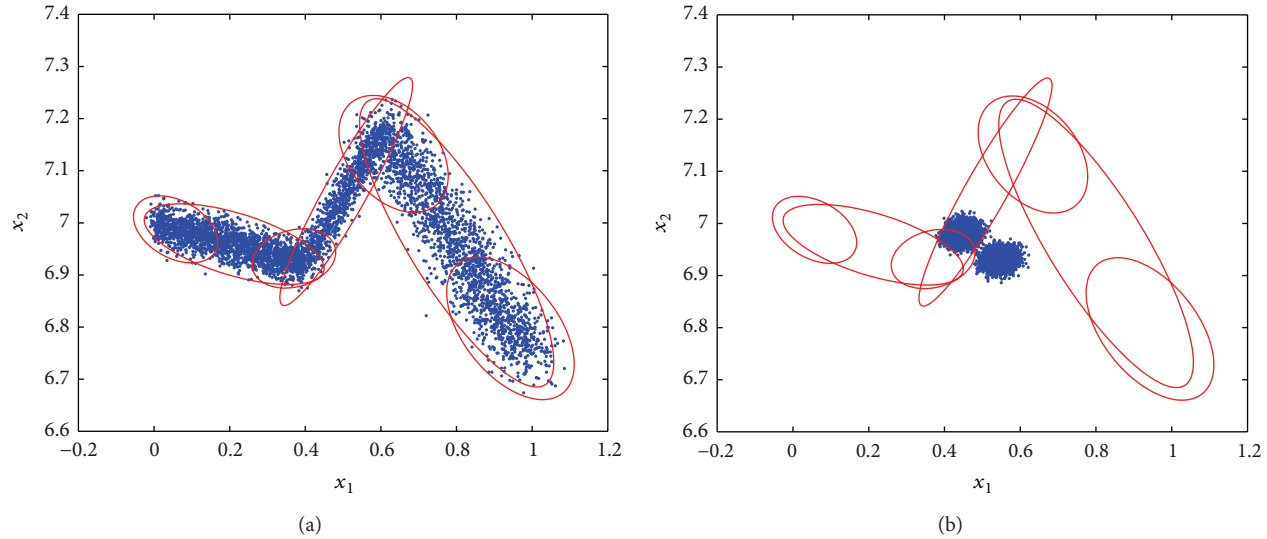

Figure 4: Training data (a) and test data (b) with a change in mean. The identified GMM model is shown in red.

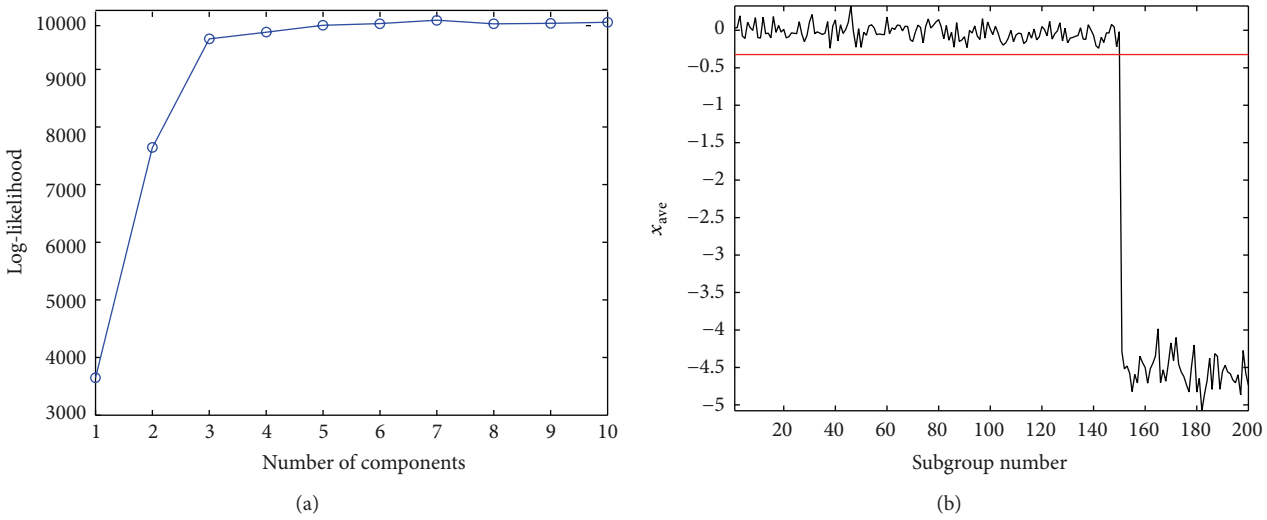

Figure 5: Log-likelihood with the penalty term (a) and Shewhart control chart for damage detection (b).

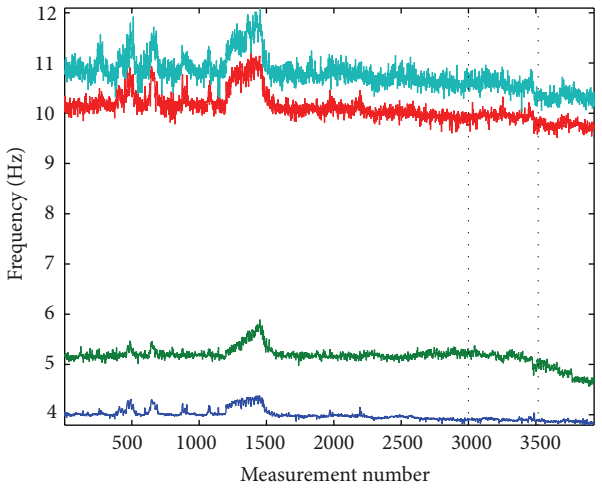

Figure 6: Identified lowest natural frequencies of the Z24 Bridge.

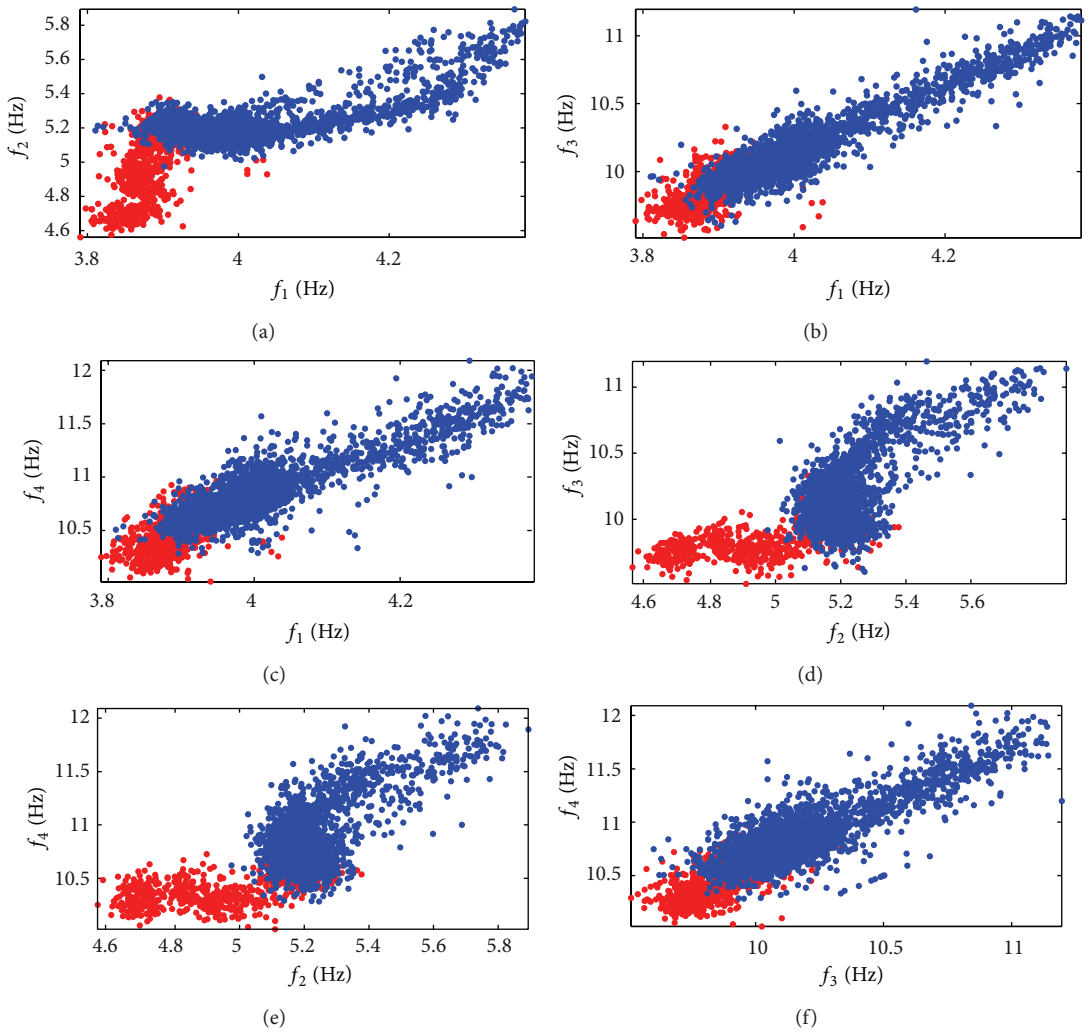

Figure 7: Correlation between the four lowest natural frequencies of the Z24 Bridge. Blue symbols indicate the training data.

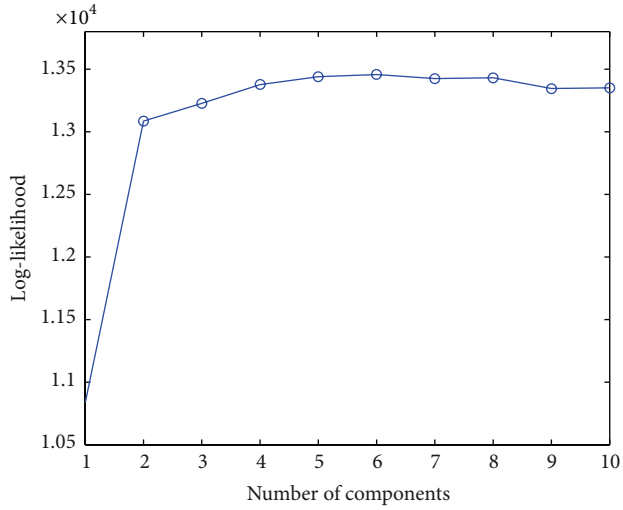

Figure 8: Log-likelihood including the penalty term.

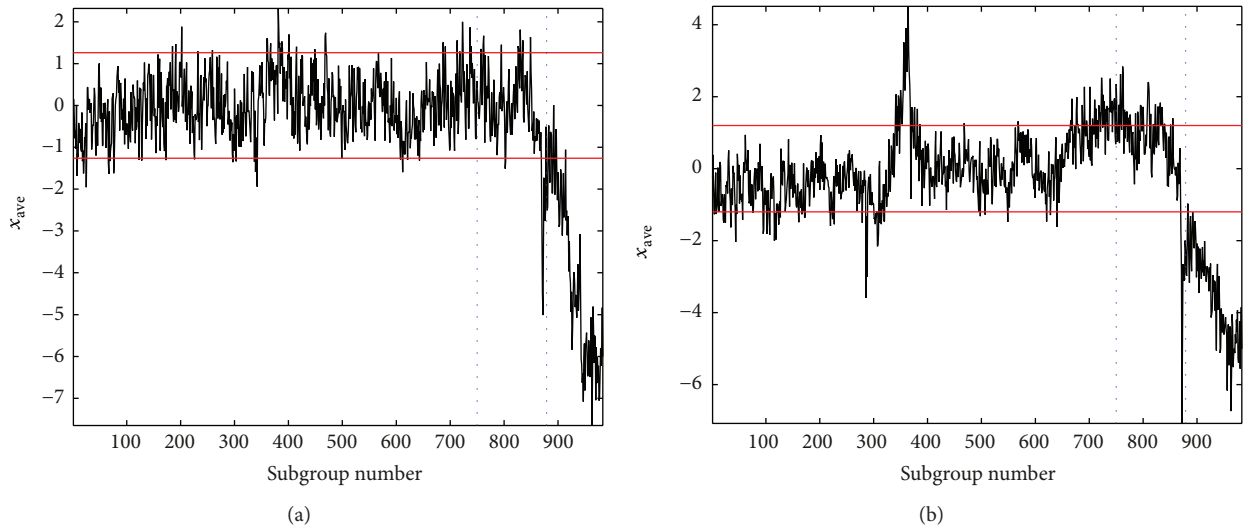

Figure 9: Shewhart control charts for damage detection using GMM (a) and a corresponding linear model (b).

the first principal component scores were used for damage detection. The Shewhart control chart was designed with a subgroup size 4 and the in-control samples 1–3,000. Damage was clearly detected (Figure 9(a)). The control limits are probably too tight resulting in several false alarms. In particular, a few false indications can be observed just prior to damage. Some activity was reported as the settlement system was installed [12], which may have changed the natural frequencies. Another control chart is shown in Figure 9(b) after using a corresponding linear model (with one component only). Compared to the chart in Figure 9(a), it can be concluded that GMM outperformed the linear model in this case.

6. Conclusion

A Gaussian mixture model was proposed to eliminate nonlinear environmental or operational influences from structural health monitoring data. The main advantages are that (1) the measurement of the underlying variables is not necessary, (2) the number of Gaussian components can be estimated, (3) the GMM model can be identified independently of the local linear models, and (4) it is a data-based method; no finite element model is needed. The main disadvantages are that the EM algorithm is not guaranteed to find the global maximum and that the training may be quite slow. Nonlinear models are most effective if the data dimensionality is low. Linear models often outperform nonlinear models for high-dimensional data [1]. The number of environmental or operational variables is usually relatively small. Therefore, their influences on the data are virtually located in a low-dimensional subspace, and a linear analysis is capable of removing this subspace from the subsequent analysis, thus eliminating the environmental or operational effects from the data.

Once the GMM model was identified, MMSE was applied to each component to take into account the local linear correlation. The Mahalanobis distance or whitening transformation [13] could also be applied to the linear components.

The question of how small damage can be detected was not addressed in this study. Detection performance depends on the signal-to-noise ratio (SNR), in which signal is the shift or variance change due to damage and noise is often the measurement error or more generally everything that cannot be explained by the model. SNR should be as low as possible. In this study, noise was decreased by building an accurate model for nonlinear data.

Damage detection comprises several functions and models, many of which are classical. Also, many methods have been applied to SHM by the author and other researchers. This paper focused on the residual generation when the data are nonlinearly correlated. The remaining functions were merely referred to by name.

Conflict of Interests

The author declares that there is no conflict of interests regarding the publication of this paper.

Acknowledgments

This research was performed in the Intelligent Structural Health Monitoring System (ISMO) project, funded by the Multidisciplinary Institute of Digitalisation and Energy (MIDE) research programme at Aalto University, Finland (http://mide.tkk.fi/en/). The natural frequencies of the Z24 Bridge were identified and provided by Dr. Bart Peeters, whose contribution is greatly acknowledged.

References

[1] J. Kullaa, "Distinguishing between sensor fault, structural damage, and environmental or operational effects in structural

health monitoring," *Mechanical Systems and Signal Processing*, vol. 25, no. 8, pp. 2976–2989, 2011.

[2] J. Kullaa, "Is temperature measurement essential in structural health monitoring?" in *Proceedings of the 4th International Workshop on Structural Health Monitoring*, pp. 717–724, Stanford University, DEStech, Stanford, Calif, USA, September 2003.

[3] Z. Ghahramani and G. E. Hinton, "The EM-algorithm for mixtures of factor analyzers," Tech. Rep. CRG-TR-96-1, University of Toronto, 1996.

[4] A.-M. Yan, G. Kerschen, P. de Boe, and J.-C. Golinval, "Structural damage diagnosis under varying environmental conditions—part II: local PCA for non-linear cases," *Mechanical Systems and Signal Processing*, vol. 19, no. 4, pp. 865–880, 2005.

[5] H. Sohn, K. Worden, and C. R. Farrar, "Statistical damage classification under changing environmental and operational conditions," *Journal of Intelligent Material Systems and Structures*, vol. 13, no. 9, pp. 561–574, 2002.

[6] M. A. Kramer, "Nonlinear principal component analysis using autoassociative neural networks," *AIChE Journal*, vol. 37, no. 2, pp. 233–243, 1991.

[7] E. Figueiredo, L. Radu, R. Westgate et al., "Applicability of a Markov-Chain Monte Carlo method for damage detection on data from the Z-24 and Tamar suspension bridges," in *Proceedings of the 6th European Workshop on Structural Health Monitoring*, C. Boller, Ed., pp. 747–754, Dresden, Germany, July 2012.

[8] C. M. Bishop, *Pattern Recognition and Machine Learning*, Springer, New York, NY, USA, 2006.

[9] J. Kullaa, "Sensor validation using minimum mean square error estimation," *Mechanical Systems and Signal Processing*, vol. 24, no. 5, pp. 1444–1457, 2010.

[10] S. Sharma, *Applied Multivariate Techniques*, John Wiley & Sons, New York, NY, USA, 1996.

[11] D. C. Montgomery, *Introduction to Statistical Quality Control*, John Wiley & Sons, New York, NY, USA, 3rd edition, 1997.

[12] B. Peeters, *System identification and damage detection in civil engineering [M.S. thesis]*, K.U.Leuven, 2000.

[13] J. Kullaa, "Whitening transformation in damage detection. Smart structures," in *Proceedings of the 5th European Conference on Structural Control (EACS '12)*, C. D. ROM, A. E. del Grosso, and P. Basso, Eds., Erredi Grafiche Editoriali, Genoa, Italy, June 2012.

Hindawi Publishing Corporation
Shock and Vibration
Volume 2014, Article ID 401942, 12 pages
http://dx.doi.org/10.1155/2014/401942

Research Article

Probabilistic Neural Network and Fuzzy Cluster Analysis Methods Applied to Impedance-Based SHM for Damage Classification

Lizeth Vargas Palomino, Valder Steffen Jr., and Roberto Mendes Finzi Neto

School of Mechanical Engineering, Federal University of Uberlândia, Campus Santa Mônica, 38400-902 Uberlândia, MG, Brazil

Correspondence should be addressed to Valder Steffen Jr.; vsteffen@mecanica.ufu.br

Received 10 July 2013; Accepted 20 January 2014; Published 27 May 2014

Academic Editor: Nuno Maia

Copyright © 2014 Lizeth Vargas Palomino et al. This is an open access article distributed under the Creative Commons Attribution License, which permits unrestricted use, distribution, and reproduction in any medium, provided the original work is properly cited.

Impedance-based structural health monitoring technique is performed by measuring the variation of the electromechanical impedance of the structure caused by the presence of damage. The impedance signals are collected from patches of piezoelectric material bonded on the surface of the structure (or embedded). Through these piezoceramic sensor-actuators, the electromechanical impedance, which is directly related to the mechanical impedance of the structure, is obtained. Based on the variation of the impedance signals, the presence of damage can be detected. A particular damage metric is used to quantify the damage. Distinguishing damage groups from a universe containing different types of damage is a major challenge in structural health monitoring. There are several types of failures that can occur in a given structure, such as cracks, fissures, loss of mechanical components (e.g., rivets), corrosion, and wear. It is important to characterize each type of damage from the impedance signals considered. In the present paper, probabilistic neural network and fuzzy cluster analysis methods are used for identification, localization, and classification of two types of damage, namely, cracks and rivet losses. The results show that probabilistic neural network and fuzzy cluster analysis methods are useful for identification, localization, and classification of these types of damage.

1. Introduction

Failures occurring in industrial equipment and structures in general are associated with friction, fatigue, impact, and crack growth or with other reasons. For an appropriate functioning of the system, the failure should be located and repaired timely. In general terms, the problem of damage monitoring consists in locating and measuring the fault and estimating the remaining life of the system (damage prognosis). One of the most important ambitions of modern engineering is to perform structural health monitoring in real time in structural components of high cost and considerable responsibility. Thus, the creation or improvement of techniques that enhance the accuracy and reliability of the tracking process is highly desirable and is the subject of several studies both in industry and academic environments [1].

There are several techniques for monitoring the occurrence and propagation of structural damage. One of these techniques is the so-called impedance-based structural health monitoring [2]. The basic idea behind this technique is monitoring the changes in the mechanical impedance of the structure as caused by the presence of damage. As the direct measurement of the mechanical impedance of the structure is a difficult task, the method uses piezoelectric ceramics (PZT patches) bonded to or incorporated into the structure, allowing the measurement of the electromechanical impedance. As this measure is related to the structure variation of the impedance signals, the presence of damage can be detected. A particular damage metric is used to quantify the damage [3].

The impedance-based SHM technique was first proposed by Liang et al. [4] and subsequently the method was extended by Chaudhry et al. [5, 6], Sun et al. [7], Park et al. [8–11], Giurgiutiu and Zagrai [12], Soh et al. [13], Bhalla et al. [14], Giurgiutiu et al. [15, 16], Moura Jr. and Steffen Jr. [17], Peairs [18], Moura Jr. [19], and Neto et al. [20].

Distinguishing damage groups from a universe containing different types of damage is a major challenge in structural health monitoring. There are various types of failures, which may occur in a given structure, such as cracks, fissures, loss of joining components (rivets), corrosion, and wear. In the case of composite structures delamination is a major concern. It is important to characterize each type of damage for defining appropriate correction efforts. In order to distinguish the different damage types, probabilistic neural network and fuzzy cluster analysis methods for classification can be used [21, 22].

An artificial neural network is a mathematical model, computational model, or metamodel that mimics the structure by using functional aspects of biological neural networks. It consists of an interconnected group of artificial neurons and processes information by using a connectionist approach for computation [23]. In most cases an artificial neural network is an adaptive system that changes its structure based on external or internal information that flows through the network during the learning phase. Modern neural networks can be understood as nonlinear statistical data modeling tools. They are usually used to model complex relationships between input and output or to find patterns in data [23]. There are several types of artificial neural network; one of them is the probabilistic neural network. This artificial neural network can be used for classification tasks. The network is an implementation of the statistical algorithm called kernel discriminate analysis [24] in which the operations are organized into a multilayered feedforward network with four layers, namely, the input layer, pattern layer, summation layer, and output layer [25].

Fuzzy clustering is an unsupervised learning operation that aims at decomposing a given set of objects into subgroups or clusters based on similarity. The goal is to divide the dataset in such a way that objects or cases belonging to the same cluster are as similar as possible, whereas objects belonging to different clusters are dissimilar [26]. The main potential of clustering is to detect the underlying structure in data, not only for classification and pattern recognition, but also for model reduction and optimization.

In the present paper, the probabilistic neural networks and the fuzzy cluster analysis methods are used for identification, localization, and classification of damage in metallic aeronautic structures. The impedance signal measurement set is used as the input of the probabilistic neural network and the output is the type of damage (crack, rivet loss, or pristine condition). The Gustafson-Kessel fuzzy clustering algorithm was also implemented. The impedance signal measurement set is used as the object to be classified by the fuzzy cluster analysis algorithm and the results represent the type of damage. The results show that the methods are useful for identification, localization, and classification of damage.

1.1. Probabilistic Neural Network. Artificial neural networks are parallel distributed systems composed of simple processing elements (neurons) that calculate given mathematical functions (usually nonlinear). Such units are arranged in one or more layers and interconnected by a large number of connections, usually unidirectional. In most models, these connections are associated with weights, which store the knowledge represented in the model and consider the input received by each neuron in the network. The operation of these networks is inspired by a physical structure designed by nature, the human brain [27]. There are different types of neural networks; the probabilistic neural network is one of them [25].

The probabilistic neural network is predominantly a classifier. It is based on the probability distribution function, and is an implementation of a statistical algorithm known as kernel discriminating analysis [24], in which the operations are organized into a multilayered feedforward network with four layers, namely, the input layer, pattern layer, summation layer, and output layer. The architecture for this system is shown in Figure 1.

When a sample X is presented, the input layer distributes this sample to the pattern layer neurons (second layer). The function described in the following equation is calculated for each j-neurons of the i-class in the pattern layer:

$$ft_{i,j}(X) = \frac{1}{(2\pi)^{d/2}\sigma_i^d} \exp\left[\frac{-\left(X - W_{i,j}\right)^T \left(X - W_{i,j}\right)}{2\sigma_i^2}\right], \quad (1)$$

where $ft_{i,j}(X)$ is the contribution of the j-neuron in the i-class; σ is the transfer function and $W_{i,j}$ is the weight of the j-neuron of the i-class. In each i-neuron of the summation layer the contribution of each neuron of the pattern layer that belongs to the i-class is added. In the output layer, the sample X is associated with the class with the highest probability [25].

The training process consists in a unique step, that is, the weight of each pattern layer neuron is formed by the characteristic vector of each training sample [25].

1.2. Fuzzy Cluster Analysis Method. In clustering analysis the sampled points (or the population) are divided into a quantity of defined groups by using the similarities between these members. In many fields of knowledge, these clustering techniques have been used to distinguish groups by their features [28]. The clustering analyses can be divided into two subclassifications, the hierarchical and nonhierarchical clustering techniques [28]. Both methods considered in the present contribution are nonhierarchical techniques.

The nonhierarchical techniques find directly the N elements of the k clusters or groups in such a way that these partitions follow two criteria, namely, the similarity (or internal cohesion) and separation of the formed groups [28]. The Gustafson-Kessel algorithm is based on the behavior of the objective function. The basic idea considers an objective or evaluation function that assigns to each possible cluster partition a quality or error value that has to be optimized. The optimal solution is the cluster partition that obtains the best evaluation. In this sense, an optimization problem is to be solved when cluster analysis is performed [29]. The corresponding objective function is given by

$$J = \sum_{i=1}^{k} \sum_{j=1}^{N} \left(u_{ij}\right)^m d^2\left(x_j, v_i\right), \quad (2)$$

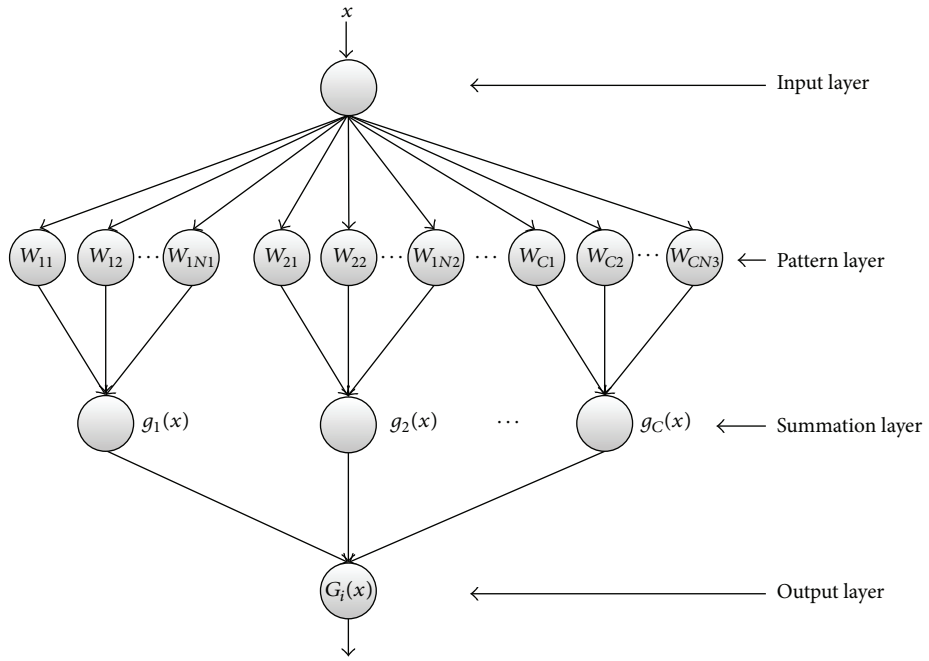

Figure 1: Probabilistic neural network architecture.

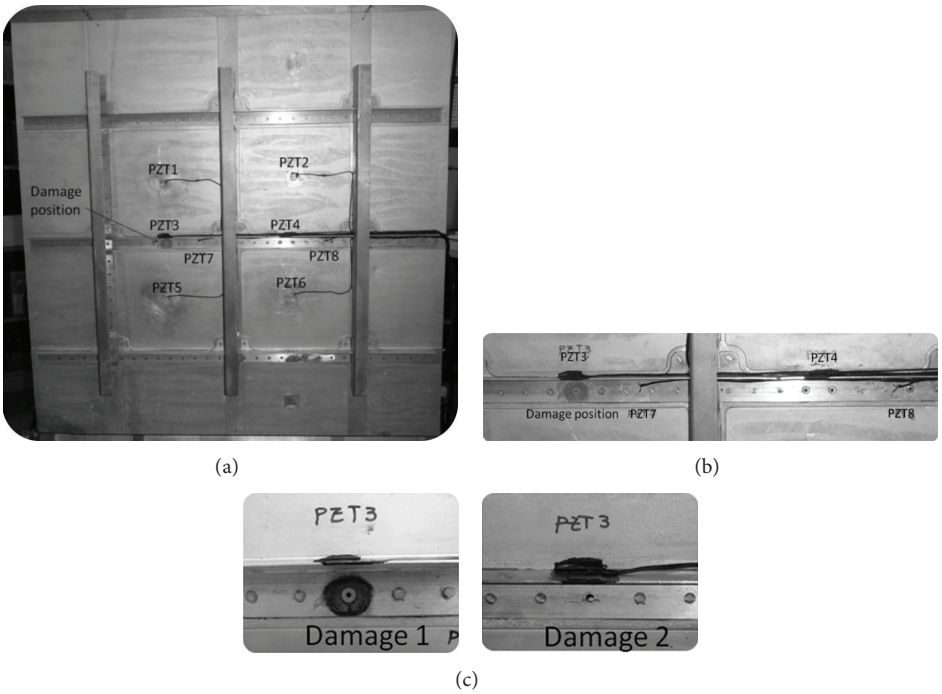

Figure 2: Aluminum aircraft panel equipped with eight PZT patches.

Table 1: States of the aircraft panel.

Number	State	Description	Measurements number
1	Baseline	The panel with all rivets	1–200
2	Damage 1	The panel without one of the rivets (Figure 2(c))	201–400
1	Baseline	The panel with all rivets	401–600
3	Damage 2	The panel with all rivets and localized corrosion	601–800

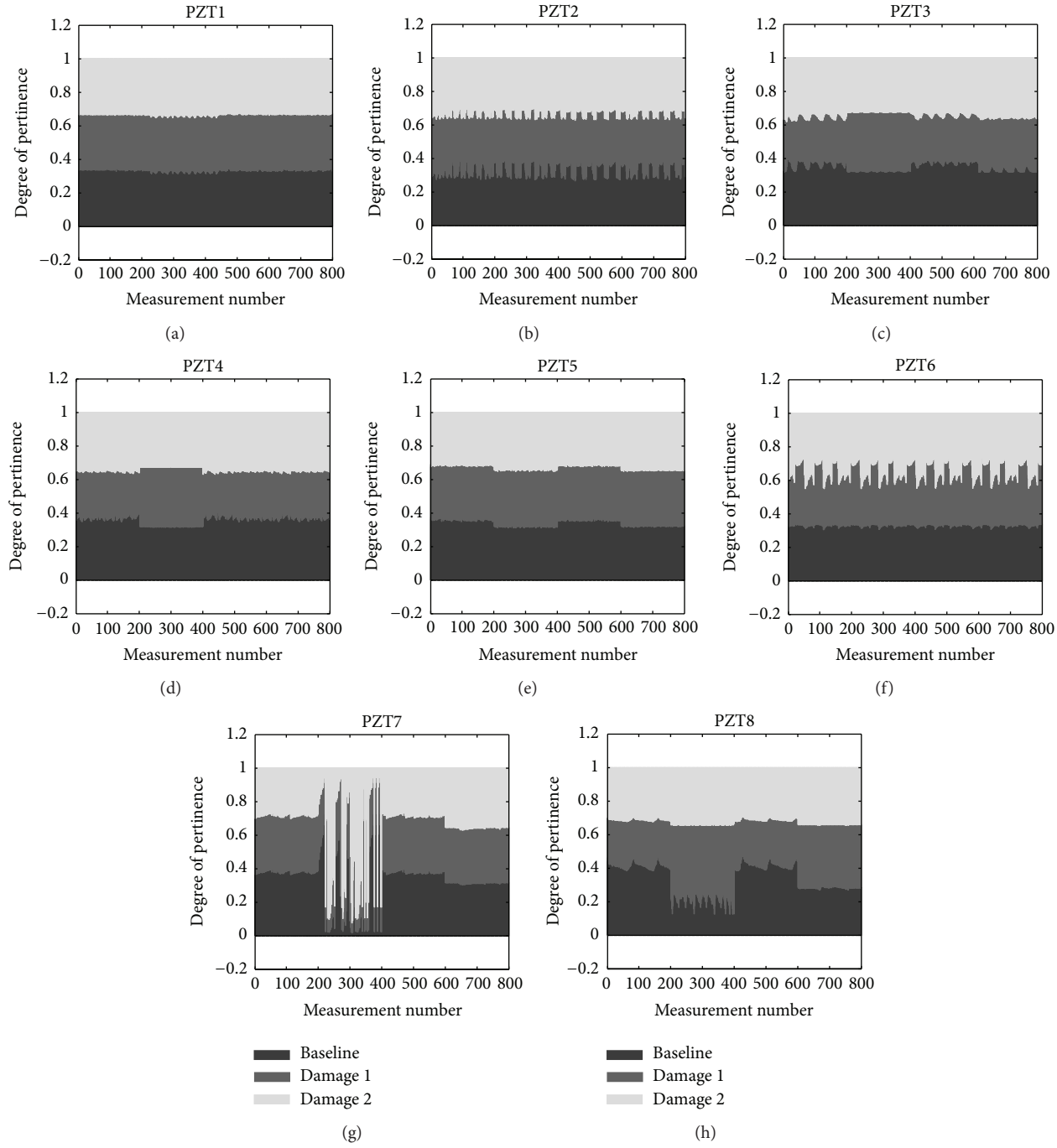

Figure 3: Initial degree of pertinence for aircraft panel.

Table 2: Probabilistic neural network for damage classification.

Layer	Number of neurons		
Input	190		
Pattern	570		
Summation	3		
Output	1		
	Baseline	Damage 1	Damage 2
Training set	360	180	180
Test set	40	20	20

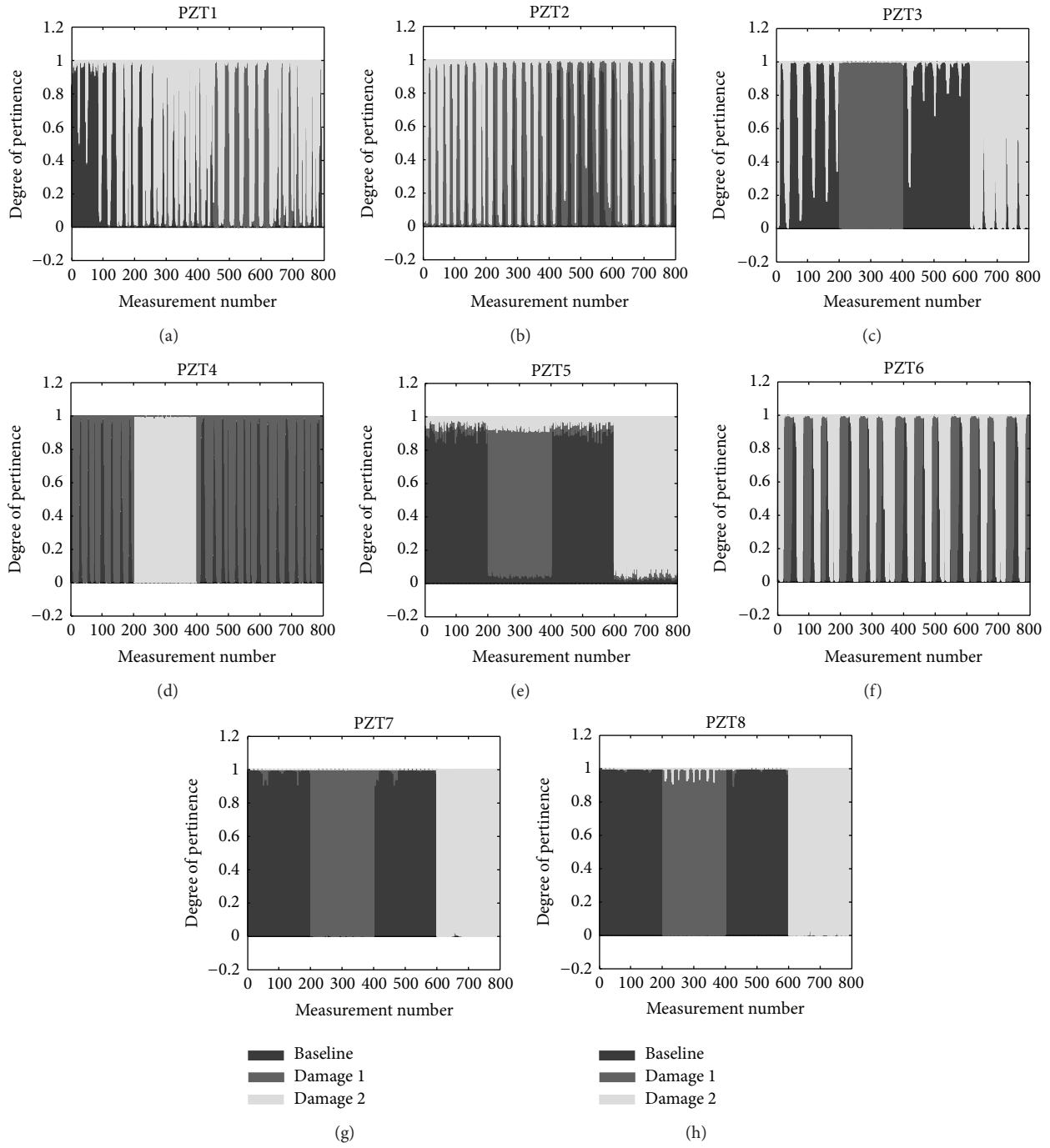

Figure 4: Final degree of pertinence for the aircraft panel.

where v_i is the center of the cluster i, x_j is the data j, $d(x_j, v_i)$ is the distance between x_j and cluster center v_i, m is the fuzzy parameter, and u_{ij} is the probability of the element x_j to pertain to the cluster i. The objective function constraints are presented in the following:

$$0 \le u_{ij} \le 1, \tag{3}$$

$$\sum_{i=1}^{k} u_{ij} = 1, \quad \forall j = 1, \ldots, N. \tag{4}$$

Mahalanobis distance used in the Gustafson-Kessel (GK) algorithm and the corresponding formulation is presented in the equation below. This technique provides greater flexibility to adapt to the shape and dimensions of each cluster but has higher computational complexity [28]. Consider the following:

$$d^2\left(x_j, v_i\right) = \left(x_j - v_i\right)^T P_i \left(x_j - v_i\right), \tag{5}$$

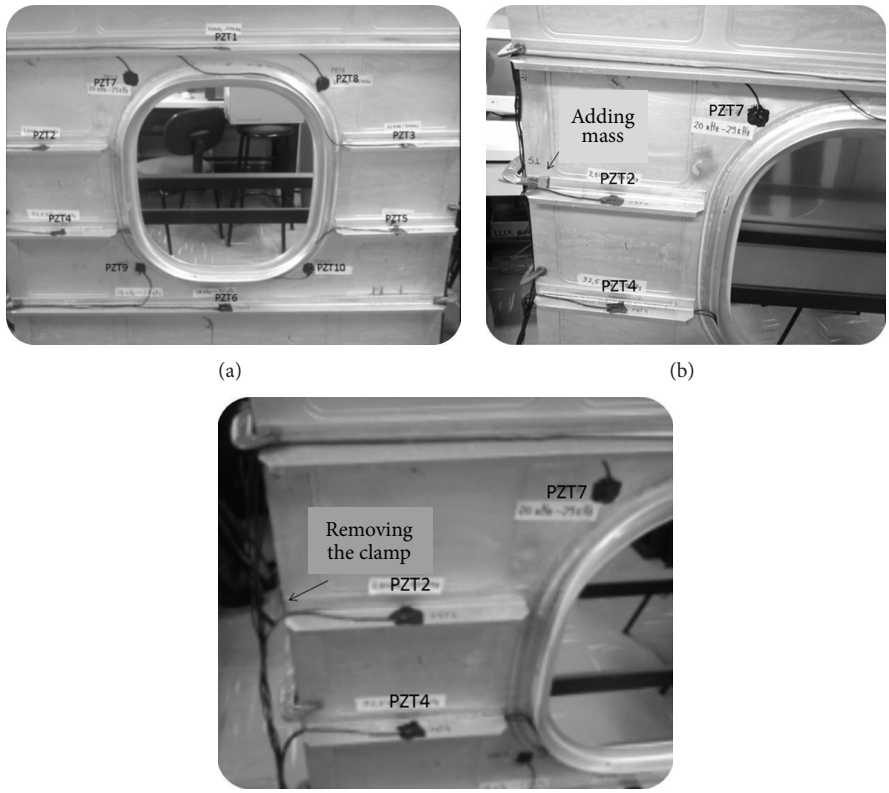

Figure 5: Aluminum aircraft window containing ten PZT patches.

where P_i are the fuzzy covariance matrices that are obtained from

$$P_i = \frac{\sum_{j=1}^{N} u_{ij}^{m} \left(x_j - v_i\right)\left(x_j - v_i\right)^{T}}{\sum_{j=1}^{N} u_{ij}^{m}}. \quad (6)$$

The process consists in minimizing the objective function, (4), and the results obtained are the cluster centers v and the pertinence matrix u.

2. Case Study Number 1: Aluminum Aircraft Panel

The first test presented in this work corresponds to an 80 × 80 cm aircraft panel, as shown in Figure 2(a). The structure was tested by using eight PZT patches to capture the impedance signals. A first type of damage was simulated by removing a rivet located close to PZT3, as shown in Figure 2(c). After the measurements have been made for this state, the rivet was reattached at its former position. Then, to simulate a corrosion type of damage, hydrochloric acid was spread in the vicinity of the rivet. A localized corrosion area was obtained (see Figure 2(c)).

A description of each state of the structure is presented in Table 1. Two hundred (200) measurements were taken for each state. Every measured signal contains 200 points.

To classify damage, the impedance signals measured in the panel were used as inputs of the neural networks. Eight probabilistic networks (one for each PZT) were implemented to analyze the structure. All these networks were built with the same architecture, since they were all intended to the same purpose (classifying the damage in the panel). The descriptions of the networks together with their training sets are presented in Table 2. The results obtained with the test set for each of the eight probabilistic neural networks are presented in Table 3. The error percentages found in damage classification for PZT1, PZT2, and PZT6 were greater than 48%, which means that they did not detect the damage. The PZT3 and PZT4 showed error percentages greater than 10%, although it should be noted that the damage 1 (loss of the rivet) was perfectly detected by both of these patches (PZT3 and PZT4). PZT3 and PZT4 were dedicated to this specific damage. The PZT5, PZT7, and PZT8 had error percentages smaller than 4%, similar to the results obtained for simpler structures (beam and plate) [30]. One can thus conclude that these three PZT patches succeeded to properly detect the types of damage that were inserted into the structure.

The initial degrees of pertinence for the Gustafson-Kessel algorithm are shown in Figure 3. After several iterations (Table 4) the algorithm was interrupted by the convergence of the process for every PZT patch that was used. One may then observe the final degree of pertinence as shown in Figure 4. The results of PZT1, PZT2, and PZT6 confirm again that these

Table 3: Classification of test set of probabilistic neural networks for each PZT patch in the aircraft panel.

		Baseline	Damage 1	Damage 2	Error%
PZT1	√	23	10	5	52,5%
	✗	17	10	15	
Total		**40**	**20**	**20**	
PZT2	√	20	9	8	55%
	✗	20	11	12	
Total		**40**	**20**	**20**	
PZT3	√	35	20	16	11,25%
	✗	5	0	4	
Total		**40**	**20**	**20**	
PZT4	√	32	20	14	17,5%
	✗	8	0	6	
Total		**40**	**20**	**20**	
PZT5	√	40	19	18	3,75%
	✗	0	1	2	
Total		**40**	**20**	**20**	
PZT6	√	40	20	18	48,75%
	✗	19	8	12	
Total		**40**	**20**	**20**	
PZT7	√	40	20	19	1,25%
	✗	0	0	1	
Total		**40**	**20**	**20**	
PZT8	√	40	20	18	2,5%
	✗	0	0	2	
Total		**40**	**20**	**20**	

Table 4: Optimization results of the Gustafson-Kessel algorithm for the aircraft panel.

	Iteration	Initial objective function value	Final objective function value
PZT1	139	3173,262	446,395
PZT2	102	831,342	118,823
PZT3	67	532244,526	5803,566
PZT4	47	602945,975	2788,759
PZT5	18	186,055	95,991
PZT6	131	3644,445	1594,554
PZT7	13	1041994,032	23013,747
PZT8	25	1452335,476	10885,113

PZTs failed to detect damage and thus made the classification impossible. The PZT3 and PZT4 correctly identified the damage 1; nevertheless the damage 2 was impossible to be distinguished from the Baseline. Finally, the PZT5, PZT7, and PZT8 managed to correctly classify the two types of damage with a degree of pertinence greater than 80%.

3. Case Study Number 2: Aluminum Aircraft Window

A second aircraft structure was used to test the artificial intelligence techniques in structural health monitoring for damage classification. For this aim a window located in an aluminum aircraft structure, as illustrated in Figure 5(a), was used. Due to the size and complexity of the structure, ten PZT patches were considered in the experiment. This number of PZT patches was arbitrary since no preliminary study was performed to optimize the test configuration. Since the beginning of the tests, the PZT10 showed poor stability and repeatability and has therefore been ignored in the test. To simulate two different types of damage in the structure, two experiments were performed as follows. First, a weight was added to the structure as shown in Figure 5(b). Second, after the mentioned weight was removed, one of the clamps (located close to the PZT2) was removed (Figure 5(c)). For every state of the structure 200 measurements were made as shown in Table 5. For every measurement 200 points were taken.

Table 5: States of the aircraft window.

Number	State	Description	Measurements number
1	Baseline	Window with all the clamps	1–200
2	Damage 1	Window with all the clamps and the weight	201–400
1	Baseline	Window with all the clamps	401–600
3	Damage 2	Window with one clamp missing near PZT2 (Figure 5(c))	601–800

Table 6: Classification of test set of probabilistic neural networks for each PZT patch of the aircraft window.

		Baseline	Damage 1	Damage 2	Error%
PZT1	√	21	8	12	
	✗	19	12	8	48,75%
Total		**40**	**20**	**20**	
PZT2	√	36	16	20	
	✗	4	4	0	10%
Total		**40**	**20**	**20**	
PZT3	√	20	3	7	
	✗	20	17	13	62,5%
Total		**40**	**20**	**20**	
PZT4	√	19	7	13	
	✗	21	13	7	51,25%
Total		**40**	**20**	**20**	
PZT5	√	21	8	13	
	✗	19	12	7	47,5%
Total		**40**	**20**	**20**	
PZT6	√	17	9	9	
	✗	23	11	11	56,25%
Total		**40**	**20**	**20**	
PZT7	√	40	19	20	
	✗	0	1	0	1,25%
Total		**40**	**20**	**20**	
PZT8	√	33	15	20	
	✗	7	8	0	18,75%
Total		**40**	**20**	**20**	
PZT9	√	33	15	20	
	✗	7	5	0	11,25%
Total		**40**	**20**	**20**	

Table 7: Optimization results of the Gustafson-Kessel algorithm for the aircraft window.

	Iteration	Initial objective function value	Final objective function value
PZT1	130	107992,545	13922,783
PZT2	44	1951882,844	3723,708
PZT3	112	11418,915	1011,319
PZT4	131	14063,77	1106,733
PZT5	105	73130,147	3914,543
PZT6	83	187017,9	8330,349
PZT7	9	209498,097	1474,566
PZT8	101	71861,057	7189,752
PZT9	40	149831,047	652,42

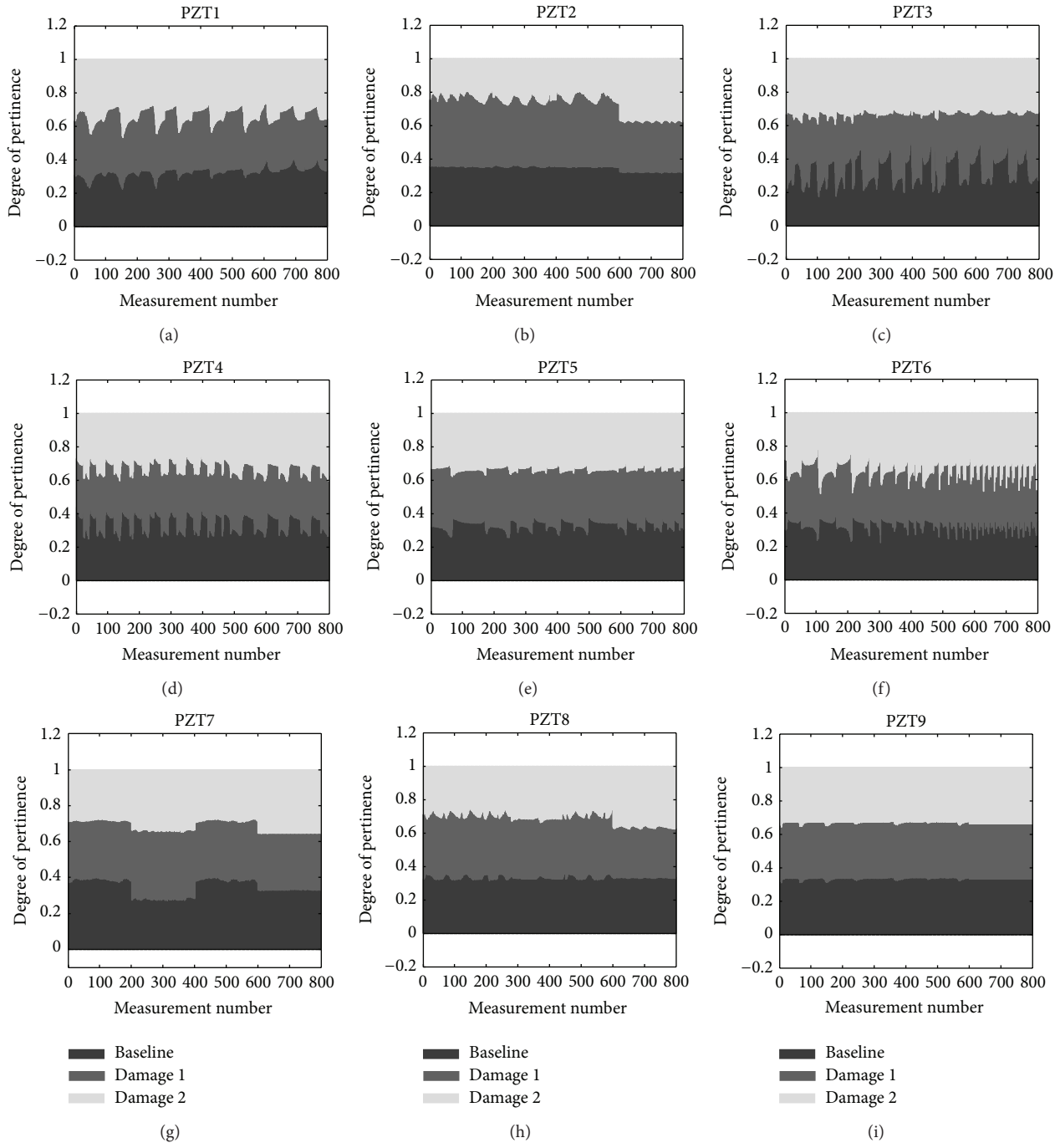

Figure 6: Initial degrees of pertinence for the aircraft window.

In this case, nine probabilistic networks were implemented (one for each PZT) to analyze this structure as shown in Table 2. The results obtained with the test set for each one of the nine probabilistic neural networks are presented in Table 6.

The damage misclassification percentages of PZT1, PZT3, PZT4, PZT5, and PZT6 were greater than 48%. These PZT patches are not meant to detect damage. The types of damage (structural modifications in this case) were inserted in the back panel and the PZT patches were bonded to the reinforcing beams. The PZT2, while installed in a reinforcement beam, was able to detect the damage 2 without errors; this success is due to the fact that this sensor is close to the clamp position. The PZT8 and PZT9 detected only the clamp removal without errors, with an overall error percentage of less than 20%. Finally, the PZT7, which was bonded directly onto the panel and close to the removed clamp, was able to identify all states with an error percentage of 1.25%.

The initial degrees of pertinence for the Gustafson-Kessel algorithm are shown in Figure 6. After several iterations (Table 7), the algorithm was interrupted by the convergence of the process for each of the PZT patches. The final degrees

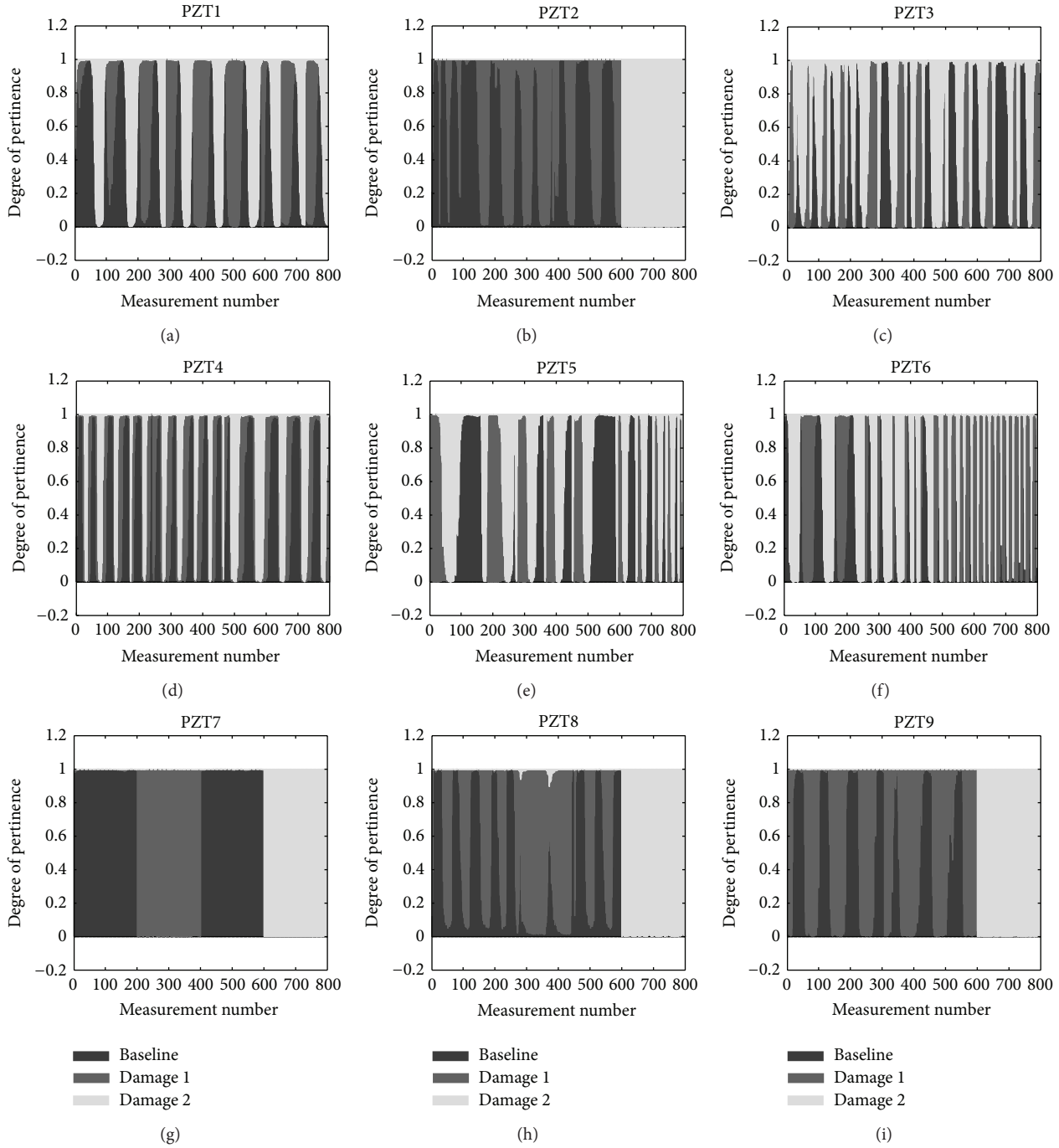

Figure 7: Final degrees of pertinence for the aircraft window.

of pertinence are shown in Figure 7. The results of the PZT1, PZT3, PZT4, PZT5, and PZT6 confirm once again that these PZT patches failed to detect damage, which made the classification impossible due to the position of the patches on the structure. The PZT2, PZT8, and PZT9 correctly classified damage 2, with a degree of pertinence of 99%. However, the damage 1 was impossible to discriminate from the baseline. Finally, for the PZT7, the Gustafson-Kessel algorithm was able to correctly classify all measurements with a degree of pertinence greater than 95%.

4. Conclusion

The probabilistic neural network and fuzzy cluster analysis methods were applied to real-world structures in the context of impedance-based structural health monitoring for damage detection, localization, and classification purposes in metallic aeronautic structures. Impedance signal responses were used as the input of the probabilistic neural network. The output was the type of damage (crack, rivet loss, or pristine condition). The Gustafson-Kessel fuzzy clustering algorithm was

also implemented. The results demonstrated the efficiency of these techniques in accomplishing these tasks. It should be pointed out that the tests were performed at constant room temperature (approximately 20°C). The PZT patches that presented the largest error percentages for both techniques used were the ones that did not succeed to detect damage due to their inappropriate location along the structure [30]. This means that the location of the PZT patches is a major concern in impedance-based structural health monitoring. Further studies will focus on temperature compensation regarding its influence on the damage classification approach. Also, the authors have designed a compact network signal analyzer for electromechanical impedance measurements, which includes post-processing computation for damage metrics calculation and temperature compensation, aiming at on board/online structural health monitoring.

Conflict of Interests

The authors declare that there is no conflict of interests regarding the publication of this paper.

Acknowledgments

The authors are thankful to FAPEMIG (TEC-APQ-00076-09) and CNPq (Proc. Nb. 574001/2008-5), research agencies in Brazil, for providing financial support to this work through the INCT-EIE.

References

[1] C. R. Farrar, N. A. J. Lieven, and M. T. Bement, "An introduction to damage prognosis," in *Damage Prognosis for Aerospace, Civil and Mechanical System*, chapter 1, Wiley, New York, NY, USA, 2005.

[2] G. Park and D. J. Inman, "Impedance-based structural health monitoring," in *Damage Prognosis for Aerospace, Civil and Mechanical System*, chapter 13, Wiley, New York, NY, USA, 2005.

[3] L. V. Palomino and V. Steffen, "Damage metrics associated with electromechanical Impedance technique for SHM applied to a riveted structure," in *Proceedings of the 20th International Congress of Mechanical Engineering (COBEM '09)*, Gramado, Brazil, 2009.

[4] C. Liang, F. P. Sun, and C. A. Rogers, "Coupled electro-mechanical analysis of adaptive material systems—determination of the actuator power consumption and system energy transfer," *Journal of Intelligent Material Systems and Structures*, vol. 5, no. 1, pp. 12–20, 1994.

[5] Z. A. Chaudhry, T. Joseph, F. P. Sun, and C. A. Rogers, "Local-area health monitoring of aircraft via piezoelectric actuator/sensor patches," in *Smart Structures and Materials: Smart Structures and Integrated Systems*, Proceedings of SPIE, pp. 268–276, San Diego, Calif, USA, March 1995.

[6] Z. Chaudhry, F. Lalande, A. Ganino, C. A. Rogers, and J. Chung, "Monitoring the integrity of composite patch structural repair via piezoelectric actuators/sensors," in *Proceedings of the 36th AIAA/ASME/ASCE/AHS/ASC Structures, Structural Dynamics, and Materials Conference and AIAA/ASME Adaptive Structures Forum*, pp. 2243–2248, April 1995.

[7] F. P. Sun, Z. Chaudhry, C. Liang, and C. A. Rogers, "Truss structure integrity identification using PZT sensor-actuator," *Journal of Intelligent Material Systems and Structures*, vol. 6, no. 1, pp. 134–139, 1995.

[8] G. Park, K. Kabeya, H. H. Cudney, and D. J. Inman, "Impedance-based structural health monitoring for temperature varying applications," *JSME International Journal, Series A: Mechanics and Material Engineering*, vol. 42, no. 2, pp. 249–258, 1999.

[9] G. Park, H. H. Cudney, and D. J. Inman, "An integrated health monitoring technique using structural impedance sensors," *Journal of Intelligent Material Systems and Structures*, vol. 11, no. 6, pp. 448–455, 2000.

[10] G. Park, H. H. Cudney, and D. J. Inman, "Feasibility of using impedance-based damage assessment for pipeline structures," *Earthquake Engineering and Structural Dynamics*, vol. 30, no. 10, pp. 1463–1474, 2001.

[11] G. Park, H. Sohn, C. R. Farrar, and D. J. Inman, "Overview of piezoelectric impedance-based health monitoring and path forward," *Shock and Vibration Digest*, vol. 35, no. 6, pp. 451–463, 2003.

[12] V. Giurgiutiu and A. N. Zagrai, "Characterization of piezoelectric wafer active sensors," *Journal of Intelligent Material Systems and Structures*, vol. 11, no. 12, pp. 959–976, 2001.

[13] C. K. Soh, K. K.-H. Tseng, S. Bhalla, and A. Gupta, "Performance of smart piezoceramic patches in health monitoring of a RC bridge," *Smart Materials and Structures*, vol. 9, no. 4, pp. 533–542, 2000.

[14] S. Bhalla, A. S. K. Naidu, C. Wee Ong, and C.-K. Soh, "Practical issues in the implementation of electro-mechanical impedance technique for NDE," in *Smart Structures, Devices, and Systems*, Proceedings of SPIE, pp. 484–494, Melbourne,Australia, December 2002.

[15] V. Giurgiutiu, A. Zagrai, and J. J. Bao, "Piezoelectric wafer embedded active sensors for aging aircraft structural health monitoring," *Structural Health Monitoring*, vol. 1, no. 1, pp. 41–61, 2002.

[16] V. Giurgiutiu, A. Zagrai, J. J. Bao, J. M. Redmond, D. Roach, and K. Rackow, "Active sensors for health monitoring of aging aerospace structures," *International Journal of the Condition Monitoring and Diagnostic Engineering Management*, vol. 6, no. 1, pp. 3–21, 2003.

[17] J. R. V. Moura Jr. and V. Steffen Jr, "Impedance-based health monitoring: frequency band evaluation," in *XXII IMAC*, Dearborn, Mich, USA, 2004.

[18] M. D. Peairs, *High frequency modeling and experimental analysis for implementation of impedance-based structural health monitoring [Ph.D. thesis]*, Virginia Polytechnic Institute and State University, Blacksburg, Va, USA, 2006.

[19] J. R. V. Moura Jr., *Contribution to structural health monitoring systems applied to aeronautic and space structures [Ph.D. thesis]*, Universidade Federal de Uberlândia, Uberlandia, Brazil, 2008.

[20] R. M. Neto, V. Steffen Jr., D. A. Rade, C. A. Gallo, and L. V. Palomino, "A low-cost electromechanical impedance-based shm architecture for multiplexed piezoceramic actuators," *Structural Health Monitoring*, vol. 10, no. 4, pp. 391–402, 2011.

[21] R. R. K. Reddy and R. Ganguli, "Structural damage detection in a helicopter rotor blade using radial basis function neural networks," *Smart Materials and Structures*, vol. 12, no. 2, pp. 232–241, 2003.

[22] P. M. Pawar and R. Ganguli, "Genetic fuzzy system for damage detection in beams and helicopter rotor blades," *Computer Methods in Applied Mechanics and Engineering*, vol. 192, no. 16-18, pp. 2031–2057, 2003.

[23] J. G. Taylor, "Neural network applications," in *Proceedings of the 2nd British Neural Network Society Meeting (NCM '91)*, Springer, London, UK, 1992.

[24] M. Rosenblatt, "Remarks on some non parametric estimates of a density function," *Annals of Mathematical Statistics*, vol. 27, pp. 832–837, 1956.

[25] D. F. Specht, "Probabilistic neural networks," *Neural Networks*, vol. 3, no. 1, pp. 109–118, 1990.

[26] R. Kruse, C. Doring, and M. J. Lesot, "Fundamentals of fuzzy clustering," in *Advances in Fuzzy Clustering and Its Applications*, Chapter 1, pp. 3–30, Wiley, New York, NY, USA, 2007.

[27] A. P. Braga, A. P. L. F. Carvalho, and T. B. Ludermir, *Redes Neurais Artificiais Teoria e Aplicacoes*, LTC, Rio de Janeiro, Brazil, 2000.

[28] S. A. Mingoti, *Análise de Dados Através de Métodos de Estatística Multivariada*, Editora UFMG, Belo Horizonte, Brazil, 2005.

[29] F. Hoppner, F. Klawonn, R. Kruse, and T. Runkler, *Fuzzy Cluster Analysis*, Wiley, New York, NY, USA, 1999.

[30] L. V. Palomino, *Artificial intelligence techniques applied to the impedance-based structural health monitoring technique for monitoring damage in aircraft structures [Ph.D. thesis]*, Federal University of Uberlândia, Uberlândia, Brazil, 2012.

Hindawi Publishing Corporation
Shock and Vibration
Volume 2014, Article ID 693593, 8 pages
http://dx.doi.org/10.1155/2014/693593

Research Article

Damage Detection in CFRP Plates Using Spectral Entropy

E. Castro,[1] P. Moreno-García,[2] and A. Gallego[3]

[1] *Applied Physics Department, Universidad Politécnica de Cartagena, 30202 Cartagena, Murcia, Spain*
[2] *INEGI, Instituto de Engenharia Mecânica e Gestão Industrial, Campus da FEUP, Rua Dr. Roberto Frias 400, 4200-465 Porto, Portugal*
[3] *Applied Physics Department, Universidad de Granada, 18071 Granada, Spain*

Correspondence should be addressed to E. Castro; enrique.castro@upct.es

Received 7 July 2013; Accepted 5 February 2014; Published 20 May 2014

Academic Editor: Nuno Maia

Copyright © 2014 E. Castro et al. This is an open access article distributed under the Creative Commons Attribution License, which permits unrestricted use, distribution, and reproduction in any medium, provided the original work is properly cited.

Damage detection techniques using vibrations are based on measuring the changes in the vibration parameters of a structure. This paper studies the viability of the spectral entropy as a new damage detection parameter to detect the presence of damage in a composite fiber reinforced polymers (CFRP) plate. To carry out this study, the vibrations in a CFRP plate with and without damage were measured and the correlation between damage and spectral entropy has been researched.

1. Introduction

Structural health monitoring (SHM) is very important in aerospace industry due to the high responsibility of the aeronautical structures and their high maintenance costs. So, the developing of reliable damage detection techniques with aerospace application is a very important issue. As composite structures are becoming very important in aerospace engineering, because their high stiffness and less weight, it is very interesting the investigation of damage detection methods for them.

This paper investigates the use of a new damage detection technique in a composite plate. The damage detection technique is based on the use of the entropy of the frequency response function (FRF), which is called spectral entropy (SE), as damage index. The FRF of a structure depends of its geometry and materials, and it is well known that a fracture or a crack produces a change in the FRF [1], which can be used to identify the damage. But in the FRF there is a lot of information, and it is necessary to analyse all this information to detect the damage. Usually the information is reduced in some way to have only one parameter which can be used as damage index. The SE is another way to do it. It is the entropy of the FRF, so it is a single parameter that characterizes the amplitude distribution of the FRF. The principal advantage over other damage indexes based on changes in the natural frequencies is that the SE depends on the distribution of amplitude of the FRF. So, a shift or a change in the global amplitude of the FRF due to external factors does not affect the value of the SE, making it very robust against a change in ambient conditions.

To evaluate the performance of the SE as a damage index, an experiment has been carried out. The vibrations of a CFRP plate with and without damage have been measured, and the FRF and SE have been obtained. As a final result, a correlation between the damage and SE has been found.

2. Experimental Description

The properties of the CFRP plate used in the experiment are listed in Table 1. The plate was excited with a random vibration of frequencies up to 1500 Hz by means of a piezoelectric actuator. The vibrations of the plate were measured with four piezoelectric sensors located symmetrically around the center of the plate. The actuator was located at the center of the plate. The positions and properties of the sensors and actuators are shown in Table 2. The four sides of the plate were clamped to a rigid frame on an antivibration table. Piezoelectric sensors were connected with STP cables to the Brüel and Kjær PULSE input channels in order to cancel out electromagnetic interference (EMI) and crosstalk

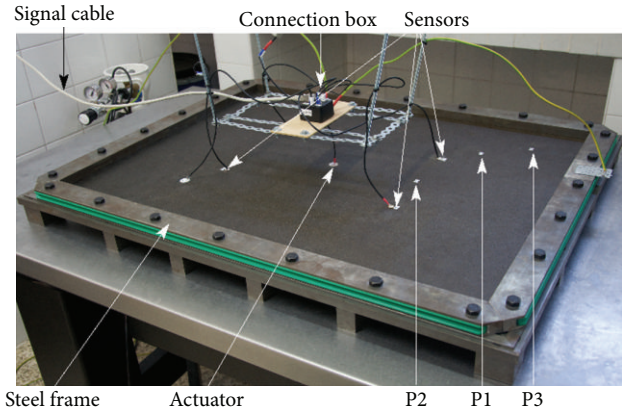

Figure 1: Plate under study and experimental arrangement.

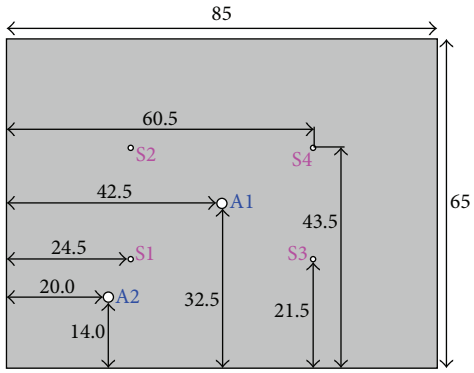

Figure 2: Dimensions of the CFRP plate and positions of the damage (P1, P2, and P3) and the actuator (A1).

Table 1: Properties of the CFRP plate.

Side (a) length	85 cm
Side (b) length	65 cm
Longitudinal Young's moduli	1.50×10^{11} Pa
Transversal Young's moduli	1.15×10^{10} Pa
Poisson's ration	0.42
Shear moduli	5.0×10^{9} Pa
Density	1560 kg/m^3
Mass	4.75 kg
Layer thickness	0.188 mm
Number of layers	12
Stacking sequence	$[0/90]_{3S}$

between neighbouring pairs and external sources. The input signal was also generated with the PULSE output port. The piezosystem EPA-104 amplifier boosted the PULSE output signal to the actuator. To minimize the EMI and electrical noise, all equipment, connection boxes, cable shields, and the frame were connected to an independent ground system. To reduce the influence of external vibrations, the frame was fixed to an antivibration table and the measurements were carried out at night with minimal ambient noise. Figure 1 shows the plate with the attached sensors, actuator, and damage locations.

The damage was simulated by masses attached to the plate with weights, 6.7 g (M1), 12.8 g (M2), 24.7 g (M3), 39.6 g (M4), 85.8 g (M5), and 192.9 g (M6), at three different positions shown in Table 3. In Figure 2 can be seen a diagram of the different positions of the damage in the plate. The plate was placed in a horizontal position and the mass was put on it without any fixing mechanism. The amplitude of the vibrations was low, so the mass stayed in its position while the experiment was performing. As the mass was free, it is possible that it can "jump" on the plate when it goes down. During the experiment no evidence of this jump was noticed.

This kind of damage has the advantages of being very well controlled and nondestructive, which is especially important to validate damage detection and evaluation methods. Furthermore, the addition of masses produces a rise of the local density, whose effect in the vibrational behaviour of the plate is similar to a reduction of the stiffness, as the vibrational frequencies depends on $\sqrt{k/\rho}$, where k is the stiffness and is the density. More details of the experiment can be found in [2, 3].

3. Spectral Entropy

Entropy is a thermodynamic magnitude that can be used to calculate the quantity of energy that cannot be transformed into work. From a microscopic point of view, it is a measure of the disorder of a system. Entropy is used too in information theory, where it is related with the uncertainty in a random variable, where it is called Shannon entropy. For our purposes, we are going to use the interpretation of entropy as a measure of the disorder of a system but applying it to the frequency distribution of a signal. The Shannon entropy can be calculated with the equation:

$$E = -\sum_{i=1}^{N} p_i \log\left(p_i\right), \tag{1}$$

where p_i is the probability of the system of being in the state i and N is the total number of states.

In order to use (1) to calculate the SE, the FRF is normalized and then each frequency peak is considered a state i and its amplitude is assumed to be its probability p_i. So, the SE is calculated using the expression:

$$\mathrm{SE} = -\sum_{i=1}^{N} \frac{A\left(f_i\right)}{A_T} \log\left(\frac{A\left(f_i\right)}{A_T}\right), \tag{2}$$

where $A(f_i)$ is the amplitude of the frequency peak f_i and $A_T = \sum_{i=1}^{N} A(f_i)$. Only the peaks in the FRF are taken into account in the calculation of the SE.

The SE measures the disorder of the amplitude distribution. If all the energy is concentrate in few frequencies, the FRF is very ordered and the SE has a low value. In the same

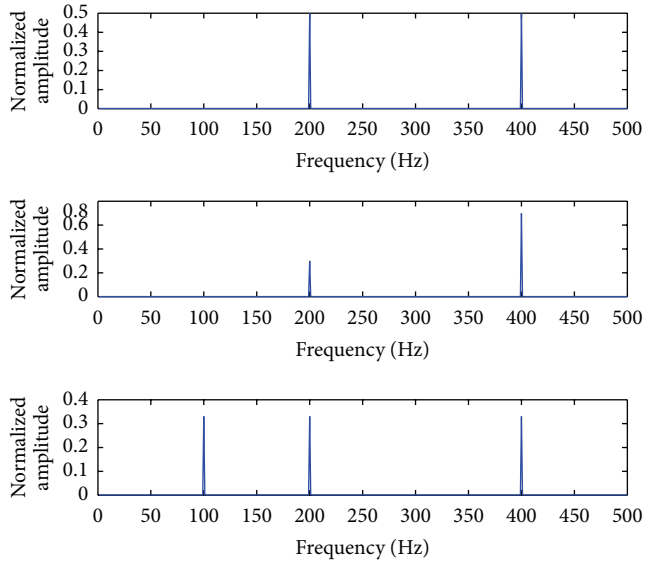

Figure 3: FRFs used as examples of the dependency of SE with the amplitude distribution. Their values of SE are 3.163, 3.108, and 3.443.

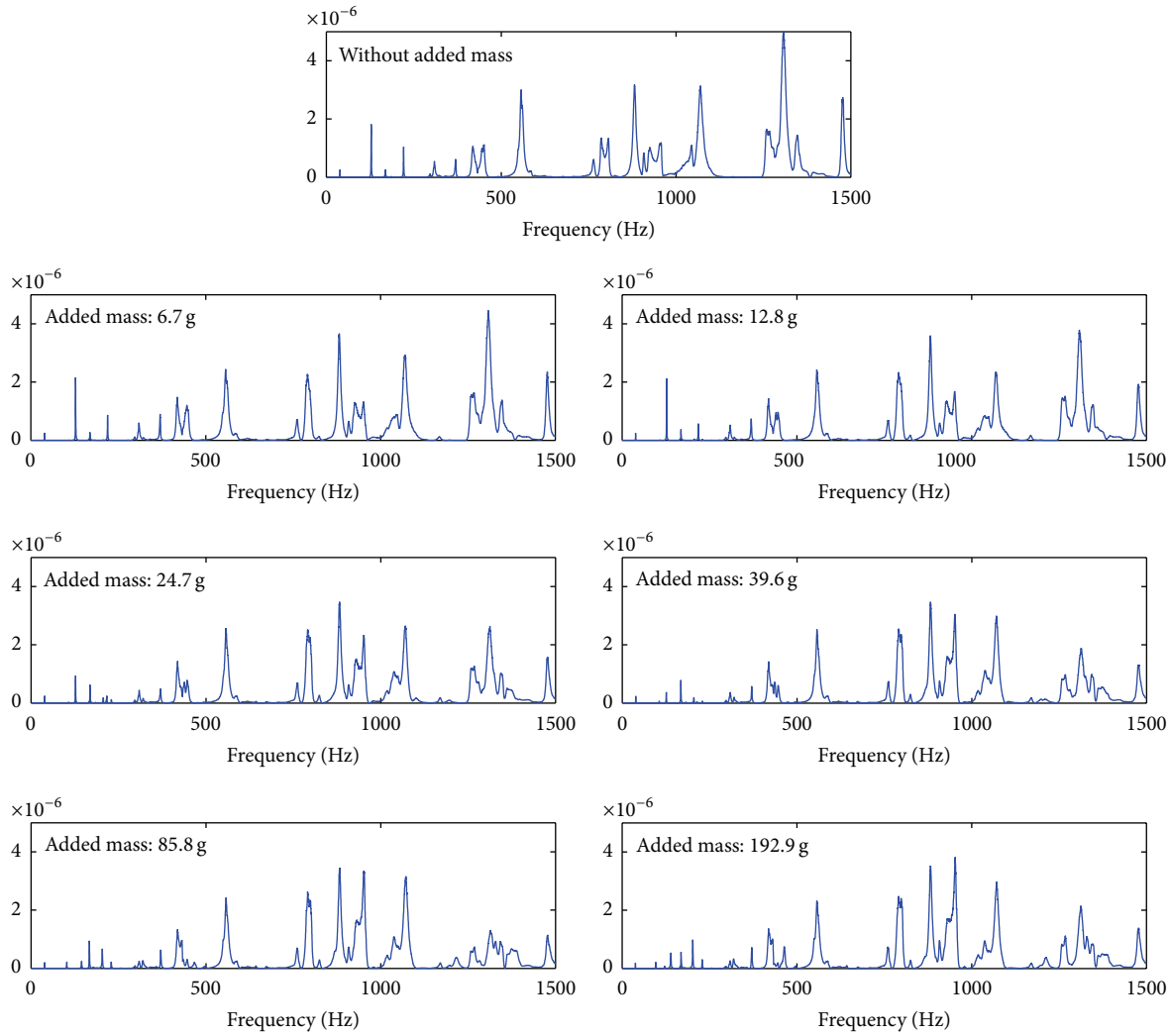

Figure 4: Examples of experimental FRFs. The examples correspond to the sensor 1 with the damage in position P1. In the figure, the added mass is indicated.

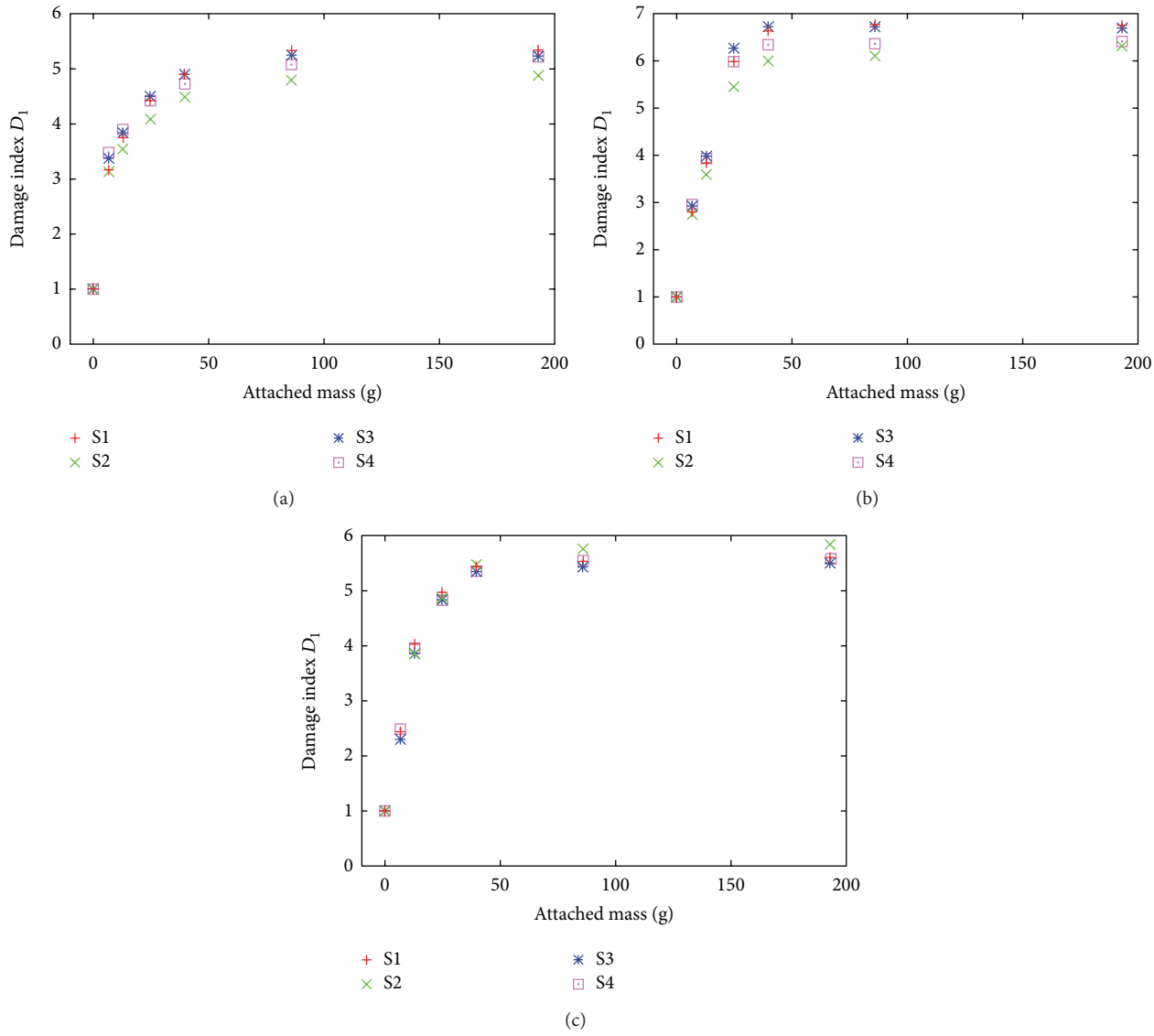

FIGURE 5: Variation of D_1 with attached mass. (a) Damage in position P1. (b) Damage in position P2. (c) Damage in position P3.

way, if the energy is distributed over many frequencies, the FRF is very disordered and the SE has a high value. Taking this into account, the SE can be seen as an indicator of the complexity of the vibration, as it will be more complex if more frequencies are involved in the movement.

As an example, in Figure 3 three normalized FRFs can be seen. The first one has only two frequencies of the same amplitude, and its SE is 3.163. The second one has the same frequencies as the previous one but one of them has higher amplitude than the other one, so it is more ordered and its SE has a value of 3.108, which is lower than the first one. The third FRF has three frequencies of equal value and its SE is 3.443. As the energy is distributed over more frequencies, the FRF is more disordered than the first one, so its SE is higher.

The SE can be used as damage index under the assumption that damage changes the amplitude distribution in the FRF of the structure. That is, if there is only a change in the value of the natural frequencies, but they have the same amplitude as the original ones, then their SE will be the same. The SE will change if the new frequencies have different amplitude than the previous ones.

To obtain the FRF the structure must be excited with an external force (input) and the vibration in a point of the structure must be measured (output). The input energy is distributed between the different natural frequencies depending on physical characteristics of the structure and the position of the actuator and the sensor. The amplitude of each frequency peak of the FRF shows which part of the input energy corresponds to that frequency.

Physically, damage decreases the stiffness of the region of the structure where it is located. It modifies the physical characteristics of the structure and the way that it vibrates,

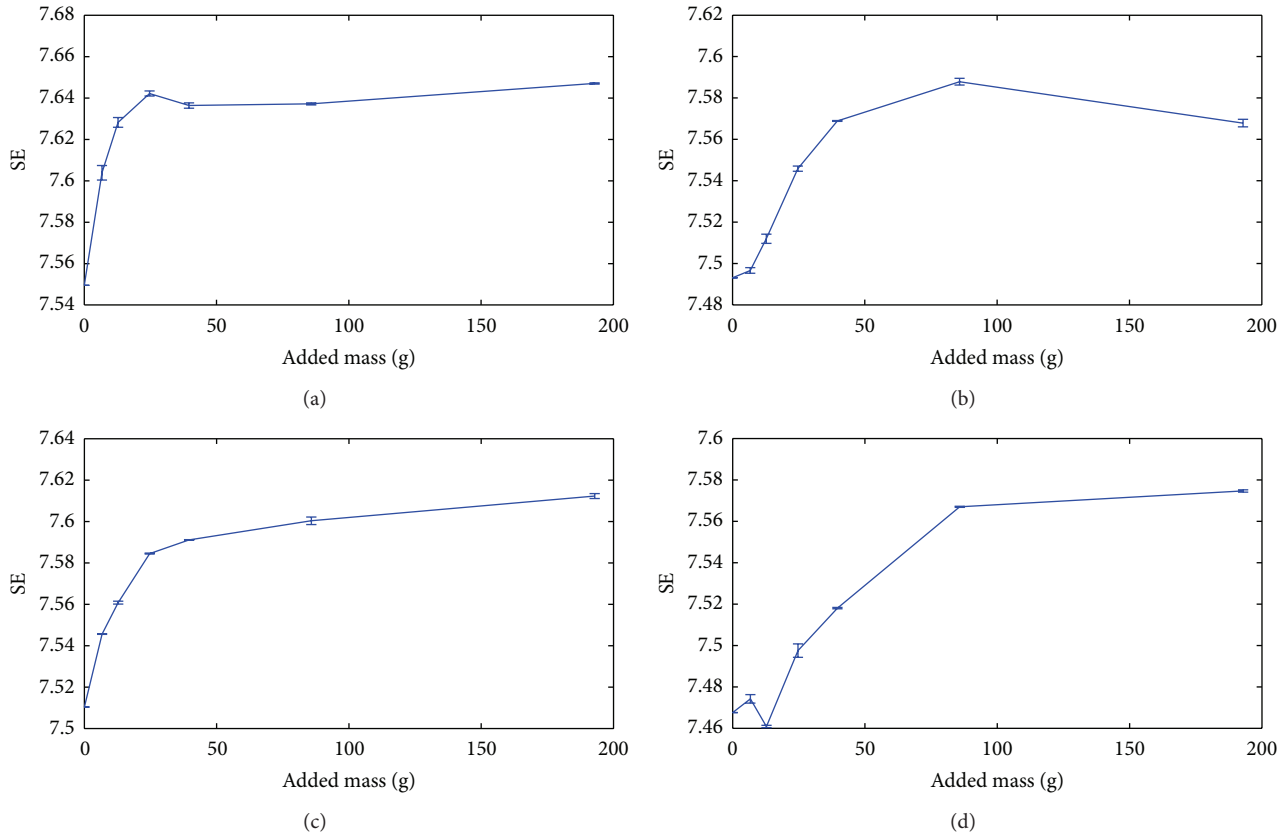

Figure 6: Variation of SE with the added mass in position 1 for: (a) Sensor S1; (b) Sensor S2; (c) Sensor S3; (d) Sensor S4.

Table 2: Properties and positions of piezoelectric sensors and actuators.

Use	Ceramics	Electrode	Thickness	Diameter	Positions	Notation
Actuator	PIC255	Ag	0.5 mm	20 mm	(42.5, 32.5) cm	A1
Sensor	PIC151	Ag	0.5 mm	10 mm	(24.5, 21.5) cm	S1
					(24.5, 43.5) cm	S2
					(60.5, 21.5) cm	S3
					(60.5, 43.5) cm	S4

Table 3: Added masses and comparison with the total mass of the plate.

Added masses (g)	Percentage of the mass of the plate
6.7	0.14
12.8	0.27
24.7	0.52
39.6	0.83
85.8	1.81
192.9	4.06

enhancing some frequencies and weakening others. So, the SE of the structure will change in the presence of damage.

Up to the authors' knowledge, the SE has not been used before to identify damage from vibrations in structures. Similar parameters with the same name have been used in other scientific fields, for example, in medicine [4, 5], ecology [6], genomics [7], and acoustics [8], but usually in each different application the SE is defined in a different way. In acoustic emission it has been used with the name of frequency entropy to analyze the obtained signals [9]. A parameter that is similar to SE is the wavelet entropy (WE), which is the Shannon entropy of the wavelet energy obtained from the continuous wavelet transform [10] or of the different frequency bands obtained with the discrete wavelet transform

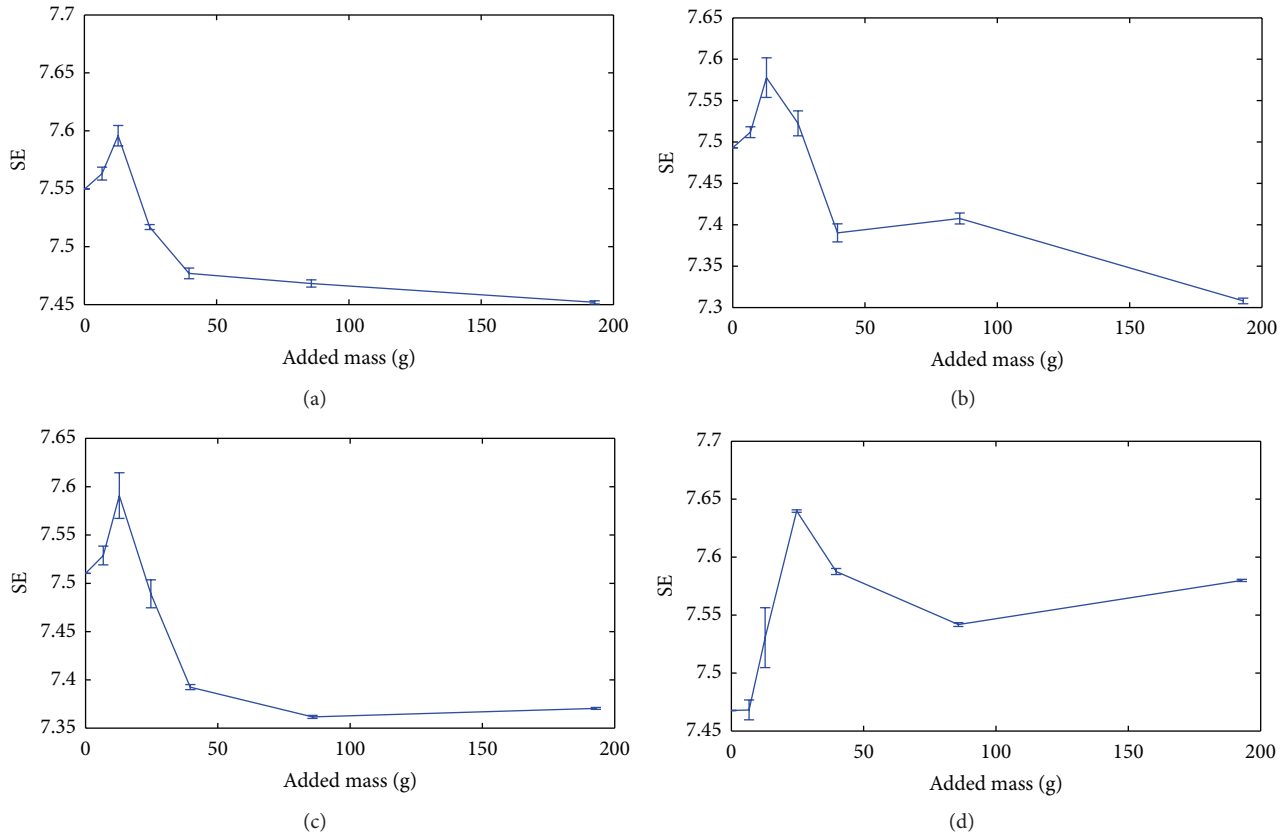

Figure 7: Variation of SE with the added mass in position 2 for (a) Sensor S1; (b) Sensor S2; (c) Sensor S3; (d) Sensor S4.

[11]. The WE have been used successfully to detect damage in structures [12].

4. Experimental Results

The experiment was repeated 15 times in the undamaged case and 5 times in each damaged plate to minimized ambient and random errors. The sample frequency was 4096 Hz and the frequency content of the excitation signal was up to 1500 Hz. The power spectral densities (PSD) of the excitation and the output were computed using Matlab and the Welch algorithm. The PSD of the output were divided by the PSD of the excitation to obtain the FRF. Some examples of FRFs of the plate with different added mass can be seen in Figure 4.

The change of these experimental FRFs with damage has been studied in previous works [2, 3]. This change was quantified using the following parameter:

$$D_1 = \sum_{f_i=f_{\min}}^{f_i=f_{\max}} \sqrt{\left|\mathrm{FRF}_{\mathrm{undamaged}}(f_i) - \mathrm{FRF}_{\mathrm{damaged}}(f_i)\right|}. \quad (3)$$

The difference between the FRF of the intact and damaged plate increases with damage, so D_1 can be used as damage index. In Figure 5 it is shown the variation of D_1 with the added mass for each damage location. It can be seen that the change in the FRF increases very fast with low damage, but for massed higher than 39.6 g, D_1 remains almost constant in all cases.

To study the performance of the SE as a damage index, it was computed for each experiment, and for each undamaged and damaged plate the mean and standard deviation were calculated. The variation of the SE with the added mass for each position of the damage is shown in Figures 6, 7, and 8, where error bars are added to show the standard deviation due to the different experiments.

As can be seen in Figures 6–8, there is a trend of the SE with the added masses. With damage in positions 1 and 3, the tendency is that the SE rises with mass, but not in monotonic form. On the other side, with damage in position 2, the tendency is that the SE decreases with mass, except in the case of sensor 4, which oscillates instead of having a trend. This means that damage in positions 1 and 3 produces more relevant frequencies in the FRF; that is, the energy distributes between more frequencies in the FRF. In the opposite side, with damage in position 2 there are less relevant frequencies. Using SE as a measure of the complexity, damage in positions 1 and 3 makes the vibration more complex, while damage in position 2 decrease its complexity.

This different behaviour of the SE with damage location can be explained by taking into account that the presence of a mass in a point of the plate makes its movement more

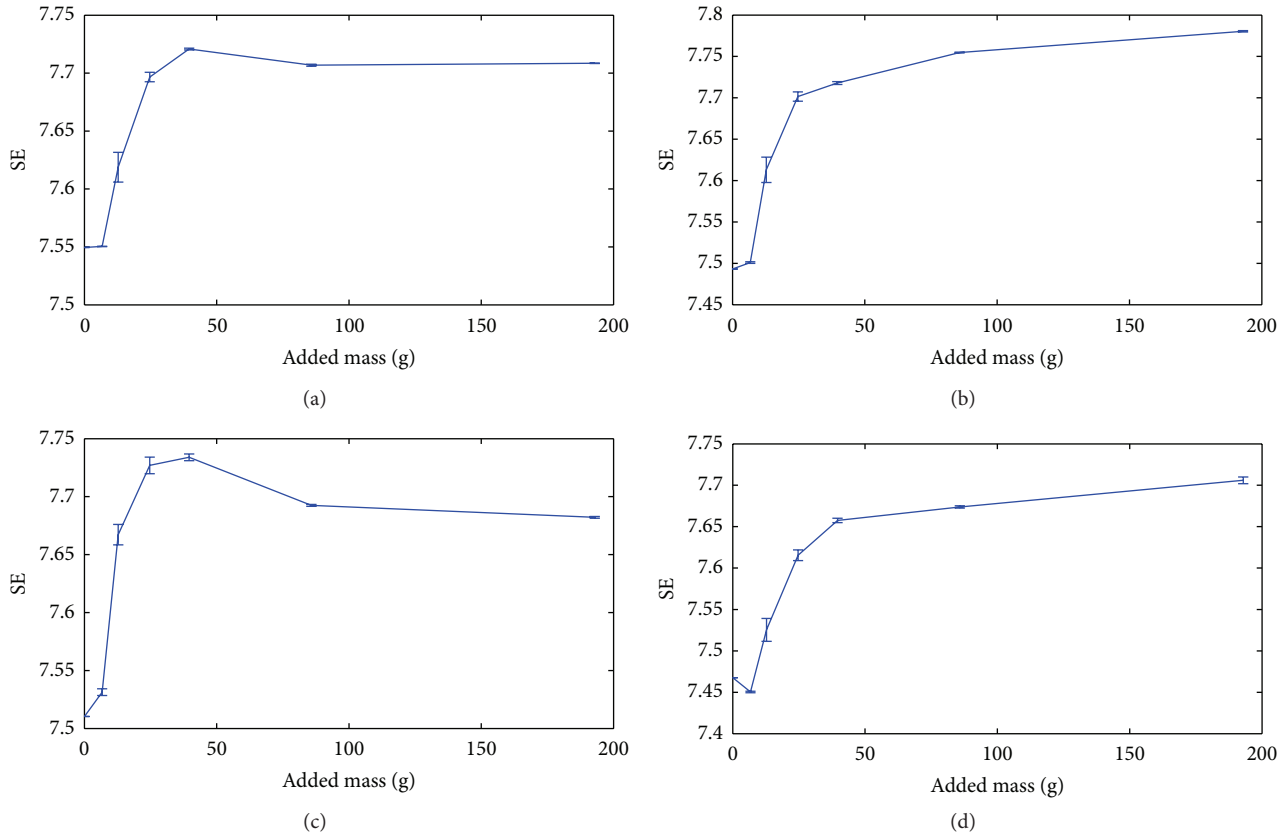

Figure 8: Variation of SE with the added mass in position 3 for (a) Sensor S1; (b) Sensor S2; (c) Sensor S3; (d) Sensor S4.

difficult. So the normal modes with an antinode which is near the damage location will be disturbed, and their influence in the vibration will decrease. In positions 1 and 3 the disturbed modes must be the principal ones, so the influence of less important modes is enhanced and the complexity of the vibration is higher. In the case of position 2, the disturbed modes have probably low relevance in the vibration and more energy goes to the principal ones, making the movement less complex. The damage index D_1 has the same behaviour in the three damage locations because it measures the difference between the FRFs of the undamaged and damaged plates, so this difference always increases with added mass.

For low added mass the SE changes very quickly, but for masses around 39.6 g and 85.8 g it becomes almost constant. It seems that when we have a high value of mass, a further increase does not change the amplitude distribution in the FRF and the SE remains constant. The same behaviour was found for damage index D_1, which is a direct measure of the change in the FRF. So it seems that the FRF changes very little when a certain value of damage is reached. The reason for this saturation of the damage indexes can be that, as have been said before, an increase of the mass in a point of the plate decreases its movement. For a low value of the mass, the point can still move. But for a high value, there is a strong limitation of the movement and it remains still. As it cannot move, a further increase of the mass will not have any effect on it.

It is possible that the results can be influenced by the fact that the masses were not fixed to the plate, but it seems that it is not the case. The possible jump of the mass on the plate could introduce a nonlinear effect that increases with weight. In the experimental results, for low masses the SE follows a trend and for high masses it has an approximately constant value. If the effect of the jumps had been important, the SE would have increased with high masses as the FRF would have been more complex.

5. Conclusions

The importance of composite structures in aerospace industry is increasing in the last years, making the development of damage identification methods adapted to this kind of materials necessary. A new damage detection technique has been experimentally tested on a CFRP plate. It is based on the use of the spectral entropy (SE) of the vibrations of the CRFP structure as damage index. This parameter measures the energy distribution between the resonant frequencies of the plate and is related with the complexity of the vibration. It has been proved that the SE changes with damage, and this change is higher than the variations in SE due to different measures of the FRF. Furthermore, the variation in the SE with damage follows a trend: the SE increases or decreases

(depending of the location) as damage increases. It means that the SE can be related with the quantity of damage in a given position and with more research, with its localization. In our experimental tests it was found that the variation of SE with damage is not always mononotic, which can make it difficult for it to be used in a real situation. It can be due to our experimental arrangement, or damage implementation, or to other reasons. To clarify this point and improve our understanding of the theoretical behaviour of the SE, a numerical investigation must be carried out.

The advantage of the SE over other damage indexes based on FRF is that a change in the ambient or external conditions of the structure (e.g., the temperature) can produce a change in the amplitude of the FRF or a translation of it, so many false positives can appear. The SE is insensitive to these changes, which makes it a very promising damage index for SHM, although more theoretical and experimental research is necessary.

Conflict of Interests

The authors declare that there is no conflict of interests regarding the publication of this paper.

References

[1] Y. J. Yan, L. Cheng, Z. Y. Wu, and L. H. Yam, "Development in vibration-based structural damage detection technique," *Mechanical Systems and Signal Processing*, vol. 21, no. 5, pp. 2198–2211, 2007.

[2] P. Moreno-García, *Simulations and experimental tests of vibrations on carbon fiber composite material plates and damage detection with frequency response function and the wavelet transform [Ph.D. thesis]*, University of Granada, 2012, (Spanish), http://hera.ugr.es/tesisugr/21009417.pdf .

[3] P. Moreno-García, E. Castro, L. Romo-Melo, A. Gallego, and A. Roldán, "Vibration tests in CFRP plates for damage detection via non-parametric signal analysis," *Shock and Vibration*, vol. 19, no. 5, pp. 857–865, 2012.

[4] M. Jiahai, W. Xueyan, X. Yonggang et al., "Spectral entropy monitoring reduces anesthetic dosage for patients undergoing off-pump coronary artery bypass graft surgery," *Journal of Cardiothoracic and Vascular Anesthesia*, vol. 26, no. 5, pp. 818–821, 2012.

[5] J. Morgaz, M. D. M. Granados, J. M. Domínguez et al., "Evaluation of spectral entropy to measure anaesthetic depth and antinociception in sevoflurane-anaesthetised Beagle dogs," *Veterinary Journal*, vol. 188, no. 3, pp. 352–355, 2011.

[6] N. Zaccarelli, B.-L. Li, I. Petrosillo, and G. Zurlini, "Order and disorder in ecological time-series: introducing normalized spectral entropy," *Ecological Indicators*, vol. 28, pp. 22–30, 2013.

[7] V. R. Chechetkin and V. V. Lobzin, "Spectral entropy criteria for structural segmentation in genomic DNA sequences," *Physics Letters A: General, Atomic and Solid State Physics*, vol. 328, no. 1, pp. 79–86, 2004.

[8] N. C. Han, S. V. Muniandy, and J. Dayou, "Acoustic classification of Australian anurans based on hybrid spectral-entropy approach," *Applied Acoustics*, vol. 72, no. 9, pp. 639–645, 2011.

[9] R. Unnthorsson, T. P. Runarsson, and M. T. Jonsson, "AE entropy for the condition monitoring of CFRP subjected to cyclic fatigue," *Journal of Acoustic Emission*, no. 26, pp. 229–239, 2008.

[10] R. Piotrkowski, E. Castro, and A. Gallego, "Wavelet power, entropy and bispectrum applied to AE signals for damage identification and evaluation of corroded galvanized steel," *Mechanical Systems and Signal Processing*, vol. 23, no. 2, pp. 432–445, 2009.

[11] D. M. Tavares and L. S. Lucena, "Entropy analysis of stochastic processes at finite resolution," *Physica A: Statistical Mechanics and Its Applications*, vol. 357, no. 1, pp. 71–78, 2005.

[12] W.-X. Ren and Z.-S. Sun, "Structural damage identification by using wavelet entropy," *Engineering Structures*, vol. 30, no. 10, pp. 2840–2849, 2008.